Nanomechanical Characterisation of Diamond-Like Carbon Coatings for Tribological Performance

Samuel James McMaster

School of Mechanical Engineering

University of Leeds

Submitted in accordance with the requirements for the degree of
Doctor of Philosophy

May 2021

The candidate confirms that the work submitted is his own, except where work which has formed part of jointly-authored publications has been included. The contribution of the candidate and the other authors to this work has been explicitly indicated below. The candidate confirms that appropriate credit has been given within the thesis where reference has been made to the work of others.

Cross-section scanning electron microscopy and preparation of samples for transmission electron microscopy was undertaken by Stuart Micklethwaite. Transmission electron microscope operation was carried out by Dr Zabeada Aslam. Assistance with MATLAB analysis scripts for the fretting data was provided by Adam Wade and Joshua Armitage. Additional scratch and calotest data was acquired by Joshua Benson and Killian Prall. Additional fretting data was acquired by Ishmaeel Ghouri, Mihhail Stotsjuk and Lei Cao.

Papers Contributing To This Thesis

In the following papers, Samuel J. McMaster is the primary author and is responsible for the collection and processing of the experimental data:

- S.J. McMaster, T.W. Liskiewicz, B.D. Beake, A. Neville, *Probing Fatigue Resistance in Multi-layer DLC Coatings by Micro-impact: Correlation to Erosion Tests*, Surf. Coatings Technol. (2020) 126319. doi:10.1016/j.surfcoat.2020.126319.

  This article is derived from Chapter 6: Nano-Scale Fatigue Determination by Comparison of Erosion and Impact Testing.

- S.J. McMaster, Tomasz W. Liskiewicz, Anne Neville, Ben D. Beake, *Investigating the Interfacial and Ploughing contributions to Friction of DLC coatings using Nano-scratch with varying Probe Radius*, In Preparation.

  This article is derived from Chapter 7: Nano-Scratch for the Determination of Interfacial Friction.

- S.J. McMaster, Shahriar Kosarieh, Tomasz W. Liskiewicz, Anne Neville, Ben D. Beake, *Multi-scale Fretting Analysis of the Friction of DLC coatings in Dry and Lubricated conditions*, In Preparation.

  This article is derived from Chapter 8: Multi-scale Fretting Testing of DLC Coatings.

In these papers, Ben D. Beake is the primary author and is responsible for the writing the article. Samuel J. McMaster was responsible for collecting parts of the experimental data and the articles were written in correlation with this project and thesis. All authors have contributed to proof reading the articles:

- B.D. Beake, S.J. McMaster, T.W. Liskiewicz, A. Neville, *Influence of Si- and W-doping on micro-scale reciprocating wear and impact performance of DLC coatings on hardened steel*, Tribol. Int. (2021) 107063. doi:10.1016/j.triboint.2021.107063.

  This article contributes to Chapter 6: Nano-Scale Fatigue Determination by Comparison of Erosion and Impact Testing and Chapter 9: Frictional Performance of DLC Coatings under Nano-Scale Reciprocating Sliding.

- B.D. Beake, A.J. Harris, T.W. Liskiewicz, J. Wagner, S.J. McMaster, S.R. Goodes, A. Neville, L. Zhang, *Friction and electrical contact resistance in reciprocating nano-scale wear testing of metallic materials*, Wear. (2021) 203866. doi:10.1016/j.wear.2021.203866.

  This article contributes to Chapter 9: Frictional Performance of DLC Coatings under Nano-Scale Reciprocating Sliding.

For my Grandfather.

Acknowledgements

Abstract

Diamond-like carbon (DLC) coatings are becoming increasingly popular in the automotive industry due to their high hardness, resistance to wear and low friction coefficient. Additionally, they have seen more recent use in the oil and gas industry as protective coatings for flow control devices such as gate and ball valves. They can suffer from poor adhesion at high loads and impact stresses. Well characterised coatings will enable the relationship between mechanical properties and tribological behaviour under different wear regimes to be studied.

To this end, three DLC variants have been produced; amorphous hydrogenated carbon, silicon-doped amorphous hydrogenated carbon and tungsten-doped amorphous hydrogenated carbon (a-C:H, Si:a-C:H and a-C:H:W) on two different substrates (316L stainless steel and hardened M2 tool steel) using the Hauzer Flexicoat 850 system located at the University of Leeds. Total thickness of the coating was varied from 1–5 μm. For the a-C:H coating, the substrate roughness was varied between 0.01 and 0.08 μm R_a. A Cr + WC/W-C:H interlayer is present in all coatings to aid adhesion to the substrate.

Mechanical characterisation has been performed using nanoindentation on the Micro Materials Nanotest Platform using a partial loading technique. Structural characterisation of the DLC was performed using Raman spectroscopy to measure graphitisation and disorder and electron energy loss spectroscopy (EELS) to determine sp^2/sp^3 ratio respectively. Throughout the testing, scanning electron microscopy (SEM) has been used to observe the deformation and failure mechanisms of the coatings.

Following this nano-scale fatigue resistance of the coatings was measured by comparing nano and micro-scale impact testing with solid particle erosion. Erosion testing was performed with a bespoke air powered flow system. Depth reached and relative depth increase with load during impact testing was compared with the amount of substrate visible (measured using optical pixel threshold method) after time-steps of erosion testing. For this application it was found that a lower H/E ratio and less severe cracking is beneficial as seen with a-C:H:W. Cross-section focused ion beam scanning electron microscopy was used to observe the coating-interlayer cracking phenomena.

Nano-scratch testing was performed to investigate the interfacial contribution to friction of various probe radii (4.5 μm, 8 μm, 72 μm and 170 μm) compared with one DLC coating, a-C:H on 316L stainless steel. All the DLC coatings were subsequently tested using the 4.5 μm probe to observe critical load failures of each coating architecture. Sub-critical load scratch tests were also performed to investigate the number of passes to failure.

Fretting tests have been performed on two length scales. Larger length-scale utilised a 5 mm radius 52100 steel ball and a displacement amplitude of ±50 μm with 20 N and 40 N loads. Both dry and lubricated conditions were employed to assess the coating's performance in the gross slip regime. Nano-wear fretting testing with a displacement amplitude of ±1 μm was performed to match the contact pressures of the larger scale fretting using the Nano-Fretting module of the Nanotest Platform.

Finally, DLC coatings previously studied, sharing similar architecture to the main DLCs produced for this study, have been tested using the NanoTriboTest module recently developed by Micro Materials Ltd. This module has allowed frictional tests to be performed on the nano-scale in the reciprocating sliding regime to compare with the fretting results. A 25 μm radius sphero-conical diamond probe was used giving larger contact pressures than typical tribological contacts (> 10 GPa) to model accelerated wear.

List of Abbreviations

AFM atomic force microscopy

BO base oil

BWF Breit-Wigner-Fano

COF coefficient of friction

CVD chemical vapour deposition

DC direct current

DLC diamond-like carbon

DLCH diamond like a-C:H

EBSD electron back scatter diffraction

ECR electrical contact resistance

EDX energy dispersive x-ray spectroscopy

EELS electron energy loss spectroscopy

FEM finite element modelling

FFO fully formulated oil

FIB focussed ion beam

GLC graphitic-like carbon

GLCH graphite-like a-C:H

GNP gross national product

HiPIMS high power impulse magnetron sputtering

HMDSO hexamethyldisiloxane

HOPG highly orientated polycrystalline graphite

HTS M2 tool steel

IOT internet of things

ISE indentation size effect

LED light emitting diode

LEMAS Leeds Electron Microscopy And Spectroscopy centre

MEMS micro-electromechanical devices

MoDTC molybdenum dialkyldithiocarbamate

PACVD plasma assisted chemical vapour depositionn

PECVD plasma enhanced chemical vapour deposition

PLCH polymer like a-C:H

POD pin-on-disk

PVD physical vapour deposition

RF radio fequency

RMS root mean square

SCPR scratch crack propagation resistance

SEAC surface engineering and advanced coatings

SEM scanning electron microscopy

SIJ submerged impingement jet

SME small-to-medium enterprise

SS 316L stainless steel

TECD triboelectric charge density

TEM transmission electron microscopy

TEM-SAD transmission electron microscopy selected area diffraction

TENG triboelectric nanogenerator

TTS tribologically transformed structure

XPS x-ray photoelectron spectroscopy

XRD x-ray diffraction

ZDDP zinc dialkyldithiophosphate

Contents

List of Figures

List of Tables

Chapter 1

Introduction, Project Background and Research Objectives

"The worthwhile problems are the ones you can really solve or help solve, the ones you can really contribute something to.... No problem is too small or too trivial if we can really do something about it."

Richard Feynman [1]

1.1 General background and Motivation for research: Climate Change

In science, problems are often pursued for their interest alone with thought to application given much later in the development and pursuit of the research. However, in engineering, more thought must be given to the practicalities of the problem and the implementation of the solution. The main driving force of much engineering research is the creation or optimisation of systems for increased efficiency or allowing components to survive in extreme environments not possible previously. To achieve this, the scale on which challenges are pursued in engineering varies widely. In more recent years, the prevalence has been toward the micro/nano-scale to understand the underlying mechanisms of phenomena. This will allow larger scale effects to be understood and optimised.

The motivation of much work in engineering is to reduce the effects of climate change as it is seen as predominant challenge affecting mankind in the present day. Though sometimes referred to as global warming, the effect is that which humans have on the climate due to the burning of fossil fuels (such as coal, oil and gas) and large scale deforestation [2]. The increase in atmospheric trace gases resulting from this activity such as carbon dioxide (CO_2), methane, nitrous oxides and chlorofluorocarbons (CFCs or "Freons") are primarily the cause of the temperature increase. They are referred to as "greenhouse gases" as they allow incoming solar radiation while restricting outgoing thermal radiation to space, in effect increasing the surface temperature of the planet. This is similar to a greenhouse's glass wherein it has the property of absorbing infrared radiation while being

transparent to visible light [2, 3].

This effect was first recognised by French scientist Jean-Baptiste Fourier in 1827. John Tyndall, a British scientist, measured the absorption of infra-red radiation by CO_2 and water vapour around 1860 and suggested ice ages may result from a decreased greenhouse effect. A Swedish chemist, Svante Arhenius calculated the effect of increasing the concentrations of greenhouse gases in 1896, estimating that doubling the concentration would increase global average temperature by 5–6 °C [2].

A simple model of how greenhouse gases function is to consider a surface modelled as a black body (an ideal emitter of radiation at every frequency that emits isotropically). The radiative power of the object is defined by the Stefan-Boltzmann law [2, 4]:

$$P_r = \varepsilon \sigma A T^4 \tag{1.1}$$

where P_r is the power radiated, A is the area of the object, σ is the Stefan-Boltzmann constant [1] and ε is the emissivity of the object. We can consider a surface of temperature T_s receiving radiation in the visible spectra equal to σT_0^4. In the absence of any blanketing $T_s = T_0$. If an absorbing layer is introduced at temperature T_a that is visible radiation transparent but absorbs infra-red at a fraction k of the radiation of the surface beneath. The layer will emit radiation equal to $k\sigma T_a^4$ upwards and downwards equally. Therefore its temperature would be $T_a^4 = 0.5kT_s^4$. Surface temperature can therefore be expressed as:

$$T_s^4 = (1 - 0.5k) T_0^4. \tag{1.2}$$

For $k = 0.5$, $T_s^4 = 1.\dot{3}T_0^4$. A layer that absorbs half the thermal radiation received will increase the absolute temperature of the surface beneath by $\approx 7.5\%$. If we take a quanta of radiative power equal to 25 °C, this equates to a surface temperature of ≈ 26.9 °C, a temperature increase of 1.9 °C.

If the absorbing layer in introduced near instantaneously, before any warming can occur, an immediate reduction in outgoing radiation is seen in the upper atmosphere equal to $0.5k\sigma T_0^4$. This quantity is known as radiative forcing and the larger it is, the more severe any warming effect will be. Under circumstances where the planet isn't experiencing an increased warming phenomenon, a fine balance exists in the absorbance, reflectance and emission of radiation that maintains the surface temperature of Earth in a reasonable range to support life [2].

The Intergovernmental Panel on Climate Change's report entitled Climate Change 2007: The Physical Science Basis [5] identified CO_2 as the most severe in radiative forcing of the long lived greenhouse gases. Methane, nitrous oxides and halocarbons are seen as the next most severe followed by ozone (both stratospheric and tropospheric). The global increase in CO_2 is primarily due to fossil fuel use whereas methane and nitrous oxide are primarily due to agriculture.

Greenhouse effects are also seen on our nearest planetary neighbours: Mars and Venus. Venus, though about the same size as Earth, has approximately 100 times the atmospheric pressure. Therefore it generates a large greenhouse effect giving it a surface temperature of about 500 °C. This is a good example of a runaway greenhouse effect where, being closer to the sun, water vapour would have been a large constituent of the atmosphere and a large positive feedback loop occurred where water boiled away from the surface increasing the water vapour in the atmosphere. Thankfully, this cannot occur on Earth [2].

Figure 1.1 shows the global temperature measured from 1850–2019 relative to the

---

[1] $\sigma = 5.6703 \times 10^{-8} \, \text{W/m}^2\text{K}^4$

average temperatures from 1961–1990. Though there is some variance on temperature year on year. From 1980 onward, it can be clearly seen that average global temperature anomaly has trended upwards reaching approximately 0.7 °C higher in 2019 as compared to the 1961–1990 baseline. This is referred to as a temperature anomaly due to its unexpected deviation from the normal heating and cooling trends of the planet. If this trend is extended back to 1850, the average temperature rise is 1.1 °C [6].
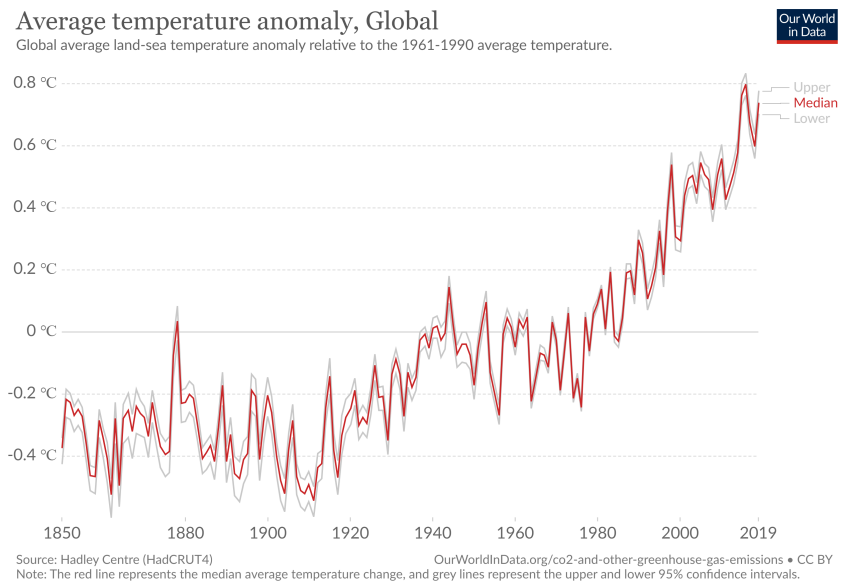
Figure 1.1: Global temperature anomaly from 1850–2019. Upper and lower confidence intervals are shown in light grey with the median line shown in red. From [6, 7].

This rise in global temperature is attributed to the increase of greenhouse gas emission, particularly CO_2 as this link has been seen throughout history [6]. Figure 1.2 shows the variation of atmospheric CO_2 concentration (in parts per million) as measured over the last 800,000 years. The periodic fluctuations in CO_2 concentration coincide with ice ages (low concentration) and interglacials (high concentration) and are caused by changed in the Earth's orbit around the sun; this is known as Milankovitch cycles. We can see that over this period, the concentration did not rise above 300 ppm but in the most recent reading, it has now exceeded 400 ppm [3, 6].
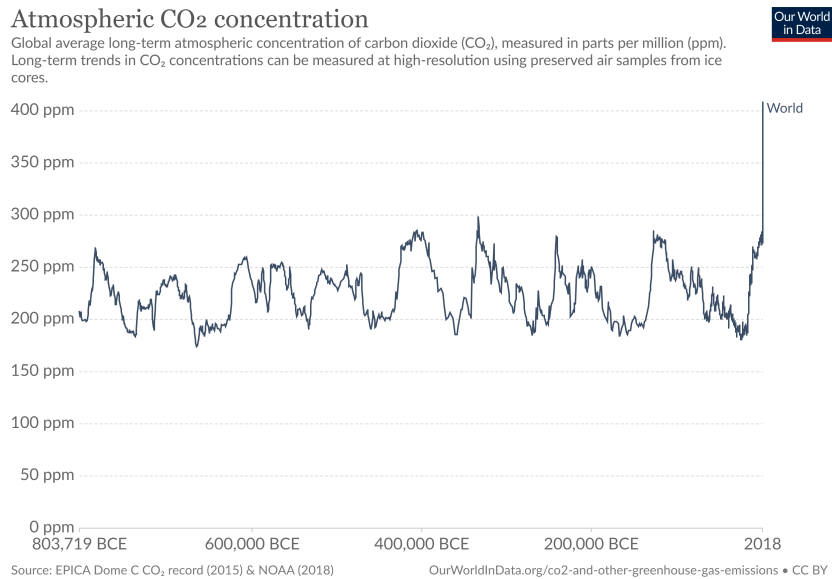
Figure 1.2: Global average long term atmospheric CO_2 concentration up to 2018. From [6, 8].

This increase in CO_2 concentration can almost entirely be attributed to human activity. Figure 1.3 shows the total annual CO_2 emissions by world region. Global emissions were 2 billion tonnes in 1900 which has increased to 36 billion tonnes in 2017 [6]. Data from 2014–2017 suggested that global emissions had stabilised however the Global Carbon Project has reported increases of 2.7 % and 0.6 % in 2018 and 2019, respectively [9].
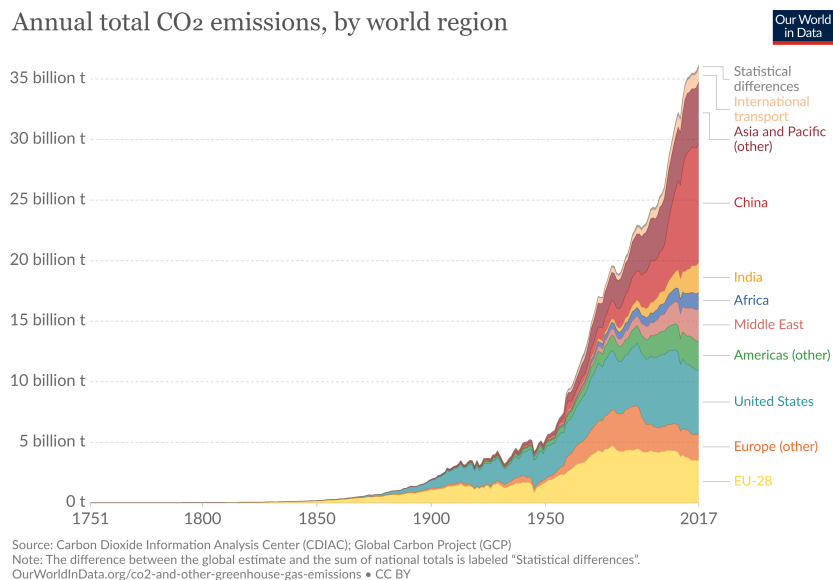
Figure 1.3: Annual CO_2 emissions in tonnes by world region. From [6, 10]

In 2015, 196 countries of the United Nations came together under the Paris Agreement to change their national development strategies to pursue sustainable development to thereby limit global warming to 1.5–2 °C above pre-industrial levels. To help achieve this goal, appropriate financial flows, a new technology framework and an enhanced capacity building framework will be put in place to aid developing countries. All parties are required to put their best efforts through nationally determined contributions. The agree-

ment came into force on the 4th November 2016, 30 days after which at least 55 Parties to the Convention accounting for approximately 55 % of the total global greenhouse has emissions deposited their instruments of ratification, acceptance, approval accession [11].

Current predictions show that the world is not on track to meet its agreed target of limiting warming to 2 °C with current trends and policy implementations showing that the expected warming will be in the range of 3.1–3.7 °C [6]. A Nature Climate Change article by Peters et al. [12] in 2020 showed that despite significant progress in low carbon technologies and reduced energy usage in some countries, fossil fuel use is continuing to grow suggesting that the full selection of policy options isn't being effectively deployed. The European Environment Agency report in 2019 [13] showed that most EU member states are not on track towards their climate and energy targets in 2020 with only 11 countries meeting all goals and only 3 countries on track currently to meet their 2030 goals. The COVID-19 pandemic has resulted in significant change in the energy demand around the world due to the closing of international borders and the lockdown restrictions to travel within countries. By early April of 2020, the daily CO_2 emissions decreased by 17 % compared to average levels in 2019. Overall emissions in 2020 are predicted to have decreased in the region of 4–7 % depending on how long restrictions remain in place worldwide [14].

A report by the RAC Foundation [15] showed that from 1971–2007 the number of cars in the UK grew by 3 % per annum to over 31 million in 2007. Over 77 % of households had access to a car with a significant increase in multi-car households with approximately 20 % having two cars and 5 % having 3 or more cars. A paper by by Ahn et al. [16] in 2008, predicted that gasoline fuelled cars would continue to be the first choice for most consumers but alternative fuel [1] vehicles will compete and their further presence in the market would lower petrol and diesel consumption. The Department for Transport noted that 599,000 vehicles were registered for the first time in Great Britain during the first quarter of 2020 which is a 30.1 % reduction on the first quarter of 2019. Diesel car registrations decreased by 45 % and petrol cars decreased by 34 %. These statistics can largely be attributed to the COVID-19 pandemic. Despite this, 33,696 ultra low emission vehicles [2] were registered for the first time (a 113 % increase on 2019) and these made up 5.6 % of all new registrations contributing to the increase of alternative fuel cars registered (65 %) [17].

Ruiz et al. [18] performed a study on climate change perceptions as it has been identified that one of the main issues with the implementation with climate change polices is the community perception as well as the poor understanding of the impact caused by these policies. Perceptions in the USA and in international cases were studied with numerous factors considered. In the international case, the largest positive influences are socio-altruistic values, observation of changed weather, support of liberal values and self perceived knowledge of climate change. In the USA, the influence of corporations is seen to be a much larger negative influence as compared to international perceptions. Education and awareness of scientific work is seen to be a far larger positive influence internationally as compared to the USA. Additionally, far smaller weighting is seen to be given to personal experience and perception in the USA compared to internationally.

---

[1] Vehicles powered by sources other than petrol or diesel.

[2] Vehicles that emit less than 75 g of CO_2 for every kilometre travelled.

1.2 Significance of Tribology and Surface Engineering

Tribology, as the study of interacting surfaces in relative motion [19], is a vitally important field to many branches of industry. Though the formalisation of tribology as a dedicated field of study is relatively new, having been introduced as a term in 1966 with the Jost report [20]. There is evidence of some knowledge of tribology being applied by the ancient Egyptians [21]. Jost and co-workers predicted that approximately £515 million (1.36 % of gross national product (GNP)) could be saved with the implementation of new tribology in machines and equipment across the country; this would equate to £9,000 million in 2017 as seen in Figure 1.4. In 2016, 50 years after the Jost report Holmberg et al. [22] reviewed the potential savings in the present day economy and concluded that approximately £12,600 million could be saved (1.39 % of GNP of the UK). In 1966, 95 % of the savings were related to wear, component breakdown and failure, maintenance and lifetime costs. Machines and equipment are much more reliable today with much less breakdown and failure with lower maintenance costs. The 5 % savings of friction reduction grew to 74 % in 2017 with a huge decrease in lifetime savings. Wear out of older products is no longer the main reason for the acquisition of new products; the adoption of new functions and designs plays a much larger role in purchasing now.
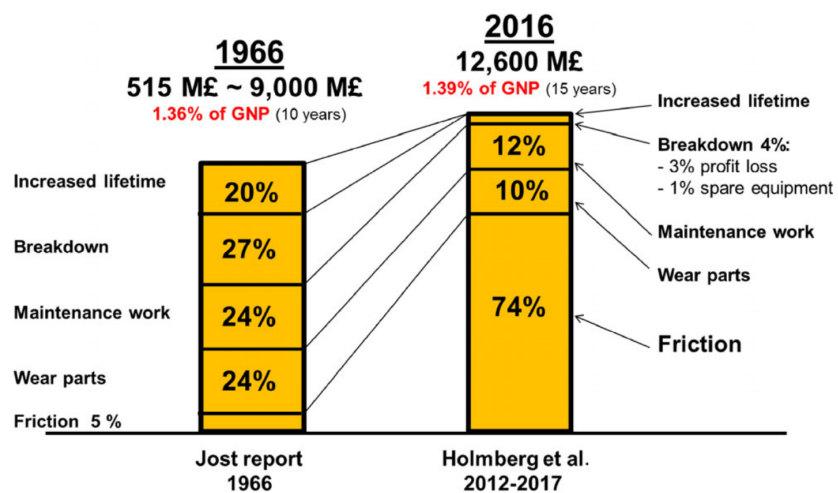
Figure 1.4: Potential savings by the implementation of new tribology in machines and equipment in 1966 vs 2016. From [22].

In a global context, Holmberg et al. [22] estimated that $\sim 23\,\%$ (119 EJ) of the world's total energy consumption originates from tribological contact. An area that quickly demonstrates the possible tribological energy savings (and therefore monetary savings) is the optimisations of passenger cars with 25 % of the potential short term savings [22]. Figure 1.5 shows the breakdown of energy consumption in a typical passenger car. Frictional losses are seen to account for 33 % of the energy converted from fuel which can be further broken down into engine losses (11.5 %), transmission (5 %), rolling resistance (11.5 %) and brakes (5 %). Though each of these areas represent relatively small amounts of energy for the vehicle, the reduction of even fraction of a percentage of any of these areas increases the the amount of energy available to move the car and reduces the "useless" energy losses. When this is stratified across the huge number of cars on the road, the cost savings both in monetary value and reduction of harmful effects on the environment speaks for itself. In comparison, global aviation (domestic and international passenger

7

and air freight) accounts for 1.9 % of greenhouse gas emissions and 2.5 % of CO_2 which is relatively small in comparison to automotive emissions worldwide. Air travel is noted as being particularly difficult to decarbonise and reduce energy losses from [23].
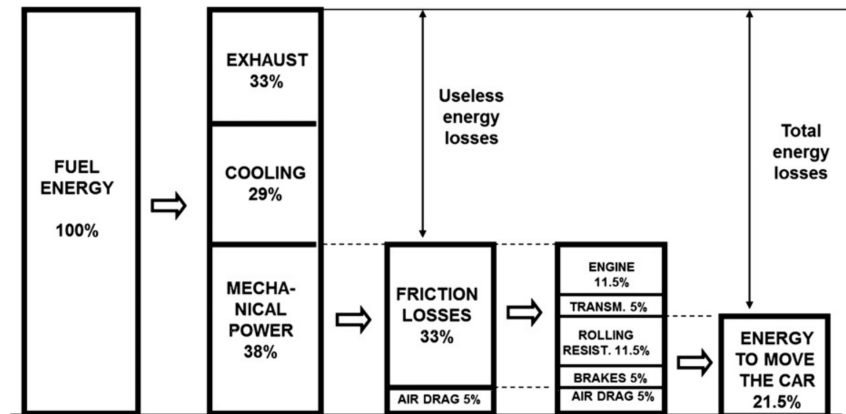
Figure 1.5: Breakdown of passenger car energy consumption. From [24].

Surface Engineering is the design of surface/substrate composite systems to achieve performance unable to be achieved by either the surface composition or substrate alone; by engineering the surface, the appearance can be improved, protection from environmental damage can be given and mechanical and physical performance of the surface can be enhanced [25]. In 2004, Artley and Matthews estimated that the value of products that incorporated surface engineering was $50 trillion per year worldwide [26]. Estimates put the UK industry's current turnover at £11.2 billion and directly affecting over £140 billion in associated goods with a compound annual growth of over 11 %. By 2025, it is estimated that the turnover will exceed £25 billion and to affect over £313 billion of associated goods. Over 46,000 people are employed in the sector in more than 2000 companies, 86 % of which are small-to-medium enterprises (SMEs) and supporting a further 150,000 jobs in the UK supply chain [27, 28].

A 2014 report by the Surface engineering and advanced coatings (SEAC) Special Interest Group reviewed the UK's surface engineering industry to evaluate how it can meet increasing demands in the coming years. Surface engineering is seen to add value to products in such varied industries as aerospace, consumer electronics, healthcare, food and drink. It was noted that some perceive SEAC technologies to be an add-on or afterthought to enhance product performance but this undervalues the potential added value of properly integrating these technologies. Furthermore, a vulnerability was identified to meet the digital gap to increase efficiency in the technology which could result in a 10–30 % loss. The report concluded with the recommendation that the UK SEAC sector must radically change to remain competitive in the global market by adapting a "design for manufacture" model and including more participants in the early prototyping and manufacturing stages [28].

The German Society for Tribology produced a report in 2019 [29] summarising the importance of tribology and the use of surface engineering in reducing economic losses and optimising technology to reduce emissions and energy losses. Lower CO_2 emissions realised by friction reduction was noted as being a key factor. The German government predicts that in total 22 million tons (6.4 % of the CO_2 reduction projected for 2030) could be saved by friction reduction alone without affecting utility value [29]. The economic importance of tribological savings was identified with 1 % of the GNP as potential savings by the German Ministry for Education and Research in 1976 [30]. This equates to

€32.7 billion in 2017. Frictional losses in the automotive powertrain are highlighted in the report, with the piston module highlighted as producing approximately 50 % of the friction of a combustion engine. Both low viscosity oils and high viscosity index oils (to maintain viscosity stability at high temperature) were identified as important development pathways to reduce friction and wear. The application of thin films such as Triondur© CN and Triodur© DLC are seen to reduce friction up to 75 % with a further 20 % achievable with low viscosity oils. Additional important areas identified in the report are hybrid drivetrains [31], alternative fuels (such as hydrogen or methane) [32] and synthetic or bio-lubricants [33].

1.3 Rationale for research: on the significance Of DLC as a coating

DLCs are an important class of coating material for many industries with varied uses beyond its tribological ones. In referring to it as a class of coating material, we are talking about the many coating structures available by tuning the structure of amorphous carbon with deposition conditions. This will be explored further in Chapter 2. At present, this section will provide a brief overview of the coatings importance in its many varied applications. Figure 1.6 shows the annual publications on DLC from 1970-2012. We can note a massive increase in the interest in this coating in the 1990s with annual publications exceeding 500 in the years 2004–2009 [34]. This in itself is a major signifier of the importance of DLC coatings. The great strength of DLC coatings is their ability for properties to be tailored based upon their deposition mechanism and deposition conditions to suit varied applications [35]. The proportion of graphitic bonded carbon, diamond bonded carbon and hydrogen thereby varies in the coating structures. The most exploited properties are high wear resistance and low friction coefficient, chemical inertness, infrared transparency high electrical resistivity and low dielectric constant. DLCs have been seen in numerous applications such as wear and corrosion protection for magnetic storage media (where nano-smooth and thin coatings are required) and protection for biological implants such as artificial heart valves (also due to their biocompatibility) [35]. Properties can be further modified by doping with various light and heavy element to give such properties as fluorine for altered surface energy, silicon for thermal stability and titanium for enhanced adhesion [36].
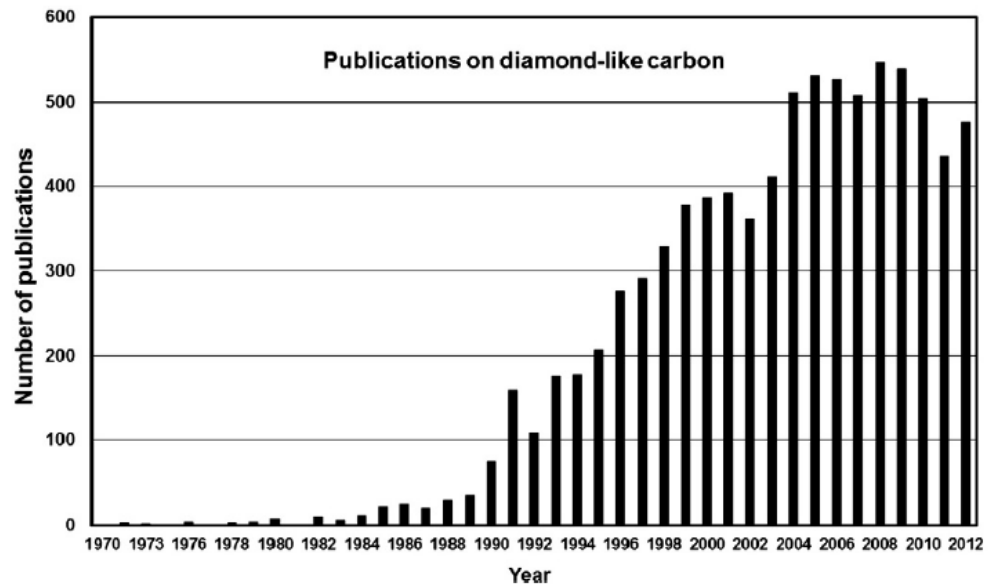
Figure 1.6: Publications on Diamond-like carbon from 1970-2012. From [34].

1.4 Nano-Tribology as a method to assess fundamental mechanisms

The length scale of work in tribology is important as it is fundamentally linked to the phenomena that can be investigated at each scale. In macroscale tribology, the real area of contact is obscured and instead we must work with an estimation of this area. As we move to the micro and further to the nano-scale, the real area of contact and apparent area of contact converge. Once the nano-scale is truly reached, single asperity interactions are possible with the scale of the interaction approaching that of the natural length scale of features on the surface [37].

This allows for the fundamental elements of tribological contact to be determined such as the tribo-chemical adhesion between two surfaces without the tribo-mechanical ploughing component of friction and wear that can be dominant on the macroscale. The great difficulty lies in uniting the behaviour seen across length scales due to different scales being dominated by different mechanisms. However the aim is that, eventually, this fundamental understanding will allow for a prediction of macroscale behaviour. In addition to a desire to understand fundamental mechanisms for tribological interactions, increasing understanding at the small scale allows for new applications such as micro-electromechanical devices (MEMS) to be exploited [37]. Figure 1.7 shows the scales of study in tribology and the phenomena that can be studied using each methodological approach.
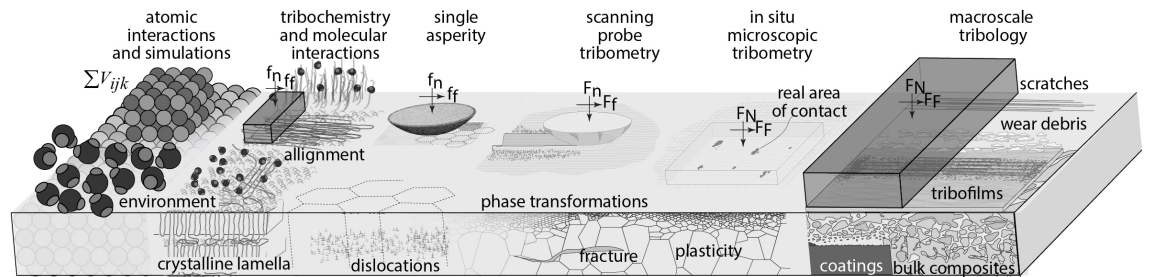
Figure 1.7: Scales of study in tribology and associated phenomena. From [38].

1.5 Aims and Objectives

This section details the aims and objectives as they were established for the completed project. The initial project plan consisted of six distinct work packages, these being:

- DLC Coating Production and Characterisation

- Nano-scratch for the Determination of Interfacial Friction

- Development of an Electrochemical Cell for Nano-scale Tribocorrosion Studies

- Nano-scale Fatigue and Fretting Testing

- Nano-scale pin-on-disk (POD) testing

- Macro-scale POD testing

As the project progressed some changes were made to the original plan which are talked about further in Section 10.1. In brief, however, POD testing was not performed, in its place multi-scale fretting testing and nano-scale reciprocating testing was performed. The development of the electrochemical cell was dropped from the project aims due to the time requirements to fully investigate the other work packages. This change in work packages was linked with product development at Micro Materials Ltd. with a high emphasis being placed on impact testing and the development of the new NanoTriboTest module allowing the nano-scale reciprocating wear testing.

1.5.1 Aims

The primary motivation of this research as described in detail in Section 1.1 is to reduce the effects of climate change however the use of coatings to combat such a large and pervasive problem seems like it would have little effect. The adoption of well optimised coatings across industry and particularly the automotive sector (where DLC has numerous applications) can have an additive beneficial effect whereby small energy savings can cumulatively reduce emissions.

Many studies focus on a few primary analytical methods to study coatings however each of these methods only captures a partial picture of the full coating performance. Practically, for many studies, it is simply not feasible to include the full roster of possible test methodologies, but the length of this project has allowed for use of multiple test

methods to produce a fuller picture of the performance of the coatings. Testing across length scales also presents difficulties as the mechanisms between the macro and nano-scale are fundamentally different; this is an ongoing research area and it will be explored throughout this thesis.

Therefore, the further study of the fundamental mechanical, structural and tribological properties of a series of DLC coating designs can expand upon the base of knowledge in literature. The coatings in this study were produced using the Hauzer Flexicoat 850 system at the University of Leeds. 3 primary DLC variants were produced with varying thickness and substrate roughness (changing the top layer coating roughness) on two substrates giving a wide range of properties to affect the coating's tribological performance.

The Micro Materials NanoTest platform is a modular system allowing a variety of tribological modes of testing to be carried out. Nanoindentation, as the core function of the system, was used to determine the whole coating structure mechanical properties in a partial load-unload method. This was used to show its benefits over standard indentation methods. Fretting, impact and scratch techniques were performed on two length scales to show the capabilities of the measurement platform and the results on each scale. Finally, a new module, the reciprocating sliding head designated the NanoTriboTest was tested to evaluate its efficacy.

As DLC coatings are amorphous, elemental proportions, carbon bonding and level of amorphization within the coating are commonly used to characterise their structure. This data, when combined with the mechanical properties, gives context to the coating's mechanical and tribological performance.

Each of these techniques will give some information on the performance of the coatings, depending on the number of dimensions of testing and load applied. By analysing the results with respect to the information provided by each technique and the length-scale being investigated, a more complete picture of the coating can be built. This will be used to show that a combination of characterisation methodologies is best for defining coating performance. The collected methodologies can also be applied to other architectures beyond DLC.

1.5.2 Objectives

The objectives of this project are:

- To perform partial load/unload indentation tests and scratch test experiments to determine the mechanical properties and adhesion of the coating structures.

- To use cross section SEM, energy dispersive x-ray spectroscopy (EDX), Raman spectroscopy, transmission electron microscopy (TEM) and EELS to determine the structure of the coatings.

- To use calotesting and correlate cross section SEM to determine the deposited coating thickness.

- To determine the difference in tribological performance of each of the coating variants depending on the top layer DLC, substrate, substrate roughness and coating thickness.

- To use instrumented impact and air-based erosion to link the fatigue effects of these processes on DLC coatings.

- To use nano-scratch testing with varying probe radii to investigate the interfacial friction contributions and assess the relation between probe radius, contact pressure and critical load failure.

- To perform micro-fretting tests at high contact pressures in both dry and lubricated conditions and compare and contrast the results to that of the same contact pressure in nano-scale fretting.

- To use Micro Materials newest module, the NanoTriboTest, to record the nano-scale reciprocating sliding friction.

- To produce a number of publications detailing the pertinent results acquired.

1.5.3 Project Structure

The structure of the project is summarised in Figure 1.8 beginning with the coating design parameters that are used in the production of the coating matrix. The coatings are produced using the Hauzer Flexicoat System at the University of Leeds. The coating designs and layer thickness are verified with the Calotest technique and SEM. As they are based on pre-existing designs [1], no repeated cycles of production and verification were required. Mechanical properties are determined with nanoindentation and scratch testing. The structure of the coatings is analyse using Raman spectroscopy and TEM/EELS. The information gained using these methods can be utilised to discuss the results gained by the nano-scale fatigue, quantitative adhesion assessment, multi-scale fretting and nano-scale reciprocating sliding studies. The techniques will be fully described in their respective sections throughout the thesis.

---

[1]Some modifications were made to the recipes such as the deposition time to achieve the various thicknesses in this study however no further design changes were made.
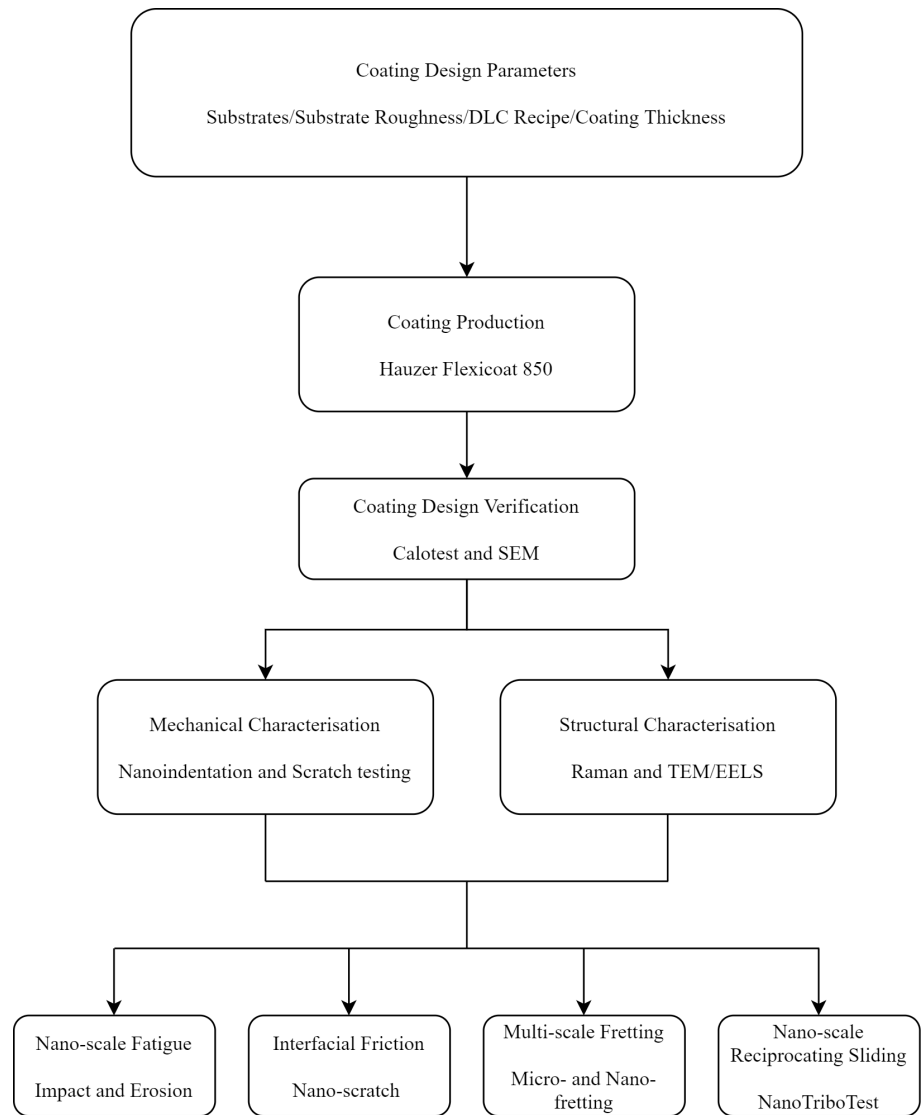
Figure 1.8: Flowchart of the main parts of the project and the associated experimental methods/parameters.

1.6 Thesis Structure

This thesis will first cover the relevant literature and theory applicable in the surface engineering and tribology of diamond-like carbon and the wear processes studied in this project. This can be found in Chapter 2. Following this theoretical overview, the production of the DLC coatings and the substrates that they are applied on in this study will be detailed in Chapter 3.

The chapters proceeding will detail each of the categories of experimental work used in the characterisation and testing of the coatings. These chapters will be written with their own standalone introduction, methodology, results and discussion (where appropriate) to allow for the results to be detailed fully in the context of that study alone. This will be as follows:

- Chapter 4: Mechanical Characterisation of DLC Coatings.

- Chapter 5: Structural Characterisation of DLC Coatings.

- Chapter 6: Nano-Scale Fatigue Determination by Comparison of Erosion and Impact Testing.

- Chapter 7: Nano-Scratch for the Determination of Interfacial Friction.

- Chapter 8: Multi-scale Fretting Testing of DLC Coatings.

- Chapter 9: Frictional Performance of DLC Coatings under Nano-Scale Reciprocating Sliding.

Chapter 10 will present an overall discussion and collected conclusions of the thesis. The effect of coating mechanical properties and structure on the tribological performance of DLC taking all the wear conditions into consideration will be addressed. Limitations of the project and recommendations for further experimental techniques (for anyone pursuing similar research) are discussed in section 10.4. Finally recommendations for future work, in reference to the possible further investigations of this work as well as rising themes in tribology and surface engineering, are presented in Chapter 11.

Chapter 2

Literature Review

This literature review covers the fundamentals of tribology, its history and more recent applications on the nano-scale. As this project is primarily focussed on the characterisation and application of coatings for improved tribological performance, discussion of fundamentals will reference coated applications as these are most relevant. Surface Engineering will be explored in its application to tribology in the production of coatings, particularly DLC.

2.1   Fundamentals of Tribology

Tribology is the science and technology of interacting surfaces in relative motion and of related subjects and practices [19] or, as is sometimes defined, the study of friction wear and lubrication [39]. "Tribology" is derived from the Greek word "tribos" meaning rubbing or sliding and "ology" meaning the study of. The term itself was introduced in 1966 in a landmark report by Jost and his associated working group formed to investigate the then current state of lubrication education and research [20, 39].

Much of tribology research is dedicated to increasing the reliability of components in large industrial systems. By analysing the operating conditions, failure of older components and assessing historical data, a model of current component performance can be established. New materials and designs alongside new monitoring methods allow improved performance alongside better prediction of failure probability and lifetime. This is accomplished by a combination of scaling down and simplifying contact geometry to test in the lab and analysing real world failures [40]. Numerical modelling methods are being used more regularly in tribological studies. An energy approach can be used at the macro-scale and when scaling down, reduction to a one dimensional problem is common. On the nano-scale, a movable cellular automata method can investigate fundamental friction and wear and changes in surface topography. This method, however, uses a large amount of computing power due to the simulation requiring small time-scales [41].

Much tribology research is concerned with industrial problems and therefore we often forget the influence that the field has on our everyday lives. Dowson [42] identified the tribological issues present in our everyday lives, this included the bio-tribology of joints and joint replacements to the tribology of teeth, clothing and shaving. Many tribological processes are understood at the macro-scale however once we progress down to smaller scales to investigate the fundamentals, the true complexity of friction and wear becomes apparent. Some fundamental questions still to be answered include why static friction is universally observed between solids, how are friction and wear related and how can we control them in practice [43].

Contact mechanics is an essential underlying component of all tribological studies as it defines the interactions between two surfaces. The peaks on surfaces are known as asperities. When two surfaces are in contact, only the highest asperities are touching. This results in the real area of contact being much lower than the apparent contact area and the stresses at these contacts being high. The stresses of contact asperities are dependent upon the shape of the asperity and the elastic and plastic properties of the contacts [19, 44].

The elastic properties of contacting materials are described by their elastic modulus (E) and the Poisson's ratio (v). When two surfaces are in contact their combined contact elastic modulus (E') is:

$$\frac{1}{E'} = \frac{1 - v_1^2}{E_1} + \frac{1 - v_2^2}{E_2} \tag{2.1}$$

where E_1, v_1 and E_2, v_2 are the elastic moduli and Poisson's ratio of each surface respectively.

Plastic properties are usually described by their hardness (H). Indentation hardness is the most useful way to describe hardness in a tribological context. This will be detailed later in this review. Hardness measured under indentation is related to the yield pressure of the material and this is also closely related to the uniaxial yield stress (σ_y or sometimes simply known as Y) [19, 44]. This is because the indenter reaches equilibrium in the hardness test when the load is just supported elastically. Therefore we can write the relation:

$$H \approx C\sigma_y \tag{2.2}$$

with $C = 2.8$ where C is the constraint factor, which holds for most metals. Fischer-Cripps [45], in his "Introduction to Contact Mechanics", notes that the relation is sometimes taken as $C \approx 3$ for metals (where E/σ_y is large) from Tabor [46]. For lower values of E/σ_y (such as glasses), $C \approx 1.5$. Chudoba et al. [47] used a combined modelling and indentation approach to analyse the H/σ_y (maximum von Mises stress) and found that C can vary depending upon the material properties namely H/E which will be detailed further in Section 2.5.8. The constraint factor arises as the mean contact pressure in hardness testing is greater than that required to initiate yield compared to uniaxial compressive stress [45, 48]. In effect, this coefficient accounts for adding the additional dimensions of yield as present in indentation.

For DLC, Chudoba et al. [47] found C to be 1.57. For higher H/E materials, C can approach unity, for example sapphire was found to have a C of 1.10. Therefore, the limiting elastic strain (ε_p) (strain for the onset of plastic deformation) is given by:

$$\varepsilon_p = \frac{H}{CE} \tag{2.3}$$

These relations are important for friction and wear [44]. In the contact between two hard surfaces, the most common contact mechanics formulation is that established by Hertz. Hertzian contact mechanics deals with the pressure between two elastic bodies placed in mutual contact [45]. In assigning a shape to the surface in a contact, certain boundary conditions are given:

- The displacements and stresses must satisfy the differential equations of equilibrium for elastic bodies, and the stresses must vanish at a great distance from the contact surface.

- The bodies are in frictionless contact.

- At the surface of the bodies, the normal pressure is zero outside and equal and opposite inside the circle of the contact.

- The distance between the surfaces of the two bodies is zero inside and greater than zero outside the contact circle.

When modelling asperities, we assume that the tips have a spherical curvature so that contact is between two spheres of radii R_1 and R_2. This can be further simplified still by assuming that one surface is flat so the model becomes contact between a sphere of radius R and a plane. An equivalence relation can be written [19, 44, 45]:

$$\frac{1}{R} = \frac{1}{R_1} + \frac{1}{R_2} \tag{2.4}$$

Under a normal load (P), the sphere and plane deform and approach each other by a distance (δ) to give a circular contact of radius (a):

$$a = \sqrt[3]{\frac{3PR}{4E'}} \tag{2.5}$$

$$\delta = \frac{a^2}{R} = \frac{1}{2}\sqrt[3]{\frac{9P^2}{16RE'^2}} \tag{2.6}$$

The maximum pressure (P_{max}) is given by:

$$P_{max} = \frac{3P}{2\pi a^2} = \sqrt[3]{\frac{6PE'^2}{\pi^3 R^2}} \tag{2.7}$$

Hardness is related to the mean contact pressure (P_{mean}) under an indenter. The mean pressure varies dependent upon the load and geometry of the indenter [1]. Information of the elastic and plastic properties of a material can be obtained with spherical indenters by plotting P_{mean} against a/R (this ratio is known as indentation strain). Three regimes can be identified [45, 48]:

1. $P_{mean} < 1.1Y$ – Fully elastic response with no permanent or residual impression left in the specimen after load removal.

2. $1.1Y < P_{mean} < CY$ – Plastic deformation exists beneath the surface but is constrained by the surrounding elastic material. The constraint factor (C) depends on the material and indenter geometry.

3. $P_{mean} = CY$ – The plastic region extends to the surface of the specimen and continues to grow in size such that the indentation contact area increases at a rate that gives little to no increase in the mean contact pressure for further increases in indentation load.

In region 1, during the initial application of load, the response is elastic and therefore the mean contact pressure (P_{mean}) can be predicted from a Hertzian relation:

$$P_{mean} = \frac{P}{\pi a^2} = \left(\frac{4}{3}\frac{E'}{\pi}\right)\frac{a}{R} \tag{2.8}$$

---

[1]Sharpness of indenter (face angles in contact with sample) changes the maximum plastic zone in terms of shear stress distribution. In combination with the relative ductility of samples being indented and the measurement of contact area, the permanent deformation (hardness) measured can vary [48, 49].

Many researchers have advanced these fundamental contact mechanics methods. Persson [50–52] has performed several analyses of contact mechanics to extend it further in looking at randomly rough surfaces and with more complex materials like rubber. Dongfeng and Koji [53] used finite element methods to analyse the contact pressure distribution in hard coatings, taking into account the effects of substrate hardness, coefficient of friction and ratio of coating thickness to contact width, to find a critical maximum contact pressure of yield. Schwarzer et al. [54] performed similar analysis to find the exact solution for the displacement and stress distribution for a coated half-space under Hertzian contact conditions.

Under the ideal contact of two surfaces, we can visualise a rough surface (as shown in Figure 2.12 on page 44) making contact with a smooth plane. In this scenario, only some asperities will make contact with the plane in different states of deformation (elastic, elasto-plastic and fully plastic). In general, as more load is applied, more asperity contact will be made such that the actual contact area is proportional to the load [44]. Greenwood and Williamson [55] established the plasticity index (φ), this gives an indicator of the relative amounts of elastic and plastic deformation in a system. This is dependent upon the ratio of hardness to elastic modulus, roughness and asperity ratio. Under normal contact load, finite element analysis shows [56]:

- when $\varphi < 0.5$, the contact is entirely elastic;

- when $0.5 < \varphi < 1.4$, the contact is elasto-plastic;

- when $\varphi \geq 8.0$, the contact is entirely plastic. Between 1.4 and 8.0, the contact is in transition between elasto-plastic and fully plastic.

More information on this can be seen in Section 2.5.8.

2.1.1   History of Tribology and Potential for the Future

Though the formalisation of tribology and unification of its aspects only occurred in the 1960s, the field itself has existed for far longer. Dowson [57], in his book 'History of Tribology' identified evidence of tribological knowledge as far back as Ancient Egypt in the movement of a large statue. Further evidence of tribological knowledge can be found in stone age fire making equipment, drilling machines and door sockets [58]. Leonardo Da Vinci famously made initial formalisations of tribology in his study of the sliding and rolling of bodies on horizontal planes [59]. The industrial evolution saw rapid technological expansion with Robert Hooke's work on friction and wear reduction in bearings and Isaac Babbitt developing low friction metals [58].

An important metric for the development of tribology throughout time is the gradual reduction of film thickness as noted by Dowson [60] in 1992. This is also noted by Spikes [61] in his 2001 review of tribology research in the twenty-first century.

Popov [62] postulated that tribology was reaching a 'Golden Age' in 2018. Despite the relative obscurity of the field new technologies such as fast Fourier transform boundary element methods have the potential to allow for direct calculation of contact conditions. Furthermore, contact mechanics theories have improved greatly looking at more complex materials. Classical tribology of bearing and gears is well understood but the field now looks towards nano- and bio-tribology for new advances. This was echoed by Stachowiak [63], in that new advances come by analysing the fundamental processes using nano-tribology.

Table 2.1: Changes in tribological film thickness with technological development. From [60].

Time Period	Development	Film thickness (m)
Late nineteenth century (1900)	Plain bearings	10^{-4}–10^{-5}
Mid-twentieth century (1950)	Steadily loaded bearings	10^{-5}
Late twentieth century (1980)	Dynamically loaded bearings	10^{-5}–10^{-6}
Late twentieth century (1990)	Elastohydrodynamics (gears; rolling bearings; cams; synovial joints)	10^{-6}–10^{-7}
End of the twentieth century (1990-2000)	Asperity lubrication; low-elastic-modulus solids; magnetic recording; plasto-elasto-hydrodynamic lubrication	10^{-7}–10^{-9}

2.1.2 Friction

Friction is the resistance to motion as one surface moves over another. Essentially, this can be stated as the resistive force encountered when asperities interact in dry contact; the theories of adhesion and ploughing define this in different ways [19, 64]. The studies of Leonardo Da Vinci and Amontons led to the development of the first two fundamental laws of friction with the third being derived from the work of Coulomb [19]. These dry friction laws are:

- The friction force (F) is directly proportional to the applied load (W).

- The friction force (F) is independent of the apparent area of contact (A).

- The friction force (F) is independent of the sliding velocity (V).

Generally these laws are only true under ideal conditions that are not representative of common tribological contacts. The ratio of the friction force to the normal load is expressed as the COF:

$$\mu = \frac{F}{W} \tag{2.9}$$

where μ is the coefficient of friction, F is the friction force and W is the normal load. These laws of friction are seen to break down at the nano-scale where instead roughness is seen to dominate [65]. Nanotribology is characterised by a light load (μN to mN) and subsequently produces little to no wear. The interaction is typically confined to the first few atomic layers [66, 67]. As a result of this, the wear mechanisms (as defined in the next section) are not applicable as they were constructed for the macro-scale. The real area of contact is vastly different between the two length scales also with macro-scale only having a fraction of the real contact of asperities [68]. A nano-scale tribological interaction can therefore be viewed as a single asperity interaction which will change the level of adhesion of asperities. On the nano-scale other mechanisms can be be present to affect the tribological interaction; these can be electronic effects, thermal effects and molecular deformation [69]. The differences in interaction between the macro and nano-scale will be investigated in this thesis.

2.1.3 Wear

Wear is the progressive damage of a material resulting in material loss. Wear rates vary hugely depending upon the material selection. Generally, there is no way to accurately predict wear from first principles therefore this is generally performed by lab and field tests [19, 44].

2.1.3.1 Wear Mechanisms

Wear can be broken down into five basic wear mechanisms, these being abrasion, adhesion, erosion, corrosion and fatigue.

2.1.3.1.1 Adhesion Bowden and Tabor established adhesive wear was due to cold welding of asperities and that shear must take place for sliding to occur [70]. Archard formulated a theoretical expression for adhesive wear [71]:

$$Q = \frac{P}{3H} \tag{2.10}$$

where Q is the total wear volume per unit distance and $P = n\pi a^2 H$ with n being the number of contact spots of radius a. From this we find the three laws of adhesive wear [19, 44]:

- The wear volume is proportional to the sliding distance.

- The wear volume is proportional to the load.

- The wear volume is inversely proportional to the hardness of the softer material.

In general, these laws are true over a limited range of conditions however the wear equation is based on the assumption of every asperity producing a wear particle. This is not the case therefore it is adapted into:

$$V = k\frac{Px}{3H} \tag{2.11}$$

where V is the total wear volume, x is the sliding distance and k is the dimensionless wear coefficient. This can be adapted into the more general form: $V = KPx$. K is the dimensional wear coefficient.

2.1.3.1.2 Abrasion Abrasive wear consists of two types: two-body and three-body abrasion [19, 44]. In two body abrasion, a hard surface rubs against a softer one. In three body abrasion, hard particle trapped between the two surfaces abrade on one or both surfaces accelerating wear. We generally think of this in terms of a hard conical asperity (of angle θ) ploughing into a softer surface:

$$V = \frac{2P\tan\theta}{\pi H} \tag{2.12}$$

2.1.3.1.3 Erosion Erosion is the removal of material due to the impingement of liquid or solid particles on a solid surface. Liquid impact generates momentary stresses that can be high enough to cause cracking. This can then proceed to form chips. Cavitation damage can also occur wherein bubbles in liquid implode on a surface [19, 44]. Sand particles, suspended in water or entrained in airflow, can cause expensive erosion damage to both the internal and external surfaces of valves, pumps and pipework [72]. It is well understood that the erosion rate of a material is dependent on its relative brittleness/ductility in addition to the velocity and angularity of the erodent material [73]. Additionally, the

impingement angle of the jet changes the erosion rate dependent upon the relative brittle-ness/ductility of the material [72, 74]. Material chipping, cracking and removal are not the only considerations in erosion wear as the large number of particle impacts is a fatigue process [75–77]. Coatings for erosion applications such as for gas turbine blades typically consist of carbide or nitride metal ceramics however high velocity oxy-fuel (HVOF) coatings are also seen in marine applications where corrosion resistance is required too [78–82]. Metal nitrides are seen in use for aerospace applications, erosion rate is seen to decrease with surface hardness for these coatings and multi-layers are beneficial [76]. The shear stress maps modelled by Zhang et al. [83] support this with higher numbers of sandwich layers lowering the maximum shear stress and Von Mises stress. Work by Shen et al. [84] has shown that extremely thick DLC layers ($\approx 50\,\mu\text{m}$) do possess the necessary wear resistance to provide good anti-sand erosion performance.

Bull [85] showed that indentation experiments can mimic processes observed in erosion and can be reasonable for the development of models. It was additionally noted that coating thickness should be chosen to match the energy of the erodent particles. A single indentation (with quasi-static loading), however, cannot mimic the high strain rates produced during impact or erosion testing [86].

2.1.3.1.4 Corrosion Corrosive wear occurs as the result of chemical reactions thereby removing material. A good example is the formation of oxide layers which and subsequently removed and reformed [19, 44]. Tribo-corrosion is the synergistic interaction between mechanical wear processes and an electrochemical and/or chemical response. Often synergistic effects occur between corrosion and other wear processes leading to increased wear rate [87]. Wood [87] defined an equation determining the synergistic relations between mechanical wear and corrosion:

$$S = T - (E + C) = (\Delta C_e + \Delta E_c) \tag{2.13}$$

where T, C and E are gravimetric terms relations to wear-corrosion, electrochemical corrosion without tribo-influence and mechanical wear mechanisms, respectively. ΔC_e and ΔE_c are the corrosion-enhanced wear and wear-enhanced corrosion respectively.

2.1.3.1.5 Fatigue Fatigue is the process by which cracks form resulting in failure when a material is subjected to cyclic stresses well below the tensile strength (σ_{TS}) and often below the yield strength (σ_y) [88]. Uniaxial fatigue testing is a standard technique to measure the fatigue strength of engineering materials. With a fixed loading ratio, the relationship between the amplitude of the fatigue load (σ_a) and the number of cycles to failure (N_f) (also known as the $S - N$ curve) can be expressed as the power law relationship [89]:

$$\sigma_a = \sigma_f \left(N_f \right)^n \tag{2.14}$$

where σ_f and n are the fatigue strength coefficient and exponent respectively. These are related to the material and its microstructure along with the testing environment and conditions. Under quasi-static loading, σ_f relates to the uniaxial fractures strength. Many tests are required to produce accurate results as each test specimen yields one data point. This type of testing is normally employed for high-cycle fatigue tests ($\gtrsim 10^4$). Under these conditions where the component is uncracked, Basquin's law can be applied [88]:

$$\Delta\sigma N_f^a = C_1 \tag{2.15}$$

where a is a constant (between $\frac{1}{8}$ and $\frac{1}{15}$ for most materials) and C_1 is also a constant. In this regime, stresses are below the yield of the component.

The Coffin-Manson Law is used to describe low cycle fatigue of uncracked components [88, 90]:

$$\Delta\varepsilon^{pl} N_f^b = C_2 \tag{2.16}$$

where $\Delta\varepsilon^{pl}$ is the change in plastic strain, N_f is the number of cycles to failure and b and C_2 are constants. With low cycle fatigue, stresses are above the general yield of the component. The data is generally plotted on a logarithmic graph.

2.1.4 Synergistic Wear Mechanisms

In real engineering component interactions, wear is complicated and more than one mechanism can occur at the same time. resulting in a greater overall effect [19]. The following are examples of such mechanisms.

2.1.4.1 Fretting

Fretting wear is the small amplitude oscillatory wear occuring between two surfaces in contact, generally under some kind of vibration [91, 92]. Depending upon the conditions seen within the fretting contact, we can observe synergism between adhesive, abrasive and corrosive wear [93]. Fretting wear typically displays 4 modes of motion: tangential, radial, rotational or torsional movement[94]. This movement can exist in different regimes dependent upon the tangential load and displacement. The partial slip regime displays the lowest movement and is typified by slight abrasive wear and fatigue. Mixed and gross slip extend the displacement displaying oxidative wear and delamination is addition to abrasion [94]. Fretting maps can be drawn of the tangential force and displacement of the moving surface to identify the regime of fretting, this is an additional method employed alongside the more traditional fretting logs of tangential force and displacement changing with numbers of cycles [95, 96]. Numerous papers by Fouvry and co-workers [97–99] have taken an analytical approach to assess the fretting damage, coefficient of friction evolution and transition criteria in different regimes. The simplest criteria is the energy ratio followed by the sliding ratio. Others also exist but they are much harder to implement [97, 100].

Wear in the gross slip fretting regime typically produces wear debris. As the test proceeds, the larger wear particles are oxidised and fragment. Below this debris layer, there exists a tribologically transformed structure (TTS) from which the debris originated. This structure is nanocrystalline in nature. A global energy approach allows the input energy required to form the TTS before the onset of wear to be predicted [101]. Liskiewicz et al. [102] performed nanoindentation mapping to assess the TTS, showing that it formed very quickly within the initial cycles. Kubiak et al. [103] found that surface roughness has a significant effect on the friction and activation energy for the onset of wear in fretting. Rougher surfaces see a lower coefficient of friction but higher wear rate. Using an wear energy approach the wear volume can be related to accumulated dissipated energy. By analysing the energy input over different displacement amplitudes and number

of cycles to failure, a chart of energy required to reach the substrate can be constructed [104]. Dynamic fretting friction can be calculated using an energy dissipation approach as performed by Liskiewicz and Fouvry [105]:

$$\mu = \frac{E_d}{2F_n d} \quad (2.17)$$

where E_d is the energy dissipated during a cycle, F_n is the applied normal load and d is the track length. Wear depth in fretting can be estimated from the cumulative energy density found by similar analysis. This can be extended to a coating endurance ranking system by analysing the number of cycles to decohesion of the coating [105].

Newer studies by Wade and co-workers have identified novel numerical methods to parametrise fretting contact and monitor regime transition in real time using acoustic emission [106, 107]. Lubrication is sometimes used to minimise wear in fretting. Grease is most commonly applied though a liquid lubricant can also be useful as it restricts oxidative wear [108].

2.1.4.2 Impact

Impact testing can be used to assess multiple parameters such as fatigue strength, creep, adhesion, residual stresses, toughness, erosive wear resistance and dynamic hardness of coatings [109–113]. Knotek et al. [114] performed some of the earliest work on assessing the impact loading of thin films. This was specifically performed to analyse the coating's resistance to dynamic loading as experienced in interruptions in machining. Bantle and Matthews [115] also investigated impact but for the wear behaviour of ceramic coatings finding that the CrN and electroless nickel-phospherous interlayers required optimising. Repetitive impact can assess fatigue resistance under repetitive loading like the impacts of erosive particles [110–112, 116–118]. Micro- and nano-impact allow for high strain rate testing and its repetitive nature is more representative of erosion under repeated particle impingement, which is particularly important as strain rate has been seen to affect the fatigue failure of thin PVD coatings [119]. Both sharp and blunt probes can be used depending on fracture and fatigue conditions being assessed [118]. Cracking evaluation and delamination assessments has also been used in the larger scale impact tests as performed by Fu et al. [120] in which 2.5 mm radius punch ball was used in a cyclic impact test. Due to the larger scale of the tests, cracking was generally centralised in the crater with some edge cracking seen. No severe delamination was recorded. Alongside physical testing of impact wear, finite element modelling (FEM) and classical mechanics models are being used to assess the dynamics of impact in varying orientations [109, 121]. Coating performance is seen to vary with architecture with ordered coatings benefiting from higher resistance to plastic deformation (H^3/E^2) [86] whereas amorphous DLC coatings benefiting from higher toughness (E/H) [122].

2.1.5 Lubrication

Lubrication is the effective interposition of a solid, fluid or gas between two bodies to reduce friction and /or wear during motion. Typical engineering lubricants can come in various forms; mineral oils, synthetic oils, grease, air or solids. Liquid lubricants can have a range of viscosities (resistance to shear). Dynamic viscosity varies with both pressure and temperature. At very high pressure the density can vary also. Other physical and

chemical properties are important to lubricant performance depending on the operating environment, these range from thermal conductivity and flashpoint to oxidation stability and pouring point [19].

The performance of oils can be further modified with additives to reduce friction and wear, maintain fluid properties and minimise contamination. Zinc dialkyldithiophosphates (ZDDPs) are common additives that have anti-oxidant and anti-wear properties. molybdenum dialkyldithiocarbamate (MoDTC) is incorporated into modern engine oils as a friction modifier. Other additives can include viscosity modifiers, anti-foaming agents and emulsifiers. Where the oil and additive combination is tailored to the operating environment, these are known as fully formulated oils [19]. Films can form on the surface on materials in tribological contact, these are known as tribofilms and are the result of physical or chemical adsorption, or chemical reaction.

There are 4 lubrication regimes that define the expected coefficient of friction depending upon the surface materials, surface texture, lubricant properties and operating conditions. With no fluid separation, the surfaces will be in dry contact giving a large coefficient of friction, this is known as boundary lubrication. [19].

Figure 2.1 shows a typical Stribeck diagram which relates the friction coefficient in different lubrication regimes to the relation between the speed (U), dynamic viscosity (η) and the load (p). The x axis is sometimes labelled as the specific film thickness (λ) which is equivalent to h_{min}/σ where h_{min} is the minimum separation between two surfaces and σ is the root mean square roughness. In this representation, it should be known as the modified Stribeck diagram.
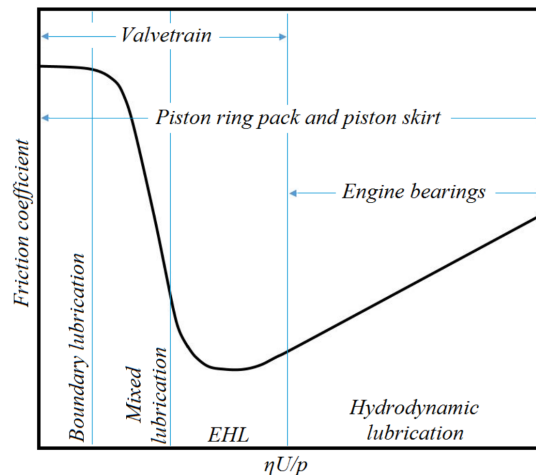
Figure 2.1: Stribeck curve noting the typical lubrication regimes of key engine components. From [123].

The identification of the mechanisms of additives in lubricants is an ongoing research area. Additives such as ZDDP and MoDTC have complex interactions with surfaces. MoDTC is generally understood to break down into MoS_2 and further into other Mo containing species with various intermediate compounds depending upon the chemical and mechanical wear interactions [124, 125]. ZDDP breaks down to form glassy phosphate pads and ongoing research is showing that shear stress can affect the rate of tribofilm formation by reducing the thermal activation barrier [126, 127]. Solid lubricants are also extensively used such as MoS_2, its basal plane orientation leading to extremely low coefficient of friction. It is typically employed for aerospace applications due to low friction at high temperatures and in vacuum conditions [128].

The use of 2D materials such as graphene or MoS_2 can produce extremely low coefficients of friction in sliding contacts [69]. A coefficient of friction below 0.01 is considered in the superlubricity regime in which there is effectively near zero friction. The application of small amounts of graphene to 440C stainless steel reduced the coefficient of friction to around 0.15–0.30 and reduced the wear wear volume by 2 orders of magnitude in ball on disk testing [129]. Various other carbon nanostructures (carbon nanotubes, nanodiamond and onion-like carbon) have also been seen to provide super lubricity [130]. Zhao and Duan [131] proposed that the application of nanodiamond between a SiO_2 surface and DLC could reduce friction via a nanoscrolling effect of graphene wrapping around nanodiamond though the introduction of nanodiamonds themselves also reduced friction. The nano-scrolling effect was seen to reduce friction by 72 % compared to nanodiamonds alone. The predicted contact area was also smaller for the nanoscrolls and they also increased the friction dissipation of the system leading to less frictional heat. Graphene nanoscroll formation was noted by Berman et al. [132], to allow for superlubricious behaviour at the macroscale.

2.2 Nano-Tribology

Nano-tribology has emerged over the past 25 years due to our improving ability to measure frictional forces and phenomena at the sub-micron scale. Nano-tribology is important to our understanding of tribology as a whole as it allows a deeper understanding of macroscopic tribological phenomena. Differences between the length scales are observed primarily by adhesion dominating at the nano-scale compared to plastic deformation and mechanical wear at the macro-scale. Analysis of lateral force microscopy data shows that on smaller length scales friction is due to a single asperity sliding over a multi-asperity surface. At the macro-scale, friction instead occurs due to collective asperity interactions and is dependent on the surface roughness. The frictional mechanisms seen in the scale up are not well understood and addressed in literature [133]. Though wear is seen at the nano-scale (generally in a reduced capacity), the energy dissipation mechanisms due to surface interaction are far more complicated. Some of the possible mechanisms were identified by Berman et al. [69] as molecular deformation, thermal effects, electronic effects, bonding, phonons, environmental or chemical interactions and structural/interlocking effects. several mechanisms may occur at once and there is the possibility of synergistic effects between them. The differences in the scale of interactions are shown in Figure 2.2.

Some of the most important work in nano-tribology has been performed in relation to measurements of coating adhesion, measurement of lubricant film thickness and magnetic forces for applications in magnetic recording media [67]. More recently nano-tribology has been used in the studies of boundary lubrication additives for aluminium [134], the study wear behaviour of single crystal silicon [135] and the characterisation of ultrathin dual-layer ionic liquid lubrication films [136].
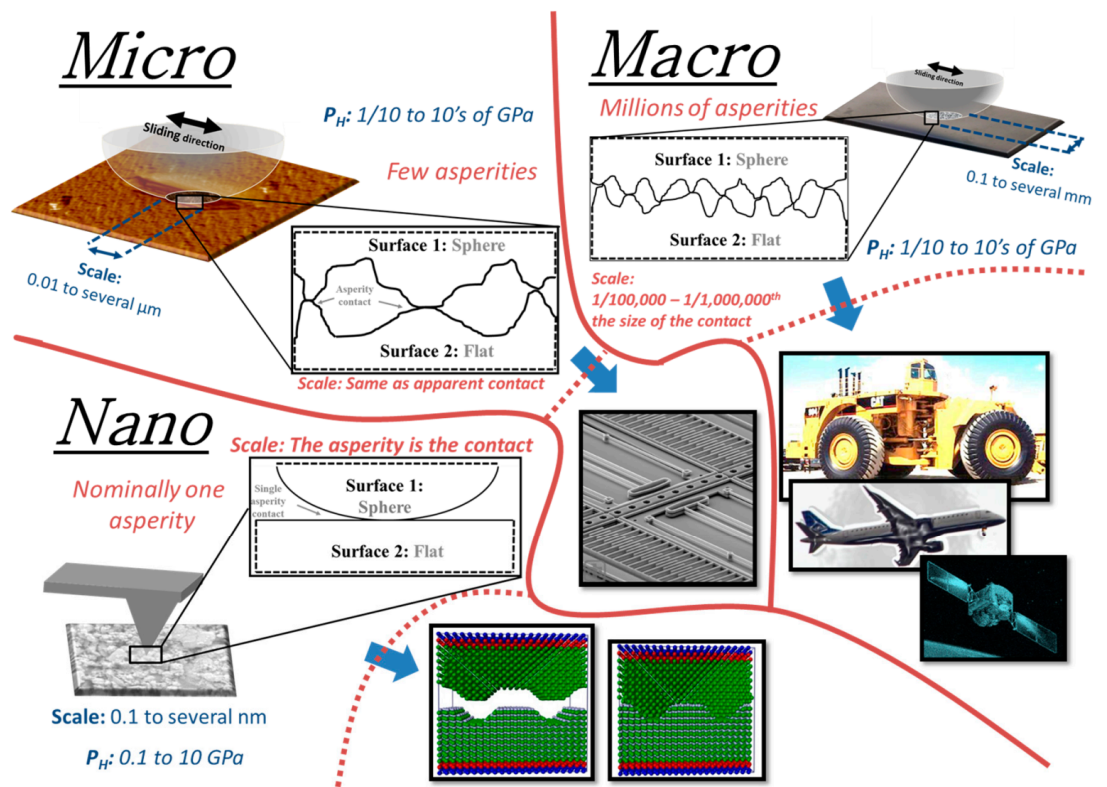
Figure 2.2: Scales of tribology with their associated asperity interactions. From [37].

2.2.1 Atomic force microscope nano-tribology

Atomic force microscopy (AFM) typically allows for relatively high contact pressures (several GPa) at low Hertzian contact areas ($10^{-5}\,\mu\text{m}^2$) due to low normal loads (nN). This allows for ultra-sensitive friction measurements [133]. This use is being seen more frequently in the literature as more fundamental interactions are being explored instead of its more typical use in topography measurements alone [137].

Much recent work is devoted to increasing the capabilties of AFM units. Such examples include the work of Bosse et al. [138] in high speed friction microscopy and nanoscale friction coefficient mapping of heterogeneous surfaces. The work of Tao et al. [139] has also extended the sliding speed capabilties of AFMs up to $200\,\text{mm}\,\text{s}^{-1}$. Other innovative work in extending AFM capabilities lies in allowing them to perform nanoindentations by increasing tip stiffness (and decreasing compliance) [140, 141], this has been performed by Tranchida et al. [142] to characterise the elastic properties of polymers.

Though AFMs are improving, some considerations must be made in the analysis of friction data due to artifacts in the measurements. Some of these are due to variation in the normal load at different locations, changes in topography and contact area during scanning and wear of the tip [138]. Some of the most innovative recent work using AFMs has been performed by Dorgham et al. [143] in their analysis of the kinetics of phosphate based tribofilms. They showed that for ZDDP the growth of phosphate glass had an exponential dependence on temperature and contact pressure whereas in the absence of zinc, a linear temperature dependence is found.

2.2.2 Nano-impact

Nano impact testing can be used to test the mechanical properties of thin films due to its smaller energy per impact. This is particularly useful for fatigue assessment as many repeated tests can be performed is a small amount of time [110, 112, 144].

2.2.3 Nano-fretting and Micro-wear

One of the first reports on nano-fretting was by Yu et al. [145] who studied the interaction of monocrystalline silicon against diamond using an AFM. Nano-fretting refers to the cyclic movements of contact interfaces with the relative displacement amplitude in the nanometre scale with the contact area and normal load being smaller accordingly. Differences in the tribological interaction will be due to the single asperity interaction. Liskiewicz et al. [146] developed a module for the Nano-Test Vantage Platform that uses a piezo stack to drive wear. This initial characterisation analysed several coatings on Si. DLC coating performance in the nano-fretting regime was analysed by Chen et al. [147] who found adhesion was a large factor in the interaction and the coating was excellent in resisting damage due to its mechanical properties. Further nano-fretting tests have been performed by Beake and coworkers [148–150] though little has been performed recently.

2.3 Triboemission, Triboplasmas and the Triboelectric effect

In addition to the more tangible tribological effects such as friction and wear, there are other surface effects that result from tribological contact. This section will briefly detail the triboemission and generation of triboplasma in addition to the triboelectric effect.

2.3.1 Triboemission and Triboplasma generation

A number of different types of particles are emitted from a sliding contact and its vicinity [151]. These particles are electrons, ions, photons, radicals and molecules. These particle emissions can be classified into three broad categories:

- triboemission from inside the contact

- triboemission from the triboplasma generated in the rear outside gap of the sliding contact

- post-emission from outside the contact

These types of particle emission are deeply connected with tribo-charging so the three types of phenomena above are termed triboelectromagnetic phenomena. Figure 2.3 shows a recent model of the triboelectromagnetic phenomena.
In a sliding contact, friction causes a temperature rise in the surface and counterface and wear is induced on both of these surfaces. Due to this heating, thermoelectrons and thermally stimulated electrons are emitted in the vicinity of the sliding contact dependent
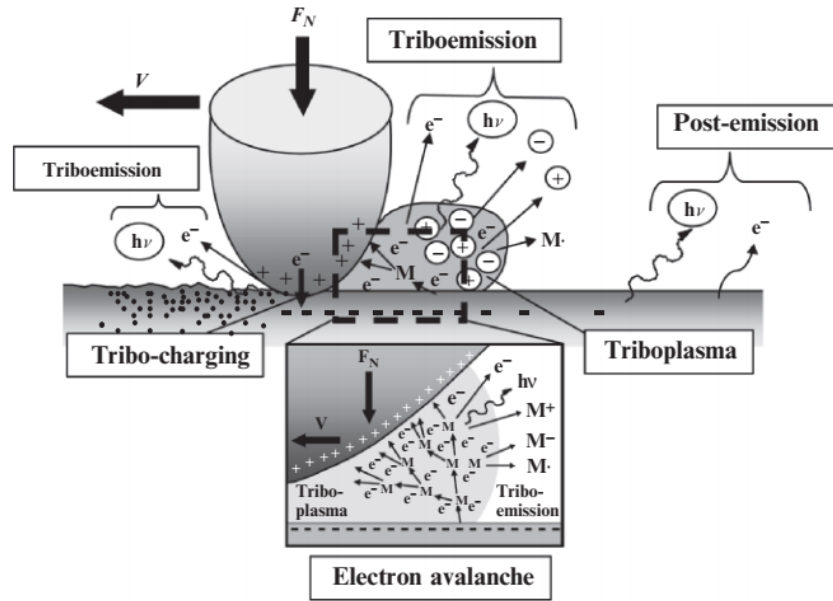
Figure 2.3: Conceptual model of triboeletromagnetic phenomena. From [151].

upon the frictional temperature rise. Additionally, chemically induced electrons are emitted due to the interaction between the newly worn surface and active molecules surrounding it. The electrons, produced by cosmic rays and other energetic events, are accelerated by the tribocharing-induced electric field. Discharge of ambient gas molecules is caused generating a triboplasma through an electron avalanche process. This triboplasma emits electrons, ions and photons. Photons are also emitted from inside the sliding contact. Post-emission electron emission is often chemically induced whereas the photon emission is theorised to be caused by surface attack by charged particles originating from the triboplasma [151].

2.3.2 Triboelectric effect

Beyond the creation of triboplasmas and emissions of charged particles, the rubbing two surfaces can transfer charge between them causing contact electrification, this is known as the triboelectric effect [152]. This is a complex phenomena due to small number of electrons transferred even on a highly charged surface, the difficulty of predicting the exact charge transfer and the number of processes occurring simultaneously. [153]. This makes it difficult to decouple all of the effects to parametrise which has the most affect.

The triboelectric process is seen to be affected by a number of factors including surface microstructure, composition, interface configuration, load, humidity and temperature [153–156]. The dependence on humidity however, has allowed for a self powered humidity detector to be created [157]. The frequency of oscillation is also seen to affect the charging characteristics [158].

The triboelectric effect has attracted a great deal of interest lately due the effect's use in the manufacture of triboelectric nanogenerators (TENGs) [159]. These devices are intended to allow for energy to be harvested to reduce power losses in systems and also to allow for microscale electronic devices to have an independent and maintenance free power source [158, 160]. The combination of thin polymers and metal sputter coating has allowed for a flexible TENG to be produced [160].

Zou et al. created a standard methodology to quantify the triboelectric charge density (TECD) to allow the materials for TENGs to be quantified. This method involves a linear motor and a 2 axis tilt and rotation platform within a Faraday cage to allow for the height and surface contact to be adjusted. The samples are oscillated against each other and the charge build up is measured by electrodes connected to an electrometer [159]. The newly established series can be seen in Figure 2.4.
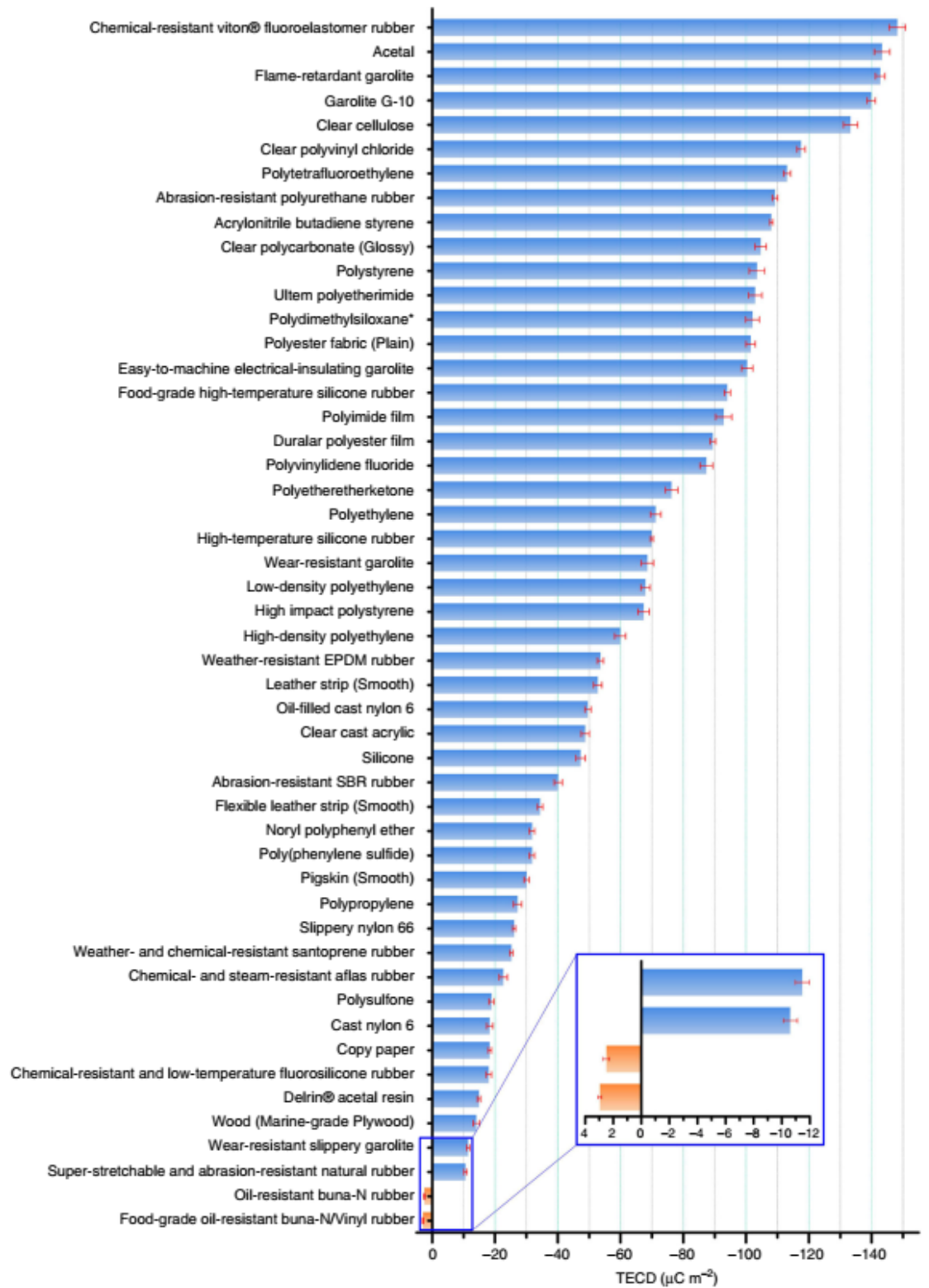
Figure 2.4: Quantification of the triboelectric series [159].

2.4 Determination of Mechanical Properties

Multiple methods exist to determine the mechanical properties of materials. The elastic modulus, tensile strength and yield strength of bulk materials is generally quantified by extension in a tensometer at constant strain rate until sample failure [161]. Hardness is assessed by indentation into a sample to determine the load for a certain indenter contact area at which permanent deformation of the sample is achieved [162].

2.4.1 Instrumented indentation

The advent of instrumented indentation has allowed for the standardisation of precise measurement of the hardness and elastic modulus of materials. Nanoindentation will be discussed in the most detail due to its use in this project.

2.4.1.1 Nanoindentation

The main goal of nanoindentation is the determination of a material's hardness and elastic modulus by experimental readings of the indenter load and penetration depth into the material. The interest in load and displacement sensing in the measurement of mechanical properties dates back to the 1970's when it was recognised that both properties could be measured by a single test [163–165]. Figure 2.5 shows a model nanoindentation load-displacement curve.
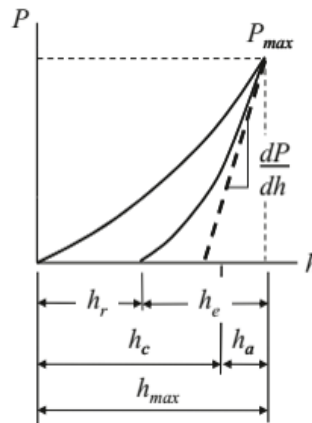
Figure 2.5: Nanoindentation load-displacement compliance curves from an experiment at maximum load. From [48].

P_{max} - Maximum load.

h_{max} - Maximum depth beneath the specimen free surface.

h_c - Depth of the contact circle.

h_a - Depth of contact circle measured from the specimen free surface.

h_r - Depth of the residual impression.

h_e - Displacement associated with elastic recovery during unloading.

The first part of the analysis begins with the fitting of the unloading curve to the power-law relation:

$$P = B\left(h - h_f\right)^m \tag{2.18}$$

where P is the indentation load, h is the displacement, B and m are empirically determined fitting parameters and h_f is the final displacement after complete unloading. The unloading stiffness (S), is determined by differentiating Equation 2.18 at the maximum depth of penetration into the sample, i.e. where $h = h_{max}$. Therefore we obtain:

$$S = \frac{dP}{dh}(h = h_{max}) = mB\left(h_{max} - h_f\right)^{m-1} \tag{2.19}$$

The contact depth is estimated from the load-displacement data with:

$$h_c = h_{max} - \varepsilon\frac{P_{max}}{S} \tag{2.20}$$

where P_{max} is the maximum indentation load and ε is a constant dependent upon the indenter geometry. For a Berkovich indenter which is most commonly used for nanoindentation, $\varepsilon \cong 0.75$.

Hardness (H) is determined by:

$$H = \frac{P_{max}}{A} \tag{2.21}$$

where A is the projected contact area for a specific indenter. Hardness is determined by the residual area impression when the indenter at applying the maximum load. Reduced elastic modulus (E_r) is determined by:

$$E_r = \frac{1}{\beta}\frac{\sqrt{\pi}}{2}\frac{S}{\sqrt{A}} = \frac{1}{2}\frac{\sqrt{\pi}}{\sqrt{A}}\frac{dP}{dh} \tag{2.22}$$

where β is is a constant dependent upon the indenter geometry ($\beta = 1.034$ for Berkovich). The gradient of the unloading curve, $\left(\frac{dP}{dh}\right)$, is equivalent to the unloading stiffness (S):

$$S = \frac{dP}{dh} = \frac{2}{\sqrt{\pi}}E_r\sqrt{A} \tag{2.23}$$

Reduced modulus is converted to a full Elastic modulus (E) by:

$$\frac{1}{E_r} = \frac{(1 - v^2)}{E} + \frac{(1 - v_i^2)}{E_i} \tag{2.24}$$

where v is the Poisson's ratio for the specimen and E_i and v_i are the respective indenter parameters.

Diamond is primarily used for room temperature indentations due to its high modulus, thereby giving it a elastic modulus difference from most samples ensuring a large stress before plastic deformation. A Berkovich geometry indenter is commonly chosen over other available geometries (such as Vickers) because it can be more readily fashioned into a sharper point [166]. The sharpest of diamond tips have a radius in the 10–100 nm range. More detail on these geometries can be found below. The predicted contact area for a Berkovich indenter is given by:

$$A = 3\sqrt{3}h_c^2\tan^2\theta \tag{2.25}$$

For a Berkovich indenter is equivalent to $\theta = 65.27°$, this is the face angle. Therefore the

projected contact area:

$$A = 24.494h_c^2 \approx 24.5h_c^2 \qquad (2.26)$$

Therefore we can use Equations 2.21 and 2.26 to find the hardness as measured by a Berkovich indenter:

$$H = \frac{P}{24.5h_c^2} \qquad (2.27)$$

This method of determination of mechanical properties is known as Oliver-Pharr analysis [48, 163, 167–169]. Figure 2.6 shows the characteristic indentation cross-section during an indentation, the physical depth measures can be seen to match with those in Figure 2.5 to provide a physical understanding of the indentation depth parameters.
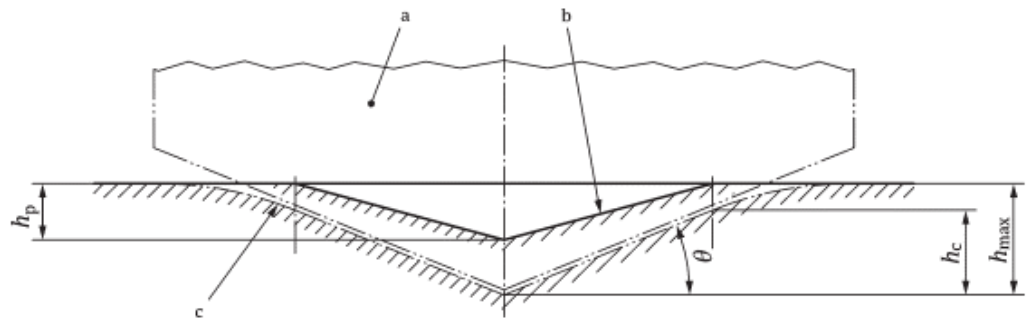
Figure 2.6: Schematic of an indentation cross-section with material "sink-in": a – indenter. b – surface of residual plastic indentation in a test piece with "perfectly plastic" response. c – surface of test piece at maximum indentation depth and load. θ – maximum angle between test piece surface and indenter. h_c – depth of contact circle. h_{max} – maximum indentation depth at maximum load. h_p – permanent indentation depth. From [162].

Despite the main aim of nanoindentation being the determination of a materials mechanical properties, there is qualitative information to be gained from the shape of the load-displacement curve of a particular material. A fully elastic solid's load-displacement profile will follow the same pattern on both the load and unload, thereby displaying no hysteresis. Recovery of residual deformation, giving a small hysteretic area, shows that a material has a visco-elastic response. The larger the area of hysteresis for a load displacement curve, the more plastic work has been required to deform the material. A changing hysteretic rate shows that the material is experiencing elasto-plastic deformation. Sudden compliance changes generally present as a pop-in event which indicates that a material is brittle. Pop-out events are also seen, showing that the material has undergone a pressure induced phase change. Non-recovering residual deformation presents as viscous-elastic-plastic behaviour and demonstrates the material experiences a creep phenomenon (whereby a material experiences irreversible deformation resulting from constant load applied over a sufficient time period) [48, 170, 171]. Rabe et al. [172] performed in-situ SEM observations of the various features of indentation curves to observe the fracture and plastic deformation. Figure 2.7 shows some of the characteristic features of different material's load-displacement curves in nanoindentation.

The behaviour of different materials is time dependent thereby making the unloading

time or unloading rate an important parameter that must be tailored to each material response. In general however, nanoindentation experiments are performed with relatively large unloading times or small unloading rates to create a quasi-static unloading test [48]. Indentation is not the only technique able to evaluate hardness. Impact testing can also be used to evaluate a "dynamic hardness" [48, 113].
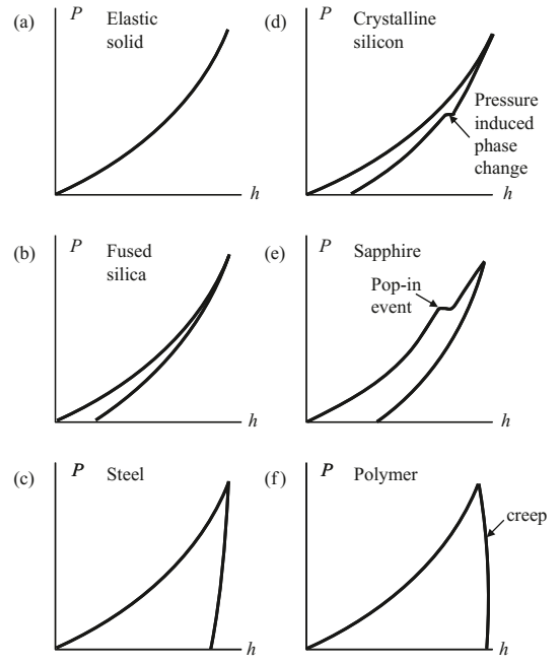
Figure 2.7: Schematic examples of load-displacement curves of different material responses and properties: (a) elastic solid, (b) brittle solid, (c) ductile solid, (d) crystalline solid, (e) brittle solid with cracking during loading, (f) polymer exhibiting creep. From [48].

A further consideration for indentation tests is the effect of material pileup around the indenter. This is particularly important for indentation into soft films on harder substrates wherein the film properties may be enhanced by substrate effects. This was investigated by Tsui and Pharr [173] in their analysis of soft aluminium films. For harder films, such as DLC, pileup is less prominent. Bharathy et al. [174] did however note that the effect was noticeable in Ti doped DLC which were softer than pure DLC (12 GPa compared to 25 GPa).

2.4.1.2   ISO 14577 Standard for Instrumented Indentation

The ISO 14577 standard defines the parameters and methodologies that should be adopted during indentation to ensure that materials can be compared in terms of the force and displacement during elastic and plastic deformation. The data analysis is performed as described above. The standard specifies the ranges of loads (F) and depths (h) in different ranges [162]. These are:

- macro range: $2\,\mathrm{N} \leqslant F \leqslant 30\,\mathrm{kN}$

- micro range: $2\,\mathrm{N} > F; h > 0.2\,\mathrm{\mu m}$

- nano range: $h \leqslant 0.2\,\mathrm{\mu m}$

36

In the micro and nano ranges, the forces are adjusted as appropriate to give the required indentation depth. Most commonly a diamond Berkovich indenter is used for indentation but the standard makes allowances for other shapes and materials; these being [162]:

- diamond indenter shaped as an orthogonal pyramid with a square base and a angle of 68° between the axis of the pyramid and one of the faces (Vickers pyramid)

- diamond pyramid with a triangular base and an angle of 65.27° between the pyramind axis and one face (Berkovich pyramid)

- hard metal ball (used specifically for the determination of the elastic behaviour of materials)

- diamond sphero-conical indenter

Two methodologies of feedback control can be employed in the measurement of the data, either force-controlled or depth-controlled. The force and displacement are to be monitored continuously throughout the test. The machine compliance and correct indenter area function should be able to be calculated by the indenter platform. The surface should be cleaned before any indentations are performed; either a dry, oil free, gas stream, the application of subliming particle stream of CO_2 or rinsing with a chemically inert solvent and leaving to dry [162].

The temperature at which the test takes place in should be monitored, typically in the range of 10–35 °C is allowable however temperature stability generally more important than the actual test temperature (unless specifically testing the hot hardness of a material). In the nano and micro range the temperature and humidity should be controlled and remain in the range 23 ± 5 °C and 45 ± 10 %.

Surface roughness affects the scatter of indentation experiments such that when the roughness value (R_a) approaches the same value of the indentation depth, the contact area will vary relative to the peaks and valleys of the surface. The surface finish should be as smooth as facilities permit with the ideal R_a value being less than 5 % of the maximum penetration depth. For indentation into thin films the maximum depth of indentation should be no more than 10 % of the film thickness [162]. Details on roughness parameters and film thickness measurement methods will be provided in Section 2.5.

The 10 % film thickness "rule" is is something of an oversimplification for instrumented indentation testing. For hard coatings on softer substrates it provides a reasonable rule of thumb however there are many caveats to its use. Fisher-Cripps [48] noted that it doesn't strictly apply for nanoindentation where the objective is modulus determination as this value is less depth sensitive than hardness. Furthermore, he stated the physical basis of the rule is dubious; its application is mainly with sharp indenters as with blunt indenters when increasing the load in successive indentations no plateau in hardness would be observed as part of the extrapolation technique [166]. Indeed in older papers such as those of Bückle [175], the ratios of the hardness values of the coating and substrate are identified as being key. Bückle summarises that this method is an approximation with debatable physical meaning. For thin coatings, we can refer to the work of Pollock and Ross and co-workers [176, 177], who found than in their development and analysis of ultra-low load hardness tester that for films less than 1 µm the plasticity of the film is difficult to estimate (particularly with soft films). Furthermore, for this case quantitative mechanical characterisation over a continuous depth range is highlighted as a using methodology as substrate effects are seen at a greater relative indentation depth (penetration depth in relation to the total film thickness) than that predicted by macroscopic theory. In the case of

hard films, the effect can be as great as 2.5 times the film thickness. This paves the way for partial load-unload indentation in Section 2.4.1.3.

The standard is extremely thorough in its specification of the abilities of the indenter platform and therefore it is recommended that the standard itself is consulted for further details. The summary provided in these paragraphs is enough to give the reader a brief overview without retreading all the details of the standard.

2.4.1.3 Partial Load-Unload Indentation

The single indentation methods used by the ISO 14577 standard are not the only method available for nanoindentation. Partial loading/unloading indentation allows for the assessment of mechanical properties with change in contact depth by performing a series of increasing load indentations to probe to larger contact depths with each cycle. This is particularly useful for mapping the effects of multiple layers in the coating structure and for the effect of the substrate [178]. This technique is not applied often in literature as the analysis of data is more involved that typical single indentation. Elastic modulus must be extrapolated back to zero contact depth to correct for the value dropping off due to substrate effects. Hardness usually sees a low value measured in the initial indentations (at low contact depth and low load), this is often ascribed to ISE however it is instead due to the roundness of the tip of this scale of testing resulting in an initial elastic contact. At larger loads, a more developed plastic zone will form causing the hardness to plateau. It is at this value that the hardness should be taken. At larger loads, the hardness will decrease due to substrate effects being seen [166].

Feng et al. [179] used this technique and developed a portable hand-held load-depth sensing micro-indentation system that does not require the load-induced indentation contact area and depth. Klapperich et al. [180] applied partial unloading indentation to study industrial polymers, allowing them to investigate how the polymer structure affects the mechanical properties and visco-elastic behaviour. Figure 2.8 shows where partial unloads may occur in a full indentation cycle. The labelled AC ripple is used in the continuous stiffness method in which a small sinusoidally varying signal is imposed upon the DC signal that drives the indenter. This allows for measurement of the contact stiffness at any point in the along the loading curve instead of being limited to the unload. This technique is ideal for nanometre thin films due to its sensitivity [181].
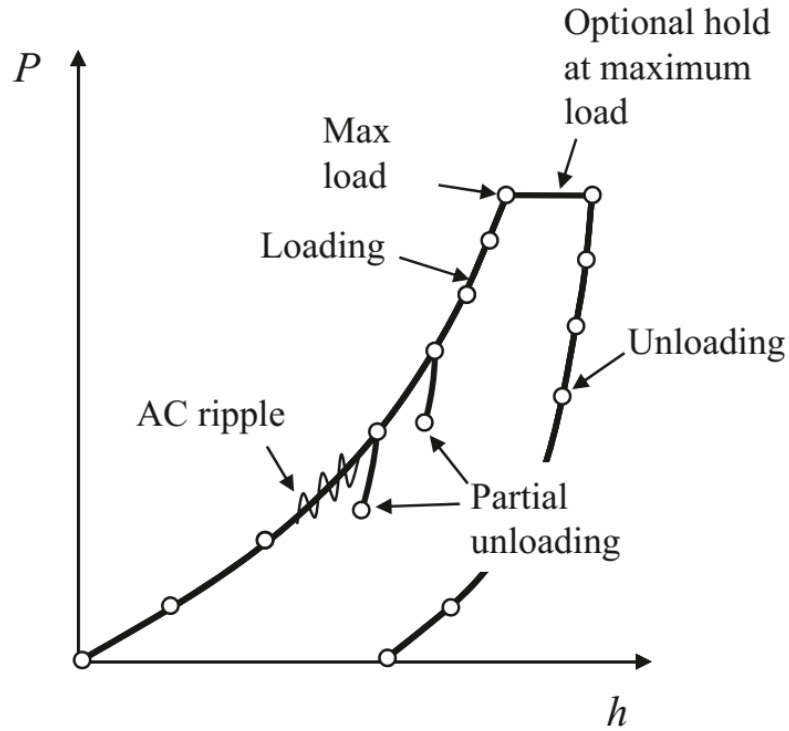
Figure 2.8: Difference in the load-displacement curve between partial unloading and single indentation. From [48].

Cyclic indentations into a material could result in some level of fatigue or work hardening. Xu et al. [89] proposed an indentation fatigue law similar to equation 2.14:

$$F_a = F_f \left(N_f\right)^m \tag{2.28}$$

where F_f and m are the indentation fatigue strength coefficient and exponent respectively. Multi-cycle indentation was utilised by Chicot et al. [171] to investigate the visco-elasto-plastic properties of magnetite on the elastic modulus; finding that the same bulk modulus value was found each time with repeated cycles at increasing indentation depths. Chicot et al. [90] also performed fatigue reliability analysis of solder joints using a cyclic indentation micro-indentation technique. They found that the indentation strain could be mapped to the Manson-Coffin fatigue law.

This methodology of indentation has the potential to better explore the coating and substrate behaviour of multi-layered systems (explored in Section 2.4.1.5) in a more elegant single test technique. ISO standard indentation can be performed in either load controlled and depth controlled modes however depth sensitivity is required in both cases as the 10 % limit with respect to total coating thickness must be respected. Partial load-unload indentation can be performed entirely in a load controlled mode (with depth sensing maintained through testing) which simplifies the experimental set up. Knowledge of the coating thickness is not required before indentation further simplifying the full coating analysis. A downside is that multi-step indentations will take longer than a complete set of individual indents but it will allow for the full coating architecture to be studied rather than the coating alone. As the indenter remains in contact with the sample surface for an extended period of time, a greater level of atmospheric control is required within the indenter system.

The lower depths probed by this indentation technique will show an undeveloped plastic region that grows to the full plasticity thereby measuring the surface hardness. The

hardness will decrease with increasing indentation depth as more substrate effects are seen [166]. As the hardness value falls with respect to depth, the level of load support can be evaluated by analysing how quickly the substrate hardness is reached relative to the total coating thickness. Modelling techniques such as those of Nix and Gao [182] and Korsunsky et al. [183] can then be applied to analyse the entire coated system mechanical properties. This method requires a more in depth understanding of the nanomechanics of indentation but can ultimately be a more information-rich technique. These factors will be explored in this study to show the overlooked importance of this indentation method.

2.4.1.4 Macro/Microindentation and Indentation Geometries

Though microindentation can refer to adapting the same methodologies detailed in ISO 14577 and applying them to thicker coatings using a larger load, it is a term more often used to apply to alternative hardness measurement methods such as Vickers and Rockwell indentation [184]. These methodologies also have their macro-scale corresponding version, the difference is the load applied. These methods will be the focus of this section. Though they are generally limited by collecting their data post-indentation by analysis of the plastic deformation of the surface, they should be detailed to provide a more complete picture of the methodologies available.

The Vickers indenter is a square based pyramid whose opposite sides meet at the apex with an angle of 136°, the edges at 148° and the faces at 68°. The Vickers diamond hardness number (HV) is calculated by:

$$HV = \frac{L}{A_c} = \frac{2L}{d^2} \sin \frac{136°}{2} = 1.8544 \frac{L}{d^2} \qquad (2.29)$$

where L is the indenter load (measured in kgf) and d (mm) is the length of the diagonal measured corner to corner on the residual impression. Vickers can be converted into more standard hardness units (MPa) by considering that the Vickers method uses the surface area of an ideal pyramid not with projected contact area. This results in a geometrical scaling factor of 0.927. Further due to the use of kgf and mm, the final relation becomes $HV = 0.094545 H_{IT}$ to convert to MPa. GPa is seen more in scientific publications as it allows for better comparison with the elastic modulus [185].

The Rockwell indentation is performed with with either a sphere or a cone depending upon the scale used. Hardness is determined by measuring the depth of penetration of an indenter under a large load compared to the penetration made by a smaller preload. The Rockell hardness (HR) is calculated by:

$$HR = N - 500h \qquad (2.30)$$

where h in mm is the difference between the two penetration depths and N is dependent upon the indenter (100 for sphero-conical and 130 for a ball). Other indentation methodologies exist such as the Knoop or Buchholz test [184].

2.4.1.5 Length Scale Effects in Multi-layered Systems

The load and size of indenter used for any particular test can affect the measured hardness of a polycrystalline material. At the macro-scale, the contact region of an indentation will sample from multiple crystalline regions therefore any inhomogeneity across the sample

is averaged. As we progress to lower length scales, this effect is seen to a lesser degree. At the micro-scale, the microstructure of a material can be examined in more detail. Once the nano-scale is reached, the experimental parameters used for indentations allow for thin films to be indented or for individual crystallites to be sampled [184]. Figure 2.9 demonstrates this.
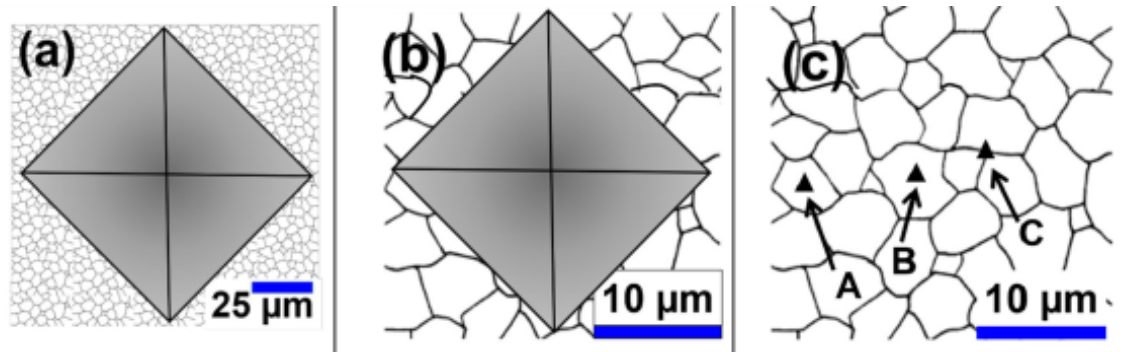
Figure 2.9: Schematic of indentations into a polycrystalline material at (a) macroscale; (b) microscale and (c) nanoscale. From [184].

These differences, depending on the length scale of testing selected, give rise to a difference in the measured hardness at low indentation load. If a fully developed plastic zone is present, the indentation hardness is seen to be greater at low load as shown in Figure 2.10. This is known as the indentation size effect (ISE) and has been attributed to several things such as high elastic recoveries, pileup, work hardening and the presence of grain precipitates [166, 184]. Zhang et al. [186] explored both modelling and experimental methods to examine the effect of roughness on ISE, finding that a rougher surface will require more energy dissipated into the surface to induce plastic deformation and therefore have a more prominent ISE.
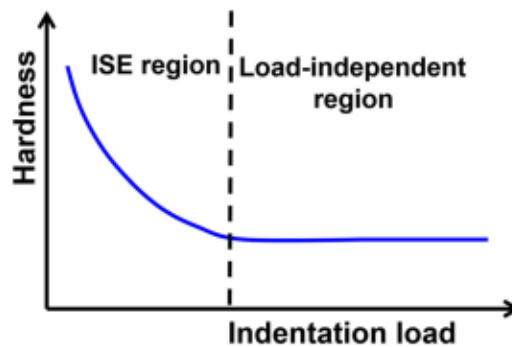
Figure 2.10: The indentation size effect. From [184].

The relation between micro-indentation hardness (H) and indentation depth (h) is shown in this model by Nix and Gao [182]:

$$\left(\frac{H}{H_0}\right)^2 = 1 + \frac{h^*}{h}$$ (2.31)

where h^* is the characteristic length (dependent on the indented material properties and angle and is on the order of microns) and H_0 is the indentation hardness for a large indentation depth ($h \gg h^*$). This model is used by many authors to explain ISE at the

micro-scale [184] but it is not valid at the nano-scale ($h < 100\,\mathrm{nm}$) because it only accounts for sharp indenters. On the nano-scale the effect of tip radius is greater at low indentation loads and depths. It also assumes that all dislocations are in a hemisphere equal to the contact radius of the indentation [187]. Recent reviews by Gouldstone et al. [188] and Pharr et al. [189] have examined work explaining the ISE at the nano-scale and found that the effect appears when the length scale of deformation approaches the critical microstructural length of the dislocation spacing. There is, however, no agreement on the prediction of ISE and much work is dedicated to modelling the behaviour.

As an indenter penetrates into a thin film, the measured mechanical response will be affected by the mechanical properties of the substrate material and it's relative penetration depth. With greater depth of penetration, the measured mechanical properties will be more proportionate to that of the substrate [184]. Several models have been proposed to model the substrate effects seen at deep penetrations into coated systems. The first to attempt this was Bückle [175] who modelled the hardness of the system (H_{fs}) as a linear interpolation of the substrate hardness (H_s) and the film hardness (H_f):

$$H_{fs} = \alpha H_f + (1 - \alpha) H_s \tag{2.32}$$

where α is a coefficient defined by:

$$\alpha = \left[1 - \frac{e^{(h-t)}}{\Delta t} \right]^{-1} \tag{2.33}$$

t is the film thickness, h is the indentation depth and Δt is the dimension of the transition region (not well defined by Bückle). This work also established the general practice of indentations being no more than $1/10$ of the film thickness that was later adopted into the ISO 14577 standard.

Korsunsky et al. [183] presented a model of fitting indentation hardness data with the relative indentation depth based on the expansion of the elastically and plastically deformed volume underneath the indenter during loading in nanoindentation [48]. The model is presented as:

$$H_{fs} = H_s + \frac{H_f - H_s}{1 + k \left(\frac{h_c}{t} \right)^2} \tag{2.34}$$

where k is a fitting parameter and h_c is the contact depth seen in the Oliver-Pharr method [163].

2.5 Surface Engineering

2.5.1 The nature of surfaces

Before detailing the various methods of surface modification, surfaces themselves must be defined. Though this may initially seem like an odd statement, surfaces have complex structure and complex properties dependent upon the nature of the solid, method of surface preparation and interaction between the surface and environment (whether it be a solid, liquid or gas interface) [64]. Figure 2.11 shows the typical composition of a solid surface.
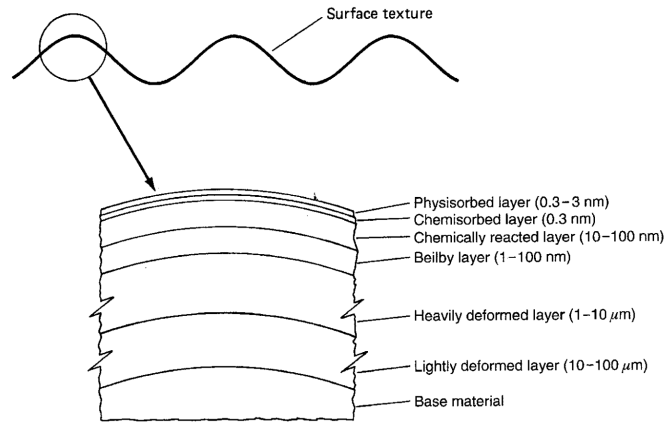
Figure 2.11: Composition of a typical solid surface structure with magnified surface texture. From [64].

Further to the composition and structure of surface layers, their topography must be addressed as well. All surfaces contain irregularities on various length scales from larger scale shape deviations to that on the order of inter-atomic distance [64]. Figure 2.12 shows a schematic of roughness, waviness and lay of a surface as part of the typical surface texture. Lay refers to the prominent directional machining marks. Waviness is the texture upon which the roughness is superimposed. Roughness itself is the irregularities in the production process left by some machining agent [44]. Numerous parameters exist to define the roughness of a surface, in fact there about 59 that are commonly used. Roughness can be defined in both two-dimensional or three-dimensional forms. The most common is the arithmetic mean height (R_a) as it is easy to define, easy to measure and gives a good general description of height variations. No information is given about the wavelength in this metric and it is not sensitive to small changes in profile. Its mathematical definition is [190]:

$$R_a = \frac{1}{l} \int_0^l |y(x)| \, dx \tag{2.35}$$

$$R_a = \frac{1}{n} \sum_{i=1}^{n} |y_i| \tag{2.36}$$

Amusingly, many researchers have complained over the past 40 years that there are a profusion of roughness parameters and that many of them are redundant. More parameters have appeared over this time and not all are related to functional properties [191].

2.5.2 Defintion of Surface Engineering

Surface engineering can be defined as the application of both traditional and innovative surface technologies to produce a composite material with properties unattainable in either the base surface materials individually [19]. These alterations can improve the appearance, provide protection from environmental damage or to enhance the mechanical or physical performance of the surface [25]. It is a multi-disciplinary subject concerned with the manufacturing process of surface layers for both technological and end use purposes, their connected phenomena and the performance effects obtained [193, 194]. With proper
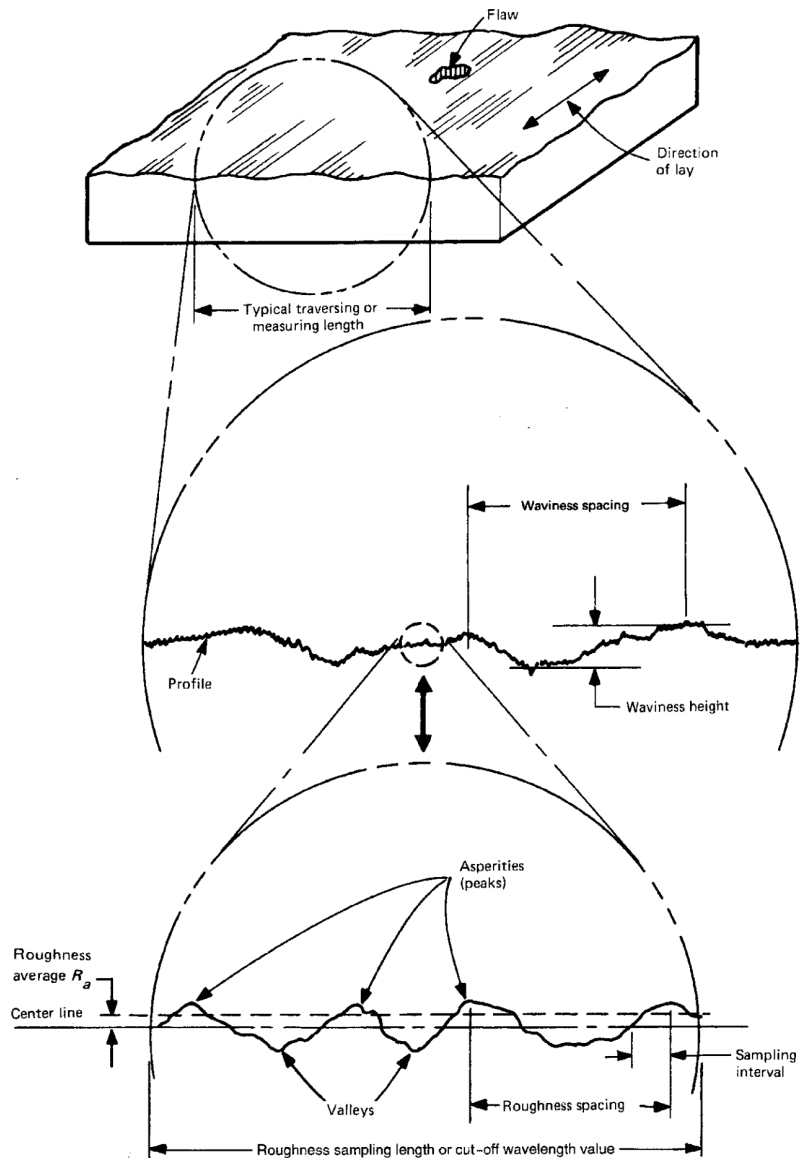
Figure 2.12: Schematic of surface patterning (lay, waviness and roughness). From [64, 192].

implementation of these technologies, entirely new products can be created to serve in extreme environments or increase the efficiency of pre-existing designs.

The field dates back to the mid 1900's with first efforts focused on modifying surface properties to reduce wear, reduce friction and improve appearance [195]. As with tribology, the formalisation of the study can relatively late; the term first appeared in late 1970s and was pioneered in the UK with the introduction of the journal Surface Engineering by Tom Bell of Birmingham University in 1985 [27, 196]. Multiple processes exist to modify surfaces. These can include methods of modifying the surface chemistry (e.g. carburizing), methods without altering the surface chemistry (e.g. flame hardening) and the coating of surfaces [197].

The application of coatings to improve the surface properties is now a well established technology however the whole coating/substrate system must be optimised to ensure the desired properties are achieved. A coating cannot be applied to a low quality bulk material with the expectation that it will perform significantly better. The substrate must

be designed for appropriate strength and toughness to avoid catastrophic failure [198]. Matthews et al. [75] expanded on this in their work on analysing the contact mechanisms and selection of particular coatings to meet the needs of the system. For example, DLCs were suggested to be excellent for fretting and lubricated contact but sub-optimal for impact and fatigue loading without the correct structural design. Dearnley [199] noted that surface engineered materials have a high potential to make high impact and meet tribological challenges across several sectors including automotive (with wear resistance coatings for piston rings, roller bearings and cam followers), tools (metal carbides and nitrides for cutting steels and cast iron) and joint replacements (TiN for Ti-6Al-4V and CrN for Co-Cr-Mo). Schwarzer [200] expanded upon previous numerical methods to provide a set of analytical tools for future coatings and surface optimisation. Beake et al. [201] detailed a series of nanomechanical test methods to aid in the optimisation of high speed machining tools. These methods included nanoindentation at room temperature and up to 500 °C and nano-impact. Some of the latest innovations in coating design lie in the application of chameleon coatings which are able to adapt to their environment by changing their chemistry and structure as required to control friction and wear in extreme environments. This makes them perfect for aerospace applications [202, 203].

2.5.3 Plasmas in Coating Technologies

Before addressing the specifics of the different coating technologies commonly applied in industry, it would be beneficial to review the fundamental theory surrounding plasmas as they are used widely in (plasma-assisted) physical and chemical vapour deposition processes. Plasmas occur throughout nature, in fact the majority of the universe exists in an ionised state. Colloquially, plasmas are known as the fourth state of matter because of this. A plasma is an ionised gas; when a gas is given enough energy such that the constituent atoms collide with each other with sufficient energy to knock electrons out of their orbitals to the continuum. This creates a gas with a mix of electrons and positively charged ions. The degree of ionisation can vary from 100 % (fully ionised) to low values (10^{-4}–10^{-6} for partially ionised gas). Plasmas have unusual properties compared to other states of matter. The separation between ions and electrons creates electric fields and flow of charged particles further creates currents and magnetic fields. The concept of local thermal equilibrium is often used to define the type of plasma, plasmas formed in laboratory conditions are generally in thermal equilibrium whereas for expansive interstellar plasmas the temperature can vary throughout the cloud. Laboratory (process) plasmas can have their parameters varied by changing the precursors gas/gases, the pressure, the electromagnetic field structure, discharge configuration and temporal behaviour (by pulsing) [204, 205].

The creation of plasmas can occur by multiple methods. Though it is possible to create a plasma by heating up a container of gas this is inefficient or generally not possible as the temperature required for the plasma exceeds that achievable by the container. Typically, in a laboratory a smaller amount of gas is heated and is ionised by some form of electric current or by a pulses of radio or microwave radiation [204, 205]. Several specific discharge methods [205] Table 2.2 shows the properties of a variety of different plasmas found throughout the universe. For deposition technologies we use process plasmas.

The electric discharge of plasmas is defined by multiple regimes depending on the voltage and current of the plasma thereby defining whether there is a dark discharge, glow discharge or arc. Most commonly glow discharge plasmas are used for process plasmas wherein the voltage is almost independent of the current over several orders of magnetude

in the discharge current. The characteristic glow is caused by excitation collisions as the electron energy is high enough [205, 206].

Table 2.2: Typical parameters for various types of plasmas. From [204].

	Length scale (m)	Particle density (m^{-3})	Electron temperature (eV)	Magnetic Field (T)
Interstellar gas	10^{16}	10^6	1	10^{-10}
Solar wind	10^{10}	10^7	10	10^{-8}
Van Allen belts	10^6	10^9	10^2	10^{-6}
Earth's ionosphere	10^5	10^{11}	10^{-1}	3×10^{-5}
Solar corona	10^8	10^{13}	10^2	10^{-9}
Gas discharges	10^{-2}	10^{18}	2	–
Process plasmas	10^{-1}	10^{18}	10^2	10^{-1}
Fusion experiment	1	10^{19}–10^{20}	10^3–10^4	5
Fusion reactor	2	10^{20}	10^4	5

Plasmas have multiple uses beyond the deposition of thin films including the surface activation and functionalisation of polymers, cleaning surfaces and surface hardening [204, 205]. Throughout the universe, regions of high plasma concentration are responsible for the creation of stars [207]. Figure 2.13 shows an image of the Orion Nebula which contains multiple dense molecular clouds which are the birth sites of high mass stars in ionised hydrogen clouds called HII regions.

2.5.4 Physical Vapour Deposition and Chemical Vapour Deposition Coatings

Thin film coatings can be applied by either physical vapour deposition (PVD) or chemical vapour deposition (CVD). PVD consists of atomistic vaporisation by which material is vaporised from a solid or liquid source in the form of a vapour through a vacuum or low pressure/plasma environment after which it condenses. Coating thickness can range from a few nanometres to thousands of nanometres. A multitude of PVD methods exist including vacuum evaporation, sputter deposition and ion plating. CVD consists of the deposition of atoms or molecules by high temperature reduction or decomposition of a chemical vapour precursor [194, 209].

Plasma enhanced chemical vapour deposition (PECVD) (sometimes known as plasma assisted chemical vapour depositionn (PACVD)) uses reactions activated by a plasma thereby bringing the temperature of the deposition down substantially. This combination of a chemical and physical process effectively bridges the gap between PVD and CVD.
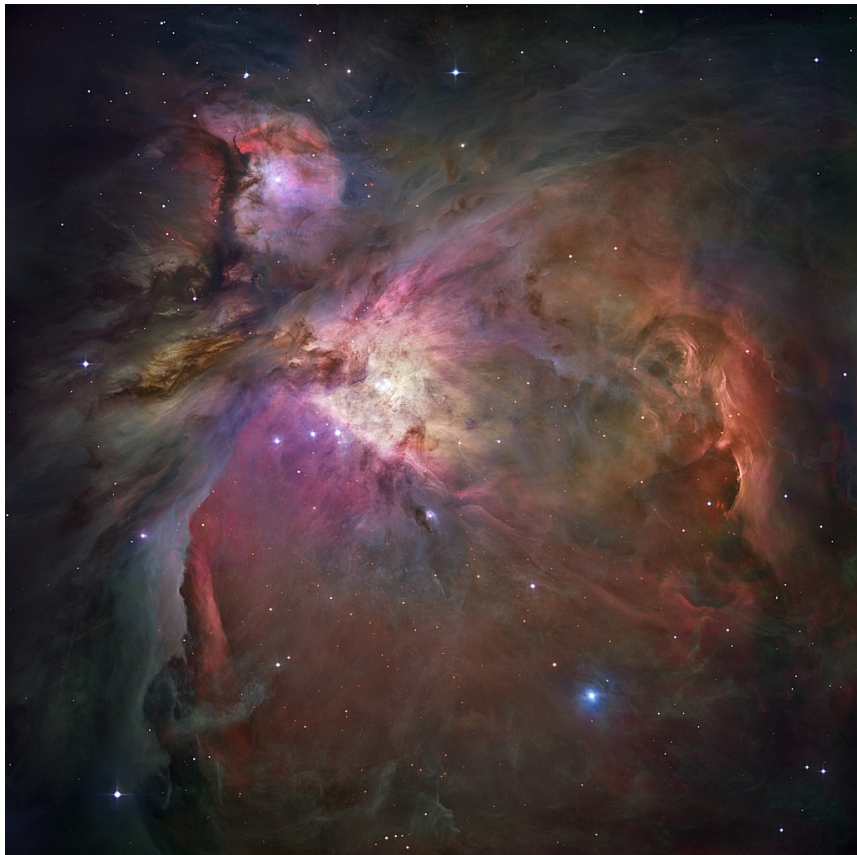
Figure 2.13: The Orion Nebula. From [208]

Two types of plasma are used in CVD, either glow discharge or arc. Glow discharge plasmas can also be generated using microwaves [209]. The plasma flow of a magnetron sputtering source can be seen in Figure 2.14.

Figure 2.14: A magnetron sputtering source. From [210]

Thornton was a prolific author in the prediction of the structure formed by thin films. In 1974 he published a paper [211] detailing how the geometry of the deposition system and the deposition conditions affects the structure and topography of sputtered coatings. His 1977 paper [212], further expanded on this establishing a structural zone model dependent upon the argon pressure and substrate temperature. Thornton and Hoffman [213] explored the stress effects in thin film deposition establishing a contribution of intrinsic growth stress and thermal stress in film deposition. Issues are encountered when high melting point coatings with low thermal expansion are deposited on polymers as the thermal expansion of the substrate will cause cracking. This can be overcome by depositing intrinsic compressive stress into the coating. The hyperthermal species responsible for film growth are affected by a multitude of factors. The subplantation model is affected by the angle of incidence of the species, crystallographic orientation of the substrate, substrate properties and temperature [214]. Ordered coatings have crystal orientations that can be assessed using electron back scatter diffraction (EBSD), this technique can also be utilised to assess the substrates themselves to provide a deeper understanding of the deposition mechanisms [215].

2.5.5   Diamond-Like Carbon

DLC is used to describe a class of mechanically hard amorphous metastable carbon materials [35, 216, 217]. Properties of DLC can vary with the ratio of sp^2 (threefold planar carbon-to-carbon bonding) to sp^3 (fourfold tetrahedral carbon-to-carbon bonding) hybridised bonding and hydrogenation of the film [216, 218, 219]. In addition to high hardness, DLC films are characterised by chemical inertness and low coefficients of friction making them ideal wear resistant coatings [217, 220]. High residual internal compressive stresses are common in harder DLC coatings, methods to reduce these stresses include the inclusion of metal doping into the DLC layer and presence of a functionally graded metallic to carbide interlayer [221–225]. Measurement of residual internal stress is typically performed by measuring the curvature of the substrate materials by applying the Stoney equation [226]. Measurement of the curvature is typically performed by a surface profilometer [227–230].

Newer methods of reducing the internal stress include the application of multilayer coatings such as that performed by Baba et al. [229] in their application of using a bilayer coating. This circumvents the issues of metallic doping wherein film properties such as hardness or roughness can change. Renzilli et al. [231] used a combination of modelling and experimental methods to tailor the residual stress profiles of Cr-CrN coatings. The application of multiple designed layers allowed for the reduction in von Mises stress throughout the multi-layer structure. Matthews et al. [232] also investigated this phenomena with the application of beam bending a multi-layered material (with the addition of FEM) to show that alternating hard and soft, or high and low modulus layers can better accommodate surface deformation.

The initial developments on DLC films were almost accidental. In 1953, Schmellenmeier was the first to note the formation of a hard black film on the cathode of his glow discharge apparatus in the study of the influence of ionised acetylene (C_2H_2) gas on the surfaces of tungsten-cobalt alloys. [233]. In a later paper he noted that these micron thick films were amorphous and using x-ray diffraction, identified some regions were diamond crystallites [234]. The major initial advance came in 1971 with the work of Aisenberg and Chabot [235], they were the first to coin the term "diamond-like carbon" in their work on forming carbon films by ion-beam deposition. Since then there were a few publications

on DLC with a huge uptake in popularity in the 1990s that has continued to present day [34, 236].

The next section will detail the terminology used to refer to DLC coatings as the initialism refers to a relatively broad class of materials. Additionally, some elements of carbon's structural chemistry should be reviewed to clarify the structures present within amorphous carbon and its various bonding types.

2.5.5.1 Terminology

It is first important to note that the term DLC can be a misnomer, the mechanical properties of amorphous carbon coatings can vary greatly depending upon their carbon composition and presence of elemental dopants and therefore the properties can vary a great deal from diamond. Some can have greater graphitic content and are sometimes referred to as graphitic-like carbon (GLC) [227]. The following classifications can be applied to the family of amorphous carbon compounds [217, 237]:

- a-C - Hydrogen free amorphous carbon films with a greater proportion of sp^2 bonding. The "a" donates an amorphous coating.

- a-C:H - Amorphous hydrogenated films containing a modest sp^3 fraction. "H" denotes an amount of hydrogenation in the coating. Several subtypes of this coating exist:

  - a-C:H films with the highest H content (40–50 %) can have up to 60 % sp^3 however the bonds are hydrogen terminated resulting in a soft material with low density; these films are known as polymer like a-C:H (PLCH).
  - a-C:H films with intermediate H content (20–40 %) have lower sp^3 content compared to polymer like a-C:H (PLCH) but more C-C sp^3 bonds; this results in better mechanical properties. These films are called diamond like a-C:H (DLCH).
  - a-C:H with low H content (<20 %). These films have high sp^2 content and sp^2 clustering and are commonly known as graphite-like a-C:H (GLCH).

- ta-C:H - Tetrahedral amorphous hydrogenated films possessing a significant sp^3 bonding fraction (> 70 %). These films can have ~ 25 % hydrogen content. These properties results in a high density (up to 2.4 g cm^{-3}) and higher Young's Modulus (up to 300 GPa).

- ta-C - Tetrahedral amorphous carbon. These films lack hydrogenation and have high sp^3 content giving them a high hardness (40–90 GPa).

Table 2.3 gives an overview of the amorphous carbons discussed in this section as well as their typical composition ranges and properties.

2.5.5.2 Carbon Chemistry

Carbon is able to form a variety of crystalline and disordered structures due to its ability to exist in three bond hybridisations. Hybridisation refers to the overlapping of electron orbitals [216]. The different physical forms (crystalline structures) that carbon can be assembled into is called its allotropes (or polymorphs). It should be clarified that the

capability of an element to assemble itself into different forms is not unique to carbon and other group 14 elements in the periodic table can also do this [238]. Figure 2.15 shows some of the various allotropes of carbon.
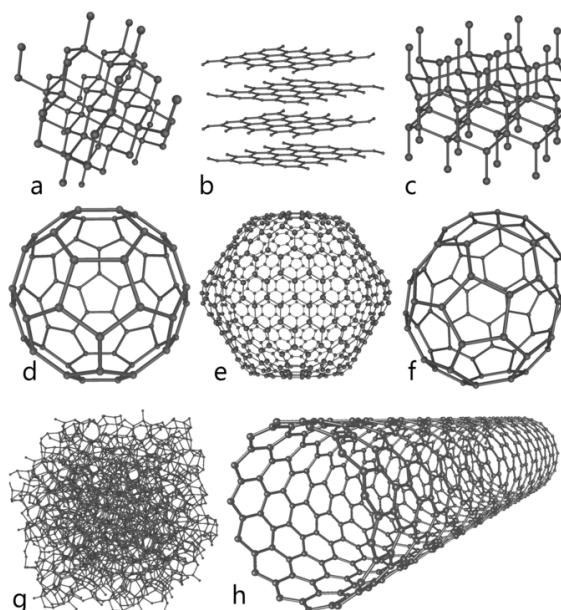
Figure 2.15: Carbon allotropes: a) diamond, b) graphite, c) lonsdaleite, d) C60 (buck-minsterfullerene or buckyball), e) C540, f) C70, g) amorphous carbon, and h) single-walled carbon nanotube (buckytube). From [239].

In sp^3 bonding, as found in diamond, the carbon atom's four valence electrons are each assigned to a tetrahedrally directed sp^3 orbital. This forms a strong σ bond to an adjacent atom. For the three-fold configuration seen in graphite, three of the four valence electrons enter trigonal sp^2 orbitals forming σ bonds in the plane The fourth electron of the sp^2 is in a pπ orbital, orientating normal to the σ bonding plane In the sp^1 config-uration, two of the four valence electrons enter σ orbitals, each one forming a σ bond in the $\pm x$-axis with the other two electrons entering pπ orbitals in the y and z directions [216, 240]. Carbon bonded in the sp^2 configuration has strong σ bonds with the plane but weak Van der Waals bonding between layers [241, 242]. This gives graphite strongly directional mechanical properties with each layer able to be easily sheared [217]. Di-amond's structure and mechanical properties are derived from its strong, directional σ bonds (with short bond length and high bond energy) [217, 243]. Figure 2.16 shows the bonding structure of the various hybridisations.
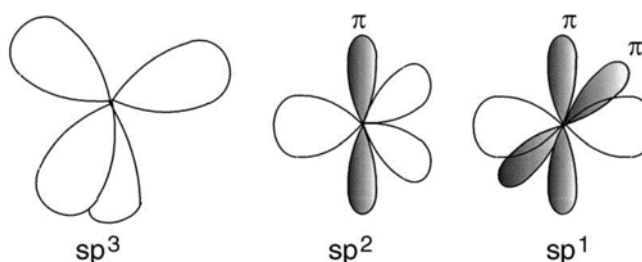
Figure 2.16: The three carbon bond hybridisations with varying numbers of π bonds. From [216].

2.5.5.3 Mechanical Properties And Structure Of DLC

DLC consists of sp^2 and sp^3 bonded carbon atoms and can also contain large amounts of hydrogen within its structure. Their mechanical and tribological properties vary due to their microstructure, composition and chemistry [217, 244, 245]. Due to DLC films nature as hard coatings, they will generally display brittle behaviour however this can change with differences in the sp^2/sp^3 ratio [216, 218, 219] and dopants [36] affecting the mechanical properties for varying coating structures. This allows DLC to be tailored to required properties to a greater degree than other coatings.

The amorphous nature of DLC films is length scale dependent. At a small enough scale it can be seen that DLC is composed of small crystallites with a local configuration of either sp^2 or sp^3 [238]. This results in a random stable network but the cluster size is sufficiently small that electron diffraction techniques show an amorphous material. DLC has no long range order [238]. The structure of an a-C:H film is shown in Figure 2.17. An sp^2 cluster can be seen highlighted and the lack of long range order can be readily observed.
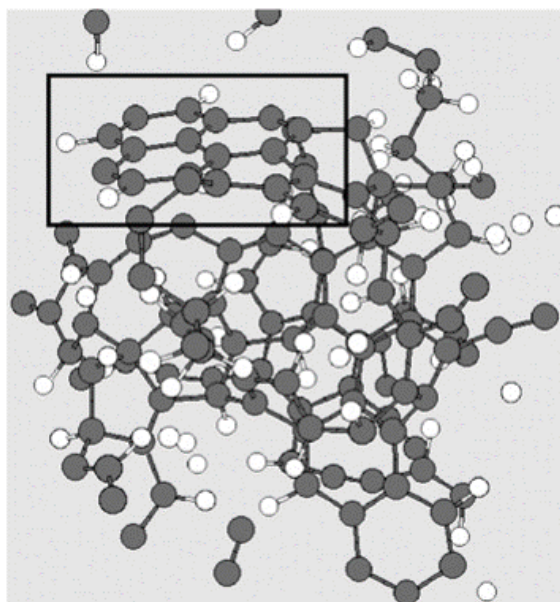
Figure 2.17: Structural model of an a-C:H film with a density of $1.7\,\mathrm{g\,cm^{-3}}$, 30 % hydrogen, 65 % sp^2, 20 % sp^3 and 15 % sp^1 bonds. A cluster consisting of graphite-like rings is highlighted. From [34]

.

Figure 2.18 shows the various types of DLC formed when the sp^2/sp^3 ratio and level of hydrogenation is varied, this phase diagram was first proposed by Jacob and Möller [246].

The range of mechanical properties can be seen in Table 2.3 (located on page 52). H/E ratios over 0.16 suggesting excellent wear rates [216] but this is rarely seen in practice [244, 247]. DLCs have been shown to have an optimum range of H/E [248] particularly under impact wear where E/H can be more important [122] as opposed to other coatings such as AlTiN and TiAlCrN [118]. This relation will be explored further is Section 2.5.8.

Table 2.3: A comparison of the properties of different DLCs with diamond and graphite. From [217].

Types	sp3 content (%)	Hydrogen content (%)	Density (g cm^{-3})	Poisson's Ratio	Young's Modulus (GPa)	Fracture Toughness (MPa m$^{1/2}$)	Residual Stress (GPa)	Hardness (GPa)
Diamond	100	0	3.515	0.07	1144	3.4	–	100
Graphite	0	0	2.267	0.2	9–15	–	–	0.2
a-C:H (Hard)	40	30–40	1.6–1.22	0.4	140–170	1.2–1.6	1–3	10–20
a-C:H (Soft)	60	40–50	1.2–1.6	0.25	50	2.9–3.3	~1	<10
ta-C	80–88	0	3.1	0.12	757$\pm$47.5	–	<12	40–90
ta-C:H	70	30	2.35	0.3$\pm$0.09	300$\pm$49	–	8.4	$\leq$50
W DLC	50	20	2.5–16.3	0.2	100–150	1.0–2.5	0.9	13.2
Si DLC	60–84	15	1.85	–	100–175	–	1.0–2.5	20–25
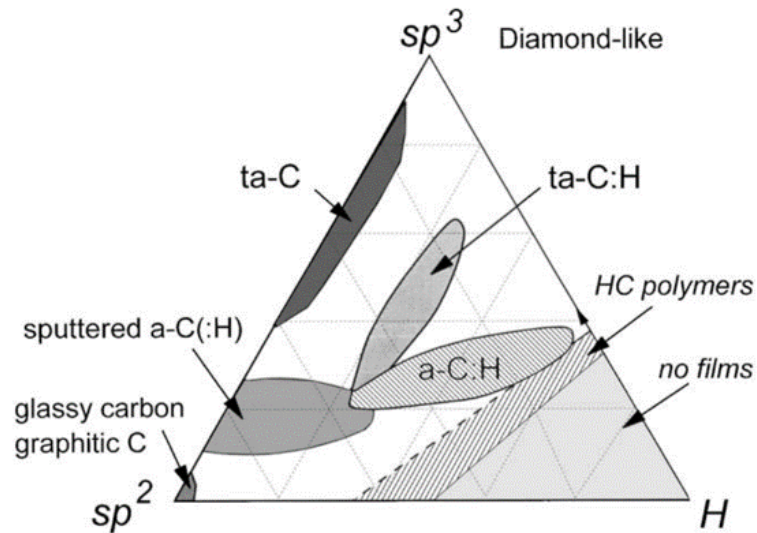
Figure 2.18: Ternary phase diagram showing the bonding present in types of diamond-like carbon [216].

2.5.5.4 Structural Characterisation Of DLC

Multiple characterisation methods can be used to determine the structural properties of DLC films. One of the most common methods is Raman spectroscopy [249]. The typical Raman frequency range for DLC is 1000–2000 cm^{-1}. In this frequency range, we observe a primary dual peak phenomenon. The D peak is around 1350 cm^{-1} and the G peak is around 1580–1600 cm^{-1} [250, 251]. The G band peak is due to the stretching of all bond pairs in sp^2 atoms (present in both chains and rings) and the D band is caused by the breathing modes of sp^2 atoms in rings [252, 253]. A smaller T peak is present around 1060 cm^{-1} and is caused by C-C sp^3 vibrations, this peak is not present in highly hydrogenated films [237]. Two main peak fittings are used for Raman spectra: Gaussian (for both peaks) and Breit-Wigner-Fano (BWF) for the G peak and Lorentzian for the D peak. Generally BWF+Lorentzian fittings use the peak height ratios whereas Gaussian fittings use the area ratio [250].

The ratio of the peaks gives us the amount of sp^2 hybridised bonding located in rings [254] with higher values indicating higher sp^2 content. From this, we can infer that in coatings with higher I_D/I_G ratio there is less sp^3 content. It should be noted that Raman spectra does not depend on just the sp^2/sp^3 ratio but also on the clustering of the sp^2 phase, bond disorder and presence of sp^2 chains or rings [250]. This is shown in Figure 2.19.
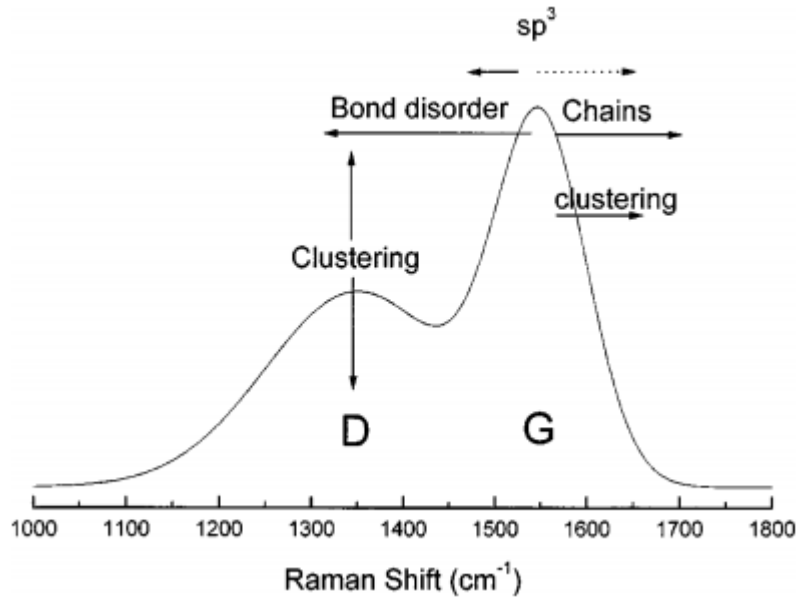
Figure 2.19: Schematic of the dual peak phenomena of carbon in Raman spectroscopy. From [250].

In general, Gaussian fittings are preferred for disordered materials and Lorentzian fits are used for crystalline materials due to its finite lifetime broadening [1] [250]. Newer Raman analysis techniques involve the use of multiple D and G peak fitting methods as it has been theorised that simple two-symmetric-line fits are not substantial enough to deconvolute the Raman spectra [255].

Electron microscopy can provide a wealth of information on the structure and composition of materials. Figure 2.20 shows a diagram of the interaction volume alongside the phenomena and information gained when an electron beam interacts with matter. The bulbous region is the electron beam excited interaction volume which can range from 0.1–10 μm in diameter [256]. scanning electron microscopy (SEM) uses an electron beam (which scans across the surface of a sample) to excite atomic electrons to be released as secondary electrons to give topographical information. transmission electron microscopy (TEM) instead uses short wavelength focussed electrons to pass through a thin sample allowing it to be imaged [257].

---

[1]No state has an infinite lifetime. The shorter the lifetime, the broader the spectral lines.
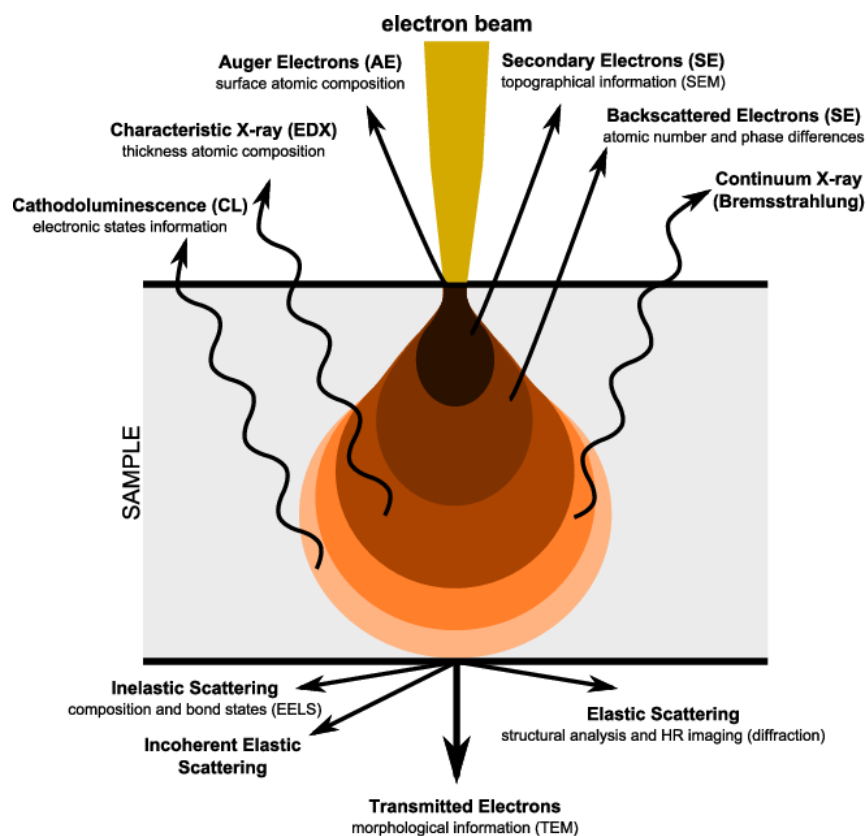
Figure 2.20: Electron matter interaction phenomena. From [258].

Multiple diffraction techniques exist to ascertain the crystallographic phase composition, grain size and lattice defect structure of a surface. X-ray diffraction (XRD) is a technique which scans x-rays over a range of angles to determine the crystal orientation and lattice spacing and thereby resolve the structure of ordered materials [259]. Transmission electron microscopy selected area diffraction (TEM-SAD) is a technique used within the TEM that diffracts the electrons depending on the structure of the material. Rings formed indicates many crystallites and spots indicate single crystals [257]. For amorphous materials, such as DLC [238], these techniques will not give a result typical of materials with a defined crystalline structure. Therefore, these techniques are typically used to confirm an amorphous structure (either entirely amorphous or a collection of smaller crystallites).

Electron energy loss spectroscopy (EELS) is a technique that involves analysing the energy distribution of mono-energetic electrons (typically of low energy in the range of 100–1000 eV) as they pass through TEM samples. This is an inelastic scattering process [260]. energy dispersive x-ray spectroscopy (EDX) involves analysing the energy of a characteristic x-rays produced by electron beam interaction in solids [256]. EDX is more sensitive to heavy elements as they produce more continuum intensity than light elements [261, 262]. EELS is preferable for light elements though it can be used for heavy elements with a higher energy electron beam [263].

EELS is the preferred method of determining the sp^3 fraction because it is also able to give the sp^2 content from the relative size of the π peak on the carbon K edge but also the valence plasmon peak (26–34 eV) giving the mass density. EELS is however a destructive and time consuming technique [264, 265]. X-ray photoelectron spectroscopy (XPS) can also be used to determine the sp^2/sp^3 ratio [266–268]. Figure 2.21 shows the deconvoluted core excitation speaks used to identify the composition of carbon films.
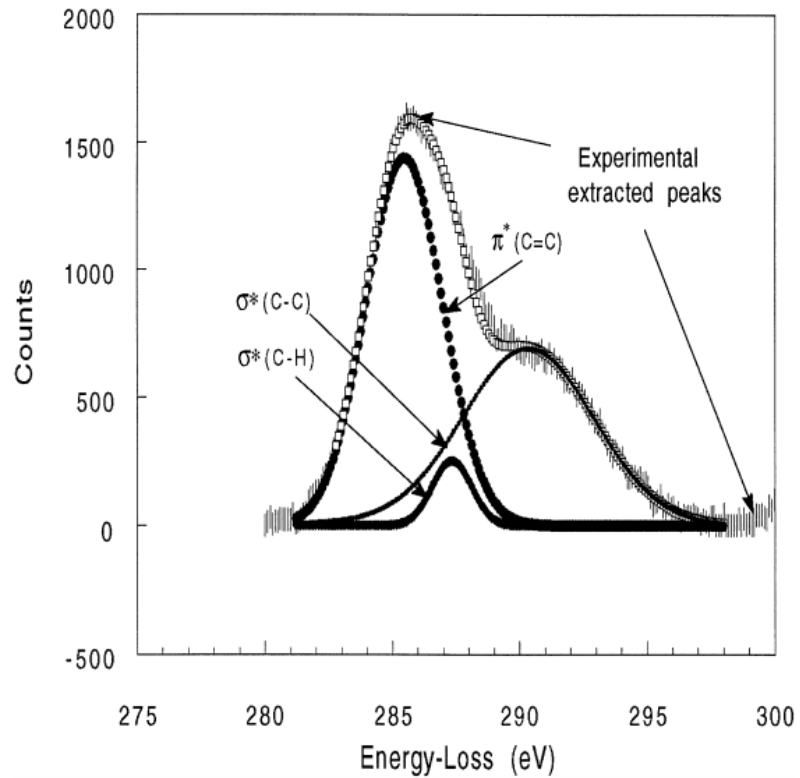
Figure 2.21: Deconvoluted core excitation peaks of carbon. From [265].

2.5.5.5 Dopants In DLC

The inclusion of dopants into DLC structures can modify properties such as the hardness, tribological properties or internal stresses to tailor it for different operating environments [36]. Doping with silicon gives improved corrosion resistance and humidity and temperature stability [269]. Si doping has also been seen to alter the sp^2/sp^3 ratio of the coating and increase adhesion to the substrate and non-lubricated performance is seen to be better than non-doped DLCs [270]. The use of metal such as tungsten as a dopant can reduce internal stresses and improve film adhesion [267, 271]. Adhesion of DLC is noted as being poor at high loads and under impact stresses [272]. In lubricated contacts, both dopants are seen to increase the wear rate however [270, 273]. Figure 2.22 shows the range of typical dopants and their effects on the structure.
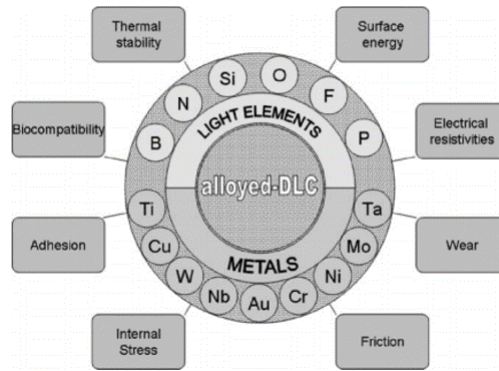
Figure 2.22: Schematic of typical doping elements and the altered properties in DLC. From [274].

2.5.5.6 Deposition Methods

DLC can be deposited by various methods and precursors such as radio fequency (RF) or direct current (DC) chemical vapour deposition (CVD), magnetron sputtering, vacuum arc and ion beam deposition [220, 245]. The use of hydrocarbon precursor introduces a level of hydrogenation into the coating structure [216, 217]. PECVD deposited films ha typically have greater levels of hydrogen content (up to 60%) [217, 220]. The ion energy (dependent upon the bias voltage and precursor gas) affects the character of the film as seen in Figure 2.23 [275, 276].
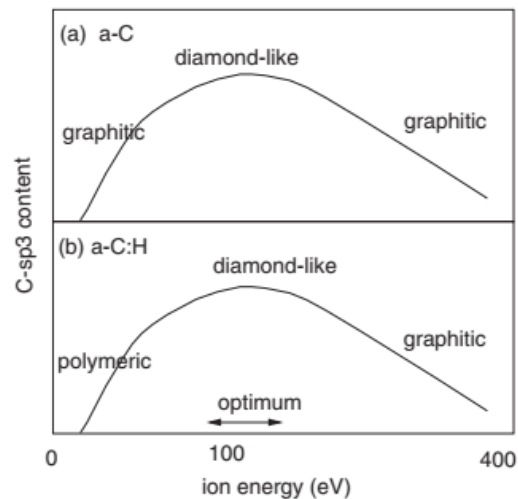
Figure 2.23: Schematic of the variation in film character depending on ion energy. From [275].

Figure 2.24 displays multiple deposition methods (PVD and CVD) specifically for the deposition of DLC.
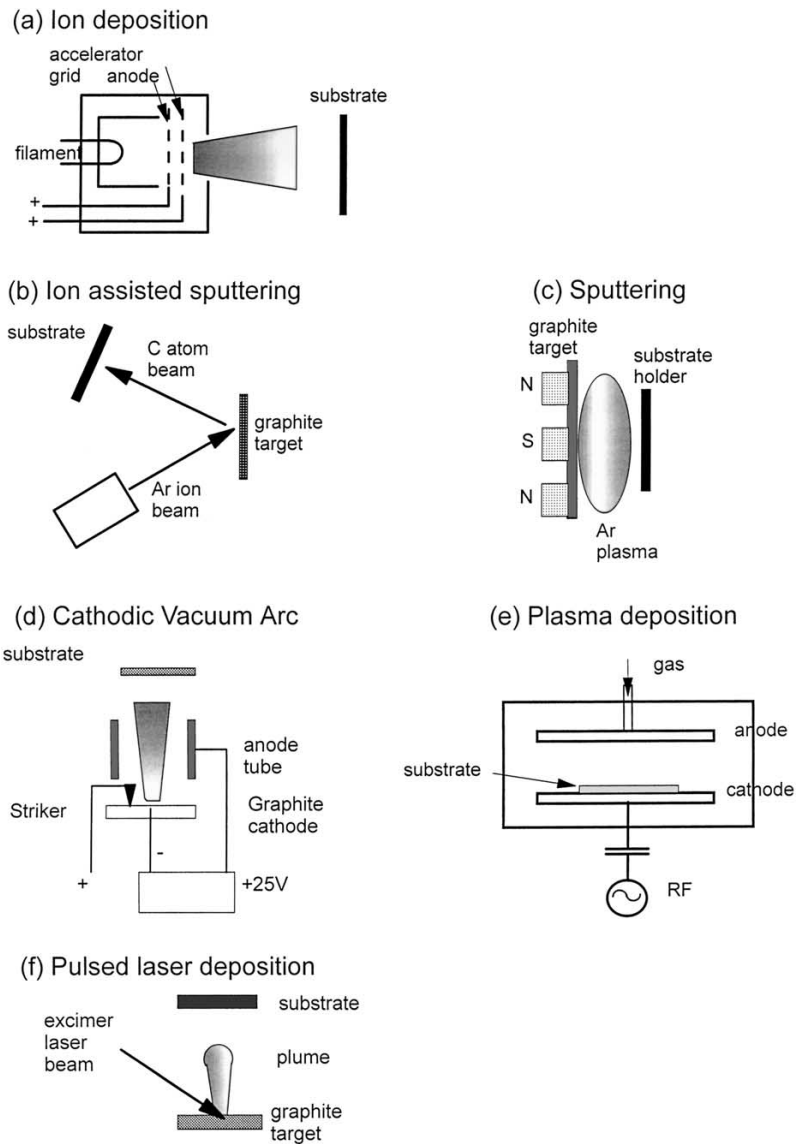
Figure 2.24: Schematics of various DLC deposition mechanisms. From [216].

2.5.5.7 Coating Growth

The coating growth and the nature of the coating is determined by an ion subplantation process. An optimum range of ion energy (which also varies depending upon the precursor hydrocarbon) exists for the maximum sp^3 content. The hydrogen content of a-C:H is always lower than the precursor hydrocarbon molecule as hydrogen is lost due to ion bombardment. Generally, ions will subplant, causing sp^3 sites initially. Some diffusion will occur as movement occurs towards the lowest energy position. If an ion has enough energy will pass through the outer layer of the growing film and cause subsurface growth. This creates a locally denser area. Ion bombardment causes the loss of H, displaced from C-H bonds to form H_2 molecules which leave the network [275, 276].

Baba et al. [229] noted that the deposition rate of their DLC coatings depended upon the precursor gas, DC voltage, application of high voltage pulses and use of RF power.

2.5.5.8　Interlayers In DLC Structures

Residual stresses in the coatings can compromise their integrity and adhesion to substrates, to improve their lifetime for tribological applications interlayers of various metals are often deposited (Ti, Zr, W, Si, Cr or WC) [277]. Initial research by Bentzon et al. [278] used a copper pretreatment on stainless steel after which depositing a carbide-metal intermediate layer. This improved the adhesion greatly. It is common to have several interlayers, these being Cr layer deposited by magnetron sputtering followed by either W or WC. Ti/TiN and Ti/TiN/TiCN has also seen to be effective [277].

2.5.5.9　Tribology Of DLC

Generally DLCs are noted for having low coefficients of friction and low wear. This is however dependent upon the structure and humidity. At low humidity, H-free DLC is seen to have a relatively high friction coefficient of approximately 0.8. Hydrogenated DLC has a much lower coefficient of friction of approximately 0.15. This is determined by the surface interactions whether it be σ or π bond dangling interaction or hydrogen terminated bonds respectively. At high humidities, H-free DLC has a much lower friction coefficient whereas that of hydrogenated DLC is seen to rise slightly [279, 280].

An increase in substrate roughness was found to increase the wear rate in ball-on-disk sliding tests in air. Increased substrate roughness changed the dominant wear mechanisms from adhesion to chip/flake and fragmentation [281]. Beake et al. conducted a study on the behaviour of DLC coatings finding a correlation between the mechanical properties and tribological behaviour in nano- and micro-scratch testing of multilayer DLC coatings [282]. A higher plasticity index was found to increase DLC crack resistance and simple modelling found failure occurs when maximum stresses are centred on the interfaces in the multilayer system. Figure 2.25 shows the typical friction coefficients of DLC variants and the effect of humidity.
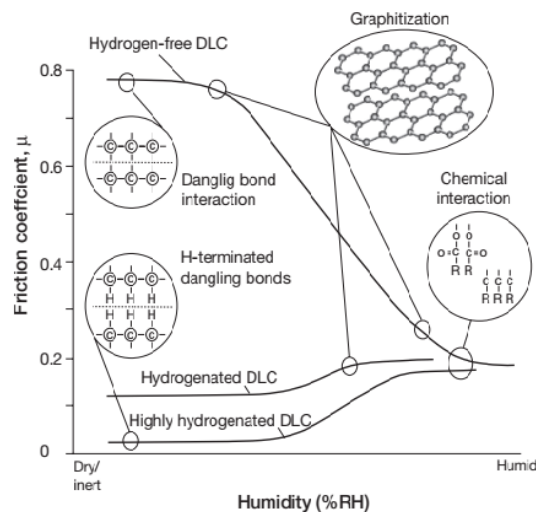
Figure 2.25: Frictional performance of DLC as a function of humidity and dominant mechanism. From [274].

Further enhancing the tribological behaviour of DLC is the formation of a carbonaceous transfer layer which reduces the friction coefficient. A high normal load and high sliding speed is seen to be most beneficial in formation, giving a thick and compact layer.

This layer tends to be graphitic in nature and have lower values of hardness and elastic modulus compared to the original coating [220, 245, 279, 283, 284].

In lubricated interactions, DLC has been found to to have an adverse reaction with oils containing MoDTC. Kosarieh et al. [125] found that the formation of an MoDTC tribofilm reduced friction but increased wear in the presence of iron. Topolovec-Miklozic et al. [285] found that when ZDDP and MoDTC were present in the lubricant a nanometre thin friction reducing film was formed. The MoDTC was seen to break down into a structure similar to MoS_2. Haque et al. [286] found that, in boundary lubrication conditions, high contact pressure will induce graphitisation and accelerate wear causing the coating to thin. Ren et al. [230] found that the addition of ZDDP to engine oil at normal operating temperatures (180 °C), caused the wear rate to decrease by two orders of magnitude and graphitisation was prevented.

2.5.5.10 Optical And Electrical Properties Of DLC

DLC coatings can have a range of electrical properties depending upon the deposition conditions and film structure. The amorphous structure of DLC allows for the adjustment of properties over a large range however the disordered structure leads to poor semiconducting properties. This allows it to be tailored to a range of applications such as protective coatings for optical devices (as they are typically transparent in the infra-red), commutators and brush assemblies and plasma switches (due to its high dielectric breakdown) [287, 288]. Grill et al. [289] noted that PECVD films display non-ohmic behaviour with their resistivities being dictated by substrate bias and the precursor used in deposition. Honglertkongsakul et al. [290] used pulsed laser ablation to investigate the electrical and optical properties of DLC and found that the properties were dependent upon the substrate temperature and laser fluences. Semenenko et al. [291] formulated DLC for coated field emission cathodes. One possible future use is to design a coating to optimise the triboelectric effect. Additionally, the coating could be used as an in-situ sensor.

2.5.5.11 DLC Applications

DLC coatings have seen wide use in engineering and medical applications where their inherent properties in dry sliding contacts have shown to be very useful [280, 292, 293].

DLC films see many practical applications across industry including razor blades, MEMs devices, cutting tools and as protective coatings for mechanical combustion engines [35, 217, 248, 294]. More recently, DLC coatings have been seen as a potential protective coating of flow control devices in oil and gas pipelines [295]. In this application, fatigue resistance is key due to repetitive stresses of hard particle impacts, particularly, sand particle impacts.

Diamond-like carbon is now seen to be deployed in extreme environments that involve high temperatures such as protective and friction reducing coatings in automotive engines [280, 296]. DLCs thermal stability is dependent on its structure with non-hydrogenated and more sp^3 rich ta-C remaining stable up to 600 °C; whereas a-C:H films only remain stable up to 400 °C [280]. In any use beyond these temperatures, the addition of dopants in thermally optimised architectures should allow it to serve in more extreme environments; titanium doping [297] and various light elements have been seen to be effective [36].

2.5.6 Coating Thickness Determination

Multiple method exist for the determination of the thickness of any applied coating as seen in Figure 2.26. Mechanical methods such as grinding or scraping can be used to partially remove a coating [298].
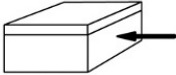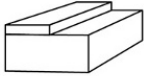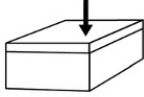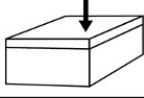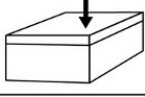
Figure 2.26: Methods of measuring coating thickness. From [299].

Cross-sectional imaging by SEM/focussed ion beam (FIB) can measure the coating thickness with a great deal of accuracy. Less common methods include ultrasonic scattering, x-ray fluorescence and capacitance sensing.

Calotesting is a ball and crater technique that wears into a coating to reveal the substrate or interlayers present beneath. The technique involves rotating a large diameter steel or tungsten carbide ball against the coating surface until the top layer of coating is worn away. Several drops of nano-crystalline diamond or SiC suspension are used to aid in the wear as the coatings are typically hard. Optical microscopy is then used to measure the dimensions of the crater [298]. Figure 2.27 shows a schematic of the Calotest apparatus and the crater profile.
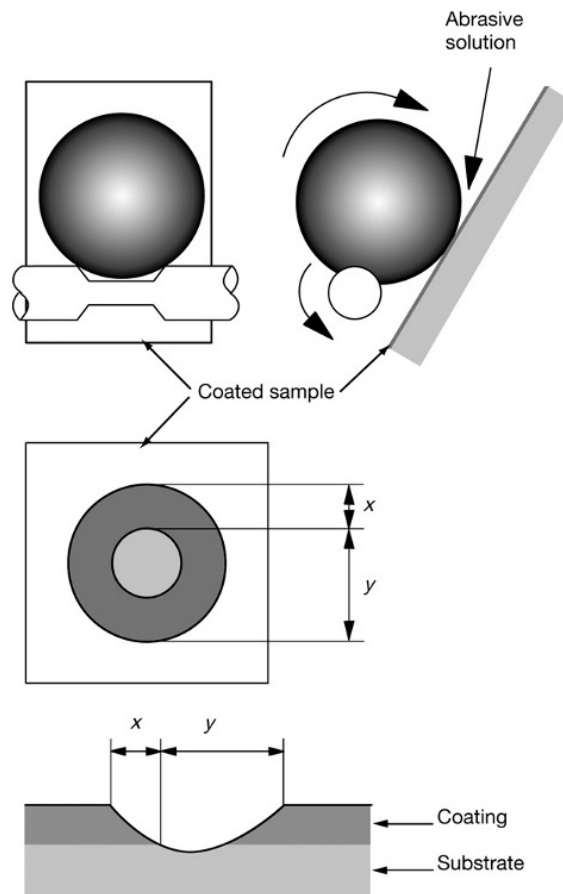
Figure 2.27: Schematic view of Calotest ball and crater apparatus and crater profile. From [299].
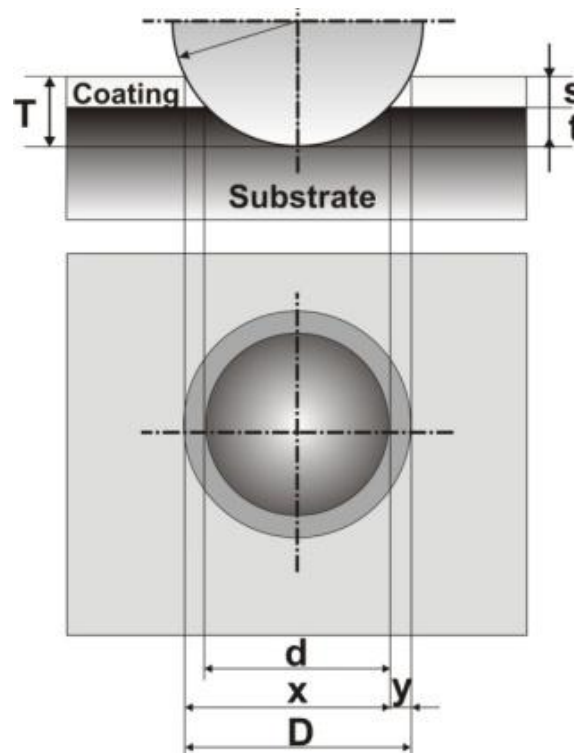
Figure 2.28: Diagram of Calotest wear scar geometry. From [300].

Considering the geometry of the wear scar shown in Figure 2.28, the coating thickness (T) can be calculated by:

$$s = T - t \tag{2.37}$$

An idealised spherical cap can be used to approximate the ball-crater volume. By analysing the geometry of the crater, we can see that T can be calculated by:

$$T = R - \frac{1}{2}\left(\sqrt{4R^2 - D^2}\right) \tag{2.38}$$

where R is the radius of the ball.
The depth reached into the substrate can be approximated by a similarly derived formula:

$$t = R - \frac{1}{2}\left(\sqrt{4R^2 - d^2}\right) \tag{2.39}$$

Therefore we can derive the coating thickness as:

$$s = \frac{1}{2}\left(\sqrt{4R^2 - d^2} - \sqrt{4R^2 - D^2}\right) \tag{2.40}$$

On the condition that $d \ll R$ and $D \ll R$ the expression can be simplified to [298]:

$$s = \frac{xy}{2R} \tag{2.41}$$

with Figures 2.27 and 2.28 showing the physical dimensions measured to obtained the coating thickness.

Diameter of the ball can be varied to test coatings of different thickness with larger ball being used to test thicker coatings. Rotation speed of the ball and wear time are varied dependant upon the hardness of the coating being tested.

2.5.7 Coating Adhesion Determination

Multiple methods of coating adhesion determination exist across the field of surface engineering, the type chosen is done to reflect the thickness of the coating being examined and the types of failures

2.5.7.1 Scratch testing

One of the first documented uses of scratch testing was by Friedrich Mohs who, in 1822, used a scratch test to rank material hardness. The relative ability of a material to leave a permanent scratch in another determined its position on the 10 point scale, the maximum hardness was set by diamond with the maximum value of 10 [48, 67].

Progressive loading scratch testing is a common technique to evaluate the adhesion of thin films. This involves the evaluation of well defined failure characteristics (such as tensile cracking, compressive spallation or gross spallation) at typical loads [301]. The primary development work in scratch testing was carried out in the 1980s. Perry [302] produced some of the first work detailing the scratch test as as applied to thin hard ceramic coatings such as TiN. This work covers the, now typical elements of scratch testing such as the measurement of critical loads and acoustic emission to detect failure. Hintermann [303] further developed the acoustic emission sensing during scratch testing,

using a piezoelectric detector fixed next to the indenter. The work of Valli, Mäkelä and Matthews contributed with further work on the adhesion of TiN to M2 tool steel and the development of a robust scratch test platform [304, 305]. The general design of modern macro-scale scratch testers are extremely similar to this platform. M Burnett and Rickerby [306] took an analytical approach to the types of failure observed on PVD deposited TiN. Their work analysed the interfacial stresses, the scratch adhesion failure modes and the various coating design factors that affect the critical load. This led to the development of the DIN-Fachberict 39 [307] which has much more detail on the failure modes involved in scratch analysis compared to the scratch test adhesion ASTM standard [308].

For a sphero-conical probe a scratch hardness (HS_p) can be calculated [67, 309]:

$$HS_p = \frac{2P_n}{A_p} \tag{2.42}$$

where P_n is the normal scratch load and A_p is the projected contact area. Pöhl et al. [309] used a scratch method to evaluate pile up and scratch resistance of soft metallic materials.

Zhang et al. [310] defined a Scratch Crack Propagation Resistance term ($L_{C1}(L_{C2} - L_{C1})$, sometimes referred to as scratch toughness). This term represents the resistant to crack initiation and propagation throughout the scratch test thereby giving a metric for the toughness of the film.

$$CPR_S = L_{C1}(L_{C2} - L_{C1}) \tag{2.43}$$

Fox-Rabinovich et al. [311] used this term to explore the resistance to crack propagation with elevated temperature on TiAlN and AlCrN coatings on a cemented carbide substrate.

2.5.7.2 Nano-Scratch testing

Nanoscratch testing is used in the assessment of the mechanical failure and it is able to discern many properties of a coating system. Beake et al. [312] concluded, in their 2013 review that the critical load for thin film adhesion can be influenced by intrinsic and extrinsic factors, friction force can be de-convoluted into interfacial and ploughing components and that film thickness is a key parameter influencing critical load in this type of testing. The exact nature of this relationship is complex however. The link between the interfacial and ploughing components can be seen in this equation [70, 312, 313]:

$$\mu_{total} = \mu_{interfacial} + \mu_{ploughing} \tag{2.44}$$

The ploughing component of a spherical indenter can be expressed as [313, 314]:

$$\mu_{ploughing} = \frac{A_p}{A_s} = \frac{R^2 \cos^{-1}\left(1 - \frac{h}{R}\right) - (R - h)\sqrt{2Rh - h^2}}{\frac{1}{2}\pi\left(2Rh - h^2\right)} \tag{2.45}$$

where A_p and A_s are the projected contact areas between the indenter and the contact surface and horizontal direction. This is similar to the model proposed by Goddard and Wilman [314]. R is the tip radius and h is the penetration depth. Lafaye and Troyon [315] discuss the applicability of this modelling with respect to the transition between sphere and cone. When the contact radius (a) is greater than the contact radius of the tip ($a_0 = R\cos\theta$), further considerations must be made taking into account the conical shape as opposed to the spherical contact when only the spherical extremity is in contact.

Several methods exist to determine the interfacial friction component [312]:

- By performing constant load friction tests at very low loads where the contact is completely elastic and the ploughing component is negligible.

- By performing repetitive scratches to eliminate the ploughing contribution.

- By performing a progressive load scratch and extrapolating the low load friction data to zero load.

At the yield point of the coating, the coefficient of friction is typically of the order of 0.05 using a diamond indenter [312]. This was also noted by Dryda et al. with their scratch testing of a range of TiN coatings [316].

The repetitive progressive load scratches present the most viable method for the determination of this friction component as they present the fewest issues with sample preparation (obtaining the optimal surface roughness) and also setting up an instrument with sufficiently low thermal drift and low external vibrations. With a well prepared surface, the load-displacement curves of nanoindentation and nano-scratch can be surprisingly similar. For a thin film, the critical load is sensitive to the film thickness [149]. Schiffmann [317] compared nanoindentation (considered as 0 dimensional testing with respect to lateral movement on the surface) with linear increasing and constant load load scratch (1 dimensional) and scanning wear (2 dimensional) noting that the physical mechanisms of these modes of wear are expected to be different. Under indentation, the elastic and plastic deformation will determine the residual depth whereas when this is extended to 1D additional shear forces and ploughing effects will be seen. For 2D testing, the distance between lines will influence the wear alongside the interactions with wear debris. The 2D tests were seen to perform differently due to the cross overs of the same wear path due to the scan line density and that wear debris must be transported across the whole wear crater with each scan before ejection.

The contact pressure in nano-scratch testing can be calculated in a method described by Beake et al. [312]. The contact depth (h_p) is given by:

$$h_p = \frac{(h_t + h_r)}{2} \tag{2.46}$$

where h_t is the on-load scratch depth and h_r is the residual depth from the final scan. The contact radius (a) is determined by:

$$a = \sqrt{2Rh_p - h_p^2} \tag{2.47}$$

The contact pressure (P_m) can then be calculated by:

$$P_m = \frac{L}{\pi a^2} \tag{2.48}$$

where L is the applied load. Several assumptions are required for this:

- The presence of the tangential load does not influence the pressure distribution too greatly such that the coefficient of friction is below 0.3. Above 0.3, the pressure distribution becomes non-Hertzian.

- The radius of the indenter is constant.

- The sliding speed is sufficiently low and the contact is sufficiently close to elastic that the load is supported on the rear of the indenter.

- The indenter can reach the bottom of the scratch track in the final topographic scan.

No standard yet exists for the nano-scratch technique but the methodology is broadly similar to larger scale testing. The geometry of the tip used in this type of testing much smaller than in macro-scale scratch testing though a sphero-conical tip is used, analogous to the Rockwell C tip used in macro-scratch testing. The radius of this tip is generally 5 μm as it promotes film failure within a reasonable load range in line with several commercial instruments [318].

Due to the scales of testing in this technique standard microscopy is difficult to implement to assess the crack phenomena. Often, SEM is used once the test has concluded as performed by Beake et al. [282] in the comparison of a-C:H. Si-a-C:H and a-C:H:W. To gain further information on the sample profile, the Micro Materials nano-scratch module uses a 3 pass technique (topography-scratch topography) to assess the pre-scratch topography, scratch depth and post-scratch topography [312].

2.5.7.3 Indentation as a Method to Assess Adhesion

The Rockwell indentation method is traditionally used to assess the hardness of steels but it has seen use as a method to determine the adhesion of relatively thick coatings. For this application a Rockwell C 120° cone with a tip radius of 200 μm is used. Other geometries such as Brinell or Vickers test can also be used. For thinner films, a Berkovich or conical indenter should, instead, be used [67].

The cracking and delamination phenomena are key in determining the adhesion in comparison to other coatings. This method does not give a quantitative value for adhesion unlike scratch testing. Sivitski et al. [319] noted the various types of cracks in indentation such as radial cracking up to delamination. Lan et al. [320] used Rockwell indentation to assess the adhesion of DLC coatings on duplex nitrided Cr12MoV steel.

2.5.8 Mechanical Properties in the Prediction of Coating Performance

In the prediction of the wear performance of coatings two main metrics are often used, these being H/E and H^3/E^2 [321–323]. Leyland and Matthews [322] were instrumental in popularising the use of H/E (the ratio of hardness to elastic modulus) in the prediction and ranking of coating wear performance. Though this was recognised by previous authors for alternative materials, this paper introduced the concept for coating studies. H/E physically relates to the elastic strain to break (or strain to failure) [322, 324]. This parameter was previously used by Oberle [325], Halling [326] and Matthews [327] fro predicting the wear of materials. H/E appears in the plasticity index as defined by Greenwoood and Williamson [55]:

$$\varphi = \frac{E}{H}\left(\frac{\sigma}{\beta}\right)^{\frac{1}{2}} \tag{2.49}$$

where σ is the surface roughness and β is the asperity radius. The plasticity index is used as a measure of the limit of elastic behaviour in the design of sliding and rolling-element bearings, making it important in the minimisation of wear [322]. Contacts with small plasticity indices must have a larger contact stress to induce significant plastic deformation. At a constant surface roughness and asperity radius, H/E is inversely proportional to the plasticity index. Therefore, a coating with a larger H/E less likely to deform

plastically at a given stress and will have a higher toughness where there is no plastic deformation [321]. Furthermore, H/E is used as a metric for fracture toughness (K_c) using pyramidal as seen in the work of Lawn, Anstis and Pharr [328, 329]:

$$K_c = \chi_r \frac{P}{c^{\frac{3}{2}}} \tag{2.50}$$

Where P is the peak load, c is the distance from the centre of the indent to the radial crack end and χ_r is a constant. This constant depends upon the square root the ratio of Young's modulus to hardness (E/H):

$$\chi_r = \S_V^R (E/H)^{\frac{1}{2}} \tag{2.51}$$

where $\S_V^R$ is a material-independent constant cracks produced using pyramidal indenters.

For a Vickers indentation, the fracture toughness can be specifically expressed as [330]:

$$K_c = 0.016 \left(\frac{E}{H_V} \right)^{0.5} P c^{-1.5} \tag{2.52}$$

A dimensionless plasticity index (PI) also exists from the work of Cheng and Cheng [201, 331] using finite element analysis relating the plastic work done during indentation (W_p) to the total elastic (W_e) and plastic work done during the indentation:

$$PI = \frac{W_p}{(W_p + W_e)} = 1 - x \left(\frac{H}{E_r} \right) \tag{2.53}$$

where x is a constant. H/E can also relate to frictional performance [332]. We assume that multi-asperity contacts can be modelled locally by either conical or spherical indentations. It is well known that the deformed surface around the indenter can exhibit pile-up or sink-in dependent upon the mechanical properties of the surface and indenter geometry [331]. For materials with a large ratio of yield strength over elastic modulus, sinking in is expected and the tendency of sink in increases with H/E [332].

As friction is widely considered to consist of two main components: an interfacial/adhesive component and ploughing component [312]; the ploughing component is needed to deform materials in the direction of sliding. The ploughing force is expected to be smaller for sinking in than for piling up, therefore the ploughing contribution to friction is expected to decrease with increasing H/E [332].

H^3/E^2 has been seen to relate to tribological performance in its relation to contact yield pressure and fracture toughness from Hertzian contact analysis [321, 333]. Rearranging Equation 2.7 with the condition of no significant plastic deformation ($P_{max} < \sigma_y$):

$$0.578 \left(\frac{PE^2}{R^2} \right)^{\frac{1}{3}} < \sigma_y = \alpha H \tag{2.54}$$

where α is some constant. Therefore we can write:

$$P < 5.168 \alpha^3 R^2 \frac{H^3}{E^2} \tag{2.55}$$

This tells us that for a given load, a coating with a larger H^3/E^2 is less likely to be plastically deformed and should therefore have higher fracture toughness.

These parameters are generally used to rank coating performance though care must be taken as some coating architectures behave differently depending on the amount of load support, an example being coating thickness affecting the load support of coated silicon. A harder and stiffer film is also more likely to have a more dramatic fracture due to the release of stored elastic strain energy per unit volume resulting in a larger delaminated area [149, 150, 318, 334, 335].

Beyond the "traditional" wear ratios of H/E and H^3/E^2, H^2/E presents an interesting alternative wear ratio to explore as discussed in the work of Eyre [336, 337] and Smart [338]. They noted that there is good correlation between erosion resistance and ultimate resilience of a material. H^2/E represents the amount of energy a material can absorb before cracking occurs. Thereby making a higher H^2/E material more erosion resistant. This can be thought of in terms of the area beneath a linear load-extension graph (P on the y axis and x as extension on the x axis), as represented by $\frac{1}{2}Px$. We can derive the energy absorbed (equivalent to $\frac{1}{2}\sigma A \varepsilon l$) from $\sigma = \frac{P}{A}$ (stress) and $\varepsilon = \frac{x}{l}$ (strain). Energy absorbed per unit volume is related to $\sigma \varepsilon$ allowing us to form $\frac{1}{2}\sigma \varepsilon V$ where V is volume. Using $E = \frac{\sigma}{\varepsilon}$ we can derive the form $\frac{1}{2}\frac{\sigma^2}{E}V$ which is proportional to H^2/E. We can therefore see that a high hardness is important in terms of resilience but also a low modulus especially if the substrate modulus is low.

2.6   Summary: State of the Art

Tribology is now a well established field of study with multiple avenues of viable research both in terms of physical experimentation and computational and mathematical modelling. Due to the complexities of many areas studied a combined approach is often employed combining both theoretical approaches and studying physical phenomena across length scales. Surface engineering for tribological performance offers many tangible benefits by creating composites with friction and wear performance that cannot be achieved with single monolithic materials.

As can be seen from the literature, considerable work has been completed on the study of nano-tribology, nanoindentation and DLC coatings. The various properties of DLC have been well studied but there is more work to be completed on minimising the effects of internal stress with multi-layer approaches [229], exploring the properties of graphene based materials [339] and the addition of nanoparticles between DLC and other surfaces [131]. Most work has focused on the tribological effects of varying few coating parameters or the study of a particular commercial coating. Examples of this include the work by Field et al. [283] on the tribological properties of Graphti-iC™ and Dymon-iC™ from Teer Coatings and Viana et al.'s [340] work on the properties of a-C:H deposited from methane and heptane precursors. Few studies undertake a more complete and comprehensive study in a similar way that this PhD project aims to do. This is partly due to the complexity and expense of coating studies but also that many coatings are deposited in smaller university systems or provided by companies, making it difficult to scale up to testing more parameters.

Previous studies have identified the need in combining several techniques (such as nanoindentation, scratch and impact testing) to characterise a coating's mechanical properties to assess performance. [122, 248]. Further to this, coatings should be designed and optimised for their environment to avoid premature failure [198], the use of multiple techniques to build a more complete picture of coating performance will aid in this. Research is trending towards the measurement of dynamic hardness of surfaces and the use

of different length-scales in testing to understand behaviour at each scale and drive failure faster [86, 110, 118]. Additionally, the use of nanoindentation mapping to assess the dynamic changes in surface hardness has been seen particular with fretting wear [102, 341]. Partial unload nanoindentation has been used in a limited capacity and could stand to be used to a greater degree in materials testing as it provides more information than a single indentation method as long as the material does not experience a large degree of fatigue.

Chapter 3

DLC Coating Production

3.1 Introduction

As covered in Chapter 2, numerous methods exist to deposit PVD and PECVD DLC coatings and the possible substrate materials are varied. The deposition system used to produce the coatings for this study is equipped with numerous technologies allowing for the production of many different types of DLC. The coating variants and substrates were chosen to allow for a large array of properties on substrates that cover a multitude of use cases to allow for the results gained in the study to be applied to many industries.

This chapter will provide an overview of the production of the DLC coated steel coupons used throughout this study. The substrate materials will be detailed first followed by the techniques used to prepare them for deposition. The architectures of the coatings will be discussed and compared with the achieved coating thickness.

3.2 Materials

This section will detail the materials used as substrates for the DLC coatings in this study. The measured mechanical properties of the substrate materials is shown in Chapter 4.

3.2.1 316L Stainless Steel

316L is the low carbon version of grade 316 stainless steel. This grade of steel is one of the standard molybdenum-bearing grades of austenitic stainless steels, after 304. The addition of molybdenum gives enhanced corrosion resistant properties, especially to pitting and crevice corrosion in chlorinated environments. In comparison to other chromium-nickel austenitic stainless steels, 316L offers higher creep resistance, fracture toughness and tensile strength at elevated temperatures [342].

Typical applications for this grade of steel include food preparation equipment, marine applications, pharmaceuticals and architectural applications [342]. Though it is regarded as the standard marine grade stainless steel, it is not entirely resistant to corrosion in warm sea water, exhibiting brown staining. The composition range of 316L stainless steel is detailed in Table 3.1a. 316L stainless steel is used for various projects throughout the School of Mechanical Engineering, as such the coupons used in this study were cut from

existing stock. Throughout this thesis, this substrate material will be addressed as SS (stainless steel).

3.2.2 M2 Tool Steel

M2 tool steel belongs in the class of high speed steels designated as Group M steels under the AISI classification system. Tungsten is present in all of this class of steels, apart from M6 and cobalt is completely absent from the composition. M2 tool steel is notable for its high carbon content and better wear resistance than M1 molybdenum high speed tool steel. Molybdenum based high speed steels have similar performance compared to tungsten high speed steels however the former is more cost effective. As the name implies, this grade of steel is used for making cutting tools [343]. The Mo and W content promotes toughness and aids in cutting performance however more precise hardening is required [344]. The round bar was sourced from J. Boyd Laurie and Son Ltd of Bradford. Vacuum hardening, hot straightening and triple tempering was performed achieve a hardness range of 62–64 HRC. The hardening temperature is in the range of 1190–1230 °C and the tempering temperature is in the range of 540–595 °C [344, 345]. Table 3.1b details the composition range of M2 tool steel. This material will be addressed as HTS for the rest of this thesis; though this material is generally referred to as HSS (high speed steel), this alternate initialism will be used to reflect the additional hardening procedures used.

Table 3.1: Composition range for 316L stainless steel and M2 Tool Steel.

(a) Composition range for 316L stainless steel. From [342].

Element	Composition Range (%)
C	0.03
Mn	2.00
Si	0.75
P	0.045
S	0.03
Cr	16.0–18.0
Mo	2.0–3.0
Ni	10.0–14.0
N	0.10
Fe	62.045–69.045

(b) Composition range for M2 tool steel. From [343].

Element	Composition Range (%)
C	0.78–1.08
Mn	0.15–0.40
Si	0.20–0.45
Cr	0.20–0.45
Ni	0.30
Mo	4.50–5.50
W	5.50–6.75
V	1.75–2.20
Cu	0.25
P	0.03
S	0.03
Fe	82.59–86.31

3.3 Methods

3.3.1 Coating Architecture Design

Three types of DLC were produced for this study on the two substrate materials presented above. The matrix of coatings produced for this study can be seen in Table 3.2 (located on page 75). The substrate materials for DLCs can vary hugely depending on the application. Some examples include alumina [346], Ti6Al4V [228] and silicon [112]. To

allow the results of this study to be applied across different areas of industry, the choice of 316L and M2 tool steel is important. Biomedical applications typically utilise 316L as well as CoCr and Ti6Al4V [318]. M2 tool steel is used in cutting tools due to its high hardness, thermostability and fatigue resistance [347]. This also allows for a range of applications relating to the substrates to the tested. Various substrate roughness values were considered by Siu et al. [348] and Peng et al. [349]. It was decided that $0.01\,\mu m$ and $0.08\,\mu m$ R_a would allow for good adhesion of the coating while still allowing the effects of higher roughness to be determined. It would also remain simple to polish to the required roughness. The coating archetypes were chosen as this project was intended to provide further tribological investigations to those performed previously by Beake [282] and Austin [324]. A range of coating thickness values are chosen for DLCs however thicker coatings are seen to increase the critical yield load (the point on a scratch track at which plastic deformation begins) [53, 350]. The choice of $1\,\mu m$ and 2–$3\,\mu m$ allowed for enough of a difference in the thickness while maintaining reasonable deposition times.

The same coating processes was utilised for coating on both SS and HTS, the only difference is the deposition time of the final step to achieve a different top layer thickness. The process details will be shown in Section 3.3.3. Therefore the other variations in coating parameters would be achieved by the selection of substrate and preparation of the substrate roughness as described in Section 3.3.2.

3.3.2 Coupon Preparation

Substrate coupons were initially cut from cylindrical steel bars ($\varnothing = 25\,mm$) to a standard-ised thickness of 6 mm per coupon. Six coupons per coating variant were produced to give enough surface area for all the required testing. Due to the cutting process, the surfaces of the substrates were heavily textured requiring polishing to obtain a flat surface as well as producing the required surface roughness. A circular grinder with varying grades of silicon carbide polishing paper was used for polishing under water lubrication. Sequentially finer grit sizes (120, 300, 450, 600, 800 and 1200) were used to remove the machining marks and achieve the correct surface finish. Grinding paper polishing leaves circular lay marks on the substrate surface that that will be present on the coating due to the nature of the coating growth and could affect DLC coating adhesion. Jiang and Arnell [281] noted that the coating roughness would be approximately half that of the substrate however care must still be taken in their preparation. Therefore, to obtain the optimal surface roughness ($R_a = 0.01\,\mu m$), samples are further polished with sequential fibre polishing cloths (VerduTex and MicroFloc) and polycrystalline diamond suspension in sequence ($9\,\mu m$ and $3\,\mu m$ VerduTex and $0.25\,\mu m$ with MicroFloc). This process removes the majority of the patterns of lay on the substrates surface to give a smooth mirror finish.

To achieve the rougher surface finish ($R_a = 0.08\,\mu m$), the same methodology was employed however the polishing with grit paper was stopped earlier in the process (800 grit). Polishing cloths were employed as before to give the mirror shine to the surface. It was found to be much easier to polish to reach the smoother finish as this is essentially the limit of what is achievable with this laboratory equipment. Measurement of the surface roughness was carried out with the Taylor-Hobson Talysurf 120L to ensure uniformity. The Talysurf 120L is equipped with a $2\,\mu m$ radius diamond tip and a scan distance of 2 mm was used. An average of 3 scans across multiple coupons was used to confirm the surface roughness.

Table 3.2: Coating design matrix.

Substrate	DLC Recipe	Nominal DLC Coating Thickness (μm)	Nominal substrate Roughness (μm R_a)	Name designation
Stainless Steel (316L)	a-C:H	1	0.01	SS-Coating A-thin-smooth
		1	0.08	SS-Coating A-thin-rough
		2-3	0.01	SS-Coating A-thick-smooth
		2-3	0.08	SS-Coating A-thick-rough
	Si-a-C:H	1	0.01	SS-Coating B-thin
		2-3	0.01	SS-Coating B-thick
	a-C:H:W	1	0.01	SS-Coating C-thin
		2-3	0.01	SS-Coating C-thick
Hardened Tool Steel (M2)	a-C:H	1	0.01	HTS-Coating A-thin-smooth
		1	0.08	HTS-Coating A-thin-rough
		2-3	0.01	HTS-Coating A-thick-smooth
		2-3	0.08	HTS-Coating A-thick-rough
	Si-a-C:H	1	0.01	HTS-Coating B-thin
		2-3	0.01	HTS-Coating B-thick
	a-C:H:W	1	0.01	HTS-Coating C-thin
		2-3	0.01	HTS-Coating C-thick

3.3.3 Coating Preparation

Coating deposition was performed with the Hauzer Flexicoat 850 PVD and PACVD system located in the School of Mechanical Engineering at the University of Leeds (as seen in Figure 3.1).

Figure 3.1: Hauzer Flexicoat 850 system in the School of Mechanical Engineering at the University of Leeds.

PVD was used to deposit the adhesive and gradient interlayers on the substrates. PACVD was used with acetylene (C_2H_2) as the precursor gas for the top DLC layer. Hexamethyldisiloxane (HMDSO), vaporized in the chamber during deposition, was utilized for silicon doped DLC. The engagement of a magnetron sputtering WC target was used for tungsten doped DLC. This will be fully detailed later in this section.

The Hauzer Flexicoat 850 was commissioned at the University of Leeds in December 2010 and upgraded to include new features in 2019. The coating system is equipped with a number of capabilities, those being [351]:

- Unbalanced magnetron sputtering

- Cathodic arc evaporation (CARC+)

- High power impulse magnetron sputtering (HiPIMS)

- High powered pulsed microwave source

- PECVD with multiple precursor sources (additional sources added in the upgrade)

- Radio-frequency bias (added in the upgrade)

- Nanoparticle source (added in the upgrade)

- Plasma diagnostics (added in the upgrade)

The Flexicoat 850 has an effective coating volume of $\varnothing$500mm x 500mm height. Four cathode positions are available, their arrangement can be seen in Figure 3.2.
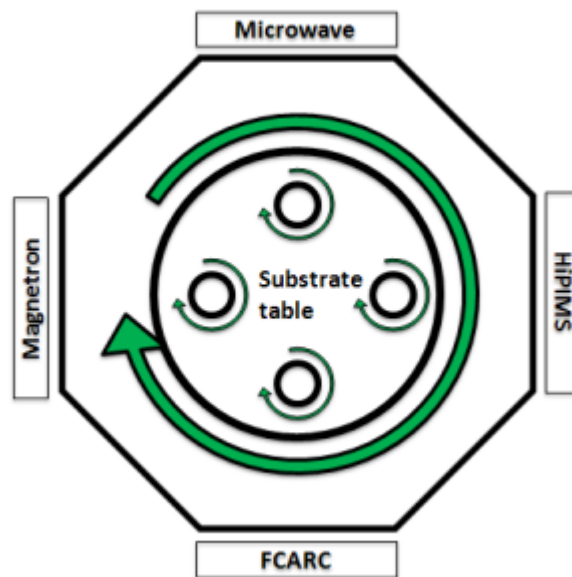
Figure 3.2: Schematic of the cathode arrangement of the Flexicoat 850 system located at the University of Leeds. From [324].

The substrate table itself with coupons mounted on it is shown in Figure 3.3.

Figure 3.3: Coupons mounted on the substrate table in the Hauzer Flexicoat 850.

The production of the coatings was broken down into multiple deposition steps for each design:

- Coating A:
    - (i) Chamber heating
    - (ii) Target cleaning
    - (iii) Plasma surface etching
    - (iv) Cr layer deposition
    - (v) Cr/WC deposition
    - (vi) a-C:H deposition

- Coating B:
    - (i) Chamber heating
    - (ii) Target cleaning
    - (iii) Plasma surface etching
    - (iv) Cr layer deposition
    - (v) Cr/WC deposition
    - (vi) Si-a-C:H deposition

- Coating C:
    - (i) Chamber heating
    - (ii) Target cleaning
    - (iii) Plasma surface etching
    - (iv) Cr layer deposition
    - (v) WC/a-C:H:W deposition

The process parameters themselves are summarised in table 3.3 (located on page 79). The chamber is pumped to 4×10^{-5} mbar (pressure is otherwise uncontrolled throughout the coating process) and heated to 200 °C in the first step. The heaters are engaged again in the plasma surface etching step otherwise the temperature is not controlled during deposition. The pump was maintained at low power throughout deposition to evacuate waste gases from the chamber. The bias voltage utilises DC current during the target cleaning step, low pulse current (PLS low) in the plasma surface etching step and high pulse current (PLS high) in the a-C:H and Si-a-C:H deposition steps. A substrate bias voltage of -100 V is applied during the deposition steps. C_2H_2 and HMDSO flow rates have a time ramp as specified in the relevant columns. The time column shows the times for both the thin and thick coating variants. These times were chosen as the standards for each of the coatings as programmed into the coating system.

3.3.4 Naming Designations

Due to the large subset of coatings being produced for this study, a naming convention was established to allow for easier reference to a particular coating architecture design. This can be seen in Table 3.2. The three DLC coating types will be referred to as:

Table 3.3: Coating deposition step parameters.

Deposition Step/Conditions	Temperature (°C)	Pressure (10^{-5} mbar)	Bias Voltage (V)	Cr target power (kW)	WC target power (kW)	Ar flow rate (sccm)	C_2H_2 flow rate (sccm)	HMDSO flow rate (sccm)	Table rotation speed (rpm)	Time (min)
Chamber heating	200	4	–	–	–	–	–	–	1	60
Target cleaning	–	–	500 (DC)	6	3	130	–	–	2	20
Plasma surface etching	150	–	200 (PLS low)	–	–	50	–	–	2	45
Cr deposition	–	–	–	3	–	130	–	–	3	25
Cr/WC deposition	–	–	–	3	3	110	–	–	3	30
a-C:H:W deposition	–	–	–	–	3	90	8–30 (30 min)	–	3	75 (A & B) / 120 / 360 (C)
a-C:H deposition	–	–	740 (PLS high)	–	–	–	380–270 (8 min)	–	1.5	150 / 360
Si-a-C:H deposition	–	–	740 (PLS high)	–	–	–	200–120 (8 min)	18–12 (8 min)	1.5	120 / 360

- a-C:H – Coating A

- Si-a-C:H – Coating B

- a-C:H:W – Coating C

The nominally 1 μm thick layer will be referred to as the thin variant and the 2–3 μm thick coating will be referred to as the thick variant. A coating with the substrate polished to 0.01 μm R_a will be referred to as the smooth variant and inversely those with 0.08 μm R_a will be the rough variant. To give an example, to refer to the first coating variant in Table 3.2 (top row), we would call it SS-Coating A-thin-smooth. Coatings B and C will not utilise the smooth and rough labels as their substrates all consist of the lower surface roughness.

3.3.5   Coating Thickness Measurement

Measurement of coating thickness was performed by several methods. The top layer coating thickness was primarily determined by the Calotest technique (using the Tribotechnic Millennium 200 as seen in Figure 3.4). In this method, a 30 mm diameter stainless steel ball is rotated against the surface of the coatings to wear into the layer structure. The diameter of the ball can be varied depending on the thickness of the coating. Nanocrystalline diamond solution is applied between the ball and coating surface to increase the wear.
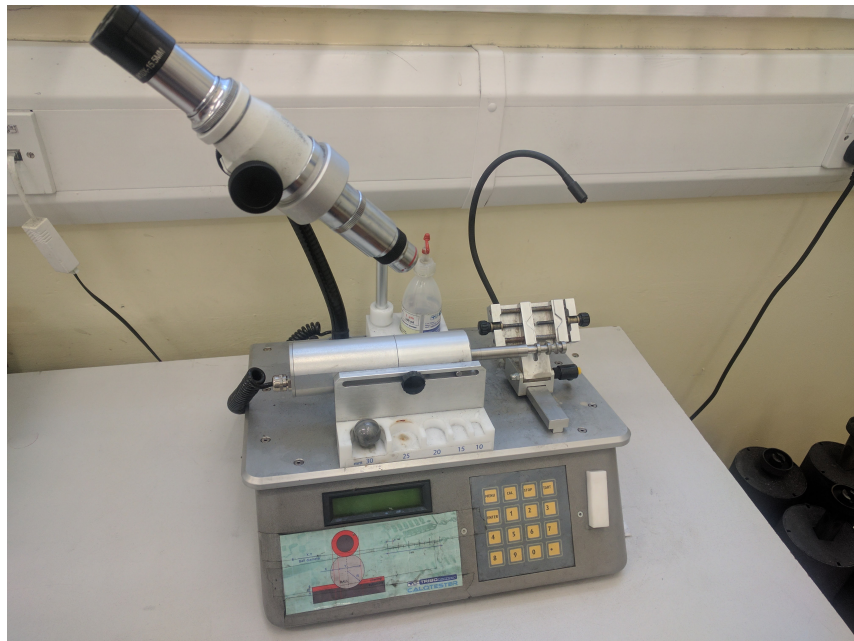
Figure 3.4: The Tribotechnic Millennium 200.

Times of between 1–10 min were used depending on the thickness of the coating. Times must be chosen carefully to wear away the material without abrasively scuffing the surface. The geometry of the wear scar is measured using optical microscopy as described in Section 2.5.6. The thick variants of Coating A on HTS and SS could not have their thickness determined using this method as the large periods of wear caused scuffing without enough wear as to determine the layer thickness. Figure 3.5 shows a failed Calotest and properly measured Calotest result for Coating B on SS.
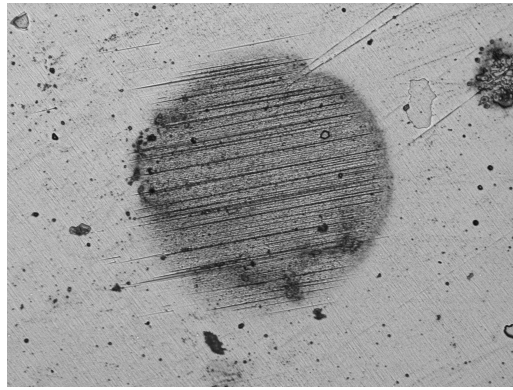
(a) Calotest with scuffing.
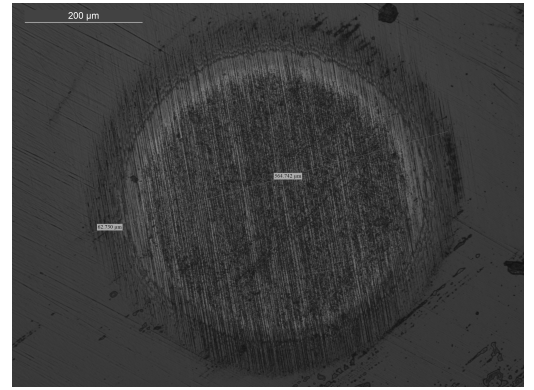
(b) Correct Calotest wear morphology.

Figure 3.5: Failed Calotest and correct morphology for Coating B on SS. Both pictures are captured at the same magnification.

The interlayer thickness (and top layer thickness of the Coating A thick variants) was determined by cross-section SEM using focussed ion beam (FIB) SEM in a FEI Helios G4 CX Dualbeam SEM located in Leeds Electron Microscopy And Spectroscopy centre (LEMAS). Platinum is deposited on the surface on the sample to protect it during material removal. The sample is tilted and a beam of Gallium ions is used to mill into the surface to reveal the substructure of the coating. A lower energy beam is used to polish the milled sample face so that the layer structure in the cross-section can be observed and the thickness of each layer measured. Figure 3.6 shows the process of cross-sectioning the coatings.

An Oxford Instruments AZtec energy dispersive x-ray spectroscopy (EDX) system was used to identify the composition of cross-section layers. Unworn areas were chosen to analyse the thickness and composition of the coatings and interlayers. The results of this methodology are seen in Section 3.4.2. This method is also applied in Chapter 6 to investigate the cross-section of impact tests.
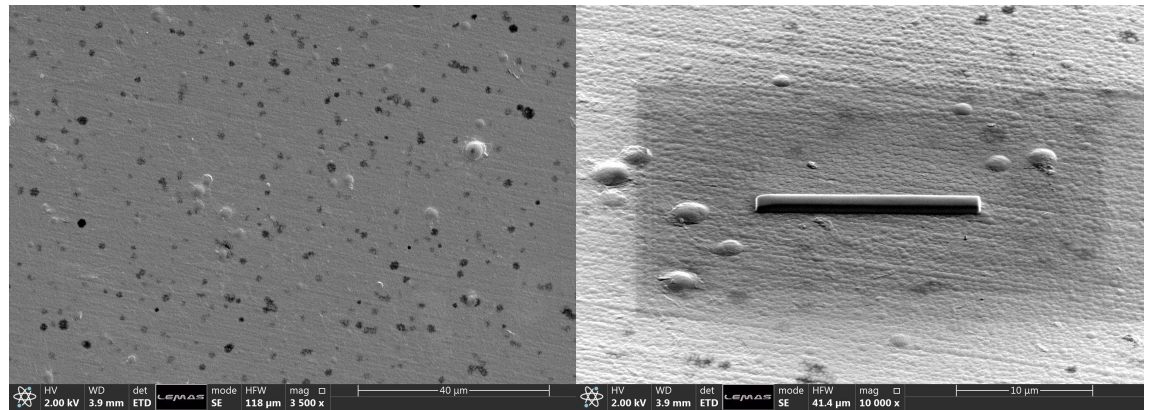
(a) Unworn area chosen for cross-section.

(b) Deposition of the protective platinum layer by ion beam.
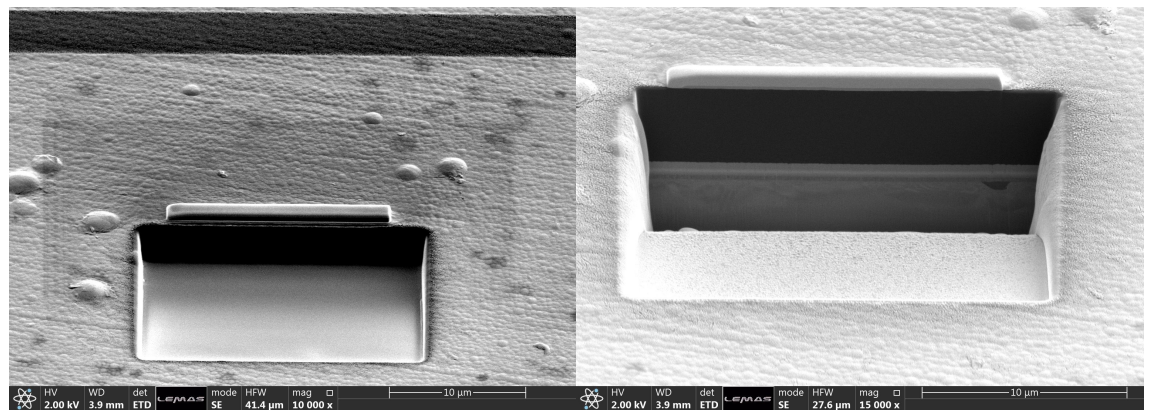
(c) Removal of material due to the gallium beam.

(d) Finer polishing of the cross-sectioned area.

Figure 3.6: Cross sectioning procedure of SS Coating A.

3.4 Results

3.4.1 Measurement of Coating Layer Thickness

Table 3.4 (located on page 84) shows the thickness of each of the constituent layers of the DLC coating structure. The adhesive (Cr) layer was, on average, 0.29 μm across all of the coatings. In Coatings A and B the WC/a-C:H:W gradient layer was 0.89 μm. This layer gradients directly into the top layer coating on Coating C resulting in a reduced thickness of 0.29 μm. The majority of the top layer coating deposited thickness were larger than intended. The only coatings seen to be close to the intended deposited thickness were Coating B on SS and Coating C on both substrates. Coating A on SS was observed to be 0.60 μm greater than the 1 μm intended thickness and approximately 2.2–2.5 μm thicker than the 2–3 μm variant. On HTS, the thinner variant was approximately 1 μm thicker and 0.80–1.50 μm thicker than the designs for the thin and thick variants, respectively. Coating B on HTS was also thicker within this same range. Overall, coatings deposited on HTS deviated from the intended thickness more often than on SS. Substrate roughness was not seen to adversely affect the deposition rate, instead the thicker coating designs

had a larger DLC layer with the rougher prepared substrate.

3.4.2   Verification of Coating Design by Scanning Electron Microscopy

Figures 3.7, 3.8 and 3.9 shows the FIB-SEM cross-sections of the unworn areas. These images were taken to corroborate the thickness measured by calotesting and to show the substructure of the coatings and interlayer system. This was only performed on one of the substrate's set of coatings as it was a verifying step. The globular structure seen at the forefront of Figure 3.8 is due to redeposition of material from the ion beam. Additionally, a Mo and V concentration can be seen at the surface of the steel and proceeding into the microstructure. The insert EDX map of Figure 3.9 shows the gradient layer present in Coating C compared to the distinct interlayer structure of Coatings A and B seen in Figures 3.7 and 3.8 respectively.

Figures 3.7, 3.8 and 3.9 show the HTS substrate microstructure from which we can discern that the hardening process has resulted in a martensitic structure [352].
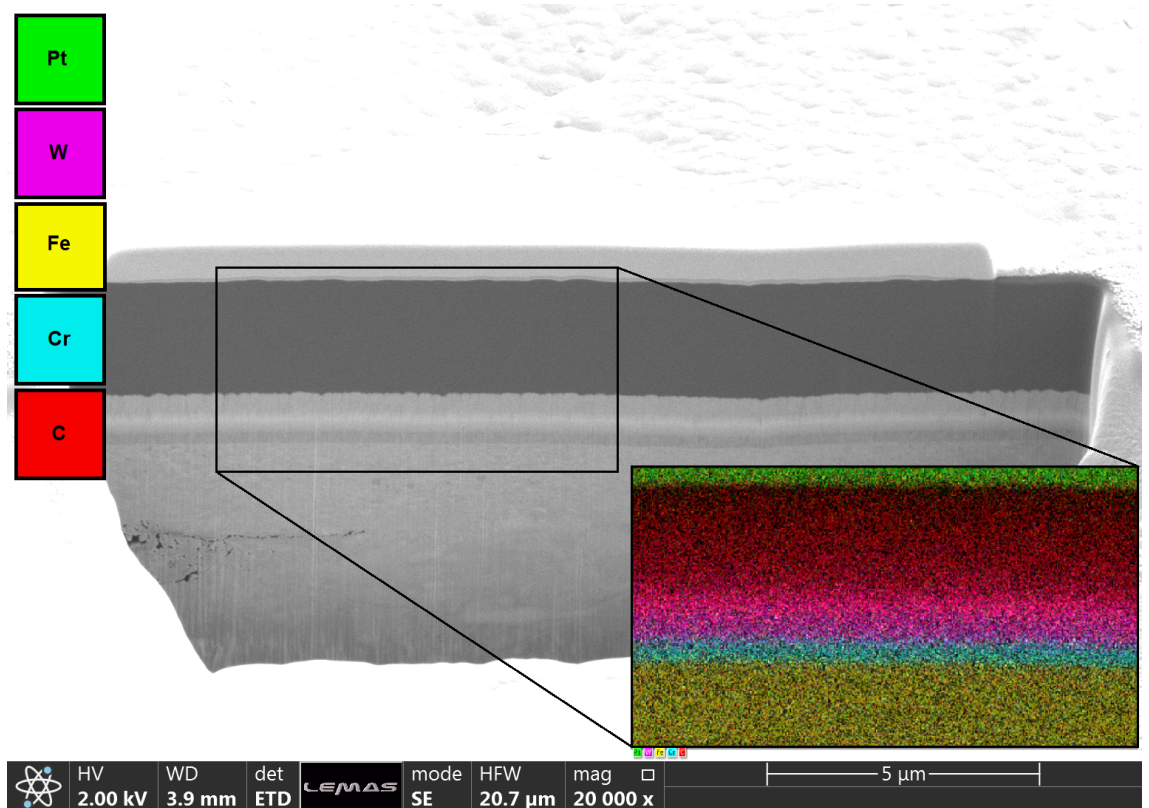
Figure 3.7: Cross-section of Coating A on HTS. Insert is an EDX map of the exposed cross-section.

Table 3.4: Measured thickness of entire coating structures.

Substrate	DLC Recipe	Nominal DLC Coating Thickness (µm)	Substrate Roughness (µm R_a)	Adhesion (Cr) layer (µm)	Gradient Layer (µm)	DLC Layer (µm)	Total Coating Thickness (µm)
SS	A	1	0.026±0.004	0.29±0.03	0.89±0.08	1.60±0.17	2.78±0.19
		1	0.0860±0.0004	0.29±0.03	0.89±0.08	1.62±0.18	2.80±0.20
		2-3	0.026±0.004	0.29±0.03	0.89±0.08	5.18±0.07	6.36±0.11
		2-3	0.0860±0.0004	0.29±0.03	0.89±0.08	5.54±0.02	6.72±0.09
	B	1	0.026±0.004	0.29±0.03	0.89±0.08	1.16±0.24	2.34±0.25
		2-3	0.026±0.004	0.29±0.03	0.89±0.08	2.88±0.17	4.06±0.19
	C	1	0.026±0.004	0.29±0.03	0.29±0.06	1.10±0.22	1.68±0.23
		2-3	0.026±0.004	0.29±0.03	0.29±0.06	2.25±0.12	2.83±0.14
HTS	A	1	0.026±0.004	0.29±0.03	0.89±0.08	2.20±0.20	3.38±0.21
		1	0.0860±0.0004	0.29±0.03	0.89±0.08	2.02±0.15	3.20±0.17
		2-3	0.026±0.004	0.29±0.03	0.89±0.08	3.82±0.09	5.00±0.12
		2-3	0.0860±0.0004	0.29±0.03	0.89±0.08	4.47±0.24	5.65±0.26
	B	1	0.026±0.004	0.29±0.03	0.89±0.08	2.17±0.16	3.35±0.18
		2-3	0.026±0.004	0.29±0.03	0.89±0.08	4.93±0.17	6.11±0.19
	C	1	0.026±0.004	0.29±0.03	0.29±0.06	1.17±0.12	1.75±0.13
		2-3	0.026±0.004	0.29±0.03	0.29±0.06	2.99±0.55	3.57±0.56
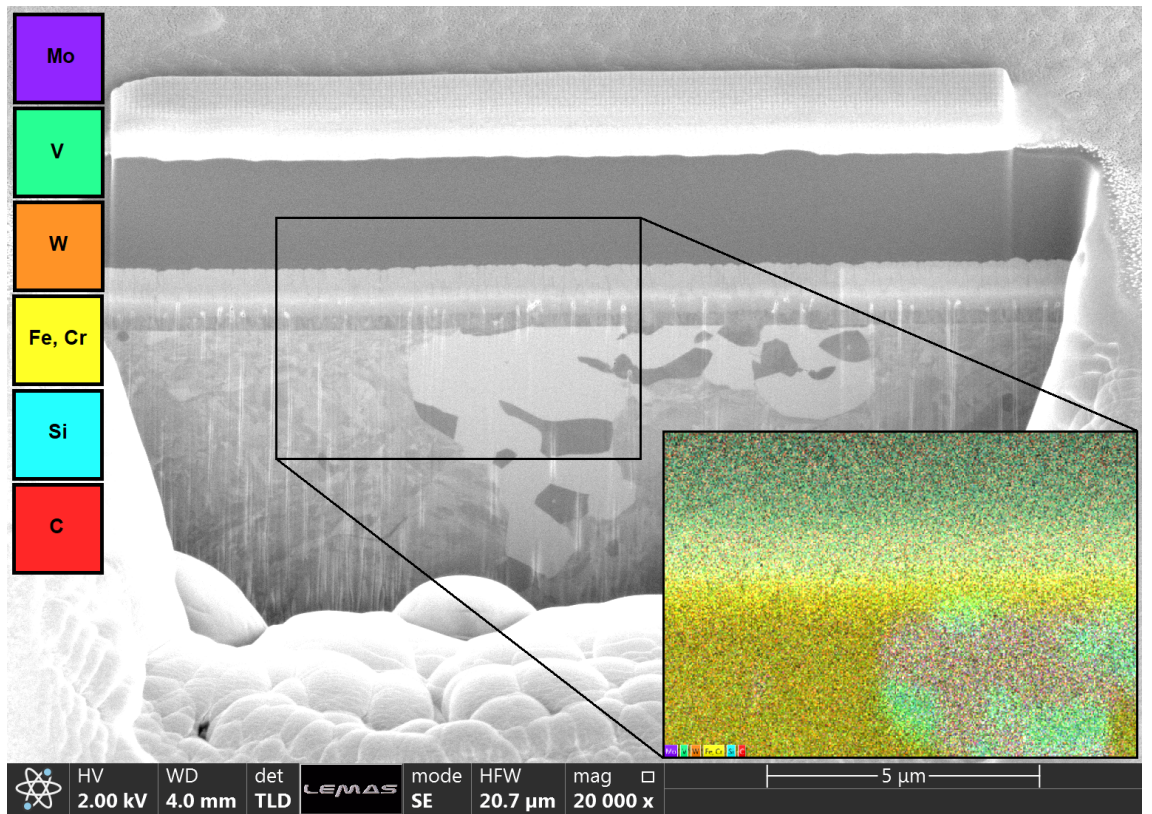
Figure 3.8: Cross-section of Coating B on HTS. Insert shows an EDX map.
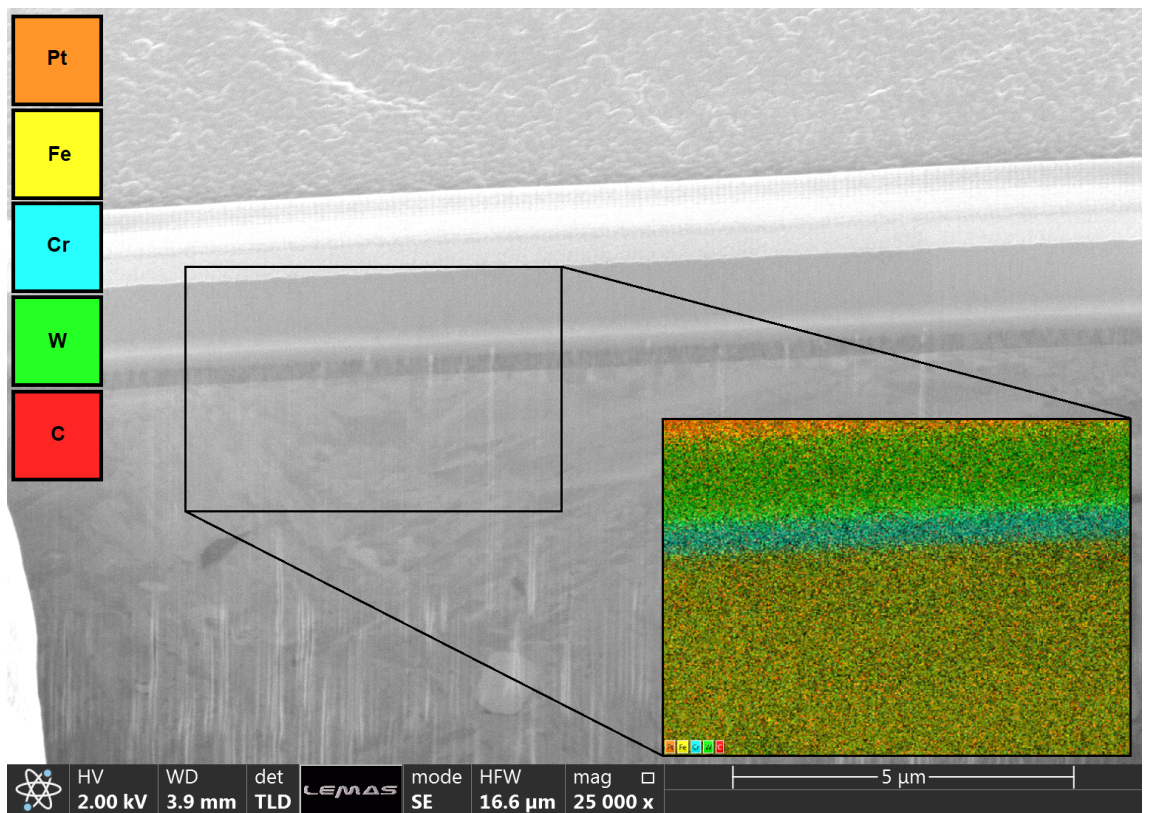
Figure 3.9: Cross-section of Coating C on HTS. Insert is an EDX map.

3.4.3 Roughness Measurements

Measurement of the smooth preparation (intended to be $0.01\,\mu m$ R_a) gave a roughness value of $0.026 \pm 0.004\,\mu m$ R_a. The rougher prepared substrate was closer to the specification with a value of $0.0860 \pm 0.0004\,\mu m$ R_a. This was measured for both substrate materials. Figure 3.10 shows a Talysurf example scan as measured on SS.
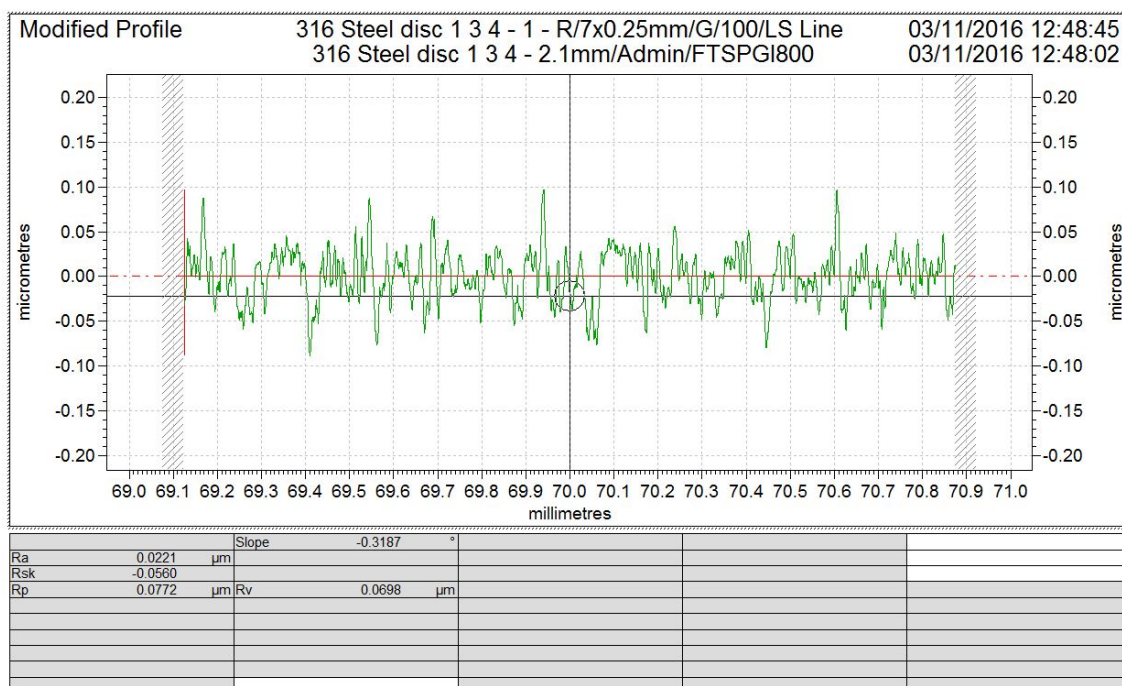
Figure 3.10: Surface roughness profile of polished SS substrate.

Chapter 7 will present the roughness values of the coatings measured on both substrates as the scan procedure, prior to a scratch, allows the roughness to be calculated.

3.5 Discussion

Table 3.4 shows that despite the standard deposition times used the achieved coating thickness was generally significantly larger than the planned thickness. Only Coating C on both substrates and Coating B on SS were within the planned thickness range. It can be seen that overall Coating A achieved a higher coating thickness based on the deposition times giving it the highest deposition rate of the coatings ($0.023\,\mu m\,min^{-1}$) for the thin coatings on HTS). The difference in coating thickness could be attributed to the increased hardness of the tool steel substrate benefiting coating growth as less ion subplantation will occur before true film growth [353]. The hardness measurements will be detailed in Chapter 4. Different electrical conductivities or substrate self-biasing could influence the coating re-sputtering rates and therefore affect the thickness.

Some clarity in the coating structures can be found in the use of structure zone diagrams (SZDs). The idea of which was first introduced by Movchan and Demchishin [354] in 1969. They showed that thick (0.3–2 mm) evaporated films could be described in terms of the homologous temperature (T_h) of the coating, T/T_m, where T is the substrate temperature in Kelvin and T_m is the melting point of the coating material in Kelvin. Three

zones were identified with distinct structural and physical properties. Low temperature zone 1 ($T_h < 0.3$) structures are made up of tapered columnar grains separated by pores or voids. At higher homologous temperatures ($0.3 < T_h < 0.5$), atomic mobility is higher and the dense columnar structures of zone 2 can form. Zone 3 ($T_h > 0.5$) occurs at yet higher homologous temperatures where recrystallisation and grain growth create large crystalline grains.

There have been several developments of SZDs. Thorton proposed a model specifically for sputtered metal coatings [211, 212]. Barna and Adamik set the boundaries differently and introduced a transition zone between zones 1 and 2 [355]. Kelly and Arnell developed a novel structure zone model for closed-field unbalanced magnetron sputtering deposition [356]. Anders [357] proposed a modified SZD wherein the linear T_h axis would be replaced by a generalised temperature with the homologous temperature and the temperature shift of particles arriving on the surface taken into account. The general linear pressure axis would be replaced with a logarithmic axis for normalised energy describing displacement and heating effects causing by kinetic energy transfer from particle bombardment. Finally, the unlabelled z axis would be replaced by net film thickness to allow the maintenance of the familiar qualitative illustration of film structure while also allowing for thickness reduction by densification, sputtering or ion etching.

DLC is amorphous [35, 216, 217] and therefore the structures proposed in the various SZDs are necessarily applicable. Additionally, PACVD was used to deposit the DLC layers from a gaseous precursor (acetylene). However, to explore the idea, carbon's melting point is 3823 K [358]. With the substrate temperature of at least 200 °C (473 K), the T_h would be 0.12 for Coating A (were it to be deposited from a solid graphite source). For the interlayer materials of Cr and WC, their melting points are 2180 K [359] and 3273 K [360] respectively. This gives T_h values of 0.22 and 0.14 for Cr and WC respectively. This produces zone 1 columnar structures.

DLC will undergo various structural transformations at different temperatures such as the conversion to nano-crystalline graphite at 300 °C in ambient air [361]. Depending upon the effective ion temperature inside the chamber, some structural changes throughout deposition may occur. The ion energy at the substrate surface (amplified by the temperature in the chamber) affects the structures of all coating methodologies. Though DLC coatings cannot be classified in the same way as polycrystalline coatings due to their amorphous structure [35, 216, 217]. Barna and Adamik [355] noted that with high levels of oxygen contamination Al will form an amorphous structure. This is similar to that seen with Coatings A and B but this is due to the coating's amorphous nature rather than contamination. Thornton [212] noted that for CVD, zone 2 columnar structures are formed when tungsten deposition was controlled by surface reactions and approximated infinite diffusion. This is similar to the structures formed for Coating C. The measurement of ion energies will, however, be able shed light onto the difference in coating thickness; the only difficulty is measuring them. The structures of the coatings can be seen in Figure 5.4 for reference.

3.6   Summary

The Hauzer Flexicoat 850 PVD/PECVD system was used to successfully deposit a series of DLC coatings on both SS and HTS. a-C:H, Si-a-C:H and a-C:H:W were deposited at two designated thickness ranges on two surface roughness preparations on the coupons.

Coating thickness was determined using the Calotest method and cross section SEM.

The measured coating thickness was found to be significantly higher than the intended thickness with Coating A having the largest deviation. Coating C was seen to be within specification. Future coatings deposited in this deposition system should have reduced deposition times to give lower coating thickness. SEM also confirmed the deposited coating architecture showing the adhesive Cr layer, gradient WC layer and the top layer DLC structure. Surface profilometry was used to confirm the prepared substrate surface roughness. The smooth preparation was seen to be slightly rougher than the specification. Automated polishing techniques would allow for the specified roughness to be reached in less time therefore making the coating preparation more efficient. Zone 1 columnar growth is predicted for the interlayer materials however the gaseous precursor (an amorphous structure of DLC) makes the homologous temperature unsuitable for predicting the structure of this particular carbon based coating.

The use of the Langmuir probe plasma diagnostics system would allow for the ion deposition energies to be monitored to aid in determining the factors that affect the final achieved coating thickness. The distortion of the electric field would have to be accounted for however. The engagement of the WC magnetron target and introduction of HMDSO into the chamber, for the deposition of coatings B and C, would affect the ion energies within the chamber (affecting the substrate ion bombardment species) and therefore altering the coating growth and structure. The presence of additional elements will also affect the mechanical properties by changing the atomic structure of the coating [225, 251, 268, 273, 362, 363]. This will be discussed further in Chapters 5 and 6.

Chapter 4

Mechanical Characterisation of DLC Coatings

4.1 Introduction

Nanoindentation is now a widely used technique to assess the mechanical properties of both bulk materials and thin films. Hardness, elastic modulus, fracture toughness, yield strength and residual stress can be determined with the correct experimental set-up. In the case of bulk materials, the test parameters can be varied to a greater degree than when testing coatings however the response of individual material must be considered. Single indentations can be performed with a specified loading time or loading rate. Partial load-unload indentation consist of multiple loading steps each defined by a maximum load and loading rate [48, 166].

ISO standard single nanoindentations and indentation using a Vickers micro-indenter were used to characterise the hardness of the substrate materials. This allowed the micro and nano-hardness to be evaluated for each material. A partial load-unload technique was used to characterise the coating's mechanical properties and subsequent change in the properties as more substrate effects are seen deeper into the material structure.

Mechanical properties are key in defining the tribological response of materials [19, 44, 71, 322] however standard indentation will only produce a single hardness value within the 10 % range specified by the ISO 14577 standard [162] which is sub-optimal for multilayer coatings whose properties change with their structure. The partial load-unload technique produces multiple indent steps within a single indent location allowing for more detailed though more complex analysis.

Adhesion testing using scratch testing is also a standardised technique used to assess the adhesion of coatings. This technique gives both qualitative information in the type of failure experienced and quantitatively in the critical loads at which failures occur. As several critical loads are measured, Fox-Rabinovich and Zhang [310, 311] have used scratch crack propagation resistance (SCPR) to assess the adhesion of coatings in their resistance to cracking under increasing progressive load.

4.2 Methods

4.2.1 Single indent methods

4.2.1.1 Coating Properties

Nanoindentation following the ISO 14577 standard was used to examine the mechanical properties of DLC deposited on SS. A depth controlled indentation with maximum of 10 % of coating thickness was used with the depth set for each coating. A maximum of 100 mN was allowed to reach this depth. An initial contact load of 0.01 mN was used with a loading and unloading rate of $0.2\,\mathrm{mN\,s}^{-1}$. A dwell period of 60 s was used for thermal drift correction post-indentation. A total of 100 indentations were performed per coating. The area function of the indenter was found by indentation into a fused silica reference sample. Hardness (H) and elastic modulus (E) were calculated by applying Oliver-Pharr analysis [168]. E and ν (0.2) are Young's modulus and Poisson's ratio for the coating. The Poisson's ratio of 0.2 was taken as an approximation from the collected values of Hainsworth and Uhure [217]. E_i (1140 GPa) and ν_i (0.07) are the same quantities for diamond respectively [167].

Figure 4.1 shows a model ISO standard single indent on SS-Coating A-thin-smooth. The contact depth can be seen to not exceed 170 nm to adhere to the specification of indents being no more than 10 % of the total coating thickness. However this specification is more valid for HTS rather than SS [48]. A pop-in event can be seen to occur at approximately 150 nm of contact depth.
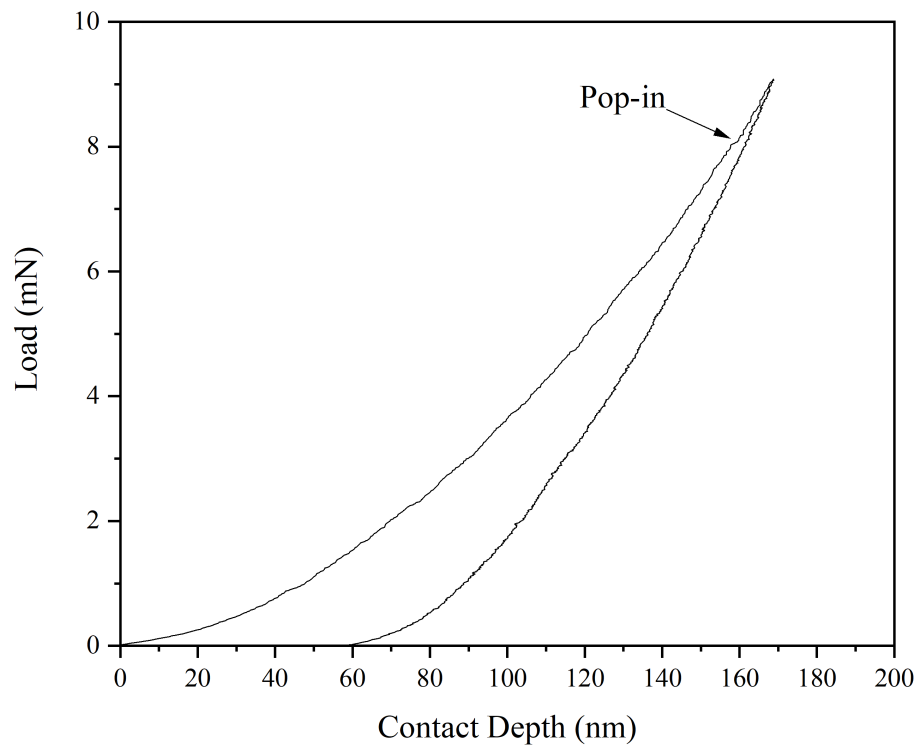
Figure 4.1: Load against contact depth hysteresis graph of SS-Coating A-thin-smooth performed using the ISO 14577 standard.

4.2.1.2 Substrate Properties

Both nanoindentation and microindentation were used to characterise the mechanical properties of the substrates. For the nanoindentations, a maximum load of 500 mN was used. The indenter contact velocity was $0.50\,\mu\text{m}\,\text{s}^{-1}$ with a load and unload time of $2\,\text{mN}\,\text{s}^{-1}$. 60 s was used for thermal drift correction as with the other single indentations. 1 s was specified for the dwell time at maximum load. 10 indentations were performed for each substrate material. A Poisson's ratio (ν) of 0.27 was used to convert from reduced modulus (E_r) for SS [364] and 0.285 for HTS [343]. A Shimadzu micro-indenter was used to measure the Vickers hardness of the substrates with a load of 0.5 kg.

4.2.2 Partial Load-unload Nanoindentation

Partial loading nanoindentation under load control was carried out using a Nanotest Vantage nanoindentation system (Micro Materials, UK) with a Berkovich diamond indenter. A total of 10 indentations with 40 loading points, in a range of 0–500 mN, per sample, was used to characterise the change in mechanical properties with depth in the coating system. A time of 2 s was used for the loading and unloading. A dwell time of 1 s was used at maximum load. Thermal drift correction was performed by a 60 s hold in the final unload step. The indenter contact velocity was set to $0.50\,\mu\text{m}\,\text{s}^{-1}$. The same analysis parameters for E are used as mentioned above.

Figure 4.2 shows a model partial load-unload on HTS-Coating A-thin-smooth. The

same broad hysteresis pattern is seen as in Figure 4.1 however the "load" section of the graph consists of multiple load and unload steps. Oliver-Pharr analysis [168] is performed on each of these steps to obtain the mechanical properties at the maximum contact depth reached for that individual step. The thermal drift correction in the final unload portion of the graph can be seen.
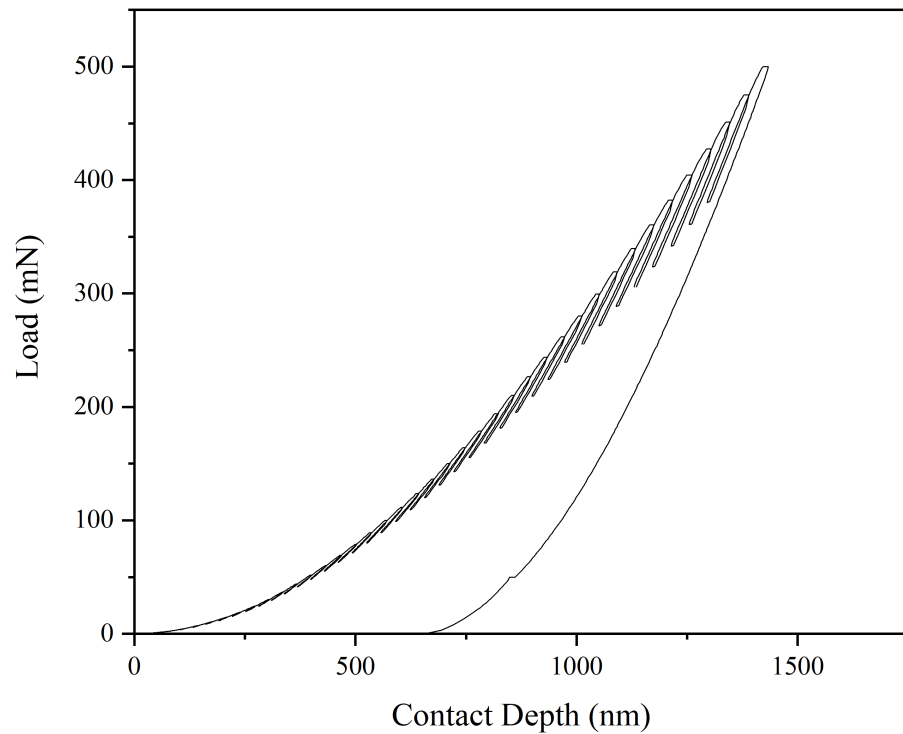
Figure 4.2: Load against contact depth hysteresis graph of SS-Coating A-thin-smooth performed using the partial load-unload method.

4.2.3 Scratch testing

Progressive loading scratch testing was performed with a Tribotechnic Millennium 200 scratch tester to assess the coating adhesion. A load of 0–50 N with a loading speed of $100\,N\,min^{-1}$ and a scratching speed of $10\,mm\,min^{-1}$ were applied. A $200\,\mu m$ radius Rockwell C diamond indenter was used for testing. L_{C1} and L_{C2} loading points were analysed. The larger scale scratch test was performed to assess the cracking resistance of the total coating structure. Smaller probe radii could be used to study inter-layer cracking phenomena [282], this will be seen in Chapter 7. Figure 4.3 (located on page 94) shows a microscopy image (taken with the Keyence VHX-6000) of a typical macro-scratch with the critical load positions annotated. Spallation is seen at L_{C1} with chevron cracking appearing before and continuing after indicating a brittle failure. Tensile cracking is seen at L_{C2}. Gross spallation is seen near the maximum load of the scratch [301, 306]. Lateral stiffness of the scratch test platform is seen to be lacking at higher loads with the track drift observed.
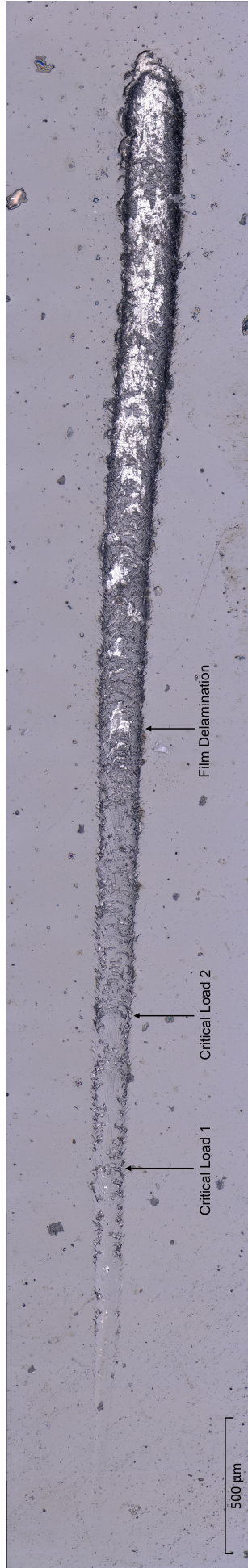
Figure 4.3: A typical macro-scratch of SS-Coating A-thin-smooth. Critical loads 1 and 2, and film delamination is annotated.

4.3   Results

4.3.1   Substrate Properties

Table 4.1 shows the comparison of the hardness data obtained by Vickers microindentation and nanoindentation methods. We can clearly note that the nano-indentation hardness of both substrates is higher than the micro-indentation hardness. This can be explained by the indentation size effect (ISE) [184].

Table 4.1: Comparison of micro-hardness and nano-hardness of the substrate materials. The micro-hardness values represent the Vickers units converted into GPa for comparison.

Substrate	Vickers Micro-hardness	Micro-hardness (GPa)	Nano-hardness (GPa)
SS	175.43 ± 13.19	1.86 ± 0.14	2.65 ± 0.10
HTS	704.67 ± 3.85	7.46 ± 0.04	9.98 ± 0.30

4.3.2   Comparing ISO Standard Indentation to Partial Load-unload

By plotting the results of hardness determined by single indent and partial load-unload on the same axis, the relative accuracy of both methods can be analysed. Figure 4.4 shows the results of both methods on SS-Coating A-thin-smooth. We can clearly see that the maximum values of the single indent method are higher. The average hardness using single indent is 21.9 ± 2.3 GPa compared to 19.4 GPa for the partial load-unload.
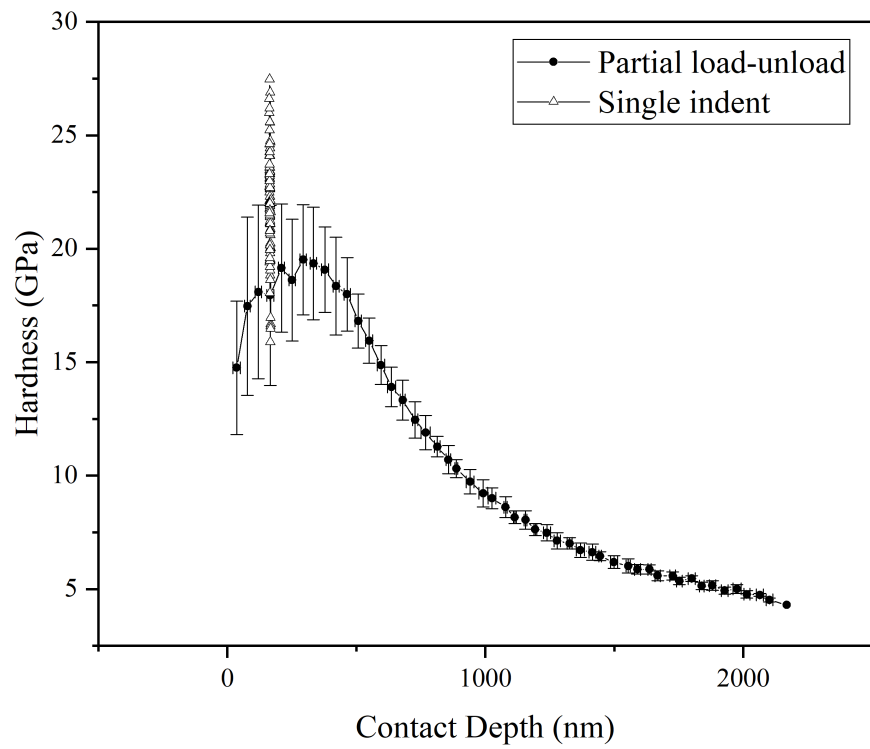
Figure 4.4: Comparison of hardness using single indent and partial load-unload on SS-Coating A-thin-smooth.

Figure 4.5 shows the results of SS-Coating B-thin-smooth by application of both indentation methods. For this coating the maxima of the partial load-unload is in the upper range of the single indent hardness. The average hardness of the single indent is 14.1 ± 1.9 GPa compared to 18.3 GPa for the partial load-unload.
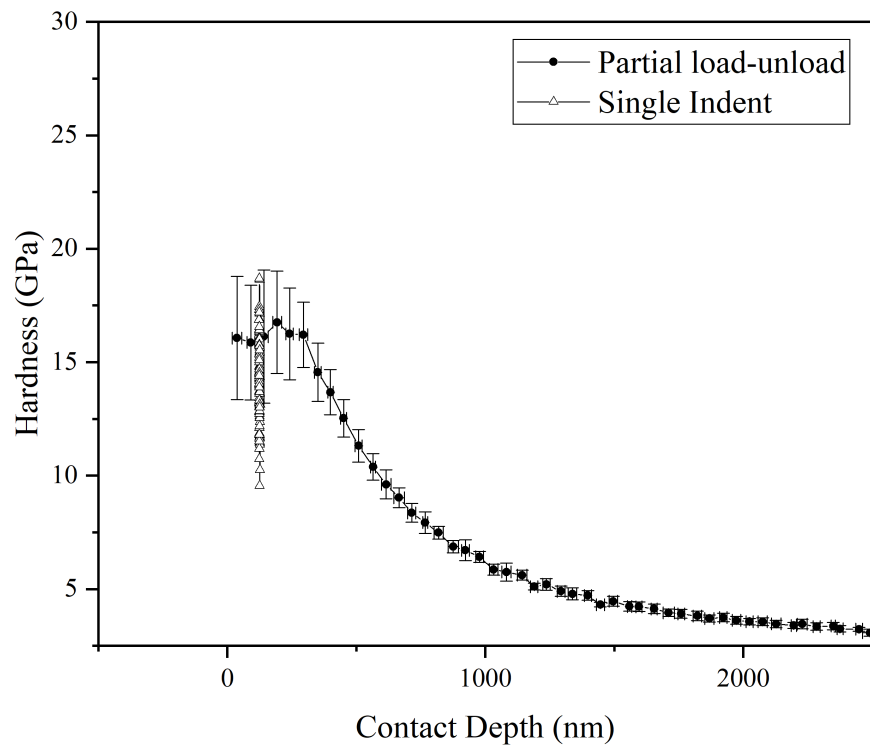
Figure 4.5: Comparison of hardness using single indent and partial load-unload on SS-Coating B-thin-smooth.

4.3.3   Coating Load Support

The coating load support provided by each substrate material can be assessed by modelling the normalised indentation depth as done by Korsunsky et al. [183]. By doing this, we can analyse how far into the coating structure the hardness data propagates.

Figure 4.6 shows the fitting of the Korsunsky model on the normalised indentation depth hardness data of HTS-Coating A-thin-smooth. The hardness data is seen to stop at approximately 0.4 normalised indentation depth. A lack of plateau at larger indentation depth shows that full substrate dominated hardness has not been reached.

Model	HTSAthinsmooth (User)
Equation	Hs + ((Hf - Hs)/(1 + k * x^2))
Plot	Mean Hardness
k	5.91031 ± 0.45802
Reduced Chi-Sqr	0.6858
R-Square (COD)	0.72061
Adj. R-Square	0.72061
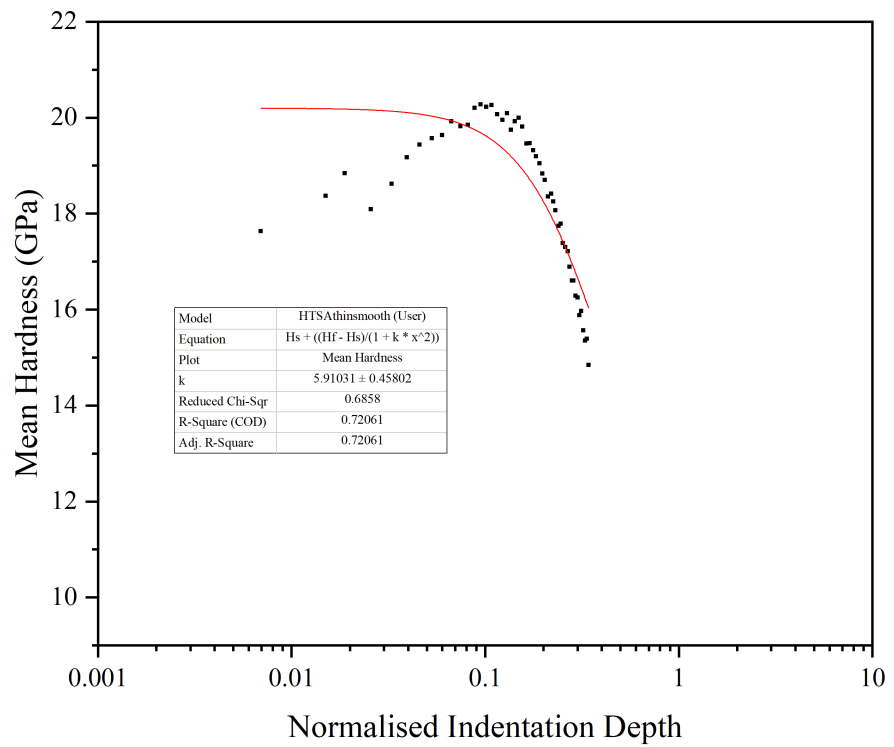
Figure 4.6: Hardness plotted against normalised indentation depth on HTS-Coating A-thin-smooth.

Figure 4.7 shows the fitting on SS-Coating A-thin-smooth. The data is seen to propagate through almost the entirety of the coating structure as it almost reaches a normalised indentation depth of 1. At this high indentation depth, the data is beginning to level off showing that substrate effects are beginning to emerge.

The table within the figure reads:

Model	SSAthinsmooth (User)
Equation	Hs + ((Hf - Hs)/(1 + k * x^2))
Plot	Mean Hardness
k	9.63652 ± 0.51779
Reduced Chi-Sqr	1.34266
R-Square (COD)	0.95062
Adj. R-Square	0.95062
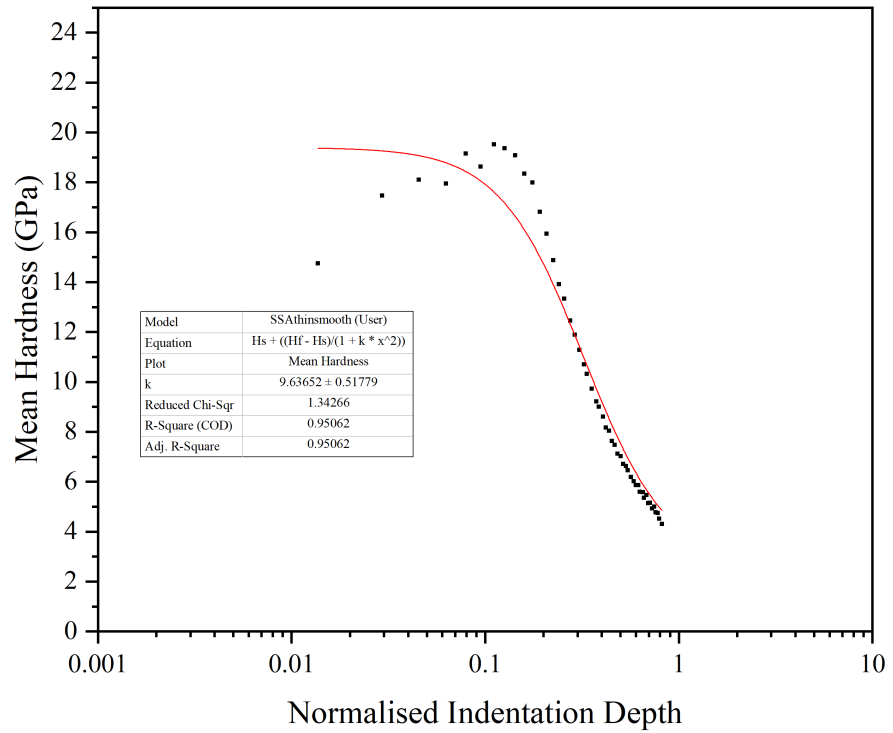
Figure 4.7: Hardness plotted against normalised indentation depth on SS-Coating A-thin-smooth.

In both Figures 4.6 and 4.7, the hardness is seen to be noticeably lower at smaller indentation depths. This can be explained by the initial contact being elastic and lacking a fully developed plastic zone [166].

4.3.4 Hardness Variation with Depth

The hardness change into the coating structure (with increasing contact depth) is seen in Figures 4.8 and 4.9. By analysing the peak hardness and extrapolating to the surface, the surface hardness can be determined [166]. We can note that the maximum contact depth is higher for the coated SS DLCs. The hardness is seen to decrease to a lower level within the contact depth range reached in the test. Generally, we see that Coating A has the highest hardness, followed by Coatings B and C respectively across both substrate materials. The rougher prepared substrate is seen to have either a slightly higher hardness value on SS (Figures 4.8a and 4.8b) or a greater uncertainty throughout the contact depth range as on HTS (Figures 4.9a and 4.9b).
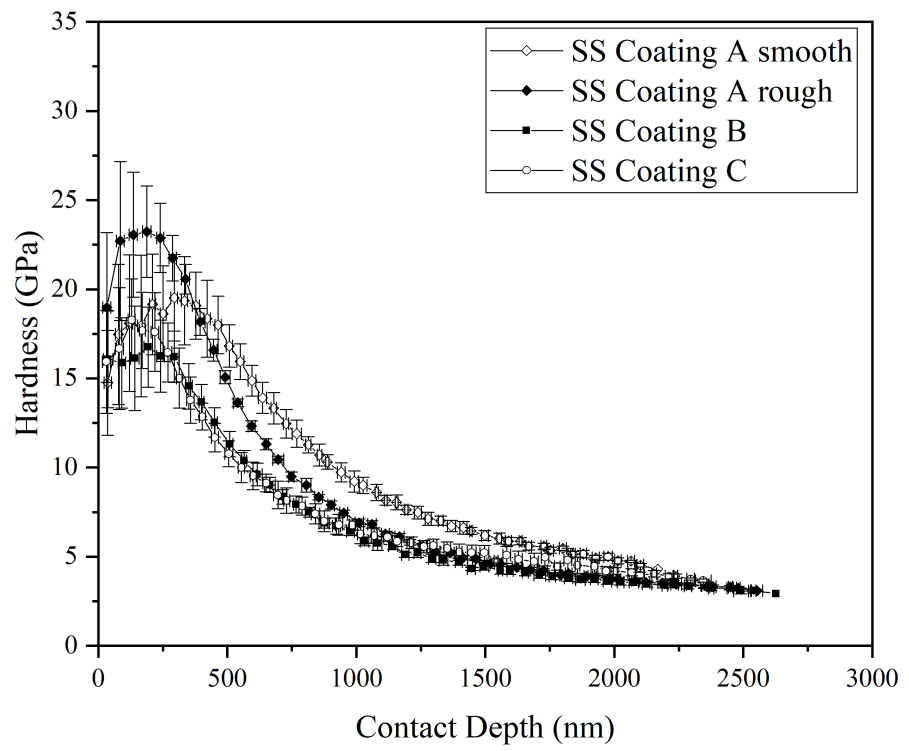
(a) SS thin
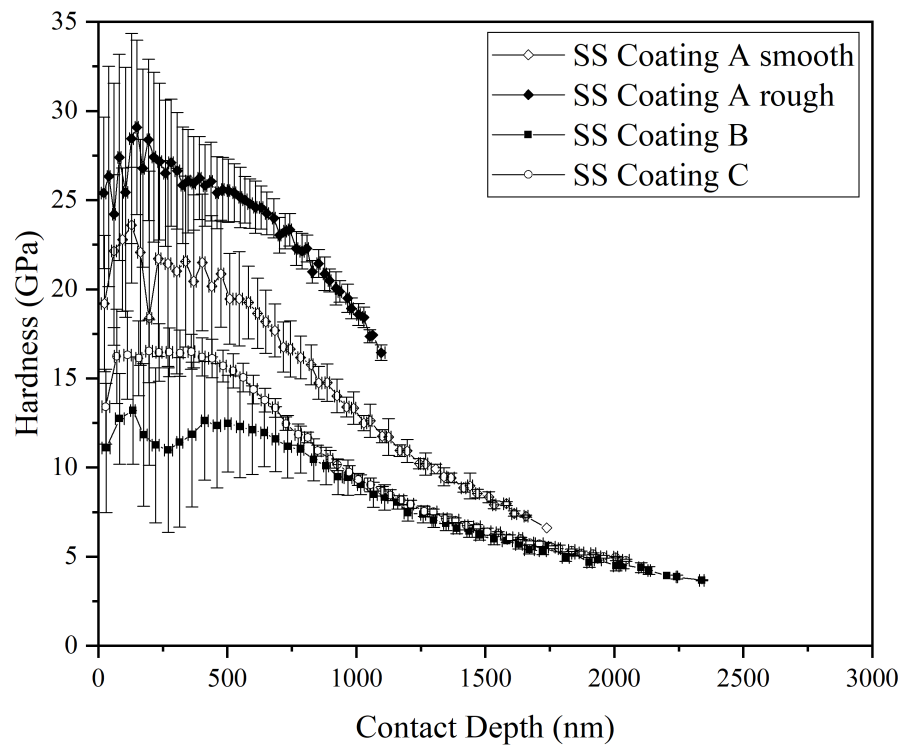
(b) SS thick

Figure 4.8: *H* varying with contact depth into coating system on SS.

100
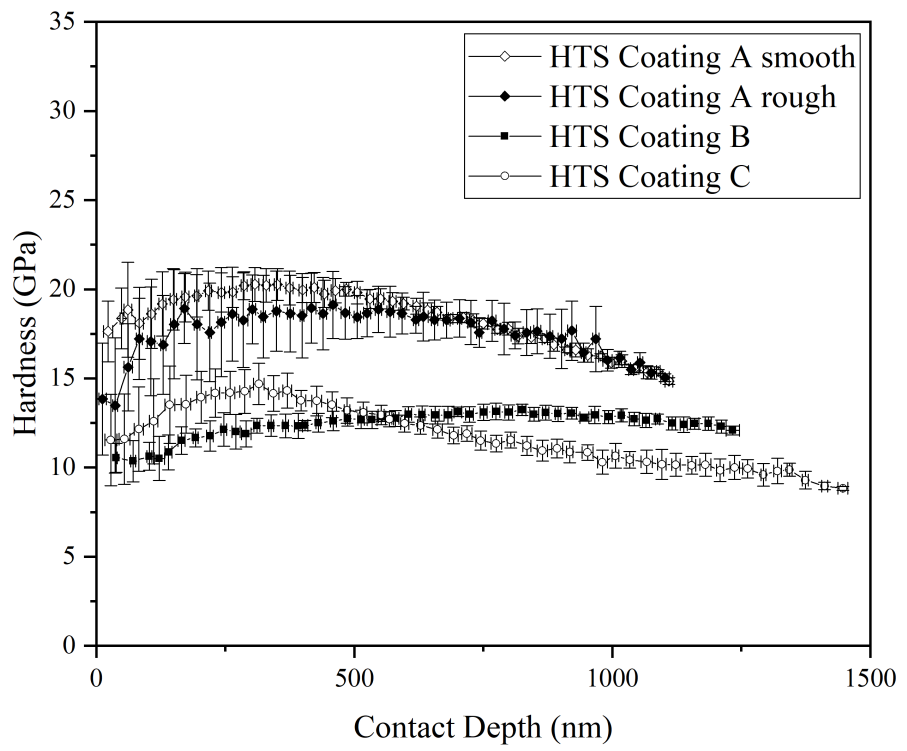
(a) HTS thin

(b) HTS thick

Figure 4.9: *H* varying with contact depth into coating system on HTS.

101

4.3.5 Elastic Modulus Variation with Depth

Elastic modulus is less dependent upon indentation depth than hardness as the determination of stiffness is taken from the gradient of the unload curve however there is still a drop off at higher penetration depths towards the substrate modulus [48, 166, 365]. Figures 4.10 and 4.11 show the elastic modulus variation with depth on both substrates on thick and thin variants of the coating. On the thin variants, Coating C is seen to have the highest elastic modulus followed by A and B respectively. On the thicker variants of SS and HTS, Coating A-rough is seen to have a higher modulus however this could be due to errors in the recognition of the surface due to roughness and the area function [166]. Coating C is seen to have the next highest elastic modulus on SS-thick however Coating A-smooth is seen to have a higher value of HTS. As with the hardness data in Figures 4.8 and 4.9, the SS data reached a higher contact depth compared to the HTS coatings. This shows the difference in coating thickness on this method of indentation but also the increased load support of the HTS substrate.
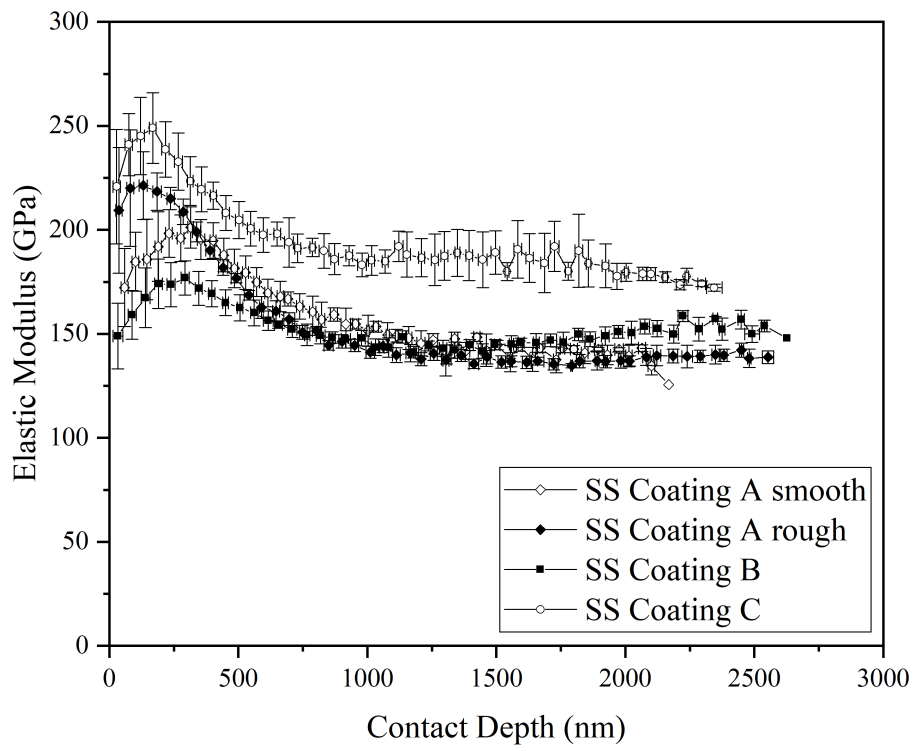
(a) SS thin
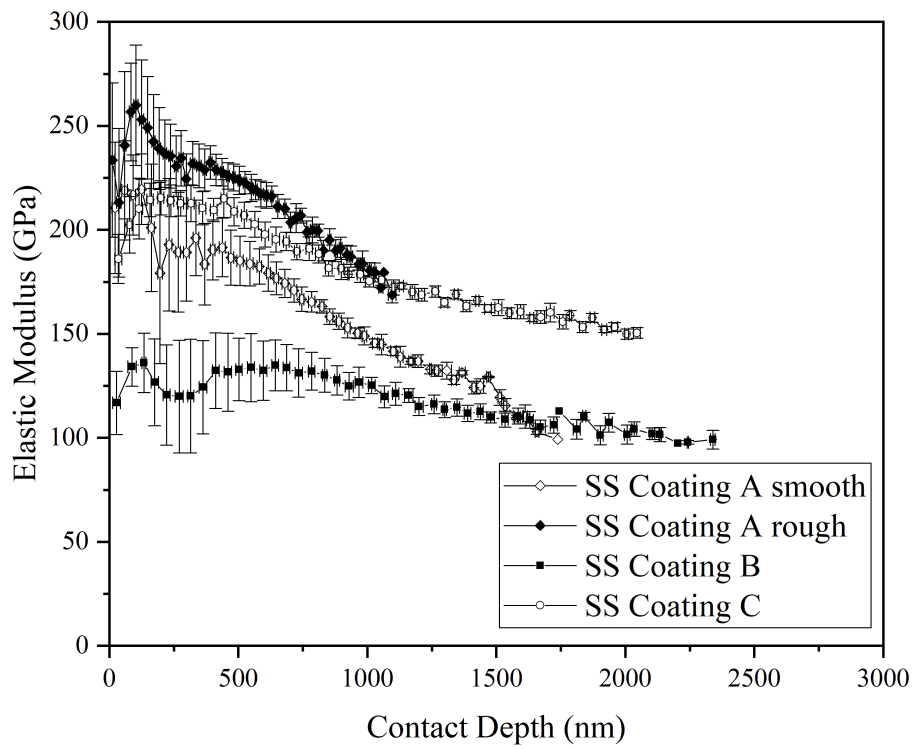
(b) SS thick

Figure 4.10: *E* varying with contact depth into coating system on SS.
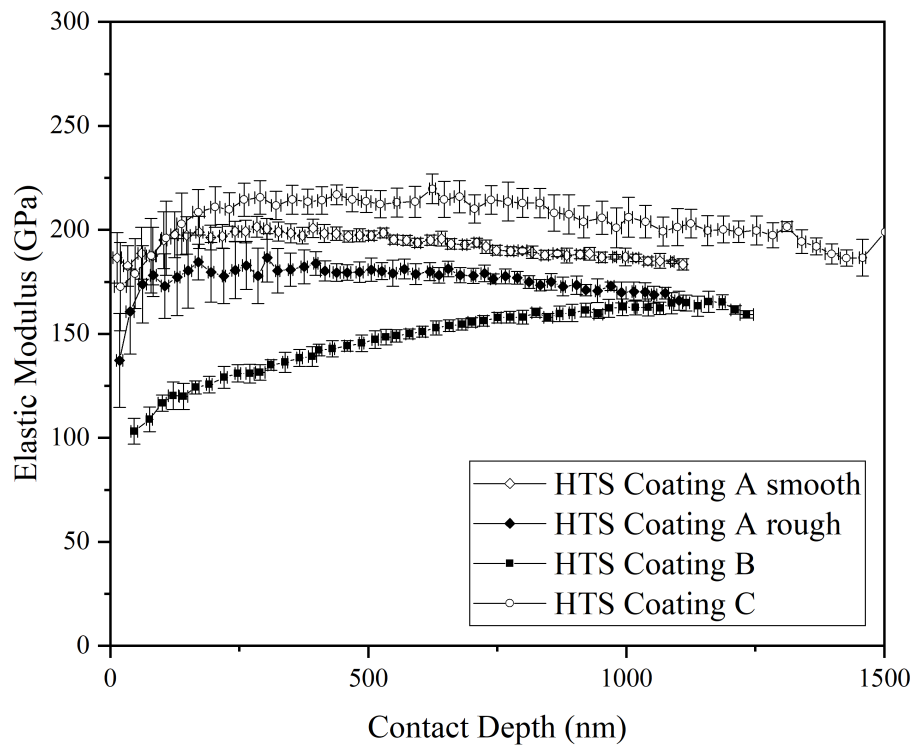
(a) HTS thin
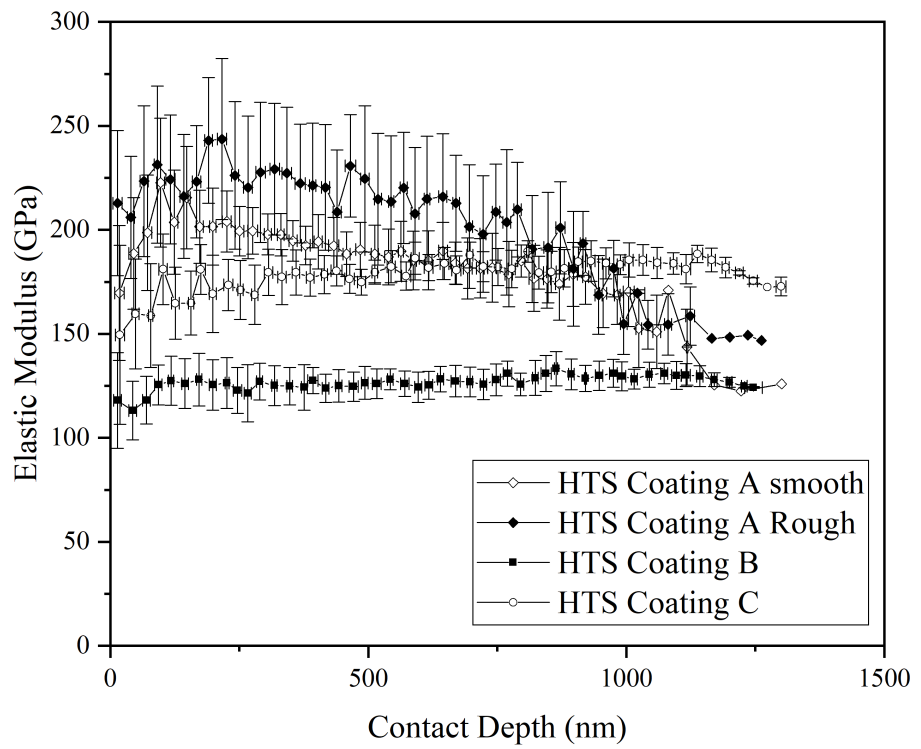
(b) HTS thick

Figure 4.11: *E* varying with contact depth into coating system on HTS.

4.3.6 H/E **Ratio Variation with Depth**

Figures 4.12 and 4.13 show the maps of H/E ratio varying with contact depth. Due to the binning process in which the data is averaged into 50 steps across the range of contact depth, some variance is expected, depending upon the depth reached for each loading step, thereby resulting in SS Coating A appearing to skip the first point. This data binning shows that on HTS (Figure 4.13a), the spacing between each point is smaller than that on SS due to the lower penetration of each indentation step. This indicates a greater amount of load support from the HTS substrate due to the smaller penetration with each repetitive indentation. In indentations on both substrates, the elastic modulus does not decrease to a large degree throughout the range of contact depth due to the measurement of contact stiffness being less affected by surface roughness and indentation depth [166, 365]. Thereby, we can surmise that the decrease in H/E ratio with contact depth is due to the decrease in hardness at higher contact depths as more substrate effects are seen [183]. Due to the thinner coatings of SS, the substrate effects are seen at lower contact depths.

On average, Coating A is seen to have the highest H/E ratio on both HTS and SS due to consistently higher hardness compared to the elastic modulus. However, it does appear to have a lower H/E at lower contact depths. This is due to both the surface roughness being higher resulting in lower measured hardness low contact depth [366] and initial elasticity in the contact due to the mean contact pressure being lower than the hardness of the film [166, 282]. Coating B could be predicted to have a smoother surface finish resulting in higher H/E at low contact depth (however this is not the case as seen in Table 7.3). Lower measured hardness except at lower contact depths results in a lower H/E values compared to Coating A. Coating C sees the consistently lowest H/E values due to its high elastic modulus throughout the contact depth range measured. These trends in H/E ratio follow that seen by Beake et al. [282] on similarly coated systems. The higher measured hardness (the higher hardness is a topographical effect) of the rougher films seen in Figures 4.8 and 4.9 is seen to give a higher H/E ratio for the same films respectively.
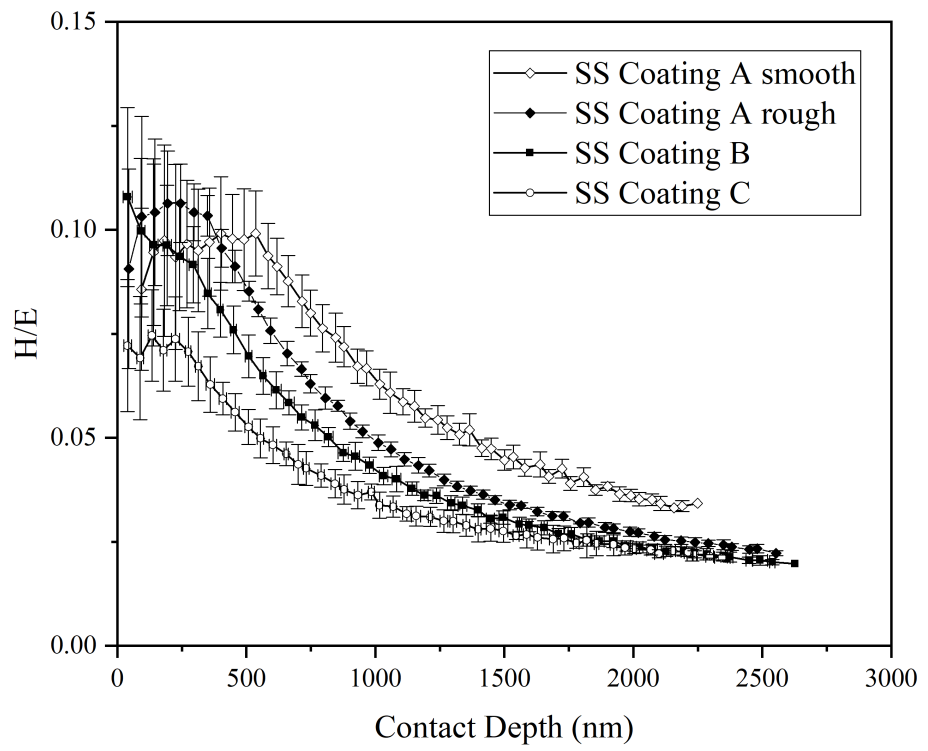
(a) SS thin
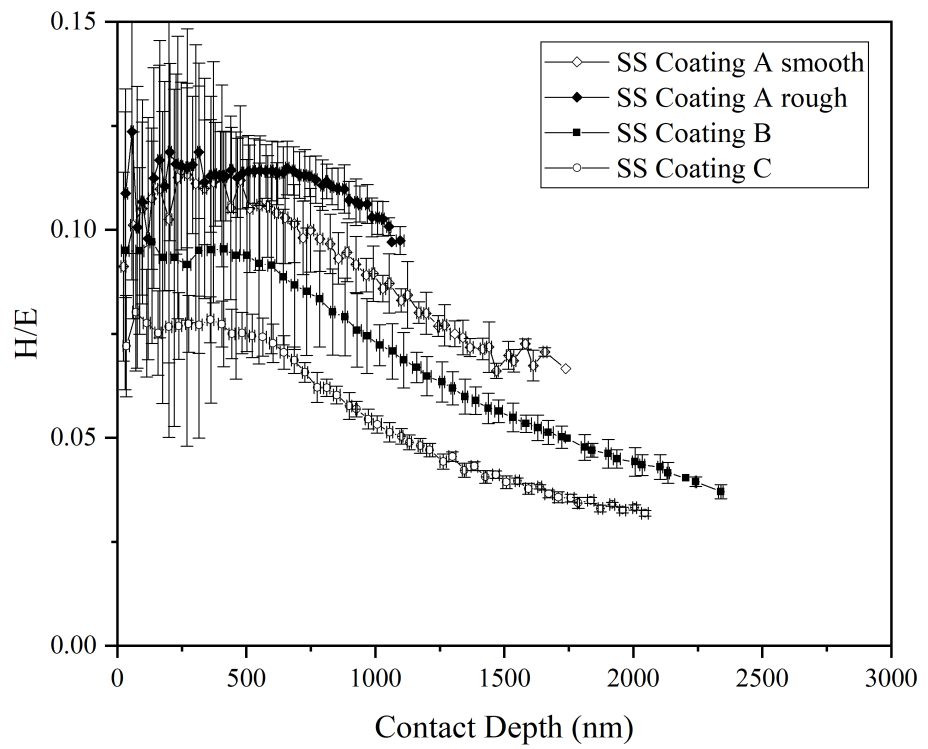
(b) SS thick

Figure 4.12: H/E ratio varying with contact depth into coating system on SS.

106
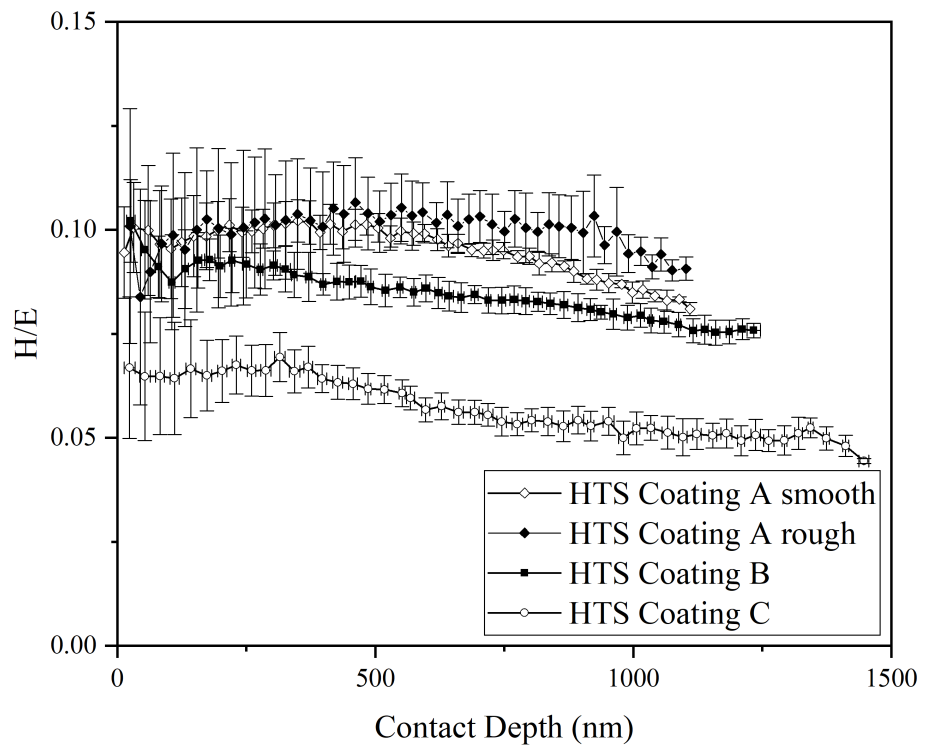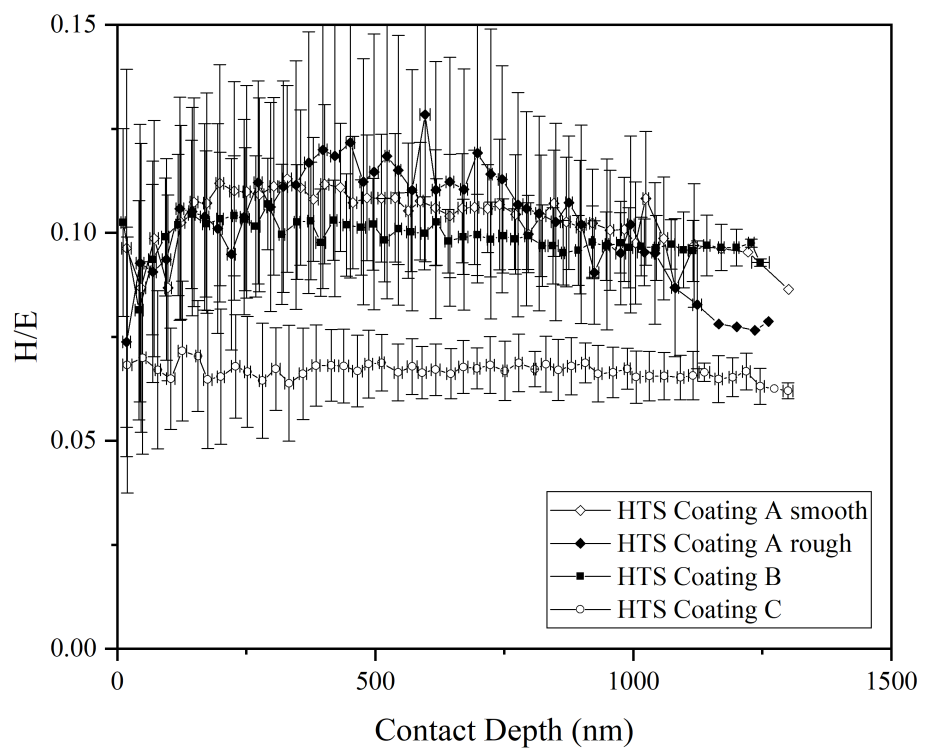
(a) HTS thin

(b) HTS thick

Figure 4.13: H/E ratio varying with contact depth into coating system on HTS.

4.3.7 Average Mechanical Properties

Surface mechanical properties of the coatings are determined by extrapolating partial loading nanoindentation to the surface (zero contact depth). Hardness (H) is found by extrapolating the maximum to the y-axis to give the surface hardness [166]. The standard deviation of the hardness is seen in Figures 4.8 and 4.9; however, due to the mathematical fitting to zero contact depth, the values of mechanical properties in Table 4.2 have no error associated with them. The elastic modulus (E) is determined by taking the mean of the maximum range to negate surface contact effects reducing the modulus at low contact depths [166]. Similar to hardness, the elastic modulus values in the table have no error associated with the single value but the errors can seen in the graphs for individual values throughout the contact depth range. The standard deviation of quantities produced by mathematical operations of others (such as H/E for the substrates) can be calculated by Gaussian error propagation, the methodologies to do this are detailed in Appendix D. This has been used throughout this thesis.

Table 4.2[1] (located on page 109) shows the nanoindentation data for both the coated and uncoated substrates. The substrates show distinct differences in their mechanical properties with HTS having surface hardness with a value of 10.0 GPa compared to 2.6 GPa for SS. The mean elastic modulus of HTS is slightly higher with a value of 229 GPa compared to 223 GPa for SS. This results in HTS having higher values of both H/E and H^3/E^2 (0.042 and 0.017 GPa respectively). The mechanical properties of the SS substrate are similar to those recorded by Ward et al.[367] prior to coating with a-C:H with Si interlayer. The hardness of the HTS after hardening is similar to that seen by Wilbur et al. [368] though a nitriding processing was used compared to the flame hardening for this study. The thin and smooth preparation of Coating A has the highest hardness value when deposited on both substrates with values of 19.4 GPa and 20.2 GPa on SS and HTS respectively. The highest mean elastic modulus for the thin coating variant is seen on Coating C on both substrates with values of 235 GPa and 218 GPa for SS and HTS respectively. Increasing the thickness of the coating reduced the hardness and stiffness of both Coatings B and C on both substrates. Conversely the thin and rough thick coating preparations of Coating A saw the higher hardness and elastic modulus with the highest values being on SS-Coating A-thick-rough with values of 26.2 GPa and 255 GPa for H and E respectively.

HTS has a much higher value of 0.418 for H^2/E (resilience) compared to 0.030 for SS. This is due to the increased hardness of the material. Generally, the thicker coatings show higher H^2/E values due to their increased hardness. This however, is not seen on Coating B on SS. The highest value is seen HTS-CoatingA-thick-rough (2.807). On average across all substrate, Coating A presents the highest resilience metric, followed by Coatings B and C respectively.

4.3.8 Scratch testing

Table 4.3[1] (located on page 111) shows the L_1, L_2 and the SCPR of the coatings. The variance in coating thickness may play a part in the difference of Scratch Crack Propagation Resistance (or Scratch Toughness as called by Zhang) (CPR$_S$, $L_{C1}(L_{C2} - L_{C1})$) [310, 311] measured across all the coatings particularly on Coating C deposited on HTS

---

[1]Each of these tables are displayed on their own page in landscape orientation due to the amount of data contained within.

Table 4.2: Mechanical properties of the coatings and uncoated substrates determined by partial load-unload nanoindentation.

Substrate	DLC Recipe	DLC Coating Thickness (μm)	Surface roughness (nm R_a)	H (GPa)	E (GPa)	H/E	H^3/E^2 (GPa)	H^2/E (GPa)
SS	Uncoated	–	26±4	2.6±0.1	223±5	0.012±0.001	0.00040±0.00003	0.030±0.002
	A	1.60±0.17	22.2±9.4	19.4	215	0.090	0.158	1.751
		1.62±0.18	47.1±10.2	22.5	210	0.107	0.260	2.411
		5.18±0.07	20.3±5.1	24.2	218	0.111	0.298	2.686
		5.54±0.02	49.6±4.5	26.2	255	0.103	0.277	2.692
	B	1.16±0.24	25.7±1.5	18.3	187	0.098	0.176	1.791
		2.88±0.17	49.2±9.7	14.9	143	0.104	0.162	1.553
	C	1.10±0.22	40.5±8.0	16.2	235	0.069	0.077	1.117
		2.25±0.12	31.7±13.7	16.9	210	0.080	0.109	1.360
HTS	Uncoated	–	26±4	10.0±0.3	239±7	0.042±0.002	0.017±0.001	0.418±0.022
	A	2.20±0.20	26.0±10.3	20.2	199	0.101	0.207	2.050
		2.02±0.15	44.7±8.5	19.4	191	0.101	0.200	1.970
		3.82±0.09	84.0±32.7	21.6	205	0.105	0.240	2.276
		4.47±0.24	82.9±19.5	25.3	228	0.111	0.311	2.807
	B	2.17±0.16	48.0±12.4	13.1	164	0.080	0.083	1.046
		4.93±0.17	96.8±15.1	12.6	129	0.098	0.120	1.231
	C	1.17±0.12	26.2±1.9	13.9	218	0.064	0.056	0.886
		2.99±0.55	39.2±23.1	13.3	183	0.073	0.071	0.967

109

which has approximately 1 μm thinner top layer DLC for the thin variant. In general, we see a larger CPR_S for the coatings deposited on HTS versus SS on the thin variant. On SS the highest value of CPR_S is for Coating C with a value of $241\,N^2$. This compares to $71.1\,N^2$ and $175\,N^2$ for Coatings A and B respectively. The values for CPR_S on HTS for Coatings A-thin-smooth and B-thin are extremely similar with values of $281\,N^2$ and $280\,N^2$ respectively. Coating C has a slightly lower value of $206\,N^2$. Increasing the roughness of the film is seen to have mixed effects across Coating A on both substrates; on the thin variant of Coating A the value increases to $214.56\,N^2$ however for the thicker coating the value decreased by approximately $13\,N^2$. Little effect was seen with HTS-Coating A-thin however the rougher variant saw a decrease in adhesion. Increasing the coating thickness, is seen to decrease the CPR_S value compared to the thinner variant of the coating implying there may be an optimum thickness range for coating adhesion.

4.4 Discussion

4.4.1 ISE

The difference in micro-indentation hardness and nano-indentation hardness demonstrated by Table 4.1 shows that with lower indentation loads (0.5 kgf (4905 mN) vs 500 mN), a higher hardness is expected with Berkovich or Vickers indenters compared to a reduction in hardness expected with spherical shapes [189]. Multiple authors have investigated numerical modelling to show how hardness varies with depth (and consequently load) such as the work of Nix and Gao [182] and more recently the work of Kim et al. [369] whose model takes into account surface roughness. For these substrate materials, the effect of sampling a larger number of grains in micro-indentation is mostly likely the cause of the effect. Neither material is known to have a high elastic recovery and a high degree of work hardening is not expected [184].

4.4.2 Comparing Single indent and Partial Load-unload

The partial load-unload technique has been used relatively infrequently throughout literature as the mechanical properties of a single layer thin film are generally determined by the ISO 14577 standard [162]. Analysing the differences in Figures 4.4 and 4.5, we can see that for Coating A, the partial load-unload technique underestimated the average hardness whereas for Coating B it found a higher surface hardness. Looking at the measured film roughness in Table 7.3, we can see that there is little difference in the DLC roughness. However Figure 4.4 does show a decrease in the surface hardness characteristic of the lack of a fully formed plastic region at lower loads and contact depths [166]. This could indicate that the technique has extreme sensitivity to surface roughness with it performing better on slightly rougher films or underestimating the hardness where low plasticity is seen early in the indentation cycles. Despite this, the technique did measure hardness within the same range as the single indentation method with the maximum hardness showing less variation than the single indent. Therefore, this technique can be ruled as being accurate but currently lacks precision and more work is required to confirm (particularly the influence of surface topography).

A possible unwanted side effect of cyclic indentations is the possibility of fatigue, this was noted by Xu et al. [89] with the development of an indentation fatigue law.

Table 4.3: Scratch testing critical loads and scratch crack propagation resistance ($L_{C1}(L_{C2} - L_{C1})$).

Substrate	DLC Recipe	DLC Coating Thickness (μm)	Surface Roughness (nm R_a)	L_{C1} (N)	L_{C2} (N)	Scratch crack propagation resistance $L_{C1}(L_{C2} - L_{C1})$ (N²)
SS	A	1.60±0.17	22.2±9.4	27.54±3.67	30.12±1.63	71.05±111.00
		1.62±0.18	47.1±10.2	26.26±2.27	34.43±1.85	214.56±79.11
		5.18±0.07	20.3±5.1	23.74±4.52	31.95±1.72	194.89±120.63
		5.54±0.02	49.6±4.5	22.71±3.47	30.69±2.44	181.21±100.31
	B	1.16±0.24	25.7±1.5	23.58±2.30	30.99±0.71	174.73±59.26
		2.88±0.17	49.2±9.7	20.43±2.45	29.67±1.62	188.72±64.11
	C	1.10±0.22	40.5±8.0	24.11±3.19	34.12±2.20	241.34±98.73
		2.25±0.12	31.7±13.7	21.00±1.64	29.78±2.13	184.47±58.26
HTS	A	2.20±0.20	26.0±10.3	23.68±2.72	35.55±2.97	281.08±100.68
		2.02±0.15	44.7±8.5	26.665±5.590	37.20±1.98	281.27±168.76
		3.82±0.09	84.0±32.7	17.98±0.84	28.56±1.20	190.30±27.77
		4.47±0.24	82.9±19.5	21.56±0.74	28.09±2.55	140.77±57.41
	B	2.17±0.16	48.0±12.4	27.19±2.25	37.50±1.22	280.33±73.36
		4.93±0.17	96.8±15.1	24.57±2.80	30.80±2.07	153.13±87.23
	C	1.17±0.12	26.2±1.9	22.10±1.77	31.41±1.28	205.75±51.01
		2.99±0.55	39.2±23.1	19.80±3.89	27.07±2.07	143.89±91.69

Chicot and co-workers [90, 171] explored the use of this technique to study fatigue and found variations in the elastic response of magnetite as a function of dwell time. This was thought to be as a result of reorganisation of dislocation networks during creep. Therefore, some unintended effects may occur as a result of cyclic indentation.

4.4.3 Load Support

The increased load support of the HTS substrate can clearly be seen in comparison of Figures 4.6 and 4.7. The hardness data points are seen to be more closely packed as normalised indentation depth increases in HTS compared to SS. Additionally, the hardness is seen to begin to decrease from its peak value to approximately 15 GPa. Whereas for SS the Korsunsky model is seen to be be more closely followed at higher normalised indentation depth as the measured mechanical properties are more representative of the substrate properties [183]. The difference in penetration into the coatings structure with coated SS (increased contact depth in Figures 4.8, 4.10 and 4.12) compared to coated HTS also indicates that there is increased load support provided by a harder substrate material. It's also interesting to note that the peak hardness is seen at 0.1 normalised indentation (Figures 4.6 and 4.7) depth corroborating the ISO 14577 specification of indentations no more than 10 % coating thickness [162]. The effect of this load support is seen to be especially prevalent in Chapter 6 where the increased hardness of the HTS substrate, greatly increased the coating resistance to erosive and impact wear. Some evidence of this was also seen in Chapter 7 with fewer critical load failures seen on coatings on HTS.

4.4.4 Mechanical Properties

In an indentation test, increasing the roughness of the film will decrease the measured hardness and elastic modulus [366]. However, depending on the methodology used by the indenter system to detect the surface and calculate the indenter area function accordingly, it is possible to see an increase the hardness and elastic modulus as seen in Figures 4.8 and 4.9 and Figures 4.10 and 4.11 respectively.

Though there are some differences due to coating thickness, load support and roughness as seen by Figures 4.8 and 4.9 and Figures 4.10 and 4.11, the general trends of Table 4.2 can be discussed. Coating A is seen to be the hardest of the coatings followed by B and C respectively. Coating C has a high E thereby reducing its H/E and H^3/E^2. The H/E and H^3/E^2 are ranked in the same order as hardness giving Coating A the best predicted friction and mechanical wear resistance [321, 322, 332]. Coating thickness is seen to be beneficial to the mechanical properties of Coating A but detrimental to those of Coatings B and C. This may be a result fo the growth dynamics of the coatings [275].

Hainsworth and Uhure collected the properties of several types of DLC, they found that hard a-C:H would have a hardness between 10–20 GPa and an elastic modulus of 140–170 GPa. For W DLC, they found a hardness and elastic modulus of 13.2 GPa and 100–150 GPa respectively. Si DLC had a hardness of 14–25 GPa and elastic modulus of 100–175 GPa [217]. Lanigan et al. [270] investigated the oxidative wear in Si doped DLCs and produced Si,O doped and Si,O,F doped variants of DLC. These coatings had measured hardness values of 13.9 GPa and 14.4 GPa respectively. Yue et al. [273] found hardness values between 15–19 GPa for W DLC depending upon the W content in the film. Elastic modulus also varied from 160–230 GPa. Hasselbruch et al. [267] produced W doped DLCs for dry rotary swaging; these coatings had hardness and elastic moduli

between 15–20 GPa and 170–210 GPa respectively. Zheng et al. [370] studied the structure and mechanical properties of W doped DLCs for space applications. Their hardness and elastic moduli values were between 9–15 GPa and 90–110 GPa respectively. An increase in C_2H_2 flow rate was seen to decrease the mechanical properties with the ratio of WC and a-C:H determining the hardness of the final coating structure.

Wei and Yen [371] noted that as film thickness increases on DLC deposited on Si without an interlayer, hardness decreases. This was also accompanied by a structural change i.e. increase in I_D/I_G ratio implying that the sp^3 content decreased. This was not the case for some of the DLC variants in this study. Coating A was seen to exhibit increasing hardness with increased film thickness (and therefore deposition time), this could be due to some effect of the energetics of ion bombardment affecting the sp^3 content though this process isn't yet fully understood [275]. There could also be some effects on the residual compressive stresses of the coatings due to ion bombardment.

4.4.5 Coating Adhesion

The SCPR proposed by Zhang and co-workers [310, 311], consists of several metrics. The full parameter itself can be used to rank coating adhesion generally with a higher value indicating a better adhered coating. The parameter, however, is very dependent upon the coating thickness and radius of the indenter. This helps to explain the relative weakness of Coating C compared to Coatings A and B. The adhesion in general follows the pattern seen by Beake et al. [282] on similar coating architectures. Coating C, despite being thinner than the other coatings, displays excellent adhesion. This is characteristic of low H^3/E^2 coatings being able to deform more elastically prior to L_{C2} failure. Zhang and co-workers [372–374] have shown that increased scratch toughness (and therefore adhesion) came at the expense of hardness and reduced compressive residual stresses improved adhesion.

Adhesion will be assessed on the nano-scale in Chapter 7 where the reduced probe radius results in greater contact pressure and this focuses the von Mises stress at a lower contact depth which will measure adhesion between the interlayers and top layer coating [282, 312]. The radius of the larger scale scratch (200 μm) instead tests the adhesion of the entire coating structure to the substrate. Therefore, in general, this scale of scratch test is primarily applicable for the assessment of the coating/substrate interfacial adhesion.

4.5 Summary

The mechanical properties of the substrates and coatings deposited upon them were determined by nanoindentation. Single indents were used to measure the properties of the uncoated substrates and partial load-unload indentation was applied on the coatings to analyse the substrate effects with increasing contact depth. A single indentation method was also employed to compare with the partial load-unload method's accuracy in determining the thin film mechanical properties. Macro-scale scratch testing was employed to assess the adhesion of the coatings.

Comparing micro-indentations to nano-indentations, the ISE can be seen to affect both SS and HTS with measured hardness increasing at the nano-scale. Partial load-unload indentation measured mechanical properties within the same range as single indentation however the analysis is more complex. Analysis of the mechanical properties of Coating

A using normalised indentation depth has shown that HTS gives more load support to the coatings due to the reduced normalised indentation depth and less substrate contribution to measured property values at larger contact depths. Generally, Coating A is seen to be the hardest of the coatings followed by B and C respectively. Coating C has a higher elastic modulus resulting is reduced H/E and H^3/E^2. Coatings A, B and C generally follow a trend of decreasing H/E and H^3/E^2 therefore predicting that Coating A will have the best wear resistance and lowest coefficient of friction (without tribochemical effects). Increased coating thickness reduces the mechanical properties for Coatings B and C but increases them for Coating A. Despite its thinner top layer compared to Coatings A and B, Coating C displays excellent scratch adhesion characteristics. Coatings A and B are generally better adhered to the substrate however; this is due to their increased thickness over Coating C.

Future studies should investigate the potential of fatigue wear and elastic effects affecting the measurement of mechanical properties using the partial load-unload technique however the use of increasing load with each indentation step does reduce this as a concern. However pile up and sink in are still concerns though material dependent as with ISO 14577 indentation [166].

Chapter 5

Structural Characterisation of DLC

Coatings

5.1 Introduction

This chapter will provide an overview of the structural characterisation of the coatings, specifically focusing on the sp^2/sp^3 ratio, I_D/I_G ratio (level of amorphisation) and proportions of the dopants in the coating. Elemental proportions were determined by multiple methods: EDX in both SEM and TEM and stitching of EELS spectra. It is well known that the coating properties are affected by the deposition conditions [216], those being the ion energy, substrate temperature and deposition rate. As the previous chapter covered the mechanical properties of the coatings, the results gained in this chapter will give context to the properties determined for each of the coating architectures.

5.2 Methods

5.2.1 Raman Spectroscopy

A Renishaw Raman microscope was used to determine the I_D/I_G ratio to provide an estimate of the amorphisation of the carbon within the coatings [250, 375]. A 488nm laser was used to target a Raman shift range of 1000–2000 cm^{-1}. In this frequency range, we observe a dual peak phenomenon. The D peak is around 1350 cm^{-1} and the G peak is around 1580–1600 cm^{-1} [250, 251]. Gaussian fitting with ratios of the peak area was used for these spectra as opposed to the Lorentzian with full width half maxima [250]. In this method, the intensities of the D and G peaks (areas beneath each peak) is referred to as I_D and I_G values respectively. Baseline subtraction and peak fitting was performed using OriginPro. The diameter of the Raman laser on the surface is determined by the Airy disk equation [376]. For a 488nm laser, we find a theoretical diameter of 397nm using a 0.75/50x lens.

The diameter of the Raman laser on the surface is determined by the Airy disk equation [376]:

$$D = \frac{1.22\lambda}{NA} \tag{5.1}$$

Where *D* is the diameter, λ is the wavelength of the laser and *NA* is the numerical aperture of the lens. For a 488nm laser, the theoretical diameter is 397nm using a 0.75/50x lens. This is important as it defines the sampling area and interaction volume of the Raman laser.

The Renishaw Raman microscope uses an optical microscope to control the focusing of the sampling laser therefore the there is no inbuilt depth sensitivity to the spectral measurements beyond the interaction volume of the laser. The laser is taken as either in focus or out of focus. The interaction volume is complex to calculate (generally perceived as not worth doing) and is normally modelled by a cylinder. True depth profiling can only be achieved with a confocal microscope which allows the sampling volume to be precisely controlled [377, 378]. The thin coating variants on both substrates were used for Raman studies.

5.2.2   SEM

SEM was performed using the Carl Zeiss EVO MA15 variable pressure SEM. It has an Oxford Instruments AZtec EDX system with mapping and linescan capability. FIB cross-sectioning was performed with the same FEI Helios G4 CX DualBeam system as detailed in Chapter 3.

5.2.3   TEM And EELS

TEM and EELS was performed using a FEI Titan Themis with a maximum power of 300 kV. A 200 keV electron beam was used along with a collection angle of 100 mrad and entrance aperture of 2.5 mm. 30 s was used for the exposure and integration time. The sp^2 and sp^3 proportions were found from the carbon K edge. The sp^2 fraction is found by calculating the area of a Gaussian fitting of the 285 eV peak (π states) and 290 eV due to the σ states. This was compared to highly orientated polycrystalline graphite (HOPG) which is 100 % sp^2 [264, 379]. EELS data processing was performed with Gatan GMS 3. TEM-SAD was also used to analyse the crystalline structure of the coatings (or apparent lack thereof due to the size of the crystallites) [238].

The Hartree-Slater model [380] was used to stitch together the EELS spectra of Si and C to determine the percentage composition of both elements in the coating. The Si edge energy was specified to be 99 eV with a fitting range from 80–154 eV. The signal sum width was 15 eV. The C edge energy was 284 eV with a fit range from 189.8–164.2 eV. The signal sum width was 40.2 eV. This method could not be utilised to determine the proportions of elements in Coating C as the major edges for W lie at 1809 eV and 1872 eV necessitating the beam energy be changed [381]. EDX was utilised instead to compare the elemental proportions for Coating C.

Preparation of the cross sections was performed using the same electron microscope as in Section 3.4.2. Figure 5.1 shows the sequence of preparation of a cross-section for TEM.The average thickness of the coating in cross sections removed for TEM analysis was $68.77 \pm 16.17 \, \mu m$ measured across the six coating variants imaged. Due to the time required to perform the FIB cross-sections and the cost of the TEM it was decided that the thicker variants of coatings A, B and C on SS and HTS. By using the thicker coatings, any depth dependence of the coating structure could be analysed.

117
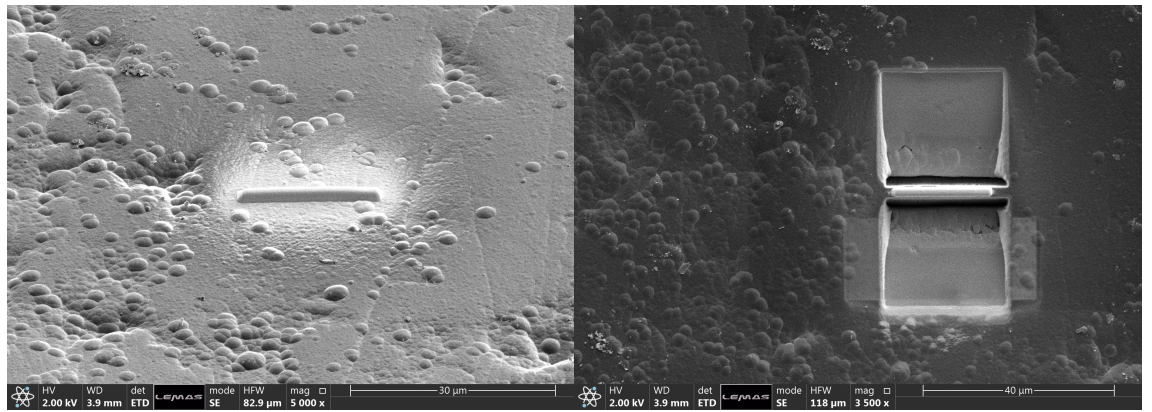
(a) Deposition of the protective Pt layervia an ion beam.

(b) Both sides are milled out around the strip to be extracted.
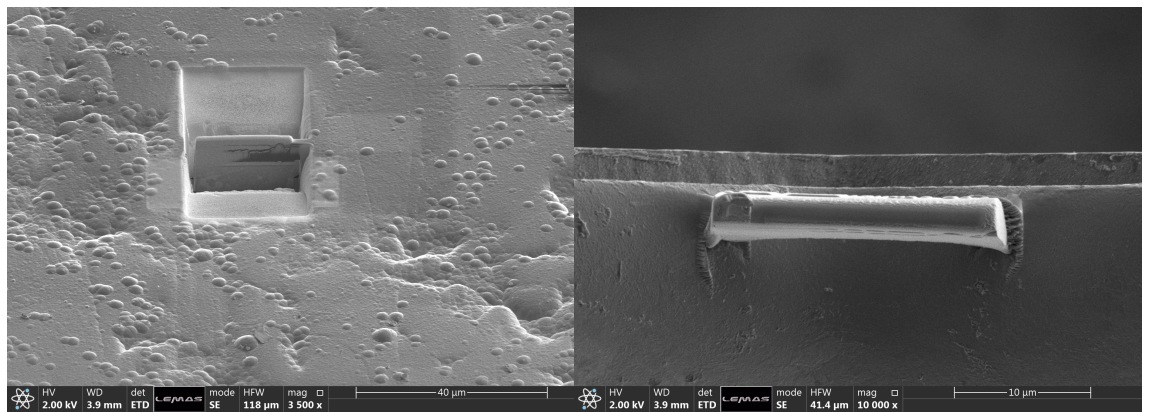
(c) One side of the strip is milled away so it can be welded to a TEM sample mount.

(d) The sample is extracted and welded to a TEM mount.
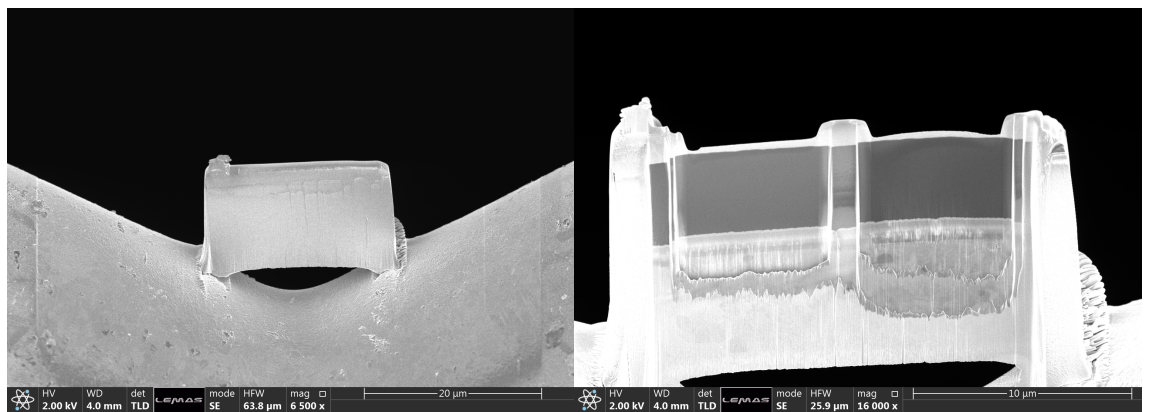
(e) The sample is reorientated to prepare for thinning and polishing.

(f) Two 'window' regions are created for TEM imaging and to maintain sample integrity.

Figure 5.1: Preparation of TEM samples. Coating shown is HTS-Coating A-thick-smooth.

5.3 Results

5.3.1 Raman Spectroscopy

5.3.1.1 I_D/I_G Ratios Determined By Raman Spectroscopy

Figure 5.2 shows the fitting of the D and G band peaks of Coating A on HTS. Table 5.1 gives the calculated I_D/I_G ratios of all three coatings on both substrates. The lowest values of I_D/I_G are seen on Coating B for both substrates (0.68 and 0.29 on SS and HTS respectively) indicating the lowest levels sp^2 carbons present in rings and therefore the lowest amorphisation. The pre-test (representative unworn area) I_D/I_G are lower on all coatings on HTS indicating that the increased hardness of the substrate gives a lower amorphisation. The pre-test values of I_D/I_G on Coating C are much higher on both substrates (3.50 and 2.96 on SS and HTS respectively) indicating a highly disordered structured rich in sp^2 carbon [362]. The difference in the Raman peak structure is shown is Figure 5.3. The I_D/I_G values are approaching that seen by Yong et al. [362] indicating a structure more like graphitic-like carbon (GLC). Additionally, they identified a closely packed nano-particulate structure [362]. This would be similar to that seen by Pei et al. [363] with nano-crystallites of WC or W_2C [362] surrounded by an amorphous matrix.
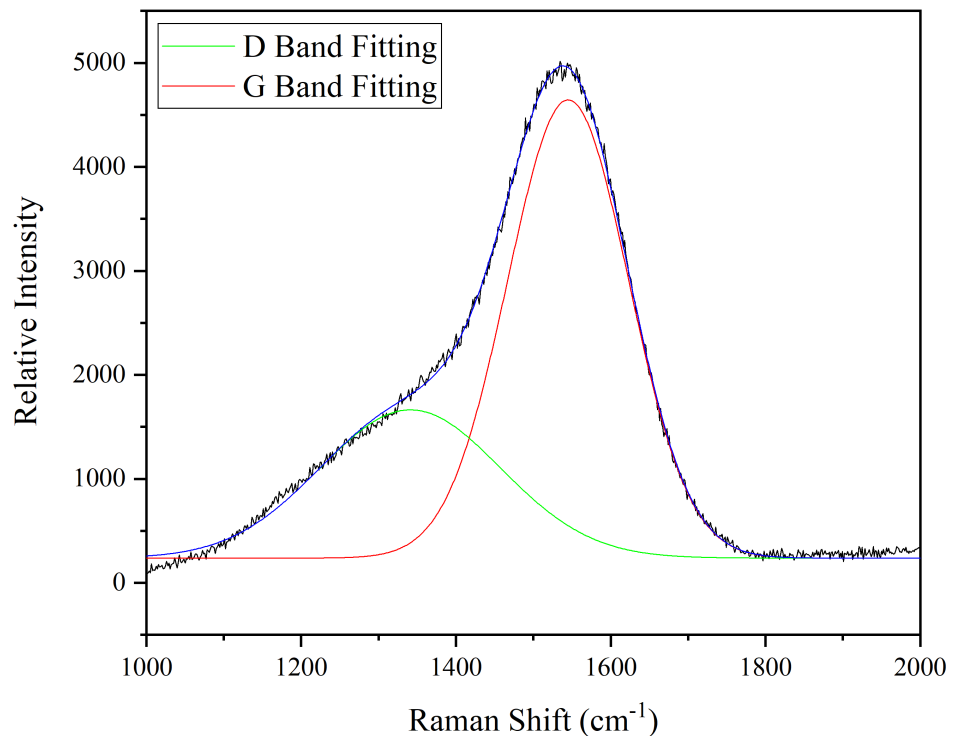
Figure 5.2: Fitting of D and G band peaks on Raman spectra of Coating A on HTS.
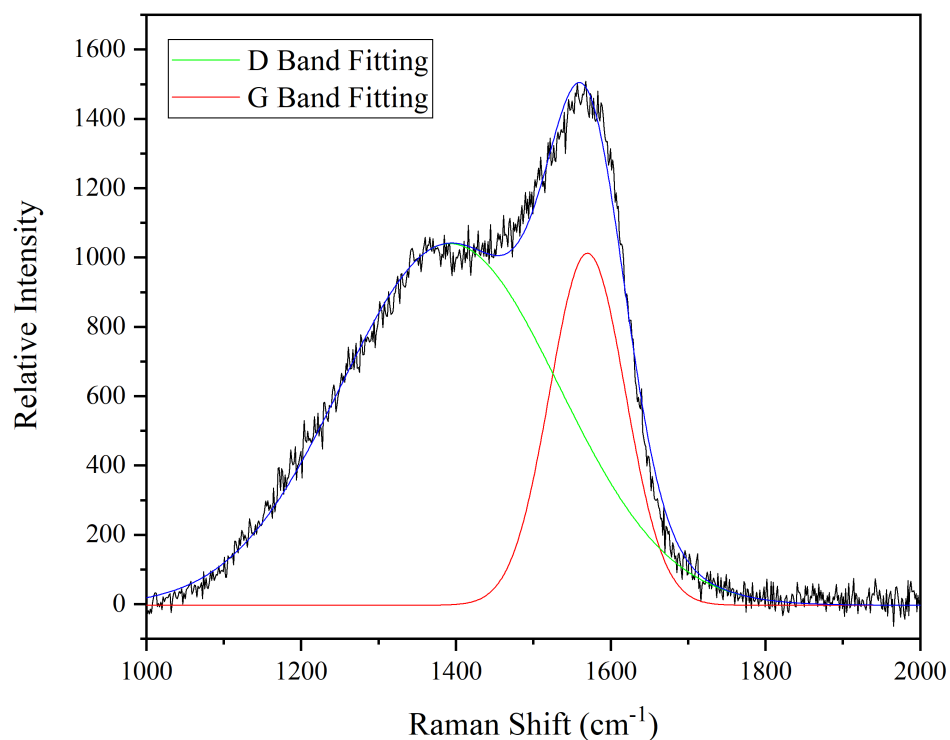
Figure 5.3: Fitting of D and G band peaks on Raman spectra of Coating C on HTS.

Table 5.1: I_D/I_G ratio of Coatings A, B and C on each substrate.

Substrate	Coating	Structure	I_D/I_G
	A	a-C:H	0.79
316L Stainless Steel	B	Si-a-C:H	0.68
	C	a-C:H:W	3.50
	A	a-C:H	0.48
Hardened M2 Tool Steel	B	Si-a-C:H	0.29
	C	a-C:H:W	2.96

5.3.1.2 Positions Of The D And G Peaks Calculated By Raman Spectroscopy

Table 5.2 shows the D and G peak positions of each coating. Taking Coating A on each substrate as the baseline we can discern how the introduction of each dopant affects the peak positions. The position of the G peak is taken to be most important as an indicator of the change in structure [250]. The Si doping in coating B is seen to decrease the wavelength value of the G peak position on both substrates. Conversely, the W doping in Coating C is seen to increase the G peak position value on both substrates.

Table 5.2: D and G peak positions of Coatings A, B and C on each substrate.

Substrate	Coating	D Peak Position (cm^{-1})	G Peak Position (cm^{-1})
	A	1367.68	1552.40
316L Stainless Steel	B	1353.94	1504.84
	C	1391.95	1567.04
	A	1344.21	1545.03
Hardened M2 Tool Steel	B	1444.26	1505.92
	C	1392.26	1570.06

5.3.2 TEM

5.3.2.1 TEM Cross-Section

Figure 5.4 shows the cross-section of the prepared DLC samples. It can be seen that SS Coating A and HTS Coating B experienced a film rupture, this is possibly due to weakening of the film due to the FIB thinning or as a result of a release of residual stress energy from the film once it was thinned enough. Coating A and B are seen to have an amorphous structure, such that no grains or crystalline structure is seen at this resolution. Coating C has a markedly different structure with a fine grain columnar structure with evidence of surface diffusion with periodic renucleation [212].
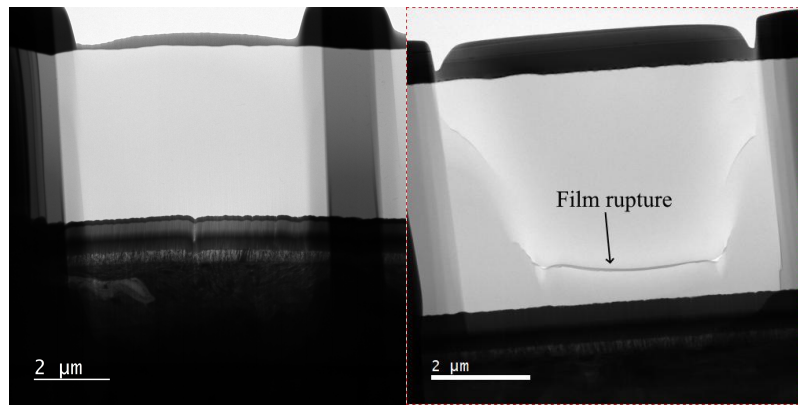
(a) HTS Coating A.

(b) SS Coating A.
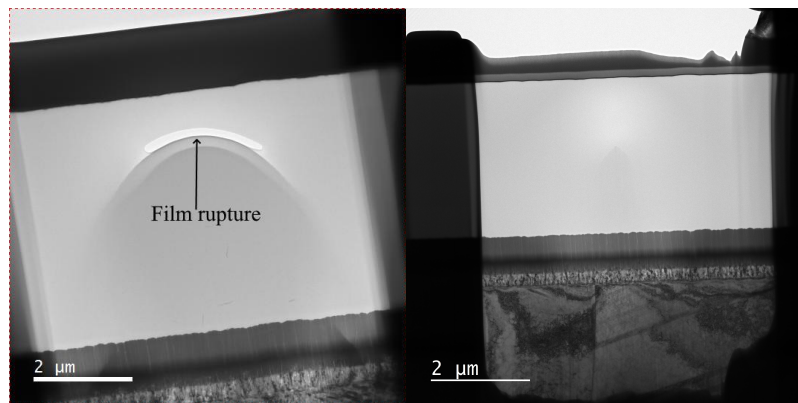
(c) HTS Coating B.
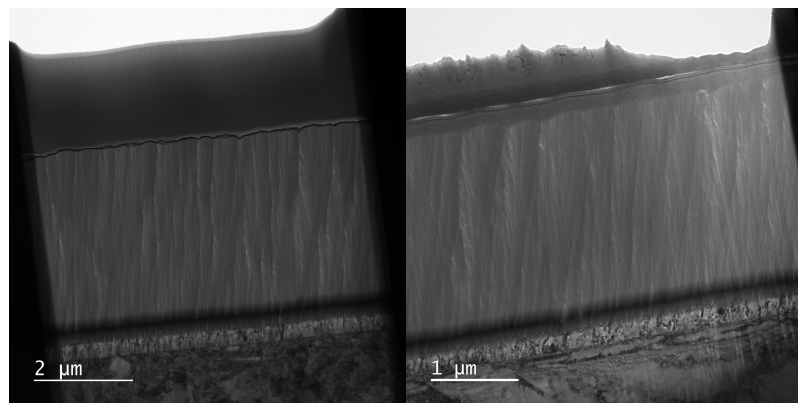
(d) SS Coating B.

(e) HTS Coating C.

(f) SS Coating C.

Figure 5.4: TEM cross-sections of Coatings A, B and C on both substrates.

5.3.2.2 TEM-SAD Verification of Amorphous Structure

Figure 5.5 shows the TEM-SAD patterns of all three coatings on both substrates. No diffraction spots are seen showing that the films lack a regular crystalline structure.

(a) HTS Coating A.   (b) SS Coating A.

(c) HTS Coating B.   (d) SS Coating B.

(e) HTS Coating C.   (f) SS Coating C.
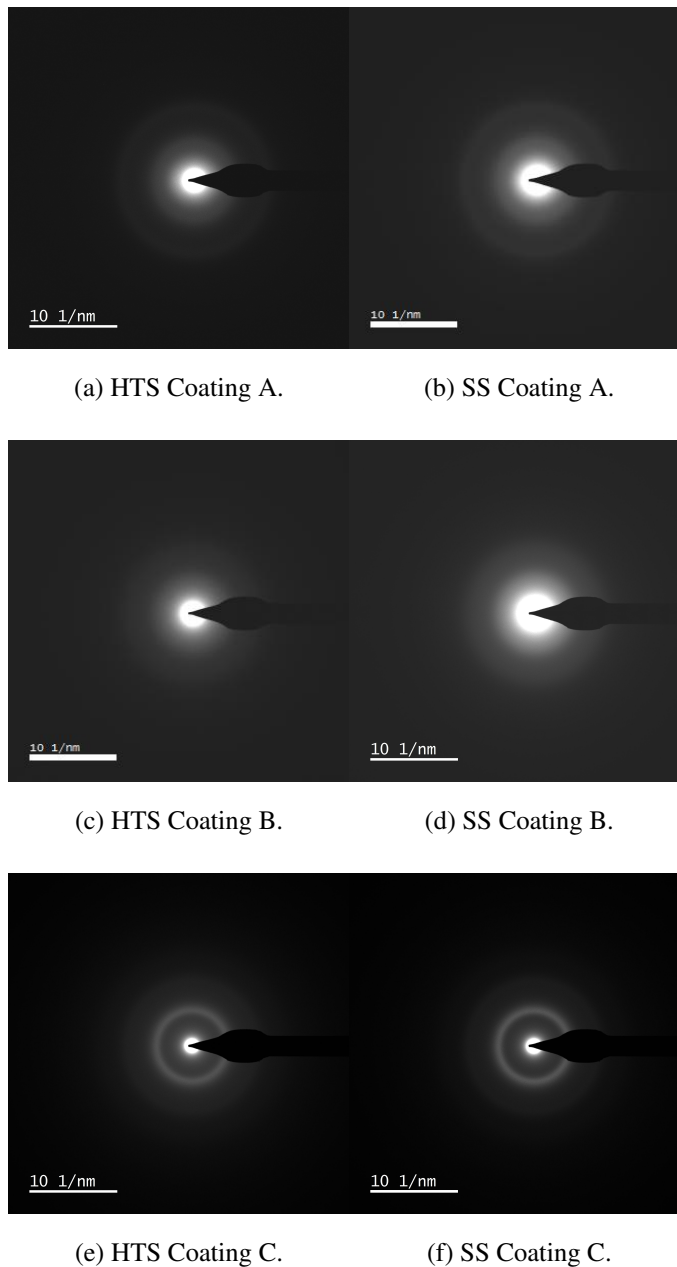
Figure 5.5: TEM-SAD patterns of Coatings A, B and C on both substrates.

5.3.2.3 sp^2/sp^3 Ratios Determined By EELS

Figure 5.6 shows the high loss EELS spectra of highly orientated polycrystalline graphite (HOPG) and HTS Coating A. These spectra are normalised relative to the total area of the high loss spectra of HOPG resulting in a lower number of counts in comparison to the low loss spectra.
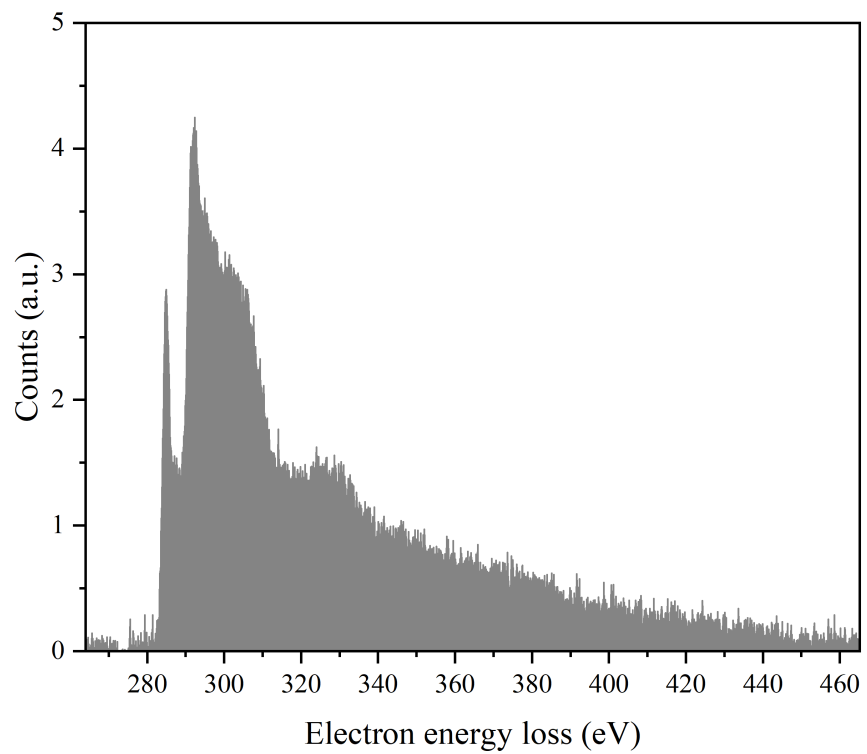
(a) High loss spectrum of HOPG.
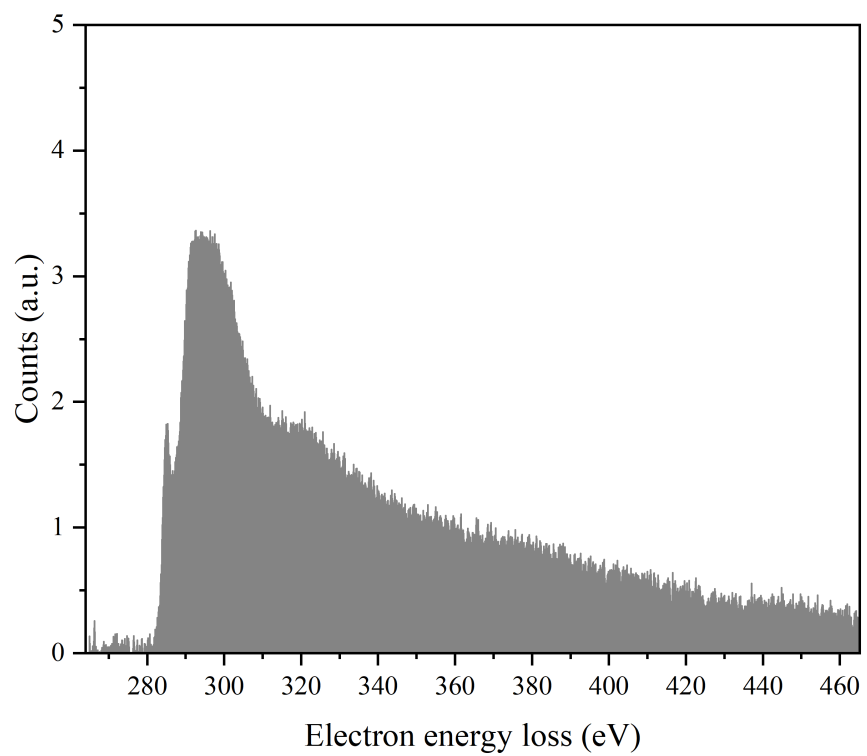
(b) High loss spectrum of HTS Coating A.

Figure 5.6: High loss EELS spectra of HOPG and HTS Coating A.

Figure 5.7 shows the low loss spectra of HTS Coating A. This spectra is not normalised and the counts shown are the raw number from the EELS detector.
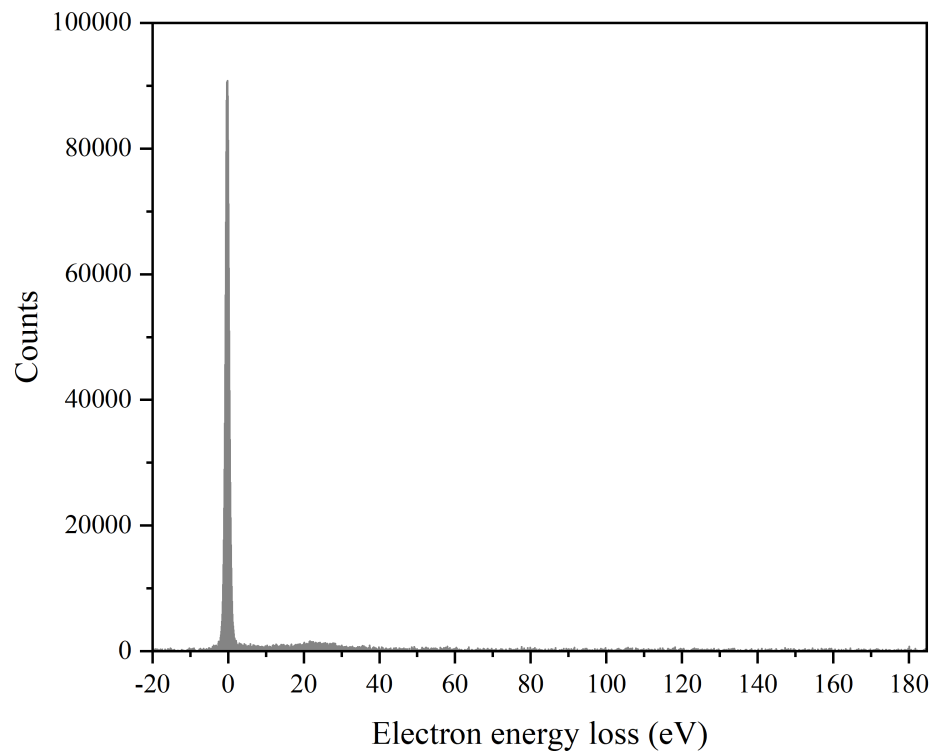
Figure 5.7: Low loss EELS spectrum of HTS Coating A.

Figure 5.8 shows the percentages of sp^2 and sp^3 content in the coatings with the associated errors of measuring multiple sites in the cross-section. No correlation was found between sp^2 and sp^3 content and depth into the coating structure.
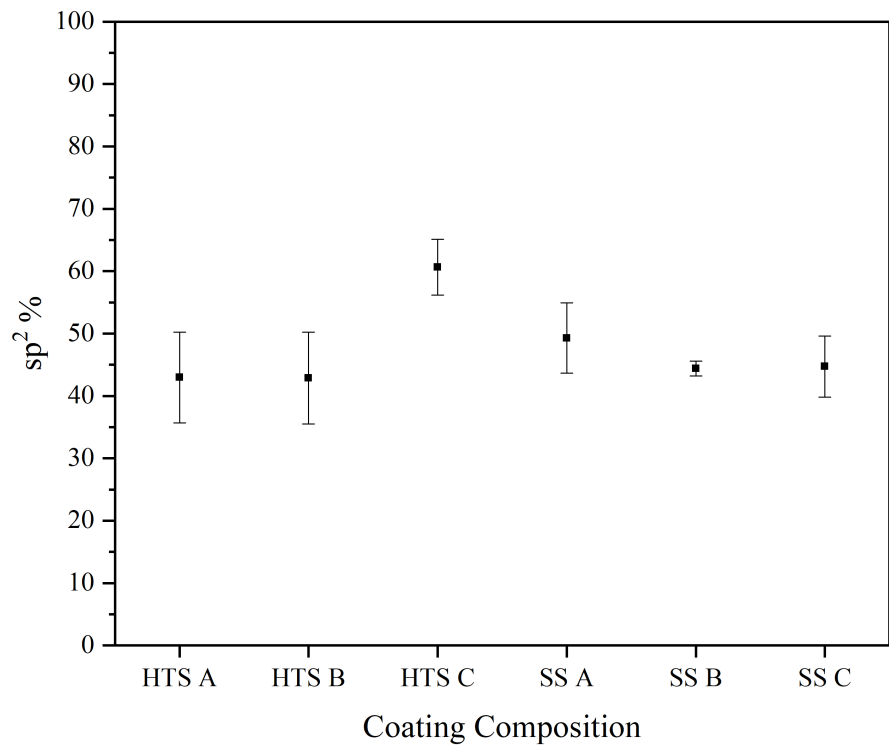
(a) sp^2 proportions.
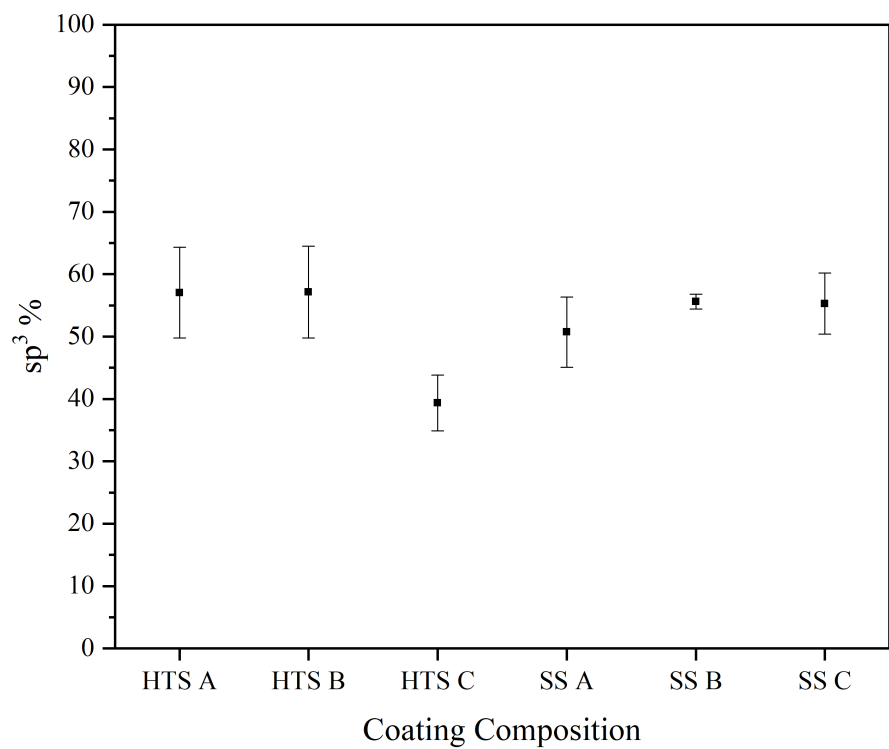
(b) sp^3 proportions.

Figure 5.8: sp^2 and sp^3 proportions of each coating with associated errors.

The sp^2/sp^3 ratio can therefore be calculated as seen in Figure 5.9. In general, the DLCs have a larger proportion of sp^3 bonding with the exception of HTS Coating C which possesses a much high proportion of sp^2 bonding within its structure. The error bars are calculated by Gaussian error propagation.
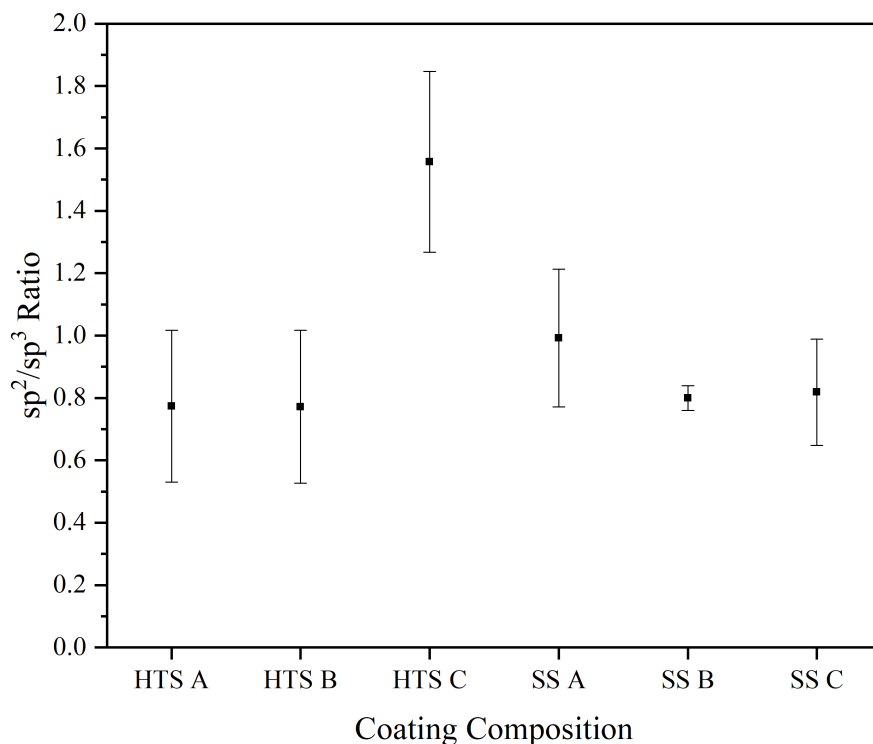
Figure 5.9: Average sp^2/sp^3 ratios.

5.3.3 Dopant Proportions

Dopant proportions were determined by multiple methods; EDX in SEM, EDX in TEM (for Coating C) and stitching of EELS spectra (for Coating B). As the TEM is set up for a specific energy range (carbon for these measurements), the range required to measure the spectra of tungsten was too high, therefore EDX was used in place.

5.3.3.1 SEM-EDX

EDX was used on unworn areas to determine the atomic proportions and atomic weights (by percentage) of all the (thinner) coatings. The images of these unworn areas can be seen in Figure 5.10.
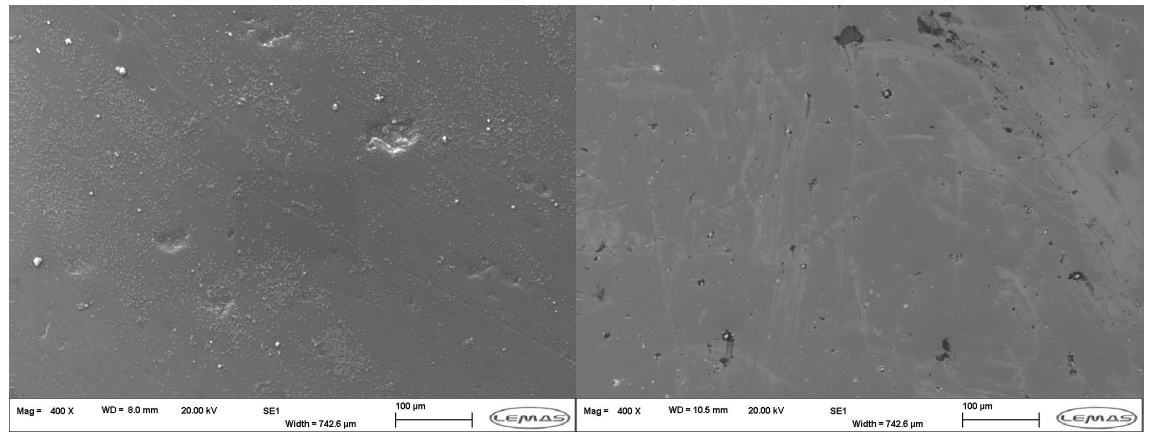
(a) HTS Coating A.

(b) SS Coating A.
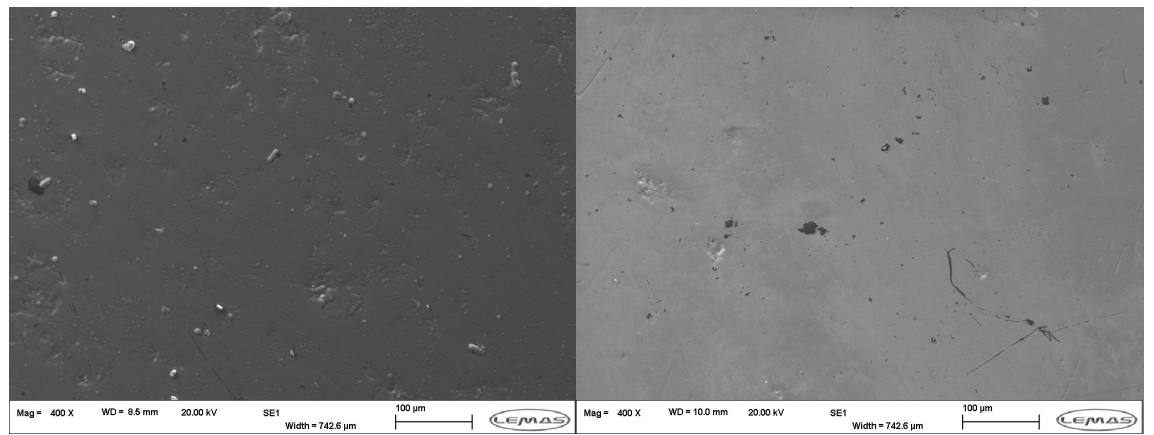
(c) HTS Coating B.
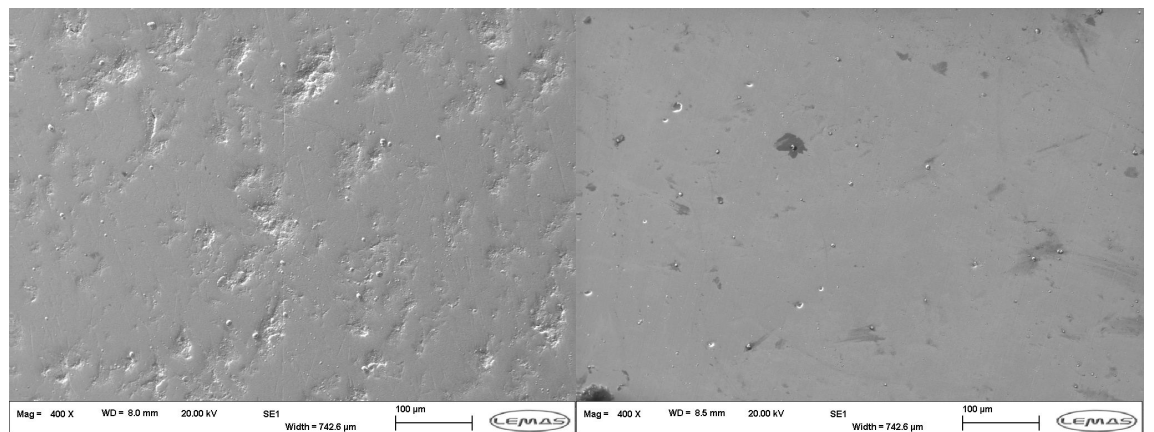
(d) SS Coating B.

(e) HTS Coating C.

(f) SS Coating C.

Figure 5.10: Unworn areas used used for elemental proportion analysis under EDX.

Table 5.3 shows the atomic composition of unworn areas of the coatings as measured by EDX before any FIB cross-sectioning has occurred. Elements that are not designed constituents of the coatings are present in the layers. In the case of Ar as seen in SS Coating B and Coating C on both substrates, some ions are embedded in the coating structure during deposition. Some amounts of Ti and O in HTS Coating C can be attributed to deposition of ions on the chamber walls from previous coating processes; Ti is used to re-coat the chamber between coating cycles using a cathodic arc process. Cr and Fe

(and W in Coatings A and B) are detected due to the interaction volume of the electron beam [256]. Some variance in the unintended elements will be due to the thickness of the coatings. Coating A on HTS and SS has 99.90 % and 99.80 % carbon composition respectively. Coating B consists of 72.06 % and 71.12 % carbon, 6.88 % and 6.13 % oxygen, and 20.84 % and 21.92 % silicon respectively. Coating C has the greatest difference in composition between HTS and SS. SS has 79.33 % carbon compared to 68.29 % as deposited on HTS. HTS Coating C has a larger proportion of W (21.14 %) compared to SS (16.31 %). The W present in HTS could explain this difference as the interaction volume of the SEM may extend to the substrate.

Table 5.3: Atomic composition of Coatings A, B and C on HTS and SS as measured by EDX.

| | Atomic Composition (%) | | | | | |
| | Coating A | | Coating B | | Coating C | |
Element	HTS	SS	HTS	SS	HTS	SS
C	99.90	99.80	72.06	71.12	68.29	79.33
O	–	–	6.88	6.13	5.93	–
Si	–	–	20.84	21.92	–	–
Ar	–	–	–	0.06	0.89	0.92
Ti	0.02	–	–	0.10	3.04	2.27
Cr	0.02	0.06	0.04	0.17	0.19	0.40
Fe	0.03	0.11	0.11	0.19	0.53	0.78
W	0.02	0.03	0.07	0.32	21.14	16.31

Table 5.4 shows the weight compositions of the coatings also determined by EDX. The same trends are present as in the previous table however the dopants make up a much larger % weight than atomic proportion. This is due to their higher atomic masses which is accounted for in the calculations performed by the Oxford Instruments AZtec software. Tungsten has an atomic mass of 183.84 compared to 28.085 for silicon [382].

Table 5.4: Weight composition of Coatings A, B and C on HTS and SS as measured by EDX.

| | Weight Composition (%) | | | | | |
| | Coating A | | Coating B | | Coating C | |
Element	HTS	SS	HTS	SS	HTS	SS
C	99.36 ± 0.17	99.76 ± 0.24	54.76 ± 0.46	51.68 ± 0.60	16.33 ± 0.51	22.90 ± 0.49
O	–	–	6.96 ± 0.25	5.93 ± 0.29	1.89 ± 0.22	–
Si	–	–	37.02 ± 0.37	37.24 ± 0.46	–	–
Ar	–	–	–	0.15 ± 0.05	0.71 ± 0.09	0.88 ± 0.08
Ti	0.100 ± 0.003	–	–	0.28 ± 0.07	2.90 ± 0.12	2.61 ± 0.11
Cr	0.11 ± 0.04	0.26 ± 0.05	0.12 ± 0.05	0.52 ± 0.08	0.19 ± 0.10	0.50 ± 0.09
Fe	0.15 ± 0.05	0.49 ± 0.06	0.38 ± 0.07	0.66 ± 0.10	0.59 ± 0.12	1.04 ± 0.12
W	0.29 ± 0.16	0.49 ± 0.23	0.78 ± 0.26	3.54 ± 0.38	77.39 ± 0.56	72.06 ± 0.51

5.3.3.2 TEM-EDX

Table 5.5 shows the elemental proportions determined by EDX in the TEM of Coating C. Some differences can be seen in the composition compared to that in SEM. This is due to the position at which the profile was taken, this being deeper into the coating structure where a high elemental proportion of the interlayer materials are present. This can be seen in Figure 5.11. A high-angle annular dark-field (HAADF) detector is enables atomic columns to be imaged with the capability to detect the atomic number of the material [260]. The signal from this detector is labelled in Figure 5.11. The position on the x axis in Figure 5.11 is taken relative to the surface of the sample ($0\,\mu m$ is the coating surface) with increasing position referring to increasing depth into the coating structure.

Table 5.5: TEM-EDX atomic and mass fractions of Coating C on HTS and SS.

Element	Atomic Fraction (%)		Mass Fraction (%)	
	HTS	SS	HTS	SS
C	59.38 ± 7.18	58.73 ± 6.62	13.23 ± 1.10	12.88 ± 1.00
Ti	4.06 ± 0.72	2.88 ± 0.50	3.29 ± 0.51	2.52 ± 0.38
Cr	10.61 ± 1.89	14.58 ± 2.53	9.27 ± 1.44	13.84 ± 2.12
Fe	1.32 ± 0.24	3.91 ± 0.68	1.24 ± 0.19	3.99 ± 0.61
W	24.63 ± 3.98	19.89 ± 3.10	72.96 ± 9.91	66.77 ± 8.86
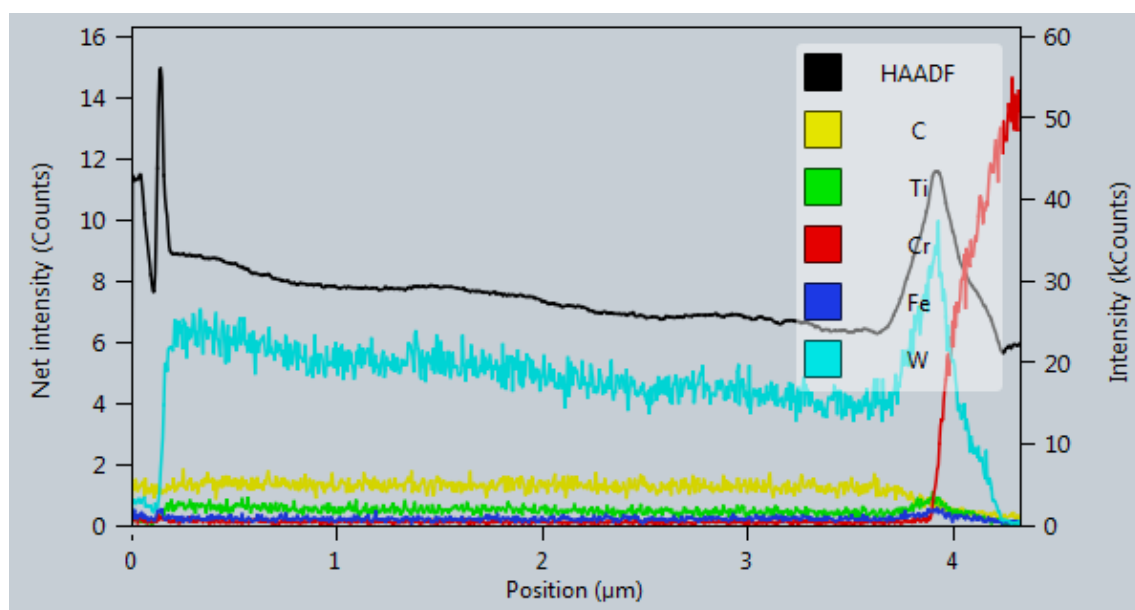
Figure 5.11: EDX elemental intensity profile of Coating C on HTS. Note this figure is extracted directly from the TEM-EDX software therefore its format does not match the other figures.

5.3.3.3 TEM-EELS Spectra Stitching

Table 5.6 shows the atomic proportions determined by the stitching of the C and Si EELS spectra of Coating B using the Hartree-Slater model. Approximately 18–19 % of the coating structure consists of Si on both substrates. The remaining structure is made up of carbon. This technique only takes into account the spectra of the chosen elements as the relative proportions of these are exclusively calculated.

Table 5.6: Atomic fraction determined by the EELS spectra stitching of C and Si spectra.

Element	Atomic Fraction (%)	
	HTS	SS
C	80.6	81.9
Si	19.4	18.1

5.4 Discussion

In Figure 5.6, we can note that there is a difference in the shape of the spectra comparing the crystalline HOPG and amorphous Coating A. A rounder spectra without sharp peaks is indicative of an amorphous carbon film [379] as is expected of a DLC film [264]. This is further exemplified by the TEM-SAD patterns shown in Figure 5.5 in which rings are seen instead of the spots expected of crystalline materials. The faint rings seen are typical of amorphous materials [383]. The cracking caused by the thinning in preparation for TEM as shown in some samples in Figure 5.4 is evidence of the residual stress commonly seen in DLC coatings [277]. Wu and Hon [268] found that Si doped DLCs exhibited residual compressive stresses dependent upon their structure. A more polymer like structure had lower stress whereas a more diamond-like structure had higher stresses.

A large difference is seen in the predicted sp^2/sp^3 ratios seen by Raman spectroscopy (Table 5.1) and the measured proportions by EELS (Figures 5.9 and 5.9). We must remember that Raman spectroscopy only gives an indication of the level of amorphisation of the coatings and that multiple elements of composition influence the Raman spectra (sp^2 clustering, bond disorder, presence of sp^2 chains or rings and sp^2/sp^3 ratio) [250, 375]. Beyond the strong correlation of higher sp^2 content (comparing Figure 2.16 and Table 5.1) in HTS Coating C, the difference in I_D/I_G ratio will be due to changes in chain and cluster structure [250]. This is further seen in Table 5.2 with lower G peak wavenumber in Coating B indicating an increase in bond disorder. An increase in G peak wavenumber indicates increased chains and clustering which is expected with some increase in sp^2 content which was seen for HTS Coating C [250]. Ferrari and Robertson's [250, 384] analysis of the structure of various carbon films do not feature the presence of dopants and therefore the trends noted by them are based on comparison of graphite, a-C and ta-C. The G peak position has been seen to inversely correlate with the hydrogen content in a-C:H [385] however the interactions of other ions during bombardment will affect the hydrogenation during deposition.

The collected DLC structural properties by Hainsworth and Uhure [217] show that for a hard a-C:H (which is expected from the measured mechanical properties in Table 4.2) around 40 % sp^3 content is expected. For W doped DLC this rises to 50 %. For Si DLC, between 60–84 % is expected. Tai et al. [375] found around equal parts sp^2/sp^3 were common for a-C:H. The sp^2/sp^3 ratio and I_D/I_G ratios are seen to be positively correlated

though the exact relation is dependent upon the analysis technique used. I_D/I_G ratios as low as 0.75 were reported corresponding to an sp^2/sp^3 ratio of 0.5. Yue et al. [273] found I_D/I_G ratios from 1.2–2.8 dependent upon the W content in W doped DLC; the W content increased the G peak wavenumber too. Zheng et al. [370] found I_D/I_G ratios from 1.17–1.49 however these were for much harder W DLCs. The higher I_D/I_G ratio also cused the G peak wavenumber to increase. Shibata et al. [386] found I_D/I_G ratios for Si DLC between 1 and 3 with higher values corresponding to higher negative pulse voltage (high power impulse magnetron sputtering (HiPIMS)).

There may be some difference in the measured spectral ratios between Raman and EELS due to the sampling difference in the interaction volume or perhaps surface structural differences though no gradient was found with EELS and any differences are supposed to be due to sampling error. Coating thickness was seen to affect the structure as noted by Wei and Yen [371]. Close examination of the structure of Coating C in Figure 5.4 shows that the predictions of Pei et al. [363] and Yong et al. [362] appear to be correct; the granular structure of Coating C does appear to be nanocrystalline in nature though higher resolution TEM would be needed to fully confirm this.

The atomic composition (Table 5.3) as determined by SEM-EDX showed that for the doped coatings (B and C) around 20 % of the coating structure consisted of the doping elements (Si and W for Coatings B and C respectively). Weight composition results (Table 5.4) showed that approximately 37 % of Coating B was Si and 72–77 % of Coating C was W. This is in good agreement with proportions determined by TEM-EDX (Table 5.5). The proportions for Coating B determined by TEM spectra stitching (Table 5.6) are also in good agreement with those determined by SEM-EDX (Table 5.3). The stitching methodology only calculates the proportions of two elements relative to each other therefore EDX is superior as it can detect all the constituent heavy elements in a coating [261, 262]. As the procedure for preparing samples for TEM is a destructive one, it is therefore preferable to determine the atomic proportions and weights via SEM-EDX. If a line profile is required (as in Figure 5.11), FIB should instead be used and an EDX profile taken after material removal and polishing.

The mechanical properties reported in Chapter 4 show that, generally, the highest hardness is observed with Coating A followed by B and C respectively. Coating C is seen to have a relatively high elastic modulus. Their ranking of H/E ratio follows the same trend as hardness. The elastic modulus and hardness' similarity to that of diamond is primarily determined by quantity of sp^3 bonding as sp^2 bonding does not contribute much to the mechanical properties [275]. Any levels of hydrogenation does not aid the C-C bond network and therefore doesn't contribute to mechanical properties [275]. We can therefore think of the mechanical properties in terms of the level of disruption to an ideal sp^3 network though we shouldn't forget that dopants affect more than mechanical properties [36]. The relative size of carbon and tungsten atoms are quite different with carbon having an atomic radius of 70 pm and a van der Waals radius of 177 pm compared to 135 pm and 249 pm for tungsten respectively [387, 388]. The breakdown of hexamethyldisiloxane (HMDSO) can occur by several mechanisms as discussed by Sonnenfeld et al. [389]. This provides, possibly multiple, precursor ionic species that can change the formation characteristics of a silicon doped DLC.

5.5 Summary

The structure of Coatings A. B and C as deposited on SS and HTS was analysed using Raman spectroscopy, SEM and TEM. TEM-SAD was used to confirm the amorphous structure of the coatings. Atomic and weight composition was measured using EDX under SEM and TEM and spectra stitching in TEM.

We can therefore conclude that for Coatings B and C the dopants were approximately 20 % of the structure by atomic proportion. Higher proportions were seen by atomic weight due to the difference in elemental mass. EDX performed in both SEM and TEM and TEM spectra stitching are in good agreement however SEM-EDX is preferred for determining constituent elements of coatings due to its ease and non-destructive nature unless line profiles through the coating structure are desired. The amorphous nature of the coatings has been confirmed with the application of TEM-SAD. Coating B is seen to have the lowest I_D/I_G ratio and Coating C had the highest on both substrates. The G peak positions reveal that the Coating B has an increase in bond disorder compared to Coating A whereas Coating C has a greater proportion of chains and clustering. Little difference is found in the sp^2/sp^3 ratios of the coatings except in HTS-Coating C where the ratio was markedly higher showing the DLC's higher sp^2 content. The difference could be due to localised differences in the structure or sampling differences between the surface and sub-surface structure. SEM images of the samples prepared for TEM showed some cracking took place indicating the residual compressive stresses of the coatings.

This study has neglected to measure the hydrogen content (EELS peak at 187.5 eV) of the coatings which has been seen to change with I_D/I_G ratio [229, 379]. Measurement of this parameter of the coating composition would allow for the correlation of friction behaviour with hydrogen content and dopant presence. Additionally, the use of x-ray photoelectron spectroscopy (XPS) to quantify the sp^2/sp^3 ratio and compare with the values determined by EELS would allow the subsurface and surface compositions to be analysed. As mentioned in the conclusion of Chapter 3, analysis of the ion energies would allow for the deposition mechanisms and intermediate ion species to be better understood.

Chapter 6

Nano-Scale Fatigue Determination by Comparison of Erosion and Impact Testing

6.1 Introduction

Multi-scale impact testing has been an emerging set of techniques used in the characterisation of the fatigue resistance, dynamic hardness and fracture properties, primarily, of coatings for the past 20 years [110, 112, 144]. Beake et al. [112] identified impact testing as a fatigue process and erosion has long been understood to have a fatigue component [76]. Therefore, as these processes both involve the study of cracking phenomena and material removal by some impacting media [76, 319], a relation can be drawn between them under the condition that approximately the same energy is imparted to the surface in each process.

In this study, the depths reached in impact testing will be correlated with the amount of substrate revealed in erosion testing to show that instrumented impact can be used to predict erosion performance of coatings. This is of use as the set up of erosion tests is complex and time consuming. Additionally, the analysis of the results either in terms of mass loss or optical analysis can be complex and time consuming. The capability to use impact testing as a proxy for erosion testing could be a boon for the oil and gas industry due to the speed of test set up and analysis. Impact and particle impingement both present similar repetitive high strain rate fatigue wear to the coating surface allowing them to be compared. Mechanical properties and structural information determined by Raman spectra will be used to inform on the coating behaviour. By using an instrumented impact method, the loading regimes tested on the coatings can be standardised allowing us to control the conditions to a greater degree than with a slurry or air-based erosion test. Additionally, immediate depth information can be acquired from the impact test as opposed to the complex post-test analysis required for erosion testing.

Erosion testing under slurry or air conditions presents difficulties in analysing the wear rate of coatings due to the difficulties in setting up a test and stopping the test to analyse the amount of coating removed. This itself is difficult due to the low mass removal rates involved therefore other techniques such as optical analysis must be employed. Appendix B will show the initial results of attempting to use mass loss in slurry erosion as a metric

to measure the coating performance under erosive conditions. Due to the variability of the results, air erosion and optical analysis was selected to be compared against impact tests for this study.

The results of this chapter have been published in Surface and Coatings Technology [390]. Some additional results have been included in additional sections of this chapter and in the relevant appendices.

6.2 Methododology

6.2.1 Materials

For this study, a smaller subset of the coatings was studied to allow for enough tests to be performed to establish the link between impact and erosion. These being the thin and smooth variants of Coatings A, B and C on SS and HTS. Table 6.1 summarises their structure and thickness for this chapter.

Table 6.1: Multilayer coating architecture design with interlayer and top layer DLC.

Substrate	Coating	Layer Structure	Adhesive (Cr) layer (μm)	Gradient Layer (μm)	DLC layer (μm)	Total (μm)
316L Stainless Steel	a-C:H (A)	Cr+WC/W-C:H+DLC	0.29 ± 0.03	0.89 ± 0.08	1.60 ± 0.17	2.65 ± 0.19
	Si-a-C:H (B)	Cr+WC/W-C:H+DLC	0.29 ± 0.03	0.89 ± 0.08	1.16 ± 0.24	2.21 ± 0.25
	a-C:H:W (C)	Cr+WC+DLC	0.29 ± 0.03	0.29 ± 0.06	1.10 ± 0.22	1.65 ± 0.23
Hardened M2 Tool Steel	a-C:H (A)	Cr+WC/W-C:H+DLC	0.29 ± 0.03	0.89 ± 0.08	2.20 ± 0.20	3.25 ± 0.22
	Si-a-C:H (B)	Cr+WC/W-C:H+DLC	0.29 ± 0.03	0.89 ± 0.08	2.17 ± 0.16	3.22 ± 0.18
	a-C:H:W (C)	Cr+WC+DLC	0.29 ± 0.03	0.29 ± 0.06	1.17 ± 0.12	1.72 ± 0.14

6.2.2 Impact Testing

Micro-impact testing was used with varying loads (400–1000 mN with a time of 300 s) to characterise the fatigue and fracture resistance of coating systems. A sphero-conical indenter of 12–15 μm radius (dependent on depth from apex) was used. A schematic of the typical geometry of a sphero-conical indenter is presented in Figure 6.1. A Micro Materials Vantage system with a micro-loading head (0.4–5 N) was used for impact testing. A solenoid connected to timed relay was used to produce repetitive impacts on the coating surface; computer control ensured that each impact was in the same location for each load and occurred every 4 s [118, 122]. Maximum testing time was 300 s resulting in 75 impacts in the test duration. Three repeats, where possible, were used in different locations on the sample. Loads of 400, 500, 600, 650, 700, 750 and 1000 mN were specified for this testing. In all impacts, the indenter was retracted 40 μm from the surface.
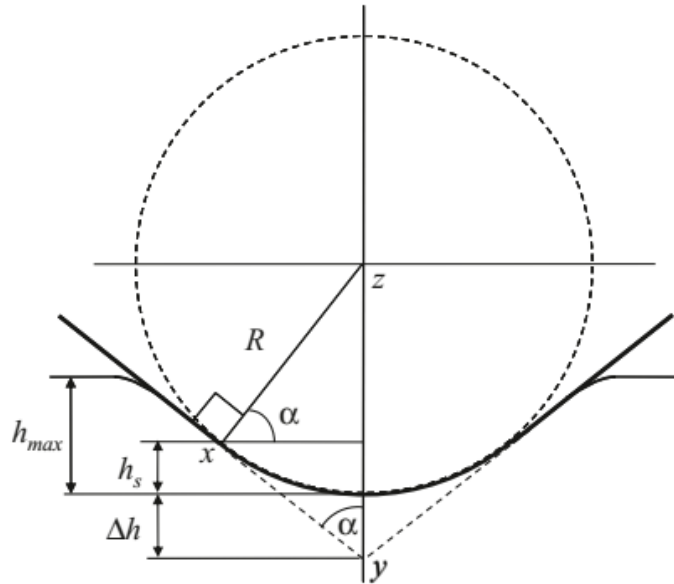
Figure 6.1: A diagram of a typical sphero-conical indenter (with radius R) during indentation. From [48].

Several features across the impact depth maps of the coatings can be highlighted to compare the performance the coatings across the selected loads. These parameters are:

- I_0 - quasi-static depth

- I_1 - the depth of the first true impact.

- I_f - depth of the final impact.

- I_δ - the ratio of final depth to initial depth normalised by the initial impact depth. This parameter shows the relative level of fatigue (depth increase due to crack formation) between each loading step.

I_δ is defined by:

$$I_\delta = \frac{I_f - I_1}{I_1} \tag{6.1}$$

Nano-impact at $100\,\text{mN}$ load with 75 impacts (corresponding to $300\,\text{s}$) was used to probe initial cracking behaviour of the coatings. 3 repeats were performed to ensure repeatability. The same indenter geometry of 12–$15\,\mu\text{m}$ was utilised for this testing. A retraction distance of $15\,\mu\text{m}$ is used for nano-impact tests. The nano-loading head has a range of 10–$100\,\text{mN}$ when used in impact mode.

6.2.3 Erosion testing

Due to the incubation period of initial mass gain in erosion tests, mass loss was unable to be used to calculate the amount of coating removed in erosion. Mass gain in erosive conditions is seen in several materials at high impingement angles ($> 45°$) due to embedding of particles [74, 391–393]. Image analysis to distinguish between the exposure of different layers is used instead.

Sand particles (HST60 silica sand of average size 250 µm) [394, 395] were used in an air-based erosion testing of the coatings at 90° impingement angle. An SEM image of the sand particles is seen in Figure 6.2. Erosion tests were performed in a bespoke air erosion rig as seen in Figure 6.3. The rig had a nozzle length of 125 mm with a diameter of 5 mm. Distance to the sample was adjustable from 0–50 mm however for this testing 5 mm distance was used. The angle of the sample holder could be varied from 30°–90° additionally.
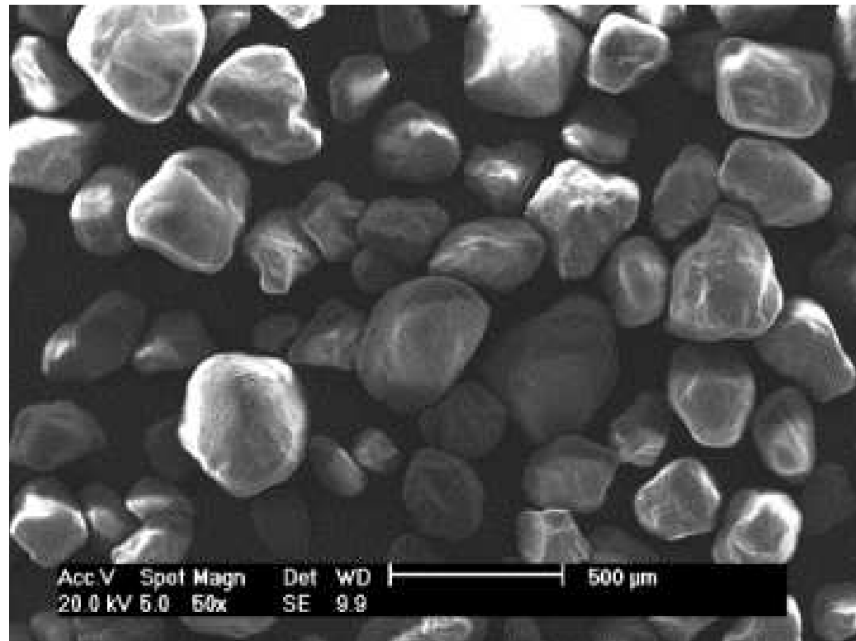
Figure 6.2: SEM image of HTS60 sand particles used in erosion testing. From [394].

Slurry erosion using a submerged impingement jet (SIJ) was initially used however this was deemed too extreme to establish a good trend as it was observed that the coating was eroded quickly and the mass loss of the substrate material was being measured. Mass gain was seen with this erosion methodology too. Further details of instrument calibration and mass measurement results can be seen in Appendix B.
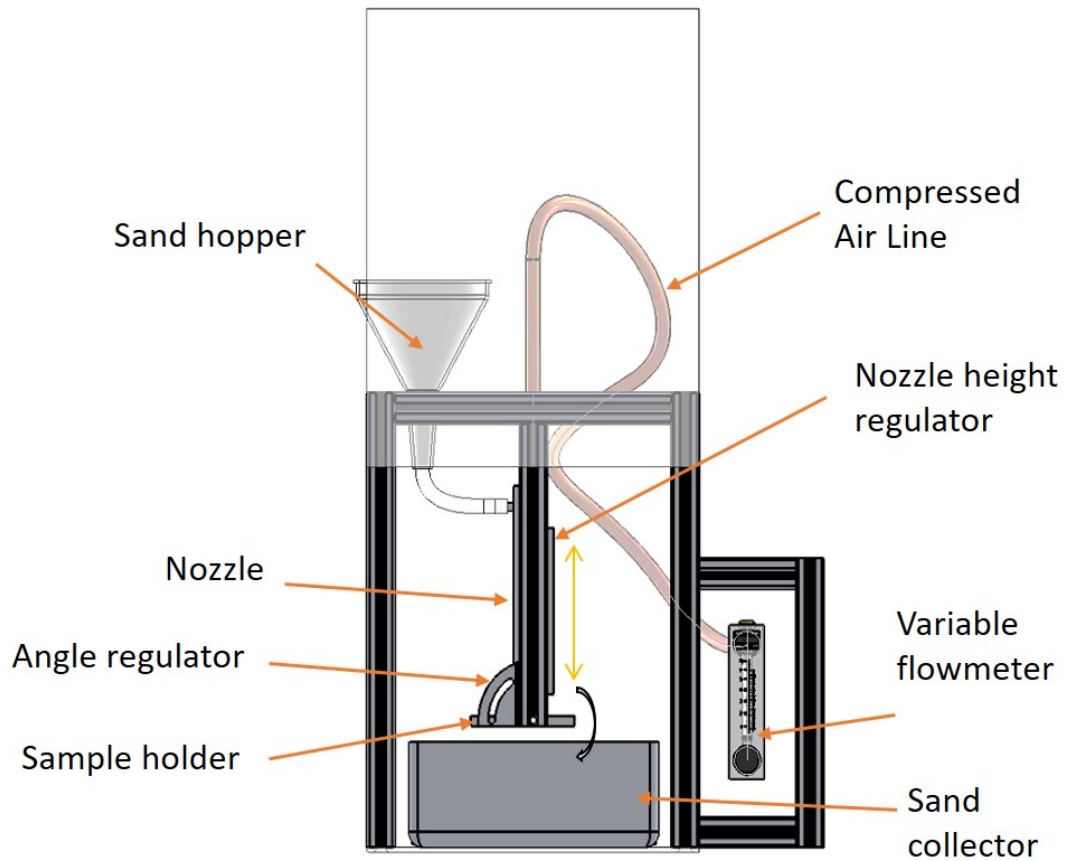
Figure 6.3: Schematic of the bespoke air erosion rig.

Speed of the particles was determined by dual exposure high shutter speed photography. The hopper was loaded full of sand and as the airflow was switched on a photograph was taken to capture the sand flow. Lighting was provided by light emitting diodes (LEDs) at the side and at the front of the nozzle.

The velocity was calculated by taking the distance travelled by the sand particles seen as a streak in the photograph measured with a pixel to distance conversion, and the time by the exposure time of the photograph. The speed was calibrated to $15\,\mathrm{m\,s^{-1}}$ with a pressure of 2.04 bar as noted by the linear fitting seen in Figure 6.4.

Equation	y = a + b*x
Plot	Particle Velocity
Weight	No Weighting
Intercept	0.35723 ± 1.22657
Slope	7.03328 ± 0.65563
Residual Sum of Squares	4.29846
Pearson's r	0.99142
R-Square (COD)	0.98292
Adj. R-Square	0.97438
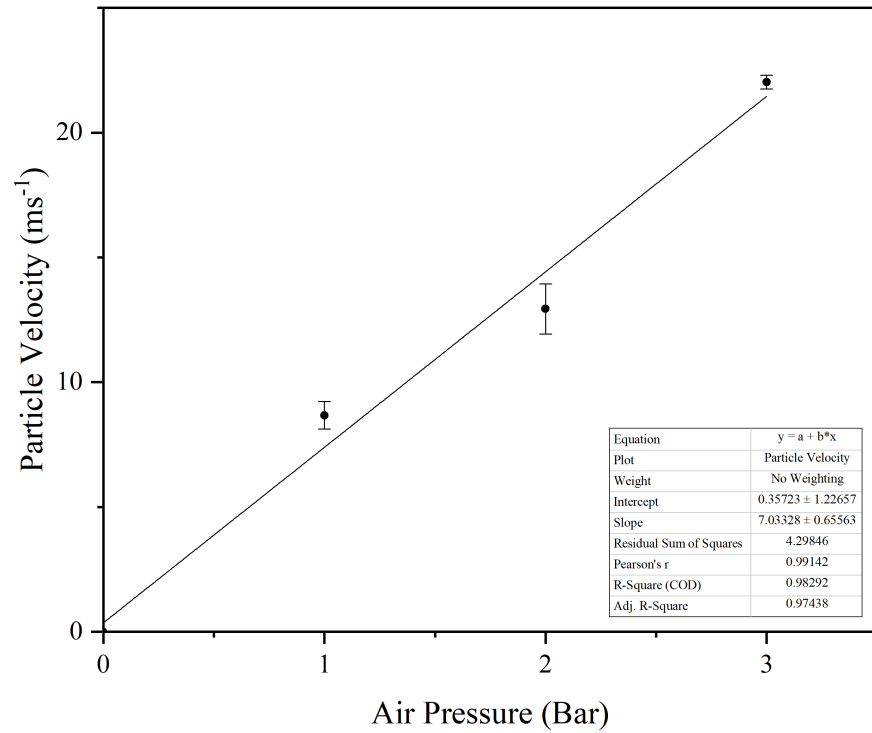
Figure 6.4: Air pressure against particle velocity as measured by dual exposure streak photography.

Figure 6.5 shows a high shutter speed photograph at an exposure of $1/800\,\mathrm{s}$, $f/4.5$ and ISO-3200 captured with a NIKON D5300 camera. At the various pressure levels, the camera settings were adjusted accordingly to capture measurable particle streaks.
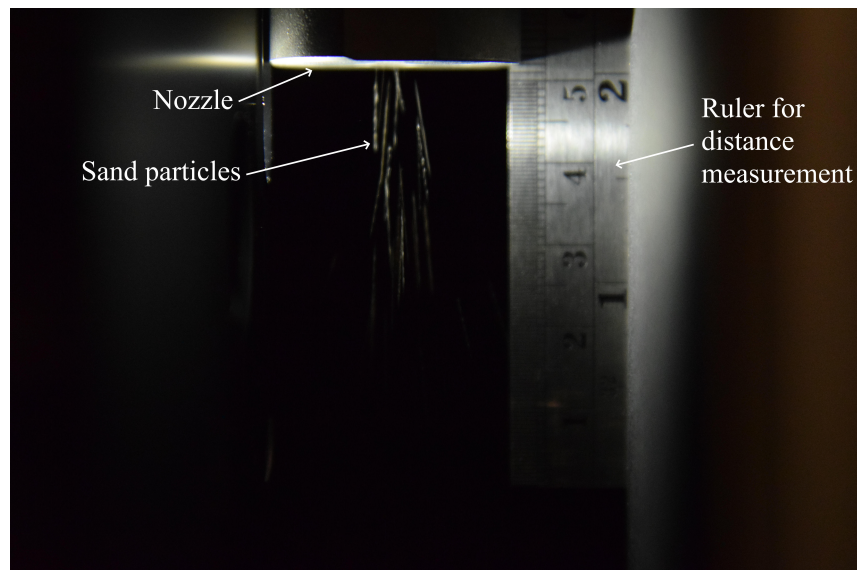
Figure 6.5: Dual exposure high shutter speed photograph of sand particle flow at 1 bar of pressure.

Erosion tests were performed for the required times (up to $420\,\mathrm{s}$) and analysed af-

ter each time step with 5 images captured of each erosion wear scar. The images were converted to 32-bit black and white images and the pixel threshold in ImageJ was used to highlight differently shaded areas corresponding to the exposure of the substrate. The threshold limit was set manually for each image. Images were captured at approximately the same exposure therefore the limit was adjusted to highlight the different coloured sections of the image. An area calculator was then used to find the amount of substrate exposed. A similar method was employed by Bouzakis et al. [396] to find the failed area ratio of impact tests. In Figure 6.6, lighter areas of the image correspond to the substrate visible after material removal due to erosion of the coating.
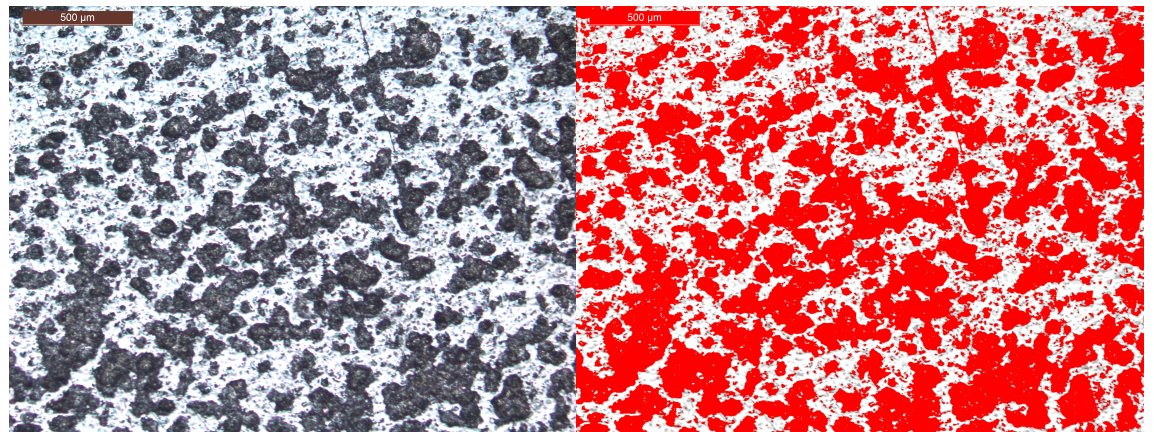
(a) Optical micrograph before thresholding.   (b) Optical micrograph after thresholding.

Figure 6.6: Erosion of Coating A after 90 seconds of particle impacts to show the effect of pixel thesholding. The scale bars in the top left of each image reads 500 μm.

Surface profilometry (Talysurf 120L) was performed at the end of the erosion testing cycle to assess the change in topography. Due to the extreme deformation of the particle impingement, wear volume could not be assessed with this method. White light interferometry (Bruker NPFLEX) was also attempted. The results of this unsuccessful post-test analysis can be found in Appendix B.

6.2.4   SEM analysis

As mentioned in Section 3.4.2, the same SEM cross sectioning was applied in the study of the morphology of impact craters. The impact craters were cross sectioned to inspect the sub-layer cracking present under cyclic loading after 75 impacts at the maximum micro-impact load of 1 N and thereby discern the differences in behaviour between the DLC coatings similar to the work of Abdollah et al. [397, 398] but in a more qualitative sense due to the on load depth already being measured by the NanoTest Platform. Abdollah and co-workers used a combination of SEM and AFM to measure the depth of their wear whereas that was not neccessary in this case.

6.3 Results

6.3.1 Micro-impact analysis

The progressive depth increase in micro-impact testing with 75 impacts at an impact load of 750 mN is seen in Figure 6.7. This is representative of the raw data in an impact test. SS Coating A fails at the first impact with a depth of 8776 nm reached showing that the load support of the substrate is insufficient for this system.
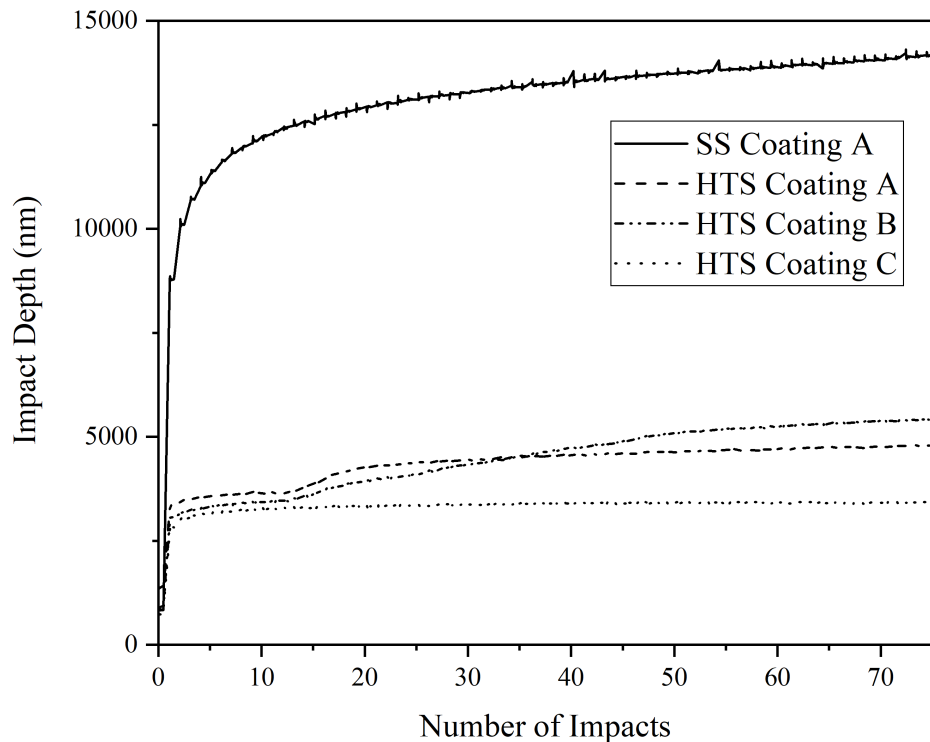
Figure 6.7: Representative micro-impact depth against number of impacts of 3 coatings on HTS and Coating A on SS. Impact load = 750 mN. Maximum number of impacts = 75 (300 s of testing).

Table 6.2 shows the number of impacts on HTS in which failure occurred against the number of full tests performed. Failure is defined by a sudden increase in depth within a short period of impact testing as with HTS Coating B (beginning at 14 impacts) in Figure 6.7. It can be noted that Coating C on HTS is less prone to failure across the full load range suggesting an increased fatigue resistance. Testing on coated SS coupons revealed eggshell type failures (immediate penetration of the coating and interlayers) under all impact loads [278], therefore they are excluded from this table. Figure 6.7 demonstrates this behaviour with SS Coating A reaching 8760 nm at second impact.

143

Table 6.2: Number of impacts tests after which fatigue failure of the coating systems occurs against the number of tests performed.

Coating and Substrate / Impact Load	400 mN	500 mN	600 mN	650 mN	700 mN	750 mN	1000 mN
HTS Coating A	0/1	0/1	2/3	0/3	1/3	1/1	1/1
HTS Coating B	2/3	3/3	3/3	2/3	2/3	2/3	2/3
HTS Coating C	1/3	0/3	1/3	0/3	1/3	0/3	1/3

Figures 6.8, 6.9 and 6.10 shows the impact parameters evaluated at each load tested. I_0 is similar across all the tests but is noticeably higher in Coating A as opposed to C. This is due to the initial crack formation in this coating at these loads. The initial and final depths reached throughout the testing is greater in Coating A and B compared to Coating C. Some degree of variability is seen in the final impact depths reached across the load range as is typical of the stochastic response for a fracture dominated process [118].
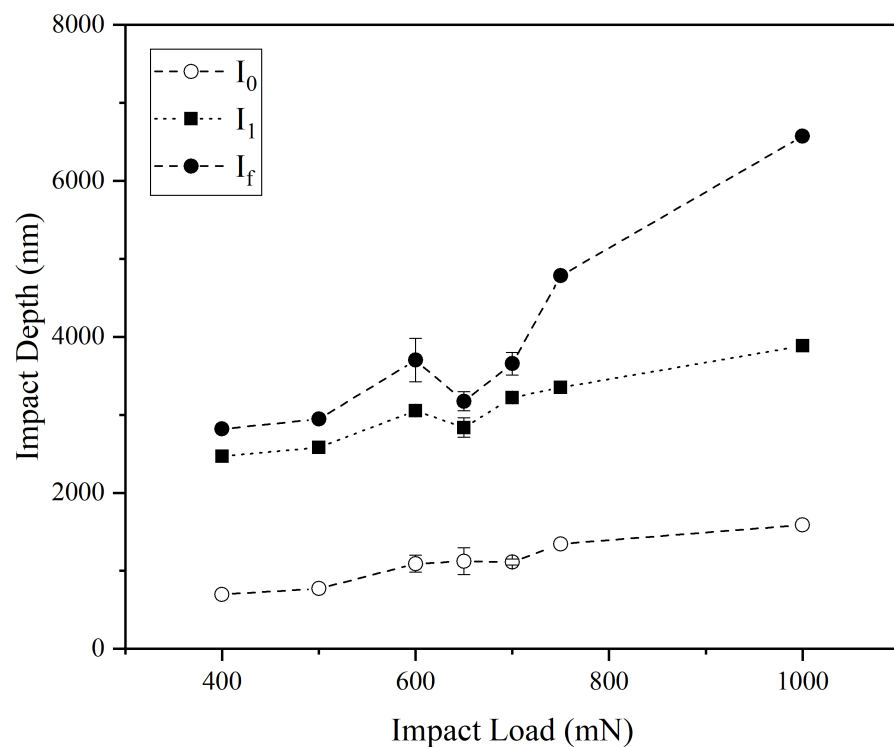
Figure 6.8: Impact parameters (I_0 – quasi-static depth, I_1 – depth of first true impact, I_f – depth of final impact) of Coating A on HTS.
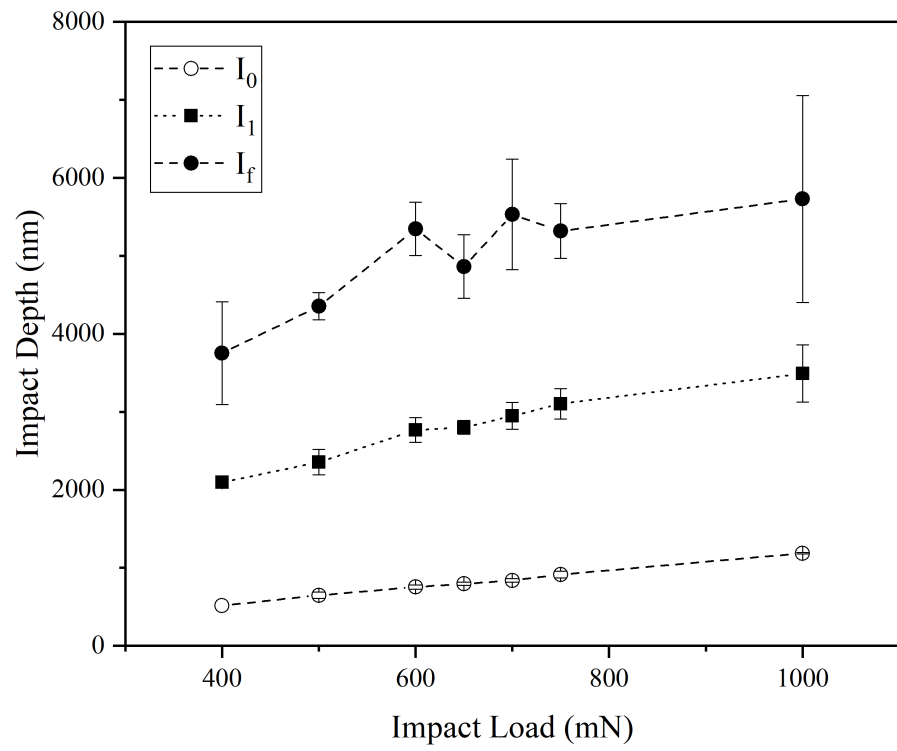
Figure 6.9: Impact parameters (I_0 – quasi-static depth, I_1 – depth of first true impact, I_f – depth of final impact) of Coating B on HTS.
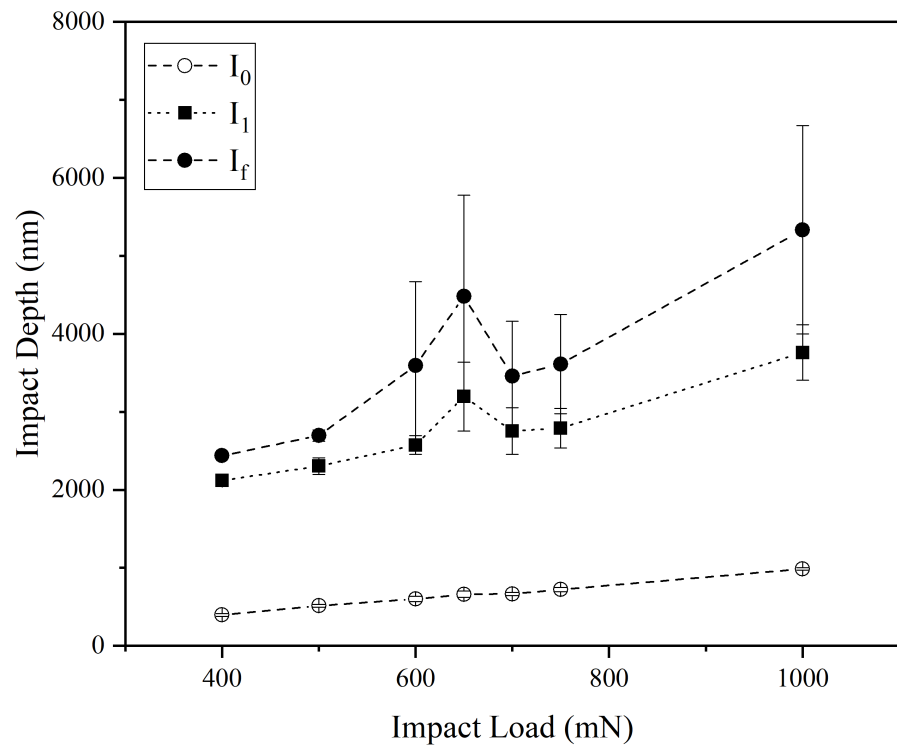
Figure 6.10: Impact parameters (I_0 – quasi-static depth, I_1 – depth of first true impact, I_f – depth of final impact) of Coating C on HTS.

The normalised difference in initial and final depth is shown in Figure 6.11 with the I_δ parameter. The use of this parameter simplifies the comparison of the impact depths and highlights the performance of each coating at the different loads. This allows the comparison of the impact and fatigue resistance of the coatings relative to each other. On HTS we can see that throughout the impact loads (Figure 6.10), Coating C remains at the lowest depth, achieving the smallest increase in depth thereby giving a low I_δ. Using this metric, a lower value is better, thereby suggesting Coating C as the best candidate for fatigue resistance. Though Coating A is seen to be better at lower load, it should be noted that raw depth reached through testing is greater giving it reduced impact resistance overall compared to Coating C.
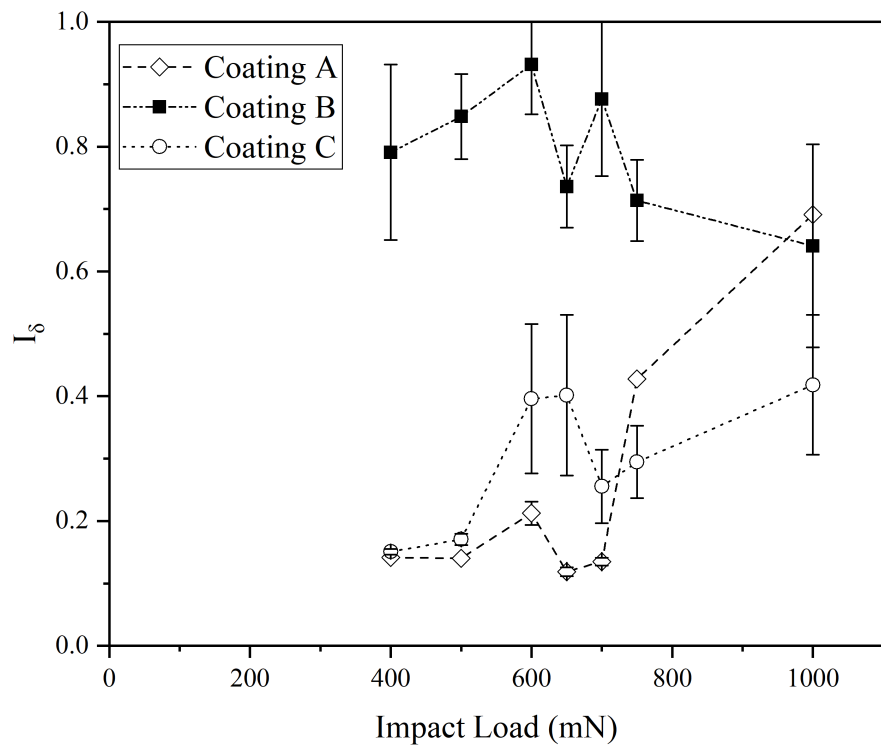
Figure 6.11: Graph of I_δ showing the change in depth from first impact to final impact normalized relative to initial impact depth to compare fatiguing of each coating on HTS.

Beake et al. [399] noted that the comparison of tests, at different applied loads and across different substrates, to determine the extent of coating failure could be performed by analysing the difference in depth between the first impact and final impact. This is shown in Figure 6.12. The same trends are seen as Figure 6.11 however the thickness of each coating must be considered in comparison rather than I_δ having a relative increase in depth. However I_δ requires consideration of the coating thickness too, a future study could consider a modification of these parameters taking into account the film thickness rather than just wear depth.
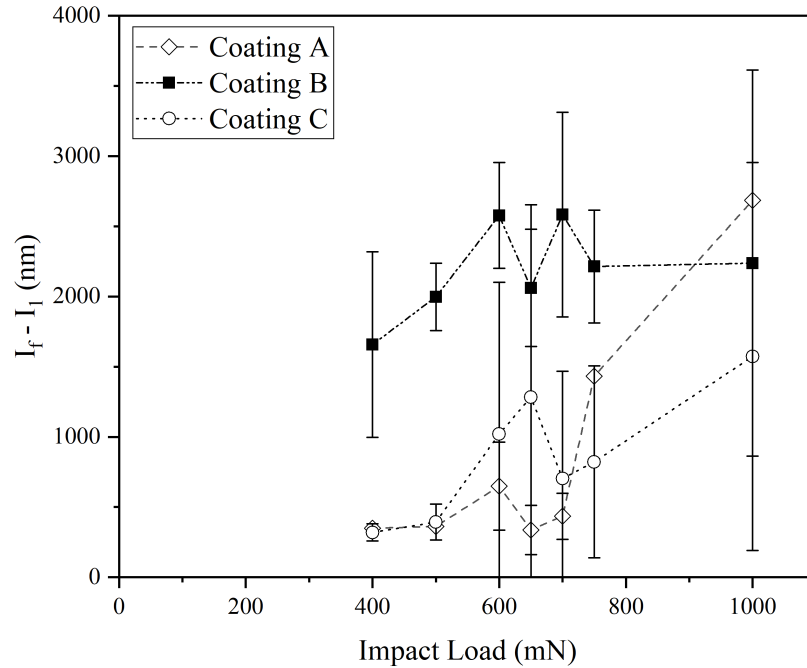
Figure 6.12: Graph of $I_f - I_1$ showing the change in depth from first impact to final impact across the load range to compare the extent of coating failure each coating on HTS.

Figures 6.13, 6.14 and 6.15 demonstrate the differences in the cracking dynamics between Coating B and C on HTS. Coating B displays larger scale cracks permeating between the interlayer structure and top layer DLC. We can also see that the top layer DLC is almost entirely removed on the right side of the crater. These features indicate that this coating is more likely to crack and completely delaminate from the interlayer and substrate. In Coating C, a greater degree of cracking can be seen when compared to Coating B but the coating has not delaminated across any of the cross-sectioned area. Much of the cracks seen are intra-layer i.e. still within the same layer instead of causing layer removal. Smaller cracking phenomena such as this is more consistent with ductile failure wherein there are smaller crack areas but more are present [301].

Voids and globular nature of the platinum deposition is due to the roughness of the coating surface after impact. Coating is seen to be removed on the right side of the impact crater. Insert shows crack formation can be seen between the interlayers and the DLC top layer indicating a mechanism that will lead to coating delamination. The inset shows a large amount of intra-layer cracking but the coating remains on the surface of the substrate.
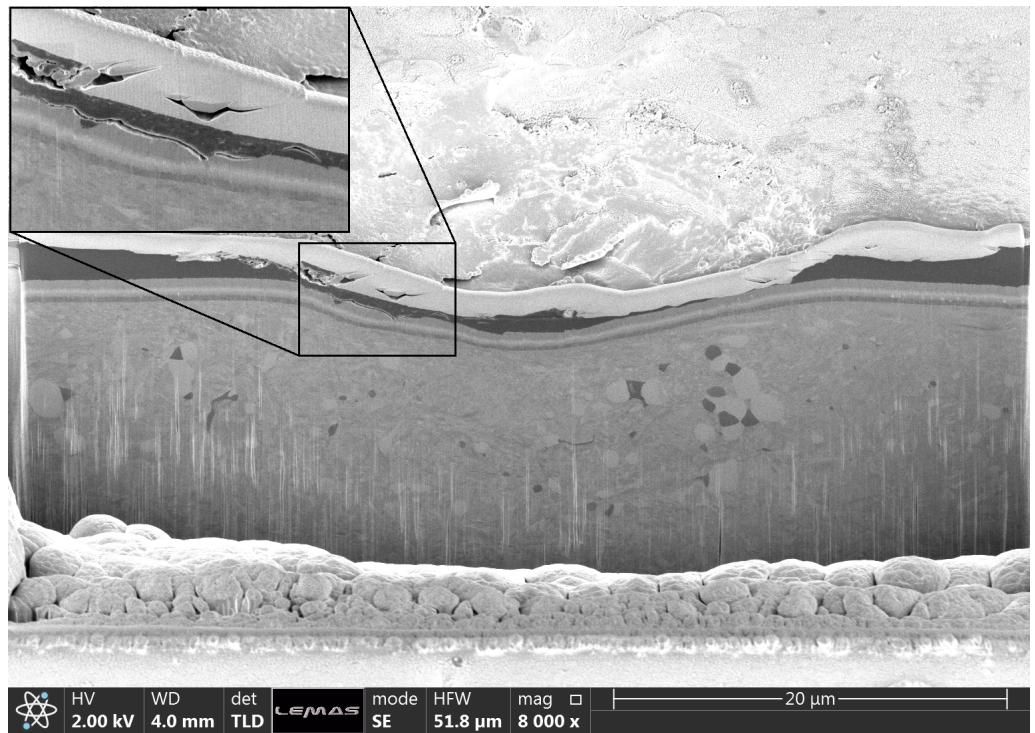
Figure 6.13: FIB-SEM cross section 75 impacts at 1 N load on Coating B on HTS. Upper light material is platinum deposited before the FIB process.
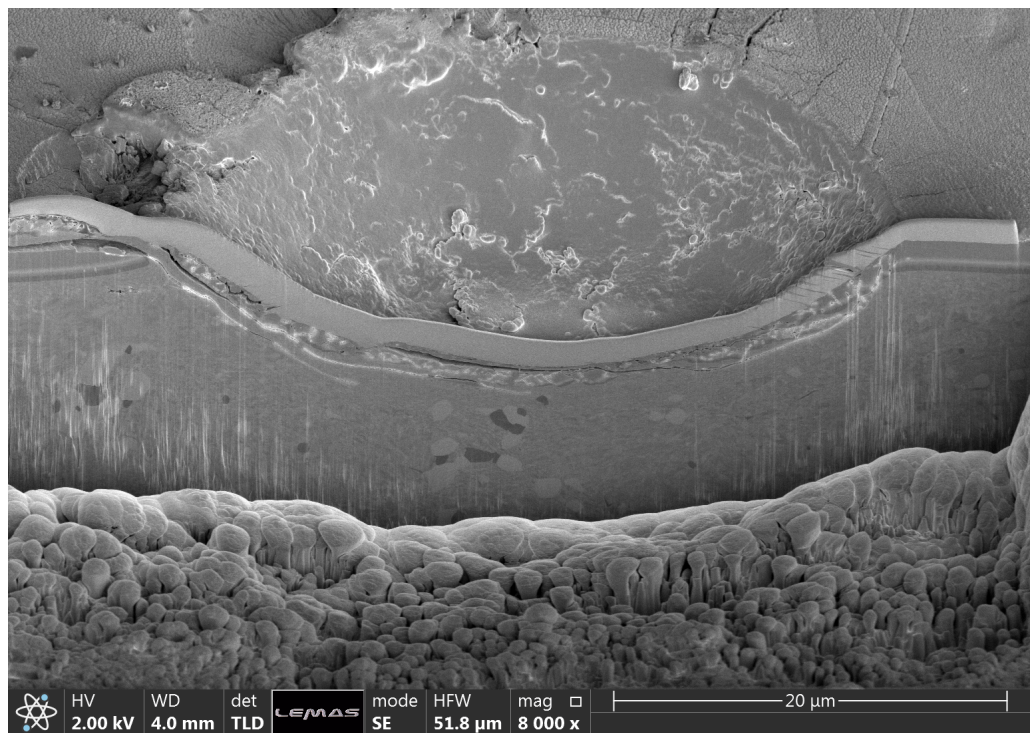
Figure 6.14: FIB-SEM cross section 75 impacts at 1 N load on Coating C on HTS. Upper light material is platinum deposited before the FIB process.
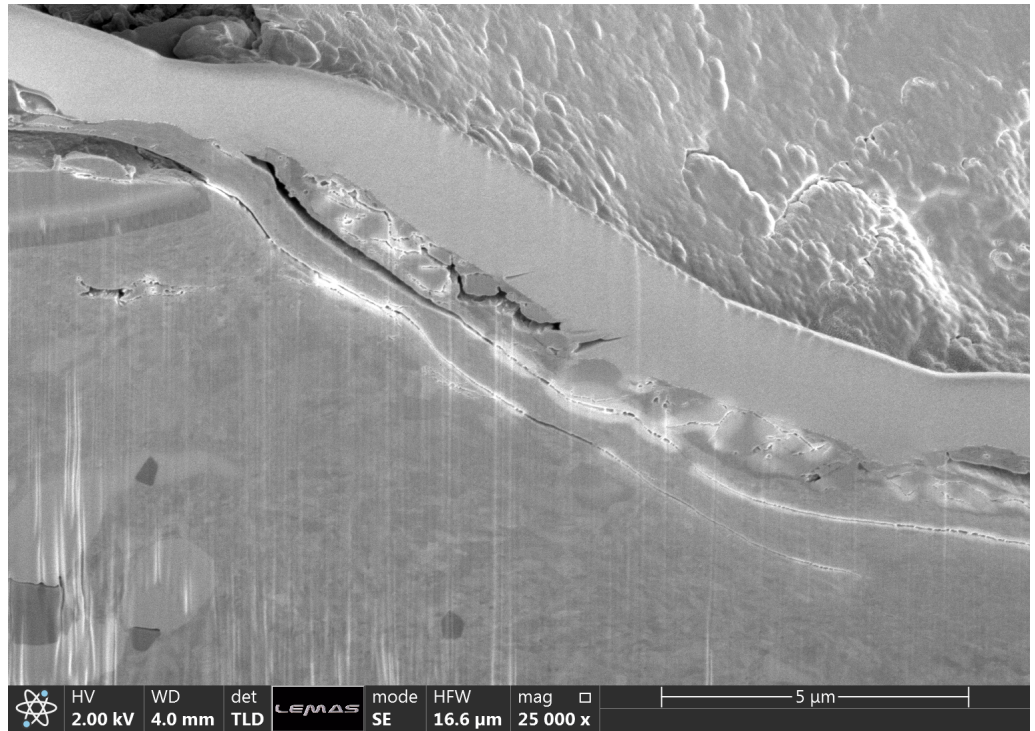
Figure 6.15: Increased magnification FIB-SEM micrograph of left side of Figure 6.14 showing 75 impacts at 1 N load on Coating C on HTS.

6.3.1.1 Raman Analysis

Using the same methodology present in Section 5.2.1, the Raman spectra of the craters at the highest micro-impact load (1 N) were analysed (when the craters could be located) to assess the maximum possible change in structure. Within the allotted time for post-test analysis, Coating A could not be located due to the relatively low magnification of the microscope station integrated in the Raman microscope.

The post-test results for coating B on HTS show a marked increase in I_D/I_G indicating graphitisation due to impact where coating C decreases in I_D/I_G suggesting higher sp^3 content and thus implies destruction of larger sp^2 clusters [400, 401].

Table 6.3: I_D/I_G ratio of Coatings A, B and C on each substrate showing the structural transformation due to repeated impacts.

Substrate	Coating	Structure	I_D/I_G (Pre-test)	I_D/I_G (Post-test)
	A	a-C:H	0.79	–
316L Stainless Steel	B	Si-a-C:H	0.68	–
	C	a-C:H:W	3.50	–
	A	a-C:H	0.48	–
Hardened M2 Tool Steel	B	Si-a-C:H	0.29	0.39
	C	a-C:H:W	2.96	1.61

By comparing the peak positions pre and post-impact, we can infer further information on the structural changes of the DLC coatings [250]. The position of the G peak can provide information on the relative levels of bond disorder, chains and clustering. Figure 6.16 shows the spectrum of Coating B on HTS with the positions of the D and G peaks annotated. The G peak position is seen to decrease from approximately $1505\,\text{cm}^{-1}$ to $1500\,\text{cm}^{-1}$, indicating a slight increase in bond disorder. The post-impact spectrum has a smaller overall peak area indicating a thinner coating due to delamination as seen in Figure 6.13. Figure 6.17 shows the spectrum of Coating C on HTS with annotated peak positions. The G peak decreased from $1570\,\text{cm}^{-1}$ to $1543\,\text{cm}^{-1}$, showing a marked increase in the bond disorder and decrease in sp^2 clustering.
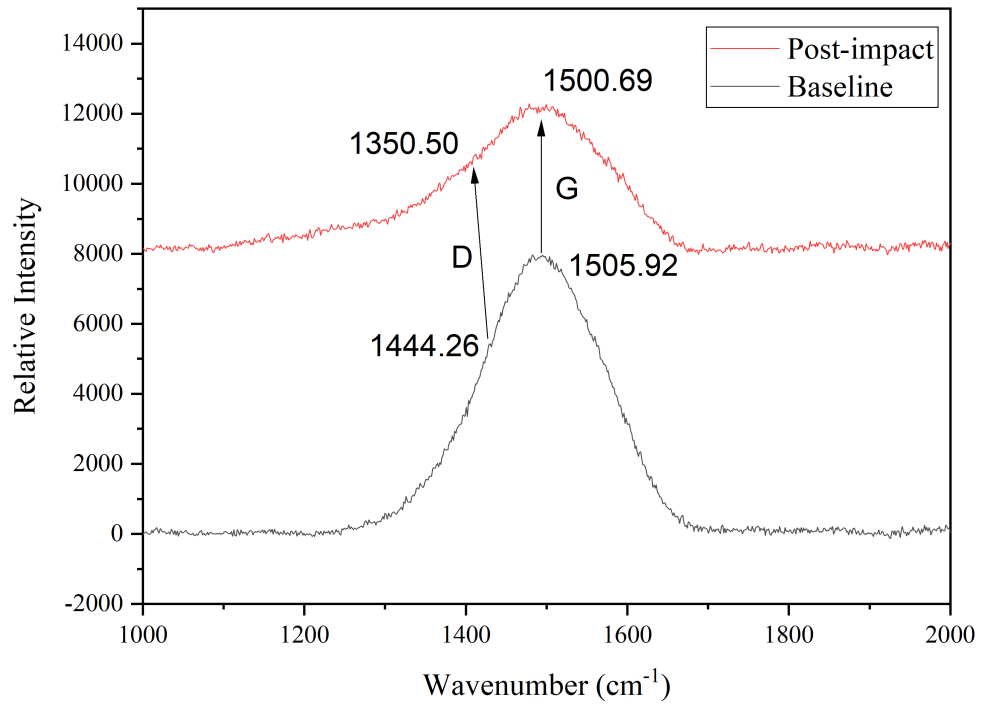
Figure 6.16: Comparative Raman spectra of the baseline and post-impact on HTS Coating B.
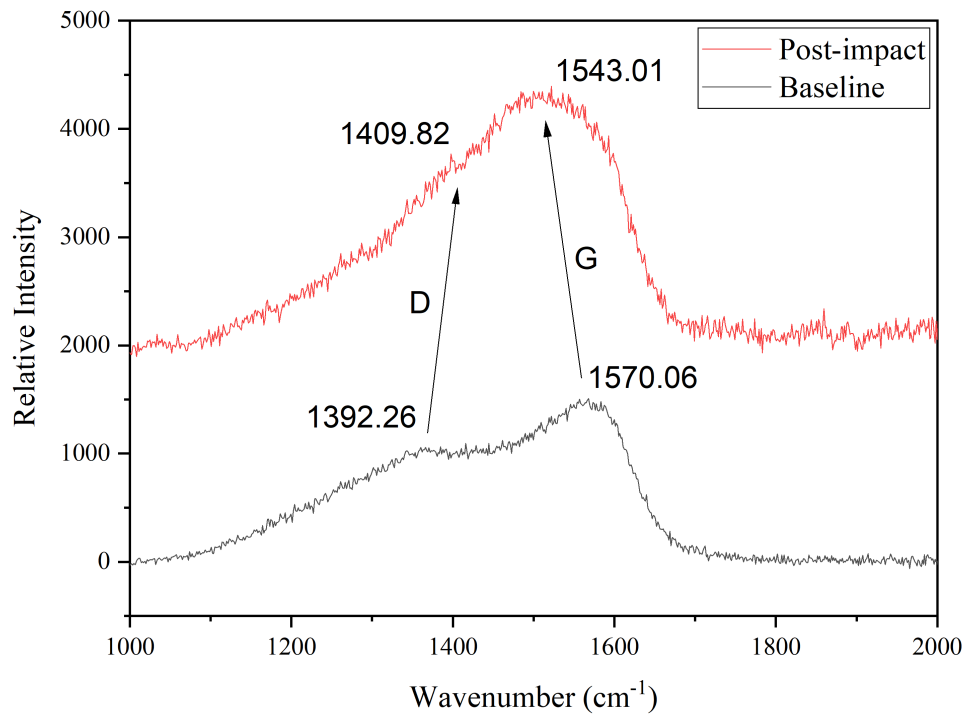
Figure 6.17: Comparative Raman spectra of the baseline and post-impact on HTS Coating C.

6.3.1.2 Nano-Impact Analysis

The results of nano-impact testing shows the level of initial cracking of the coatings due to the smaller loads imparting less energy impact into the system with each impact. Figures 6.18 and 6.19 shows the progressive depth increase of Coatings A, B and C on both HTS and SS with 75 impacts at a load of 100 mN. Observing the difference in Figures 6.18 and 6.19 under the same impact load, the deeper penetration in the SS coating is immediately apparent due to eggshell failure with the substrate unable to provide the necessary load support. As seen in Figure 6.18 and Table 6.4, Coating A on HTS has the smallest increase from I_1 (429 nm) to I_f (535 nm) resulting in an I_δ value of 0.18. Coating B is seen to have the largest increase in depth from 559 nm at I_1 to 917 nm at the end of testing giving an I_δ value of 0.64. Coating C has a more gradual increase in depth, though a higher value of I_1 of 661 nm, progressing to 910 nm. This gives an I_δ value of 0.38. Observing the I_δ values on the SS substrate, we see values that fall within the same range of the HTS substrate, however by the end of the impact testing only Coating A has not completely broken though all the coating layers with a final impact depth of approximately 2.05 μm compared to the total thickness of 2.65 μm. On SS, both Coatings B and C penetrate the top DLC layer at first true impact (1.54 μm and 1.86 μm for I_1 with top DLC layers of 1.16 μm and 1.10 μm respectively). In addition to the relative depth increase in impact testing, the absolute depth relative to the coating thickness must be observed.
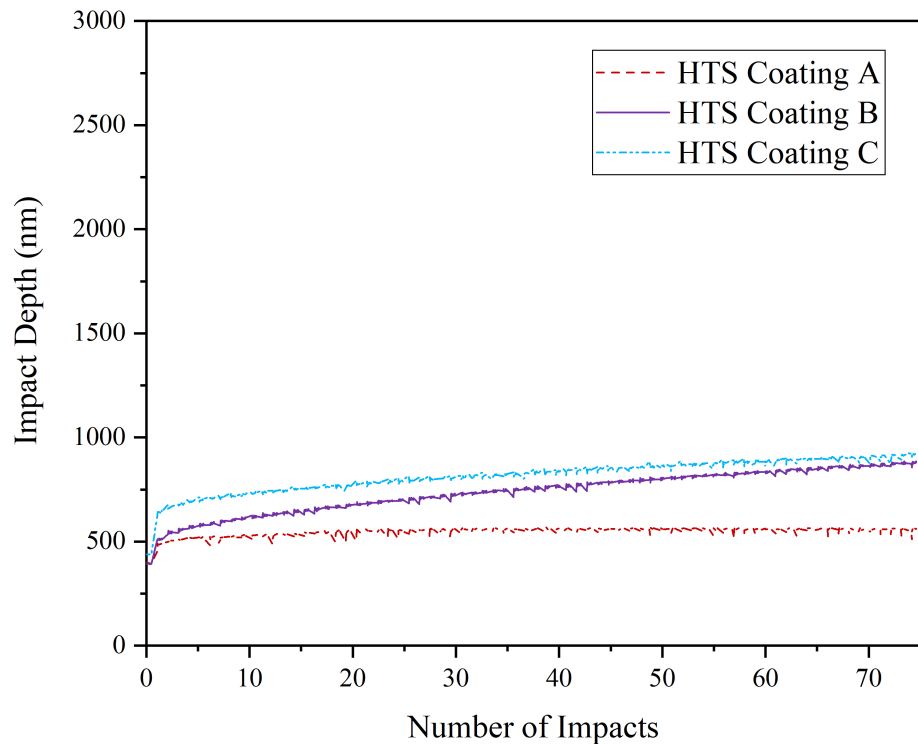
Figure 6.18: Representative nano-impact depth versus number of impacts for coatings A–C on HTS. Impact load = 100 mN. Total number of impacts = 75 (300 s of testing).
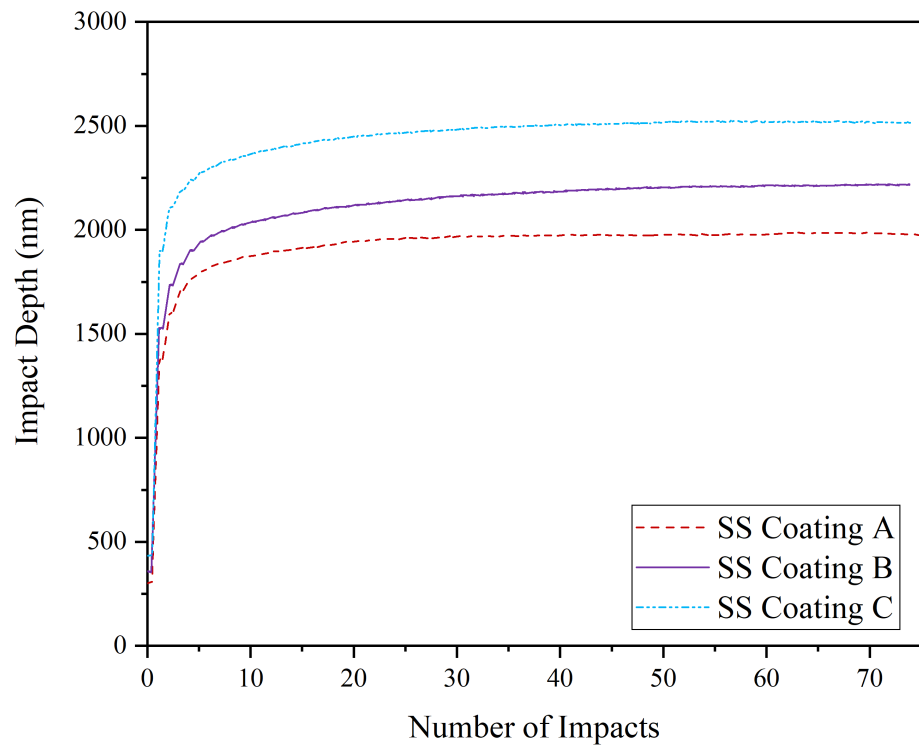
Figure 6.19: Graph of nano-impact depth versus number of impacts for Coatings A-C on SS. Impact load = 100 mN. Total number of impacts = 75 (300 s of testing).

Table 6.4: Comparison of impact parameters (I_0 – quasi-static depth, I_1 – depth of first true impact, I_f – depth of final impact, I_δ – normalised difference between the first and final impact) in nano-impact tests at 100 mN load.

Substrate and Coating/Impact Parameter	I_0 (nm)	I_1 (nm)	I_f (nm)	I_δ
HTS Coating A	350.0 ± 23.0	429.0 ± 15.9	535.0 ± 31.8	0.18 ± 0.01
HTS Coating B	383.0 ± 28.8	559.0 ± 40.4	917.0 ± 66.3	0.64 ± 0.07
HTS Coating C	421.0 ± 25.5	661.0 ± 11.3	910.00 ± 9.93	0.38 ± 0.01
SS Coating A	327.0 ± 24.7	1402.0 ± 31.6	2058.0 ± 92.0	0.47 ± 0.02
SS Coating B	352.0 ± 16.7	1549.0 ± 28.1	2271.0 ± 65.8	0.47 ± 0.02
SS Coating C	420.0 ± 44.3	1864.0 ± 47.3	2511.0 ± 32.0	0.35 ± 0.01

154

6.3.1.3 Solid Particle Erosion

In Figure 6.20, it is noted that the substrate exposure quickly climbs to approximately 100 % for all coatings. At 5 s, all three coatings have completely failed by completing exposing the substrate, once again demonstrating the lessened load support of the SS substrate and showing the same behaviour between impact and erosion. Figure 6.21 shows that Coating C can withstand erosive condition to a greater degree than Coatings A and B. After 400 s of solid particle impingement the substrate exposure is around 50 % compared to Coating A reaching 94 % at 210 s and Coating B reaching 97 % at 150 s. The substrate exposure value does vary over the period of testing, but this is attributed to the small-scale cracking and deformation occurring on the surface of coating as opposed to the larger scale removal in the other coatings. As less of the substrate is exposed, a thicker layer of DLC remains on the surface.
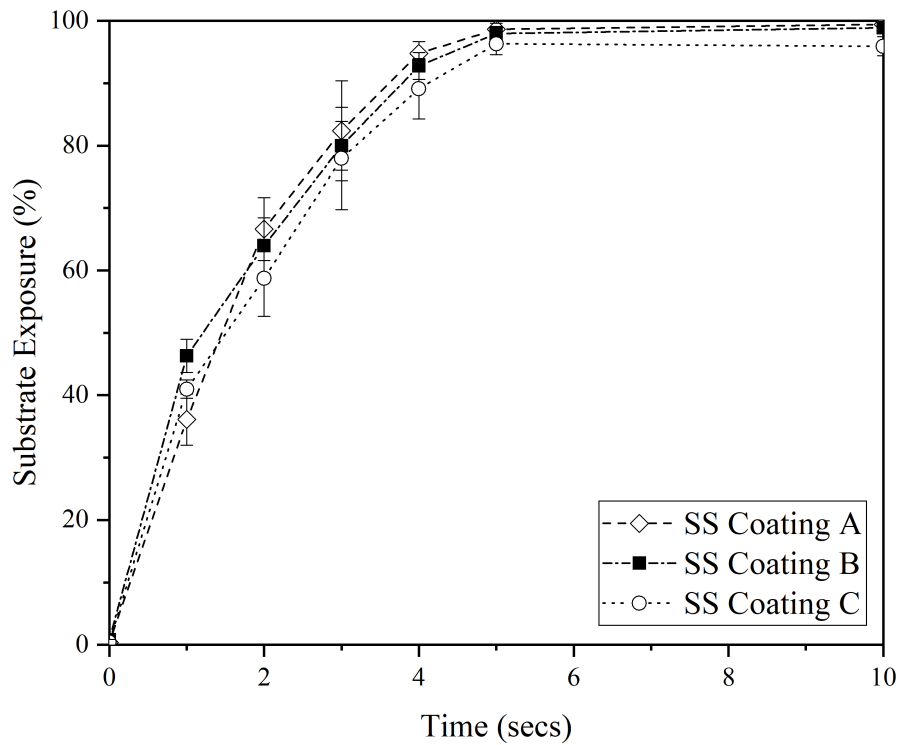
Figure 6.20: Substrate exposure of coatings on SS as measured by optical image analysis.
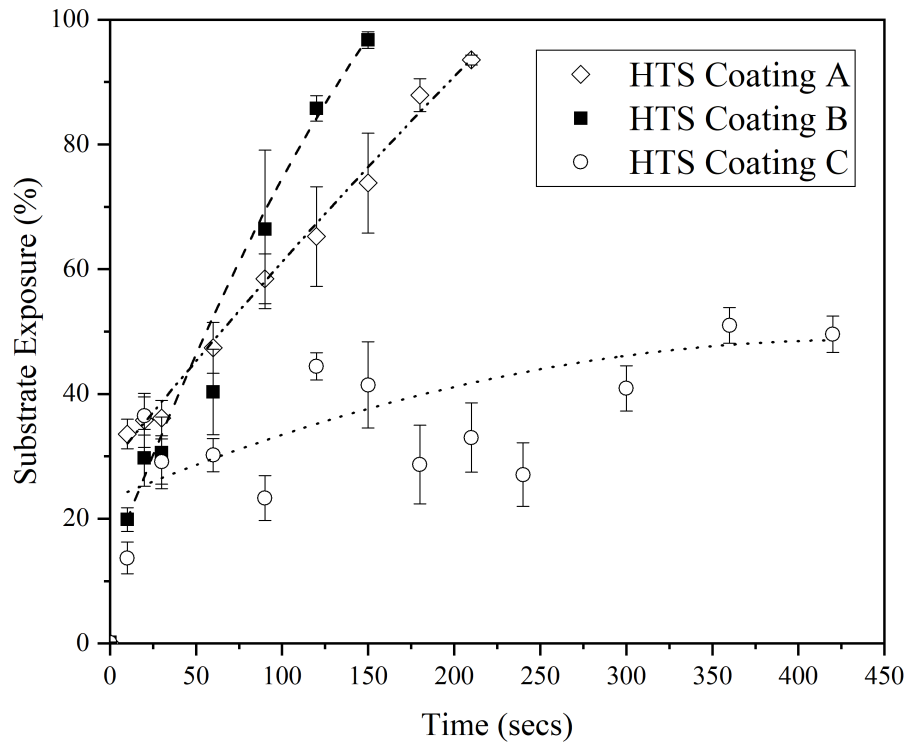
Figure 6.21: Substrate exposure of coatings on HTS as measured by optical image analysis.

6.3.2 Energy Quantification

The energy supplied by the impact module can be quantified as performed by Beake et al. [111].

$$E_i = P_s \times F \qquad (6.2)$$

Where E_i is the energy per impact (in J), P_s is the pendulum swing distance (in m) and F is the force (in N). The total energy supplied (E_T) can then be calculated by multiplying the energy per impact (E_i) with the total number of impacts (N_i):

$$E_T = N_i \times E_i \qquad (6.3)$$

Using the retraction distance of 15 μm and 40 μm for nano and micro-impact, respectively, as the P_s values and 75 as the total number of impacts (corresponding to 300 s of testing), the total energy (E_T) can be calculated. Table 6.5 shows the results of these calculations.

Table 6.5: Calculated energies imparted in impact testing. Note that the 100 mN force is applied via nano-impact with a P_s of 15 μm resulting in lower E_i and E_T values.

Force (mN)	E_i (J)	E_T (J)
100	0.0015	0.1125
400	0.0160	1.2000
500	0.0200	1.500
600	0.0240	1.800
650	0.0260	1.950
700	0.0280	2.100
750	0.0300	2.250
1000	0.0400	3.000

Appendix C shows a mathematical derivation of the estimated number of particle impacts based on the geometry of the nozzle set up and mass flow rate. This model predicts 2096 particles per second impacting on the surface at a flow velocity of 15 m s^{-1} under slurry conditions. When adjusted for the density of particles in air flow, 1220 particles per second are predicted to impact on the surface each second. Ukpai [402] used acoustic emission to measure the number of particle impacts per second, he found for a flow velocity of 15 m s^{-1} with a sand density of 500 mg L^{-1}, approximately 2000 acoustic emission counts were measured corresponding to the same number of particles per second. Therefore, we can be reasonably that the model has preliminary accuracy.

Using similar basic numerical modelling, the energy imparted to the sample surface in erosion can be calculated. The energy per particle impact can be estimated with:

$$E_p = m \times a \times d_n \qquad (6.4)$$

This is an expanded version of $E = F \times d$ where $F = m \times a$; m is taken as the mass of an individual sand particle (see Appendix C for this value), d_n is the distance to the nozzle (5 mm). The deceleration (a) is calculated by dividing the particle velocity (15 m s^{-1}) by the time for each impact. The time is approximated by the nozzle distance by the particle velocity. The energy per second (E_s) can be calculated by:

$$E_s = I_s \times m \times d_n \times a \qquad (6.5)$$

This gives 6 mJ s^{-1}. Erosion for 10 s (as seen on coatings on SS) gives an energy input

of 0.058 J. Erosion up to 150 s, 210 s and 420 s (for Coatings B, A and C respectively on HTS) gives 0.863 J, 1.208 J and 2.416 J respectively. In comparison to Table 6.5, we can see that similar energies are imparted to the surface. Applying the same model to slurry erosion, a total energy of 17.78 J is imparted after 30 min and therefore 284 J is imparted after 8 h (with the assumptions of this ideal model). Clearly, the slurry erosion conditions are too extreme (much higher energy input) to provide a good comparison with impact conditions for the times tested.

6.4 Discussion

6.4.1 On the Significance of Substrate Hardness

Once a sufficient load-bearing substrate is present the fatigue resistance of the coating structure can be studied, by either instrumented impact or solid particle impingement. Marked differences are seen in the behaviour of the SS and HTS substrates under the same conditions as evidenced by Figures 6.7 , 6.18, 6.19, 6.20 and 6.21. Higher depths are reached on SS under both micro and nano-impact with near instantaneous coatings failure seen under erosive conditions too.

This effect is known as egg-shelling (sometimes referred to as crème brûlée effect) where impact stress causes the coating structure collapse, presumed to collapse into the substrate due to it yielding and plastically deforming underneath the coating [278, 403, 404]. The softer SS substrate cannot elastically support the stress induced by impact or erosion testing. This is further supported by sub-surface plastic deformation being common in impact wear [112]. The HTS substrate, therefore, allows for the analysis of the coating system in addition to giving a more fatigue resistant system due less variation in the hardness and elastic modulus data across the system as seen in Figure 4.13a in comparison to Figure 4.12a where little drop in H/E ratio is seen with increase in depth. We can also note the higher surface hardness (10 GPa vs 2.6 GPa) and H/E and H^3/E^2 values (0.042 and 0.017 vs 0.012 GPa and 0.0004 GPa respectively) of HTS compared with SS in Table 4.2. It is interesting to note that SS has a higher Mean Elastic Modulus of 223 GPa compared with 204 GPa suggesting that stiffness alone does not benefit substrate support. The detrimental effects of low substrate hardness were also seen with investigation of erosion resistance on TiN coatings on tool steel [77]. Ramalingam and Zheng [405, 406] noted that matching the elastic moduli of coatings and substrates will reduce tensile flexural stresses and therefore reduce film cracking alongside thicker coatings further reducing this stress. Therefore, it can be concluded coating fatigue resistance is first controlled by the substrate's ability to support the coating structure and substrate properties must be considered for a well performing composite [198].

6.4.2 Coating Mechanical Properties

Nanoindentation and scratch tests were used to measure the nanomechanical properties and adhesion of the coatings. Using the measured mechanical properties [321, 322] and scratch cracking parameters [310, 311], we aim to predict the impact and erosion performance of the DLC coatings. Coating A possessed the highest hardness, H/E and H^3/E^2 (as seen in Table 4.2 and Figure 4.13a); this can be attributed to the I_D/I_G ratio correlating with high sp^3 content [375]. Using the predictions of Leyland and Matthews [322] and

Chen et al. [321], we would say this would predispose Coating A to have the best wear resistance as it would possess the highest elastic strain-to-break (H/E) [122]. Further to this, metal ceramic coatings with high H^3/E^2 ratios performed well under impact conditions [118, 407]. However, in the treatment of Lawn (and co-workers) and Pharr, fracture toughness follows an E/H (lower H/E) relationship thereby positioning Coating C to be the best performing with less chance of fracture [122, 163, 322, 328]. The difference in coating hardness and substrate hardness may also play a part as with the work of Bousser et al. [408] where a smaller difference in the hardness of the coating and substrate allowed the coating to accommodate plastic deformation of the substrate without cracking. The difference in dependence in these parameters theoretically depends on influence of the applied stress and behaviour observed where crack resistance is benefited by a low E or crack propagation where high stiffness would stop the cracking though a combination of these factors is probably at play [163]. The CPR$_S$ provides valuable information on the predicted behaviour of the coatings too. On SS Coating C is seen to have the highest CPR$_S$ (Table 4.3) which can relate to the fracture toughness of the film [310, 311]. The decrease in CPR$_S$ in Coating C HTS can be explained by the change in the position of maximum stress due to the difference in coating thickness compared to the Coatings A and B [83].

Structural considerations must be made too. W doping in DLC films increases the fraction of sp^2 bonding present in the coating structure thereby giving it a more graphitic structure and softening the coating; clearly seen in Table 4.2 and Figures 4.12a and 4.13a. The sp^2 ring structure and presence of tungsten in its microstructure imparts a high elastic modulus to the coating while also giving it a lower surface hardness with the added likelihood of the presence of nanocrystalline WC or W_2C [225, 251, 273, 362, 363]. Superior fatigue resistance is seen in tungsten doped DLC due to non-planar sp^2 carbon-carbon bonding allowing for greater compensation of shear stress [409]. The post impact Raman results (Table 6.3 and Figures 6.16 and 6.17) show a decrease in I_D/I_G corresponding to higher sp^3 content and destruction of larger sp^2 clusters [401]. There could also be a degree of hardening that occurs due to the Hall Petch effect (material strengthening by a change in grain size) or by compression of the nanocrystallites under impact [310, 363, 410]. Conversely, Si doping increases sp^3 fraction in a coating structure [269, 411, 412] however this doesn't result in a harder coating due to it developing a polymer like structure [268] and further softening with graphitisation (increase in I_D/I_G in Table 6.3) [400].

In considering H^2/E as resilience during erosion tests as seen in Table 4.2; we would assume that Coating A on HTS would perform best under these repetitive fatigue conditions. Additionally, following this metric, the coatings deposited on SS should also perform well as already stated when analysing the values of H/E and H^3/E^2. These metrics (H/E, H^3/E^2 and H^2/E) are most applicable to ordered crystalline coatings [86] such as metal ceramics [118, 407]. Toughness (E/H) has previously been shown to be paramount to amorphous coating fatigue resistance such as DLC [122]. We can therefore surmise that any coatings with high resistance to plastic deformation (H^3/E^2) will also have a high resilience (H^2/E) due to the mathematically similar nature of both metrics. H^2/E should therefore be used in future erosion and impact studies when appropriate for the material.

6.4.3 Micro- and Nano-impact

Multi-scale instrumented impact testing allows for varying strain rates and energies to be modelled in a method able to simulate fatigue conditions experienced in service far closer than other methods. It allows for individual impacts to be studied and for time-to-fail and on-load depth to be measured [110, 144]. Rueda-Ruiz et al. [113] recently showed that impact testing could be utilised to evaluate dynamic hardness at high strain rates. Due to the lower load and therefore lower strain, nano-impact allows us to see the initial repetitive strain resistance of the coatings. Figure 6.18 and Table 6.4 suggest that initially Coating A on HTS performs better as the higher H^3/E^2 minimises plasticity [86]. This indicates initial load support in Coating A as also seen in the lower loads of micro-impact (Figures 6.11 and 6.12). In other nano/micro scale comparisons it is typical to change the probe geometry between length scales in order to drive failure rapidly [282], by maintaining the same probe throughout we can study the load dependent fatigue behaviour without pursuing film failure. We can also note that the comparison of the impact depths of HTS and SS seen in Figures 6.18 and 6.19 and Table 6.4 shows that egg-shelling also occurs in nano-impact.

Micro-impact allows for a far greater amount of energy to be fed into the system with greater loads for each impact. This allows for more dramatic failures to be seen and the loads to be parametrised to a greater degree as with Figures 6.8, 6.9 and 6.10. The number of failures seen under multiple loads and repeats of the testing conditions (Table 6.2) compared with the depth parameters (Figures 6.8, 6.9 and 6.10) and I_δ (Figure 6.11) and $I_f - I_1$ (Figure 6.12) show that throughout the testing Coating C has consistently performed the best with an overall lower impact depth at end of test, lower impact depth increase during testing and less probability of failure within the given time [112]. Beake et al. [330] showed that impact testing could be used to probe the fracture toughness of ceramic coatings. It is noted in this paper that the fracture toughness follows an inverse relationship with the probe depth reached, further supporting Coating C as the superior architecture. Figure 6.7 demonstrates the full extent of eggshell failure between SS and HTS at micro-impact loads. Figures 6.13 and 6.14 give greater insight into the cracking dynamics seen between Coatings B and C on HTS. Coating B has partly delaminated compared to Coating C where intralayer cracking is present. The cracked coating is still adhering to the surface. From this we can gather that the multiple processes suggested earlier are seen with the lower H/E value and CPR_S benefitting fracture toughness and reducing the amount of crack propagation while the impact hardening benefits in fatigue resistance [122, 144, 328]. The reduced severity of cracking suggests a more semi-brittle nature rather than the brittle fracture seen in the other coatings.

6.4.4 Impact-Erosion Link and Wear Resistance

Erosion tests with a bespoke air particle impingement jet showed that on HTS, Coating C had the most coating remaining on the surface and the least amount of substrate exposed (Figure 6.21), a combination of beneficial mechanical properties and the ability to structurally transform (as seen under impact wear) make this coating more erosive and fatigue resistant to particle impact. Repetitive impact induces fatiguing and fracture in materials intrinsically linking impact and erosion wear [75–77, 110–112, 116, 117]. Furthermore, Figures 6.11 and 6.12 and Figure 6.21 show a link in the lowest increase in depth across the load range (with I_δ and $I_f - I_1$) and most coating remaining in erosion testing correlating to a coating that is less likely to catastrophically crack and delaminate in either wear

regime. Figure 6.14 corroborates this with less severe cracking seen within the coating layer. The same egg-shelling seen with micro- and nano-impact (Figure 6.7, Figure 6.18 and Figure 6.19 respectively) is seen under erosive conditions so that repetitive impacts either by sand particles or an indenter tip cause the coating structure collapse due to lack of substrate support [278, 403, 404]. Using all these parameters together it is possible to rank the relative performance under the repetitive fatigue conditions of impact and erosive wear, we can clearly see that Coating C is the superior coating for resistance to these wear regimes, followed by A and B, specifically on HTS as substrate support is first required.

Initial numerical modelling as presented in Section 6.3.2 shows that the energies imparted under impact and erosion are in the same order of magnitude, reinforcing that these processes can be linked and compared. More complex modelling will be required to precisely calculate the energy input of impact and erosion respectively. The model is limited by assuming that all particles hitting the surface have the same energy, the flow dynamics are not considered (affecting the angle of impacts) and the geometry of the process (size of particles versus size of indenter) is neglected. The sizes of the particles (and their overall impacting area) is very different to that of the impacting indenter therefore the energy density is different and this may affect deformation. A representative volume could be considered from the Hertzian indentation strain volume (to approximate the plastic strain region) with height $2.4a$ (where a is the contact radius) and area πa^2. [413]. A further extension to the simplified modelling performed here would be to consider impulse (force integrated over time) in order to consider time dependence during impact (which may have rebound characteristics) and particle impingement (time for energy transfer and number of particle impacts per unit time). Particle size and particle shape are well known to affect the erosion process. More angular particles causing a cutting effect as opposed to simple crack generation and larger particles causing greater mass loss [414]. Numerous erosion models exist with each factoring in various different physical properties, a systematic approach comparing these [414] alongside the application of Bull's [85] work of indentation model applied to impact may provide further insights into these processes to draw them closer together and increase the accuracy of the impact method to predict performance under erosive conditions. The size and angularity of particles could be tailored to the impacting indenter size with sharp particles modelled with a cube corner. Angled impact testing could also be investigated to compare different particle approach angles with impacts normal to the surface.

The use of a combination of nanomechanical techniques [122] paired with cross sectional SEM, to understand the cracking dynamics of coatings [397, 398], can inform on how a specific coating structure behaves and how its properties drive different failure mechanisms (crack initiation or propagation) [122, 144, 328]. This is useful for other coatings beyond DLC where standardised instrumented impact can remove some of the randomness of erosion testing to make future coating architecture optimisation easier and the ranking of fatigue resistance possible.

6.5   Summary

Multi-scale instrumented impact testing was used to compare fatigue resistance against erosion testing to find a link between the processes to allow for impact to be used as a more standardised method in future testing.

Correlation between the relative depth increase in instrumented impact and substrate exposure in erosion allows linking of the two wear processes and for the use of impact to

inform fatigue behaviour of coating under erosive conditions. The methodologies adopted in this work can be applied to other coating architectures to assess their relative erosive and impact resistance to allow for future coating optimisation. Though it should be noted that a combination of techniques provides the capability for a more complete characterisation of the behaviour of the system.

Differences in the relative fatigue resistance can be observed between coatings A, B and C correlating between erosion and impact testing. Coating C (with tungsten metallic doping) is seen to be the most resistant to fatigue wear due to its semi-brittle nature of smaller intralayer cracking. It follows that for DLC coatings, a lower H/E ratio is favourable for fatigue resistance. This lower H/E ratio correlates with increased toughness (E/H) rather than elastic strain to break (H/E). Additionally, impact and erosion testing shows that the resistance to wear in these two techniques is first dominated by the substrate's hardness and load bearing support, a harder substrate is most beneficial to fatigue resistance under repetitive loading conditions. The difference in hardness between the SS substrate and DLC top layer is such that an eggshell type failure is seen under both impact and erosive wear.

Robust surface profilometry would allow for the amount of substrate exposure to be correlated to wear volume. Future studies could investigate the impact/erosion relation with thicker coatings or multi-top-layer coatings. Modelling to compare between the two methods and analyse the energy input into the system would allow for the fatigue behaviour to be further investigated. Additional post-test structural Raman and nanomechanical topographical mapping would allow for the dynamic structural transformation to be discerned as performed with fretting wear previously [102, 341]. Future impact work could investigate the scenarios under which I_δ or $I_f - I_1$ functions best as a wear parameter; additionally a modification of the parameters could be investigated to take the penetration into the total coating thickness into account.

Chapter 7

Nano-Scratch for the Determination of Interfacial Friction

7.1 Introduction

Traditionally, nano-scratch testing has been used to investigate the critical load failures of thin films (to the nm scale) and to test the adhesion of upper portions of the coating structure (top film layer and interlayer) as opposed to the whole film and substrate. In the NanoTest platform, to drive failure generally a smaller probe is used to increase the maximum Hertzian contact pressure and induce film failure. Additionally, the load could be increased by moving to the micro-load head (with maximum load of 5 N) which allows for significantly larger normal forces in the scratch test [282]. Numerical modelling has been performed to predict the ploughing and interfacial components of friction of various probe radii [313, 415]. Experimental studies have been performed to investigate the abrasive, shear and ploughing components of friction on various materials [416, 417]. The partition of friction into interfacial and ploughing components originated with Bowden and Tabor [70]; the interfacial component was formulated as the shearing of metallic junctions formed in the contact between metal surfaces. The ploughing component is expressed as the friction in displacing the softer material in the contact. However for dissimilar materials, this interfacial component (sometimes called the adhesive component) can be expressed as the breaking of multiple types of bonds including covalent, electrostatic and hydrogen bonds [64, 418].

However, no systematic studies have been performed to investigate these phenomena as most research institutes do not possess the selection of probes needed due to their expense. Additionally, AFMs are traditionally used to model the work of adhesion [1] as the pull off force can be more readily measured [420–422] however this is generally limiting as the probe radii are much smaller than those used for scratch testing. By performing this study, the fundamental contact conditions (in terms of adhesion) between two surfaces can be assessed without an AFM. The use of small radius probes to induce plastic deformation in coatings allows their yield stresses to be calculated which is invaluable for coating design. Furthermore, the relation between H and Y is a useful input parameter for modelling applications to analyse the stresses within coating structures, this has not been performed with such a large array of coating designs previously. Y/E may also present

---

[1]The work of adhesion is the reversible thermodynamic work required to separate the interface from the equilibrium state of two media in contact to a separation distance of infinity [419, 420]. This is effectively the adhesive energy of two surfaces in contact.

as a useful wear parameter as it is sensitive to the full coating structure rather than the mechanical properties of the coating alone.

In this study, 4 probe radii of diamond sphero-conical geometry (4.5 µm, 8 µm, 72 µm and 170 µm) were used to assess the interfacial component of the coefficient of friction relative to each probe on one DLC design variant. The 4.5 µm probe was used to test the whole set of coating structures to measure the yield and critical load failures and correlate this with the parametric change of each coating design. The scratch friction and scratch recovery are also investigated to further explore each design's resistance to scratch. Multi-pass sub-critical load scratches were also performed to evaluate the coatings surface roughness change with each pass and its correlation to the coefficient of friction. The results presented in this chapter will be published at a later date [423].

7.2 Methods

7.2.1 Nano-scratch module

The nano-scratch module consists of the normal loading head as part of the NanoTest Platform with the addition of a friction probe (in the form of a Wheatstone Bridge strain gauge). The typical methodology for this type of testing is a 3 pass technique known as topography-scratch-topography [312, 424]. In the topography steps an extremely low load is used to ensure that no surface deformation takes place. Constant load scratch or progressive load scratches can be performed depending on whether cracking/topography change or critical load failures are to be investigated. Table 7.1 shows the typical range of conditions achievable with the nano-scratch module.

Table 7.1: Typical experimental conditions of nano-scratch module [425].

Probe radii (µm)	5–25
Applied Load (mN)	0–500
Sliding Speed ($\mu m\,s^{-1}$)	1–100
Scan Distance per cycle (µm)	10
Number of cycles	1–20
Total sliding distance (µm)	1–1000

A probe scanning velocity of $10\,\mu m\,s^{-1}$ and scan length of 1000 µm was used with all passes. The topography steps use a load of 0.10 mN. The scratch step had a maximum load of 500 mN applied after 200 µm with a loading rate of $8\,mN\,s^{-1}$. A total scan length of 1000 µm was used. 5 repeated scratches were performed with a separation of 200 µm. The same methodology is used to measure friction in Chapter 8 whereby the normal friction force triggers a change in electrical resistance which is measured by the platform. The multi-pass scratch tests used an altered experimental technique, a total of 21 passes were used to give 10 scratch passes with topography passes pre and post scratch. A maximum load of 150 mN with a loading rate of $2.5\,mN\,s^{-1}$ was used. All other experimental parameters were the same as specified above.

To investigate the interfacial component of friction for each probe radius (4.5 μm, 8 μm, 72 μm and 170 μm), progressive load scratches were performed on one DLC coating design (SS-Coating A-thin-smooth). The probe area functions (and effective radius) was determined by indentation into fused silica. This material is used because it is isotropic and has little variation in its elastic properties across the nano load range [167, 168, 426]. The interfacial component of friction is determined by extrapolating the low load friction to zero load [312]. Following this, the rest of the coating architectures were tested using the 4.5 μm radius probe to determine their surface roughness (via the topography scan), adhesion (via determination of the critical load points), contact pressure and friction. Repetitive multi-pass scratches (10 passes) were used to analyse the effect on friction and contact pressure on SS-Coating A-thin-smooth. Critical load points are determined by analysis of the depth and friction data for sudden increases in either value. Correlation with microscopy to assess the cracking phenomena is also used. The contact depth and subsequent contact pressure by Hertzian analysis is calculated using equations 2.46 and 2.48 respectively. The probe depth data is corrected to remove any slope, topographic or instrument compliance contribution [282].

Figure 7.1 shows the uncorrected profile of HTS-Coating A-thin-smooth. The pre-scratch profile can be used to generate a surface roughness value of the coatings. Observations in changes in the on-load profile can be indicative of critical loads. Comparison with microscopy of the scratch track is generally used to check that a critical load failure is being reached. The post-scratch residual profile can be used to find both the yield point and estimate the contact pressure.
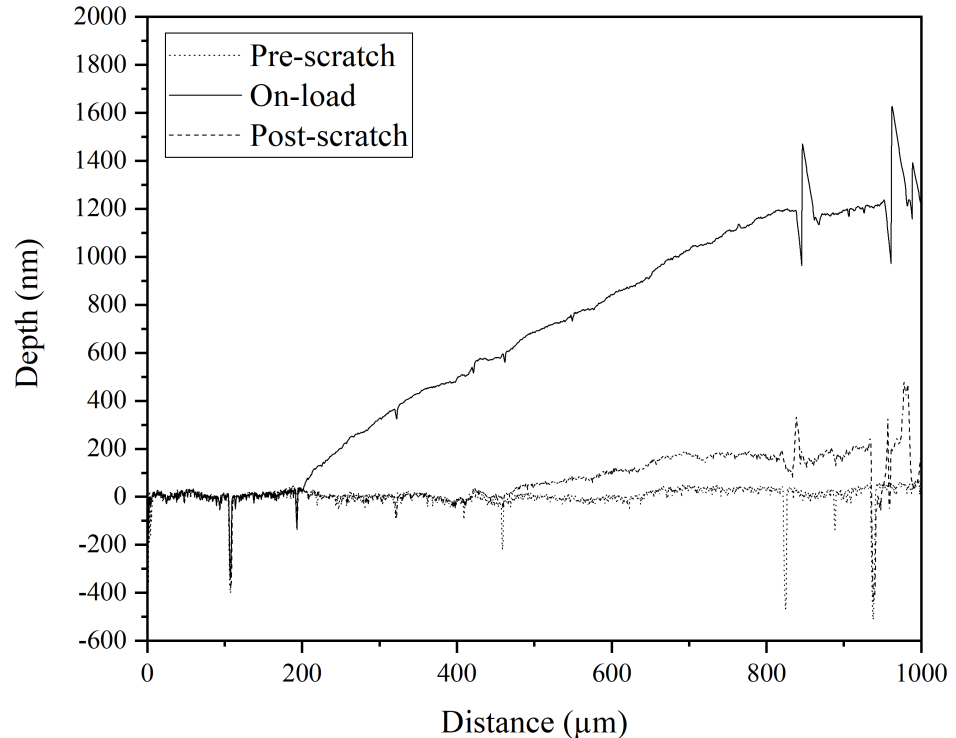
Figure 7.1: Pre- and post-scratch topographies along with the on-load scratch depth (uncorrected for instrument compliance, sample slope or topography) on HTS-Coating A-thin-smooth.

The difference in the corrected profile is seen in Figure 7.2. We can see that some features, such as the spike at approximately 100 μm distance, are much less dramatic once the topographic and instrument compliance corrections are added. The point at which the coating yields is also visible in the post-scratch topography scan at approximately 400 μm.
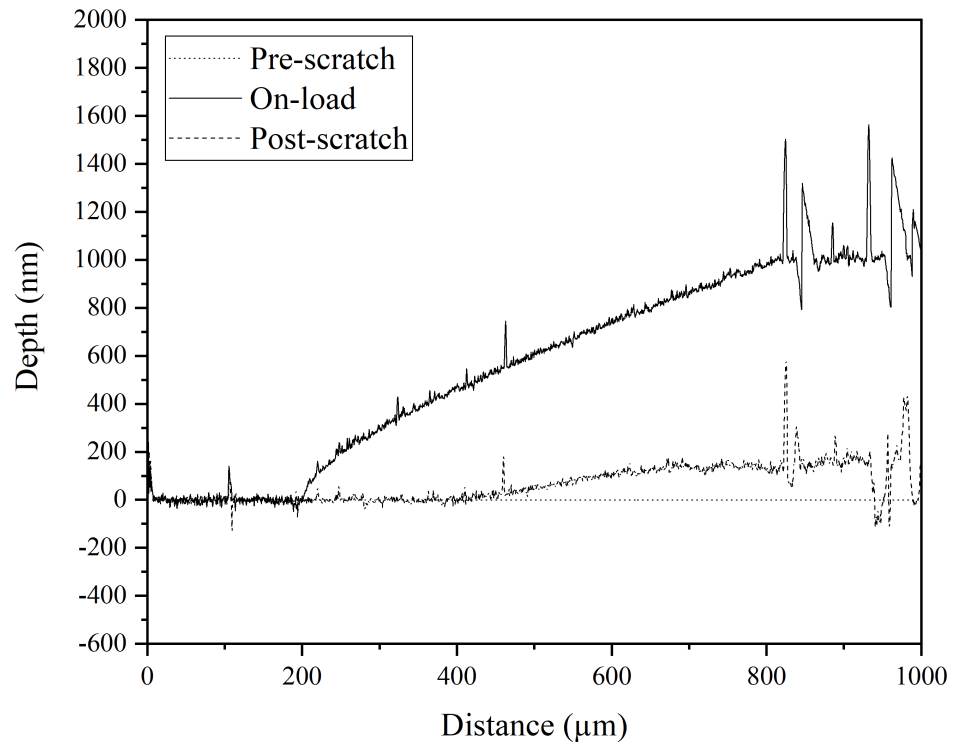
Figure 7.2: Pre- and post-scratch topographies along with the on-load scratch depth (with corrections) on HTS-Coating A-thin-smooth.

Figure 7.3 shows the COF change with applied load for each of the coatings on HTS. The friction sensor reached a software limit on Coating C after approximately 350 mN therefore the friction trace has been cut off as it appears to reduce in COF after this point. This could be caused by a calibration issue however the measured COF for each coating are similar to that measured by Beake et al. [282] on comparable DLC architectures.
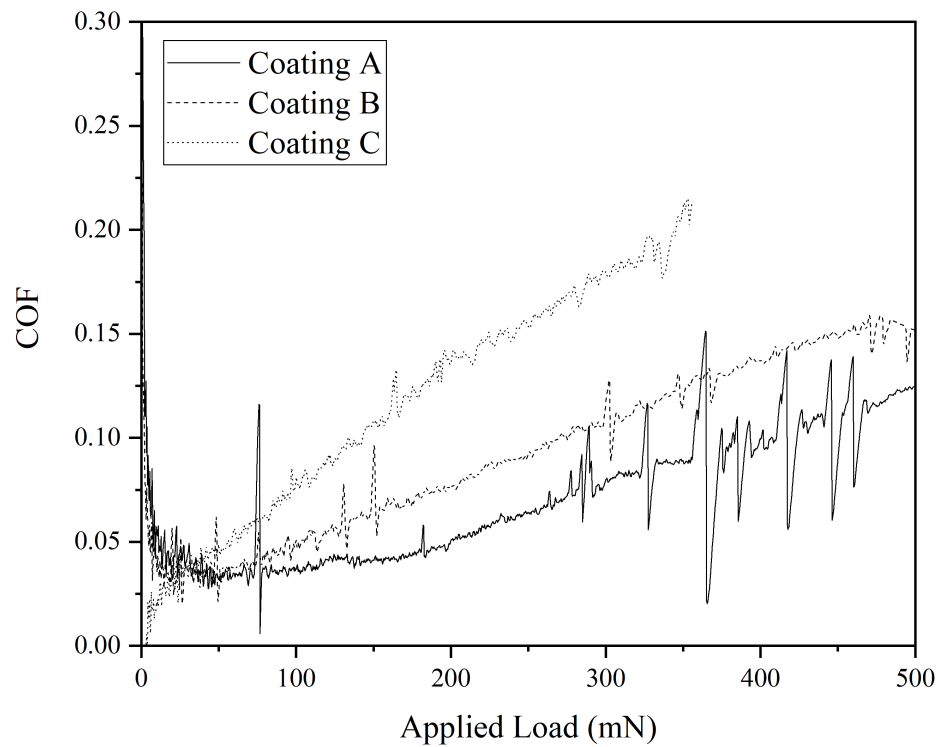
Figure 7.3: Friction coefficient against applied load for Coating A, B and C thin-smooth variants on HTS.

7.3 Results

7.3.1 Predicting the Ploughing Friction Component

Using Equation 2.45, the ideal ploughing friction components with each of the probe radii can be calculated. Figure 7.4 shows the results of these calculations with each of the probes showing a near zero ploughing contribution at zero depth. The ploughing contribution is seen to increase as each probe radius decreases. The ploughing component is seen to increase at a greater rate once the nominal radius of the probe is approached as with the 4.5 µm probe. This is due to the $(R - h)\sqrt{2Rh - h^2}$ component of Equation 2.45 decreasing rapidly past 2000 nm and the denominator plateauing as it approaches 4000 nm. This gives a limit of applicability for this equation. Modelling at higher contact depths must apply the considerations of Lafaye and Troyon [315] with transitions to conical contact.

168
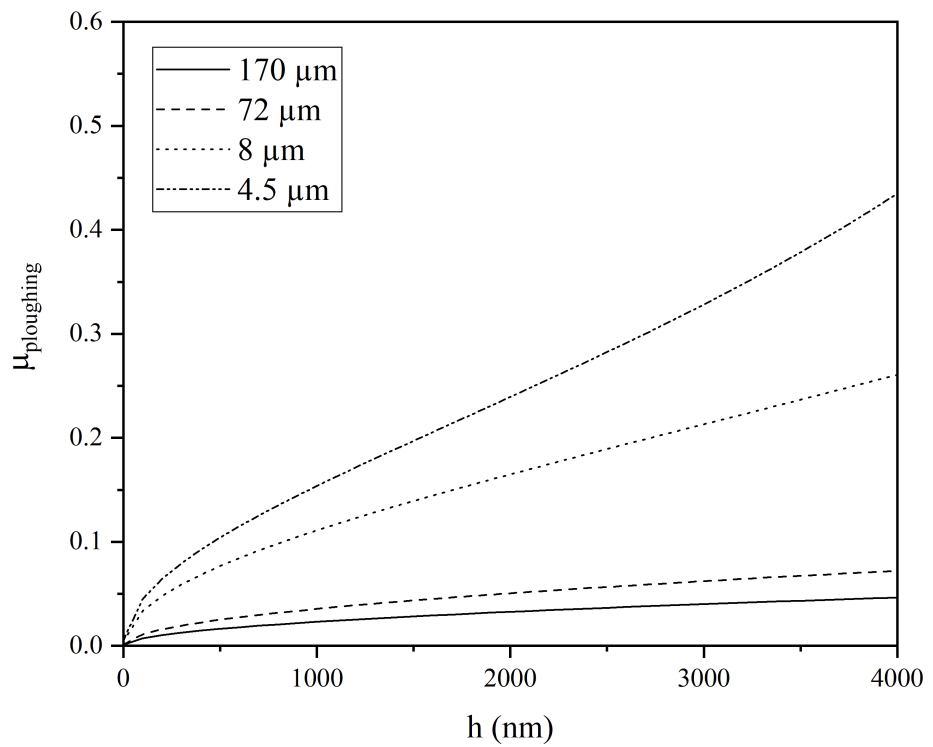
Figure 7.4: Calculated components of ploughing friction with varying probe radius.

7.3.2 Interfacial Friction Components

Table 7.2 shows the results of extrapolating the friction data to zero load on SS-Coating A-thin-smooth to estimate the interfacial friction component. The interfacial friction is seen to increase as the probe radius decreases with the largest value of 0.125 seen with the 4.5 μm probe. As the probe radius decreases the ploughing component of friction is seen to increase more dramatically with increasing depth.

Table 7.2: Estimated interfacial friction component of SS-Coating A-thin-smooth with varying probe radius.

Probe radius (μm)	$\mu_{interfacial}$
170	0.017 ± 0.003
72	0.029 ± 0.019
8	0.069 ± 0.042
4.5	0.125 ± 0.029

7.3.3 Surface Roughness

Table 7.3 [1] (located on page 181) shows the surface roughness measured during the first scan step of the scratch procedure. On the smoother prepared substrates, all coatings showed an increase in surface roughness compared to the substrate roughness. with the highest being seen on HTS-Coating B-thick. The most dramatic roughening in comparison to the substrate (26 nm R_a), however, was HTS-Coating A-thick-smooth with a value of 84 nm R_a. Many of the thicker coating variants saw roughness values double that of the thinner variant such as Coating B on both substrates. Coating C on both substrates displayed unusual behaviour with a decrease in roughness on SS and an increase in roughness on HTS.

7.3.4 Coating Adhesion

Table 7.4 (located on page 182) shows the critical loads and and calculated SCPR from the nano-scratch. The highest SCPR value was found on SS-Coating A-thin-smooth with a value of $0.049\,N^2$. The lowest was recorded with SS-Coating B-thin with a value of $0.025\,N^2$. Despite its thinner structure (compared to Coatings A and B) Coating C recorded relatively high SCPR values. We can note the benefit of increasing its thickness in the increase from $0.030\,N^2$ to $0.042\,N^2$ on SS. Some of the thicker produced coatings and those deposited on HTS were unable to show a critical load failure within this load range. For the thicker coatings, this is entirely normal and shows that higher contact pressures are required. This was noticed by Beake et al. [282] in nano-scratch testing of similar coating architectures. A switch to a 25 μm probe on the micro-loading stage (up to 5 N) was required in order to capture the full critical load performance due to its increased contact pressure at the interface as this is what controls film failure.

Figure 7.5 shows the various different failure modes seen with the different coating architectures tested under nano-scratch. SS-Coating A-thin-smooth is typified by Hertzian

---

[1]Please note that the tables in the following sections until Table 7.8 in Section 7.3.7 are displayed in landscape format for clarity and are therefore found at the end of the chapter.

cracking within the scratch track with some compressive spallation. Coating B instead sees some tensile cracking and compressive spallation. Both are brittle in their failure. Coating C displays ductile failure with some buckling. The lateral rigidity on this sample is lacking compared to the others tested. When the rougher variant of Coating A is tested much more pronounced spallation occurs. The thicker variant does not display a critical load failure [301]. The increase in roughness causing more extreme failure was noted by Weidner et al. [427] in their use of spherical nanoindentation on DLC coated soda-lime glass. The increase in roughness caused more severe ring and lateral cracking as well as increasing the severity of sub-interface damage. Extremely high roughness ($R_a > 500 \, \text{nm}$) was show to form cavities in the coating during deposition.
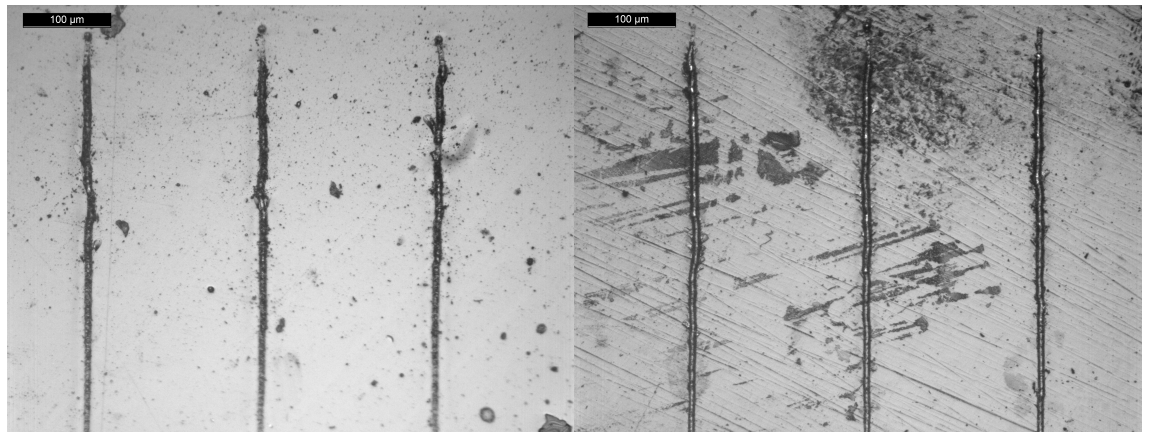
(a) SS-Coating A-thin-smooth.

(b) SS-Coating B-thin-smooth.
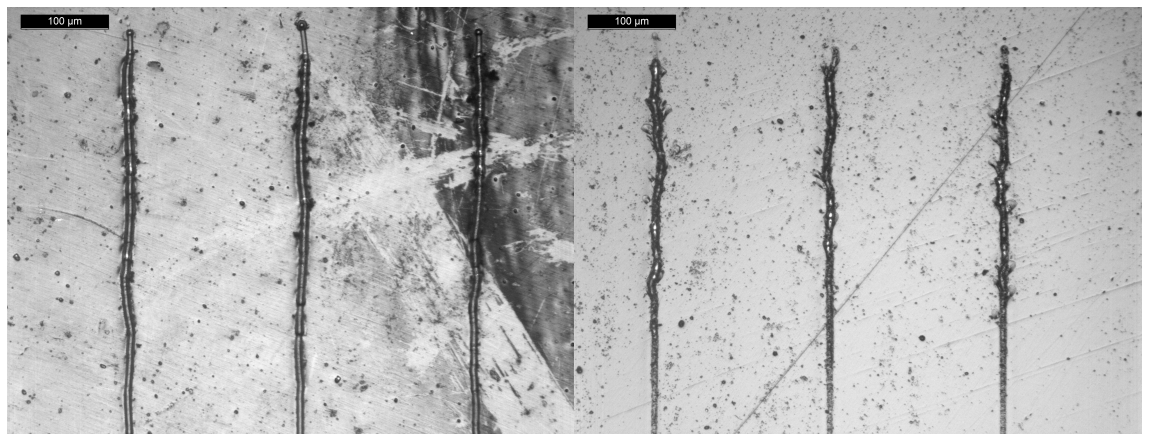
(c) SS-Coating C-thin-smooth.

(d) SS-Coating A-thin-rough.
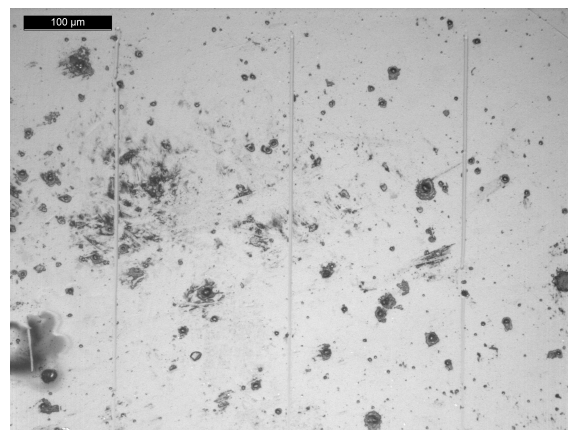
(e) SS-Coating C-thick-smooth.

Figure 7.5: Micrographs of the scratch morphology for various coating architectures. Images are captured approximately 555 μm into the scan therefore the load at the bottom of the image is approximately 280 mN.

The coatings deposited on HTS displayed the same failure morphologies however the critical loads were generally higher positioning these failure events further along the scratch.

7.3.5 Scratch Friction

Table 7.5 (located on page 183) shows the results of the maximum measured COF during the scratch pass. We can see that, on each substrate for the thin coating variant, Coating A displayed the lowest friction followed by B and C respectively. Increasing the coating thickness was seen to affect the COF for each coating differently. For Coating A, the friction decreased (as in SS-Coating A-thin-smooth) where the friction decreased from 0.213 to 0.098. For Coating B on HTS the friction increased from 0.157 to 0.161.

7.3.6 Contact Pressure, Contact Depth And Scratch Recovery

Analysis of the on-load depth and residual depth, once corrections for instrument compliance, slope and topography have been carried out, can be used to estimate the maximum Hertzian contact pressure, contact depth and scratch recovery. Scratch recovery (*SR*) is defined as [318]:

$$SR = \frac{h_t - h_r}{h_t} \qquad (7.1)$$

The parameters are defined in Section 2.5.7.2. Table 7.6 (located on page 184) shows the contact depth (h_p), contact pressure (*Pmean*) at yield and the scratch recovery at maximum applied load. For all variants, the yield is seen to occur in the upper regions of the coating. The increase in substrate roughness decreases the contact depth at yield for the thinner preparation of Coating A on SS and HTS. Increasing the coating thickness produces the opposite effect suggesting that increased roughness is detrimental to depth reached at yield. Increasing the coating thickness decreases the contact depth with the smooth preparation of Coating A on SS however the opposite is true for HTS. Coating B reaches a lower contact depth on SS with increased coating thickness seeming to be detrimental though there is a large error associated with SS-Coating B-thin (requiring more repeats to provide statistical significance). Coating B on HTS shows increased contact depth with increased DLC thickness mirroring the behaviour of Coating A. Coating C displays lower contact depth on average with approximate h_p values of 194 nm and 136 nm for SS and HTS respectively on the thinner coating preparation. Increasing the coating thickness results in increased contact depth at yield for both substrates. The contact pressures at yield are generally within the same range as that seen previously by Beake et al. [282] on similar coatings however increasing the DLC thickness caused the contact pressure at load to increase. Rougher coatings generally display a higher contact pressure at yield also. SS-Coating C-thin has an anomalously small contact pressure, using the constraint factor for DLC of Chudoba et al. [47] and using the hardness relation of Equation 2.2, it would be expected to be approximately 10.2 GPa. As this still falls short of the measured surface hardness the constraint factor must therefore be different. These values have been be calculated for each of the coatings.

Scratch recovery is generally in the range of 60–70 % on Coatings A and B on both substrates. Coating C displays reduced scratch recovery across both substrates which is in line with its more ductile properties.

By applying $P_{mean} \approx 1.1Y$ for the onset of plasticity (as discussed in Section 2.1) expected to occur at a depth of $\approx 0.47a$ [46, 166, 282], the yield pressures can be calculated. The relation to hardness can therefore be calculated (H/Y) to analyse the constraint factor for each coating. The relation between the yield and elastic modulus (Y/E) can also be calculated. Liskiewicz et al. [428] showed that this parameter correlated to favourable

wear resistance, particularly under nano-fretting wear. Table 7.7 shows the results of these parameters. Generally the highest yield stresses are seen on coating A on both substrates though the thin variant on SS has lower values of 12.34 GPa and 13.77 GPa for the smooth and rough variants respectively. The highest yield stress is seen on HTS-Coating A-thin-smooth with a value of 22.33 GPa. Apart from the small Y seen with SS-Coating C-thin (due to its small mean contact pressure), the range of values for Coatings B and C are generally similar. Due to the approximate relation between the contact pressure and Y, the same patterns are seen with each of the quantities. H/Y values are higher on SS generally. Overall, Y/E is higher across the HTS coatings with the highest value of 0.112 occurring on HTS-Coating A-thin-smooth.

7.3.7 Repetitive Multi-Pass Scratch

The results of the multi-pass increasing load scratch are shown in Table 7.8. The roughness in seen to increase with successive cycles from the unworn value of 22.2 nm as seen in Table 7.3 to 79.8 nm after 10 passes. The coefficient of friction also increased with each pass up to a maximum of 0.134. The contact pressure decreased with each pass reaching a final value of 9.74 GPa. The scratch recovery was nearly constant with a value of 62 % however this dramatically increased in the final cycle to 77 %. From analysis of the residual depth profile, this is likely due to the entrapment of wear debris within the track causing the residual depth to appear lower than it would otherwise.

Table 7.8: Evolution of surface roughness, COF, contact depth, contact pressure and scratch recovery with repetitive scratch cycles.

Scratch cycle	R_a (nm)	COF	h_p (nm)	P_m (GPa)	% Scratch Recovery
1	48.1 ± 15.4	0.075 ± 0.005	372.49 ± 106.20	15.84 ± 4.32	62.47 ± 22.92
5	54.5 ± 0.7	0.090 ± 0.017	557.56 ± 102.42	10.37 ± 1.52	62.74 ± 12.64
10	79.8 ± 27.4	0.134 ± 0.028	619.01 ± 191.98	9.74 ± 2.14	77.67 ± 6.50

Figure 7.6 shows the effect of multiple sub-critical load scratches on the SS-Coating A-thin-smooth. Though an individual scratch doesn't achieve the loading necessary to induce a critical load failure, multiple passes will induce failure and generate a large amount of wear debris. Analysis of the track depths for failure criteria reveals that a single cycle doesn't induce a dramatic failure event, the debris is ejected over multiple passes during the scratch test.
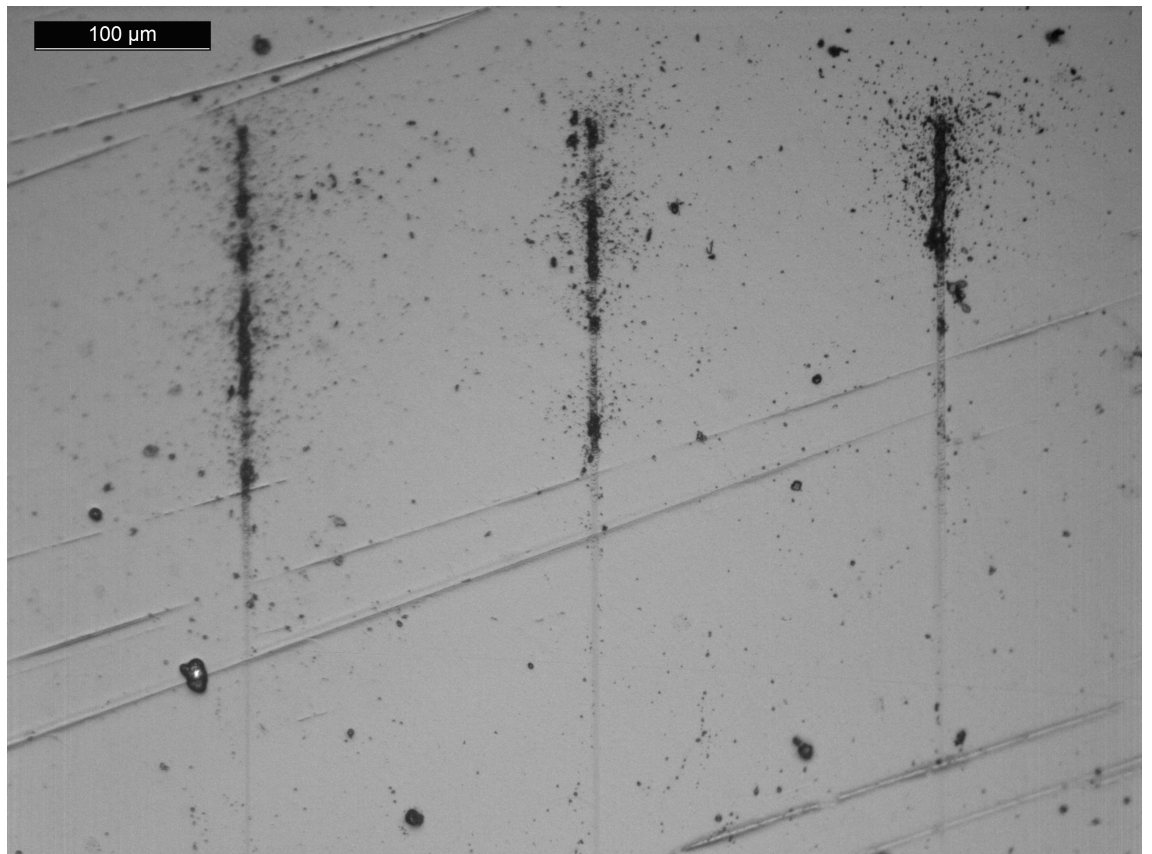
Figure 7.6: Micrograph of 3 tracks each with 10 scratch passes on SS-Coating A-thin-smooth. The micrograph is captured at approximately the same location as in Figure 7.5.

7.4 Discussion

7.4.1 Determination of Interfacial Friction

As shown in Table 7.2, an inverse correlation is seen between the probe radius and interfacial coefficient of friction. This at first seems counter-intuitive as we would expect a larger probe to have a greater interfacial interaction; however there is a difference between the expected area of contact and real area of contact that is normally seen in different length scales but is apparent here with different probe sizes [68]. The 170 μm probe is clearly far from a single asperity contact, this is even seen with smaller AFM probes wherein the fractal nature of surfaces gives rise to multi-asperity interactions [422]. Gao et al. [421] noted that the work of adhesion was larger with smaller tip radii in AFM studies of the atomic scale friction of diamond. This correlates to more interfacial interactions occurring requiring more energy to remove the probe from the surface. Thus resulting in a larger real contact area producing higher interfacial friction. Beake et al. stated [312] that a 5 μm probe was an effective choice particularly for affecting film failure, these results also show that it also is more similar to a true single asperity interactions and superior for measuring interfacial friction.

Interfacial/adhesive friction determination was performed by Ronkainen [429] with successive scratches with a 200 μm radius probe at 5 N and 10 N. At 5 N, the component of adhesion was approximately 0.045 and increased to 0.049 at 10 N thereby showing that

175

the component has some sensitively to the load employed. Though the primary shape of indenter is sphero-conical, Zhang et al. [415] employed a Berkovich indenter alongside a spherical indenter to assess the differences in determining the ploughing and interfacial components of friction on silicon carbide ceramic. They found that the ploughing component had a more significant role when using a sharp Berkovich tip and that for a spherical indenter the two components (ploughing and interfacial) are extremely similar a low contact depth. This is seen in the model present in Figure 7.4. Any fluctuation in the friction coefficient results from the material composition. In the case of the SiC with Zhang's work [415], the pores lead to a collapse in the cutting process.

7.4.2 Coating Roughness

As noted in Table 3.3, a plasma surface etching step is employed in the deposition of all the coatings therefore we expect that there will be some increase in the coating roughness due to this. Peng et al. [349] noted that the ion impingement energy affects the roughness. If the impinging ion energy is below a critical level for atomic displacement, the ions will instead remain in the surface layers generating thermal spikes and promoting surface diffusion. This leads to ordered sp^2 rich clusters and raising the roughness. Inversely, the ions will penetrate the surface, reducing diffusion leading to higher density structures with lower sp^2 content, increased compressive stresses and smoother surfaces. This effect may explain some of the surface roughening of the as-deposited coatings. Borodich et al. [430] noted that DLC films produced by pulsed DC magnetron sputtering are smooth at the micrometre scale due to the ion energies leading to flatter surfaces and compact morphologies. Ali et al. [431] found that for RF plasma glow discharge deposition, DLC roughness was controlled by electrode position in the chamber.

7.4.3 Coating Adhesion and Scratch Resistance

Adhesion has been determined on two length scales, the macro scale (as shown in Table 4.3) and in this Chapter, the nano-scale as seen in Table 7.4. Despite the critical loads for some coatings being unmeasurable within the 500 mN loading range, the data available tells us plenty regarding the adhesion and scratch resistance. Adhesion on the nano-scale is broadly similar to that on the macro-scale noted in Chapter 4. Though yielding at a lesser load due to its reduced hardness, Coating C is seen to be very scratch resistant with higher critical load values [282, 372–374]. The reduced thickness will also affect it but analysis of its failure mechanisms in Figure 7.5 show a more ductile response indicating that the coating can deform beneficially to stop more extreme cracking occurring as seen on the two harder coatings. This was also noted by Beake et al. [282] on a similar tungsten doped DLC.

The lack of critical load failure on the thickest of the coatings shows that the location of critical yield stress within the coating structure is not at a point where decohesion or cracking will occur. Moving to a micro-scratch test could remedy this allowing the full critical load failures to be captured [282]. A sharper probe could also be used but these tend to be more sensitive to blunting and this could inhibit the application of Hertzian analysis for other testing.

7.4.4 Friction

Friction results (Table 7.5) can be seen to correspond to the coating's H/E and H^3/E^2 ratios as seen in Table 4.2. This corresponds to the strain to break and plastic deformation respectively [321, 322]. Additionally, we can note that for the coatings with higher H/E and H^3/E^2, the ploughing component is expected to decrease [332]. Though the interfacial component of friction will be different with each of the coatings due their composition varying, there will be less variance than with an entirely different coating family. Therefore the friction can be explained by a combination of the H/E ratio and contact depth (Table 7.6) as this will affect the ploughing component.

Dyrda and Sayer [316] performed larger scale scratch testing on TiN on M2 tool steel. One of the aspects of their work of interest to this study is the analysis of the coefficient of friction with respect to the depth and critical load failure. They found that a change in the gradient of friction coefficient with increasing load can indicate a critical load failure. Inspection of the gradients of Figure 7.3 shows that the coatings were not completely delaminated by this nano-scratch testing. Additionally, it was noted that spikes in the friction during scratch can indicate particularly large asperities. Irregularities in the friction signal can indicate the breakdown (significant cracking) of coating.

7.4.5 Contact Pressure and Yield

The contact pressures at yield calculated in Table 7.6 shows values that are within the same range and show roughly the same trends as those seen by Beake et al. [282] on similar DLCs when compared to the thinner coatings in this study. Previous modelling has shown that increasing the film thickness requires a higher contact pressure (and consequently higher stresses) in order to deform the contact and cause it to yield at the onset of plasticity [53, 406]. The results of this study support this and additionally have shown that, in general, yield pressure is measured to be higher with higher surface roughness.

Plastic deformation is generally expected to occur when $P_{mean} \approx 1.1\sigma_y$ however at higher loads (with more developed plasticity), P_{mean} is related to the constraint factor (H/Y), which is dependent upon the material properties [45, 47, 48, 282]. Chudoba et al. [47] found that, for a 2.1 µm DLC, this constraint factor $(H/\sigma_{M,crit})$[1] was 1.57. For SS-Coating A-thin-smooth, the same value of H/Y was found. Thicker coatings and those on HTS have a lower value (in some cases unity or lower) indicative of yield occurring at a different point in the coating structure; stress modelling is required to fully explore this. The von Mises stress modelling presented in Section 9.3.3 (later in this Thesis) assumes a H/Y value of 1.2 which is congruous with the thicker coatings on HTS due to their similarity in coating thickness. The contact yield pressures are seen to be higher on the HTS coatings suggesting that the improved mechanical properties of this substrate gives additional load support as also seen in Chapters 4 and 6. This further supports the conclusions of Meneve et al. [198] in that the substrate properties can be tailored to avoid catastrophic failure. The application of multilayer coatings is another method of altering the critical stresses in coatings requiring higher stresses to cause yield [83, 231]. Multilayer coatings also reduce the internal stress of coating architectures which is beneficial to adhesion [229].

The calculation of contact pressure is only applicable up to yield in coatings as the Hertzian analysis utilised assumes elastic contact and is therefore not applicable once

---

[1] $\sigma_{M,crit}$ is the maximum von Mises stress which is equivalent to the yield stress (Y) in this case.

plasticity has been induced. This is particularly seen in more ductile coatings such as HTS-Coating C-thick where the the contact pressure on the sample surface at maximum load was predicted to be 50 GPa which is clearly not a reasonable value. The high contact depths otherwise resulting in the lowered scratch recovery (due to its more ductile nature) contributes to this high contact pressure estimation beyond the yield point.

The further calculation of yield stress as seen in Table 7.7, allows extremes of the coating's wear performance to be analysed. In addition to scratch testing, yield stress can also be determined by nanoindentation experiments. Several authors have analysed the relation between H/E and Y/E and have analysed the relation between Y/E and the constraint factor and elastic work with respect to the work hardening of the material. Higher values of Y/E tend to have a lower constraint factor and also a higher proportion of elastic work [432, 433]. Haq and co-workers analysed the yield of DLCs on Si substrates and noted that the geometry of the indenter has a greater effect than the thickness of the coating. Analysis by TEM showed that with a 5 μm radius spherical indenter the localised compressive plastic strain was relatively low (4 %) [434–437]. Scratch testing with a larger indenter would reduce this further and, with a larger load range, allow all the critical load behaviours to be captured. Schwarzer et al. [438] proposed that the failure of coating systems under spherical indenters proceeds as follows:

1. Initial plastic flow occurs within the material wherever the critical von Mises stress (yield strength) is exceeded. This failure cannot be detected by the test equipment or microscope as there is no severe visible or otherwise detectable macroscopic damage.

2. With increasing load, the plastic zone grows until it reaches the interface region between the substrate and first coating layer. This weakens the integrity of the coating system.

3. If there is additional sufficiently high tensile stresses at the surface that coincide with the weakening due to plastic flow at the first interface, mode-I fractures could propagate to this interface. This causes the system to fail globally due to shearing off of large coating areas (corresponding to a L_C failure).

Surface roughness is seen to have a minimal effect on the on contact pressure at yield and consequently Y values however coating thickness and coating structure gives a large variance in the values. Generally, Coating A is seen have the highest Y followed by B and C respectively. Conversion of H/E into Y/E shows the same trends while also highlighting the higher values of Y/E seen on HTS. The additional load support of this substrate material has been noted throughout this thesis and this wear parameter could serve in addition to H/E though taking into account the load support of the substrate. Its previous use by Liskiewicz [428] et al. for nano-fretting wear, integrating modelling, support its efficacy for this use.

The results gained in this chapter could be applied to further improve the integration of mechanical testing with predictive wear modules [47, 200, 428] particularly the integration of the Micro Materials NanoTest and SIO Film Doctor software packages as results importing is possible. The depths reached in the scratch test, mechanical properties and calculated yield stresses are fed into the SIO software. This allows for more detailed modelling in Film Doctor.

Four conditions are generally required to apply this type of Hertzian analysis, those being: (i) the tangential load not influencing the pressure distribution too greatly so the COF is well below 0.3, (ii) the radius of the indenter is constant, (iii) the sliding speed

is sufficiently slow and the contact close to elastic so that the load is supported on the rear of the indenter and (iv) the indenter can reach the bottom of the scratch track in the final topographic scan [312]. In evaluating the test specifications with respect to Beake's [439] previous Hertzian analysis we can say that the tangential load does not influence the pressure distribution to great degree. As the $4.5\,\mu m$ probe was new, it is unlikely that the radius of the probe changed to a large degree throughout testing, there were no indications in the results to support this as the calculated yield results are within a sensible range. The depths measured by the scratch test indicate the indenter could reach the bottom of the track. However, the sliding speed of $10\,\mu m\,s^{-1}$ is much faster than the $2\,\mu m\,s^{-1}$ originally applied by Beake et al. [439] therefore this may have had some affect on the results as the load would be not be entirely supported on the rear of the indenter. Repeated testing at a lower sliding speed would be required to fully investigate this as no results were observed to be adversely affected by the higher speed.

7.4.6 Effect of Sub-Critical Load Passes

The results of the multi-pass scratches as seen in Table 7.8 differ from those seen in nano-wear tests performed by Beake et al. [312, 318] though these were constant load tests employing the nano-fretting module. However, we would still expect decreasing resistance to cracking with repeated passes due to gradual failing of the coating structure. On 316L stainless steel, the scratch recovery was seen to decrease over the course of 10 wear cycles from 27 % to 14 % and the mean pressure decreased from 4 GPa to 2 GPa. Constant load subs-critical load passes on TiN on M42 steel showed an increase in the on-load probe depth with wear cycles [424]. The friction coefficient was also seen to increase after 1 cycle at 100 mN load before decreasing. At a higher load of 300 mN, the friction coefficient decreased from 0.14 to 0.09 over the wear cycles [424]. In similar testing on thin carbon films Shi et al. [440] found that the scratch recovery decreased with increasing load cycles. In repetitive scratch tests on WC/Co metals, Gee and Nimishakavi found [441] the scratch track increased in area with successive passes thereby decreasing the contact pressure. The generated debris seen in Figure 7.6 may have affected the scratch recovery by their build up in the track giving the unexpected response.

The difference could be attributed to the entirely different dynamics of applying an increasing load scratch as opposed to maintaining the same load in the fretting regime (in addition to smaller amplitudes and higher probe speeds). Ronkainen et al. [429] performed multi-pass tests with a $200\,\mu m$ radius tip and 5 N and 10 N and found that the coefficient decreased with successive cycles likely due to the reduction of the ploughing component and increased track area. Wei et al. [442] performed multi-pass micro-scratches on austenitic steel and found that penetration depth and residual depth increased monotonously with each pass but coefficient of friction decreases monotonously with each pass.

7.5 Summary

In this study, nano-scratch testing was performed using a range of probe radii to analyse the interfacial and ploughing components of friction of one DLC coating with the same roughness thickness and substrate maintained throughout. Following the analysis of the interfacial friction components, the matrix of DLC coatings above was tested to anal-

yse the effects of changing the substrate, surface roughness, coating thickness and DLC recipe. Sub-critical load scratches were also performed to investigate their affect on the contact pressure, surface roughness and cracking phenomena with successive scratches.

By extrapolating the low load friction data in an increasing load scratch with different probe radii, it was shown that as probe radius decreases the interfacial component of friction increases as increased real contact is made with the asperities. The topography scanning step found that the roughness of the coatings increased for all coating preparations. Increasing the thickness of the coating generally increased the top layer roughness. This was presumed to be due to the energetics of sustained ion bombardment during longer depositions processes. The reduced hardness of Coating C resulted in it yielding at lower load than Coatings A and B however it does display excellent adhesion compared to the other coatings. The failure characteristics of Coating C are more ductile in nature than Coatings A and B. Some coatings could not have their SCPR determined as the second critical load was beyond the loads range achievable in the nano-scratch. Moving to the micro-scratch would remedy this for future testing. HTS saw fewer critical load failures once again indicating its increased load support compared to SS. COF under scratch loading related to the coatings' H/E and H^3/E^2 ratios and contact depth with Coating A seeing the lowest friction. Contact pressure at yield was seen to be within the range of previous testing by Beake et al. [282] also following similar trends (Coating A having the highest yield followed by B and C respectively) and is in good agreement with the relation to the coating hardness. Increasing the film thickness and surface roughness caused the measured yield contact pressure to increase. Though a smaller effect is seen with surface roughness. Contact pressure at yield can be converted to yield stress which allows the extremes of the coating's wear performance to be analysed. The constraint factor (H/Y) of SS-Coating A-thin-smooth was found to be same as that determined by Chudoba et al. [47] for DLC. Thicker coatings and those on HTS, have lower H/Y values. Y/E values can also be calculated which has been seen to relate to wear resistance in nano-fretting [428]. In this application, Y/E was seen to be sensitive to substrate load support which shows it may be a tribological metric that could be used to assess the complete coating system. Sub-critical load passes caused roughening of the track, this combined with the increased contact depth with successive scratches increased the COF with each pass. Contact pressure was seen to decrease with track deformation. Scratch recovery remained relatively constant though the formation of wear debris caused an apparent increase in recovery in later cycles.

Future studies analysing the adhesive component of friction could integrate AFM studies into the experimental methods as this allows for easier measurement of the work of adhesion and extrapolation to zero load friction due to the lower forces used. This is typically performed in AFM studies such as that performed by Gao et al. [421]. Further tests could also assess the other two methods of determining interfacial friction proposed by Beake et al. [312], those being constant load friction tests at extremely low load with an elastic contact and zero ploughing and repetitive scratches to eliminate the ploughing contribution.

Table 7.3: Surface roughness of the coating architectures measured in the initial scan step of the scratch procedure.

Substrate	DLC Recipe	DLC Coating Thickness (μm)	Substrate Roughness (μm R_a)	R_a (nm)
		1.60±0.17	0.026±0.004	22.2±9.4
	A	1.62±0.18	0.0860±0.0004	47.1±10.2
		5.18±0.07	0.026±0.004	20.3±5.1
SS		5.54±0.02	0.0860±0.0004	49.6±4.5
	B	1.16±0.24	0.026±0.004	25.7±1.5
		2.88±0.17	0.026±0.004	49.2±9.7
	C	1.10±0.22	0.026±0.004	40.5±8.0
		2.25±0.12	0.026±0.004	31.7±13.7
		2.20±0.20	0.026±0.004	26.0±10.3
	A	2.02±0.15	0.0860±0.0004	44.7±8.5
		3.82±0.09	0.026±0.004	84.0±32.7
HTS		4.47±0.24	0.0860±0.0004	82.9±19.5
	B	2.17±0.16	0.026±0.004	48.0±12.4
		4.93±0.17	0.026±0.004	96.8±15.1
	C	1.17±0.12	0.026±0.004	26.2±1.9
		2.99±0.55	0.026±0.004	39.2±23.1

Table 7.4: Yield, critical loads and SCPR for the coatings determined by nano-scratch testing. Blank entries for the critical load indicate that the load could not be reached within the load range.

Substrate	DLC Recipe	DLC Coating Thickness (μm)	Surface Roughness (nm R_a)	L_y (mN)	L_{C1} (mN)	L_{C2} (mN)	SCPR (N^2)
SS	A	1.60±0.17	22.2±9.4	127.14±20.22	176.70±4.73	453.05±4.25	0.049±0.001
		1.62±0.18	47.1±10.2	108.97±10.27	208.87±10.66	410.92±21.67	0.042±0.005
		5.18±0.07	20.3±5.1	203.37±142.64	–	–	–
		5.54±0.02	49.6±4.5	205.98±59.07	–	–	–
	B	1.16±0.24	25.7±1.5	94.87±39.14	169.40±30.61	318.09±33.77	0.025±0.006
		2.88±0.17	49.2±9.7	92.54±29.20	339.94±30.00	–	–
	C	1.10±0.22	40.5±8.0	35.88±7.82	215.90±51.48	356.37±31.50	0.030±0.005
		2.25±0.12	31.7±13.7	82.67±12.34	321.06±43.17	451.48±20.22	0.042±0.010
HTS	A	2.20±0.20	26.0±10.3	200.45±16.22	339.53±83.89	–	–
		2.02±0.15	44.7±8.5	142.66±42.77	238.75±56.22	–	–
		3.82±0.09	84.0±32.7	192.72±52.90	391.20±98.19	–	–
		4.47±0.24	82.9±19.5	268.57±53.10	–	–	–
	B	2.17±0.16	48.0±12.4	165.96±23.83	332.21±33.65	–	–
		4.93±0.17	96.8±15.1	217.47±36.13	443.36±14.28	–	–
	C	1.17±0.12	26.2±1.9	52.23±9.01	261.71±43.12	408.65±53.15	0.038±0.009
		2.99±0.55	39.2±23.1	116.05±25.87	355.69±26.97	–	–

Table 7.5: Maximum COF measured under scratch load for each coating architecture.

Substrate	DLC Recipe	DLC Coating Thickness (μm)	Surface Roughness (nm R_a)	Max COF
		1.60±0.17	22.2±9.4	0.213±0.005
	A	1.62±0.18	47.1±10.2	0.218±0.002
		5.18±0.07	20.3±5.1	0.098±0.002
		5.54±0.02	49.6±4.5	0.097±0.002
SS		1.16±0.24	25.7±1.5	0.258±0.004
	B	2.88±0.17	49.2±9.7	0.180±0.003
		1.10±0.22	40.5±8.0	0.279±0.008
	C	2.25±0.12	31.7±13.7	0.209±0.002
		2.20±0.20	26.0±10.3	0.128±0.003
	A	2.02±0.15	44.7±8.5	0.137±0.002
		3.82±0.09	84.0±32.7	0.103±0.003
		4.47±0.24	82.9±19.5	0.108±0.003
HTS		2.17±0.16	48.0±12.4	0.157±0.002
	B	4.93±0.17	96.8±15.1	0.161±0.003
		1.17±0.12	26.2±1.9	0.208±0.004
	C	2.99±0.55	39.2±23.1	0.207±0.002

Table 7.6: Contact depth (h_p) and contact pressure (P_{mean}) at yield. Scratch recovery is calculated at maximum load.

Substrate	DLC Recipe	DLC Coating Thickness (μm)	Surface Roughness (nm R_a)	h_p (nm)	P_{mean} (GPa)	% Scratch Recovery
	A	1.60±0.17	22.2±9.4	343.24±23.73	13.58±1.43	72.72±15.35
		1.62±0.18	47.1±10.2	269.35±60.58	15.15±2.41	46.76±5.78
		5.18±0.07	20.3±5.1	314.80±165.51	21.21±7.27	76.13±7.06
SS		5.54±0.02	49.6±4.5	333.37±98.17	22.92±3.03	76.05±15.75
	B	1.16±0.24	25.7±1.5	302.90±179.13	11.05±1.17	76.62±12.57
		2.88±0.17	49.2±9.7	240.70±53.33	13.83±1.87	76.15±13.14
	C	1.10±0.22	40.5±8.0	194.60±72.95	6.98±1.07	59.06±16.80
		2.25±0.12	31.7±13.7	212.00±36.73	14.34±2.37	47.55±15.55
	A	2.20±0.20	26.0±10.3	299.52±21.72	24.54±1.96	67.67±9.59
		2.02±0.15	44.7±8.5	235.91±45.89	21.63±3.03	51.33±9.49
		3.82±0.09	84.0±32.7	347.77±73.15	20.99±6.36	72.13±17.30
HTS		4.47±0.24	82.9±19.5	428.26±51.58	23.48±5.00	72.30±21.68
	B	2.17±0.16	48.0±12.4	352.18±37.46	17.52±3.36	71.85±6.89
		4.93±0.17	96.8±15.1	533.52±45.42	15.26±1.26	65.21±10.55
	C	1.17±0.12	26.2±1.9	136.49±20.79	13.75±0.90	44.11±14.26
		2.99±0.55	39.2±23.1	255.96±38.74	16.55±3.30	48.41±27.81

Table 7.7: Calculated yield stress (Y), ratio of hardness to yield (H/Y) and ratio of yield to elastic modulus (Y/E).

Substrate	DLC Recipe	DLC Coating Thickness (μm)	Surface Roughness (nm R_a)	Y (GPa)	H/Y	Y/E
SS	A	1.60±0.17	22.2±9.4	12.34±1.30	1.57±0.17	0.057±0.006
		1.62±0.18	47.1±10.2	13.77±2.19	1.63±0.26	0.066±0.010
		5.18±0.07	20.3±5.1	19.29±6.61	1.25±0.43	0.088±0.030
		5.54±0.02	49.6±4.5	20.84±2.76	1.26±0.17	0.082±0.011
	B	1.16±0.24	25.7±1.5	10.04±1.06	1.82±0.19	0.054±0.006
		2.88±0.17	49.2±9.7	12.57±1.70	1.19±0.16	0.088±0.012
	C	1.10±0.22	40.5±8.0	6.35±0.98	2.55±0.39	0.027±0.004
		2.25±0.12	31.7±13.7	13.04±2.16	1.30±0.21	0.062±0.010
HTS	A	2.20±0.20	26.0±10.3	22.31±1.78	0.91±0.07	0.112±0.009
		2.02±0.15	44.7±8.5	19.67±2.76	0.99±0.14	0.103±0.014
		3.82±0.09	84.0±32.7	19.08±5.78	1.13±0.34	0.093±0.028
		4.47±0.24	82.9±19.5	21.35±4.54	1.19±0.25	0.094±0.020
	B	2.17±0.16	48.0±12.4	15.93±3.05	0.82±0.16	0.097±0.019
		4.93±0.17	96.8±15.1	13.88±1.15	0.91±0.08	0.108±0.009
	C	1.17±0.12	26.2±1.9	12.50±0.82	1.11±0.07	0.057±0.004
		2.99±0.55	39.2±23.1	15.05±3.00	0.88±0.18	0.082±0.016

Chapter 8

Multi-scale Fretting Testing of DLC Coatings

8.1 Introduction

The relation between H/E ratio and frictional performance is well understood across length scales in full sliding reciprocating wear tests and pin-on-disk (POD) [321, 322, 331, 332] tests however little research has been performed to assess this relation in the fretting regime, specifically in the gross slip fretting regime where it is a step below reciprocating sliding with the additional contribution of surface fatigue. The addition of lubricants to fretting tests is also rarely studied [108]. Furthermore, there has been little research to investigate applying the same contact pressure and fretting regime across length scales, in this case, adapting the same approximate sliding ratio and maximum Hertzian contact pressure from the micro-scale to the nano-scale. Though it is clear that, at the nano-scale, the surface roughness of the material will play a key role in determining the frictional dynamics [443, 444], the effect of multi-asperity to single asperity interactions can be properly assessed. The assessment of lubricated fretting performance will be useful in optimising oils for electric vehicle power trains and bearings which are required to be more complex than their petrol or diesel fuelled counterparts [31]. Little research has been carried out recently using the nano-fretting module with some of the last publications utilising it between 2010 and 2013 [146, 149, 318]. The testing as part of this work project will allow for its capabilities to be assessed and recommendations made for future developments of the module.

In this study, an electro-dynamic shaker fretting tester was used to assess the fretting performance of a series of DLC coatings at high contact pressures in dry and lubricated conditions. The lubricants were a base oil (a Group III mineral oil designated Yubase 4) and a fully formulated oil (Yubase 4 with an additional additive pack), with and without MoDTC. A piezo-driven nano-scale fretting tester (a modular component of the Micro Materials NanoTest Platform) [146] was used to measure the coefficient of friction evolution over the same number of cycles and the same nominal contact pressure as the micro-scale test to investigate the affect of surface roughness and length-scale in the interaction. A smaller probe was also utilised to cross-check the sensor readings and the effect of yet more extreme contact pressure. The results in this chapter will be published at a later date [445].

8.2 Methods

8.2.1 Micro-fretting

Micro-fretting tests [1] were performed with a bespoke electrodynamic shaker driven fretting rig as seen in Figure 8.1. The system is controlled with a bespoke LabVIEW program. The normal load is manually placed on the arm (at W). Tangential force during testing is monitored with a load cell. The optical displacement sensor adjusts the displacement of the electrodynamic shaker via a feedback loop to maintain it within the parameters specified. All micro-fretting tests were performed in laboratory conditions with a temperature of 22 °C and a humidity of 34 %.
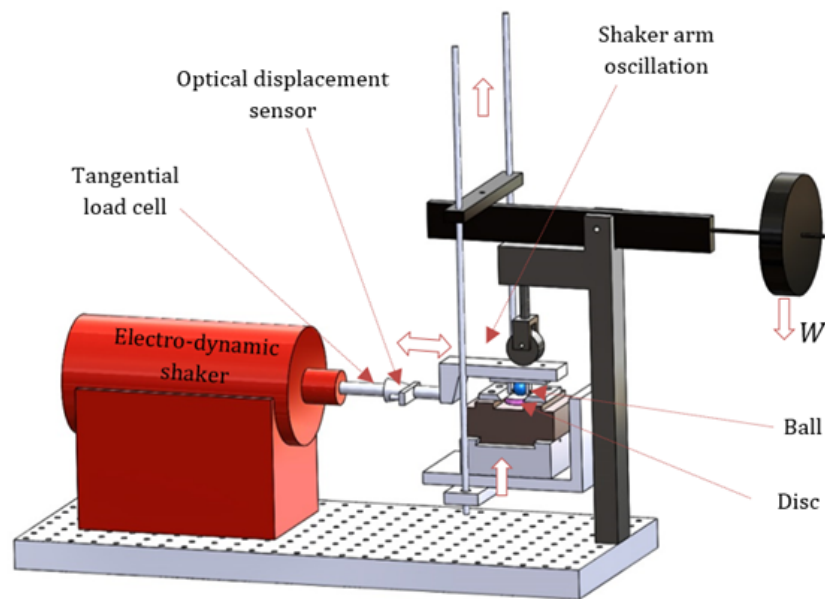
Figure 8.1: 3D schematic of the micro-fretting experimental set up. From [106].

The counterfaces for the testing was 10 mm diameter 52100 steel balls (chosen because the lubricant is designed for ferrous materials). Testing was performed in dry conditions and with various formulations of the lubricants:

- Base oil (BO): Yubase 4 without any additives.

- Base oil (BO) + MoDTC: Yubase 4 with the addition of a friction modifier (MoDTC).

- Fully formulated oil (FFO): Yubase 4 with an additional additive package and viscosity modifier.

- Fully formulated oil (FFO) + MoDTC: Yubase 4 with the additive package, viscosity modifier and friction modifier.

The lubricants were provided by Croda. The FFO differs from the BO by the addition of a viscosity modifier and unspecified package of further additives. MoDTC was added

---

[1]Fretting with displacement on the micron scale typical of most fretting tests with large diameter counterfaces (mm or greater).

to 1 % weight which is equivalent to 500 ppm. The loading conditions and lubricant combinations are summarised in Table 8.1 (located on page 190); blank entries in the table represent sets of test variables that were omitted. In choosing this test matrix, the affect of the presence of DLC and the type of DLC, coating thickness and substrate roughness could be assessed. This allowed for the maximum efficiency of testing time without exhaustively testing all coating variants and lubricant combinations. However, the doped DLCs were not tested as it was deemed that enough variables were changed to produce a good comparative study. 20 N and 40 N loads were used, with 40 N loads used on the HTS variants alongside the lower load. In all tests 15,000 cycles wear cycles were performed at a frequency of 5 Hz resulting in a test time of 50 min. The amplitude was set to $\pm 50\,\mu\mathrm{m}$ giving wear in the gross slip fretting regime [1]. The effective velocity was $250\,\mu\mathrm{m\,s}^{-1}$. At least two repeats were performed to confirm repeatability of the results. Table 8.2 summarises the sliding ratios and contact pressures in each of the test conditions [2]. The Poisson's ratios for the 52100 steel, SS, HTS and DLC were 0.285 [446], 0.27 [364], 0.285 [343] and 0.2 [217] respectively. The elastic moduli for the DLC, SS and HTS can be found in Table 4.2. The elastic modulus used for 52100 steel was 200 GPa.

---

[1]As determined by the sliding ratio [97] which is calculated by $\frac{\delta_0}{\delta^*}$. δ_0 is the displacement amplitude at zero force. δ^* is the maximum displacement amplitude. At values equal to or below 0.26, the fretting is in the partial slip regime. Above 0.26, the fretting is in the gross slip regime.

[2]p_{max} was calculated using Equation 2.7.

Table 8.1: Micro-fretting test matrix showing the loads and lubricant combinations used.

Substrate	DLC Recipe	DLC Coating Thickness (μm)	Surface Roughness (nm R_a)	Dry	BO	BO + MoDTC	FFO	FFO + MoDTC
SS	Uncoated	–	26 ± 4	20 N	20 N	20 N	20 N	20 N
	A	1.60 ± 0.17	22.2 ± 9.4	20 N	20 N	20 N	20 N	20 N
		1.62 ± 0.18	47.1 ± 10.2	20 N				
		5.18 ± 0.07	20.3 ± 5.1	20 N				
		5.54 ± 0.02	49.6 ± 4.5	20 N				
	B	1.16 ± 0.24	25.7 ± 1.5	20 N				
		2.88 ± 0.17	49.2 ± 9.7	20 N				
	C	1.10 ± 0.22	40.5 ± 8.0	20 N				
		2.25 ± 0.12	31.7 ± 13.7	20 N				
HTS	Uncoated	–	26 ± 4	20 N / 40 N	20 N / 40 N	20 N / 40 N	20 N / 40 N	20 N / 40 N
	A	2.20 ± 0.20	26.0 ± 10.3	20 N / 40 N	20 N / 40 N	20 N / 40 N	20 N / 40 N	20 N / 40 N
		2.02 ± 0.15	44.7 ± 8.5	20 N / 40 N				
		3.82 ± 0.09	84.0 ± 32.7	20 N / 40 N				
		4.47 ± 0.24	82.9 ± 19.5	20 N / 40 N				
	B	2.17 ± 0.16	48.0 ± 12.4	20 N / 40 N				
		4.93 ± 0.17	96.8 ± 15.1	20 N / 40 N				
	C	1.17 ± 0.12	26.2 ± 1.9	20 N / 40 N				
		2.99 ± 0.55	39.2 ± 23.1	20 N / 40 N				

Table 8.2: Predicted contact pressures and sliding ratio conditions for micro-fretting testing.

Load (N)	Substrate	Coating	p_{max} (GPa)	Sliding ratio
		Uncoated	1.26	0.58
		A	1.24	0.57
	SS	B	1.18	0.56
		C	1.29	0.58
20		Uncoated	1.23	0.57
		A	1.20	0.56
	HTS	B	1.12	0.54
		C	1.24	0.57
		Uncoated	1.55	0.45
		A	1.52	0.45
40	HTS	B	1.42	0.43
		C	1.56	0.45

All the lubricant combinations were tested with uncoated SS and HTS variants and the Coating A-thin-smooth variants. This allowed the lubricant affects on the coefficient of friction to be evaluated on DLC. The other coating variants were tested only in dry conditions.

8.2.2 Nano-fretting

The nano-fretting[1] module uses a function generator to drive a piezo-based vibration stage. The function generator is fed into the sample stage controller of the NanoTest

---

[1]Fretting with displacement on the nano-scale with μm radius probes generally achievable with an AFM or piezo-based vibration stage.

Vantage so the oscillations can be switched on and off as dictated by software control. The signal from the sample stage controller is fed into an amplifier and step-up transformer before finally being received by the fretting stage. The amplifier is used to ensure the full sine wave produced by the function generator is available for the fretting stage. The step-up transformer is required to step up the supply voltage to the piezo stack that drives the fretting stage. Table 8.3 shows the typical experimental conditions possible of the nano-fretting module. It should be noted that care must be taken, as with the micro-scale fretting rig, to calculate the correct experimental conditions pre-test to ensure that the theoretical predictions give the correct fretting regime.

Table 8.3: Typical experimental conditions of Nano-fretting module [425].

Probe radii (µm)	10–200
Applied Load (mN)	0–500
Sliding Speed ($\mu m\,s^{-1}$)	10
Scan Distance per cycle (µm)	20
Number of cycles	1000–200000
Total sliding distance (µm)	10000–100000

Figure 8.2 shows the nano-fretting module before mounting in the NanoTest Platform.
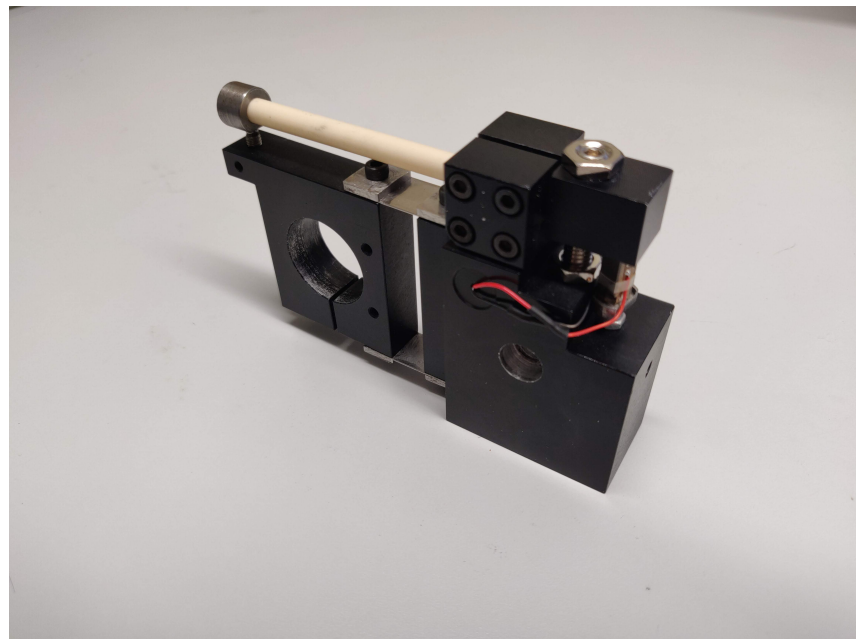
Figure 8.2: The nanofretting module.

Before the module can be used it must be calibrated. To do this, the module is mounted

as shown in Figure 8.3. This allows the depth sensing capabilities of the instrument to measure the track length of the module across the range of frequencies and amplitudes available. This method allows the total track displacement to be measured. This value must then be halved for the applied oscillation distance for fretting testing.
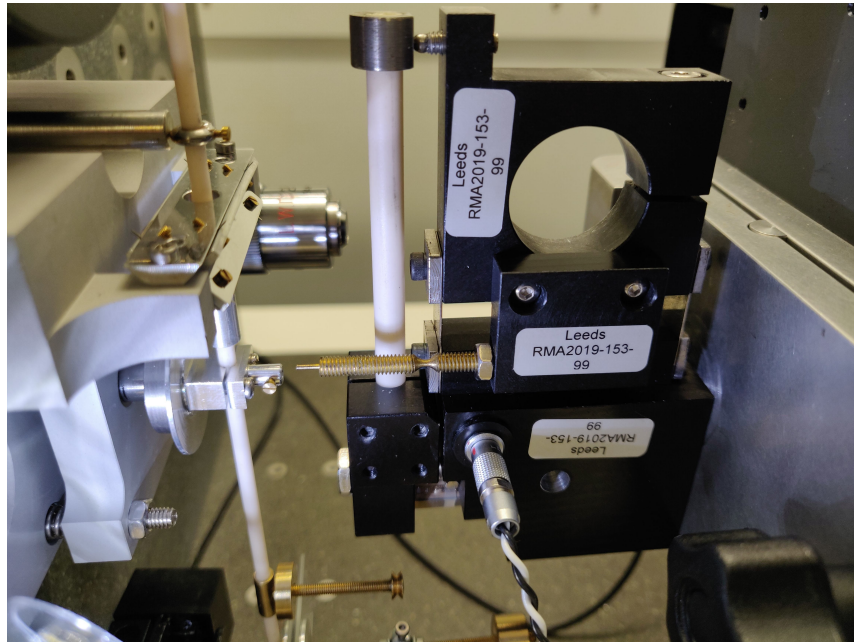
Figure 8.3: The nano-fretting module mounted in the calibration position.

A typical calibration involves testing the full range of amplitudes and frequencies produced by the function generator that give measurable track lengths while driving the piezo stack. The range of calibrations produced for this study can be seen in Figure 8.4.
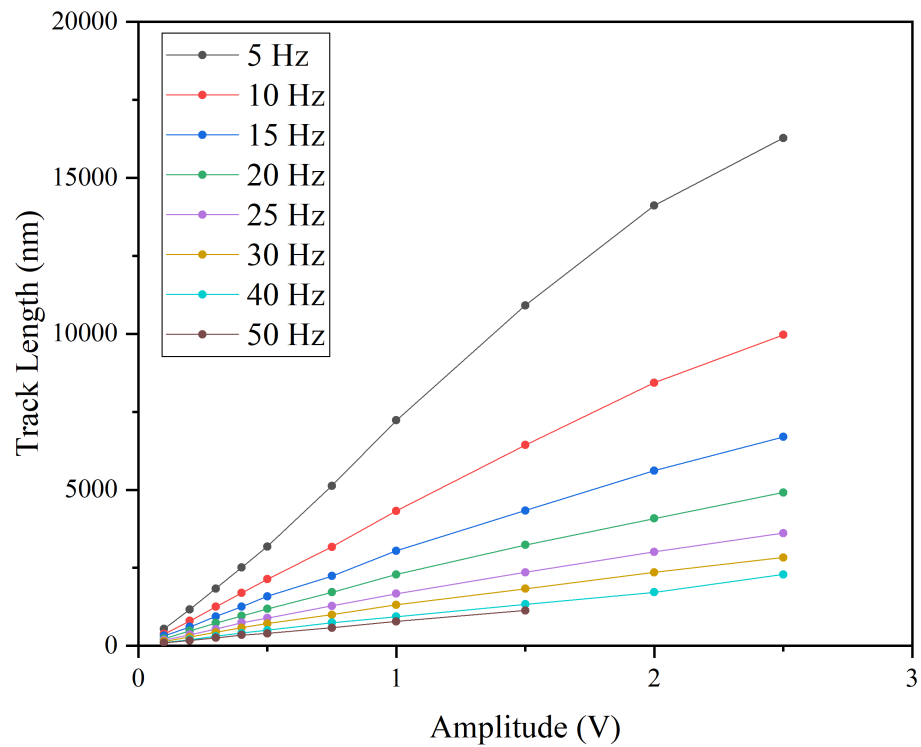
Figure 8.4: Nano-fretting track length calibrations produced by varying the frequency and amplitude of a frequency generator.

To ensure the track length calibration corresponds to physical wear scars on the surface, tests were performed on uncoated HTS with $2.5\,\mathrm{V}$ and $5\,\mathrm{Hz}$ applied. The track length calibration measured a track length of $16\,275\,\mathrm{nm}$; when this was physically tested track lengths of $15\,812\,\mathrm{nm}$ and $15\,959\,\mathrm{nm}$ were produced [1] (Figure 8.5). Therefore we can surmise that the physical track length will be slightly smaller than predicted by calibration. As it does not exceed the calibration and is smaller by approximately $200\,\mathrm{nm}$, the calibrated values are deemed to be sound.

---

[1]Two values were measured to assess repeatability in the the wear track length on the material surface compared to depth sensor calibration.
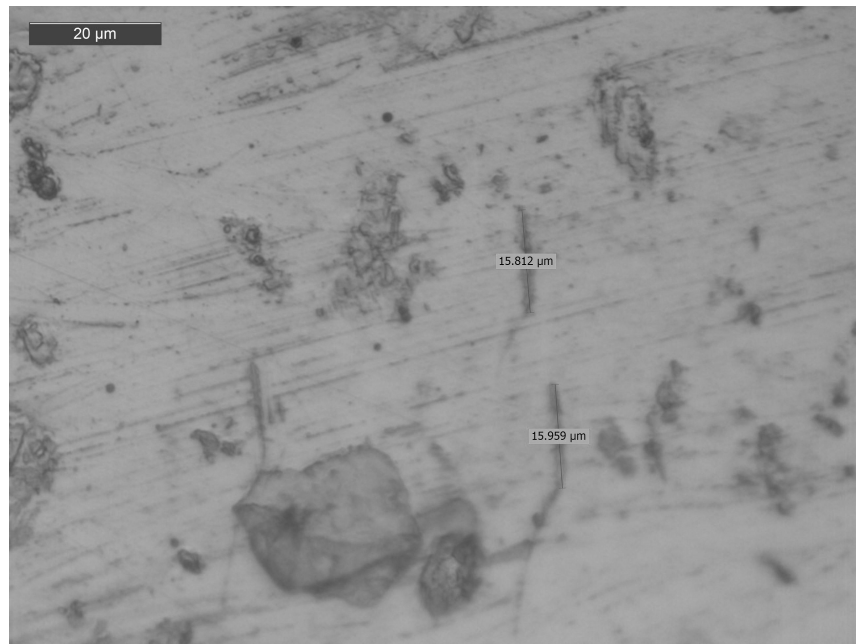
Figure 8.5: Track length verification of the nano-fretting calibration.

Once calibration is complete the fretting stage can be mounted in the test position as seen in Figure 8.6. The friction probe can be seen to be mounted in the figure. A range of probes can be used depending on the contact pressure range required or speed at which wear is to be imparted on the surface.
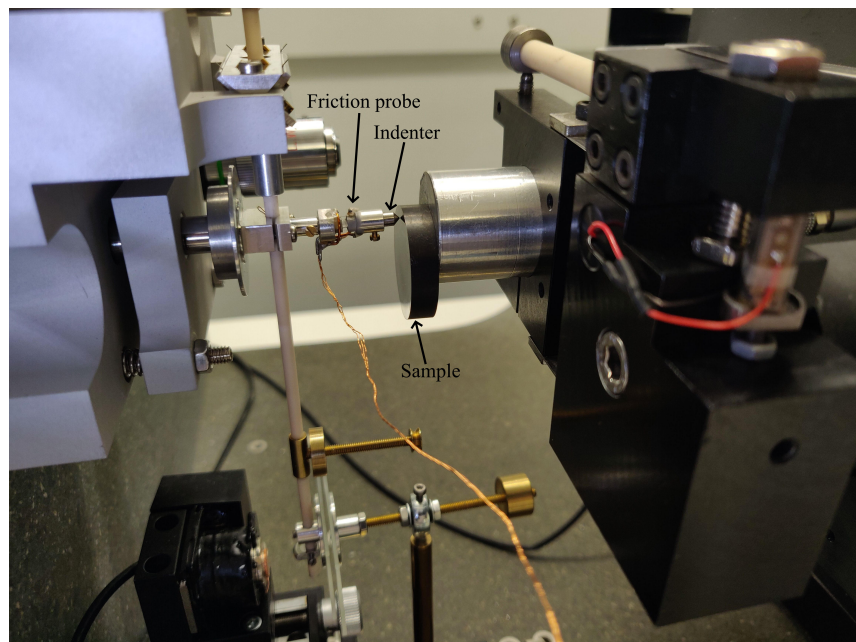
Figure 8.6: The nanofretting module mounted in the experimental set-up with a DLC coating.

Figure 8.7 shows the morphology of accelerated wear tests performed with the nano-fretting module on 316L stainless steel as part of a previous study [318].
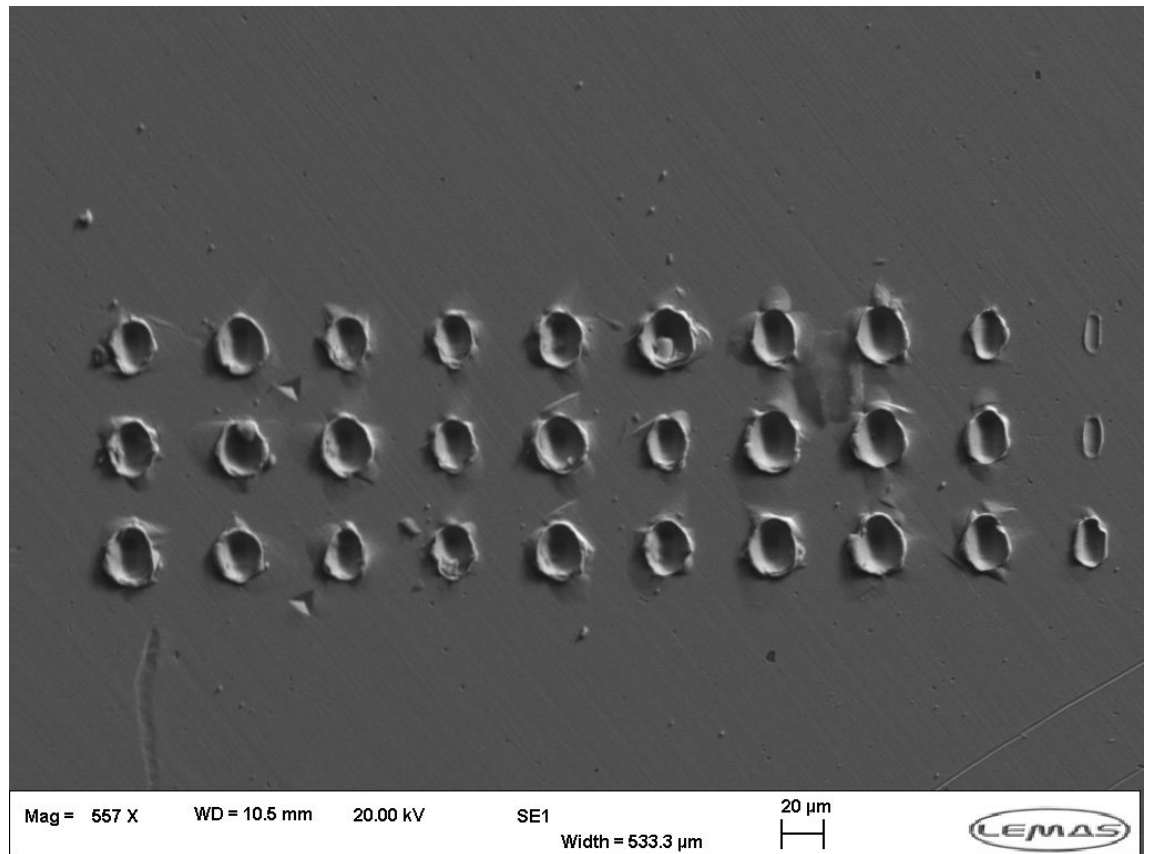
Figure 8.7: Typical morphology of nano-fretting tests on 316L stainless steel as performed by Beake and Liskiewicz in 2013 [318].

The test conditions used for the coating variants are summarised in Table 8.4 (located on page 198), as with the micro-fretting test matrix, blank entries show omitted tests. Using this combination of test conditions allowed the affect of applied load, coating variant, coating thickness and substrate roughness to be studied without testing all of the DLCs.

A 170 µm radius sphero-conical diamond probe was primarily used in this testing. The signal generator was set to a frequency of 25 Hz and an amplitude of 1.23 V giving a track length of 2100 nm. The effective velocity was 52.5 $\mu m\,s^{-1}$ (approximately 1/5th of the velocity of the micro-fretting). The total sampling time was 800 s with the generator being on for 120 s and off for 30 s. 5 on periods were used giving a total on sample oscillation time of 600 s. This was used to avoid thermal expansion of the stage during testing but will likely affect tribofilm formation due to due cooling down periods. 15,000 cycles of oscillation resulted on the sample surface to match the micro-fretting tests in terms of the number of cycles. At 10 mN, the sliding ratio predicts testing in the gross slip fretting and for 100 mN the regime was predicted to be in the partial slip regime. The 10 mN load gives approximately the same contact pressure as in the micro-fretting testing however with 5 times lower sliding velocity and an amplitude of $\pm 1\,\mu m$ compared to $\pm 50\,\mu m$ for the micro-fretting. 3 repeats were used per set of conditions/sample with a separation of 100 µm. For the load of 10 mN, a load and unload rate of 1 $mN\,s^{-1}$ was used. For 100 mN, load and unload rates of 10 $mN\,s^{-1}$ was used. These changes in loading and unloading rates were used to maintain the loading times between 10 mN and 100 mN. A 4.5 µm radius probe was also used to check the friction signal with a 10 mN load on uncoated SS. Friction was monitored during testing via a Wheatstone bridge strain gauge. This is in the reciprocating wear regime as the sliding ratio is greater than 1 and gives a maximum Hertzian contact pressure of 15.95 GPa. Table 8.5 shows the predicted initial contact

pressures and sliding ratios for the nano-fretting test parameters. All nano-fretting tests were performed in laboratory conditions with a temperature of 23 °C and a humidity of 19 %, this was controlled within the test room. Before tests were performed the Nanotest Platform chamber was allowed to thermally stabilise for 15 min prior to testing.

Table 8.4: Nano-fretting test matrix with showing the loads tested for each coating variant.

Substrate	DLC Recipe	DLC Coating Thickness (μm)	Surface Roughness (nm R_a)	Loads applied (mN)
	Uncoated	–	26 ± 4	10 / 100
		1.60 ± 0.17	22.2 ± 9.4	10 / 100
	A	1.62 ± 0.18	47.1 ± 10.2	10 / 100
		5.18 ± 0.07	20.3 ± 5.1	–
SS		5.54 ± 0.02	49.6 ± 4.5	10 / 100
	B	1.16 ± 0.24	25.7 ± 1.5	10
		2.88 ± 0.17	49.2 ± 9.7	–
	C	1.10 ± 0.22	40.5 ± 8.0	10
		2.25 ± 0.12	31.7 ± 13.7	–
	Uncoated	–	26 ± 4	10 / 100
		2.20 ± 0.20	26.0 ± 10.3	10 / 100
	A	2.02 ± 0.15	44.7 ± 8.5	10 / 100
		3.82 ± 0.09	84.0 ± 32.7	10 / 100
HTS		4.47 ± 0.24	82.9 ± 19.5	10 / 100
	B	2.17 ± 0.16	48.0 ± 12.4	10 / 100
		4.93 ± 0.17	96.8 ± 15.1	–
	C	1.17 ± 0.12	26.2 ± 1.9	10 / 100
		2.99 ± 0.55	39.2 ± 23.1	–

Table 8.5: Predicted contact pressures and sliding ratio conditions for nano-fretting testing.

Load (mN)	Substrate	Coating	p_{max} (GPa)	Sliding ratio
10	SS	Uncoated	1.38	0.54
		A	1.33	0.53
		B	1.23	0.51
		C	1.40	0.54
	HTS	Uncoated	1.32	0.53
		A	1.27	0.52
		B	1.14	0.49
		C	1.34	0.53
100	SS	Uncoated	2.98	0.25
		A	2.86	0.24
		B	–	–
		C	–	–
	HTS	Uncoated	2.85	0.24
		A	2.74	0.24
		B	2.46	0.23
		C	2.89	0.25

8.3 Results

8.3.1 Micro-fretting

8.3.1.1 Fretting Logs and Sliding Ratio

By plotting the tangential force (Q) against number of cycles and displacement, logs of the fretting process are obtained which can be used to visualise the fretting regime the system is in and whether this changes throughout the test. These logs were constructed in MATLAB. The tangential force data was processed through the de-trend function as the LabVIEW program compares the difference in the maxima and minima in tangential force per cycle to calculate friction resulting in some load cell drift throughout the test. Figure 8.8 shows the fretting logs for different sample configurations. Each of the logs are seen to be in the gross slip fretting regime. With the addition of the DLC coating and lubricant, we can see the tangential force decrease resulting in lower energy dissipation [101, 447]. Some variability is seen at the start of each test as the rig requires a few cycles to adjust to the specified parameters.
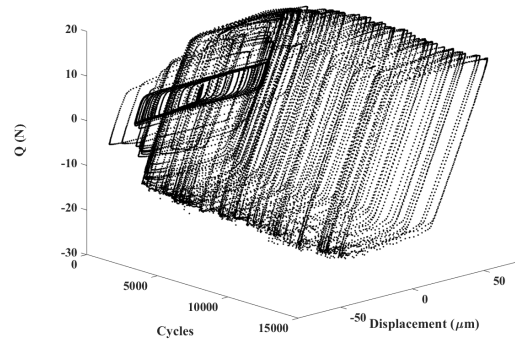
(a) HTS Dry
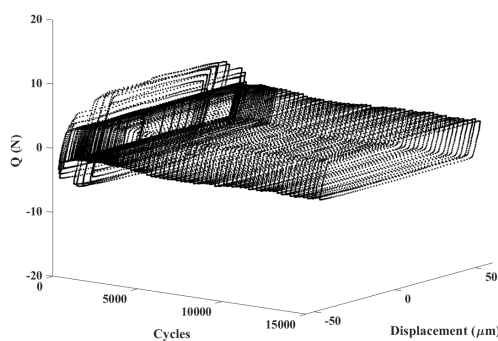
(b) HTS-Coating A-thin-smooth Dry
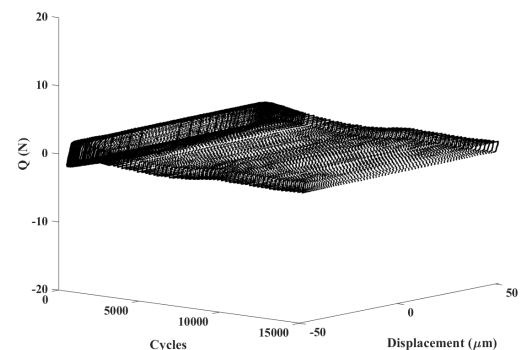
(c) HTS Coating A in BO

Figure 8.8: Fretting logs of various samples at 20 N.

Figure 8.9 shows how the sliding ratio changes throughout the test. As the value remains above 0.26 through the entirety of the test, we can be sure that the gross slip

regime is maintained throughout [97]. The relative stability of each test configuration can be assessed by analysing how smooth the sliding ratio progression is. HTS dry is seen to be the most unstable corresponding to the variability of its respective fretting map. As with the fretting logs for the coated and lubricated samples, the sliding ratio was stable throughout the test.
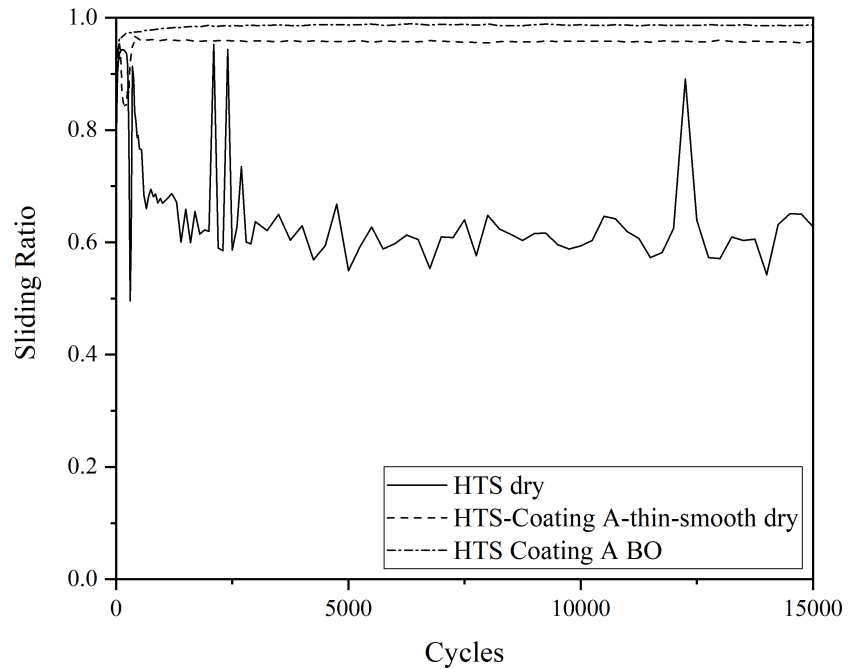
Figure 8.9: Sliding ratio variation with cycles for uncoated substrate, coating and lubricant variants.

8.3.1.2 Coefficient of Friction

In gross slip fretting it is common to have some instability in the friction especially during the early parts of a test where friction is high. Generally, it will then reduce to a lower steady state value [448]. Discontinuity or change in COF indicate that there are severe metal/substrate interactions [105]. This can indicate that there is wear through or decohesion of the coating.

Figure 8.10 shows the unlubricated fretting friction results of the thin coating variants and uncoated substrates at 20 N and 40 N. The uncoated HTS is seen to have a high COF of approximately 0.9 and 0.8 at 20 N and 40 N respectively. This is typical of unlubricated steel-on-steel contact [103]. The smooth preparation of Coating A is seen to have a COF of 0.15 and 0.2 at the lower and higher load respectively. The higher load sees more instability at the start of the cycles marked by it being in the mixed fretting regime before settling into the gross slip regime once the friction stabilised. The rougher preparation of Coating A is seen to have lower friction due to the reduced asperity contact [103]. Coating B is seen to have a slightly lower COF but its running period is much more pronounced thereby giving a larger amount of dissipated energy (overall larger area of the friction log). Coating C has a less pronounced running in period at each load however, towards the end of the cycles, the friction is seen to climb. This is much more pronounced at 40 N

with a high level of instability post 1000 cycles. This is indicative of coating decohesion and wear through as seen in Figure 8.19c.
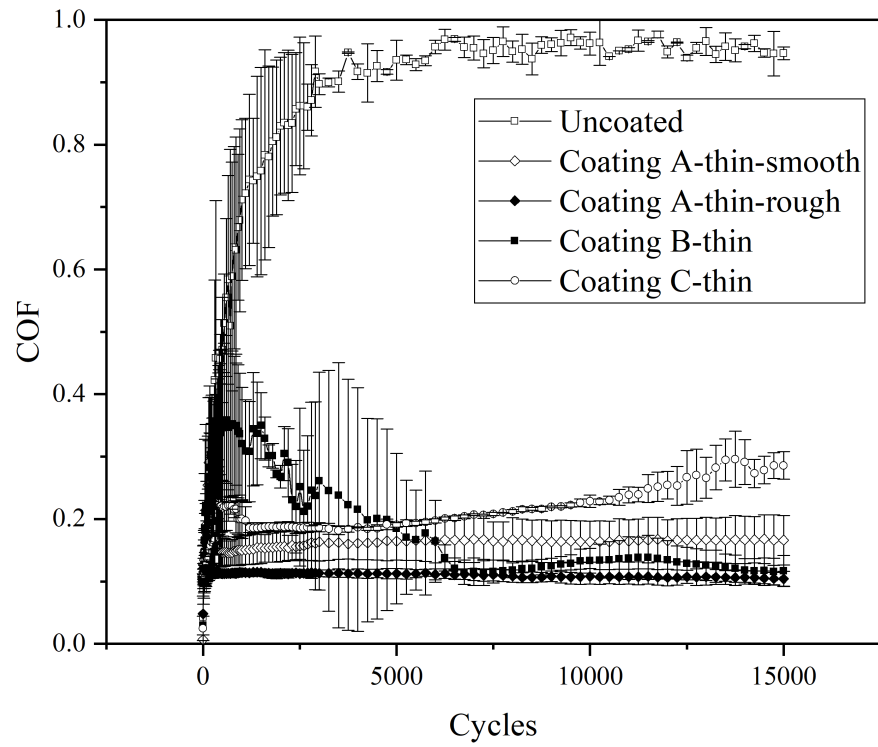
(a) HTS-thin-unlubricated-20 N.

Figure 8.10: COF evolution of HTS-thin at 20 N and 40 N (continued on next page).
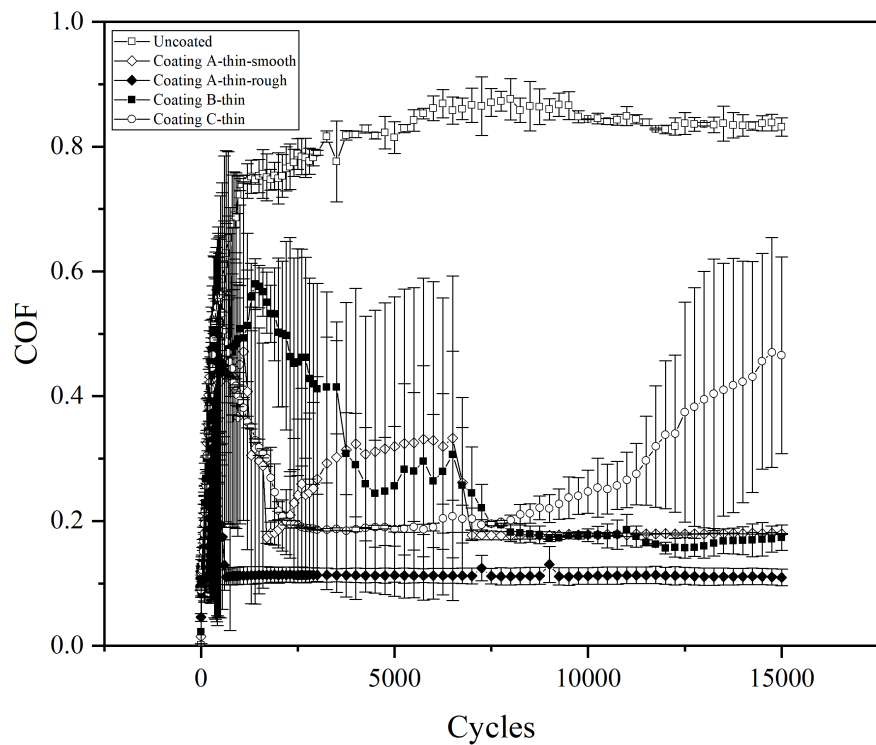
(b) HTS-thin-unlubricated-40 N.

Figure 8.10: COF evolution of HTS-thin at 20 N and 40 N (cont.).

The COF results for the thick preparations of the HTS coatings is presented in Figure 8.11. Due to the increased thickness, Coating C does not experience layer wear through and maintains a more stable COF throughout testing though it does have a longer running in period compared to the other coatings. Coating A is seen to have a steady decrease in friction until a steady state is seen. This steady state is at the same COF as Coating B (approximately 0.14). The rough preparation once again has a low COF due to reduced asperity interaction. The high load results are similar to those of the thinner coating preparation however Coating C doesn't experience decohesion and wear through. Both Coatings B and C had a large running in period. Coating A-smooth had a steady decrease to steady state at the same value as the rough preparation.
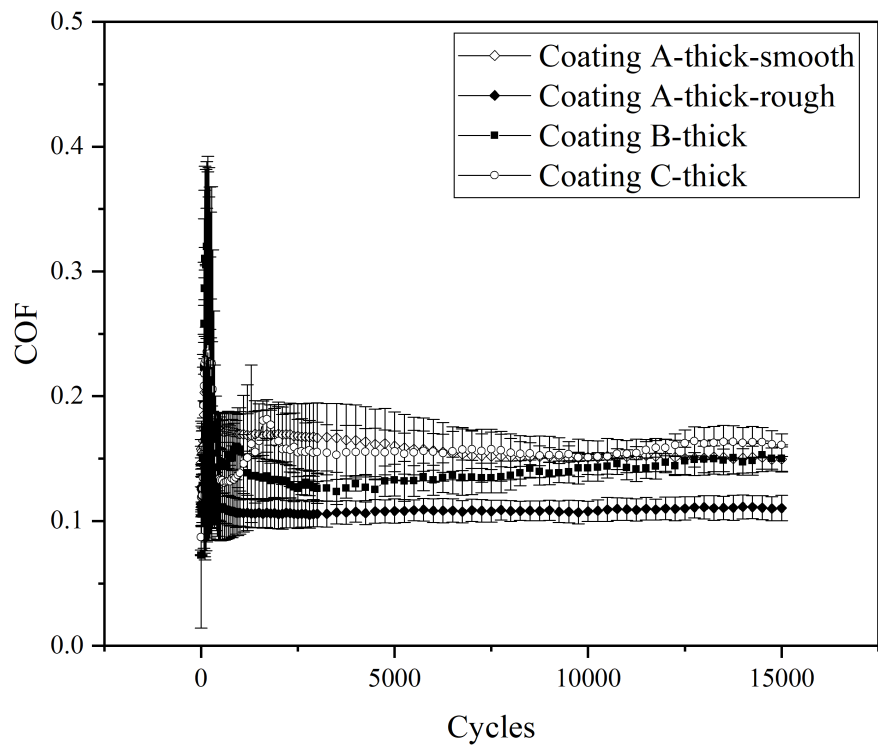
(a) HTS-thick-unlubricated-20 N.
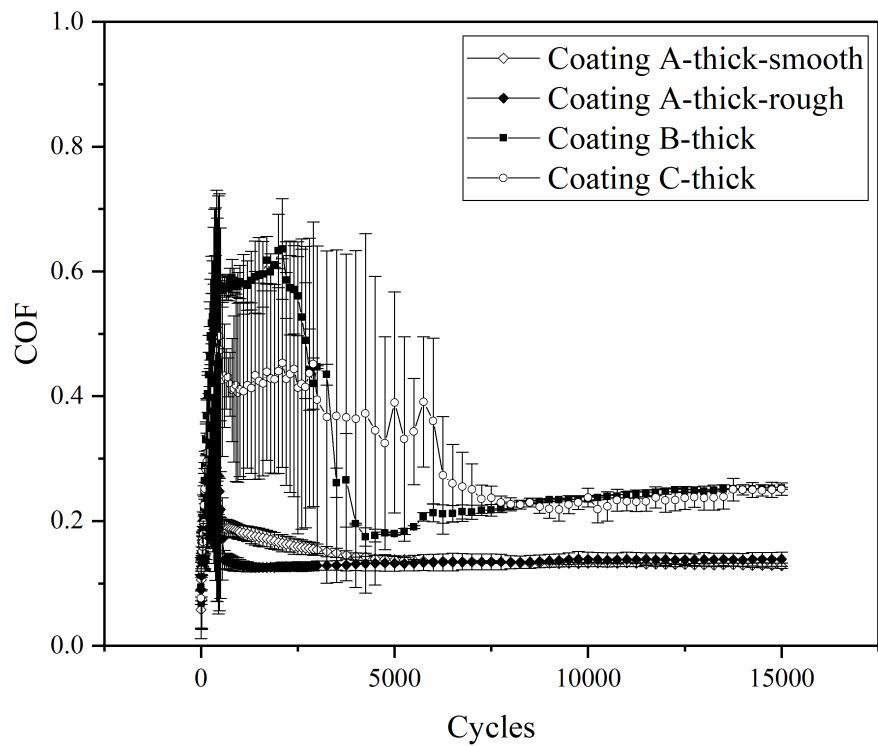
(b) HTS-thick-unlubricated-40 N.

Figure 8.11: COF evolution of HTS-thick at 20 N and 40 N.

The lubricated COF results of uncoated HTS at 20 N and 40 N are shown in Figure 8.12. Both loads display a high COF at the start of the cycles corresponding to a stick-slip phenomena before friction stabilises in the gross slip regime [108, 449]. This period is more pronounced at 40 N. FF + MoDTC is seen to produce the lowest COF at both loads. BO is seen to have the highest COF at 20 N however the consistently highest for the 40 N was the FF oil. FF + MoDTC was seen to have a large running in before slowly reducing its COF to approximately 0.1.
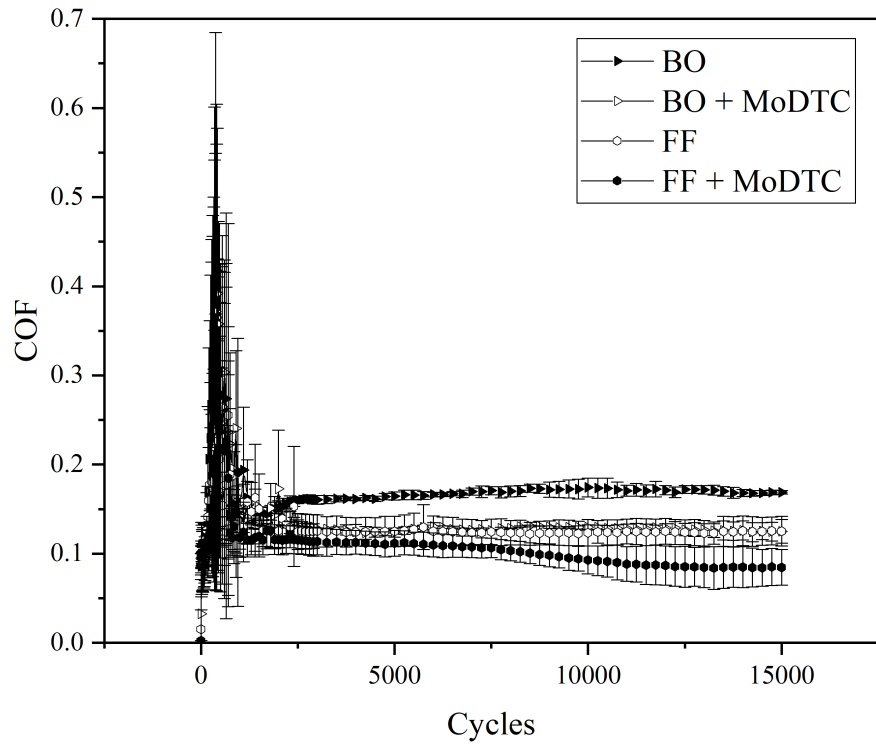
(a) HTS-uncoated-lubricated-20 N.

Figure 8.12: COF evolution of HTS-uncoated-lubricated at 20 N and 40 N (continued on next page).
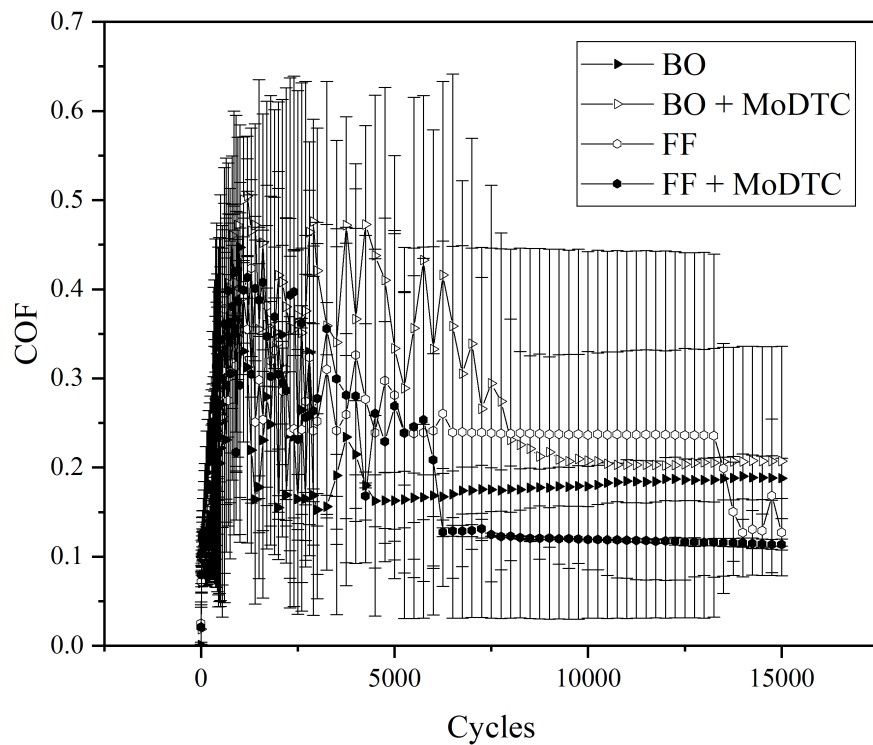
(b) HTS-uncoated-lubricated-40 N.

Figure 8.12: COF evolution of HTS-uncoated-lubricated at 20 N and 40 N (cont.).

The COF result of HTS-Coating A lubricated under both loads is presented in Figure 8.13. The friction is noted to be more stable than the unlubricated tests with a no spikes in COF during run-in. The fully formulated oils are seen to perform relatively poorly, showing higher friction than their base oil variants. FF + MoDTC and BO + MoDTC performed similarly though the FF oil has a higher friction during run-in. Overall, at both loads, BO + MoDTC was seen to produce the lowest COF once stable friction was established.
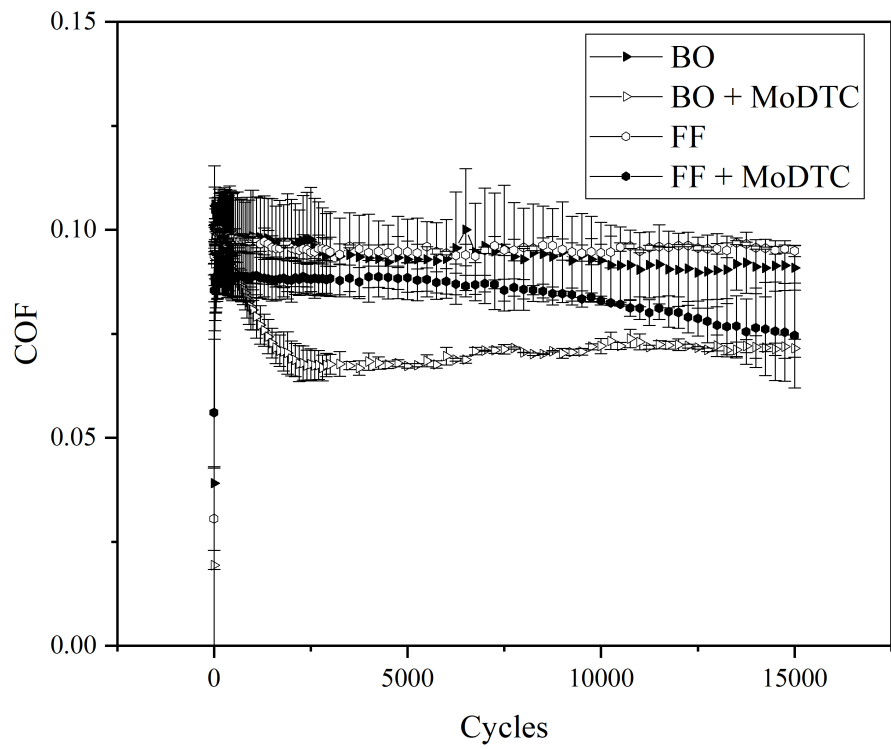
(a) HTS-A-lubricated-20 N.
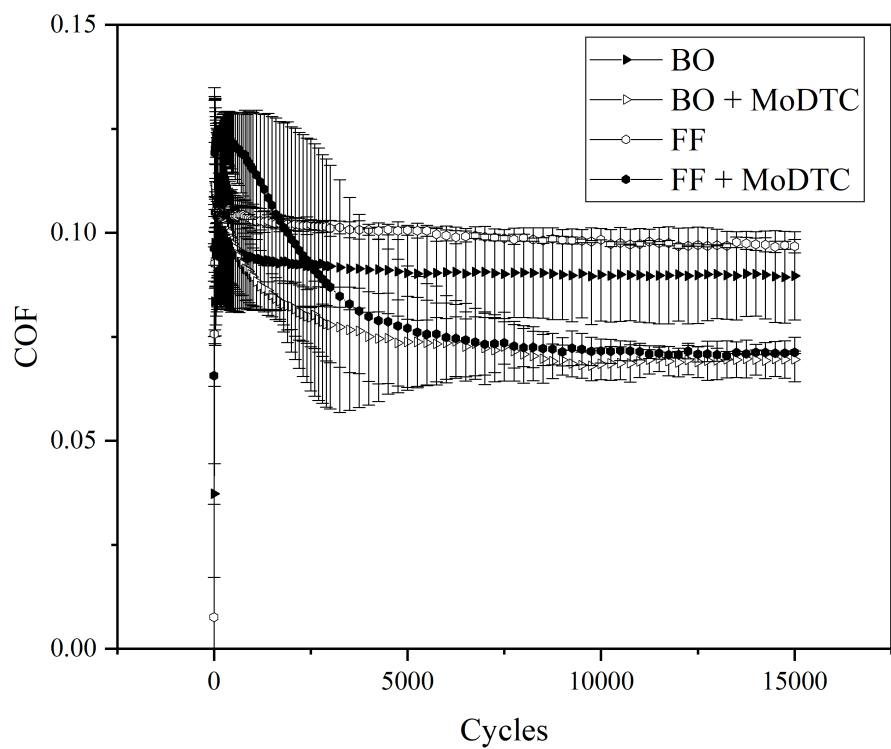
(b) HTS-A-lubricated-40 N.

Figure 8.13: COF evolution of HTS-A-lubricated at 20 N and 40 N.

207

The COF results for unlubricated SS are shown in Figure 8.14. The thin preparation of the SS coatings displays similar behaviour as seen in Figure 8.10a. Little difference is noted in changing the substrate material though the rise in the COF near the end of the cycles does indicate wear through. The behaviour of the smooth and rough preparations of Coating A in the thick coating variants is the opposite of what is expected as noted by Kubiak et al. [103]; they found that lower coefficient of friction was was observed with a rough surfaces. Additionally, wear rate increased with surface roughness was increased. Higher wear activation energy was required for smoother surfaces.
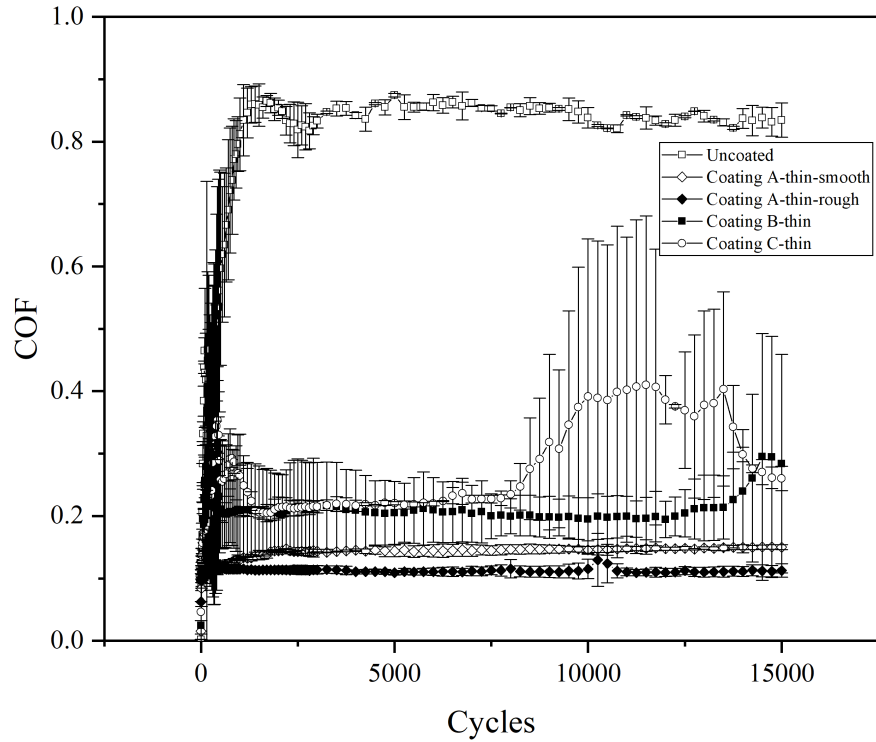
(a) SS-thin-unlubricated-20 N.

Figure 8.14: COF evolution of SS-unlubricated at 20 N (continued on next page).
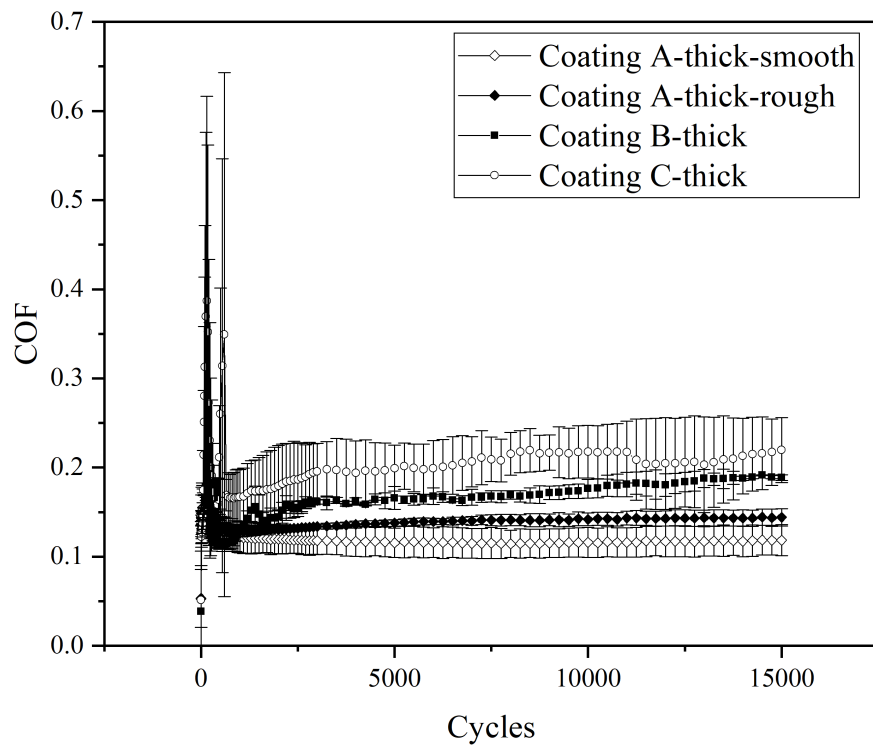
(b) SS-thick-unlubricated-20 N.

Figure 8.14: COF evolution of SS-unlubricated at 20 N (cont.).

The lubricated COF results for SS are seen in Figure 8.15. Compared to HTS, FF oil was seen to perform best against the uncoated substrate. On the uncoated substrate, there was a large COF spike for all lubricant corresponding to the running-in period followed by close packing of the steady state COF values. Applying the same lubricants to Coating A, sees BO perform best compared to BO + MoDTC on HTS. Once again the FF oils performed relatively poorly compared to the base oil variants applied to the coatings.
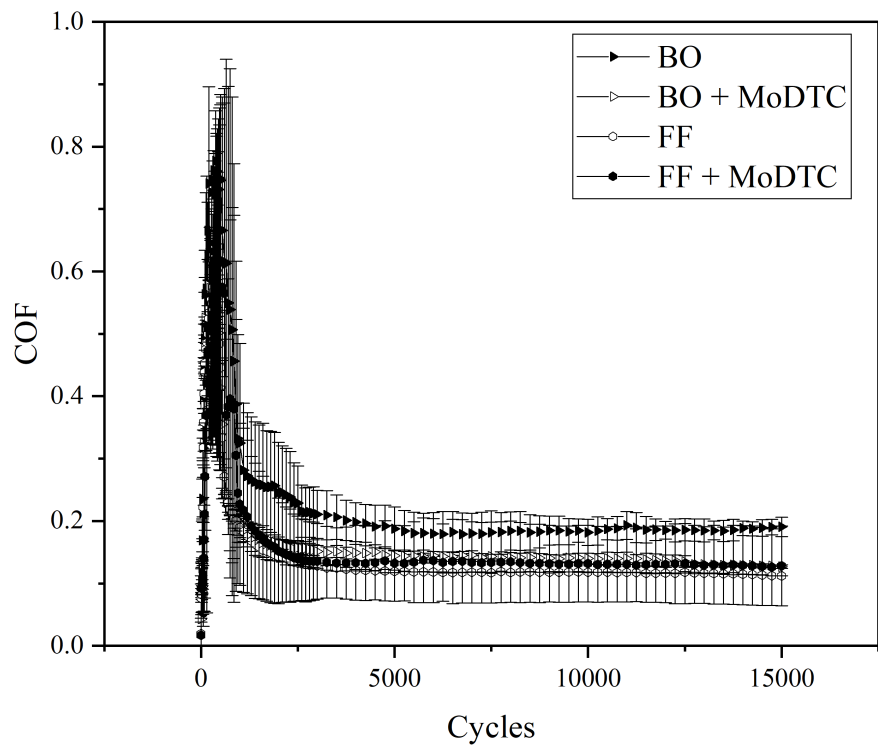
(a) SS-uncoated-lubricated-20 N.
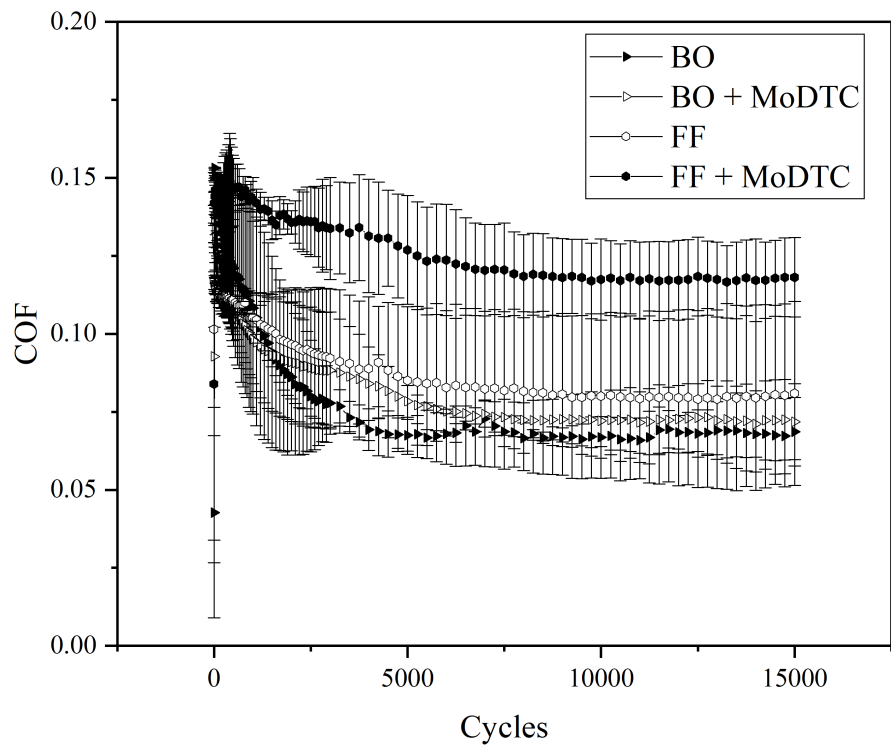
(b) SS-Coating A-lubricated-20 N.

Figure 8.15: COF evolution of SS-lubricated at 20 N.

8.3.1.3 Dissipated Energy

By integrating the frictional force and displacement of each loop and cumulatively summing the energies, the total dissipated fretting energy can be calculated. This can be used as a metric to compare the resistance to wear of each system [105]. The lower the dissipated energy, the lower the fretting wear. Consistently lower COF will correspond to a lower value of dissipated energy as less energy is expended during the entire fretting cycle. By comparing this quantitative metric with the wear morphology of each fretting scar a more complete picture of the system performance can be obtained. Abbreviations have been used to ensure the labels all fit; 's' and 'r' refer to the smooth and rough substrate preparations respectively. 'U' refers to uncoated and 'M' signifies the addition of MoDTC into the lubricant formulation.

Figure 8.16 shows the total dissipated energy of the lubricated and dry tests on the HTS samples at 20 N. The highest amount of dissipated energy is with the uncoated substrate in dry conditions with approximately 30 J. This corresponds to the high level of wear seen in Figure 8.19d. The highest amount of dissipated energy with a coating in dry conditions is the thin preparation of Coating C. The thin-rough and thick-rough preparations of Coating A show the same level of dissipated energy due to the benefit of increased surface roughness decreasing the coefficient of friction and therefore energy [103]. In the application of lubricants to the uncoated substrate, the progression through the lubricants (BO, BO + MoDTC, FF, FF + MoDTC) showed decreasing levels of energy with each application indicating that with the smoother prepared substrate the increased viscosity and additive action is beneficial. The additives were less effective on Coating A with the FF and FF + MoDTC showing almost the same energy as BO. BO + MoDTC was very effective at reducing the energy however.
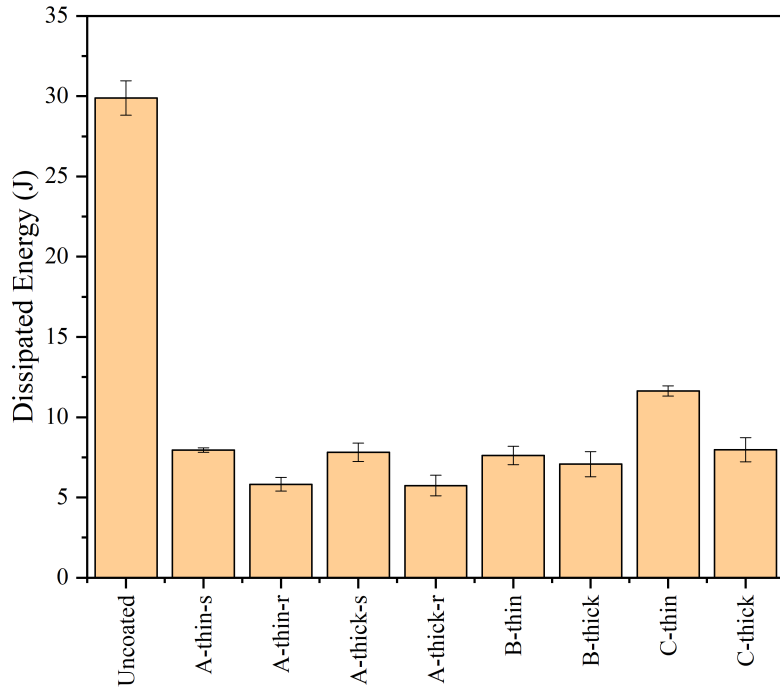
(a) HTS unlubricated.
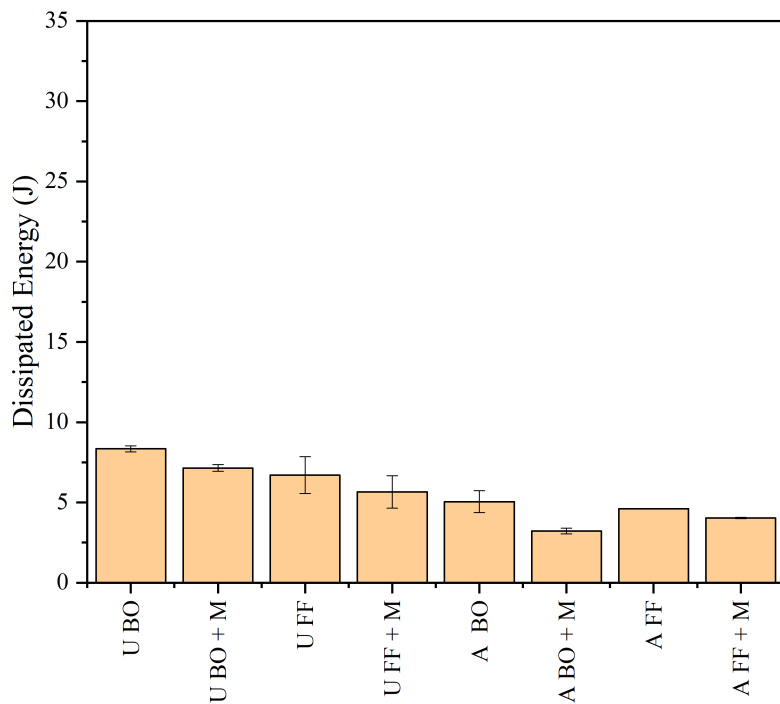
(b) HTS lubricated.

Figure 8.16: Dissipated energy of HTS in dry and lubricated conditions at 20 N.

In increasing the load to 40 N as in Figure 8.17 we can see that the dissipated energy is higher for all the test conditions. In the dry conditions, the uncoated substrate had around the same level of dissipated energy as B-thick and both thicknesses of Coating C

indicating the poor performance of the coatings. With Coating A, the increase in coating thickness was beneficial at higher load but both substrate surface roughness preparations showed the same dissipated energy (as their DLC surface roughness was the same from Table 7.3). The increased roughness with the thin preparation did reduce the energy by almost half at this load. The higher load decreased the effectiveness of all lubricants on the uncoated substrate however for Coating A, the addition of MoDTC saw decreases in the energy with both oil variants.
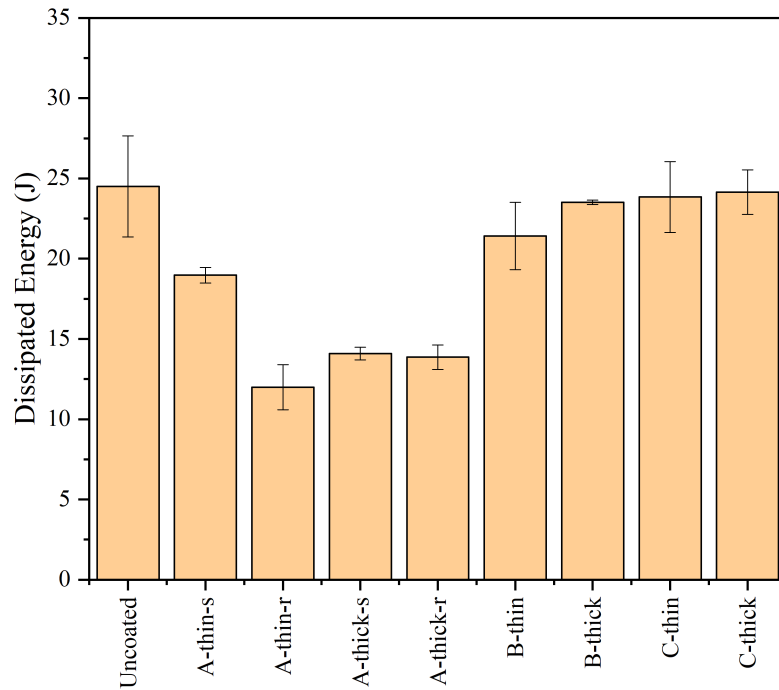
(a) HTS unlubricated.

Figure 8.17: Dissipated energy of HTS in dry and lubricated conditions at 40 N (continued on next page).
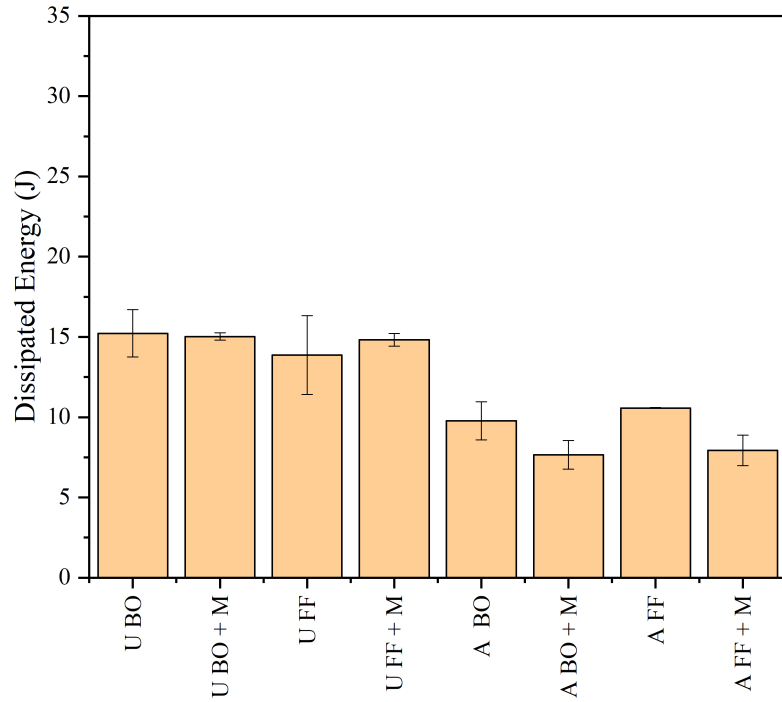
(b) HTS lubricated.

Figure 8.17: Dissipated energy of HTS in dry and lubricated conditions at 40 N (cont.).

Figure 8.18 shows the dissipated energy for the SS coated and uncoated substrates. As with HTS, the uncoated SS performed poorly with a larger dissipated energy corresponding to large wear. Coating C-thin was seen to have a larger dissipated energy than the rest of the coatings due to wear through.

In the lubricated tests on the uncoated substrate, a broadly similar trend is seen as the uncoated HTS.
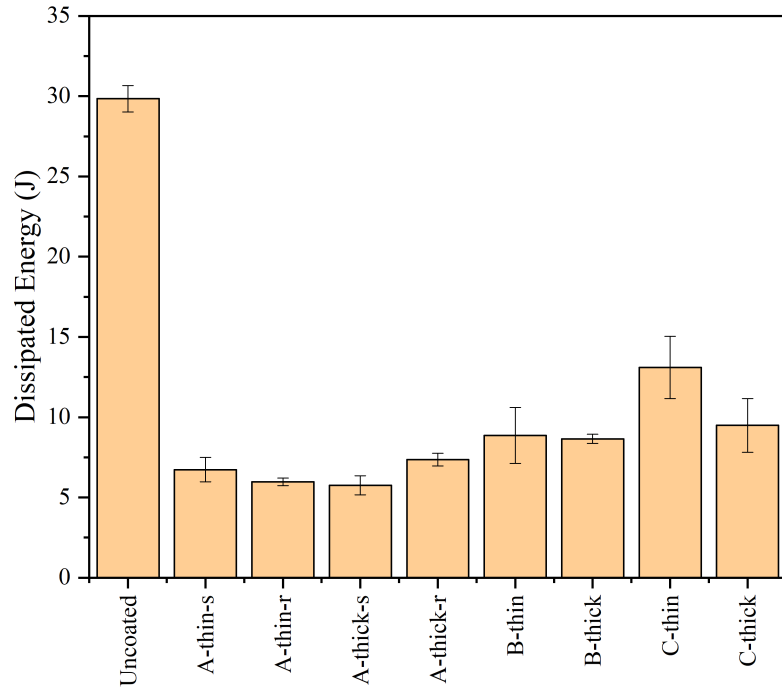
(a) SS unlubricated.
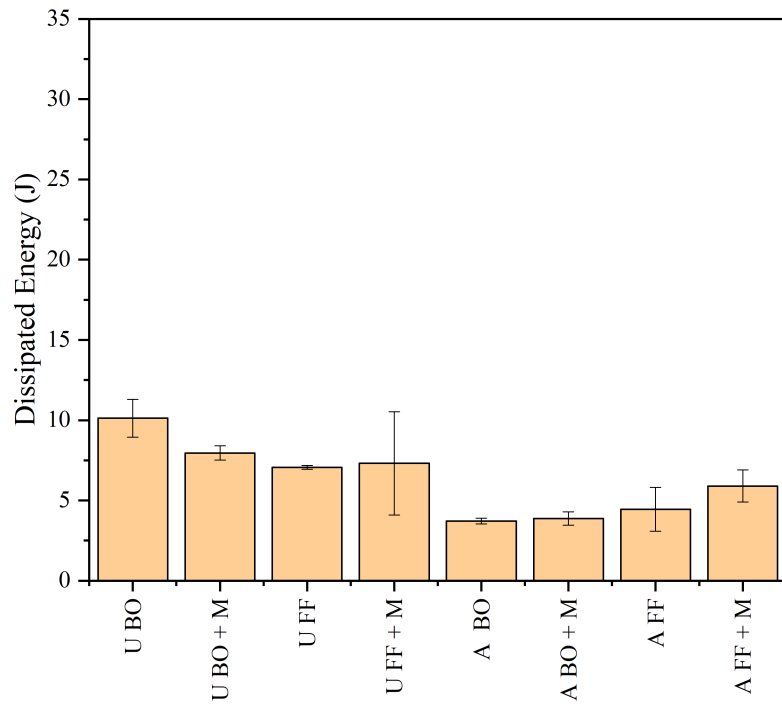
(b) SS lubricated.

Figure 8.18: Dissipated energy of SS in dry and lubricated conditions.

8.3.1.4 Wear Morphology

Optical microscopy was used to image the micro-fretting wear scars to qualitatively assess their morphology. The nano-fretting wear scars were too small to be able to image with the optical microscope and the AFM was unavailable for use therefore they have not been imaged.

Figure 8.19 shows the morphology of the fretting scars of different coating architectures on HTS. Coating A displays abrasive marks in the centre of the wear scar with some ejected wear debris. This is similar for Coating B however the volume of ejected wear debris is greater in the case of B. Coating C displays a far larger volume of wear debris and the coating is seen to be worn through in the middle of the wear scar. Uncoated HTS is seen to have the largest wear in this set of fretting scars. There is evidence of large oxidised wear debris being ejected from the fretting surface alongside an oxidised contact circle.

(a) HTS-Coating A-thin-smooth Dry.

(b) HTS-Coating B-thin-smooth Dry.

(c) HTS-Coating C-thin-smooth Dry.

(d) HTS-uncoated Dry.
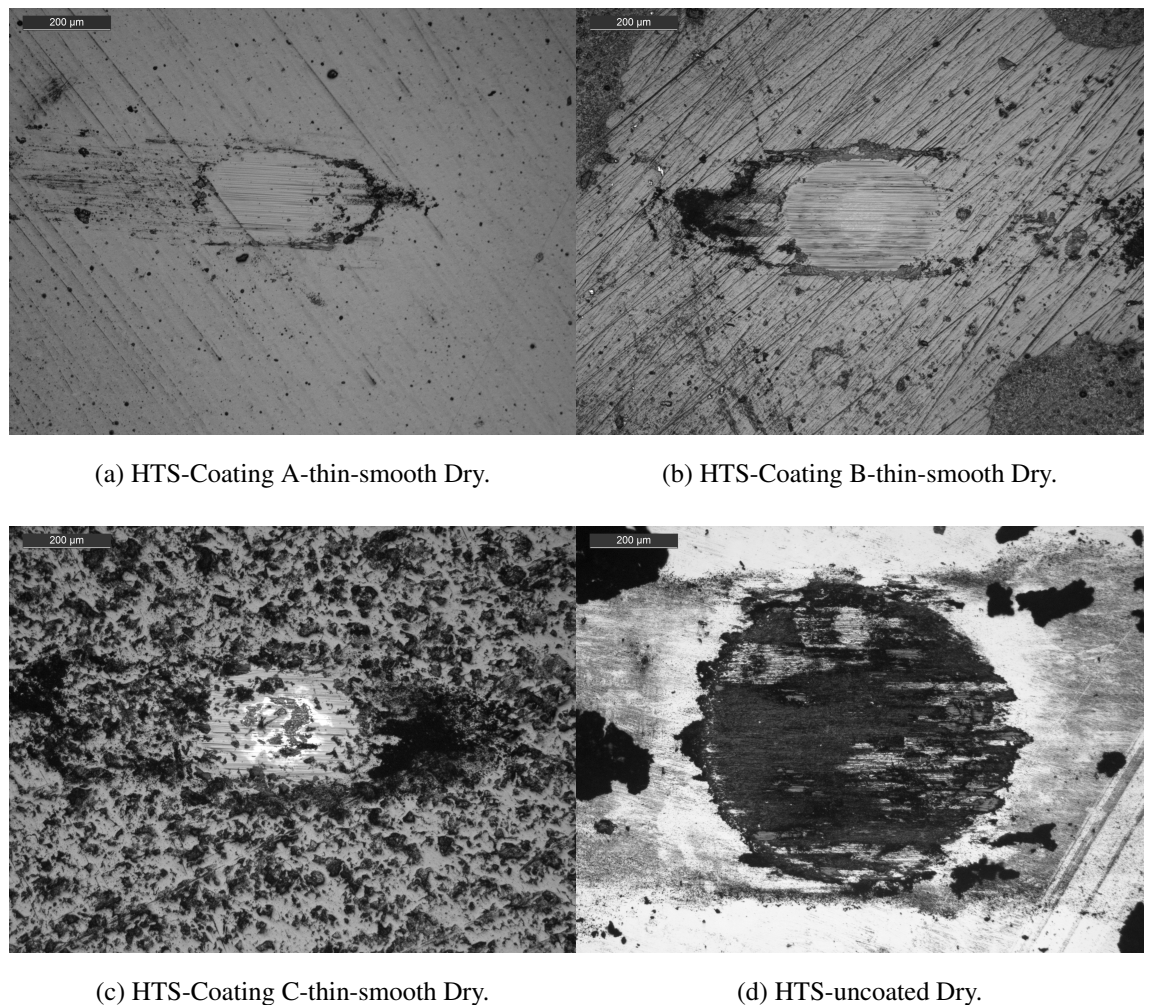
Figure 8.19: Morphology of micro-fretting wear scars on HTS.

Figure 8.20 shows the morphology of fretting scars on SS. The wear morphology seen on each coating architecture is seen to be broadly similar to displayed on HTS in the previous figure. Coating A is seen to have a larger amount of wear debris that isn't ejected from the wear scar as readily due to their small size. Coatings B and C both display evidence of coating wear through (decohesion) in the centre of the wear scar.
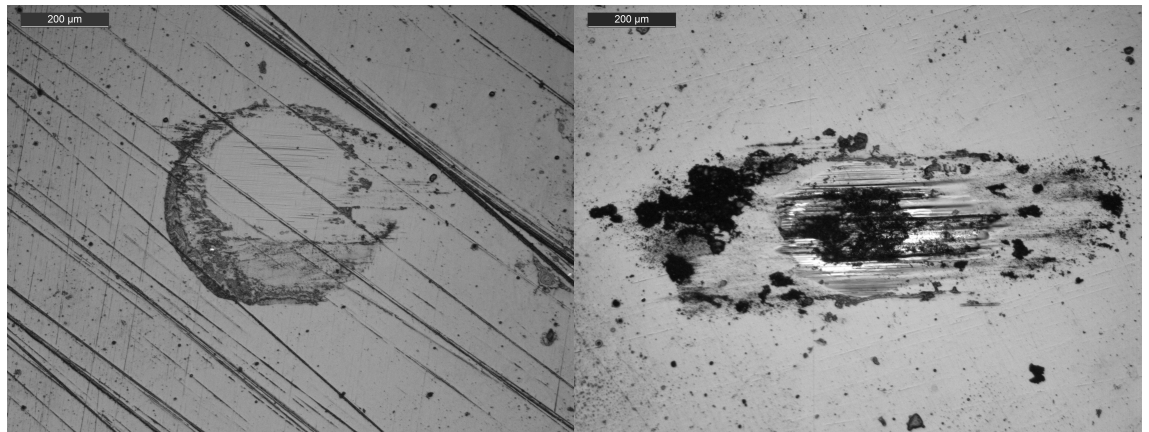
(a) SS-Coating A-thin-smooth Dry.

(b) SS-Coating B-thin-smooth Dry.
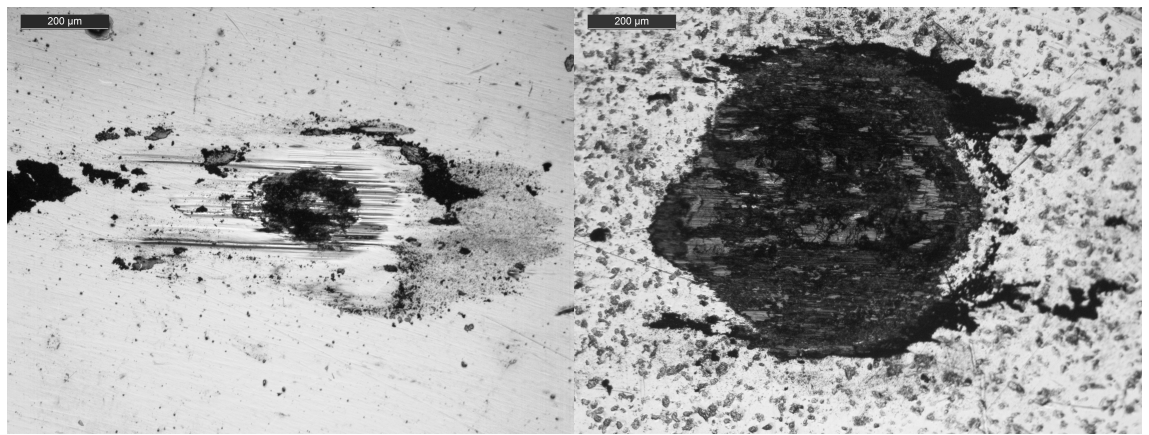
(c) SS-Coating C-thin-smooth Dry.

(d) SS-uncoated Dry.

Figure 8.20: Morphology of micro-fretting wear scars on SS.

Figure 8.21 shows the morphology of fretting wear scars on HTS when lubricants were present. We can immediately see that the wear is less severe. The fully formulated oil shows some evidence of residue being left despite cleaning with acetone being imaging. The use of base oil on HTS-Coating A-thin-smooth shows that no wear debris was produced suggesting that the oil served to cool the contact down so no thermal graphitisation occurred [411]. Raman spectroscopy would have to be performed to confirm, however. Some small fatigue cracks are observed in the centre of the wear scar with abrasive marks surrounding.
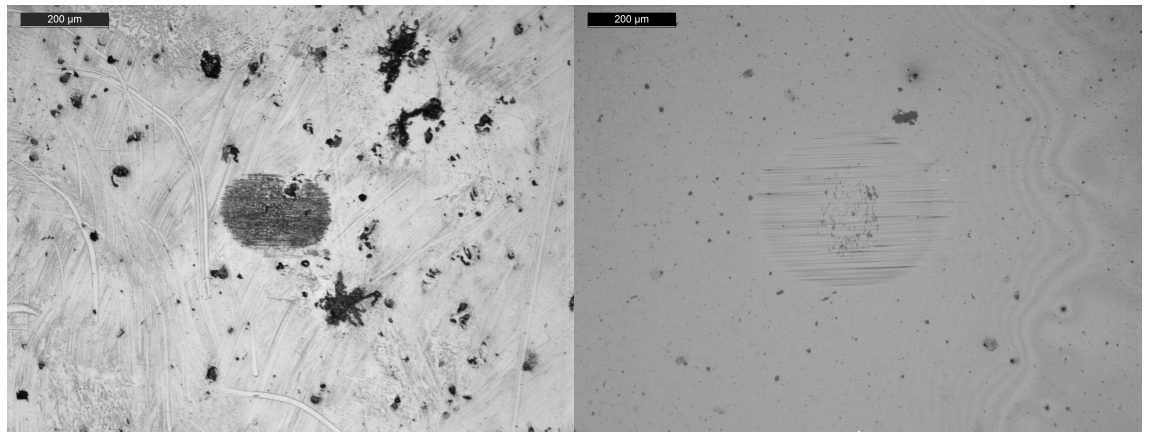
(a) HTS-uncoated FF oil.   (b) HTS-Coating A-thin-smooth BO.

Figure 8.21: Morphology of lubricated micro-fretting scars on HTS.

8.3.2 Nano-fretting

8.3.2.1 Coefficient of Friction Evolution

The coefficient of friction was processed using MATLAB from the raw friction data outputted from the NanoTest Platform. After the data is imported, the friction data was processed through the de-trend function to remove any variations due to probe positioning and the root mean square (RMS) friction was calculated to find the magnitude from the positive and negative data. The final step involved removing the time steps in which the probe was not moving to stitch all of the data together into a continuous data set. Figure 8.22 shows the COF evolution with uncoated SS at 10 mN load utilising a 4.5 μm radius probe. The friction is seen to be highly variable throughout the time tested with numerous larger spikes at random intervals.
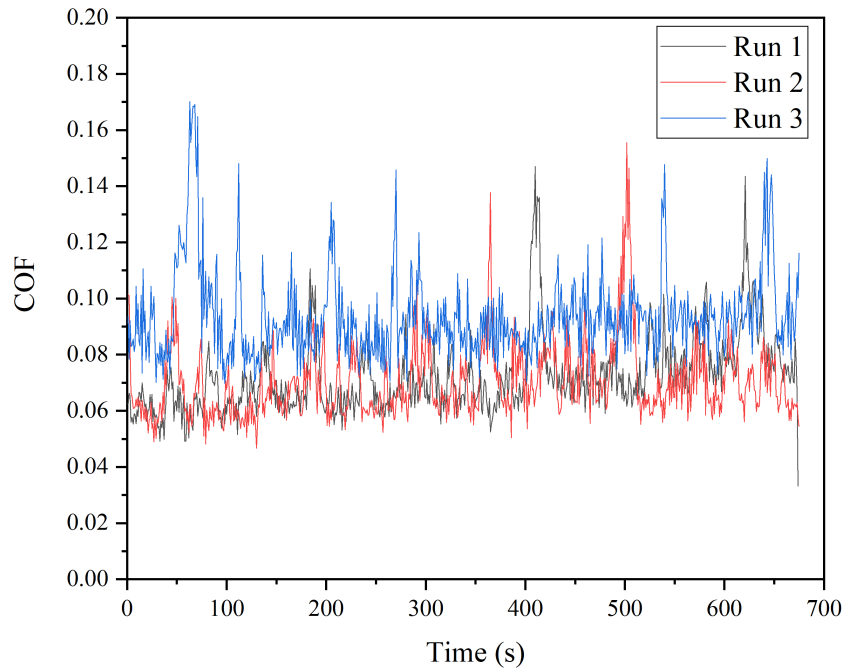
Figure 8.22: COF of uncoated SS under nanofretting with 10 mN load using a 4.5 μm radius probe.

Figure 8.23 shows the difference in switching to a 170 μm probe. A marked reduction in the coefficient of friction is observed though broadly the same morphology is seen.
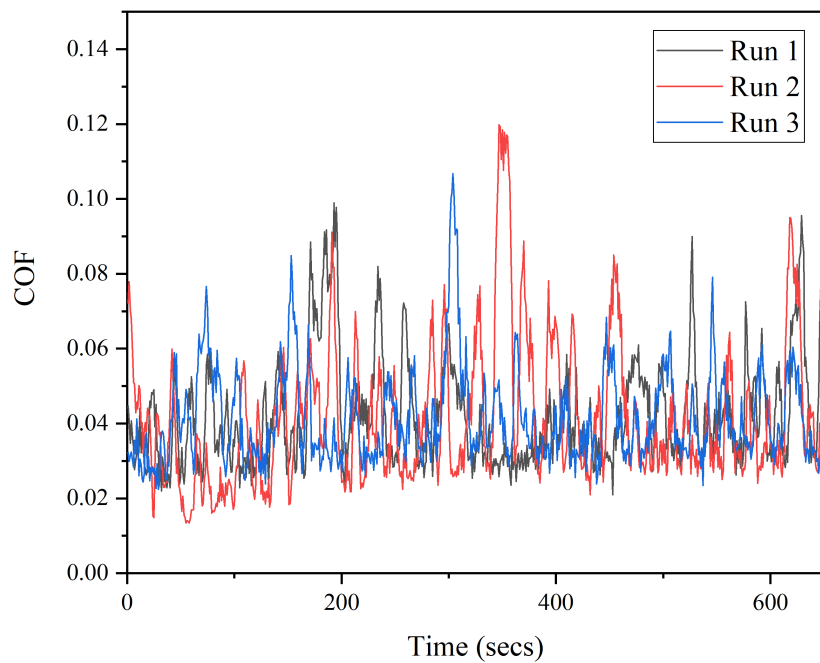
Figure 8.23: COF of HTS-Coating A-thin-smooth under nanofretting with 10 mN load using a 170 μm radius probe.

219

The effect of a larger load is seen in Figure 8.24 where friction is seen to be reduced further. The spikes in friction are seen less frequently across the fretting time.
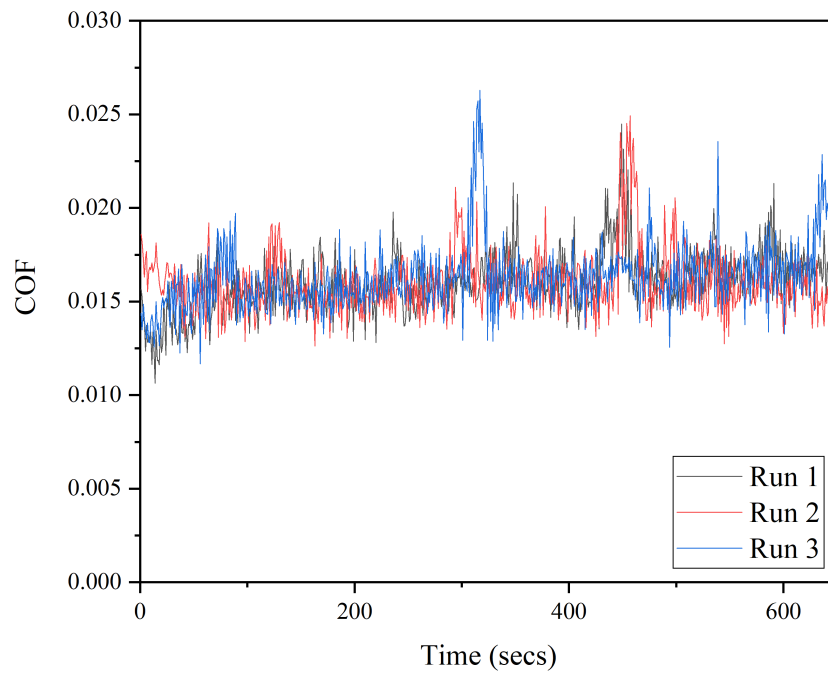
Figure 8.24: COF of HTS-Coating A-thin-smooth under nanofretting with 100 mN load using a 170 μm radius probe.

The difference in average coefficient of friction is seen in Figure 8.25. The average COF for 10 mN was 0.04 and for 100 mN was 0.015.
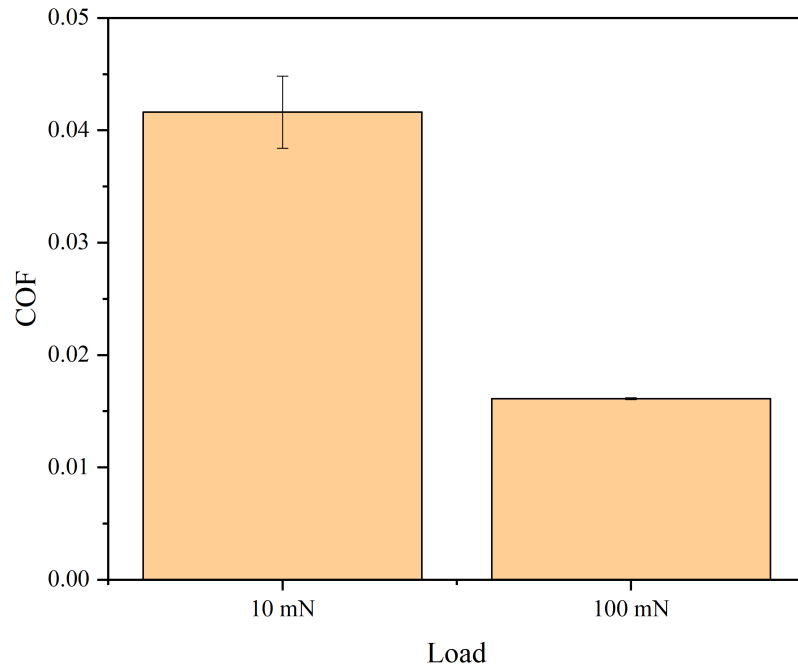
Figure 8.25: Comparison of the average COF of HTS-Coating A-thin-smooth under nanofretting at 10 mN and 100 mN.

8.3.2.2 Average Coefficient of Friction

Considering the morphology of the friction evolution with time seen in Figure 8.23 and 8.24, it makes sense to condense the friction data to average COF results for easier comparison. Figure 8.26 shows the average friction of the HTS samples tested at 10 mN load. Very different behaviour is seen compared with that of the micro-scale fretting across the board. The highest friction is instead seen with the rough coating preparations on Coating A with a value of approximately 0.055. Coating A-thin-smooth sees the lowest friction with a COF of 0.04. Larger error bars are seen in all tests corresponding to the unstable friction signals displayed with Figure 8.23.
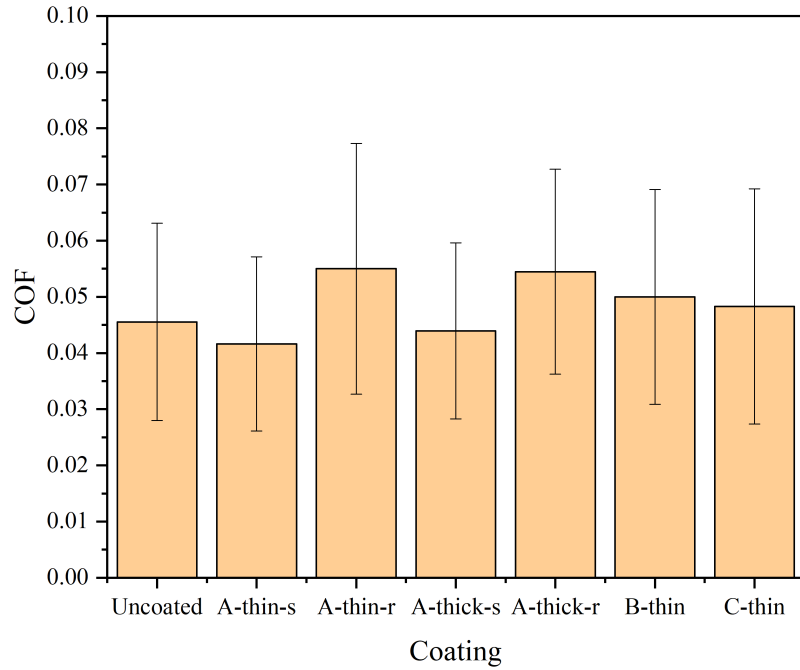
Figure 8.26: Average COF of coatings on HTS at 10 mN load.

Increasing the load counter-intuitively decreases the COF (in comparison to macro-scale tribology) as seen in Figure 8.27. Additionally, the opposite behaviour is seen in comparison with tests at 10 mN with Coating A-thin-rough having the lowest friction of 0.010. The highest COF was with the uncoated substrate, Coating A-thick smooth and rough with a value of approxiamtely 0.018. Smaller error bars are seen corresponding to the slightly smoother signal of Figure 8.24 compared to the 10 mN load.
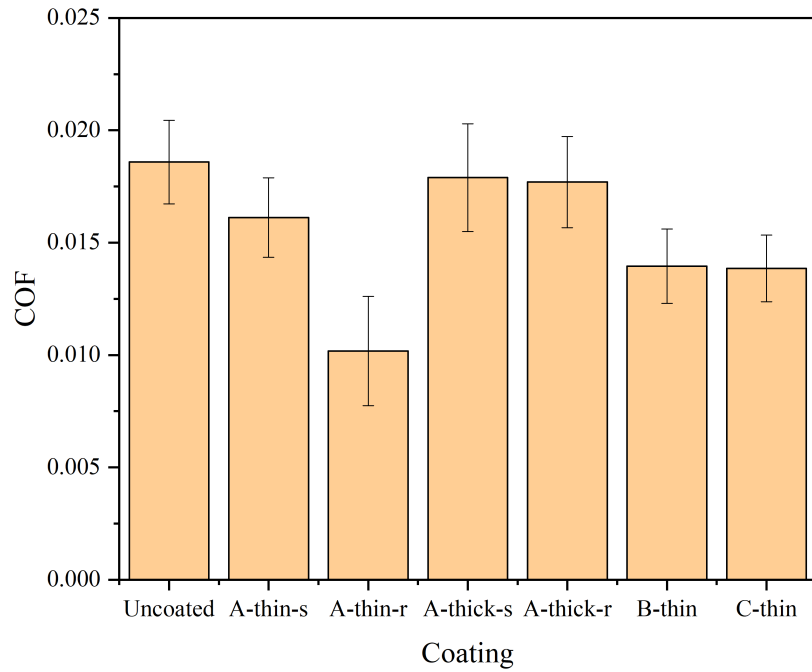
Figure 8.27: Average COF of coatings on HTS at 100 mN load.

The coatings deposited on SS tested at 10 mN are shown in in Figure 8.28. These display high error in their average COF similar to HTS as shown in Figure 8.26.
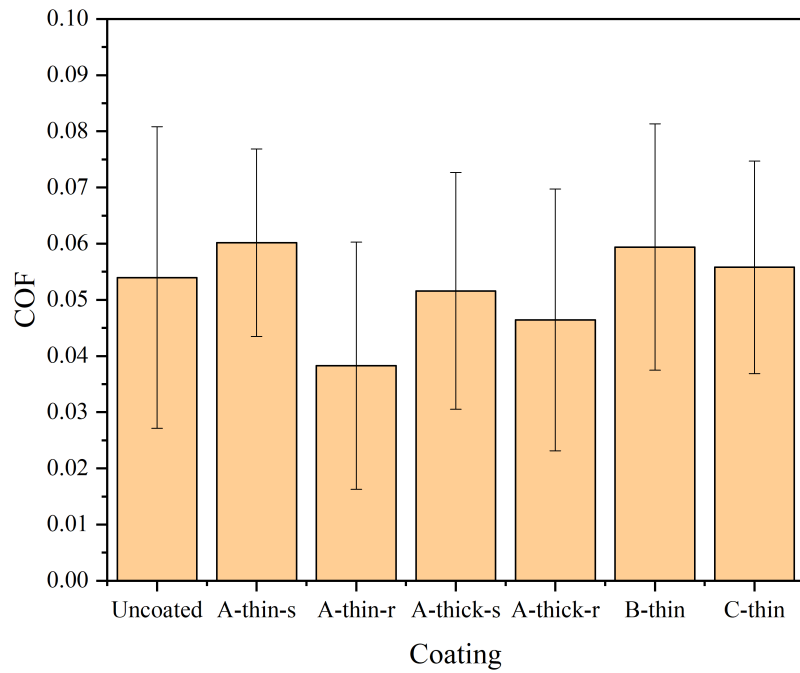
Figure 8.28: Average COF of coatings on SS at 10 mN load.

Figure 8.29 shows the average COF with 100 mN load. An extremely small COF is

recorded with these samples however less variance is noted per sample than with the HTS coatings.
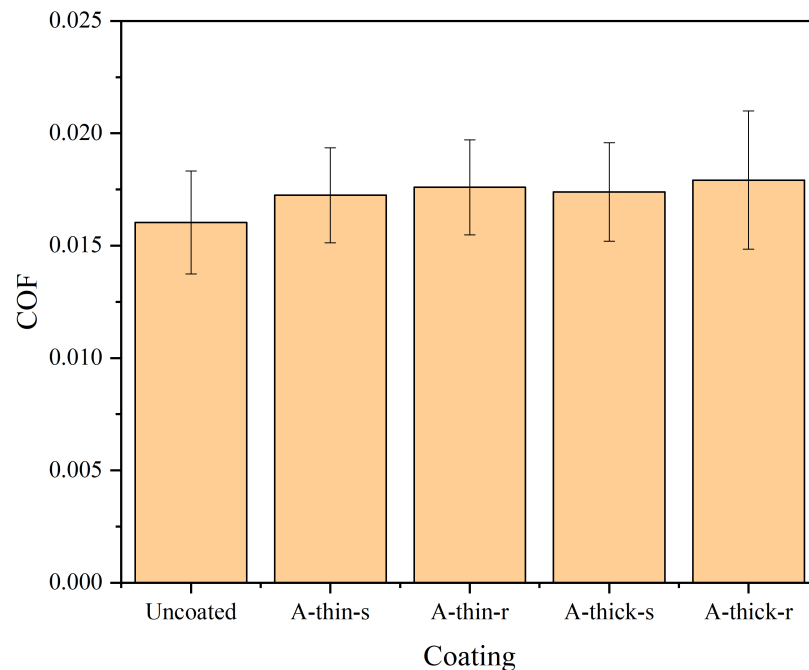
Figure 8.29: Average COF of coatings on SS at 100 mN load.

8.4 Discussion

8.4.1 Micro-fretting

8.4.1.1 Performance of Different DLC Types

Friction coefficient is generally not directly measured as often as wear in fretting tests. Wear is a far more present issue due to its severity by either crack nucleation and propagation (under cyclic fatigue conditions) and eventual formation of wear debris [98]. Friction does however play a part in determining the regime of fretting currently being experienced alongside the displacement relative to the contact area [95–97, 450]. An energy based approach is often favourable as this can quantify the fretting lifetime and predicted wear depth [450]. The application of coatings to protect against fretting damage has been long understood. Coatings that have residual compressive stresses can be particularly useful as they protect against cracking phenomena [451].

Liskiewicz et al. [452] analysed the durability of a series of hard coatings under fretting wear establishing the total dissipated energy density allowable to the coating system before failure occurs. The mechanical properties of these coatings were noted to affect their durability with a high Young's Modulus producing the highest wear (on TiN). The difference in modulus between the substrate and coating negatively affected wear performance, leading to easier deformation of the substrate and brittle cracking generating wear

particles. Comparing the modulus differences in Table 4.2, this is less of a concern with these coatings however the tests were not ran till failure so this could be investigated with longer scale tests.

In an approach where a coating is being chosen to protect a surface, a reduction in tangential force (when visualised as part of a fretting loop/map) will result in a lower coefficient of friction and therefore reduce the dissipated energy over a number of fretting cycles [100]. This should reduce the amount of wear and increase coating lifetime. Therefore an investigation into the relation between mechanical properties and their prediction of frictional and wear performance is beneficial for future coating optimisation in fretting wear scenarios.

Surface roughness is seen to be a key factor in the fretting control. Though a lower COF is seen with a higher surface roughness, the wear rate is seen to be higher with increased surface roughness and this also decreases the activation energy (energy required for the onset of cracking) required for wear. Therefore though the coefficient of friction is generally seen to be higher, a smoother surface is more beneficial in the reduction of wear [103]. Increased wear is probably, in part, due to the increased maximum contact pressure seen with rougher films which may also increase the formation of wear debris (asperity deformation, work hardening and tensile cracking at the asperity root leading to fracture and generation of debris) as noted by Jiang and Arnell [281]. This does however explain the lower COF seen with the rougher coatings. The application of a thicker coating will change the maximum tensile stress of a coating system with a thicker coating allowing it to occur at the substrate/coating interface rather than at the surface for a thin coating [83]. In a fretting contact, this effectively reduces the amount of wear debris created. This would additionally mean a greater dissipated energy density to fail the coating [105, 450].

Taking into account both the surface roughness and thickness and analysing the friction in Figures 8.10, 8.11 and 8.14, we can see that Coating A (with the highest H/E) ratio is seen to perform the best across both substrates. Further differences in the dissipated energy (Figures 8.16, 8.17 and 8.18) can be seen to correspond with the surface roughness of the coatings as seen in Table 7.3. The friction of uncoated metals under fretting conditions is generally seen to be high with values of around 0.8 seen for AISI1034 and Ti-6Al-4V alloys with a 52100 steel ball (with diameter of 25.4 mm) [103]. This is similar to the two uncoated substrates.

Fretting tests were performed previously on W-doped DLC (Balinit C Star, Oerlikon Balzers) on Ti-6Al-4V and SCMV steel by Mohd Tobi et al. [453], though at a lower contact pressure (due to the larger contact area). No delamination of the coating was observed and a COF of 0.3 was seen for the DLC layer. This is within the range seen in Figures 8.10 and 8.14 though increases in friction were seen due to layer wear through. This increase in friction was also seen with Balinit C Star. Blanpain et al. [454] compared the fretting wear of a series of carbon coatings and found that the COF was between 0.05 and 0.10 (with a 10 mm diameter corundum ball) depending on the deposition methodology employed to create the DLC (either radio fequency (RF), arc or laser). Additionally, the wear rate was found to be smaller compared to TiN. The low friction was supposed to be due to the formation of a graphitised transfer layer. The formation of wear debris in Figures 8.19 and 8.20, point towards that a lubricating third body could be present in the DLC coatings.

8.4.1.2 Effect of Changing the Loading Conditions

Increasing the load from 20 N to 40 N on the coated and uncoated HTS samples saw an increase in the maximum contact pressure to approximately 1.5 GPa and a reduction in

the sliding ratio to approximately 0.45. This reduction in sliding ratio is a result of the higher predicted contact area due to the high load, thereby creating conditions in which crack propagation is more likely. The initially high friction values seen early in the tests at this higher load (Figures 8.10b and 8.11b) correspond with transitions to the partial slip regime and back to gross slip thereby forming the mixed slip regime before settling into the gross slip regime once relatively stable friction conditions have been established [99]. Normal contact pressure was seen to affect the lubricating oil film and it has been shown that higher load reduces the effectiveness of the lubricant and increases COF [449, 455].

8.4.1.3 Effect of the Addition of Lubricants

Lubricants have been seen to be an effective method of reducing friction and wear in fretting contacts [451]. All lubricated contacts displayed instability in the COF at the beginning of the fretting cycles due to stick slip (Figures 8.12, 8.13 and 8.15). The performance of oils when applied to fretting contacts has been seen to be greatly affected by viscosity though their presence reduces wear drastically [108, 449, 455]. Neyman [455] investigated the effect of changing viscosity and boundary lubrication properties of oil in fretting mild steel. He found that the boundary lubrication properties affected the wear volume to a greater degree than the viscosity. Shima et al. [449] found that the viscosity affected the friction coefficient after stick-slip with higher viscosity showing higher COF. This was assessed to be due to oxygen access inhibition but could also be due to the increased viscosity affecting entrainment into the contact. This explains the decreased performance (increased COF) of the FF oil and those with MoDTC added (as its an extremely viscous additive and increases the viscosity of the oil blend).

As dissipated energy relates to wear in a fretting contact, we would expect any adverse interactions with the MoDTC additive to see a drastic increase in dissipated energy however this was not the case comparing Figures 8.12, 8.13 and 8.15. The addition of MoDTC generally reduced the friction and dissipated energy particularly with the uncoated samples. MoDTC is seen to readily react on hydrogenated carbonaceous surfaces to form MoS_2 and MoO_3 though some other Mo and C containing containing compounds have been noted with steel counterparts. The MoS_2 is only found in the contact however [456, 457]. Differences in the wear behaviour with MoDTC/DLC interactions are reported, Kosarieh et al. [125] found that the formation of the MoDTC tribofilm reduced the friction but increased the wear with a DLC film. The interaction with iron accelerated this interaction by the possible formation of molybdenum containing species that lead to the breaking of C-C/C-H bonds from the DLC matrix; the exact mechanism, however, is an ongoing area of study. Al-Jeboori et al. [458] reported on high wear with DLC and found that tribofilm build-up was related to the ratio of rolling to sliding with MoS_2 seen in pure sliding. The reduction in displacement with fretting may affect the additive breakdown and formation of commonly found tribofilm components. Kassim et al. [124] found that the COF changed with the formation of different intermediate materials which was not seen with this fretting testing. Longer scale tests and analysis of possible film formation with Raman spectroscopy or x-ray near edge structure technique [459] would be helpful for future characterisation.

8.4.2   Nano-fretting

Previous nano-fretting (or nano-wear as it was sometimes called), using the NanoTest platform, focused inducing accelerated wear and measuring the resulting wear depth [148,

149, 318, 460]. Nano-fretting tests on DLC coatings similar to those produced for this study showed increasing friction with wear cycles and COF behaviour ranked with H/E ratio however a smaller radius probe was used (5 μm radius) with a larger track length (13.4 μm) [428]. Yu et al. [145] performed nano-fretting using an AFM and were able to record friction; however, they were limited by the loads and number of cycles employed. As can clearly been seen in observing the friction differences compared to the micro-scale fretting (comparing Figures 8.23 and 8.24 with 8.10 and 8.14), despite nominally the same contact pressure employed there is no link between the two length scales with the parameters employed in this testing. In the testing of thin coatings (TiN and DLC) on three length scales, Drees et al. [461], found that the nano-friction was not dominated by deformation and third body influences but adhesion and molecular interactions.

Though dry fretting in the micro-scale shows excellent correlation with the coating mechanical properties, this is not the case with nano-fretting in these tests [462]. Due to the large radius of the probe employed in this testing, a significantly reduced ploughing component is seen. Comparing the interfacial component of friction measured with this probe 0.017 in Table 7.2), we can see almost zero ploughing is experienced in some tests (Figure 8.29). At lower loads, on this length scale, increased roughness is seen to correlate with lower friction whereas when the load is increased the opposite occurs. The measured mechanical properties as seen in Table 4.2 appear to have little bearing on tribological properties however it is well known that at the nano-scale stick-slip and the formation of meniscus bridges are more dominant in friction especially at low velocities (under lubrication) [422]. With smaller AFM tips (generally up to 15 μm radius [463]) the friction coefficient of DLC at high velocities can be as high as 0.5 [464] however at higher humidities (50 %) 0.15 is more common (with Si_3N_4 AFM tips) [422]. This is due to graphisation and interposition of water molecules whose interaction with the DLC hydrogen-terminated dangling bonds with weak van der Waals reduces the friction [279]. Bhushan and Sundararajan [463] found that tip radius and relative humidity had an effect on the nano-friction of thin films.

The tests performed at 10 mN display higher friction than those performed at a 100 mN (clearly demonstrated in Figures 8.23, 8.24 and 8.25). Several mechanisms could be at work to explain the decrease in COF at higher loads. As seen in Figure 8.24, there is some instability in the friction which corresponds to the lower COF generally seen with partial slip fretting at lower displacement amplitudes [465]. Additionally, the use of a larger probe with mN loads will give a scenario more like a macro-scale tribological test with reduced real contact area and contact pressure [68] though the contact pressure of a single asperity may be high. Tambe and Bhushan noted that even with AFM tips, there is the possibility for multi-asperity interactions despite it generally being considered single asperity [422]. Therefore with the higher load, it is likely that there is less conformal contact with the probe contacting with fewer asperities causing the lower COF. Garabe-dian et al. [466] presented a method of fabricating and calibrating larger AFM probes (approximately 30 μm radius) capable of mN force measurements however little work has been performed with them. The use of these larger probes along with the sensitivity of an AFM may be able to further investigate this phenomenon.

Chen et al. [147] found that the phase transformation to form a graphitised transfer layer could not occur in the slipping interface of DLC/SiO_2 pairs during nanofretting. They attributed the low friction of the DLC to its high hardness and hydrophobic properties. A much smaller radius of tip was used in this study resulting in more conformal asperity contact giving a steady state COF of approximately 0.2. Though tested in at a higher length scale (using a 10 mm diameter 52100 steel ball as a counterface) Blanpain et al. [454] indicated that the low friction and wear seen with CVD diamond was due to

the formation of a transfer layer on the diamond surface. This could be beneficial to low friction in a DLC/diamond contact as seen in these tests. Extremely low friction (within the realms of superlubricity[1] has been seen with DLC previously (as low as 0.001 with self-mated a-C:H [130]). DLC on DLC contacts with high levels of hydrogenation show extremely low friction due to the repulsion of positively charged hydrogen protons. The formation of an sp^2 rich carbonaceous transfer film is noted to be universal though it is affected by the contact parameters and environmental conditions [130].

The shape of friction signals in Figures 8.22 and 8.24 resemble that seen by Berman et al. [132] in the evaluation of graphene nano-scroll formation in humid environments. It is extremely unlikely there are any similarities between the two processes as no nanodiamonds were introduced for this study (as were used by Berman et al. [132]) but it could be possible that fractured particles from rougher DLC surfaces could provide similar function. TEM or high magnification SEM would be ideal to further investigate the interface as performed previously in superlubricity studies [69, 132]. The adaptation for in-situ electron microscopy would answer further key questions for this puzzling behaviour particularly the reduction in friction seen with larger radius probes.

8.5   Summary

In this study, multi-scale fretting testing was performed with micro-scale testing utilising an electro-dynamic shaker and nano-scale utilising a piezo-driven vibratory stock to assess the relation between coating H/E ratio and coefficient of friction. Various lubricant combinations were also employed to assess their effect on the coefficient of friction and whether the additives used were of benefit to reducing friction in the gross slip fretting regime.

Under dry conditions in micro-scale fretting, the coatings perform according to their H/E ratio with Coating A displaying the lowest COF and dissipated energy. An increase in surface roughness is seen to further decrease the steady state COF. Coating C is worn through on both HTS and SS. No load support effects were seen in changing the substrate. Increasing the normal load increased the length of time the coatings spend in the stick-slip regime before steady state friction is established and also increases the dissipated energy over the fretting cycles. The rough preparation of Coating A is seen to perform well under higher normal load. Increased surface roughness was seen to be more beneficial to reducing COF and dissipated energy than increased coating thickness.

At a lower normal load the addition of lubricants is seen to be more effective than at a higher load though the COF was reduced in both cases. The time to stabilise the friction was far greater under higher normal load. The COF results with the lubricants tended to show that the less viscous lubricant (i.e. without the MoDTC additive) was more effective. The inclusion of additives did however decrease the dissipated energy. No adverse wear was seen as a decrease in dissipated energy was observed (correlating to less wear) with the addition of the MoDTC additive. The increased wear of DLC observed by Kosarieh et al. [125] was not seen in the tests performed here.

The effects of friction modifiers present in the lubricants in the micro-fretting was shown however characterisation of the exact composition of the tribofilm was not performed as the main aim of this study was to simply assess the frictional performance of the coating lubricant system and evaluate the factors affecting the coefficient of friction of each test. It would be beneficial in future work to analyse the tribofilm formed and

---

[1]Superlubricity is defined as a coefficient of friction value below 0.01 [69]).

assess the dynamics of it throughout the testing time. The possibility of modifying a Raman microscope to assess the in-situ tribofilm formation would allow for analysis without extraneous repeats. Further study should also analyse the lubricant interactions on the doped DLC coatings as the addition of the doping elements will affect the surface chemical interactions with the lubricants.

At the nano-scale, surface roughness is seen to be the main variable determining the COF. Tests performed with the 200 µm radius probe show a marked reduction in the measured coefficient of friction due to the reduced ploughing component and interaction more akin to macro-tribological interaction with limited asperity interaction. At lower loads the COF corresponds to lower surface roughness however at higher loads the opposite is true. At higher loads the combination of limited asperity contact and partial-slip fretting explains the low COF with, in some cases, nearly zero ploughing component. There is also the possibility of the formation of a graphitised layer. Friction was more stable with the larger load however variability attributed to surface roughness effects was seen at both loads.

Due to the use of a piezo-driven oscillator to induce the displacement of the wear counterface in the nano-fretting module no real time displacement data can be obtained. Though the pre-test calibration ensures that, at maximum, the module will reach the desired oscillation distance it would be beneficial to further develop the capabilities of this module allow it to measure displacement in real time. Additionally, the thermal expansion of the stage affected the depth measurements meaning that accurate wear depth could not be measured in this project using the nano-fretting module. Section 11.5 will detail possible improvements to this module.

Future studies utilising nano-fretting should investigate a greater number of cycles with a thinner coating so that failure can be induced and observed using either SEM or AFM. A greater number of cycles should also be employed to properly investigate the wear through of the coatings and evaluate the global energy input required to cause failure as employed previously by Liskiewicz and Fouvry [105]. Post-test Raman spectroscopy could be used to identify the level of graphitisation experienced by the coatings (measurable change in the I_D/I_G ratio within the wear scar) [286] and this could be correlated with nanoindentation mapping of the fretting scars [102] to track the dynamic change the coating structure with wear (measurable softening of the coating due to the change of structure). Contact profilometry would be another excellent addition to the roster of techniques used to characterise the fretting wear, white light interferometry was attempted for these samples however the roughening due to wear made it difficult to acquire accurate wear volume data.

Chapter 9

Frictional Performance of DLC Coatings under Nano-Scale Reciprocating Sliding

9.1   Introduction

Wear tests in the reciprocating regime (with pins or balls) are generally seen on the macro-scale where the true contact area is obscured and is presumed to be a fraction of the apparent contact area [50, 68]. The result is that the true contact pressure will be much higher in parts of the contact than the calculated nominal pressure. Generally, this motion is chosen to replicate specific test conditions such as sections of a piston in an engine. By moving to smaller scale, the contact conditions can be simplified to a nominally single asperity interaction allowing for the onset of wear and fundamental friction to be studied with respect to topography and mechanical properties [37, 68]. This brings us closer to the underlying mechanisms in tribology as wear begins at the asperity contacts [55, 191]. The probe geometry and load can be varied to greater degree to match larger scale conditions or (as is more often the case) to drive failure at a faster rate than macro-scale tests [282]. AFMs are typical of this test scale due to the small radius of probes resulting in high contact pressures however the tips for performing nano-wear tests tend to be much more expensive and are more susceptible to wear and deformation from the nominal radius and shape [133, 138].

To bridge the gap in high cycle reciprocating wear tests in the mN range, Micro Materials have developed a new NanoTriboTest module for the NanoTest Platform [467]. Gee and co-authors [468, 469] developed a similar system that is able to be operated in-situ with an SEM however it is limited in its load range and total number of cycles. Others have also shows that reciprocating wear tests in the mN range have benefit in determining underlying tribological mechanisms [133, 137, 460, 470, 471]. Due to the specifications of the NanoTest platform it is ideal for reciprocating wear tests as it has a varied load range and high thermal and mechanical stability. DLC coatings generally show a strong correlation to mechanical properties in their tribological performance however the test conditions (contact pressure) can show differences that are interesting to investigate particularly as longer sliding distances on smaller length scales have not yet been explored [150, 282, 428]. The results presented form part of an recently published in Tribology International [472].

9.2 Methods And Materials

9.2.1 Materials

The coatings studied in this chapter share similar structure and composition to the DLCs produced for this study and were, in fact, the designs upon which they were based having been produced for an earlier study before the start of this project [282]. Table 9.1 shows the coating layer structures and measured thickness. Designated coatings A and B share approximately the same adhesive (Cr) layer and a slight increase in the thickness of the gradient (W-C:H) layer. Coating C's design deviates the most from the main coatings in this study with only a CrN adhesive layer (of 1 μm thickness) and no gradient layer present. The top DLC layer is closer to the amount deposited for the thicker coatings of this study. Coatings A and B were deposited using PECVD with the Hauzer Flexicoat 850 system. Coating C was a sputter deposited commercial coating (Balinit C Star, Oerlikon Balzers) with alternating carbon and WC layers giving a microlamellar structure [473]. All the coatings were deposited on hardened M2 tool steel. The surface roughness (R_a) was 11–12 nm for all coatings [282].

Table 9.1: Multilayered coating architecture and thickness for NanoTriboTest coatings. Adapted from [282].

Coating Architecture	Layer Structure	Adhesive layer thickness (μm)	Gradient Layer thickness (μm)	DLC layer thickness (μm)	Total thickness (μm)
a-C:H (A)	Cr + W-C:H + DLC	0.3 (Cr)	0.7 (W-C:H)	2.9 (DLC)	3.9
Si-a-c:H (B)	Cr + W-C:H + Si-DLC	0.3 (Cr)	0.7 (W-C:H)	2.8 (Si-DLC)	3.8
a-C:H:W (C)	CrN + a-C:H:W	1.0 (CrN)	–	2.0 (a-C:H:W)	3.0

The following tables will present data pertinent to the discussion of the results gained using the NanoTriboTest methodology but were obtained as part of an earlier study [282]. Table 9.2 shows the coating mechanical properties determined by nanoindentation using a Berkovich diamond indenter following the ISO14577 standard. Area function of the indenter and frame compliance were calibrated by indentation into a fused silica and single tungsten crystal reference samples. A maximum indentation load of 20 mN was used resulting in contact depths in the range of 4–8 % of the total coating thickness. 10 repeats were carried out at this load each with a loading time of 20 s, hold time of 5 s at maximum load and an unload time of 20 s. Thermal draft was corrected with a 60 s hold period 60 s prior to the load ramp and after 90 % unloading [282]. The hardness (H) and elastic modulus (E) values were determined by applying Oliver-Pharr analysis with $E = 1140$ GPa and $\nu = 0.07$ for the diamond indenter [168]. Errors in the H/E and H^3/E^2 values were calculated using Gaussian error propagation.

Table 9.2: Coating mechanical properties determined at nanoindentation load of 20 mN. Contact depths were 4–8 % of the total coating thickness. Adapted from [282, 474].

Coating Architecture	H (GPa)	E (GPa)	H/E	H^3/E^2 (GPa)
A	23.4 ± 1.2	226 ± 13	0.104 ± 0.008	0.251 ± 0.030
B	16.2 ± 0.6	157 ± 4	0.103 ± 0.005	0.172 ± 0.013
C	11.5 ± 0.9	161 ± 7	0.071 ± 0.006	0.059 ± 0.009

Nano-scratch tests were performed using a progressive load technique (3 pass, topography-scan-topography) up to a maximum load of 500 mN with a sphero-conical diamond of radius 5 μm. [282]. Table 9.3 shows the critical load values determined by nano- and micro-scratch test.

Table 9.3: Nano-scratch (500 mN peak load) and micro-scratch (5000 mN peak load) critical loads. Adapted from [282, 474].

Coating	Nano-scratch (R = 5 μm)			Micro-scratch (R = 25 μm)			
	L_y (mN)	L_C1 (mN)	L_{C2} (mN)	L_y (mN)	L_C1 (mN)	L_{C2} (mN)	CPR$_S$ $L_{C1}(L_{C2}-L_{C1})$ (N^2)
A	206 ± 5	422 ± 4	> 500	356 ± 9	2179 ± 120	2612 ± 127	0.94 ± 0.38
B	110 ± 10	445 ± 12	> 500	383 ± 52	1827 ± 111	2830 ± 367	1.83 ± 0.71
C	68 ± 4	> 500	> 500	375 ± 49	2256 ± 116	3695 ± 132	3.25 ± 0.43

Friction was measured on-load using a strain gauge probe as part of the scratch methodology. Measurements were performed using both the nano-scratch and micro-scratch methodologies however only the micro-scratch friction is reproduced here as the probe used matches that used on the NanoTriboTest [282]. Table 9.4 shows the friction values determined under micro-scratch testing at different loads.

Table 9.4: Friction coefficient at 100 mN and 500 mN loads in micro-scratch testing. Adapted from [282, 474].

Coating	μ at 100 mN	μ at 500 mN
A	0.067 ± 0.015	0.077 ± 0.013
B	0.084 ± 0.021	0.082 ± 0.003
C	0.079 ± 0.015	0.108 ± 0.003

9.2.2 NanoTriboTest

The reciprocating tests were carried out using a NanoTriboTest module installed into a NanoTest Vantage platform. In the NanoTriboTest module, the reciprocating stage (Physik Instrumente, Germany) is controlled independently of the instrument loading head. A 25 μm radius diamond probe was used to perform 500 cycle reciprocating wear tests at loads of 10–500 mN on three DLC coatings.Table 9.5 shows the range of experimental conditions available with the NanoTriboTest module. Figure 9.1 shows an image of the NanoTriboTest module installed in the NanoTest Vantage.

Table 9.5: Typical experimental conditions of NanoTriboTest module [425].

Probe radii (μm)	25–5000
Applied Load (mN)	0–500
Sliding Speed ($mm\,s^{-1}$)	1–10
Scan Distance per cycle (mm)	1–40
Number of cycles	100–30000
Total sliding distance (m)	1–300
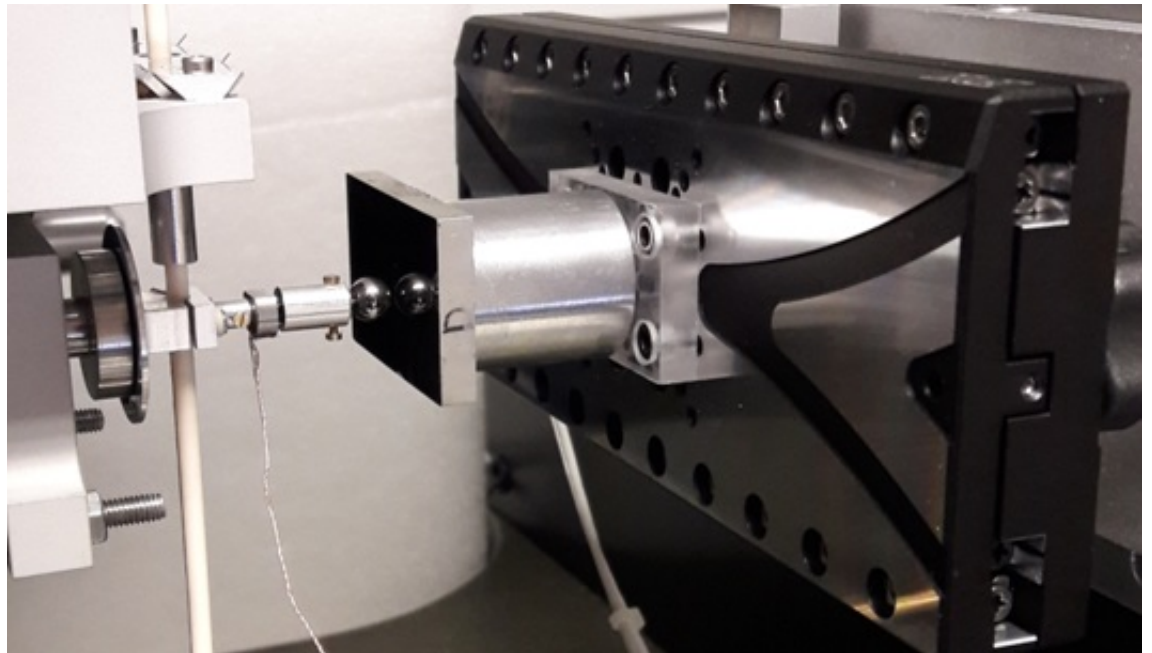
Figure 9.1: NanoTriboTest module in the Nanotest platform. From [425].

The track length was set to 1 mm in the NanoTriboTest with a maximum velocity of $0.5\,mm\,s^{-1}$ thereby giving a total sliding distance of 500 mm. The velocity was at maximum over the central 90 % of the track and linearly reduced to zero at the turn-around points. Each coating was tested at 10, 100 and 500 mN with 3 repeats. Additional tests at 50 mN and 200 mN were used for Coatings A and 50, 200 and 300 mN for Coating B. The friction force and the raw (unlevelled and lacking instrument drift or frame compliance corrections) probe displacements were monitored continuously and recorded over the entire wear track. As the reciprocating stage expands during the test, the on load depth data was only used to assess the topography change. The dynamic friction was calculated in software using Equation 2.17 [105]. The static friction measurement was approached in a similar way to that of Burris and Sawyer [475] to account for any transducer misalignment. Table 9.6 shows the calculated initial Hertzian contact pressures on each coating at each load. The Poisson's ratios used were 0.07 and 0.2 for diamond and DLC respectively. An E value of 1141 GPa was used for diamond and Table 9.2 shows the moduli values used for each of the coatings.

Table 9.6: Calculated initial contact pressures.

	Contact Pressure (GPa)		
Load (mN)	Coating A	Coating B	Coating
10	4.90	3.99	4.24
50	8.37	6.83	–
100	10.55	8.60	9.14
200	13.29	10.84	–
300	–	12.41	–
500	18.04	14.71	15.63

9.2.3 Confocal Microscopy

A Keyence VHX-6000 digital optical microscope with confocal capabilities was utilised to scan the surface of the samples to assess the wear volume (where measurement was possible), change in surface roughness and wear depth. As some of the wear volumes were below the range at which the resolution of the microscope is able to measure, these results are not available.

9.2.4 Stress Distribution Analysis

The Surface Stress Analyser (SSA, from the Saxonian Institute of Surface Mechanics) was used to determine the simulated stress distributions of von Mises, tensile and shear stresses at 100 mN with a 5 μm radius probe. This system uses a physical-based analytical method. The input parameters were:

- The Mechanical properties of the coatings (assumed to be monolayered) and substrate, i.e. H, E and H/Y (1.2 for coatings and 2.5 for the steel substrate).

- The coating thickness.

- Poisson's ratio.

- Probe radius, applied load and friction (taken from previous nano and micro-scratch data [282]).

9.3 Results

9.3.1 Friction

9.3.1.1 Friction Sensing

Before the friction behaviour of the individual coatings can be analysed, we must first assess the friction sensing capabilities of the new instrument. Figure 9.2 shows the unprocessed friction force varying with displacement across the surface of Coating A at 500 mN load. It can be clearly seen that the increase in amplitude after 25 mm is characteristic of a transition to higher friction coefficient. The ability to sense this change in friction within a few cycles demonstrates the systems use in measuring minute changes in the friction.
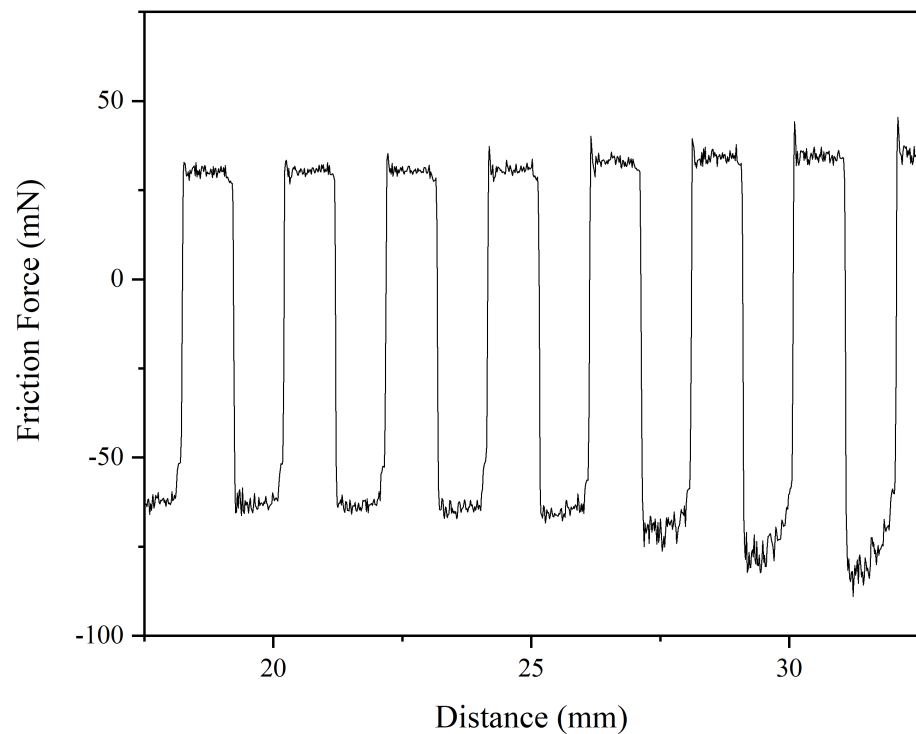
Figure 9.2: Unprocessed friction data of Coating A at 500 mN load.

Friction loops can been seen to also demonstrate this sensitivity to frictional changes as seen in Figure 9.3. The total contact stiffness of the system can also be measured at the extremities of track displacement. For Coating A at 500 mN, this was approximately 2000 N m^{-1}. Figure 9.3 is primarily to demonstrate the cycle to cycle sensitivity to friction changes however it must be noted that the track displacement is greater than the specified value of 1 mm. This is because the corrections normally applied to account for frame compliance and stage heating during testing have not yet been applied.
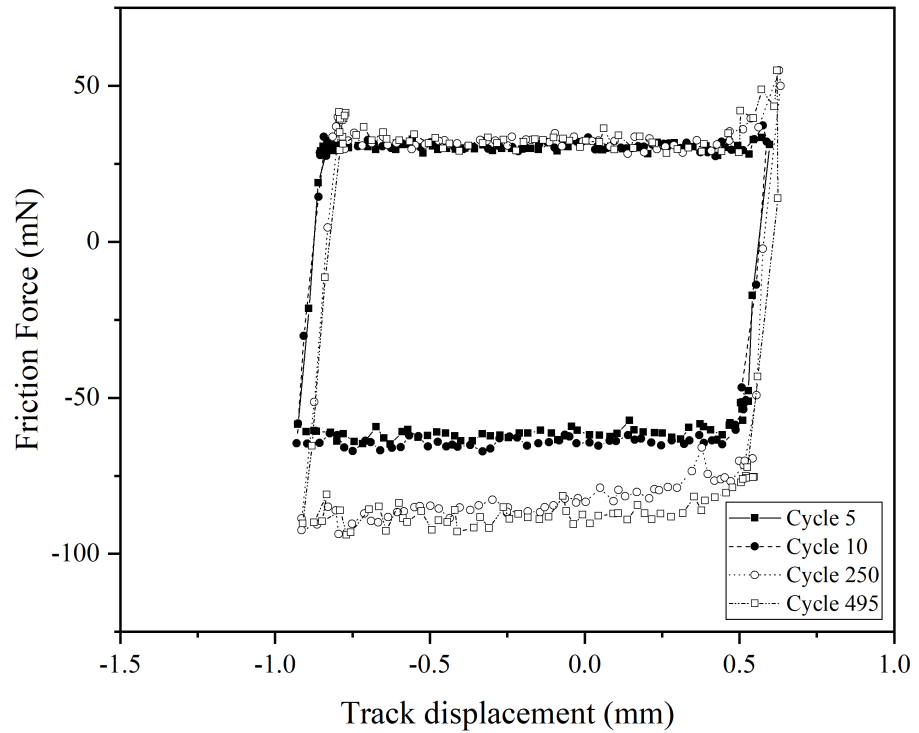
Figure 9.3: Raw (without corrections for thermal drift and frame compliance) friction loops on Coating A at 500 mN.

9.3.1.2 Coating A

The average friction of all loads on Coating A is displayed in Figure 9.4. The average COF is seen to be approximately 0.08 for all loads at the beginning of the cycles. The 10 mN load is seen to have more variability across the cycles than any other load. Apart from 500 mN, the friction coefficient is seen to decrease with increasing cycles with each load step.
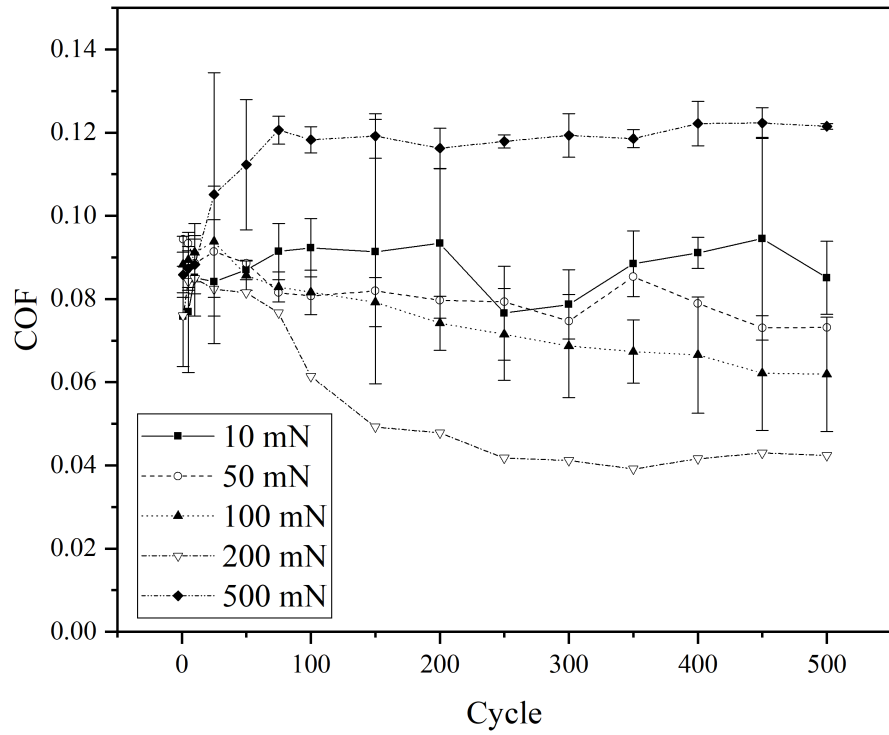
Figure 9.4: Average COF values for all loads on Coating A.

Figure 9.5 shows the COF evolution with cycles of the three wear tracks at 500 mN load. The COF has been averaged every 5 cycles. Repeat 1 shows a greater running in period and greater variability of friction across the sampling time. This run corresponded with the coating failing, the morphology of which can be seen in the next section.
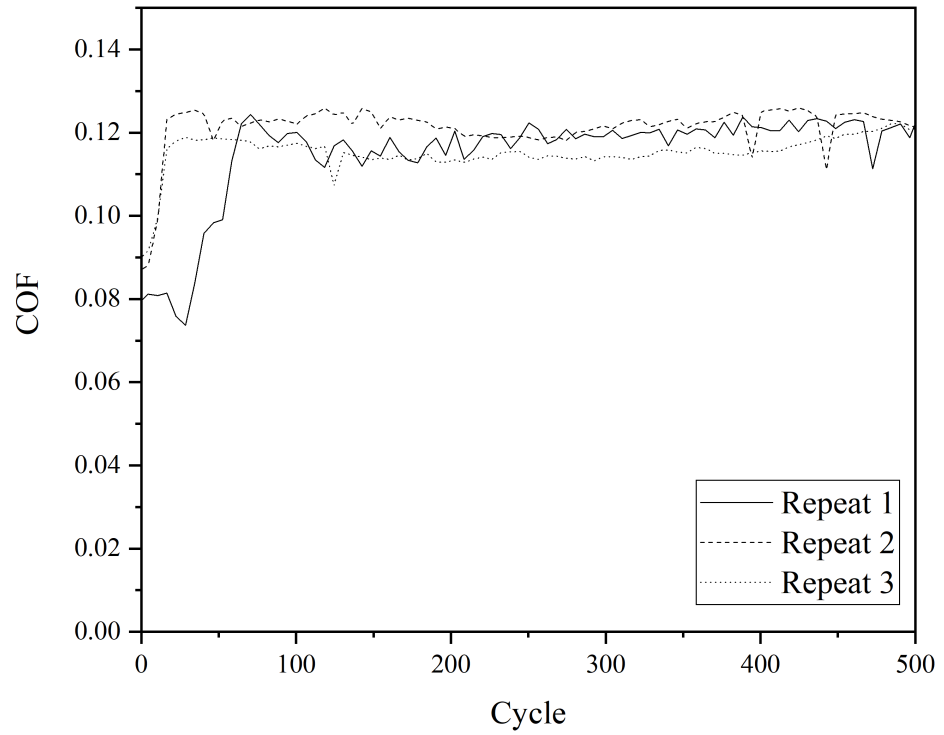
Figure 9.5: COF measurements for 3 repeats at 500 mN on Coating A.

Table 9.7 shows the average COF values across all the cycles at each load. This corroborates the observation of decreasing COF in Figure 9.4. The lowest COF value is seen at 200 mN load with a value of 0.051; conversely the highest value is seen at 500 mN with a value of 0.117.

Table 9.7: Average COF of Coating A measured at each of the applied loads.

Load (mN)	Average COF
10	0.087 ± 0.008
50	0.080 ± 0.005
100	0.073 ± 0.009
200	0.051 ± 0.014
500	0.117 ± 0.006

9.3.1.3 Coating B

The friction evolution at each load across all the cycles is seen in Figure 9.6. All loads saw approximately the same COF of 0.95 at the beginning. Little variation is seen otherwise apart from the 10 mN load which saw higher spikes in friction.
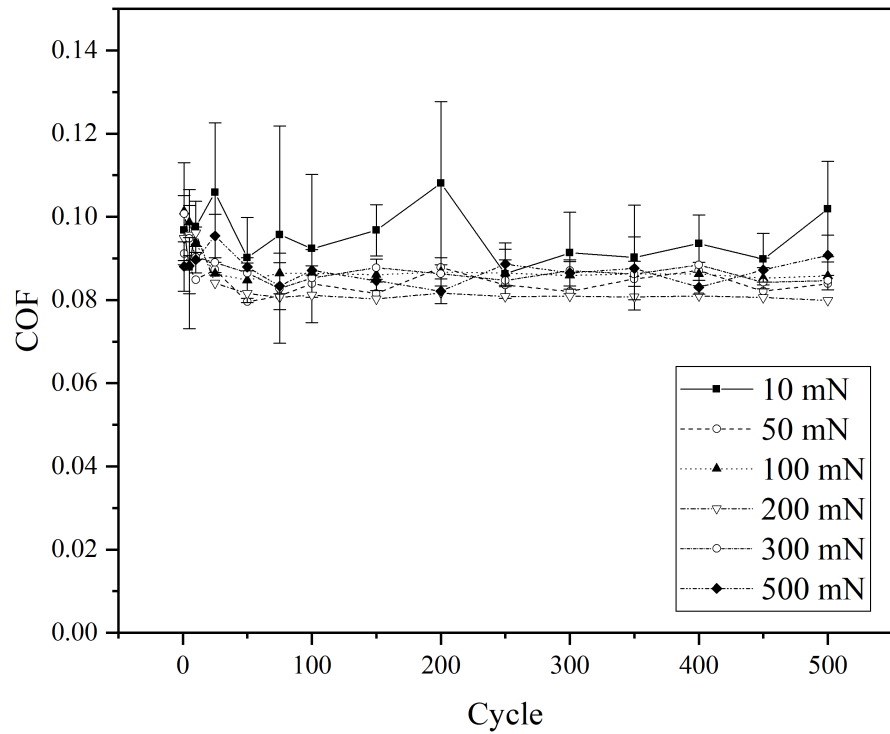
Figure 9.6: Average COF values for all loads on Coating B.

Figure 9.7 shows that the COF values across all repeats at 500 mN has little variance though some periodicity in the friction is observed.
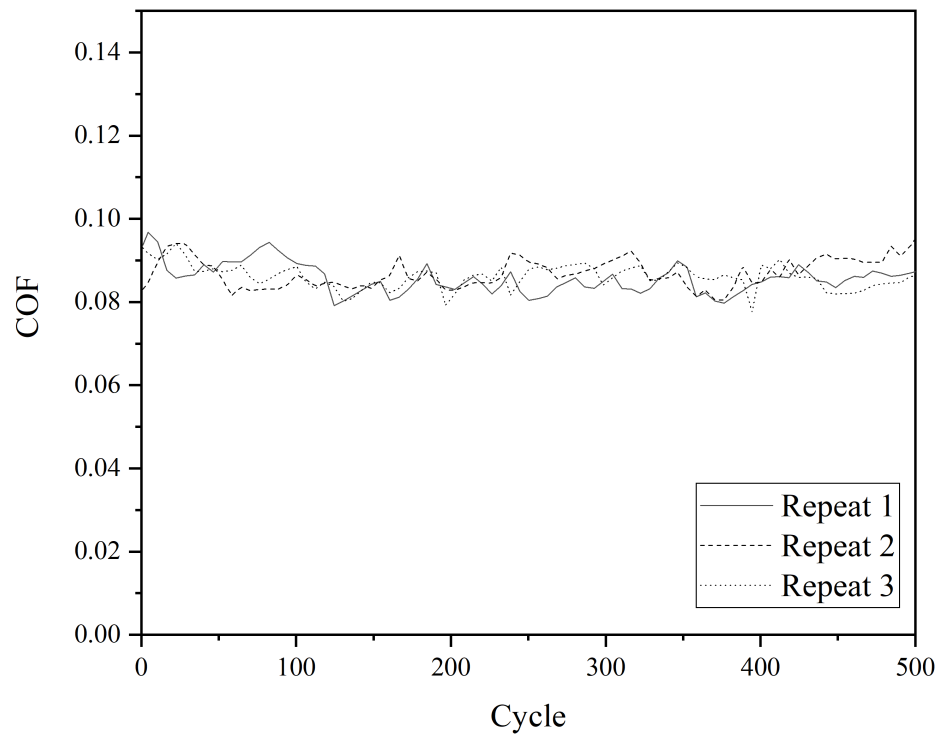
Figure 9.7: COF measurements for 3 repeats at 500 mN on Coating B.

Table 9.8 shows the average COF values across all the measured cycles for Coating B. Little change is seen in the average COF. The 10 mN load saw a high average friction coefficient of 0.093.

Table 9.8: Average COF of Coating B measured at each of the applied loads.

Load (mN)	Average COF
10	0.093 ± 0.005
50	0.083 ± 0.002
100	0.086 ± 0.002
200	0.081 ± 0.003
300	0.087 ± 0.002
500	0.087 ± 0.003

9.3.1.4 Coating C

Figure 9.8 shows that for the 10 mN load, there is more variance in the friction as it spikes to approximately 0.11 at 25 and 200 cycles. The highest COF at the start of the cycles is seen at 100 mN with a value of 0.1.
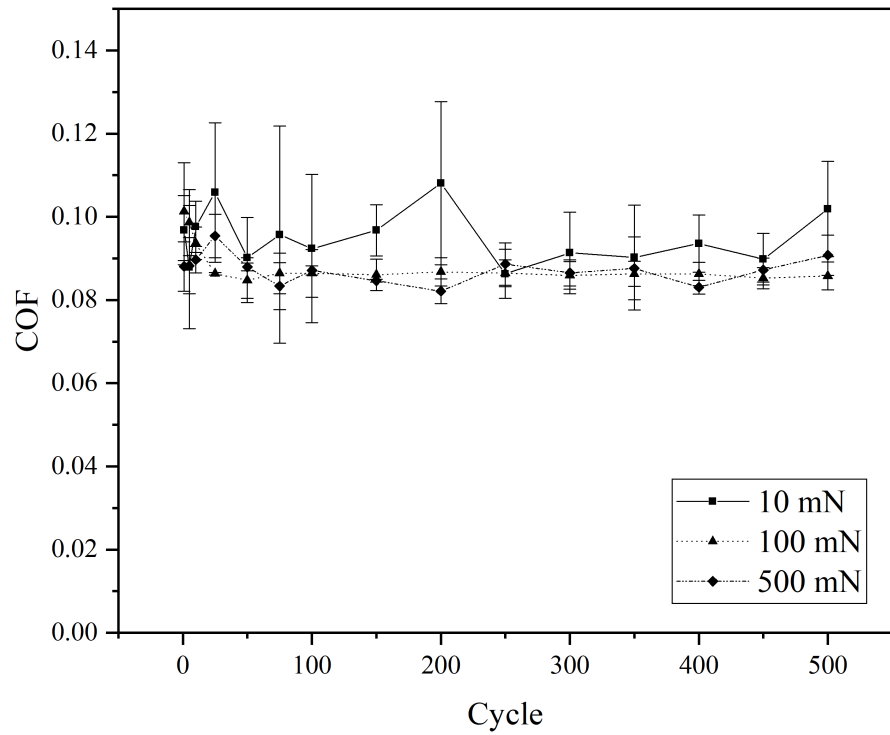
Figure 9.8: Average COF values for all loads on Coating C.

Figure 9.9 shows that for each repeat at 500 mN the friction decreases steadily from approximately 0.85 to 0.75 over the range of 500 cycles.
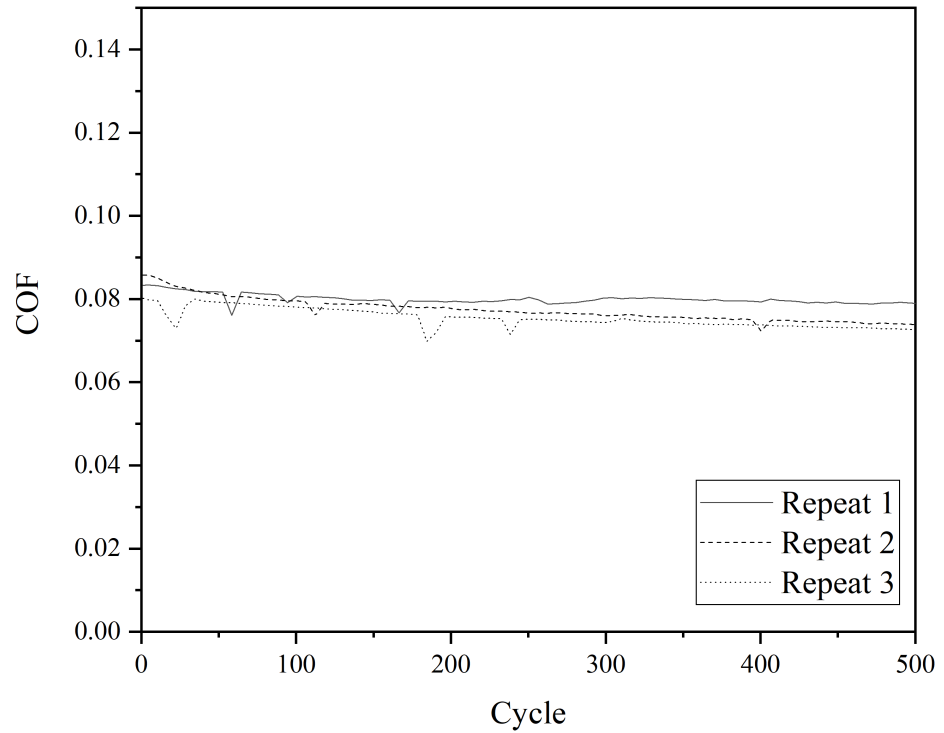
Figure 9.9: COF measurements for 3 repeats at 500 mN on Coating C.

Table 9.9 shows that as the load increases the average COF decreases. The lowest value with the lowest standard deviation is seen at 500 mN with a value of 0.078 ± 0.002.

Table 9.9: Average COF of Coating C measured at each of the applied loads.

Load (mN)	Average COF
10	0.094 ± 0.008
100	0.091 ± 0.003
500	0.078 ± 0.002

9.3.2 Wear And Surface Morphology

Figure 9.10 shows a confocal microscope image of one of the sets of wear tracks on Coating A. On the 100 mN and 200 mN tracks, a small amount of wear debris can be observed ejected around the edges of the tracks. The bottom (500 mN) track has failed over the majority of the track length.
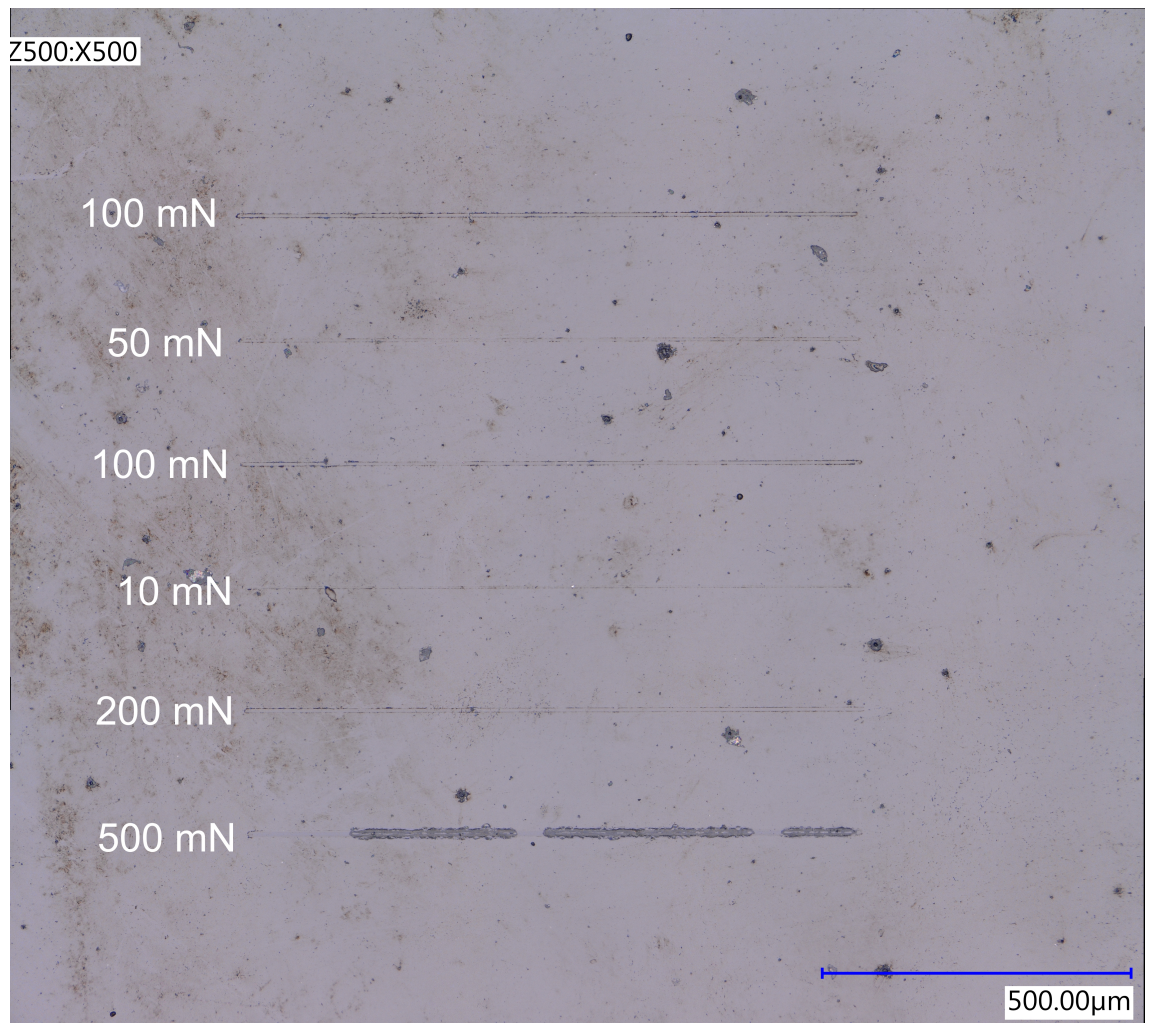
Figure 9.10: Micrograph of the wear tracks on Coating A. Loads are annotated on the figure. The 500 mN wear track shows the test in which the sample failed.

Figure 9.11 shows an SEM micrograph of the failed 500 mN load track. Abrasive wear tracks can be observed within the normal track on the left of the micrograph. The transition to failure appears to be abrupt however analysis of the depth during sliding showed a progressive increase in depth across the failed regions with increasing cycles. This depth was seen to be 1.5 μm greater than the abrasively worn regions. EDX analysis in these regions showed Cr and W exposure further demonstrating the thinning of the failed coating. In the failed regions, abrupt changes in friction were seen in the transition from the fractured to abrasive wear regions.
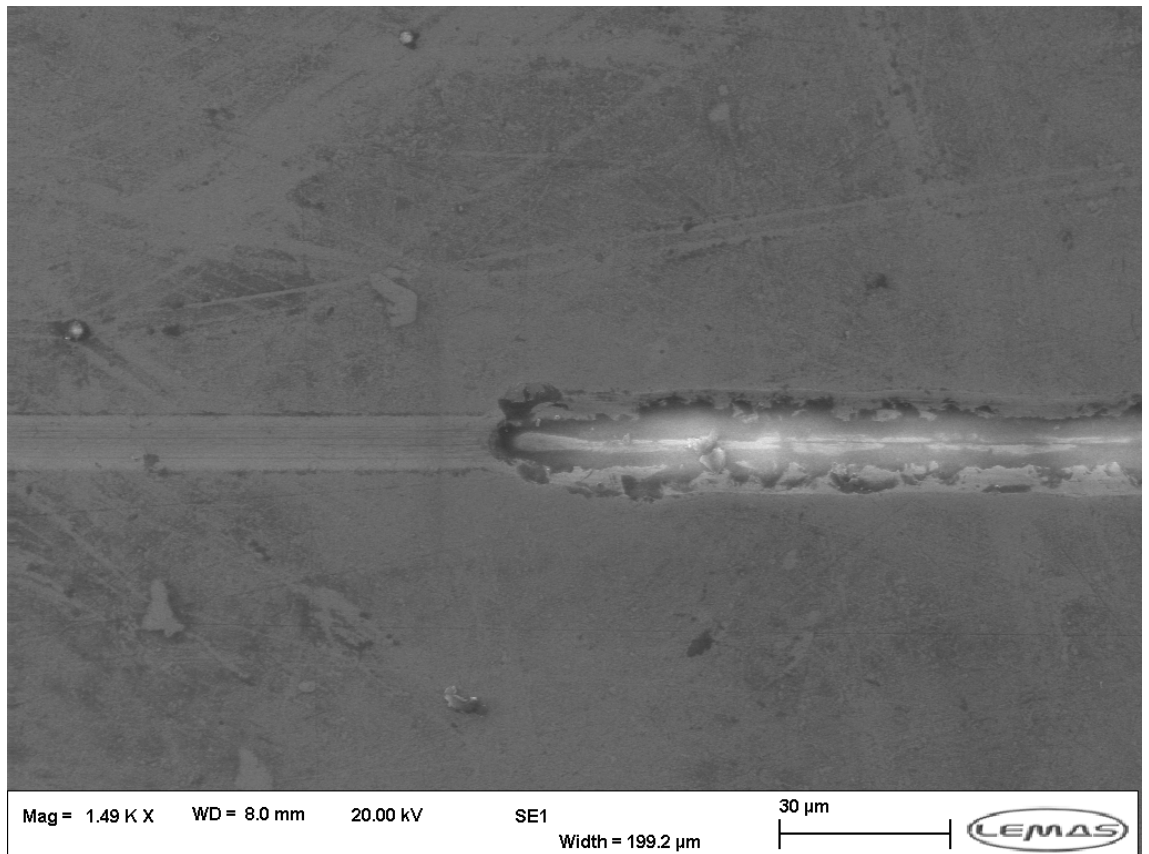
Figure 9.11: SEM micrograph of 500 mN failed track on Coating A.

Figure 9.12 shows a confocal microscopy micrograph of the wear tracks on Coating B. Some abrasive marks are present within the tracks and a small amount of debris has been seen to be ejected surrounding the wear.
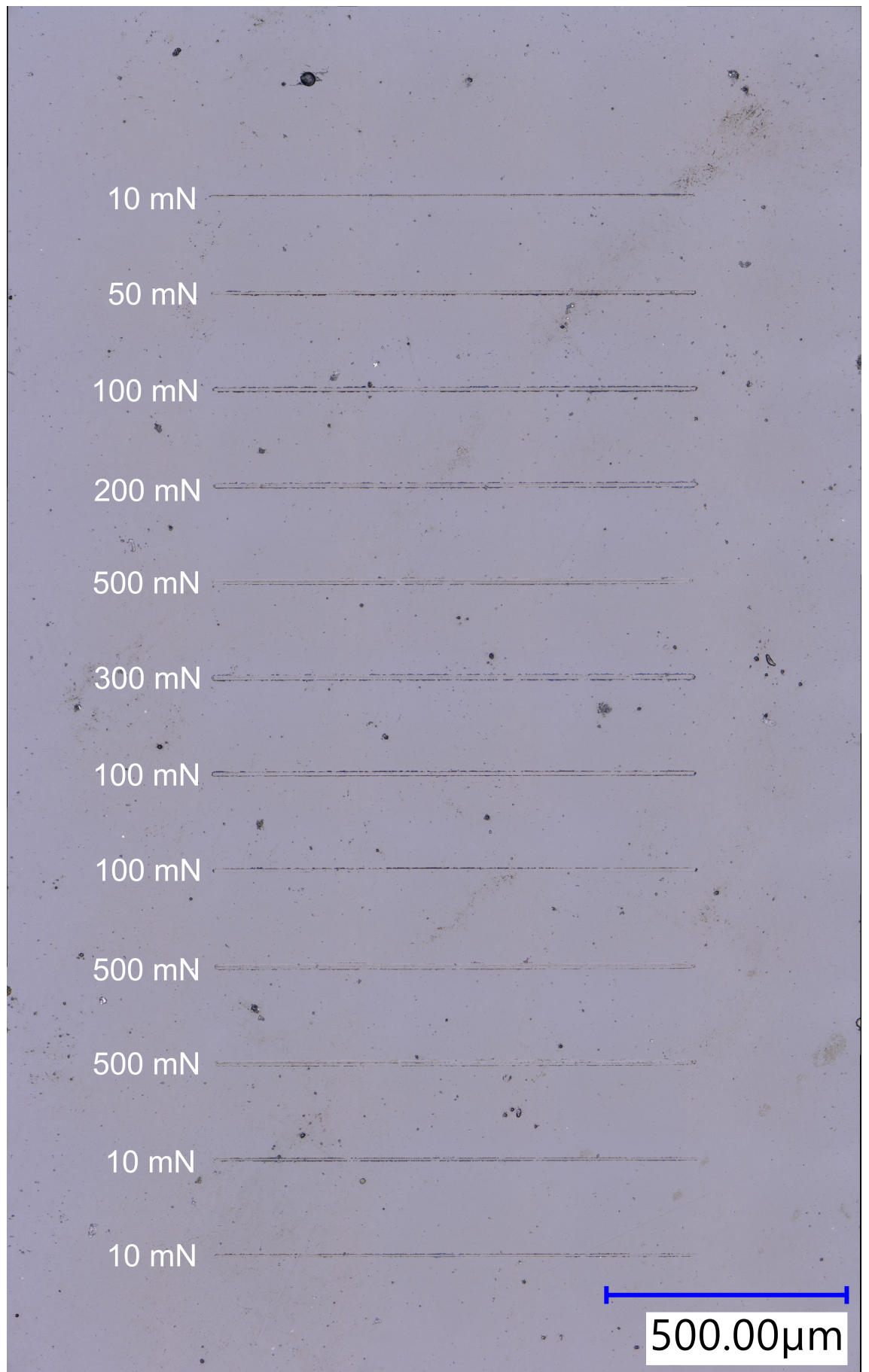
Figure 9.12: Micrograph of the wear tracks on Coating B. Loads are annotated on the figure.

Figure 9.13 shows an SEM micrograph of a 500 mN wear track on Coating B. Generally, this coating shows poor contrast under SEM due to its low metallic content in the top layers however the small amount of ejected wear debris can be observed on the edge of the wear track.
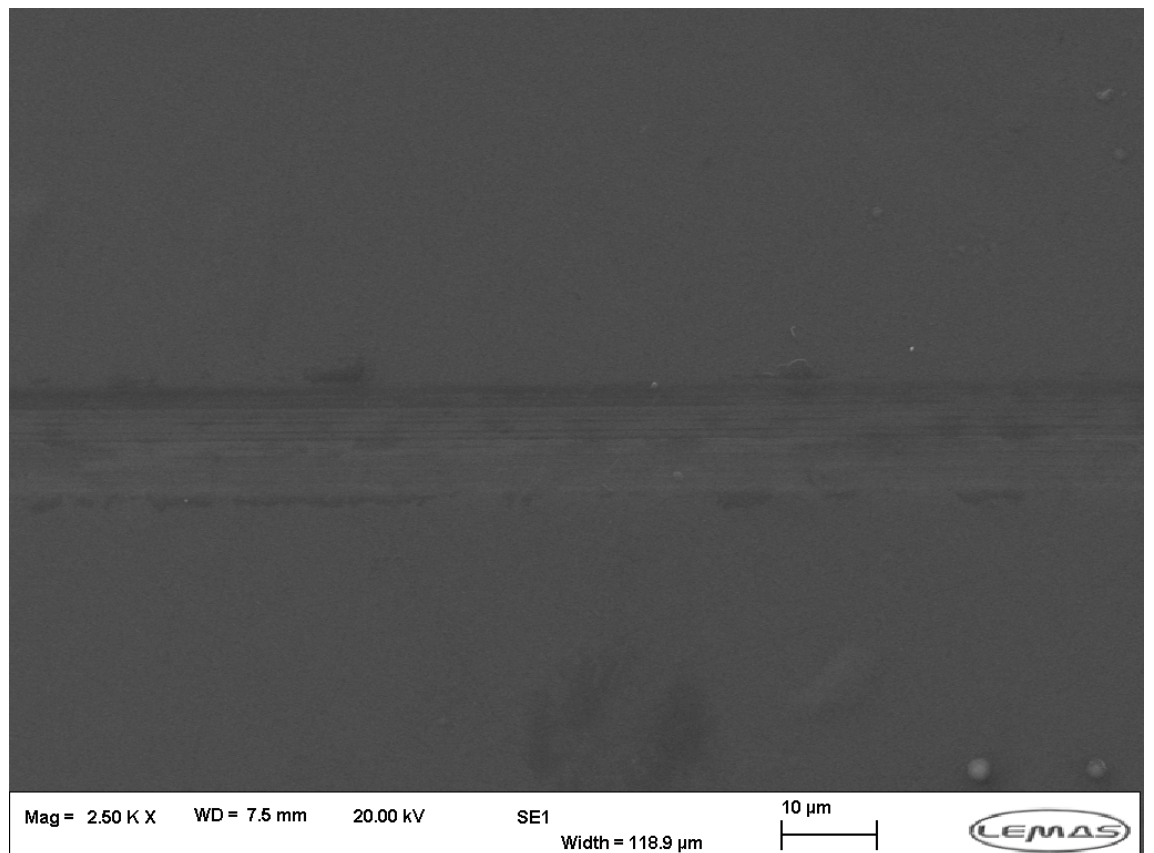
Figure 9.13: SEM micrograph of 500 mN track on Coating B.

Figure 9.14 shows a micrograph captured by confocal microscope of the wear tracks on Coating C. The morphology of the tracks can be clearly observed to be smooth with no wear debris at the sides.
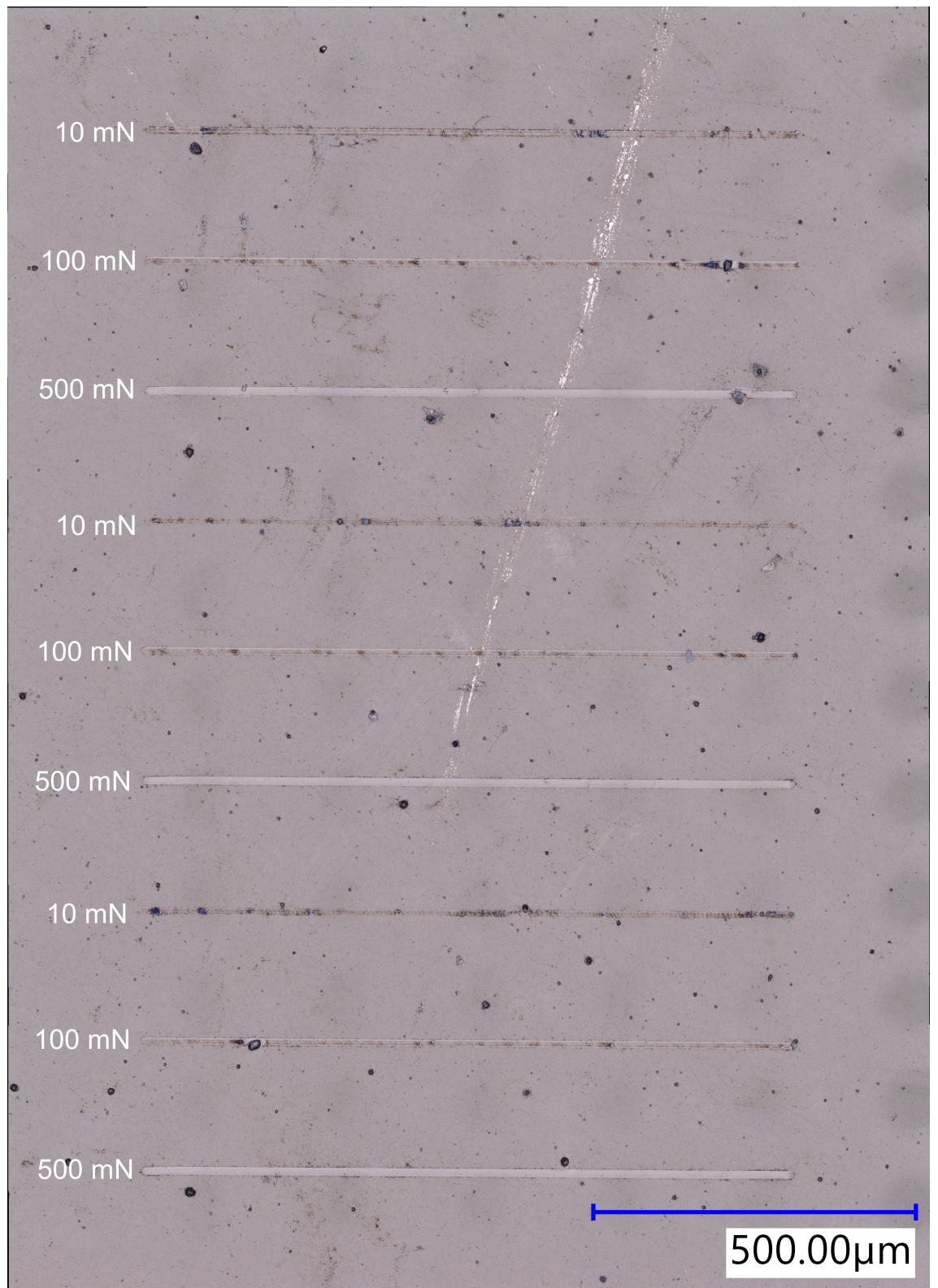
Figure 9.14: Micrograph of the wear tracks on Coating C. Loads are annotated on the figure.

Figure 9.15 shows a SEM micrograph of wear track at 500 mN on Coating C. The contrast of this image is improved compared to Coating B due to the tungsten doping and thereby the smoothness of the wear track can be seen.
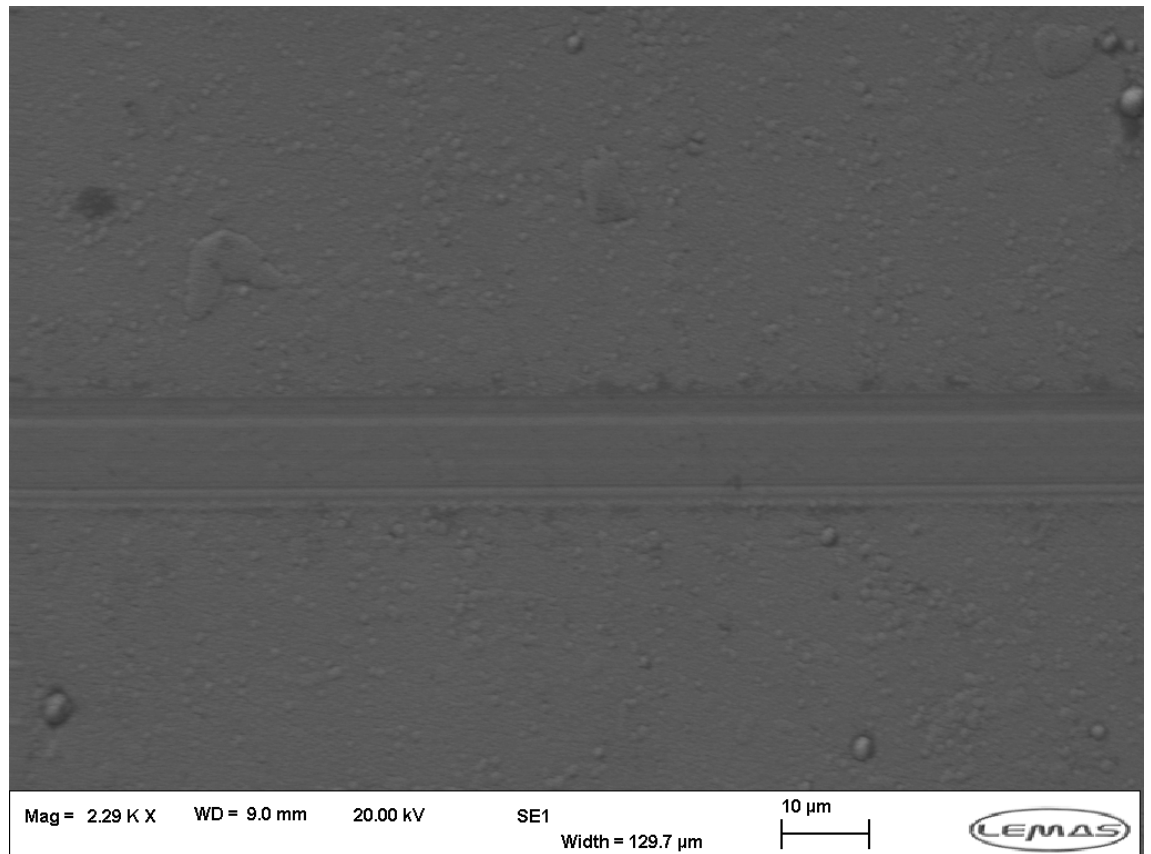
Figure 9.15: SEM micrograph of 500 mN track on Coating C.

Using the Hertzian contact pressure calculations introduced in Section 2.5.7.2, the contact pressure at the end of the testing cycles can be estimated. Table 9.10 shows the contact pressure estimated for Coatings A, B and C at 500 mN load. The residual depths (h_r) and on-load depths (h_t) are taken from the instrument output and used in Equation 2.46 to calculate contact depth (h_p). The contact pressure (P_m) using Equation 2.48. These P_m values are found from the calculated values of a. The measured values of a (via confocal microscopy) are provided as a comparison. The initially high contact pressures are seen to decrease drastically due to the plastic deformation of the coating. From the measured track widths and depths we can surmise that Coating A has the lowest wear rate followed by Coating B and C respectively.

Table 9.10: Residual depth (h_r), on-load depth (h_t), contact depth (h_p) calculated contact radius (a) and measured contact radius (from confocal microscopy) and the resultant final contact pressures (P_m) at 500 mN.

Coating	h_r (nm)	h_t (nm)	h_p (nm)	a Calculated (μm)	a Confocal (μm)	P_m (GPa)
A	100	1400	750	6.1	6.3	4.31
B	100	1400	750	6.1	6.8	4.31
C	700	1500	110	7.3	7.5	2.96

9.3.3 Stress Model

Figure 9.16 shows the analytical model of the von Mises stresses on each of the three coatings at 100 mN. Highlighted regions show where the von Mises stresses are greater than the yield stress, overloading the system and indicating where plastic flow is expected. The stress distribution in the coating structure can help in understanding the physical wear behaviour. This modelling however assumes that the coatings are mono-layered with single asperity sphere-on-plate geometry with perfectly flat surfaces. The model helps in the understanding of how the coating properties can control the yield location in scratch and reciprocating tests. We can interpret the deformation of small scale scratch tests (as seen in this model) as an effective single asperity contact primarily influenced by ploughing friction with minimal third body wear due to the smoothness of both the diamond indenter and DLC surfaces. Coating A is seen to be elastic, Coating B is seen to have a small region of yield within the coatings and Coating C has a much more extensive yield region. The yield determined by scratch testing for each coating is seen in Table 9.3.
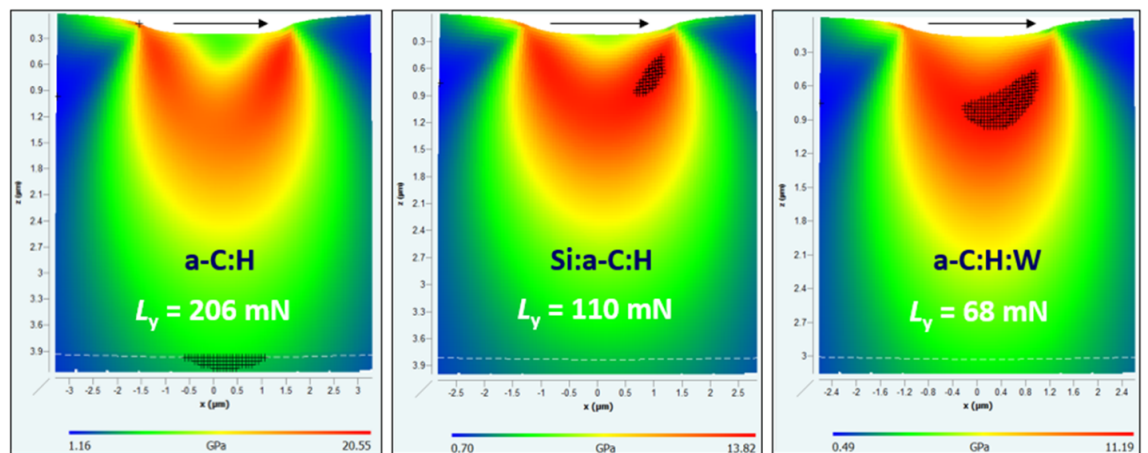
Figure 9.16: Analytical stress maps of the three coatings at 100 mN with a 5 μm radius probe.

9.4 Discussion

9.4.1 Friction

We can see in Figures 9.4, 9.6 and 9.8 that the initial COF was in the region 0.08–0.10 with no load dependence observable. These coefficients of friction were close to that observed in micro-scratch testing (with the same 25 μm radius probe as presented in Table 9.4). All coatings possess more variability and higher friction at 10 mN (relative to the preceding higher loads), this is due to greater influence of surface roughness where relative steps will see increases and decreases in friction [443, 444]. At this load, it can presumed that the ploughing term of friction is relatively small due to the low penetration into the sample (the confocal microscope was unable to measure a wear volume). Achanta and co-workers [133, 137] found similar results with friction variability at the smaller scale due to geometrical changes (continuous track changes) and adhesion (changing contact area). They also noted that during the early cycles of a reciprocating sliding test, friction increases in the initial cycles due to changing asperity angle and roughness of the coatings. Once the two surfaces become conformal, sliding energy stabilises and so does friction. Any debris trapped in the contact will affect the friction depending upon their size and morphology. Holmberg et al. [476] found that the increase in friction early in the sliding cycles was due to increasing surface roughness, change in contact area and topographical disturbance in generating a low friction tribolayer.

At higher load, running-in effects are seen where material is removed and the track geometry changes thereby affecting the contact area [477]. Hsia et al. [478] noted that when high conformity is seen between two surfaces with a low gap between them adhesion becomes increasingly dominant. Figure 9.12 illustrates the wear morphology of Coating B which has minimal ploughing and smoothing of the track at each load which fits with this, explaining its friction reduction in Figures 9.6 and Table 9.8.

The friction of Coating A (Figure 9.4) could be categorised into 2 regimes. A small-scale friction regime in which the increase in applied load decreases the COF due to the reduced influence of surface roughness. This was noted by Achanta et al. [133] in the comparison of as deposited DLC and TiN coatings compared to polished coatings as measured by lateral force microscopy. The measured tangential friction force was reduced and the friction loops were more stable with fewer fluctuations and spikes. As load increases the topography influence decreases. At higher loads the fiction is seen to increase rapidly. This is due to the onset of plastic deformation leading to high deformation after which a more defined wear track is formed with reduced ploughing [471]. Similar results were noted in nano-fretting on this coating with increasing friction before levelling out [428]. More spikes in the friction trace are seen in the case of Coating A (Figure 9.5). Some variability is also noted in Coating B (Figure 9.7), this could be the result of micro-cracking. Santner et al. [479] found that the topography can affect the friction signal when surface features such as step height changes are seen.

No direct evidence of a graphitised transfer layer was found as no Raman spectroscopy was performed to assess the change in the coating structure. However, AFM studies have produced evidence of phase transformation to a lower friction low shear graphitised layer after tribological contact [480]. The low friction seen in Coating A from 50–200 mN (Table 9.7) is indicative of this effect too. Holmberg et al. [476] recorded low COF values in POD tests and reciprocating sliding that are evident of graphitisation reducing friction.

Coating C displays different behaviour compared to the two harder coatings. As seen

in Figure 9.9, the friction decreases steadily with increasing cycles. This is different from the nano-fretting results, where friction increased with cycles [428]. The sharpness of the probe and modification of the topography with changing angle of the probe may be the cause [479]. Korres et al. [481] attributed such behaviour to be the result of minimal third body interaction with track widening and a reduction in the ploughing component of friction. Figure 9.14 indicates that that the smoothness of the wear track supports this. The microlamellar structure of Coating C further backs this up alongside its morphology in previous scratch tests [282, 473]. Gee et al. [469] found coefficients of friction from 0.04–0.08 on DLC with a diamond counterface with little correlation to macroscopic tests. Adhesion, molecular interactions and humidity is seen to be more influential in smaller scale friction tests however [461, 463]. Comparing the mesoscasle to the nanoscale, we generally see a higher COF with the mesocale (0.16 for DLC) compared to 0.064 at the nanoscale [461].

9.4.2 Wear Resistance

Previous testing under the nano-fretting regime showed that at 100 mN load Coating C was less wear resistant with its larger on-load depth increase (813 nm) with a 5 μm radius probe [428]. Scratch testing also revealed that greater contact depths were reached in Coating C compared to the other coatings [282]. By analysing the yield depths presented in Table 9.3, we can see that with the 25 μm probe used in this testing only the highest load would cause immediately plasticity of the coatings; yield loads were in the range of 350–375 mN [282]. Therefore we can clearly see that at the lower loads tested here, the sliding contact was initially elastic. The previously performed Hertzian analysis shows that the von Mises stress is located within the coating structure for all architectures but modelling can show different behaviour as the initial yield was seen to be within the substrate.Coating C was seen to yield within the coating though Coatings A and B remain below the yield stress.

Figure 9.16 shows analytical modelling performed at 100 mN with 5 μm radius probe. The highlighted regions show where the von Mises stress exceeds the the yield stress of the coating thereby giving regions where plasticity is expected. Single asperity interaction is assumed as is the perfect smoothness of the surfaces but modelling can be a useful tool in showing how properties affect the yield. Though wear is normally the process of asperity smoothing, a scratch test with smooth diamond probes can give an effective single asperity interaction relative to ploughing friction and generally little third body effects [282, 312]. This can provide further information on the behaviour seen during sliding wear. The yield loads are found from the previous nano-scratch testing [282]. Coating A was seen to have an entirely elastic response. Coating B had a small yield region and Coating C showed much more extensive yielding. Table 9.3 shows the experimental yield loads. The same trends are seen in the experimental results as in the modelling however when the load is increased behaviour of the system will change. Table 9.6 shows that the initial Hertzian contact pressures are high especially at 500 mN. Deformation due to wear will reduce the contact pressure throughout the test as wear occurs. Table 9.10 shows that at the maximum load the contact pressure has reduced to 4.31 GPa for Coatings A and B. Coating C has a lower contact pressure of 2.96 GPa. Nano-fretting at 100 mN produced initial pressures of 15.1, 12.7 and 11.2 GPa for Coatings A, B and C respectively. After 4500 cycles, the pressures reduced on all coatings to 7.5, 5.1 and 3.8 GPa for A, B and C respectively [428]. Analysis of the residual depth as seen in Table 9.10 can give us the wear depth and therefore allows us to tell which of the coatings wore faster. Due

to Coating C reaching a higher on load depth at 500 mN and having a larger residual depth along with its higher contact radius, the wear track can be seen to be larger in all dimensions (in comparison to non-failed tests). The relative softness of Coating C (as seen in Table 9.2) and its more ductile behaviour as noted by Beake et al. [282] contributes to the high residual and on-load depth in comparison to Coatings A and B. This tendency to deform results in lower contact pressures after the full wear cycles (Table 9.10). The ploughing component on this coating was found to be particularly small especially as it was previously found that its interfacial friction component is higher than Coating A or B [282]. For cases without extremely high contact pressure, causing the onset of drastic wear, we can therefore see that wear resistance is related to the mechanical properties (H/E but primarily H^3/E^2 as resistance to plastic deformation) as well as the shear stress distribution relative to the load and probe geometry used in testing.

Cyclic tests such as these could induce fatigue which would be present as micro-fracture in the wear track [312]. However analysis of the wear tracks in Figures 9.10, 9.12 and 9.14 show no evidence of this wear morphology. Analysis of the scratch tracks performed previously [282] show that Coating C displays small cracking consistent with what may be seen with low cycle fatigue. Micro-cracking degrading the coating micro-structure was found by Koskinen [482] in tests on ta-C. This is evidence of low cycle fatigue. Wear is seen to be a combination of displaced material (generally by debris creation) or by plastic deformation. Schiffmann found that on the micro-scale, plastic deformation is the primary cause of wear primarily within the first few cycles leading to higher friction coefficients initially. Plastic deformation was seen to contribute greatly to residual wear depth, at lower loads this can entirely dominate with little to no material loss seen [470, 471].

H/E ratio as popularised by Leyland and Matthews is a key parameter in evaluating wear resistance [322]. Gee et al. found this to be in good agreement with tests on various ceramic, amorphous carbon and soft coatings with a 1 μm radius diamond probe. Balinit C Star (Coating C) displayed low wear resistance in 25 cycle reciprocating tests [469]. Michler and Black [483] noted that the ratio of coating layer thickness to indenter radius was also an important parameter in determining the where cracking begins in contact with spherical indenters. For thin layers, plasticity was first noted in the substrate before moving to (or below) the interface. Shi et al. [440] showed that applied load is another important factor particularly in repetitive scratch nano-wear as it can determine the locus of failure. Under 50 mN loading, the peak stress was within the coatings wherein better mechanical properties (i.e. hardness) of the coating determined performance. At 150 mN, the stresses were located at the interface and fracture dominated. Due to the reduced hardness of Coating C, it was seen to perform better as the hardness more closely matched that of the substrate.

9.5 Summary

The newly developed NanoTriboTest module was utilised to assess the friction and wear performance of previously produced DLC coatings [282] sharing similar architectures to those produced for this study. A wide variety of loads were applied to evaluate coating performance over a range of contact pressures and analyse the dominant wear mechanisms in each load range. The wear scars produced were imaged with both SEM and confocal microscopy.

The development of this module for the NanoTest platform has added the capability

for high cycle, high speed and high sliding displacement at the mN level to its roster of capabilities. The high lateral rigidity of the loading head and thermal stability of the platform aid in obtaining accurate friction results. The module has proven capable of sensing the change of friction within a few cycles and its capacity for longer tests will allow for the modelling of different phenomena throughout the stages of wear. The performance of the coatings can be analysed with a combination of their H/E ratio (relating to strain to failure), H^3/E^2 (resistance to plastic deformation) and analysis of the contact pressures and yield of each coating relative to the load and radius of probe applied. Below 500 mN load, Coating A was seen to perform best with the lowest recorded coefficient of friction. This was presumed to be due to the formation of a graphitised layer though no direct evidence of one was found. At the 500 mN the higher initial contact pressures caused by the coating's high stiffness increased the friction and caused failure in one of the tests. Coating C was seen to perform well at 500 mN, this is likely due to its more ductile structure allowing it to deform favourably, thereby reducing the contact pressure. This results in larger measured contact radius and depth indicating higher wear of the coating. Due to the high cycle wear, micro-scale fatigue wear was a possibility however little evidence of this was found in the tracks.

Due to the low wear imparted on the surface during the sliding cycles, the confocal microscope was unable to measure the wear volumes of some wear scars. Follow up analysis on these wear scars should instead use AFM with a tip radius small enough to be able to grant high enough resolution. Future studies analysing the behaviour of DLC coatings using this technique should additionally employ Raman spectroscopy to analyse the I_D/I_G ratios of the wear tracks to compare to that of the unworn areas to assess whether an increase in the ratio is seen across all samples and to what degree. Future uses of this module could investigate the use of larger radius probes or investigating surface roughness orientation and its effect on friction within the mN load range.

Chapter 10

General Discussion and Conclusions

10.1   Evaluation of the Project Aims

Section 1.5 details the wide scope of this project at the outset. As with most projects some changes were made to the scope as magnitude of some tasks became apparent however the majority of objectives were met and studied to some degree.

The use of the various modules in the NanoTest platform proved the simplicity and elegance of this single system. Calibration and set up in a new experimental configuration was quick. Combined with the scheduling feature of the system. this allowed experiments to be ran almost continuously allowing for the large amount of data held presented within this thesis to be collected. The greatest amount of time was spent during this project in the use of bespoke pieces of equipment in the impact and erosion study (air-based erosion system) and fretting study (macro-scale fretting).

The development trajectory at Micro Materials pointed towards nano-scale reciprocating wear as a key area which resulted in the development on the Nano-Tribo-Test, the results of which can be seen in Chapter 9. Furthermore, the planned fretting studies were expanded cover across multiple length scales at high contact pressures. These results could therefore be compared with the ultra high contact pressures attained with the Nano-Tribo-Test module.

The structural characterisation performed in this project produced sufficient data on the composition, cross-section, amorphisation and phases of carbon bonding within the coating to give additional context to the coating performance. True knowledge of the ion energies and species within the chamber during deposition. Some knowledge of this can be estimated using a structure zone diagram however more full structural coating characterisation in any future studies should not neglect this.

Of note is the multiple distinct work projects that make up this thesis, though this has allowed for a rarely compiled full coating characterisation, it did increase the workload in data analysis and writing. Researchers working on similar projects should evaluate the detail desired along with the time investment necessary in their work.

Further to the experimental work, it was clearly stated that dissemination of the results of the project should be done at both national and international conferences. Multiple conferences at national and international level were attended during the project and results gained at various stages of the project were presented. Appendix A details the conferences attended and the oral presentations and poster presentations given. Multiple journal articles, derived from and adjacent to the project work, have been produced and are currently at various stages of publication.

10.2 General Discussion

This discussion will break down the effect of varying each parameter of the coating design and how it affected the whole system performance. Each chapter's discussion section goes into much more detail than what is presented here however this will serve as an overall summary.

10.2.1 Influence of the Substrate

Partial load-unload nanoindentation was used primarily because of its ability to map mechanical property changes with depth however when applying the model of Korsunsky et al. [183] as in Section 4.3.3, the difference in load support can be analysed with the relative depth of indentation reached as well as the density of data across the depth range. The increased coating thickness of the HTS coatings plays a part in maintaining a higher measured hardness at increased depth. The substrate support is still noticeable particularly as the mechanical properties do not fall off to the same degree with the harder substrate.

As seen in Chapter 6, under repetitive strain fatigue conditions, substrate support defines the ability of the coating structure to survive under these conditions. When the substrate is too soft, the coating structure will fail after extremely small energy input (on small time-scales) in both impact and erosive conditions due to eggshell failure [278, 403, 404]. With the enhanced substrate hardness giving a smaller difference in the hardness between HTS and Coating C, the substrate can accommodate the deformation better. Bousser et al. [408] found that the less the substrate plastically deforms relative to the coating (with a smaller the ratio of coating to substrate hardness), the less cracking will occur and therefore the coating will be more wear resistant to erosive conditions. This follows with the results of the impact and erosion tests in Chapter 6. As the impact stress is normal to the surface orientation in the testing performed in this study, this is the most extreme scenario in which the substrate support is tested.

The nano-scratch critical load failures (Table 7.4) appear to be sensitive to substrate load support as fewer critical load failures were observed on the HTS substrates. This is further exemplified with the calculated contact pressures at yield (Table 7.6), yield stress and Y/E (Table 7.7) with higher values seen with HTS compared to SS. The difference in the H/Y values indicate there is a difference in the location of the von Mises stress in the coating structure which may affect the stress propagation throughout the coating structure and thereby the plastic flow that leads to a critical load failure [47, 438]. The load support of the substrate may have an influence on this also.

10.2.2 Effect of Surface Roughness

Surface roughness was initially varied by polishing the substrate to different degrees; however, it was also found that the coating deposition influenced the surface roughness. The initial scanning step in the the nano-scratch testing allowed for the calculation of the surface roughness of the coatings (Table 7.3). DLC surface roughness varied across the range of thicknesses of coatings deposited possibly due to deposition time, which ranged from 2–6 h.

Increased roughness produced more variance in hardness at the low load steps in the partial load-unload nanoindentation. Figure 4.8 shows this well. The increased roughness

affects the peak hardness due to differences in detecting the surface. This is seen in Table 4.2. Small variances in SCPR are seen in Table 4.3 but no trend can otherwise be observed.

In nano-scratch testing, Coating A on SS saw a reduction in SCPR (Table 7.4) however overall trends cannot be determined due to the lack of critical load failures on the other coatings. Table 7.5 shows that a rougher surface produces higher scratch friction which makes sense due to the increased surface roughness effects on asperity-asperity contact at this length scale. Generally, contact pressure at yield (as seen in Table 7.6) was seen to increase with surface roughness, this is probably due to the increased pressure required to smooth the asperities before further yield is seen. Y, H/Y and Y/E are therefore affected in the same way.

Surface roughness is the key variable in the friction measured under nano-fretting with the large probes as seen in Section 8.3.2. At smaller loads, decreased roughness produces a lower average COF whereas the opposite effect is seen at higher loads. The regimes of fretting and their mechanisms are different with each of these loads. Roughness in micro-fretting has less of an overall effect on the COF but provide a small reduction as noted by Kubiak et al. [484].

10.2.3 Effect of Coating Thickness

Undoped DLC benefits from increased hardness (Table 4.2) due to the reduction of substrate effects and the peak hardness occurring within the common $1/10$ of coating thickness rule of thumb [162, 175, 183]. The increased deposition time for Coatings B and C must affect the structure of the coating to thereby either soften the coating (as with B) or increase the thickness which has a minimal effect on increasing hardness as the coating is relatively soft (as with C). Macro-scale scratch (Table 4.3) is affected by coating thickness, generally the thicker the coating the less well adhered it is. This is unusual as typically, critical load increases with coating thickness indicating better adhesion [302]. Wei and Yen [371] found that critical load in nano-scratch testing decreased with increased coating thickness; structural changes (increased I_D/I_G ratio with thicker coatings) was highlighted as a factor and could also be the case in this study. Due to the scale of test (macro-scale) and contact pressure applied, yield will occur first further into the coating structure and shear will occur between the coating and substrate thereby reducing its adhesion [282, 312, 438]. In smaller scale scratch tests as in Chapter 7, increased thickness is beneficial as the yield is generally focused in the upper regions of the coating which also increases the stress required to initiate failure.

In the impact and erosion testing, the same category of coating thickness were tested to maintain comparability between the coating types using coatings more typically found in industry (i.e. a few microns thickness). Extremely thick DLC performed well under erosive conditions which makes it a topic of investigation for future work [84].

In micro-fretting (Section 8.3.1), increased thickness of coating increases the wear resistance as a larger number of fretting cycles are required to induce layer delamination. The friction was also seen to be more stable with a lessened running in period, this could possibly due to a change in the locus of stress in coatings but modelling would be required to fully investigate. The energy dissipation is not affected greatly by this change.

10.2.4   Effect of DLC Coating Type

In all wear modes tested (besides nano-fretting and impact and erosion), tribological properties are seen to relate to H/E and H^3/E^2 in terms of resistance to fracture, elastic strain to break or friction (with respect to pile up and sink in) [321–323, 332]. Y/E and H/E are linked, with higher ratios of both favouring good friction and wear performance [332, 428]. The nano-scratch results in Table 7.7 also indicates that the substrate support is present in Y/E allowing it to act a metric more inclusive of entire system performance rather than simply measuring coating performance. Nano-fretting, due to its less conformal tribological contact, is heavily dependent upon surface roughness (Section 8.3.2) and the use of a relatively large probe means the contact will be dominated by interfacial friction with a small ploughing friction component. Contrary to crystalline coatings such as TiN or TiAlCrN where impact and erosion performance scales with resistance to fracture (H^3/E^2) [80, 118], DLCs impact performance scales with E/H giving increased fracture toughness [122, 163, 322, 328]. Therefore a lower H/E ratio is beneficial for repetitive stresses of particle impingement or indenter impact.

10.2.5   Altering the Length Scale of Testing

Length scale effects were investigated across numerous aspects of this project. The results of Section 4.3.1 showed that altering the scale of indentation used produces a much different result with nano-scale hardness being higher for the substrate materials. This provides a good demonstration of the indentation size effect (ISE) which has been attributed to several causes such as pileup or work hardening [166, 184].

Scratch testing was performed on both the macro-scale and nano-scale. As the macro-scale scratch was able to induce critical load failures in all the coatings (as seen in Table 4.3), we can therefore say that the failure process proposed by Schwarzer et al. [438] was able to induce plastic flow to cause coating cracking or fracture. However, nano-scale testing (Table 7.4), showed that for some of the coatings the contact pressure was not high enough to induce a critical load failure. In this case, the typical step would be to increase the scale of the test as done by Beake et al. in moving to a 25 μm radius probe with a larger load range [282]. It must be noted however that the SCPR values cannot be directly compared between the macro-scratch and nano-scratch because this metric is specific to the scale and probe size used in each test [310, 311].

Impact testing was performed on both the micro- and nano-scale in investigating the link to erosion wear (Chapter 6). As the same radius of impacting indenter was utilised between the length scales, the change in load and retraction distance between the two methods allowed for different levels of energy input as seen in Section 6.3.2. The nanoscale results presented in Section 6.3.1.2 with lower energy input per impact are able to capture smaller scale fatigue phenomena. The micro-scale impact in Section 6.3.1 with its larger energy input delivers similar energy to erosion in approximately the same time (with relatively simple modelling).

Fretting testing was performed on the micro and nano-scale. The nominal contact pressures (as seen in Tables 8.2 and 8.5) were predicted to be similar as effort to assess the effect of maintaining the same contact pressure across length scales. It is well known that the mechanisms at different length scales are quite different with the contact pressures generally being higher at the nano-scale. Due to the complexity of the interactions at the nano-scale, it is much more difficult to ascertain its mechanisms and these do not scale up to larger length scales [37, 69, 133].

The nano-scale reciprocating sliding of Chapter 9, displayed varying behaviour depending on the load used in testing. At lower loads across all 3 coatings, the effects of surface roughness were more prominent with larger variance of the friction signal throughout the sliding cycles. As the load was increased, the predicted contact pressures grew to allow for more accelerated wear testing, as is typical of nano-scale testing [37, 68]. Coating A, which was stiffer than the other coatings, was shown to have the chance of failure at these loads as the resultant contact pressure was extremely high.

10.3   Research Conclusions

In this project a matrix of coatings was produced which varied the substrate (HTS and SS), substrate roughness (0.01 and 0.08 $\mu m R_a$), DLC recipe (a-C:H, Si-a-C:H and a-C:H:W) and DLC top layer coating thickness. Coating thickness was evaluated with calotesting and cross section FIB. Mechanical properties of the coatings and substrate were characterised by nanoindentation. Structural characterisation of the coatings was performed with Raman and EELS. Adhesion was assessed on the macro and nano-scale with macro and nano-scratch testing. Nano-scratch was also used to investigate the interfacial coefficients of friction with different radii of indenters. Impact testing was used to investigate the relation to the fatigue characteristics as seen under erosive conditions. Multi-scale fretting testing was used to investigate the relation between mechanical properties and friction alongside matching contact pressure between length scales. Nano-scale reciprocating sliding was performed with a novel testing module to investigate the wear resistance and friction of a similar set of DLC coatings.

The summary sections of the results chapters present the research outcomes of each methodology used. The following highlights the novel aspects of the work of this thesis:

- Chapter 3: DLC Coating Production conclusions:

  The large matrix of coatings produced for the project allowed for a wide range of parametric variations to be investigated in the successively results chapters. DLC coatings deposited on HTS were observed to generally be thicker than their counterparts on SS possibly due to different electrical conductivities or substrate self-biasing effects. Analysis of the coating using structure zone models gave some insight to the differences between the layers however much work is required to clarify the ion energies responsible for the different thicknesses.

- Chapter 4: Mechanical Characterisation of DLC Coatings conclusions:

  The use of partial load-unload nanoindentation was shown to be a good methodology for analysis of the mechanical properties of multi-layer coating systems. Using load controlled indentation, a multi-stage indentation is able to find the hardness and elastic modulus with respect to depth. This allows for faster visualisation of the whole coating structure mechanical properties, substrate effects and load support. However, it must be noted that the analysis of the data is more complex as extrapolation to zero contact depth is required (instead of a fitting of single unload curves) and allowances must be made of the size of the plastic zone.

- Chapter 5: Structural Characterisation of DLC Coatings conclusions:

  The elemental composition of the coatings was verified using both EDX in SEM and EELS spectra stitching. All techniques were found to be in good agreement;

for future studies scanning electron microscopy EDX is recommended due to its simplicity. All coatings were shown to be amorphous using TEM-SAD. Differences were noted between the predicted amorphisation determined by Raman spectroscopy and sp^2/sp^3 ratio (using EELS) though this could be due to differences in the excitation volume between the two techniques.

- Chapter 6: Nano-Scale Fatigue Determination by Comparison of Erosion and Impact Testing conclusions:

  The use of impact testing was shown to be a valid alternative to the time-consuming and awkward set up of erosion tests so long as the energies of particle impacts are known. Substrate hardness was identified to be key to providing load support to repetitive fatigue strain. Optical analysis of the coating removal was successfully used in place of mass loss for erosion analysis. The energy comparison between single impacts and particle impingement was shown with simplified modelling. The use of impact/erosion plastic volume, consideration of impulse and rebound dynamics can improve future models.

- Chapter 7: Nano-Scratch for the Determination of Interfacial Friction conclusions: The extrapolation of the low load friction in progressively increasing load nano-scratch testing was used to show that with smaller radius probes, the interfacial component of friction increased. This was due to the increase in real contact area. Yield stresses were calculated from Hertzian contact pressure at yield. Using yield stress and hardness the constraint factor (H/Y) can be found which is a key value for feeding into models of the stresses experienced during scratch testing. Y/E shows potential as a tribological metric as it takes the substrate support into account allowing for assessment of the performance of the complete structure of the coating.

- Chapter 8: Multi-scale Fretting Testing of DLC Coatings conclusions: Fretting tests were compared across length scales (on the micro and nano-scale) with the same nominal contact pressure maintained between the two test methods to assess any similarities between the scales of testing. On the micro-scale, fretting performance is determined by the coating mechanical properties with no substrate support effects observed. The addition of lubricants was observed to be beneficial to reduced friction and wear in the fretting contact. Conversely, on the nano-scale, friction was determined to be affected by the surface roughness of the coatings. Extremely low friction was measured between the sphero-conical diamond probe and DLC surface. Due to the different mechanisms responsible for tribological interaction at each length scale, no direct links were found between the micro and nano-fretting.

- Chapter 9: Frictional Performance of DLC Coatings under Nano-Scale Reciprocating Sliding conclusions:

  The new reciprocating sliding module (NanoTriboTest) for the NanoTest platform was tested on DLC coatings sharing similar design architectures to the main DLCs in this thesis. This module was shown to be capable of friction sensing up to high cycle counts at high speeds. The module was shown to be sensitive to friction sensing within a few cycles allowing it to be used for the investigation of fundamental tribological mechanisms at the micro and nano-scales. The coating's performance was found to relate to their strain to break (H/E) and plastic deformation (H^3/E^2). Performance was also found to be particularly sensitive to contact pressure with stiffer coatings showing more wear and failure events.

10.4 Limitations and Recommendations

Due to the time considerations of managing the multiple work projects that has made up this project, there are some experimental methods that weren't utilised which would have been extremely useful for additional data acquisition.

The first of these techniques is FEM of the principle stresses during indentation and scratch testing. Commercial software such as ANSYS or COMSOL Multiphysics could be used to to model the coating deformation and stress propagation within the layer structure. Furthermore, SIO Film Doctor integrates with Micro Materials to analyse the data measured by the Nanotest indentation platform to allow for more precise modelling of coating failure and stresses. The integration of modelling methods alongside careful coating design will allow the coating properties or design to be tuned to allow them to be better optimised for the operating environment.

AFM utilised as both a friction sensing technique and post-test volume and topography measurement method would allow for extension of the aims of this project to smaller length scales. Confocal microscopy, stylus profilometry and white light interferometry were used to quantify the surface roughness and wear volume. These methods were unable to quantify the wear down to the smallest loads applied in this project making AFM the ideal method to the used. Any projects continuing in the themes of this one should makes this consideration early in their conception.

10.5 Closing Statement

The techniques developed and refined in this study will allow for the more complete characterisation of coating architectures for harsh or extreme environments. Though DLCs were the main focus of this project, the methodologies adopted could be applied to any hard coating architecture. It is hoped that the techniques used can be adopted into a more complete characterisation system. The results have reinforced that coatings must be tailored to their operating environment and that application of a coating to a pre-existing design (with bulk material defined) may result in poor performance. To attain the best performance, surface engineering techniques must be factored into the design process and the whole coating layer structure (substrate included) should undergo scrutiny.

Chapter 11

Future Work

The work contributing to this thesis has spanned multiple wear test methods and length scales to improve the understanding on DLC's tribological performance. The suggestions of future work are both informed by the work packages performed in this study and additionally those seen to be required by the current state of the art. Each of these sections feature several themes of possible continued research.

11.1   Plasma Analysis To Determine The Ion Deposition Energies

Ion energies are key to achieving optimum mechanical properties and coating density in the deposition of DLC [216]. The target power, plasma bias voltage and temperature will all affect the ion energy and subsequently affect the deposition rate and coating properties. This was not investigated in this study as standard coating procedures were used however analysis of the plasma constituents and ion energies would allow for further optimised coatings and provide further insight into the deviations in the coating thickness. The integration of a langmuir probe into the deposition system or time of flight mass spectrometer would allow the ion energies to be measured during deposition. Some considerations must be made for the presence of these elements in the chamber as they will affect the dynamics of the plasma.

Furthermore, the investigation of ion energies throughout deposition and as deposited coating structure can be further expanded by analysing the structure (sp^2/sp^3 ratio) at the surface of the coating and comparing to that at various depths. This can be achieved by using both XPS and EELS. EELS relies upon a FIB or some other cross sectioning methods to be able to create a sample thin enough for electron penetration in a TEM, this also allows for the structural analysis to be performed at different depths relative to the substrate. XPS is an entirely surface sensitive technique. The information gained could be fed into existing coating growth models to further improve them.

11.2   Additional mechanical testing and modelling

With the deployment of DLC coatings in thermally demanding environments, their thermal stability and change in mechanical properties with temperature requires optimisation.

Measurement of the change in mechanical properties with increased temperature will allow its dynamic performance to be assessed.The Micro Materials NanoTest platform is capable of high temperature indentation and impact testing up to 1000 °C [201, 485–487]. A vacuum chamber can be utilised with different materials such as cubic boron nitride or sapphire to allow for the indenter to survive the indentation without degradation [488]. Though the maximum achievable temperature is beyond the range at which DLC coatings are are thermally stable, this is normally in the range of 400–600 °C (dependent upon the DLC structure) [280], it this does allow for a wide range of potential operating environments to be assessed.

The newly developed Nanopositioning stage on the NanoTest Platform allows for rapid indentation and the generation of in-situ 3D profiles with an accuracy of up to 3 nm [489]. These capabilities allow for the generation of 3D topographies paired with mechanical property data that will allow for greater resolution in analysing nano-fretting and impact after the test has been completed to investigate structural changes due to the high strain rate and fatigue of these test methods. Under impact conditions, this mechanical property mapping could be correlated with dynamic hardness measurements determined by the impact testing to test the accuracy of these two methods. Further assessment of the change of mechanical properties could extend to the metallic interlayers to evaluate work hardening under repetitive strain and how this contributes to the assessment of interlayers as addressed in Section 11.3.

Micro- to nano-scale friction and wear was investigated in this project, this could be extended further with the use of AFM. It is also possible to use AFM as indentation method (given depth sensing capabilities) to allow for mechanical properties down to the picoscale to be determined [490]. Due to the sensitivity of such methods, the properties and morphologies of various tribofilms formed on DLC surfaces can also be studied. This could aid in determining the adverse reaction (increased wear rate) between DLC and MoDTC as noted by various authors [125, 286, 491]. This is likely a chemical interaction between the MoDTC additive and DLC causing the DLC structure to decompose however this mechanism is not understood yet.

The impact and erosion studies in Chapter 6 were performed at a 90° impingement angle to establish the initial link between the two processes. However, the rate of material loss in erosion tests varies based on a number of factors including the brittleness/ductility of the material, the shape of the erodent particle and the angle of impingement [72, 74]. It would therefore, be useful to further explore the link between the two processes at varying angles. A new sample mounting solution would be required to allow for the angle to be changed and fixed during testing. Additionally, the angularity of the impinging particles could be explored to see how sharper particles affects the wear resistance under erosive conditions. Angularity can be investigated under SEM. This can be correlated with performing micro/nano-impact tests using a cube corner indenter (as a sharper indenter) as opposed to a sphero-conical geometry (blunt indenter).

To augment the work of determining the interfacial and ploughing friction contributions in nano-scratch testing, a modelling approach can be integrated. As stated in Section 10.4 the NanoTest platform integrates (export of experimentally determined data to the modelling software) with the SIO Film Doctor Software to more accurately model the indentation and scratch stresses with measured data. This was originally to be performed in that work project but due to both time constraints and software availability, it was decided to perform an entirely experimental study. Combined experimental and modelling studies will aid in the digitalisation of surface engineering to improve future coating design and deployment.

11.3 Further study of the structural changes in DLC and their effects

The coatings produced in this study were varied by the addition of dopants which will alter the H/E ratio and structure of the coatings as well as the tribochemistry. It can be inferred that the levels of hydrogenation will vary between the coatings due to the variation in ion subplantation [276] however no direct study was made for this set of coatings. Similar studies could look at the relation between H/E ratio and DLC performance under various wear regimes where the DLC coating has more dramatic structural differences such as ta-C or ta-C:H. Hydrogenation in DLCs can be measured by either XPS or EELS.

Various interlayer designs are regularly chosen to serve to reduce the intrinsic residual stress in DLC coatings and improve adhesion to the substrate material [277, 278, 371, 492, 493]. A single interlayer design was produced and tested for the coatings in this study with the omission of Ti as an interlayer material. In light of the conclusions reached in Chapter 6, it would be of particular interest to assess the role of interlayers in fatigue compensation (changing the distribution of stresses within the coating structure to reduce cracking) under repetitive cyclic conditions. To achieve this a different target material would be selected for the magnetron sputtering step of the interlayer deposition. As emphasised in that chapter the whole coating structure must be optimised to increase lifetime under impact and particle impingement and a change in the interlayer may benefit future coating design.

This project has focused on changing the design of coating parameters to assess their impact on the tribological performance. The M2 tool steel was hardened out of necessity after discovering the eggshelling of the coating in the impact and erosion testing. Future studies could focus on altering or testing a wider range of substrates to investigate the optimum substrate for a particular coating architecture and application. 3D printed parts and aplymers are prime candidates for investigation. This will be useful to fill in the knowledge gap of designing a full coating system focusing on all aspects of the composite system as opposed to depositing a coating on an established substrate [198].

It has been shown that multi-layer coating architectures provide better impact resistance than the single monolithic layers present in the coatings in this study as seen with testing on TiN and AlTiN coatings [319, 494]. Therefore to further investigate the relationship between impact and erosive wear and correlations to mechanical properties, multilayer/sandwich (top layer) DLC coatings could be investigated to this end. There are many design options to achieve this, one option would be alternating magnetron sputtered Cr layers and PACVD DLC layers. The deposition time for each layer would be reduced in order to have multiple thinner layers giving a similar overall coating thickness.

11.4 Analysis of the structural changes in DLC under different wear regimes

FIB cross sectioning was used to observe the microstructural cracking after impact testing, this revealed a lot about the performance of each of the coatings under cyclic impact. This technique could also be extended to inform on the microstructural changes after erosion,

sliding and fretting wear. The same procedure would be used here as in Chapter 6 whereby the sites to be cross-sectioned would be located and a dual-stage SEM would be used to remove the material and polish the revealed microstructure. This would be useful to physically investigate the yielding of coatings under scratch testing and to compare with modelling.

Both Raman spectroscopy and EELS have been utilised in this project however only micro-impact craters were tested using the Raman microscope to quantify the graphitisation of the surface. Future studies should track the tribological transformation of the coating surface using both methods throughout testing. This would involve running tests for specific intervals, stopping the test and performing the spectroscopy before return the sample to continue testing.

11.5 Further fretting studies on DLC and development of the nano-fretting module

The fretting studies in this project have targeted the gross slip fretting regime in order to accelerate the wear due to the relatively small testing times compared to other fretting studies. To provide a more complete understanding of the coating performance under fretting conditions, the regime can be varied (by changing the load and displacement) alongside longer tests measuring the number of cycles to failure. This can be coupled with a changes in the interlayer and top layer coating design to inform on more optimised coating parameters for fretting resistance.

Several studies have been conducted to assess the performance of materials under dynamic loading (varying the load and displacement throughout) conditions under fretting wear [104, 495]. This can act as a further development of the testing of different fretting regimes by changing the fretting regime deliberately while maintaining contact between the sample and counterface. This is of interest to DLC characterisation due to the mestability of the coating, allowing it to graphitise, more readily form a transfer film and self lubricate the contact. This will affect wear performance under the cyclic abrasion and adhesion that dominates fretting. The entire coating structure's effect on the fretting fatigue resistance and amount of energy dissipated into the coating structure can be analysed to assess the crack and debris generation.

At the time of this project, few publications exist using the nanofretting module with the last being published between 2010 and 2013 [146, 149, 318]. One of the objectives of this project was to evaluate this module and suggest possible improvements and new capabilities. Though it is a easy module to set up and use, there are several improvements that stand to be made. The module lacks a method of measuring the displacement in real-time and entirely relies upon a pre-test calibration to set the desired displacement. Due to the length scales and frequencies that this module operates on, it is a challenging prospect to further instrument the module. Doing so would allow for the dissipated energy to be calculated on a per cycle basis and allow for the fretting maps to be plotted giving more data for potential future studies. This would be especially useful for any work spanning multiple length scales. An optical or laser sensor could provide the resolution required to detect the change of displacement during fretting. A strain gauge based friction probe is used to measure the friction per fretting cycle. Currently, the NanoTest software doesn't implement any kind of data processing to allow for the RMS friction to be calculated. Any processing was carried out using MATLAB; the processing methodologies adopted

for this work could be implemented into the NanoTest software to aid in data processing for future work.

11.6   Electrical and emissive effects of DLC

With the advent of the internet of things (IOT) and collected monitoring technologies, coatings are a prime use case for the development of smart sensors. DLC is already used as a protective coating for MEMS devices [147, 282] and further development could allow the coating itself to act as a sensor. The investigation of the effect of load and coating structure on capacitance/resistivity will allow for its use as an integrated sensor to be assessed. Electrical contact resistance (ECR) (measured with an electrically conductive probe) could be used to assess the change in DLC structure with wear as graphitisation should be measurable by a change in the resistivity of the coating. Additionally, the investigation of DLC as a possible material pair for the TENG sensors could expand its abilities further. The electrical breakdown of DLC can be measured by the application of a voltage across the coating and substrate; by varying the voltage and analysing the current response the structural breakdown of the coating can be found.

It is noted that the oscillation frequency of triboelectric pairs affects the charging characteristics observed in contact electrification [158]. Fretting can having varying amplitude and frequency but a generally small displacement and high frequency could aid in triboelectric charge build up for well placed TENGs. A fretting rig with an integrated electrometer would allow for the charge build up to be measured during the fretting cycles. Additionally, to expand on the idea from the previous paragraph, the integration of sensors into systems well known to have fretting issues could allow us to monitor the system better and help prevent undue system failure.

Various types of particles are emitted from the surfaces under sliding contact and the area around them including electron, ions, photons, radicals and molecules [151]. It is well known that DLC produces triboemission but further study of this phenomena could help to narrow down the root causes of the triboelectric effect and understand the fundamentals of surface interaction. A charger detector with a photomultiplier located near the contact zone in a sliding contact would allow for particle emission to be measured.

References

[1] Richard P Feynman. *Perfectly reasonable deviations from the beaten track: the letters of Richard P. Feynman*. Perseus Books, 2005. doi: 10.5860/choice.43-1530. 2

[2] John Houghton. Global warming. *Reports Prog. Phys.*, 68(6):1343–1403, 2005. ISSN 00344885. doi: 10.1088/0034-4885/68/6/R02. 2, 3

[3] Qiancheng Ma. NASA GISS: Science Briefs: Greenhouse Gases: Refining the Role of Carbon Dioxide, 1998. URL `https://www.giss.nasa.gov/research/briefs/ma{_}01/`. 3, 4

[4] P A Tipler and G Mosca. *Physics for Scientists and Engineers*. Physics for Scientists and Engineers: Standard. W. H. Freeman, 2007. ISBN 9781429201247. URL `https://books.google.co.uk/books?id=AttDBYgLeZkC`. 3

[5] Jonathan Gregory Richard Alley, Terje Berntsen, Nathaniel L. Bindoff, Zhenlin Chen, Amnat Chidthaisong, Pierre Friedlingstein, Ulrike Lohmann Gabriele Hegerl, Martin Heimann, Bruce Hewitson, Brian Hoskins, Fortunat Joos, Jean Jouzel, Vladimir Kattsov, Venkatachalam Martin Manning, Taroh Matsuno, Mario Molina, Neville Nicholls, Jonathan Overpeck, Dahe Qin, Graciela Raga, Ronald J. Ramaswamy, Jiawen Ren, Matilde Rusticucci, Susan Solomon, Richard Somerville, Thomas F. Stocker, Peter Stott, and David Wratt Stouffer, Penny Whetton, Richard A. Wood. Climate Change 2007. The Physical Science basis: Summary for policymakers. Contribution of Working Group I to the Fourth Assessment Report of the Intergovernmental Panel on Climate Change. Technical report, 2007. 3

[6] Hannah Ritchie and Max Roser. CO2 and Greenhouse Gas Emissions. *Our World Data*, 2017. URL `https://ourworldindata.org/co2-and-other-greenhouse-gas-emissions`. 4, 5, 6

[7] Colin P Morice, John J Kennedy, Nick A Rayner, and Phil D Jones. Quantifying uncertainties in global and regional temperature change using an ensemble of observational estimates: The HadCRUT4 data set. *J. Geophys. Res. Atmos.*, 117(8), 2012. ISSN 01480227. doi: 10.1029/2011JD017187. 4

[8] NOAA. Global Monitoring Laboratory - Carbon Cycle Greenhouse Gases, 2019. URL `https://www.esrl.noaa.gov/gmd/ccgg/trends/`. 5

[9] Pierre Friedlingstein, Matthew W. Jones, Michael O'Sullivan, Robbie M. Andrew, Judith Hauck, Glen P. Peters, Wouter Peters, Julia Pongratz, Stephen Sitch, Corinne Le Quéré, Orothee C.E. DBakker, Josep G. Canadell1, Philippe Ciais1, Robert B. Jackson, Peter Anthoni1, Leticia Barbero, Ana Bastos, Vladislav Bastrikov, Meike Becker, Laurent Bopp, Erik Buitenhuis, Naveen Chandra, Frédéric Chevallier, Louise P. Chini, Kim I. Currie, Richard A. Feely, Marion Gehlen, Dennis Gilfillan,

Thanos Gkritzalis, Daniel S. Goll, Nicolas Gruber, Sören Gutekunst, Ian Harris, Vanessa Haverd, Richard A. Houghton, George Hurtt, Tatiana Ilyina, Atul K. Jain, Emilie Joetzjer, Jed O. Kaplan, Etsushi Kato, Kees Klein Goldewijk, Jan Ivar Korsbakken, Peter Landschützer, Siv K. Lauvset, Nathalie Lefèvre, Andrew Lenton, Sebastian Lienert, Danica Lombardozzi, Gregg Marland, Patrick C. McGuire, Joe R. Melton, Nicolas Metzl, David R. Munro, Julia E.M.S. Nabel, Shin Ichiro Nakaoka, Craig Neill, Abdirahman M. Omar, Tsuneo Ono, Anna Peregon, Denis Pierrot, Benjamin Poulter, Gregor Rehder, Laure Resplandy, Eddy Robertson, Christian Rödenbeck, Roland Séférian, Jörg Schwinger, Naomi Smith, Pieter P. Tans, Hanqin Tian, Bronte Tilbrook, Francesco N. Tubiello, Guido R. Van Der Werf, Andrew J. Wiltshire, and Sönke Zaehle. Global carbon budget 2019. *Earth Syst. Sci. Data*, 11(4):1783–1838, dec 2019. ISSN 18663516. doi: 10.5194/essd-11-1783-2019. 5

[10] Global Carbon Atlas. CO2 Emissions — Global Carbon Atlas, 2018. URL `http://www.globalcarbonatlas.org/en/CO2-emissions`. 5

[11] United Nations. The Paris Agreement — UNFCCC, 2018. URL `https://unfccc.int/process-and-meetings/the-paris-agreement/the-paris-agreementhttps://unfccc.int/process/the-paris-agreement/what-is-the-paris-agreement`. 6

[12] G. P. Peters, R. M. Andrew, J. G. Canadell, P. Friedlingstein, R. B. Jackson, J. I. Korsbakken, C. Le Quéré, and A. Peregon. Carbon dioxide emissions continue to grow amidst slowly emerging climate policies. *Nat. Clim. Chang.*, 10(1):3–6, jan 2020. ISSN 17586798. doi: 10.1038/s41558-019-0659-6. URL `https://www.nature.com/articles/s41558-019-0659-6`. 6

[13] EEA. Trends and projections in Europe 2019: Tracking progress towards Europe's climate and energy targets. Technical report, 2019. URL `https://www.eea.europa.eu//publications/trends-and-projections-in-europe-1papers2://publication/uuid/542F7834-5B03-4EAA-91FA-FC2D26B37746`. 6

[14] Corinne Le Quéré, Robert B. Jackson, Matthew W. Jones, Adam J.P. Smith, Sam Abernethy, Robbie M. Andrew, Anthony J. De-Gol, David R. Willis, Yuli Shan, Josep G. Canadell, Pierre Friedlingstein, Felix Creutzig, and Glen P. Peters. Temporary reduction in daily global CO2 emissions during the COVID-19 forced confinement. *Nat. Clim. Chang.*, 10(7):647–653, jul 2020. ISSN 17586798. doi: 10.1038/s41558-020-0797-x. URL `https://doi.org/10.1038/s41558-020-0797-x`. 6

[15] David Leibling. Royal Automobile Club Foundation for Motoring Car ownership in Great Britain. Technical report, 2008. URL `www.racfoundation.org`. 6

[16] Jiwoon Ahn, Gicheol Jeong, and Yeonbae Kim. A forecast of household ownership and use of alternative fuel vehicles: A multiple discrete-continuous choice approach. *Energy Econ.*, 30(5):2091–2104, sep 2008. ISSN 01409883. doi: 10.1016/j.eneco.2007.10.003. 6

[17] Department for Transport. Vehicle Licensing Statistics: 2020 Quarter 1 (Jan - Mar), 2020. 6

[18] Itxaso Ruiz, Sérgio H. Faria, and Marc B. Neumann. Climate change perception: Driving forces and their interactions. *Environ. Sci. Policy*, 108:112–120, jun 2020. ISSN 18736416. doi: 10.1016/j.envsci.2020.03.020. 6

[19] John Williams. *Engineering tribology*, volume 9780521609. Cambridge University Press, Cambridge, 2005. ISBN 9780511805905. doi: 10.1017/CBO9780511805905. URL http://ebooks.cambridge.org/ref/id/CBO9780511805905. 7, 17, 18, 19, 21, 22, 23, 24, 26, 43, 90

[20] Peter Jost. Lubrication (tribology), education and research. A Report on the present position and industry's needs. Technical report, Department of Education and Science, London, 1966. 7, 17

[21] Bharat Bhushan. History of Tribology and Micro/Nanotribology. In *Micro/Nanotribology Its Appl.*, pages 1–16. Springer Netherlands, 1997. doi: 10.1007/978-94-011-5646-2_1. 7

[22] Kenneth Holmberg and Ali Erdemir. Influence of tribology on global energy consumption, costs and emissions. *Friction*, 5(3):263–284, sep 2017. ISSN 22237704. doi: 10.1007/s40544-017-0183-5. 7

[23] Hannah Ritchie. Climate change and flying: what share of global CO2 emissions come from aviation?, 2020. URL https://ourworldindata.org/co2-emissions-from-aviationhttps://ourworldindata.org/co2-emissions-from-aviation{%}0Ahttps://ourworldindata.org/co2-emissions-from-aviation{#}licence. 8

[24] Kenneth Holmberg, Peter Andersson, and Ali Erdemir. Global energy consumption due to friction in passenger cars. *Tribol. Int.*, 47:221–234, mar 2012. ISSN 0301679X. doi: 10.1016/j.triboint.2011.11.022. 8

[25] Tsao Cheng Huang, Jui Ming Yeh, and Cheng Yuan Lai. Polymer nanocomposite coatings. In *Adv. Polym. Nanocomposites Types Appl.*, pages 605–638. Elsevier Inc., jan 2012. ISBN 9781845699406. doi: 10.1533/9780857096241.3.605. 8, 43

[26] R.J. Artley and A. (Allan) Matthews. 2005 revisited: the UK surface engineering industry to 2010 report. Technical report, Hampshire, 2010. 8

[27] IOM3. The Surface Engineering Leadership Forum — IOM3. *Mater. World Mag.*, 2019. URL https://www.iom3.org/materials-world-magazine/feature/2019/may/10/surface-engineering-leadership-forum. 8, 44

[28] Special Interest Group: Surface Engineering and Advanced Coatings. Time for Strategic Change: UK Surface Engineering and Advanced Coatings Industry. Technical report, 2014. 8

[29] M. Woydt, Thomas Gradt, Tim Hosenfeldt, Rolf Luther, Adrian Rienäcker, Franz-Josef Wetzel, and Christoph Wincierz. Tribology in Germany: Interdisciplinary technology for the reduction of CO2-emissions and the conservation of resources. Technical report, German Society for Tribology, 2019. 8

[30] Oscar Pinkus and Donald F Wilcock. Strategy for energy conservation through tribology. Technical report, American Society of Mechanical Engineers, New York, 1977. 8

[31] Leonardo Israel Farfan-Cabrera. Tribology of electric vehicles: A review of critical components, current state and future improvement trends. *Tribol. Int.*, 138 (April):473–486, 2019. ISSN 0301679X. doi: 10.1016/j.triboint.2019.06.029. URL `https://doi.org/10.1016/j.triboint.2019.06.029`. 9, 187

[32] S. Douvartzides and I. Karmalis. Working fluid selection for the Organic Rankine Cycle (ORC) exhaust heat recovery of an internal combustion engine power plant. In *IOP Conf. Ser. Mater. Sci. Eng.*, volume 161, page 012087. Institute of Physics Publishing, dec 2016. doi: 10.1088/1757-899X/161/1/012087. URL `https://iopscience.iop.org/article/10.1088/1757-899X/161/1/012087https://iopscience.iop.org/article/10.1088/1757-899X/161/1/012087/meta`. 9

[33] H M Mobarak, E Niza Mohamad, Hassan H Masjuki, M A Kalam, K A H Al Mahmud, Md Habibullah, and A M Ashraful. The prospects of biolubricants as alternatives in automotive applications. *Renew. Sustain. energy Rev.*, 33:34–43, 2014. 9

[34] Klaus Bewilogua and Dieter Hofmann. History of diamond-like carbon films - From first experiments to worldwide applications. *Surf. Coatings Technol.*, 242:214–225, mar 2014. ISSN 02578972. doi: 10.1016/j.surfcoat.2014.01.031. URL `https://www.sciencedirect.com/science/article/pii/S0257897214000474{#}f0030`. 9, 10, 49, 51

[35] Alfred Grill. Diamond-like carbon: state of the art. *Diam. Relat. Mater.*, 8(2-5):428–434, mar 1999. ISSN 09259635. doi: 10.1016/S0925-9635(98)00262-3. URL `http://www.sciencedirect.com/science/article/pii/S0925963598002623http://linkinghub.elsevier.com/retrieve/pii/S0925963598002623`. 9, 48, 60, 87

[36] Juan Carlos Sánchez-López and Asuncion Fernández. Doping and alloying effects on DLC coatings. In *Tribol. Diamond-Like Carbon Film. Fundam. Appl.*, pages 311–328. Springer US, Boston, MA, 2008. ISBN 9780387302645. doi: 10.1007/978-0-387-49891-1_12. URL `http://link.springer.com/10.1007/978-0-387-49891-1{_}12`. 9, 51, 56, 60, 133

[37] Pantcho Stoyanov and Richard R. Chromik. Scaling effects on materials tribology: From macro to micro scale. *Materials (Basel).*, 10(5):550, may 2017. ISSN 19961944. doi: 10.3390/ma10050550. URL `www.mdpi.com/journal/materials`. 10, 28, 231, 260, 261

[38] Tribology Laboratory at Lehigh University:. URL `https://www.lehigh.edu/{~}intribos/materialstribology.htmlhttp://www.lehigh.edu/{~}intribos/tribodesign.html`. 11

[39] G. W. Stachowiak and A. W. Batchelor. *Engineering Tribology*. Butterworth-Heinemann, 4 edition, 2014. ISBN 978-0-12-397047-3. doi: https://doi.org/10.1016/C2011-0-07515-4. URL `https://www.sciencedirect.com/science/book/9780123970473`. 17

[40] K. Holmberg. Reliability aspects of tribology. *Tribol. Int.*, 34(12):801–808, dec 2001. ISSN 0301679X. doi: 10.1016/S0301-679X(01)00078-0. 17

[41] V. L. Popov and S. G. Psakhie. Numerical simulation methods in tribology. *Tribol. Int.*, 40(6):916–923, jun 2007. ISSN 0301679X. doi: 10.1016/j.triboint.2006.02. 020. 17

[42] D Dowson. A tribological day. *Proc. Inst. Mech. Eng. Part J J. Eng. Tribol.*, 223 (3):261–273, 2009. ISSN 13506501. doi: 10.1243/13506501JET557. 17

[43] Michael Urbakh, Joseph Klafter, Delphine Gourdon, and Jacob Israelachvill. The nonlinear nature of friction. *Nature*, 430(6999):525–528, jul 2004. ISSN 00280836. doi: 10.1038/nature02750. 17

[44] D. Arnell. Mechanisms and laws of friction and wear. In *Tribol. Dyn. Engine Powertrain Fundam. Appl. Futur. Trends*, pages 41–72. Elsevier Ltd., jan 2010. ISBN 9781845693619. doi: 10.1533/9781845699932.1.41. 18, 19, 20, 21, 22, 23, 43, 90

[45] Anthony C. Fischer-Cripps. *Introduction to Contact Mechanics*. Mechanical Engineering Series. Springer US, Boston, MA, 2000. ISBN 0-387-98914-5. doi: 10.1007/b97709. URL http://link.springer.com/10.1007/b97709. 18, 19, 177

[46] David Tabor. *The hardness of metals*. Oxford university press, 1951. 18, 173

[47] T. Chudoba, N. Schwarzer, and F. Richter. Steps towards a mechanical modeling of layered systems. *Surf. Coatings Technol.*, 154(2-3):140–151, 2002. ISSN 02578972. doi: 10.1016/S0257-8972(02)00016-6. 18, 173, 177, 178, 180, 258

[48] Anthony C. Fischer-Cripps. *Nanoindentation*. Springer, 2004. ISBN 9780387220451. 18, 19, 33, 35, 36, 37, 39, 42, 63, 90, 91, 102, 138, 177

[49] Milton C. Shaw and Gabriel J. DeSalvo. The Role of Elasticity in Hardness Testing. *Metallogr. Microstruct. Anal.*, 1(6):310–317, 2012. ISSN 2192-9262. doi: 10. 1007/s13632-012-0047-3. 19

[50] B. N.J. Persson. Relation between interfacial separation and load: A general theory of contact mechanics. *Phys. Rev. Lett.*, 99(12):125502, sep 2007. ISSN 00319007. doi: 10.1103/PhysRevLett.99.125502. 20, 231

[51] B. N.J. Persson. Theory of rubber friction and contact mechanics. *J. Chem. Phys.*, 115(8):3840–3861, aug 2001. ISSN 00219606. doi: 10.1063/1.1388626. URL http://aip.scitation.org/doi/10.1063/1.1388626.

[52] B. N.J. Persson. Contact mechanics for randomly rough surfaces. *Surf. Sci. Rep.*, 61(4):201–227, jun 2006. ISSN 01675729. doi: 10.1016/j.surfrep.2006.04.001. 20

[53] Diao Dongfeng and Kato Koji. Interface yield map of a hard coating under sliding contact. *Thin Solid Films*, 245(1-2):115–121, jun 1994. ISSN 00406090. doi: 10.1016/0040-6090(94)90886-9. 20, 74, 177

[54] N. Schwarzer, F. Richter, and G. Hecht. The elastic field in a coated half-space under Hertzian pressure distribution. *Surf. Coatings Technol.*, 114(2-3):292–303, may 1999. ISSN 02578972. doi: 10.1016/s0257-8972(99)00057-2. 20

[55] J. A. Greenwood and J. B. P. Williamson. Contact of Nominally Flat Surfaces. *Proc. R. Soc. A Math. Phys. Eng. Sci.*, 295(1442):300–319, dec 1966. ISSN 1364-5021. doi: 10.1098/rspa.1966.0242. URL `http://rspa.royalsocietypublishing.org/cgi/doi/10.1098/rspa.1966.0242`. 20, 66, 231

[56] Lior Kogut and Izhak Etsion. A finite element based elastic-plastic model for the contact of rough surfaces. *Tribol. Trans.*, 46(3):383–390, 2003. ISSN 1547397X. doi: 10.1080/10402000308982641. 20

[57] Duncan Dowson. *History of Tribology , 2nd Edition.* Wiley, 1998. ISBN 9781860580703. URL `https://www.wiley.com/en-gb/History+of+Tribology{%}2C+2nd+Edition-p-9781860580703`. 20

[58] Javier Echávarri, Eduardo De La Guerra, and Enrique Chacón. Tribology: A Historical Overview of the Relation between Theory and Application, 2015. ISSN 18753426. URL `https://link.springer.com/chapter/10.1007/978-94-017-9645-3{_}8`. 20

[59] Ian M. Hutchings. Leonardo da Vinci's studies of friction. *Wear*, 360-361:51–66, aug 2016. ISSN 00431648. doi: 10.1016/j.wear.2016.04.019. URL `https://www.sciencedirect.com/science/article/pii/S0043164816300588`. 20

[60] Duncan Dowson. Developments in lubrication - the thinning film. *J. Appl. Phys. D Appl. Phys.*, 25:334–339, 1992. ISSN 0002-9505. doi: 10.1119/1.1933017. URL `https://iopscience.iop.org/article/10.1088/0022-3727/25/1A/050`. 20, 21

[61] H. Spikes. Tribology research in the twenty-first century. *Tribol. Int.*, 34(12):789–799, dec 2001. ISSN 0301679X. doi: 10.1016/S0301-679X(01)00079-2. 20

[62] Valentin L. Popov. Is Tribology Approaching Its Golden Age? Grand Challenges in Engineering Education and Tribological Research. *Front. Mech. Eng.*, 4:16, nov 2018. ISSN 2297-3079. doi: 10.3389/fmech.2018.00016. URL `https://www.frontiersin.org/article/10.3389/fmech.2018.00016/full`. 20

[63] Gwidon W. Stachowiak. How tribology has been helping us to advance and to survive, sep 2017. ISSN 22237704. URL `http://link.springer.com/10.1007/s40544-017-0173-7`. 20

[64] Bharat Bhushan. *Modern tribology handbook.* CRC Press, 2001. ISBN 0849377870. URL `https://books.google.co.uk/books?hl=en{&}lr={&}id=h6X0NM7ME8IC{&}oi=fnd{&}pg=PP1{&}dq=modern+tribology+handbook{&}ots=JCCwWibE2k{&}sig=hJV6GQS8QMxi{_}R-Mudh4mu260Yk{#}v=onepage{&}q=moderntribologyhandbook{&}f=false`. 21, 42, 43, 44, 164

[65] Yifei Mo, Kevin T. Turner, and Izabela Szlufarska. Friction laws at the nanoscale. *Nature*, 457(7233):1116–1119, 2009. ISSN 00280836. doi: 10.1038/nature07748. URL `http://dx.doi.org/10.1038/nature07748`. 21

[66] Bharat Bhushan. *Nanotribology and Nanomechanics*, volume 366. Springer, 2008. ISBN 9788578110796. doi: 10.1098/rsta.2007.2170. URL `http://rsta.royalsocietypublishing.org/cgi/doi/10.1098/rsta.2007.2170`. 21

[67] Bharat Bhushan. *Handbook of Micro/Nanotribology*. CRC Press, 2 edition, 1998. ISBN 9788578110796. doi: 10.1017/CBO9781107415324.004. URL `https://www.crcpress.com/Handbook-of-MicroNano-Tribology/Bhushan/p/book/9780849384028`. 21, 27, 63, 64, 66

[68] W Gregory Sawyer and Kathryn J Wahl. Accessing inaccessible interfaces: In situ approaches to materials tribology. *MRS Bull.*, 33(12):1145–1150, 2008. ISSN 08837694. doi: 10.1557/mrs2008.244. 21, 175, 227, 231, 261

[69] Diana Berman, Ali Erdemir, and Anirudha V. Sumant. Approaches for Achieving Superlubricity in Two-Dimensional Materials. *ACS Nano*, 12(3):2122–2137, 2018. ISSN 1936086X. doi: 10.1021/acsnano.7b09046. 21, 27, 228, 260

[70] Frank Philip Bowden and David Tabor. *The friction and lubrication of solids*. Oxford Clarendon Press, 1950. 22, 64, 164

[71] J. F. Archard. Contact and rubbing of flat surfaces. *J. Appl. Phys.*, 24(8):981–988, 1953. ISSN 00218979. doi: 10.1063/1.1721448. 22, 90

[72] R.J.K. Wood. The sand erosion performance of coatings. *Mater. Des.*, 20(4):179–191, aug 1999. ISSN 02613069. doi: 10.1016/S0261-3069(99)00024-2. URL `https://www.sciencedirect.com/science/article/pii/S0261306999000242{#}FIG1http://dx.doi.org/10.1016/S0261-3069(99)00024-2`. 22, 23, 266

[73] Ian M Hutchings. Ductile-brittle transitions and wear maps for the erosion and abrasion of brittle materials. *J. Phys. D. Appl. Phys.*, 25(1):A212–A221, jan 1992. ISSN 13616463. doi: 10.1088/0022-3727/25/1A/033. URL `http://stacks.iop.org/0022-3727/25/i=1A/a=033?key=crossref.556b6a5096eac390e5b0a2da9ef04d77`. 22, n

[74] Joseph Zahavi and George F. Schmitt. Solid particle erosion of polymeric coatings. *Wear*, 71(2):191–210, sep 1981. ISSN 00431648. doi: 10.1016/0043-1648(81)90338-0. URL `https://www.sciencedirect.com/science/article/pii/0043164881903380`. 23, 138, 266, n

[75] A Matthews, S Franklin, and K Holmberg. Tribological coatings: Contact mechanisms and selection. *J. Phys. D. Appl. Phys.*, 40(18):5463–5475, sep 2007. ISSN 00223727. doi: 10.1088/0022-3727/40/18/S07. URL `http://stacks.iop.org/0022-3727/40/i=18/a=S07?key=crossref.8c8ff780076e33881f7eb5900b1d1245`. 23, 45, 160

[76] E. Bousser, L. Martinu, and J. E. Klemberg-Sapieha. Solid particle erosion mechanisms of protective coatings for aerospace applications. *Surf. Coatings Technol.*, 257:165–181, oct 2014. ISSN 02578972. doi: 10.1016/j.surfcoat.2014.08.037. 23, 136

[77] Michael Bromark, Per Hedenqvist, and Sture Hogmark. The influence of substrate material on the erosion resistance of TiN coated tool steels. *Wear*, 186-187(PART 1):189–194, jul 1995. ISSN 00431648. doi: 10.1016/0043-1648(95)07163-6. 23, 158, 160

[78] B. S. Mann, Vivek Arya, A. K. Maiti, M. U.B. Rao, and Pankaj Joshi. Corrosion and erosion performance of HVOF/TiAlN PVD coatings and candidate materials for high pressure gate valve application. *Wear*, 260(1-2):75–82, jan 2006. ISSN 00431648. doi: 10.1016/j.wear.2004.12.045. 23

[79] M. S. Mahdipoor, F. Tarasi, C. Moreau, A. Dolatabadi, and M. Medraj. HVOF sprayed coatings of nano-agglomerated tungsten-carbide/cobalt powders for water droplet erosion application. *Wear*, 330-331:338–347, may 2015. ISSN 00431648. doi: 10.1016/j.wear.2015.02.034.

[80] Michael W. Reedy, Timothy J. Eden, John K. Potter, and Douglas E. Wolfe. Erosion performance and characterization of nanolayer (Ti,Cr)N hard coatings for gas turbine engine compressor blade applications. *Surf. Coatings Technol.*, 206(2-3): 464–472, oct 2011. ISSN 02578972. doi: 10.1016/j.surfcoat.2011.07.063. 260

[81] G. Barbezat, A. R. Nicol, and A. Sickinger. Abrasion, erosion and scuffing resistance of carbide and oxide ceramic thermal sprayed coatings for different applications. *Wear*, 162-164(PART A):529–537, apr 1993. ISSN 00431648. doi: 10.1016/0043-1648(93)90538-W.

[82] K. S. Tan, J. A. Wharton, and R. J.K. Wood. Solid particle erosion-corrosion behaviour of a novel HVOF nickel aluminium bronze coating for marine applications - Correlation between mass loss and electrochemical measurements. In *Wear*, volume 258, pages 629–640. Elsevier, jan 2005. doi: 10.1016/j.wear.2004.02.019. 23

[83] X. C. Zhang, B. S. Xu, H. D. Wang, Y. X. Wu, and Y. Jiang. Hertzian contact response of single-layer, functionally graded and sandwich coatings. *Mater. Des.*, 28(1):47–54, jan 2007. ISSN 18734197. doi: 10.1016/j.matdes.2005.06.018. 23, 159, 177, 225

[84] Yongqing Shen, Bin Liao, Zhiqiang Zhang, Xianying Wu, Minju Ying, and Xu Zhang. Anti-sand erosion and tribological performance of thick DLC coatings deposited by the filtered cathodic vacuum arc. *Appl. Surf. Sci.*, 533(July): 147371, 2020. ISSN 01694332. doi: 10.1016/j.apsusc.2020.147371. URL https://doi.org/10.1016/j.apsusc.2020.147371. 23, 259

[85] S J Bull. Using work of indentation to predict erosion behavior in bulk materials and coatings. *J. Phys. D. Appl. Phys.*, 39(8):1626–1634, apr 2006. ISSN 00223727. doi: 10.1088/0022-3727/39/8/023. URL http://stacks.iop.org/0022-3727/39/i=8/a=023?key=crossref.fcbddd3fe8667130cfd8945d4ce605a4. 23, 161

[86] B. D. Beake, V. M. Vishnyakov, and J. S. Colligon. Nano-impact testing of TiFeN and TiFeMoN films for dynamic toughness evaluation. *J. Phys. D. Appl. Phys.*, 44 (8), 2011. ISSN 00223727. doi: 10.1088/0022-3727/44/8/085301. URL https://iopscience.iop.org/article/10.1088/0022-3727/44/8/085301. 23, 25, 69, 159, 160

[87] Robert J K Wood. Tribo-corrosion of coatings: A review. *J. Phys. D. Appl. Phys.*, 40(18):5502–5521, sep 2007. ISSN 00223727. doi: 10.1088/0022-3727/40/18/S10. URL http://stacks.iop.org/0022-3727/40/i=18/a=S10?key=crossref.f9f8bd124d6ea1476517812134aa1547. 23

[88] David R.H. Jones and Michael F. Ashby. *Engineering materials 1: An introduction to properties, applications and design.* Butterworth-Heinemann, 2019. ISBN 9780081020517. doi: 10.1016/C2015-0-04446-X. 23, 24

[89] Baoxing Xu, Akio Yonezu, and Xi Chen. An indentation fatigue strength law. *Philos. Mag. Lett.*, 90(5):313–322, 2010. ISSN 09500839. doi: 10.1080/09500831003662495. 23, 39, 110

[90] D. Chicot, K. Tilkin, K. Jankowski, and A. Wymysłowski. Reliability analysis of solder joints due to creep and fatigue in microelectronic packaging using microindentation technique. *Microelectron. Reliab.*, 53(5):761–766, may 2013. ISSN 00262714. doi: 10.1016/j.microrel.2013.01.008. 24, 39, 112

[91] R. B. Waterhouse. Fretting fatigue. *Mater. Sci. Eng.*, 25(C):201–206, sep 1976. ISSN 00255416. doi: 10.1016/0025-5416(76)90071-9. URL https://www.sciencedirect.com/science/article/pii/0025541676900719. 24

[92] R. B. Waterhouse. Fretting wear. *Wear*, 100(1-3):107–118, dec 1984. ISSN 00431648. doi: 10.1016/0043-1648(84)90008-5. URL https://www.sciencedirect.com/science/article/pii/0043164884900085. 24

[93] P. L. Hurricks. The mechanism of fretting - A review, jun 1970. ISSN 00431648. URL https://www.sciencedirect.com/science/article/pii/0043164870902358. 24

[94] M. H. Zhu and Z. R. Zhou. On the mechanisms of various fretting wear modes. In *Tribol. Int.*, volume 44, pages 1378–1388. Elsevier, oct 2011. ISBN 0301679X. doi: 10.1016/j.triboint.2011.02.010. URL https://www.sciencedirect.com/science/article/pii/S0301679X1100051X. 24

[95] Olof Vingsbo and Staffan Söderberg. On fretting maps. *Wear*, 126 (2):131–147, sep 1988. ISSN 00431648. doi: 10.1016/0043-1648(88)90134-2. URL https://www.sciencedirect.com/science/article/pii/0043164888901342?via{%}3Dihub. 24, 224

[96] Z. R. Zhou, K. Nakazawa, M. H. Zhu, N. Maruyama, Ph. Kapsa, and L. Vincent. Progress in fretting maps. *Tribol. Int.*, 39(10): 1068–1073, oct 2006. ISSN 0301679X. doi: 10.1016/j.triboint.2006.02.001. URL https://www.sciencedirect.com/science/article/pii/S0301679X0600051X?via{%}3Dihub{#}fig2. 24

[97] S. Fouvry, Ph. Kapsa, and L. Vincent. Analysis of sliding behaviour for fretting loadings: determination of transition criteria. *Wear*, 185(1-2):35–46, jun 1995. ISSN 00431648. doi: 10.1016/0043-1648(94)06582-9. URL https://www.sciencedirect.com/science/article/pii/0043164894065829. 24, 189, 201, 224

[98] Siegfried Fouvry, Philippe Kapsa, and Leo Vincent. Quantification of fretting damage. *Wear*, 200(1-2):186–205, dec 1996. ISSN 00431648. doi: 10.1016/S0043-1648(96)07306-1. URL https://www.sciencedirect.com/science/article/pii/S0043164896073061. 224

[99] S. Fouvry, Ph. Kapsa, and L. Vincent. Developments of fretting sliding criteria to quantify the local friction coefficient evolution under partial slip condition. In *Tribol. Ser.*, volume 34, pages 161–172. Elsevier, jan 1998. ISBN 9780444500335. doi: 10.1016/s0167-8922(98)80071-0. URL `https://www.sciencedirect.com/science/article/pii/S0167892298800710`. 24, 226

[100] Lifeng Ma, Kilho Eom, Jean Geringer, Tea Sung Jun, and Kyungmok Kim. Literature review on fretting wear and contact mechanics of tribological coatings. *Coatings*, 9(8):1–20, 2019. ISSN 20796412. doi: 10.3390/coatings9080501. 24, 225

[101] S Fouvry, Ph Kapsa, E Sauger, J.M Martin, L Ponsonnet, and L Vincent. Tribologically transformed structure in fretting. *Wear*, 245(1-2):39–52, oct 2002. ISSN 00431648. doi: 10.1016/s0043-1648(00)00464-6. URL `https://www.sciencedirect.com/science/article/pii/S0043164800004646`. 24, 200

[102] T. Liskiewicz, K. Kubiak, and T. Comyn. Nano-indentation mapping of fretting-induced surface layers. *Tribol. Int.*, 108:186–193, 2017. ISSN 0301679X. doi: 10.1016/j.triboint.2016.10.018. URL `https://www.sciencedirect.com/science/article/pii/S0301679X16303826`. 24, 69, 162, 229

[103] K. J. Kubiak, T. W. Liskiewicz, and T. G. Mathia. Surface morphology in engineering applications: Influence of roughness on sliding and wear in dry fretting. *Tribol. Int.*, 44(11):1427–1432, oct 2011. ISSN 0301679X. doi: 10.1016/j.triboint.2011.04.020. URL `https://www.sciencedirect.com/science/article/pii/S0301679X11001228`. 24, 201, 208, 211, 225

[104] T. Liskiewicz, S. Fouvry, and B. Wendler. Impact of variable loading conditions on fretting wear. *Surf. Coatings Technol.*, 163-164: 465–471, jan 2003. ISSN 02578972. doi: 10.1016/S0257-8972(02)00643-6. URL `https://www.sciencedirect.com/science/article/pii/S0257897202006436{#}FIG1`. 25, 268

[105] T. Liskiewicz and S. Fouvry. Development of a friction energy capacity approach to predict the surface coating endurance under complex oscillating sliding conditions. *Tribol. Int.*, 38(1):69–79, jan 2005. ISSN 0301679X. doi: 10.1016/j.triboint.2004.06.002. URL `https://www.sciencedirect.com/science/article/pii/S0301679X0400115X?via{%}3Dihub`. 25, 201, 211, 225, 229, 235

[106] A. Wade, R. Copley, A. Alsheikh Omar, B. Clarke, T. Liskiewicz, and M. Bryant. Novel numerical method for parameterising fretting contacts. *Tribol. Int.*, jun 2019. ISSN 0301679X. doi: 10.1016/j.triboint.2019.06.019. URL `https://www.sciencedirect.com/science/article/pii/S0301679X19303330{#}fig1https://linkinghub.elsevier.com/retrieve/pii/S0301679X19303330`. 25, 188

[107] A. Wade, R. Copley, B. Clarke, A. Alsheikh Omar, A. R. Beadling, T. Liskiewicz, and M. G. Bryant. Real-time fretting loop regime transition identification using acoustic emissions. *Tribol. Int.*, 145:106149, may 2020. ISSN 0301679X. doi: 10.1016/j.triboint.2019.106149. 25

[108] Z. R. Zhou and L. Vincent. Lubrication in fretting - A review, 1999. ISSN 00431648. 25, 187, 205, 226

[109] Georgios Skordaris, Antonios Bouzakis, and Konstantinos-Dionysios Bouzakis. Impact Test Applications Supported by FEA Models in Surface Engineering for Coating Characterization. *Mater. Proc.*, 2(1):13, 2020. doi: 10.3390/ciwc2020-06809. 25

[110] B. D. Beake, S. R. Goodes, and J. F. Smith. Micro-impact testing: A new technique for investigating thin film toughness, adhesion, erosive wear resistance, and dynamic hardness. *Surf. Eng.*, 17(3):187–192, jun 2001. ISSN 02670844. doi: 10.1179/026708401101517755. URL http://www.tandfonline.com/doi/full/10.1179/026708401101517755. 25, 29, 69, 136, 160

[111] B. D. Beake, S. R. Goodes, J. F. Smith, R. Madani, C. A. Rego, R. I. Cherry, and T. Wagner. Investigating the fracture resistance and adhesion of DLC films with micro-impact testing. *Diam. Relat. Mater.*, 11(8):1606–1609, aug 2002. ISSN 09259635. doi: 10.1016/S0925-9635(02)00107-3. URL http://www.sciencedirect.com/science/article/pii/S0925963502001073. 156

[112] Ben D. Beake, S. P. Lau, and James F. Smith. Evaluating the fracture properties and fatigue wear of tetrahedral amorphous carbon films on silicon by nano-impact testing. *Surf. Coatings Technol.*, 177-178:611–615, jan 2004. ISSN 02578972. doi: 10.1016/S0257-8972(03)00934-4. URL https://www.sciencedirect.com/science/article/pii/S0257897203009344. 25, 29, 73, 136, 158, 160

[113] Mario Rueda-Ruiz, Ben D. Beake, and Jon M. Molina-Aldareguia. New instrumentation and analysis methodology for nano-impact testing. *Mater. Des.*, page 108715, apr 2020. ISSN 02641275. doi: 10.1016/j.matdes.2020.108715. URL https://linkinghub.elsevier.com/retrieve/pii/S0264127520302495. 25, 36, 160

[114] O. Knotek, B. Bosserhoff, A. Schrey, T. Leyendecker, O. Lemmer, and S. Esser. A new technique for testing the impact load of thin films: the coating impact test. *Surf. Coatings Technol.*, 54-55:102–107, 1992. ISSN 02578972. doi: 10.1016/S0257-8972(09)90035-4. URL http://dx.doi.org/10.1016/S0257-8972(09)90035-4. 25

[115] R. Bantle and A. Matthews. Investigation into the impact wear behaviour of ceramic coatings. *Surf. Coatings Technol.*, 74-75(PART 2):857–868, 1995. ISSN 02578972. doi: 10.1016/0257-8972(95)08314-6. 25

[116] Ben D. Beake, Tomasz W. Liskiewicz, Andrew Bird, and Xiangru Shi. Micro-scale impact testing - A new approach to studying fatigue resistance in hard carbon coatings. *Tribol. Int.*, apr 2019. ISSN 0301679X. doi: 10.1016/j.triboint.2019.04.016. URL https://www.sciencedirect.com/science/article/pii/S0301679X19302105. 25, 160

[117] Qing Zhou, Weichao Han, Yin Du, Hongxing Wu, Andrew Bird, Xiaoxing Zhao, Xianzong Wang, Haifeng Wang, and Ben D. Beake. Enhancing fatigue wear resistance of a bulk metallic glass via introducing phase separation: A micro-impact test analysis. *Wear*, 436-437:203037, oct 2019. ISSN 0043-1648. doi: 10.1016/J.WEAR.2019.203037. URL https://www.sciencedirect.com/science/article/pii/S0043164819309949?dgcid=rss{_}sd{_}all{&}utm{_}source=researcher{_}app{&}utm{_}medium=referral{&}utm{_}campaign=RESR{_}MRKT{_}Researcher{_}inbound. 160

[118] Ben D. Beake, Luis Isern, Jose L. Endrino, and German S. Fox-Rabinovich. Micro-impact testing of AlTiN and TiAlCrN coatings. *Wear*, 418-419:102–110, jan 2019. ISSN 00431648. doi: 10.1016/j.wear.2018.11.010. URL `https://www.sciencedirect.com/science/article/pii/S0043164818308469`. 25, 51, 69, 137, 144, 159, 260

[119] K.-D. Bouzakis, M Pappa, S Gerardis, G Skordaris, and E Bouzakis. PVD Coatings' Strength Properties at Various Temperatures by Nanoindentations and FEM Calculations Determined. *Tribol. Ind.*, 34 (1):29–35, 2012. URL `https://www.researchgate.net/publication/283779545{_}PVD{_}Coatings{%}27{_}Strength{_}Properties{_}at{_}Variou` 25

[120] T. Fu, Z. F. Zhou, Y. M. Zhou, X. D. Zhu, Q. F. Zeng, C. P. Wang, K. Y. Li, and J. Lu. Mechanical properties of DLC coating sputter deposited on surface nanocrystallized 304 stainless steel. *Surf. Coatings Technol.*, 207:555–564, aug 2012. ISSN 02578972. doi: 10.1016/j.surfcoat.2012.07.076. URL `https://www.sciencedirect.com/science/article/pii/S0257897212007669`. 25

[121] Mehdi Akhondizadeh, Majid Fooladi Mahani, Masoud Rezaeizadeh, and Hoseyn S. Mansouri. Theoretical and experimental modeling of impact wear. *Ind. Lubr. Tribol.*, 70(3):490–498, 2018. ISSN 00368792. doi: 10.1108/ILT-06-2017-0159. 25

[122] Ben D. Beake. Evaluation of the fracture resistance of DLC coatings on tool steel under dynamic loading. *Surf. Coatings Technol.*, 198(1-3 SPEC. ISS.):90–93, aug 2005. ISSN 02578972. doi: 10.1016/j.surfcoat.2004.10.048. URL `https://www.sciencedirect.com/science/article/pii/S0257897204010448`. 25, 51, 68, 137, 159, 160, 161, 260

[123] Cristiana Delprete and Abbas Razavykia. Piston dynamics, lubrication and tribological performance evaluation: A review. *Int. J. Engine Res.*, 21(5):725–741, jun 2020. ISSN 20413149. doi: 10.1177/1468087418787610. 26

[124] K. A.M. Kassim, T. Tokoroyama, M. Murashima, and N. Umehara. The wear classification of MoDTC-derived particles on silicon and hydrogenated diamond-like carbon at room temperature. *Tribol. Int.*, page 106176, jan 2020. ISSN 0301679X. doi: 10.1016/j.triboint.2020.106176. 26, 226

[125] Shahriar Kosarieh, Ardian Morina, Jonathan Flemming, Emmanuel Lainé, and Anne Neville. Wear Mechanisms of Hydrogenated DLC in Oils Containing MoDTC. *Tribol. Lett.*, 64(1), 2016. ISSN 10238883. doi: 10.1007/s11249-016-0737-0. 26, 60, 226, 228, 266

[126] H. Spikes. The history and mechanisms of ZDDP. *Tribol. Lett.*, 17(3):469–489, 2004. ISSN 10238883. doi: 10.1023/B:TRIL.0000044495.26882.b5. 26

[127] Jie Zhang and Hugh Spikes. On the Mechanism of ZDDP Antiwear Film Formation. *Tribol. Lett.*, 63(2):1–15, 2016. ISSN 10238883. doi: 10.1007/s11249-016-0706-7. 26

[128] Mohammad R. Vazirisereshk, Ashlie Martini, David A. Strubbe, and Mehmet Z. Baykara. Solid lubrication with MoS2: A review. *Lubricants*, 7(7), 2019. ISSN 20754442. doi: 10.3390/LUBRICANTS7070057. 26

[129] Diana Berman, Ali Erdemir, and Anirudha V. Sumant. Reduced wear and friction enabled by graphene layers on sliding steel surfaces in dry nitrogen. *Carbon N. Y.*, 59:167–175, 2013. ISSN 00086223. doi: 10.1016/j.carbon.2013.03.006. URL `http://dx.doi.org/10.1016/j.carbon.2013.03.006`. 27

[130] Xinchun Chen and Jinjin Li. Superlubricity of carbon nanostructures. *Carbon N. Y.*, 158:1–23, mar 2020. ISSN 00086223. doi: 10.1016/j.carbon.2019.11.077. 27, 228

[131] Weili Zhao and Fangli Duan. Friction properties of carbon nanoparticles (nanodiamond and nanoscroll) confined between DLC and a-SiO2 surfaces. *Tribol. Int.*, 145:106153, may 2020. ISSN 0301679X. doi: 10.1016/j.triboint.2019.106153. 27, 68

[132] Diana Berman, Sanket A. Deshmukh, Subramanian K.R.S. Sankaranarayanan, Ali Erdemir, and Anirudha V. Sumant. Macroscale superlubricity enabled by graphene nanoscroll formation. *Science (80-.).*, 348(6239):1118–1122, 2015. ISSN 10959203. doi: 10.1126/science.1262024. 27, 228

[133] Satish Achanta, Dirk Drees, and Jean Pierre Celis. Friction from nano to macroforce scales analyzed by single and multiple-asperity contact approaches. *Surf. Coatings Technol.*, 202(24):6127–6135, aug 2008. ISSN 02578972. doi: 10.1016/j.surfcoat.2008.07.020. 27, 28, 231, 252, 260

[134] D. Devaprakasam, O. P. Khatri, N. Shankar, and S. K. Biswas. Boundary lubrication additives for aluminium: A journey from nano to macrotribology. *Tribol. Int.*, 38(11-12 SPEC. ISS.):1022–1034, nov 2005. ISSN 0301679X. doi: 10.1016/j.triboint.2005.07.030. URL `https://www.sciencedirect.com/science/article/pii/S0301679X0500201X`. 27

[135] Philippe Stempflé and Jamal Takadoum. Multi-asperity nanotribological behavior of single-crystal silicon: Crystallography-induced anisotropy in friction and wear. In *Tribol. Int.*, volume 48, pages 35–43. Elsevier, apr 2012. doi: 10.1016/j.triboint. 2011.03.027. URL `https://www.sciencedirect.com/science/article/pii/S0301679X11000922`. 27

[136] Jibin Pu, Deming Huang, Liping Wang, and Qunji Xue. Tribology study of dual-layer ultrathin ionic liquid films with bonded phase: Influences of the self-assembled underlayer. *Colloids Surfaces A Physicochem. Eng. Asp.*, 372 (1-3):155–164, dec 2010. ISSN 09277757. doi: 10.1016/j.colsurfa.2010. 10.017. URL `https://www.sciencedirect.com/science/article/pii/S0927775710005881`. 27

[137] Satish Achanta, Dirk Drees, and Jean Pierre Celis. Friction and nanowear of hard coatings in reciprocating sliding at milli-Newton loads. In *Wear*, volume 259, pages 719–729. Elsevier, jul 2005. doi: 10.1016/j.wear.2005.02.078. 28, 231, 252

[138] James L Bosse, Sungjun Lee, Andreas Sø Andersen, Duncan S Sutherland, and Bryan D Huey. High speed friction microscopy and nanoscale friction coefficient mapping. *Meas. Sci. Technol.*, 25(11):115401, oct 2014. ISSN 13616501. doi: 10.1088/0957-0233/25/11/115401. URL `https://iopscience.iop.org/article/10.1088/0957-0233/25/11/115401https://iopscience.iop.org/article/10.1088/0957-0233/25/11/115401/meta`. 28, 231

[139] Zhenhua Tao and Bharat Bhushan. New technique for studying nanoscale friction at sliding velocities up to 200 mms using atomic force microscope, 2006. ISSN 00346748. 28

[140] L. Calabri, N. Pugno, C. Menozzi, and S. Valeri. AFM nanoindentation: Tip shape and tip radius of curvature effect on the hardness measurement. *J. Phys. Condens. Matter*, 20(47), 2008. ISSN 09538984. doi: 10.1088/0953-8984/20/47/474208. 28

[141] Zhixin Zeng and Jin Chong Tan. AFM Nanoindentation to Quantify Mechanical Properties of Nano- and Micron-Sized Crystals of a Metal-Organic Framework Material. *ACS Appl. Mater. Interfaces*, 9(45):39839–39854, 2017. ISSN 19448252. doi: 10.1021/acsami.7b13402. 28

[142] Davide Tranchida, Stefano Piccarolo, and Maria Soliman. Nanoscale mechanical characterization of polymers by AFM nanoindentations: Critical approach to the elastic characterization. *Macromolecules*, 39(13):4547–4556, 2006. ISSN 00249297. doi: 10.1021/ma052727j. 28

[143] Abdel Dorgham, Pourya Parsaeian, Abdullah Azam, Chun Wang, Ardian Morina, and Anne Neville. Single-asperity study of the reaction kinetics of P-based triboreactive films. *Tribol. Int.*, 133:288–296, may 2019. ISSN 0301679X. doi: 10.1016/j.triboint.2018.11.029. 28

[144] Ben D. Beake and James F. Smith. Nano-impact testing - An effective tool for assessing the resistance of advanced wear-resistant coatings to fatigue failure and delamination. *Surf. Coatings Technol.*, 188-189(1-3 SPEC.ISS.):594–598, nov 2004. ISSN 02578972. doi: 10.1016/j.surfcoat.2004.07.016. URL `https://www.sciencedirect.com/science/article/pii/S0257897204005596`. 29, 136, 160, 161

[145] J. X. Yu, L. M. Qian, B. J. Yu, and Z. R. Zhou. Nanofretting behaviors of monocrystalline silicon (1 0 0) against diamond tips in atmosphere and vacuum. *Wear*, 267(1-4):322–329, jun 2009. ISSN 00431648. doi: 10.1016/j.wear.2008.11.008. URL `https://www.sciencedirect.com/science/article/pii/S0043164809000544`. 29, 227

[146] T. W. Liskiewicz, B. D. Beake, and J. F. Smith. In situ accelerated micro-wear - A new technique to fill the measurement gap. *Surf. Coatings Technol.*, 205 (5):1455–1459, nov 2010. ISSN 02578972. doi: 10.1016/j.surfcoat.2010.07.109. URL `https://www.sciencedirect.com/science/article/abs/pii/S0257897210006316`. 29, 187, 268

[147] Lei Chen, Mingchu Yang, Jiaxin Yu, Linmao Qian, and Zhongrong Zhou. Nanofretting behaviours of ultrathin DLC coating on Si(100) substrate. *Wear*, 271(9-10):1980–1986, jul 2011. ISSN 00431648. doi: 10.1016/j.wear.2010.11.016. URL `https://www.sciencedirect.com/science/article/pii/S0043164811000834`. 29, 227, 269

[148] B.D. Beake, T.W. Liskiewicz, N.J. Pickford, and J.F. Smith. Accelerated nanofretting testing of Si(1 0 0). *Tribol. Int.*, 46(1):114–118, feb 2012. ISSN 0301-679X. doi: 10.1016/J.TRIBOINT.2011.05.027. URL `https://www.sciencedirect.com/science/article/pii/S0301679X11001599`. 29, 226

[149] B. D. Beake, T. W. Liskiewicz, and J. F. Smith. Deformation of Si(100) in spherical contacts - Comparison of nano-fretting and nano-scratch tests with nano-indentation. *Surf. Coatings Technol.*, 206(7):1921–1926, dec 2011. ISSN 02578972. doi: 10.1016/j.surfcoat.2011.10.035. URL `https://www.sciencedirect.com/science/article/pii/S0257897211010413`. 65, 68, 187, 227, 268

[150] B. D. Beake, M. I. Davies, T. W. Liskiewicz, V. M. Vishnyakov, and S. R. Goodes. Nano-scratch, nanoindentation and fretting tests of 5-80nm ta-C films on Si(100). *Wear*, 301(1-2):575–582, 2013. ISSN 00431648. doi: 10.1016/j.wear.2013.01.073. URL `http://dx.doi.org/10.1016/j.wear.2013.01.073`. 29, 68, 231

[151] Keiji Nakayama. Triboemission and triboplasma generation with dlc films. In *Tribol. Diamond-Like Carbon Film. Fundam. Appl.*, pages 291–310. Springer US, Boston, MA, 2008. ISBN 9780387302645. doi: 10.1007/978-0-387-49891-1_11. URL `http://link.springer.com/10.1007/978-0-387-49891-1{_}11`. 29, 30, 269

[152] Peng Bai, Guang Zhu, Yu Sheng Zhou, Sihong Wang, Jusheng Ma, Gong Zhang, and Zhong Lin Wang. Dipole-moment-induced effect on contact electrification for triboelectric nanogenerators. *Nano Res.*, 7(7):990–997, jun 2014. ISSN 19980000. doi: 10.1007/s12274-014-0461-8. 30

[153] Shuaihang Pan and Zhinan Zhang. Fundamental theories and basic principles of triboelectric effect: A review, feb 2019. ISSN 22237704. 30

[154] Yuanjie Su, Jun Chen, Zhiming Wu, and Yadong Jiang. Low temperature dependence of triboelectric effect for energy harvesting and self-powered active sensing. *Appl. Phys. Lett.*, 106(1):013114, jan 2015. ISSN 00036951. doi: 10.1063/1.4905553. URL `http://aip.scitation.org/doi/10.1063/1.4905553`.

[155] Mihai Lungu. Electrical separation of plastic materials using the triboelectric effect. *Miner. Eng.*, 17(1):69–75, jan 2004. ISSN 08926875. doi: 10.1016/j.mineng.2003.10.010.

[156] Vu Nguyen and Rusen Yang. Effect of humidity and pressure on the triboelectric nanogenerator. *Nano Energy*, 2(5):604–608, jun 2013. ISSN 22112855. doi: 10.1016/j.nanoen.2013.07.012. 30

[157] Yuanjie Su, Guangzhong Xie, Si Wang, Huiling Tai, Qiuping Zhang, Hongfei Du, Hulin Zhang, Xiaosong Du, and Yadong Jiang. Novel high-performance self-powered humidity detection enabled by triboelectric effect. *Sensors Actuators, B Chem.*, 251:144–152, nov 2017. ISSN 09254005. doi: 10.1016/j.snb.2017.04.039. 30

[158] Sihong Wang, Long Lin, and Zhong Lin Wang. Nanoscale triboelectric-effect-enabled energy conversion for sustainably powering portable electronics. *Nano Lett.*, 12(12):6339–6346, dec 2012. ISSN 15306984. doi: 10.1021/nl303573d. 30, 269

[159] Haiyang Zou, Ying Zhang, Litong Guo, Peihong Wang, Xu He, Guozhang Dai, Haiwu Zheng, Chaoyu Chen, Aurelia Chi Wang, Cheng Xu, and Zhong Lin Wang. Quantifying the triboelectric series. *Nat. Commun.*, 10(1):1–9, dec 2019. ISSN 20411723. doi: 10.1038/s41467-019-09461-x. 30, 31, 32

[160] Feng Ru Fan, Zhong Qun Tian, and Zhong Lin Wang. Flexible triboelectric generator. *Nano Energy*, 1(2):328–334, mar 2012. ISSN 22112855. doi: 10.1016/j.nanoen.2012.01.004. 30

[161] Michael F. Ashby and David R.H. Jones. Yield Strength, Tensile Strength, and Ductility. In *Eng. Mater. 1*, pages 115–133. Butterworth-Heinemann, 2012. ISBN 9780080966656. doi: 10.1016/b978-0-08-096665-6.00008-8. 33

[162] ISO. ISO 14577-1:2015 Metallic materials – Instrumented indentation test for hardness and materials parameters – Part 1: Test method, 2015. URL `https://www.iso.org/standard/56626.html`. 33, 35, 36, 37, 90, 110, 112, 259

[163] G. M. Pharr. Measurement of mechanical properties by ultra-low load indentation. *Mater. Sci. Eng. A*, 253(1-2):151–159, sep 1998. ISSN 09215093. doi: 10.1016/s0921-5093(98)00724-2. 33, 35, 42, 159, 260

[164] A. P. Ternovskii, V. P. Alekhin, M. Kh Shorshorov, M. M. Krushchov, and V. N. Skvortsov. MICROMECHANICAL TESTING OF MATERIALS BY DEPRESSION. *Ind Lab*, 39(10):1620–1624, 1973.

[165] S. I. Bulychev, V. P. Alekhin, M. Kh Shorshorov, A. P. Ternovskii, and G. D. Shnyrev. DETERMINING YOUNG'S MODULUS FROM THE INDENTOR PENETRATION DIAGRAM. *Ind Lab*, 41(9):1409–1412, 1975. 33

[166] A. C. Fischer-Cripps. Critical review of analysis and interpretation of nanoindentation test data. *Surf. Coatings Technol.*, 200(14-15):4153–4165, apr 2006. ISSN 02578972. doi: 10.1016/j.surfcoat.2005.03.018. 34, 37, 38, 40, 41, 90, 99, 102, 105, 108, 110, 114, 173, 260

[167] G. M. Pharr and W. C. Oliver. Measurement of thin film mechanical properties using nanoindentation. *Mrs Bull.*, 17(7):28–33, jul 1992. ISSN 08837694. doi: 10.1557/S0883769400041634. URL `http://www.journals.cambridge.org/abstract{_}S0883769400041634http://journals.cambridge.org/abstract{_}S0883769400041634`. 35, 91, 166

[168] W. C. Oliver and G. M. Pharr. An improved technique for determining hardness and elastic modulus using load and displacement sensing indentation experiments. *J. Mater. Res.*, 7(6):1564–1583, jun 1992. ISSN 20445326. doi: 10.1557/JMR.1992.1564. URL `http://www.journals.cambridge.org/abstract{_}S0884291400017039`. 91, 93, 166, 232

[169] A.C Fischer-Cripps. A review of analysis methods for sub-micron indentation testing. *Vacuum*, 58(4):569–585, sep 2000. ISSN 0042207X. doi: 10.1016/S0042-207X(00)00377-8. URL `https://www.sciencedirect.com/science/article/pii/S0042207X00003778http://linkinghub.elsevier.com/retrieve/pii/S0042207X00003778`. 35

[170] Michelle L. Oyen and Robert F. Cook. A practical guide for analysis of nanoindentation data. *J. Mech. Behav. Biomed. Mater.*, 2(4):396–407, aug 2009. ISSN 17516161. doi: 10.1016/j.jmbbm.2008.10.002. URL `https://www.sciencedirect.com/science/article/pii/S1751616108000805`. 35

[171] D. Chicot, F. Roudet, A. Zaoui, G. Louis, and V. Lepingle. Influence of visco-elasto-plastic properties of magnetite on the elastic modulus: Multicyclic indentation and theoretical studies. *Mater. Chem. Phys.*, 119(1-2):75–81, jan 2010. ISSN 02540584. doi: 10.1016/j.matchemphys.2009.07.033. 35, 39, 112

[172] R. Rabe, J. M. Breguet, P. Schwaller, S. Stauss, F. J. Haug, J. Patscheider, and J. Michler. Observation of fracture and plastic deformation during indentation and scratching inside the scanning electron microscope. *Thin Solid Films*, 469-470 (SPEC. ISS.):206–213, 2004. ISSN 00406090. doi: 10.1016/j.tsf.2004.08.096. 35

[173] T. Y. Tsui and G. M. Pharr. Substrate effects on nanoindentation mechanical property measurement of soft films on hard substrates. *J. Mater. Res.*, 14(1):292–301, 1999. ISSN 08842914. doi: 10.1557/JMR.1999.0042. 36

[174] P. Vijai Bharathy, D. Nataraj, Paul K. Chu, Huaiyu Wang, Q. Yang, M. S.R.N. Kiran, J. Silvestre-Albero, and D. Mangalaraj. Effect of titanium incorporation on the structural, mechanical and biocompatible properties of DLC thin films prepared by reactive-biased target ion beam deposition method. *Appl. Surf. Sci.*, 257(1): 143–150, 2010. ISSN 01694332. doi: 10.1016/j.apsusc.2010.06.052. URL http://dx.doi.org/10.1016/j.apsusc.2010.06.052. 36

[175] H. Bückle. Progress in micro-indentation hardness testing. *Metall. Rev.*, 4(1):49–100, 1959. ISSN 00766690. doi: 10.1179/095066059790421746. URL https://www.tandfonline.com/doi/abs/10.1179/095066059790421746. 37, 42, 259

[176] J. D.J. Ross, H. M. Pollock, J. C. Pivin, and J. Takadoum. Limits to the hardness testing of films thinner than 1 μm, 1987. ISSN 00406090. 37

[177] D. Newey, M. A. Wilkins, and H. M. Pollock. An ultra-low-load penetration hardness tester. *J. Phys. E.*, 15(1):119–122, 1982. ISSN 00223735. doi: 10.1088/0022-3735/15/1/023. 37

[178] T. Y. Tsui, G. M. Pharr, W. C. Oliver, C. S. Bhatia, R. L. White, S. Anders, A. Anders, and I. G. Brown. Nanoindentation and nanoscratching of hard carbon coatings for magnetic disks. In *Mater. Res. Soc. Symp. - Proc.*, volume 383, pages 447–452. Materials Research Society, 1995. doi: 10.1557/proc-383-447. 38

[179] C. Feng, J. M. Tannenbaum, B. S. Kang, and M. A. Alvin. A load-based multiple-partial unloading micro-indentation technique for mechanical property evaluation. *Exp. Mech.*, 50(6):737–743, 2010. ISSN 00144851. doi: 10.1007/s11340-009-9271-4. 38

[180] C. Klapperich, K. Komvopoulos, and L. Pruitt. Nanomechanical properties of polymers determined from nanoindentation experiments. *J. Tribol.*, 123(3):624–631, jul 2001. ISSN 15288897. doi: 10.1115/1.1330736. 38

[181] Xiaodong Li and Bharat Bhushan. A review of nanoindentation continuous stiffness measurement technique and its applications, feb 2002. ISSN 10445803. URL http://www.sciencedirect.com/science/article/pii/S1044580302001924. 38

[182] William D. Nix and Huajian Gao. Indentation size effects in crystalline materials: A law for strain gradient plasticity. *J. Mech. Phys. Solids*, 46(3):411–425, mar 1998. ISSN 00225096. doi: 10.1016/S0022-5096(97)00086-0. 40, 41, 110

[183] A. M. Korsunsky, M. R. McGurk, S. J. Bull, and T. F. Page. On the hardness of coated systems. *Surf. Coatings Technol.*, 99(1-2):171–183, feb 1998. ISSN 02578972. doi: 10.1016/S0257-8972(97)00522-7. 40, 42, 97, 105, 112, 258, 259

[184] Esteban Broitman. Indentation Hardness Measurements at Macro-, Micro-, and Nanoscale: A Critical Overview. *Tribol. Lett.*, 65(1):23, mar 2017. ISSN 10238883. doi: 10.1007/s11249-016-0805-5. URL http://link.springer.com/10.1007/s11249-016-0805-5. 40, 41, 42, 95, 110, 260

[185] Thomas Chudoba. Measurement of Hardness and Young's Modulus by Nanoindentation. pages 216–260. Springer, New York, NY, 2006. doi: 10.1007/978-0-387-48756-4_6. URL https://link.springer.com/chapter/10.1007/978-0-387-48756-4{_}6. 40

[186] Tong Yi Zhang, Wei Hua Xu, and Ming Hao Zhao. The role of plastic deformation of rough surfaces in the size-dependent hardness. *Acta Mater.*, 52(1):57–68, jan 2004. ISSN 13596454. doi: 10.1016/j.actamat.2003.08.026. 41

[187] Y. Huang, F. Zhang, K. C. Hwang, W. D. Nix, G. M. Pharr, and G. Feng. A model of size effects in nano-indentation. *J. Mech. Phys. Solids*, 54(8):1668–1686, aug 2006. ISSN 00225096. doi: 10.1016/j.jmps.2006.02.002. 42

[188] Andrew Gouldstone, Nuwong Chollacoop, Ming Dao, Ju Li, Andrew M. Minor, and Yu Lin Shen. Indentation across size scales and disciplines: Recent developments in experimentation and modeling. *Acta Mater.*, 55(12):4015–4039, jul 2007. ISSN 13596454. doi: 10.1016/j.actamat.2006.08.044. 42

[189] George M. Pharr, Erik G. Herbert, and Yanfei Gao. The indentation size effect: A critical examination of experimental observations and mechanistic interpretations. *Annu. Rev. Mater. Res.*, 40(1):271–292, jun 2010. ISSN 15317331. doi: 10.1146/annurev-matsci-070909-104456. URL http://www.annualreviews.org/doi/10.1146/annurev-matsci-070909-104456. 42, 110

[190] E. S. Gadelmawla, M. M. Koura, T. M.A. Maksoud, I. M. Elewa, and H. H. Soliman. Roughness parameters. *J. Mater. Process. Technol.*, 123(1):133–145, apr 2002. ISSN 09240136. doi: 10.1016/S0924-0136(02)00060-2. 43

[191] T. R. Thomas. Roughness and function. *Surf. Topogr. Metrol. Prop.*, 2(1):10, jan 2014. ISSN 2051672X. doi: 10.1088/2051-672X/2/1/014001. URL https://iopscience.iop.org/article/10.1088/2051-672X/2/1/014001https://iopscience.iop.org/article/10.1088/2051-672X/2/1/014001/meta. 43, 231

[192] ASME. B46.1 Surface Texture (Surface Roughness, Waviness, and Lay), 2019. URL https://www.asme.org/codes-standards/find-codes-standards/b46-1-surface-texture. 44

[193] Tadeusz. Burakowski and Tadeusz Wirzchon. *Surface Engineering of Metals: Principles, Equipment, Technologies.* CRC Press, 1999. ISBN 9780849382253. URL https://www.crcpress.com/Surface-Engineering-of-Metals-Principles-Equipment-Technologies/Burakowski-Wierzchon/p/book/9780849382253. 43

[194] Donald M. Mattox. *Handbook of Physical Vapor Deposition Processing*. William Andrew, 2009. ISBN 9780815520375. doi: 10.1016/B978-0-8155-2037-5.00025-3. URL http://www.sciencedirect.com/science/book/9780815520375http://www.elsevier.com/wps/find/bookdescription.cws{_}home/717814/description{#}description. 43, 46

[195] Peter M. Martin. *Introduction to Surface Engineering and Functionally Engineered Materials*. John Wiley & Sons, Inc., Hoboken, NJ, USA, aug 2011. ISBN 9780470639276. doi: 10.1002/9781118171899. URL http://doi.wiley.com/10.1002/9781118171899. 44

[196] Binshi Xu and Wei Zhang. Progress and application of nano-surface engineering in china. In *Nov. Mater. Process. by Adv. Electromagn. Energy Sources*, pages 339–343. Elsevier Science Ltd, jan 2005. ISBN 9780080445045. doi: 10.1016/B978-008044504-5/50070-2. 44

[197] Gordon England. Surface Engineering in a Nutshell, 2007. URL http://www.surfaceengineer.co.uk/. 44

[198] J. Meneve, K. Vercammen, E. Dekempeneer, and J. Smeets. Thin tribological coatings: Magic or design? *Surf. Coatings Technol.*, 94-95:476–482, oct 1997. ISSN 02578972. doi: 10.1016/S0257-8972(97)00430-1. URL https://www.sciencedirect.com/science/article/pii/S0257897297004301. 45, 68, 158, 177, 267

[199] P. A. Dearnley. Meeting tribological challenges with surface engineered materials. *Tribol. - Mater. Surfaces Interfaces*, 1(1):18–27, mar 2007. ISSN 1751-5831. doi: 10.1179/175158407x181516. 45

[200] Norbert Schwarzer. Completely analytical tools for the next generation of surface and coating optimization. *Coatings*, 4(2):253–281, 2014. ISSN 20796412. doi: 10.3390/coatings4020253. 45, 178

[201] B. D. Beake, G. S. Fox-Rabinovich, S. C. Veldhuis, and S. R. Goodes. Coating optimisation for high speed machining with advanced nanomechanical test methods. *Surf. Coatings Technol.*, 203(13):1919–1925, mar 2009. ISSN 02578972. doi: 10.1016/j.surfcoat.2009.01.025. URL https://www.sciencedirect.com/science/article/pii/S025789720900053X. 45, 67, 266

[202] C. Muratore and A.A. Voevodin. Chameleon Coatings: Adaptive Surfaces to Reduce Friction and Wear in Extreme Environments. *Annu. Rev. Mater. Res.*, 39(1):297–324, aug 2009. ISSN 1531-7331. doi: 10.1146/annurev-matsci-082908-145259. URL http://www.annualreviews.org/doi/10.1146/annurev-matsci-082908-145259. 45

[203] C. C. Baker, J. J. Hu, and A. A. Voevodin. Preparation of Al2O3/DLC/Au/MoS2 chameleon coatings for space and ambient environments. *Surf. Coatings Technol.*, 201(7 SPEC. ISS.):4224–4229, 2006. ISSN 02578972. doi: 10.1016/j.surfcoat.2006.08.067. 45

[204] Robert J Goldston and Paul H Rutherford. *Introduction to Plasma Physics*. 1995. doi: 10.1887/075030183x. URL https://www.amazon.co.uk/Introduction-Plasma-Physics/dp/075030183X. 45, 46

[205] Annemie Bogaerts, Eric Neyts, Renaat Gijbels, and Joost Van der Mullen. Gas Discharge Plasmas and Their Applications. *Spectrochim. Acta Part B*, 57:609 – 658, 2002. 45, 46

[206] Electric glow discharge — Plasma-Universe.com. URL `https://www.plasma-universe.com/electric-glow-discharge/{#}cite{_}note-2https://www.plasma-universe.com/electric-glow-discharge/`. 46

[207] Steven W. Stahler and Francesco Palla. *The Formation of Stars*. Wiley, nov 2008. ISBN 9783527618675. doi: 10.1002/9783527618675. URL `https://onlinelibrary.wiley.com/doi/book/10.1002/9783527618675`. 46

[208] NASA, ESA, and M. Robberto. Orion Nebula - Hubble 2006, 2006. URL `https://commons.wikimedia.org/wiki/File:Orion{_}Nebula{_}-{_}Hubble{_}2006{_}mosaic{_}18000.jpg`. 47

[209] Hugh O. Pierson. *Handbook of Chemical Vapor Deposition*. Noyes Publications, 1999. ISBN 9780815514329. doi: 10.1016/b978-0-8155-1300-1.50009-x. URL `http://www.sciencedirect.com/science/book/9780815514329`. 46, 47

[210] Immodus. Magnetron sputtering source, 2013. URL `https://commons.wikimedia.org/wiki/File:Magnetron{_}sputtering{_}source.jpg`. 47

[211] John A. Thornton. Influence of apparatus geometry and deposition conditions on the structure and topography of thick sputtered coatings. *J. Vac. Sci. Technol.*, 11 (4):666–670, jul 1974. ISSN 0022-5355. doi: 10.1116/1.1312732. URL `http://avs.scitation.org/doi/10.1116/1.1312732`. 48, 87

[212] J A Thornton. High Rate Thick Film Growth. *Annu. Rev. Mater. Sci.*, 7(1): 239–260, aug 1977. ISSN 0084-6600. doi: 10.1146/annurev.ms.07.080177. 001323. URL `http://www.annualreviews.org/doi/10.1146/annurev.ms.07.080177.001323`. 48, 87, 121

[213] John A. Thornton and D. W. Hoffman. Stress-related effects in thin films. *Thin Solid Films*, 171(1):5–31, apr 1989. ISSN 00406090. doi: 10.1016/0040-6090(89)90030-8. URL `https://www.sciencedirect.com/science/article/pii/0040609089900308`. 48

[214] Y. Lifshitz, S. R. Kasi, J. W. Rabalais, and W. Eckstein. Subplantation model for film growth from hyperthermal species. *Phys. Rev. B*, 41(15):10468–10480, may 1990. ISSN 01631829. doi: 10.1103/PhysRevB.41.10468. URL `https://link.aps.org/doi/10.1103/PhysRevB.41.10468`. 48

[215] Wenting He, Georg Mauer, Alexander Schwedt, Olivier Guillon, and Robert Vaßen. Advanced crystallographic study of the columnar growth of YZS coatings produced by PS-PVD. *J. Eur. Ceram. Soc.*, 38(5):2449–2453, 2018. ISSN 1873619X. doi: 10.1016/j.jeurceramsoc.2017.12.054. URL `https://doi.org/10.1016/j.jeurceramsoc.2017.12.054`. 48

[216] J. Robertson. Diamond-like amorphous carbon. *Mater. Sci. Eng. R Reports*, 37(4-6):129–281, may 2002. ISSN 0927796X. doi: 10.1016/S0927-796X(02)00005-0. URL `http://www.sciencedirect.com/science/article/pii/S0927796X02000050`. 48, 49, 50, 51, 53, 57, 58, 87, 116, 265

[217] S. V. Hainsworth and N. J. Uhure. Diamond like carbon coatings for tribology: production techniques, characterisation methods and applications. *Int. Mater. Rev.*, 52(3):153–174, may 2007. ISSN 0950-6608. doi: 10.1179/174328007X160272. URL `http://www.tandfonline.com/doi/full/10.1179/174328007X160272`. 48, 49, 50, 51, 52, 57, 60, 87, 91, 112, 132, 189

[218] J. Robertson. Properties of diamond-like carbon, feb 1992. ISSN 02578972. URL `http://www.sciencedirect.com/science/article/pii/025789729290001Q`. 48, 51

[219] Y. Lifshitz. Diamond-like carbon — present status. *Diam. Relat. Mater.*, 8(8-9):1659–1676, aug 1999. ISSN 09259635. doi: 10.1016/S0925-9635(99)00087-4. URL `http://www.sciencedirect.com/science/article/pii/S0925963599000874http://linkinghub.elsevier.com/retrieve/pii/S0925963599000874`. 48, 51

[220] A. Grill. Review of the tribology of diamond-like carbon. *Wear*, 168(1-2):143–153, sep 1993. ISSN 00431648. doi: 10.1016/0043-1648(93)90210-D. URL `http://www.sciencedirect.com/science/article/pii/004316489390210D`. 48, 57, 60

[221] Wolfgang Tillmann, Nelson Filipe Lopes Dias, and Dominic Stangier. Tribomechanical properties of CrC/a-C thin films sequentially deposited by HiPIMS and mfMS. *Surf. Coatings Technol.*, 335:173–180, feb 2018. ISSN 02578972. doi: 10.1016/j.surfcoat.2017.12.035. 48

[222] M. Antonov, I. Hussainova, F. Sergejev, P. Kulu, and A. Gregor. Assessment of gradient and nanogradient PVD coatings behaviour under erosive, abrasive and impact wear conditions. *Wear*, 267(5-8):898–906, jun 2009. ISSN 00431648. doi: 10.1016/j.wear.2008.12.045.

[223] S. Yang, X. Li, N. M. Renevier, and D. G. Teer. Tribological properties and wear mechanism of sputtered C/Cr coating. *Surf. Coatings Technol.*, 142-144:85–93, jul 2001. ISSN 02578972. doi: 10.1016/S0257-8972(01)01147-1.

[224] M. Diesselberg, H. R. Stock, and P. Mayr. Friction and wear behaviour of PVD chromium nitride supported carbon coatings. *Surf. Coatings Technol.*, 188-189(1-3 SPEC.ISS.):612–616, nov 2004. ISSN 02578972. doi: 10.1016/j.surfcoat.2004.07.023.

[225] Xinchun Chen, Zhijian Peng, Zhiqiang Fu, Sudong Wu, Wen Yue, and Chengbiao Wang. Microstructural, mechanical and tribological properties of tungsten-gradually doped diamond-like carbon films with functionally graded interlayers. *Surf. Coatings Technol.*, 205(12):3631–3638, mar 2011. ISSN 02578972. doi: 10.1016/j.surfcoat.2011.01.004. 48, 88, 159

[226] George Gerald Stoney. The tension of metallic films deposited by electrolysis. *Proc. R. Soc. London. Ser. A, Contain. Pap. a Math. Phys. Character*, 82(553):172–175, may 1909. ISSN 0950-1207. doi: 10.1098/rspa.1909.0021. URL `https://royalsocietypublishing.org/doi/10.1098/rspa.1909.0021`. 48

[227] Xiangru Shi, Tomasz W. Liskiewicz, Ben D. Beake, Jian Chen, and Chun Wang. Tribological performance of graphite-like carbon films with varied thickness. *Tribol. Int.*, feb 2019. ISSN 0301679X. doi: 10.1016/j.triboint.

2019.01.045. URL `https://www.sciencedirect.com/science/article/pii/S0301679X19300593`. 48, 49

[228] L. F. Bonetti, G. Capote, L. V. Santos, E. J. Corat, and V. J. Trava-Airoldi. Adhesion studies of diamond-like carbon films deposited on Ti6Al4V substrate with a silicon interlayer. *Thin Solid Films*, 515(1):375–379, sep 2006. ISSN 00406090. doi: 10.1016/j.tsf.2005.12.154. 73

[229] Koumei Baba, Ruriko Hatada, Stefan Flege, and Wolfgang Ensinger. Diamond-like carbon films with low internal stress by a simple bilayer approach. *Coatings*, 10(7):1–10, 2020. ISSN 20796412. doi: 10.3390/coatings10070696. 48, 58, 68, 134, 177

[230] Siming Ren, Shaoxian Zheng, Jibin Pu, Zhibin Lu, and Guangan Zhang. Study of tribological mechanisms of carbon-based coatings in antiwear additive containing lubricants under high temperature. *RSC Adv.*, 5(81):66426–66437, jul 2015. ISSN 20462069. doi: 10.1039/c5ra08879h. URL `http://xlink.rsc.org/?DOI=C5RA08879H`. 48, 60

[231] Marco Renzelli, Muhammad Zeeshan Mughal, Marco Sebastiani, and Edoardo Bemporad. Design, fabrication and characterization of multilayer Cr-CrN thin coatings with tailored residual stress profiles. *Mater. Des.*, 112:162–171, 2016. ISSN 18734197. doi: 10.1016/j.matdes.2016.09.058. URL `http://dx.doi.org/10.1016/j.matdes.2016.09.058`. 48, 177

[232] Allan Matthews, Richard Jones, and Stephen Dowey. Modelling the deformation behaviour of multilayer coatings. *Tribol. Lett.*, 11(2):103–106, 2001. ISSN 10238883. doi: 10.1023/A:1016667932251. 48

[233] H Schmellenmeier. Die Beeinflussung von festen Oberflachen durch eine ionisierte. *Exp. Tech. Phys*, 1:49–68, 1953. 48

[234] H Schmellenmeier. Carbon films with diamond structure. *J. Phys. Chem*, 205:349–350, 1956. 48

[235] Sol Aisenberg and Ronald Chabot. Ion-beam deposition of thin films of diamondlike carbon. *J. Appl. Phys.*, 42(7):2953–2958, jun 1971. ISSN 00218979. doi: 10.1063/1.1660654. URL `http://aip.scitation.org/doi/10.1063/1.1660654`. 48

[236] J. Vetter. 60years of DLC coatings: Historical highlights and technical review of cathodic arc processes to synthesize various DLC types, and their evolution for industrial applications. *Surf. Coatings Technol.*, 257:213–240, oct 2014. ISSN 02578972. doi: 10.1016/j.surfcoat.2014.08.017. URL `https://www.sciencedirect.com/science/article/pii/S0257897214007257`. 49

[237] C. Casiraghi, F. Piazza, A. C. Ferrari, D. Grambole, and J. Robertson. Bonding in hydrogenated diamond-like carbon by Raman spectroscopy. In *Diam. Relat. Mater.*, volume 14, pages 1098–1102. Elsevier, mar 2005. doi: 10.1016/j.diamond.2004.10.030. URL `https://www.sciencedirect.com/science/article/pii/S0925963504003991{#}fig1`. 49, 53

[238] Hugh O. Pierson. *Handbook of Carbon, Graphite, Diamonds and Fullerenes: Processing, Properties and Applications (Materials Science and Process Technology).* Noyes Publications, 1993. ISBN 978-0-8155-1339-1. doi: http://dx.doi.org/10.1016/B978-0-8155-1339-1.50008-6. URL `https://www.sciencedirect.com/book/9780815513391/` `handbook-of-carbon-graphite-diamonds-and-fullereneshttp://` `www.sciencedirect.com/science/article/pii/B9780815513391500086.` 50, 51, 55, 117

[239] Lumen. Allotropes of Carbon — Introduction to Chemistry, 2019. URL `https://courses.lumenlearning.com/introchem/chapter/` `allotropes-of-carbon/.` 50

[240] John C. Angus. Empirical categorization and naming of "diamond-like" carbon films. *Thin Solid Films*, 142(1):145–151, aug 1986. ISSN 00406090. doi: 10.1016/0040-6090(86)90310-X. URL `https://www.sciencedirect.com/science/` `article/pii/004060908690310X.` 50

[241] M. S. Dresselhaus, G. Dresselhaus, and P. C. Eklund. *Science of fullerenes and carbon nanotubes.* Academic Press, 1996. ISBN 978-0-12-221820-0. doi: https://doi.org/10.1016/B978-0-12-221820-0.X5000-X. 50

[242] B. T. (Brian Thomas) Kelly. *Physics of graphite.* Springer, 1981. ISBN 0853349606. URL `https://inis.iaea.org/search/search.aspx?` `orig{_}q=RN:13661340.` 50

[243] John C. Angus and Cliff C. Hayman. Low-pressure, metastable growth of diamond and "diamondlike" phases. *Science (80-.).*, 241(4868): 913–921, aug 1988. ISSN 00368075. doi: 10.1126/science.241.4868. 913. URL `http://www.ncbi.nlm.nih.gov/pubmed/17731439http://www.` `sciencemag.org/cgi/doi/10.1126/science.241.4868.913.` 50

[244] Ali Erdemir, Osman L. Eryilmaz, and G. Fenske. Synthesis of diamondlike carbon films with superlow friction and wear properties. *J. Vac. Sci. Technol. A*, 18(4): 1987, jul 2000. ISSN 07342101. doi: 10.1116/1.582459. URL `http://0-avs.` `scitation.org.wam.leeds.ac.uk/doi/abs/10.1116/1.582459.` 51

[245] Y. Liu, A. Erdemir, and E I Meletis. A study of the wear mechanism of diamond-like carbon films 1. *Surf. Coatings Technol.*, 82(1-2):48–56, jul 1996. ISSN 02578972. doi: 10.1016/0257-8972(95)02623-1. URL `http://www.` `sciencedirect.com/science/article/pii/0257897295026231.` 51, 57, 60

[246] W. Jacob and W. Möller. On the structure of thin hydrocarbon films. *Appl. Phys. Lett.*, 63(13):1771–1773, sep 1993. ISSN 00036951. doi: 10.1063/1.110683. URL `http://aip.scitation.org/doi/10.1063/1.110683.` 51

[247] Sriram Sundararajan and Bharat Bhushan. Micro/nanotribology of ultra-thin hard amorphous carbon coatings using atomic force/friction force microscopy. *Wear*, 225-229(I):678–689, apr 1999. ISSN 00431648. doi: 10.1016/S0043-1648(99) 00024-1. URL `https://www.sciencedirect.com/science/article/abs/` `pii/S0043164899000241.` 51

[248] Ben D. Beake and Tomasz Liskiewicz. Nanomechanical Characterization of Carbon Films. In *Appl. Nanoindentation Adv. Mater.*, chapter 2, pages 19–68. 2017. doi: 10.1002/9781119084501.ch2. 51, 60, 68

[249] Sajid Bashir and Jingbo Liu. Nanocharacterization. In *Adv. Nanomater. Their Appl. Renew. Energy*, pages 117–180. Elsevier Inc., aug 2015. ISBN 9780128017081. doi: 10.1016/B978-0-12-801528-5.00003-8. 53

[250] A. Ferrari and J. Robertson. Interpretation of Raman spectra of disordered and amorphous carbon. *Phys. Rev. B - Condens. Matter Mater. Phys.*, 61(20):14095–14107, may 2000. ISSN 1550235X. doi: 10.1103/PhysRevB.61.14095. URL `https://link.aps.org/doi/10.1103/PhysRevB.61.14095`. 53, 54, 116, 121, 132, 151

[251] C. Rincón, G. Zambrano, A. Carvajal, P. Prieto, H. Galindo, E. Martínez, A. Lousa, and J. Esteve. Tungsten carbide/diamond-like carbon multilayer coating on steel for tribological applications. *Surf. Coatings Technol.*, 148(2-3):277–283, dec 2001. ISSN 02578972. doi: 10.1016/S0257-8972(01)01360-3. 53, 88, 116, 159

[252] Andrea Carlo Ferrari and John Robertson. Raman spectroscopy of amorphous, nanostructured, diamond-like carbon, and nanodiamond, nov 2004. ISSN 1364503X. URL `http://www.ncbi.nlm.nih.gov/pubmed/15482988`. 53

[253] Andrea Carlo Ferrari. Determination of bonding in diamond-like carbon by Raman spectroscopy. *Diam. Relat. Mater.*, 11(3-6):1053–1061, mar 2002. ISSN 09259635. doi: 10.1016/S0925-9635(01)00730-0. URL `https://www.sciencedirect.com/science/article/pii/S0925963501007300`. 53

[254] C. Casiraghi, A. C. Ferrari, and J. Robertson. Raman spectroscopy of hydrogenated amorphous carbons. *Phys. Rev. B - Condens. Matter Mater. Phys.*, 72(8):085401, aug 2005. ISSN 10980121. doi: 10.1103/PhysRevB.72.085401. 53

[255] F. C. Tai, S. C. Lee, J. Chen, C. Wei, and S. H. Chang. Multipeak fitting analysis of Raman spectra on DLCH film. *J. Raman Spectrosc.*, 40(8):1055–1059, 2009. ISSN 03770486. doi: 10.1002/jrs.2234. 54

[256] Joseph I. Goldstein, Dale E. Newbury, Joseph R. Michael, Nicholas W.M. Ritchie, John Henry J. Scott, and David C. Joy. *Scanning electron microscopy and x-ray microanalysis*. Springer New York, jan 2017. ISBN 9781493966769. doi: 10.1007/978-1-4939-6676-9. 54, 55, 129

[257] R.F. Egerton. *Physical Principles of Electron Microscopy*. 2016. ISBN 2005924717. doi: 10.1007/978-3-319-39877-8. 54, 55

[258] Claudionico~commonswiki. Electron Interaction with Matter, 2013. URL `https://commons.wikimedia.org/wiki/File:Electron{_}Interaction{_}with{_}Matter.svg`. 55

[259] Donald M. Mattox. Substrate ("Real") Surfaces and Surface Modification. In *Handb. Phys. Vap. Depos. Process.*, chapter 2, pages 25–72. 2010. ISBN 9780815520375. doi: 10.1016/b978-0-8155-2037-5.00002-2. 55

[260] R. F. Egerton. *Electron Energy Loss spectroscopy in the Electron Microscope*. Springer, 2011. ISBN 978-1-4419-9582-7. doi: 10.1007/ 978-1-4419-9583-4. URL `http://home.ustc.edu.cn/{~}yanglh/{%}5BR.F. {_}Egerton{%}5D{_}Electron{_}Energy-Loss{_}Spectroscopy{_}i(BookFi) .pdf`. 55, 130

[261] Bob Hafner. Energy Dispersive Spectroscopy on the SEM: A Primer. 55, 133

[262] Manuel Scimeca, Simone Bischetti, Harpreet Kaur Lamsira, Rita Bonfiglio, and Elena Bonanno. Energy dispersive X-ray (EDX) microanalysis: A powerful tool in biomedical research and diagnosis. *Eur. J. Histochem.*, 62(1):89–99, 2018. ISSN 20388306. doi: 10.4081/ejh.2018.2841. 55, 133

[263] Ryosuke Senga and Kazu Suenaga. Single-atom electron energy loss spectroscopy of light elements. *Nat. Commun.*, 6:1–6, 2015. ISSN 20411723. doi: 10.1038/ ncomms8943. 55

[264] A.C Ferrari, B Kleinsorge, G Adamopoulos, J Robertson, W.I Milne, V Stolojan, L.M Brown, A LiBassi, and B.K Tanner. Determination of bonding in amorphous carbons by electron energy loss spectroscopy, Raman scattering and X-ray reflectivity. *J. Non. Cryst. Solids*, 266-269:765–768, may 2003. ISSN 00223093. doi: 10.1016/s0022-3093(00)00035-1. URL `https://www.sciencedirect. com/science/article/pii/S0022309300000351`. 55, 117, 132

[265] L Ponsonnet, C Donnet, K Varlot, J. M. Martin, A Grill, and V Patel. EELS analysis of hydrogenated diamond-like carbon films. *Thin Solid Films*, 319 (1-2):97–100, apr 1998. ISSN 00406090. doi: 10.1016/S0040-6090(97) 01094-8. URL `https://www.sciencedirect.com/science/article/pii/ S0040609097010948{#}FIG1`. 55, 56

[266] Zhencheng Ren, Haifeng Qin, Yalin Dong, G.L. Doll, and Chang Ye. A boron-doped diamond like carbon coating with high hardness and low friction coefficient. *Wear*, 436-437:203031, oct 2019. ISSN 0043-1648. doi: 10.1016/J.WEAR. 2019.203031. URL `https://www.sciencedirect.com/science/article/ pii/S004316481831648X`. 55

[267] Henning Hasselbruch, Marius Herrmann, Andreas Mehner, Hans Werner Zoch, and Bernd Kuhfuss. Development, characterization and testing of tungsten doped DLC coatings for dry rotary swaging. In *MATEC Web Conf.*, volume 21, page 8012, 2015. ISBN 9782759818235. doi: 10.1051/matecconf/20152108012. URL `http://dx.doi.org/10.1051/matecconf/20152108012`. 56, 112

[268] Weng Jin Wu and Min Hsiung Hon. The structure and residual stress in Si containing diamond-like carbon coating. *Thin Solid Films*, 307(1-2):1–5, oct 1997. ISSN 00406090. doi: 10.1016/S0040-6090(97)00251-4. 55, 88, 132, 159

[269] Junho Choi, Masahiro Kawaguchi, Takahisa Kato, and Masami Ikeyama. Deposition of Si-DLC film and its microstructural, tribological and corrosion properties. In *Microsyst. Technol.*, volume 13, pages 1353–1358, may 2007. doi: 10.1007/s00542-006-0368-8. 56, 159

[270] J. L. Lanigan, C. Wang, A. Morina, and A. Neville. Repressing oxidative wear within Si doped DLCs. *Tribol. Int.*, 93:651–659, jan 2016. ISSN 0301679X. doi: 10.1016/j.triboint.2014.11.004. 56, 112

[271] K. Bewilogua, C. V. Cooper, C. Specht, J. Schröder, R. Wittorf, and M. Grischke. Erratum to: 'Effect of target material on deposition and properties of metal-containing DLC (Me-DLC) coatings' [Surf. Coat. Technol. 127 (2000) 224-234], oct 2000. ISSN 02578972. 56

[272] Takahiro Horiuchi, Kentaro Yoshida, Makoto Kano, Masao Kumagai, and Tetsuya Suzuki. Evaluation of adhesion and wear resistance of DLC films deposited by various methods. In *Plasma Process. Polym.*, volume 6, pages 410–416, jul 2009. doi: 10.1002/ppap.200930004. URL `http://onlinelibrary.wiley.com/doi/` `10.1002/ppap.200930004/abstract`. 56

[273] Wen Yue, Chunyue Liu, Zhiqiang Fu, Chengbiao Wang, Haipeng Huang, and Jiajun Liu. Effects of tungsten doping contents on tribological behaviors of tungsten-doped diamond-like carbon coatings lubricated by MoDTC. *Tribol. Lett.*, 58(2): 1–10, may 2015. ISSN 10238883. doi: 10.1007/s11249-015-0508-3. 56, 88, 112, 133, 159

[274] Christophe Donnet and Ali Erdemir. *Tribology of Diamond-Like Carbon Films*. Springer US, Boston, MA, 2008. ISBN 978-0-387-30264-5. doi: 10.1007/978-0-387-49891-1. URL `http://link.springer.com/10.1007/` `978-0-387-49891-1http://www.springerlink.com/index/10.1007/` `978-0-387-49891-1`. 57, 59

[275] John Robertson. Classification of diamond-like carbons. In *Tribol. Diamond-Like Carbon Film. Fundam. Appl.*, pages 13–24. Springer US, Boston, MA, 2008. ISBN 9780387302645. doi: 10.1007/978-0-387-49891-1_1. URL `http:` `//link.springer.com/10.1007/978-0-387-49891-1{_}1`. 57, 58, 112, 113, 133

[276] John Robertson. The deposition mechanism of diamond-like a-C and a-C: H. *Diam. Relat. Mater.*, 3(4-6):361–368, apr 1994. ISSN 09259635. doi: 10.1016/ 0925-9635(94)90186-4. URL `http://www.sciencedirect.com/science/` `article/pii/0925963594901864`. 57, 58, 267

[277] Yves Pauleau. Residual stresses in DLC films and adhesion to various substrates. In *Tribol. Diamond-Like Carbon Film. Fundam. Appl.*, pages 102–136. Springer US, Boston, MA, 2008. ISBN 9780387302645. doi: 10.1007/978-0-387-49891-1_ 4. URL `http://link.springer.com/10.1007/978-0-387-49891-1{_}4`. 59, 132, 267

[278] M. D. Bentzon, K. Mogensen, J. Bindslev Hansen, C. Barholm-Hansen, C. Træholt, P. Holiday, and S. S. Eskildsen. Metallic interlayers between steel and diamond-like carbon. *Surf. Coatings Technol.*, 68-69(C):651–655, dec 1994. ISSN 02578972. doi: 10.1016/0257-8972(94)90232-1. URL `https:` `//www.sciencedirect.com/science/article/pii/0257897294902321`. 59, 143, 158, 161, 258, 267

[279] Helena Ronkainen and Kenneth Holmberg. Environmental and thermal effects on the tribological performance of DLC coatings. In *Tribol. Diamond-Like Carbon Film. Fundam. Appl.*, pages 155–200. Springer US, Boston, MA, 2008. ISBN 9780387302645. doi: 10.1007/978-0-387-49891-1_6. URL `http://link.` `springer.com/10.1007/978-0-387-49891-1{_}6`. 59, 60, 227

[280] Ali Erdemir and Christophe Donnet. Tribology of diamond-like carbon films: Recent progress and future prospects, sep 2006. ISSN 00223727. URL `http://stacks.iop.org/0022-3727/39/i=18/a=R01?key=crossref. 9af827cc7f4ea226ffcf654a7b79e6d5`. 59, 60, 266

[281] Jiaren Jiang and R. D. Arnell. The effect of substrate surface roughness on the wear of DLC coatings. *Wear*, 239(1):1–9, apr 2000. ISSN 00431648. doi: 10.1016/ S0043-1648(99)00351-8. URL `https://www.sciencedirect.com/science/ article/abs/pii/S0043164899003518`. 59, 74, 225

[282] B. D. Beake, T. W. Liskiewicz, V. M. Vishnyakov, and M. I. Davies. Development of DLC coating architectures for demanding functional surface applications through nano- and micro-mechanical testing. *Surf. Coatings Technol.*, 284:334–343, dec 2015. ISSN 02578972. doi: 10.1016/j.surfcoat. 2015.05.050. URL `http://www.sciencedirect.com/science/article/pii/ S0257897215005034`. 59, 66, 74, 93, 105, 113, 160, 164, 166, 167, 170, 173, 176, 177, 180, 231, 232, 233, 234, 236, 253, 254, 259, 260, 269

[283] S. K. Field, M. Jarratt, and D. G. Teer. Tribological properties of graphite-like and diamond-like carbon coatings. *Tribol. Int.*, 37(11-12 SPEC.ISS.): 949–956, nov 2004. ISSN 0301679X. doi: 10.1016/j.triboint.2004. 07.012. URL `https://www.sciencedirect.com/science/article/pii/ S0301679X04001306{#}FIG6`. 60, 68

[284] Yunhai Liu, Lei Chen, Bin Zhang, Zhongyue Cao, Pengfei Shi, Yong Peng, Ningning Zhou, Junyan Zhang, and Linmao Qian. Key role of transfer layer in load dependence of friction on hydrogenated diamond-like carbon films in humid air and vacuum. *Materials (Basel).*, 12(9):1–12, 2019. ISSN 19961944. doi: 10.3390/ma12091550. 60

[285] Ksenija Topolovec-Miklozic, Frances Lockwood, and Hugh Spikes. Behaviour of boundary lubricating additives on DLC coatings. *Wear*, 265(11-12):1893–1901, 2008. ISSN 00431648. doi: 10.1016/j.wear.2008.04.051. 60

[286] T. Haque, A. Morina, A. Neville, R. Kapadia, and S. Arrowsmith. Effect of oil additives on the durability of hydrogenated DLC coating under boundary lubrication conditions. *Wear*, 266(1-2):147–157, 2009. ISSN 00431648. doi: 10.1016/j.wear.2008.06.011. 60, 229, 266

[287] C. Venkatraman, A. Goel, R. Lei, D. Kester, and C. Outten. Electrical properties of diamond-like nanocomposite coatings. *Thin Solid Films*, 308-309(1-4):173–177, oct 1997. ISSN 00406090. doi: 10.1016/S0040-6090(97)00384-2. 60

[288] A Grill. Electrical and optical properties of diamond-like carbon. *Thin Solid Films*, 355:189–193, nov 1999. ISSN 00406090. doi: 10.1016/S0040-6090(99) 00516-7. URL `https://www.sciencedirect.com/science/article/pii/ S0040609099005167`. 60

[289] A. Grill, V. Patel, and S. Cohen. Electrical resistivities of diamond-like carbon. *Diam. Relat. Mater.*, 3(3):281–284, feb 1994. ISSN 09259635. doi: 10.1016/ 0925-9635(94)90093-0. 60

[290] K. Honglertkongsakul, P. W. May, and B. Paosawatyanyong. Electrical and optical properties of diamond-like carbon films deposited by pulsed laser ablation. *Diam. Relat. Mater.*, 19(7-9):999–1002, jul 2010. ISSN 09259635. doi: 10.1016/j.diamond.2010.03.007. URL `https://www.sciencedirect.com/science/article/pii/S0925963510001330`. 60

[291] M. Semenenko, G. Okrepka, O. Yilmazoglu, H. L. Hartnagel, and D. Pavlidis. Electrical conditioning of diamond-like carbon films for the formation of coated field emission cathodes. *Appl. Surf. Sci.*, 257(2):388–392, nov 2010. ISSN 01694332. doi: 10.1016/j.apsusc.2010.06.089. 60

[292] F.Z Cui and D.J Li. A review of investigations on biocompatibility of diamond-like carbon and carbon nitride films. *Surf. Coatings Technol.*, 131(1-3):481–487, sep 2000. ISSN 02578972. doi: 10.1016/S0257-8972(00)00809-4. URL `https://www.sciencedirect.com/science/article/pii/S0257897200008094http://linkinghub.elsevier.com/retrieve/pii/S0257897200008094`. 60

[293] M. Azzi, M. Paquette, J. A. Szpunar, J. E. Klemberg-Sapieha, and L. Martinu. Tribocorrosion behaviour of DLC-coated 316L stainless steel. *Wear*, 267(5-8):860–866, jun 2009. ISSN 00431648. doi: 10.1016/j.wear.2009.02.006. URL `https://www.sciencedirect.com/science/article/pii/S0043164809001458`. 60

[294] S. V. Johnston and S. V. Hainsworth. Effect of DLC coatings on wear in automotive applications. *Surf. Eng.*, 21(1):67–71, feb 2005. ISSN 0267-0844. doi: 10.1179/174329405X30039. URL `http://www.tandfonline.com/doi/full/10.1179/174329405X30039http://www.maneyonline.com/doi/abs/10.1179/174329405X30039`. 60

[295] Tomasz Liskiewicz and Amal Al-Borno. DLC Coatings in Oil and Gas Production. *J. Coat. Sci. Technol.*, 1(1):59–68, jun 2014. ISSN 2369-3355. doi: http://dx.doi.org/10.6000/2369-3355.2014.01.01.7. URL `http://www.lifescienceglobal.com/pms/index.php/jcst/article/view/2122`. 60

[296] Ankit Tyagi, R. S. Walia, Qasim Murtaza, Shailesh M. Pandey, Pawan K. Tyagi, and Bharat Bajaj. A critical review of diamond like carbon coating for wear resistance applications, jan 2019. ISSN 22133917. URL `https://www.sciencedirect.com/science/article/pii/S0263436818303597`. 60

[297] Natthaphong Konkhunthot, Pat Photongkam, and Pornwasa Wongpanya. Improvement of thermal stability, adhesion strength and corrosion performance of diamond-like carbon films with titanium doping. *Appl. Surf. Sci.*, 469:471–486, mar 2019. ISSN 01694332. doi: 10.1016/j.apsusc.2018.11.028. URL `https://www.sciencedirect.com/science/article/pii/S0169433218330988`. 60

[298] Zuzana Mala, Tomas Vitu, and Danuse Novakova. Determination of coating thickness - industrial standard in the physics practical education. In *Phys. Teach. Eng. Educ.*, page 4, 2011. 61, 63

[299] K. (Kenneth) Holmberg and A. (Allan) Matthews. *Coatings tribology : properties, mechanisms, techniques and applications in surface engineering*. Elsevier Science, 2009. ISBN 9780080931463. 61, 62

[300] Luis Carlos Hernández, Luis Ponce, Abel Fundora, Enrique López, and Eduardo Pérez. Nanohardness and residual stress in TiN coatings. *Materials (Basel).*, 4(5):929–940, may 2010. ISSN 19961944. doi: 10.3390/ma4050929. URL http://www.ncbi.nlm.nih.gov/pubmed/28879958http://www.pubmedcentral.nih.gov/articlerender.fcgi?artid=PMC5448585. 62

[301] S. J. Bull. Failure modes in scratch adhesion testing. *Surf. Coatings Technol.*, 50(1):25–32, jan 1991. ISSN 02578972. doi: 10.1016/0257-8972(91)90188-3. URL https://www.sciencedirect.com/science/article/pii/0257897291901883. 63, 93, 148, 171

[302] A. J. Perry. Scratch adhesion testing of hard coatings. *Thin Solid Films*, 107(2):167–180, 1983. ISSN 00406090. doi: 10.1016/0040-6090(83)90019-6. 63, 259

[303] H. E. Hintermann. Adhesion, friction and wear of thin hard coatings. *Wear*, 100(1-3):381–397, 1984. ISSN 00431648. doi: 10.1016/0043-1648(84)90023-1. 63

[304] J. Valli, U. Makela, A. Matthews, and V. Murawa. TiN coating adhesion studies using the scratch test method. *J. Vac. Sci. Technol. A Vacuum, Surfaces, Film.*, 3(6):2411–2414, 1985. ISSN 0734-2101. doi: 10.1116/1.572848. 64

[305] Juhani Valli, Ulla Makela, and Allan Matthews. Assessment of coating adhesion. *Surf. Eng.*, 2(1):49–54, 1986. ISSN 17432944. doi: 10.1179/sur.1986.2.1.49. 64

[306] P. J. Burnett and D. S. Rickerby. The relationship between hardness and scratch adhesion. *Thin Solid Film.*, 154:403–416, 1987. ISSN 1556-5068. doi: 10.2139/ssrn.2782847. 64, 93

[307] DIN. Fachbericht 39 - Charakterisierung dunner Schichten. Technical report, Beuth Verlag GmbH Berlin, Berlin, 1993. 64

[308] ASTM. C1624 - Standard Test Method for Adhesion Strength and Mechanical Failure Modes of Ceramic Coatings by Quantitative Single Point Scratch Testing, 2012. 64

[309] Fabian Pöhl, Corinna Hardes, and Werner Theisen. Scratch behavior of soft metallic materials. *AIMS Mater. Sci.*, 3(2):390–403, 2016. ISSN 23720468. doi: 10.3934/matersci.2016.2.390. 64

[310] Sam Zhang, Deen Sun, Yongqing Fu, and Hejun Du. Effect of sputtering target power on microstructure and mechanical properties of nanocomposite nc-TiN/a-SiNx thin films. In *Thin Solid Films*, volume 447-448, pages 462–467. Elsevier, jan 2004. doi: 10.1016/S0040-6090(03)01125-8. 64, 90, 108, 113, 158, 159, 260

[311] G. S. Fox-Rabinovich, B. D. Beake, J. L. Endrino, S. C. Veldhuis, R. Parkinson, L. S. Shuster, and M. S. Migranov. Effect of mechanical properties measured at room and elevated temperatures on the wear resistance of cutting tools with TiAlN and AlCrN coatings. *Surf. Coatings Technol.*, 200(20-21):5738–5742, may 2006. ISSN 02578972. doi: 10.1016/j.surfcoat.2005.08.132. URL https://www.sciencedirect.com/science/article/pii/S0257897205010182. 64, 90, 108, 113, 158, 159, 260

[312] B. D. Beake, A. J. Harris, and T. W. Liskiewicz. Review of recent progress in nanoscratch testing. *Tribol. - Mater. Surfaces Interfaces*, 7(2):87–96, jun 2013. ISSN 17515831. doi: 10.1179/1751584X13Y.0000000037. 64, 65, 66, 67, 113, 165, 166, 175, 179, 180, 253, 254, 259

[313] Jin Kun Xiao, Lei Zhang, Ke Chao Zhou, and Xin Ping Wang. Microscratch behavior of copper-graphite composites. *Tribol. Int.*, 57:38–45, jan 2013. ISSN 0301679X. doi: 10.1016/j.triboint.2012.07.004. 64, 164

[314] J Goddard and H Wilman. A theory of friction and wear during the abrasion of metals. *Wear*, 5:114–135, 1961. 64

[315] Sébastien Lafaye and Michel Troyon. On the friction behaviour in nanoscratch testing. *Wear*, 261(7-8):905–913, 2006. ISSN 00431648. doi: 10.1016/j.wear.2006.01.036. 64, 168

[316] Katia Dyrda and Michael Sayer. Critical loads and effective frictional force measurements in the industrial scratch testing of TiN on M2 tool steel. *Thin Solid Films*, 355:277–283, nov 1999. ISSN 00406090. doi: 10.1016/S0040-6090(99)00450-2. 65, 177

[317] Kirsten Ingolf Schiffmann. Microtribological/mechanical testing in 0, 1 and 2 dimensions: A comparative study on different materials. *Wear*, 265(11-12):1826–1836, 2008. ISSN 00431648. doi: 10.1016/j.wear.2008.04.043. 65

[318] B. D. Beake and T. W. Liskiewicz. Comparison of nano-fretting and nano-scratch tests on biomedical materials. In *Tribol. Int.*, volume 63, pages 123–131. Elsevier, jul 2013. ISBN 0301679X. doi: 10.1016/j.triboint.2012.08.007. URL https://www.sciencedirect.com/science/article/pii/S0301679X12002794?via{%}3Dihub. 66, 68, 74, 173, 179, 187, 195, 196, 227, 268

[319] A Sivitski, A Gregor, M Saarna, P Kulu, and F Sergejev. Application of the indentation method for cracking resistance evaluation of hard coatings on tool steels. *Est. J. Eng.*, 15(4):309, 2009. ISSN 1736-6038. doi: 10.3176/eng.2009.4.08. URL http://www.kirj.ee/?id=16273{&}tpl=1061{&}c{_}tpl=1064. 66, 136, 267

[320] Rui Lan, Zhifeng Ma, Chunji Wang, Guoying Lu, Yanyan Yuan, and Changlun Shi. Microstructural and tribological characterization of DLC coating by in-situ duplex plasma nitriding and arc ion plating. *Diam. Relat. Mater.*, 98:107473, oct 2019. ISSN 09259635. doi: 10.1016/j.diamond.2019.107473. 66

[321] Xinjie Chen, Yao Du, and Yip Wah Chung. Commentary on using H/E and H3/E2 as proxies for fracture toughness of hard coatings. *Thin Solid Films*, apr 2019. ISSN 00406090. doi: 10.1016/j.tsf.2019.04.040. URL https://www.sciencedirect.com/science/article/pii/S0040609019302500. 66, 67, 112, 158, 159, 177, 187, 260

[322] A Leyland and A Matthews. On the significance of the H/E ratio in wear control: A nanocomposite coating approach to optimised tribological behaviour. *Wear*, 246(1-2):1–11, nov 2000. ISSN 00431648. doi: 10.1016/S0043-1648(00)00488-9. URL https://www.sciencedirect.com/science/article/pii/S0043164800004889. 66, 90, 112, 158, 159, 177, 187, 254, 260

[323] A. Leyland and A. Matthews. Design criteria for wear-resistant nanostructured and glassy-metal coatings. *Surf. Coatings Technol.*, 177-178:317–324, 2004. ISSN 02578972. doi: 10.1016/j.surfcoat.2003.09.011. 66, 260

[324] Louise Beth Austin. *Evaluation and Optimisation of Diamond-Like Carbon for Tribological Applications*. PhD thesis, University of Leeds, 2014. URL `http://etheses.whiterose.ac.uk/7713/`. 66, 74, 77

[325] T. L. Oberle. Wear of Metals. *JOM*, 3(6):438–439, jun 1951. ISSN 1047-4838. doi: 10.1007/BF03397325. URL `http://link.springer.com/10.1007/BF03397325`. 66

[326] J Halling. Surface films in tribology. *Tribologia*, 1(2):15, 1982. 66

[327] A Matthews. The value of deposition processes for industrial tools. *Mater. Eng.*, pages 175–182, 1984. 66

[328] G. R. ANSTIS, P. CHANTIKUL, B. R. LAWN, and D. B. MARSHALL. A Critical Evaluation of Indentation Techniques for Measuring Fracture Toughness: I, Direct Crack Measurements. *J. Am. Ceram. Soc.*, 64(9):533–538, sep 1981. ISSN 15512916. doi: 10.1111/j.1151-2916.1981.tb10320.x. URL `http://doi.wiley.com/10.1111/j.1151-2916.1981.tb10320.x`. 67, 159, 160, 161, 260

[329] B. R. LAWN, A. G. EVANS, and D. B. MARSHALL. Elastic/Plastic Indentation Damage in Ceramics: The Median/Radial Crack System. *J. Am. Ceram. Soc.*, 63(9-10):574–581, sep 1980. ISSN 15512916. doi: 10.1111/j.1151-2916.1980.tb10768.x. 67

[330] Ben D. Beake, James F. Smith, and Maria Jes s.Ibaez García. Micro-impact testing: A new technique for investigating fracture toughness. *Thin Solid Films*, 398-399:438–443, nov 2001. ISSN 00406090. doi: 10.1016/S0040-6090(01)01397-9. 67, 160

[331] Yang Tse Cheng and Che Min Cheng. Scaling, dimensional analysis, and indentation measurements. *Mater. Sci. Eng. R Reports*, 44(4-5):91–149, 2004. ISSN 0927796X. doi: 10.1016/j.mser.2004.05.001. 67, 187

[332] Wangyang Ni, Yang Tse Cheng, Michael J Lukitsch, Anita M Weiner, Lenoid C Lev, and David S Grummon. Effects of the ratio of hardness to Young's modulus on the friction and wear behavior of bilayer coatings. *Appl. Phys. Lett.*, 85(18):4028–4030, 2004. ISSN 00036951. doi: 10.1063/1.1811377. URL `https://doi.org/10.1063/1.1811377`. 67, 112, 177, 187, 260

[333] Kenneth Langstreth Johnson. *Contact mechanics*. Cambridge University Press, 1985. 67

[334] Xiangru Shi, Ben D. Beake, Tomasz W. Liskiewicz, Jian Chen, and Zhengming Sun. Failure mechanism and protective role of ultrathin ta-C films on Si (100) during cyclic nano-impact. *Surf. Coatings Technol.*, 364:32–42, apr 2019. ISSN 02578972. doi: 10.1016/j.surfcoat.2019.02.082. URL `https://www.sciencedirect.com/science/article/pii/S025789721930235X{#}f0015`. 68

[335] B. D. Beake, V. M. Vishnyakov, and A. J. Harris. Relationship between mechanical properties of thin nitride-based films and their behaviour in nano-scratch tests. *Tribol. Int.*, 44(4):468–475, apr 2011. ISSN 0301679X. doi: 10.1016/j.triboint. 2010.12.002. 68

[336] T. S. Eyre. Wear characteristics of metals. *Tribol. Int.*, 9(5):203–212, 1976. ISSN 0301679X. doi: 10.1016/0301-679X(76)90077-3. 68

[337] T. S. Eyre. The mechanisms of wear. *Tribol. Int.*, 11(2):91–96, 1978. ISSN 0301679X. doi: 10.1016/0301-679X(78)90135-4. 68

[338] R. F. Smart. Selection of surfacing treatments. *Tribol. Int.*, 11(2):97–104, 1978. ISSN 0301679X. doi: 10.1016/0301-679X(78)90136-6. 68

[339] Leysan Kh Rysaeva, Dmitry S. Lisovenko, Valentin A. Gorodtsov, and Julia A. Baimova. Stability, elastic properties and deformation behavior of graphene-based diamond-like phases. *Comput. Mater. Sci.*, 172:109355, feb 2020. ISSN 09270256. doi: 10.1016/j.commatsci.2019.109355. 68

[340] W. E.S.S. Viana, A. E. Elzubair, M. M. Wysard, D. F. Franceschini, and S. S. Camargo. Comparison of the properties of a-C:H films deposited from methane and heptane precursors: study of the mechanical, chemical and structural properties. *Thin Solid Films*, 695:137733, feb 2020. ISSN 00406090. doi: 10.1016/j.tsf.2019. 137733. 68

[341] Yanfei Liu, Tomasz W. Liskiewicz, and Ben D. Beake. Dynamic changes of mechanical properties induced by friction in the Archard wear model. *Wear*, 428-429: 366–375, 2019. ISSN 00431648. doi: 10.1016/j.wear.2019.04.004. 69, 162

[342] Azom. Stainless Steel - Grade 316L - Properties, Fabrication and Applications (UNS S31603), 2013. URL https://www.azom.com/article.aspx? ArticleID=2382. 71, 73

[343] AZoM. M2 Molybdenum High Speed Tool Steel (UNS T11302), 2012. URL https://www.azom.com/article.aspx?ArticleID=6174. 72, 73, 92, 189

[344] MatWeb. AISI Type M2 Molybdenum High Speed Tool Steel (UNS T11302). URL http://www.matweb.com/search/DataSheet.aspx?MatGUID= 28fdb77f07524170ab825dff9fda8a84. 72

[345] West Yorkshire Steel. M2 High Speed Steel. Technical report, 2020. URL www.tcpdf.org. 72

[346] Ay Ching Hee, Yue Zhao, Dipankar Choudhury, Subir Ghosh, Qiang Zhu, and Hongtao Zhu. Tribological behavior of hydrogenated diamond-like carbon on polished alumina substrate with chromium interlayer for biomedical application. *Biotribology*, 7:1–10, sep 2016. ISSN 23525738. doi: 10.1016/j.biotri.2016.06. 001. 73

[347] Ying Chen and Xueyuan Nie. Study on fatigue and wear behaviors of a TiN coating using an inclined impact-sliding test. *Surf. Coatings Technol.*, 206(7):1977–1982, dec 2011. ISSN 02578972. doi: 10.1016/j.surfcoat.2011.09.032. URL https://www.sciencedirect.com/science/article/pii/S0257897211009078. 74

[348] Jaffee H.W Siu and Lawrence K.Y Li. An investigation of the effect of surface roughness and coating thickness on the friction and wear behaviour of a commercial MoS2-metal coating on AISI 400C steel. *Wear*, 237(2):283–287, feb 2000. ISSN 00431648. doi: 10.1016/S0043-1648(99)00349-X. URL `http://linkinghub.elsevier.com/retrieve/pii/S004316489900349X`. 74

[349] X. L. Peng, Z. H. Barber, and T. W. Clyne. Surface rough of diamond-like carbon films prepared using various techniques. *Surf. Coatings Technol.*, 138(1):23–32, apr 2001. ISSN 02578972. doi: 10.1016/S0257-8972(00)01139-7. URL `https://www.sciencedirect.com/science/article/pii/S0257897200011397`. 74, 176

[350] Kee Sung Lee. Effect of elastic modulus mismatch on the contact crack initiation in hard ceramic coating layer. *KSME Int. J.*, 17(12):1928–1937, dec 2003. ISSN 1226-4865. doi: 10.1007/bf02982432. 74

[351] University of Leeds. Facilities — Surface engineering — School of Mechanical Engineering — University of Leeds, 2019. URL `https://engineering.leeds.ac.uk/info/201538/institute{_}of{_}functional{_}surfaces/331/surface{_}engineering/3`. 76

[352] Alan M Bayer, Bruce A Becherer, and Teledyne Vasco. High Speed Tool Steels. *ASM Handb.*, 16:51–59, 1989. 83

[353] Y. Lifshitz, G. D. Lempert, E. Grossman, I. Avigal, C. Uzan-Saguy, R. Kalish, J. Kulik, D. Marton, and J. W. Rabalais. Growth mechanisms of DLC films from C + ions: experimental studies. *Diam. Relat. Mater.*, 4(4):318–323, apr 1995. ISSN 09259635. doi: 10.1016/0925-9635(94)05205-0. URL `https://www.sciencedirect.com/science/article/pii/0925963594052050`. 86

[354] B A Movchan and A V Demchishin. STRUCTURE AND PROPERTIES OF THICK CONDENSATES OF NICKEL, TITANIUM, TUNGSTEN, ALUMINUM OXIDES, AND ZIRCONIUM DIOXIDE IN VACUUM. *Fiz. Met. Met. 28 653-60 (Oct 1969).*, 1969. 86

[355] P. B. Barna and M. Adamik. Fundamental structure forming phenomena of polycrystalline films and the structure zone models. *Thin Solid Films*, 317(1-2):27–33, 1998. ISSN 00406090. doi: 10.1016/S0040-6090(97)00503-8. 87

[356] P. J. Kelly and R. D. Arnell. Development of a novel structure zone model relating to the closed-field unbalanced magnetron sputtering system. *J. Vac. Sci. Technol. A Vacuum, Surfaces, Film.*, 16(5):2858–2869, 1998. ISSN 0734-2101. doi: 10.1116/1.581432. 87

[357] André Anders. A structure zone diagram including plasma-based deposition and ion etching. *Thin Solid Films*, 518(15):4087–4090, 2010. ISSN 00406090. doi: 10.1016/j.tsf.2009.10.145. URL `http://dx.doi.org/10.1016/j.tsf.2009.10.145`. 87

[358] The Editors of Encyclopaedia Britannica. Carbon - Facts, Uses, & Properties, 2021. URL `https://www.britannica.com/science/carbon-chemical-element`. 87

[359] RSC. Chromium - Element information, properties and uses — Periodic Table, 2021. URL `https://www.rsc.org/periodic-table/element/24/chromiumhttp://www.rsc.org/periodic-table/element/24/chromium.` 87

[360] AZO Materials. Properties: Tungsten Carbide - An Overview, 2002. URL `https://www.azom.com/properties.aspx?ArticleID=1203http://www.azom.com/properties.aspx?ArticleID=1203.` 87

[361] D R Tallant, J E Parmeter, M P Siegal, and R L Simpson. The thermal stability of diamond-like carbon. *Diam. Relat. Mater.*, 4(3):191–199, 1995. ISSN 09259635. doi: 10.1016/0925-9635(94)00243-6. 87

[362] Qingsong Yong, Guozheng Ma, Haidou Wang, Shuying Chen, and Binshi Xu. Influence of tungsten content on microstructure and properties of tungsten-doped graphite-like carbon films. *J. Mater. Res.*, 31(23):3766–3776, dec 2016. ISSN 20445326. doi: 10.1557/jmr.2016.433. 88, 119, 133, 159

[363] Y. T. Pei, D. Galvan, and J. Th M. De Hosson. Nanostructure and properties of TiC/a-C:H composite coatings. *Acta Mater.*, 53(17):4505–4521, oct 2005. ISSN 13596454. doi: 10.1016/j.actamat.2005.05.045. URL `http://linkinghub.elsevier.com/retrieve/pii/S1359645405003551.` 88, 119, 133, 159

[364] The A to Z of Materials. Properties: Stainless Steel - Grade 316 (UNS S31600), 2013. URL `https://www.azom.com/properties.aspx?ArticleID=863.` 92, 189

[365] Yang Xia, Maxence Bigerelle, Julie Marteau, Pierre Emmanuel Mazeran, Salima Bouvier, and Alain Iost. Effect of surface roughness in the determination of the mechanical properties of material using nanoindentation test. *Scanning*, 36(1):134–149, jan 2014. ISSN 01610457. doi: 10.1002/sca.21111. URL `http://doi.wiley.com/10.1002/sca.21111.` 102, 105

[366] Wu Gui Jiang, Jian Jun Su, and Xi Qiao Feng. Effect of surface roughness on nanoindentation test of thin films. *Eng. Fract. Mech.*, 75(17):4965–4972, nov 2008. ISSN 00137944. doi: 10.1016/j.engfracmech.2008.06.016. 105, 112

[367] Liam Ward, Fabian Junge, Andreas Lampka, Mark Dobbertin, Christoph Mewes, and Marion Wienecke. The Effect of Bias Voltage and Gas Pressure on the Structure, Adhesion and Wear Behavior of Diamond Like Carbon (DLC) Coatings With Si Interlayers. *Coatings*, 4(2):214–230, apr 2014. ISSN 2079-6412. doi: 10.3390/coatings4020214. URL `http://www.mdpi.com/2079-6412/4/2/214http://www.mdpi.com/2079-6412/4/2/214/.` 108

[368] P. J. Wilbur, J. A. Davis, R. Wei, J. J. Vajo, and D. L. Williamson. High current density, low energy, ion implantation of AISI-M2 tool steel for tribological applications. *Surf. Coatings Technol.*, 83(1-3):250–256, sep 1996. ISSN 02578972. doi: 10.1016/0257-8972(95)02830-7. 108

[369] Ju Young Kim, Seung Kyun Kang, Jung Jun Lee, Jae il Jang, Yun Hee Lee, and Dongil Kwon. Influence of surface-roughness on indentation size effect. *Acta Mater.*, 55(10):3555–3562, jun 2007. ISSN 13596454. doi: 10.1016/j.actamat.2007.02.006. 110

[370] Jun Zheng, Hui Zhou, Zhi Hua Wan, and Rui Peng Sang. Structure and mechanical properties of tungsten-containing hydrogenated diamond like carbon coatings for space applications. In *Phys. Procedia*, volume 18, pages 245–250. Elsevier B.V., jan 2011. doi: 10.1016/j.phpro.2011.06.089. 113, 133

[371] Chehung Wei and Jui Ying Yen. Effect of film thickness and interlayer on the adhesion strength of diamond like carbon films on different substrates. *Diam. Relat. Mater.*, 16(4-7 SPEC. ISS.):1325–1330, apr 2007. ISSN 09259635. doi: 10.1016/j.diamond.2007.02.003. 113, 133, 259, 267

[372] S Zhang, X L Bui, Y Fu, and H Du. Extremely High Toughness With Good Hardness. 3:571–578, 2004. 113, 176

[373] Yu Xi Wang and Sam Zhang. Toward hard yet tough ceramic coatings. *Surf. Coatings Technol.*, 258:1–16, 2014. ISSN 02578972. doi: 10.1016/j.surfcoat.2014.07.007. URL https://doi.org/10.1016/j.surfcoat.2014.07.007.

[374] Sam Zhang, Xuan Lam Bui, Yongqing Fu, David L. Butler, and Hejun Du. Bias-graded deposition of diamond-like carbon for tribological applications. *Diam. Relat. Mater.*, 13(4-8):867–871, 2004. ISSN 09259635. doi: 10.1016/j.diamond.2003.10.043. 113, 176

[375] F. C. Tai, S. C. Lee, C. H. Wei, and S. L. Tyan. Correlation between ID/IG Ratio from Visible Raman Spectra and sp2/sp3 Ratio from XPS Spectra of Annealed Hydrogenated DLC Film. *Mater. Trans.*, 47(7):1847–1852, 2006. ISSN 1345-9678. doi: 10.2320/matertrans.47.1847. URL https://www.jstage.jst.go.jp/article/matertrans/47/7/47{_}7{_}1847/{_}article. 116, 132, 158

[376] Max Born and Emil Wolf. *Principles of optics : electromagnetic theory of propagation, interference and diffraction of light*. Pergamon, 1999. 116

[377] Ewen. Smith and Geoffrey. Dent. *Modern Raman Spectrocopy: A Practical Approach*. J. Wiley, 2005. ISBN 9780471497943. doi: 10.1002/0470011831. 117

[378] V. Presser, M. Keuper, C. Berthold, and K. G. Nickel. Experimental Determination of the Raman Sampling Depth in Zirconia Ceramics. *Appl. Spectrosc.*, 63(11):1288–1292, 2009. ISSN 0003-7028. doi: 10.1366/000370209789806975. 117

[379] H. Daniels, R. Brydson, B. Rand, and A. Brown. Investigating carbonization and graphitization using electron energy loss spectroscopy (EELS) in the transmission electron microscope (TEM). *Philos. Mag.*, 87(27):4073–4092, 2007. ISSN 14786435. doi: 10.1080/14786430701394041. 117, 132, 134

[380] G. Duscher, M. E. Hmielewski, and J. D.O. Oduor. Reliable quantification of EELS spectra with a simple model-based approach. *Microsc. Microanal.*, 15(SUPPL. 2):446–447, 2009. ISSN 14319276. doi: 10.1017/S1431927609094884. 117

[381] Gatan. Tungsten - EELS Atlas. URL https://eels.info/atlas/tungsten. 117

[382] Royal Society of Chemistry. Periodic Table – Royal Society of Chemistry, 2020. URL https://www.rsc.org/periodic-table. 129

[383] MyScope. Diffraction patterns. URL `https://myscope.training/legacy/tem/background/concepts/imagegeneration/diffractionimages.php`. 132

[384] A. C. Ferrari and J. Robertson. Resonant Raman spectroscopy of disordered, amorphous, and diamondlike carbon. *Phys. Rev. B - Condens. Matter Mater. Phys.*, 64 (7):075414, jul 2001. ISSN 1550235X. doi: 10.1103/PhysRevB.64.075414. URL `https://link.aps.org/doi/10.1103/PhysRevB.64.075414`. 132

[385] J Schwan, S Ulrich, V Batori, and H Ehrhardt. Raman spectroscopy on amorphous carbon films. *J. Appl. Phys.*, 80(1), 1996. 132

[386] Yuki Shibata, Takashi Kimura, Setsuo Nakao, and Kingo Azuma. Preparation of silicon-doped diamond-like carbon films with electrical conductivity by reactive high-power impulse magnetron sputtering combined with a plasma-based ion implantation system. *Diam. Relat. Mater.*, 101:107635, jan 2020. ISSN 09259635. doi: 10.1016/j.diamond.2019.107635. 133

[387] WebElements and Mark Winter. Carbon: radii of atoms and ions, 2020. URL `https://www.webelements.com/carbon/atom{_}sizes.html`. 133

[388] WebElements and Mark Winter. Tungsten: radii of atoms and ions, 2020. URL `https://www.webelements.com/tungsten/atom{_}sizes.html`. 133

[389] J. F. Behnke A. Sonnenfeld, T. M. Tun, L. Zajíčková, K. V. Kozlov, H.-E. Wagner and R. Hippler. Deposition Process Based on Organosilicon Precursors in Dielectric Barrier Discharges at Atmospheric Pressure—A Comparison. *Plasmas Polym.*, 6(4):237–266, 2001. ISSN 1084-0184. doi: 10.1023/A:1014414016164. URL `http://link.springer.com/10.1023/A:1014414016164http://www.springerlink.com/content/wu9y42hbt9jjl418/?MUD=MP`. 133

[390] Samuel J. McMaster, Tomasz W. Liskiewicz, Ben D. Beake, and Anne Neville. Probing Fatigue Resistance in Multi-layer DLC Coatings by Micro-impact: Correlation to Erosion Tests. *Surf. Coatings Technol.*, 402:126319, nov 2020. ISSN 02578972. doi: 10.1016/j.surfcoat.2020.126319. URL `https://linkinghub.elsevier.com/retrieve/pii/S0257897220309889`. 137

[391] J. B. Zu, G. T. Burstein, and I. M. Hutchings. A comparative study of the slurry erosion and free-fall particle erosion of aluminium. *Wear*, 149(1-2):73–84, sep 1991. ISSN 00431648. doi: 10.1016/0043-1648(91)90365-2. URL `https://www.sciencedirect.com/science/article/pii/0043164891903652`. 138, n

[392] I. M. Hutchings. A model for the erosion of metals by spherical particles at normal incidence. ,, 70(3 , Aug. 15, 1981):269–281, aug 1981. ISSN 00431648. doi: 10.1016/0043-1648(81)90347-1. URL `https://www.sciencedirect.com/science/article/pii/0043164881903471`.

[393] A.W. Ruff and S.M Wiederhorn. Erosion by solid particle impact. *Treatise Mater. Sci. Technol.*, 16:69–126, 1979. URL `http://www.dtic.mil/docs/citations/ADA066525`. 138, n

[394] Richard James Barker. *Erosion-corrosion of carbon steel pipework on an offshore oil and gas facility*. PhD thesis, University of Leeds, 2012. URL `http://etheses.whiterose.ac.uk/4444/`. 139, c

[395] Joshua James Owen. *Erosion-Corrosion of Carbon Steel in Complex Flow Geometries in Oil & Gas CO2 Environments*. PhD thesis, University of Leeds, 2018. 139, c

[396] K.-D. Bouzakis, A. Siganos, T. Leyendecker, and G. Erkens. Thin hard coatings fracture propagation during the impact test. *Thin Solid Films*, 460(1-2):181–189, jul 2004. ISSN 00406090. doi: 10.1016/j.tsf.2004.02.009. URL `http://linkinghub.elsevier.com/retrieve/pii/S0040609004002329http://www.scopus.com/inward/record.url?eid=2-s2.0-2942593904{&}partnerID=tZOtx3y1`. 142

[397] Mohd Fadzli Bin Abdollah, Yuto Yamaguchi, Tsuyoshi Akao, Naruhiko Inayoshi, Takayuki Tokoroyama, and Noritsugu Umehara. The Effect of Maximum Normal Impact Load, Absorbed Energy, and Contact Impulse, on the Impact Crater Volume/Depth of DLC Coating. *Tribol. Online*, 6(6):257–264, aug 2011. ISSN 1881-2198. doi: 10.2474/trol.6.257. URL `http://joi.jlc.jst.go.jp/JST.JSTAGE/trol/6.257?from=CrossRef`. 142, 161

[398] Mohd Fadzli Bin Abdollah, Yuto Yamaguchi, Tsuyoshi Akao, Naruhiko Inayoshi, Nobuyuki Miyamoto, Takayuki Tokoroyama, and Noritsugu Umehara. Deformation-wear transition map of DLC coating under cyclic impact loading. *Wear*, 274-275:435–441, jan 2012. ISSN 00431648. doi: 10.1016/j.wear.2011.11.007. 142, 161

[399] B D Beake, L Isern, J L Endrino, T W Liskiewicz, and X Shi. Micro-scale impact resistance of coatings on hardened tool steel and cemented carbide. *Mater. Lett.*, 284:129009, 2021. ISSN 0167-577X. doi: 10.1016/j.matlet.2020.129009. URL `https://doi.org/10.1016/j.matlet.2020.129009`. 147

[400] Papken Eh Hovsepian, Paranjayee Mandal, Arutiun P. Ehiasarian, G. Sáfrán, R. Tietema, and D. Doerwald. Friction and wear behaviour of Mo-W doped carbon-based coating during boundary lubricated sliding. *Appl. Surf. Sci.*, 366:260–274, mar 2016. ISSN 01694332. doi: 10.1016/j.apsusc.2016.01.007. 150, 159

[401] Mohd Fadzli Bin Abdollah, Yuto Yamaguchi, Tsuyoshi Akao, Naruhiko Inayoshi, Noritsugu Umehara, and Takayuki Tokoroyama. Phase transformation studies on the a-C coating under repetitive impacts. *Surf. Coatings Technol.*, 205(2):625–631, oct 2010. ISSN 02578972. doi: 10.1016/j.surfcoat.2010.07.062. URL `https://www.sciencedirect.com/science/article/pii/S0257897210005840`. 150, 159

[402] Jonathan I Ukpai. *Erosion-corrosion characterisation for pipeline materials using combined acoustic emission and electrochemical monitoring*. PhD thesis, University of Leeds, 2014. URL `http://etheses.whiterose.ac.uk/7328/http://etheses.whiterose.ac.uk/7328/1/Thesis.200564637.Final.pdf`. 157

[403] Zhenyu Hu, Alexej Schubnov, and Frank Vollertsen. Tribological behaviour of DLC-films and their application in micro deep drawing. *J. Mater. Process. Technol.*, 212(3):647–652, mar 2012. ISSN 09240136. doi: 10.1016/j.jmatprotec.2011.10.012. URL `https://www.sciencedirect.com/science/article/pii/S0924013611003013{#}fig0005`. 158, 161, 258

[404] Teresa Wright and Trevor F. Page. Nanoindentation and microindentation studies of hard carbon on 304 stainless steel. *Surf. Coatings Technol.*, 54-55:557–562, jan 1992. ISSN 02578972. doi: 10.1016/S0257-8972(07)80082-X. 158, 161, 258

[405] Lanshi Zheng and S. Ramalingam. Multi-layer and composite structures for advanced coatings. *Surf. Coatings Technol.*, 81(1):52–71, may 1996. ISSN 02578972. doi: 10.1016/0257-8972(95)02618-5. 158

[406] S. Ramalingam and Lanshi Zheng. Film-substrate interface stresses and their role in the tribological performance of surface coatings. *Tribol. Int.*, 28(3):145–161, may 1995. ISSN 0301679X. doi: 10.1016/0301-679X(95)98963-E. 158, 177

[407] Jian Chen, Heng Li, and Ben D. Beake. Load sensitivity in repetitive nano-impact testing of TiN and AlTiN coatings. *Surf. Coatings Technol.*, 308:289–297, dec 2016. ISSN 02578972. doi: 10.1016/j.surfcoat.2016.05.094. URL https://www.sciencedirect.com/science/article/pii/S0257897216307319. 159

[408] E. Bousser, M. Benkahoul, L. Martinu, and J. E. Klemberg-Sapieha. Effect of microstructure on the erosion resistance of Cr-Si-N coatings. *Surf. Coatings Technol.*, 203(5-7):776–780, 2008. ISSN 02578972. doi: 10.1016/j.surfcoat.2008.08.012. URL http://dx.doi.org/10.1016/j.surfcoat.2008.08.012. 159, 258

[409] Siavash Soltanahmadi, Thibaut Charpentier, Ileana Nedelcu, Vishal Khetan, Ardian Morina, Helen M. Freeman, Andrew P. Brown, Rik Brydson, Marcel C.P. Van Eijk, and Anne Neville. Surface Fatigue Behavior of a WC/aC:H Thin-Film and the Tribochemical Impact of Zinc Dialkyldithiophosphate. *ACS Appl. Mater. Interfaces*, 11(44):41676–41687, 2019. ISSN 19448252. doi: 10.1021/acsami.9b14669. 159

[410] J Rao, T Rose, M Craig, and J. R. Nicholls. Wear coatings for high load applications. In *Procedia CIRP*, volume 22, pages 277–280, 2014. doi: 10.1016/j.procir.2014.07.005. URL www.sciencedirect.com. 159

[411] A. A. Ogwu, R. W. Lamberton, S Morley, P Maguire, and J McLaughlin. Characterization of thermally annealed diamond like carbon (DLC) and silicon modified DLC films by Raman spectroscopy. *Phys. B Condens. Matter*, 269(3-4):335–344, sep 1999. ISSN 09214526. doi: 10.1016/S0921-4526(99)00138-6. URL https://www.sciencedirect.com/science/article/pii/S0921452699001386. 159, 217

[412] Sekhar C. Ray, W. F. Pong, and P. Papakonstantinou. Iron, nitrogen and silicon doped diamond like carbon (DLC) thin films: A comparative study. *Thin Solid Films*, 610:42–47, jul 2016. ISSN 00406090. doi: 10.1016/j.tsf.2016.04.048. 159

[413] Surya R. Kalidindi and Siddhartha Pathak. Determination of the effective zero-point and the extraction of spherical nanoindentation stress-strain curves. *Acta Mater.*, 56(14):3523–3532, aug 2008. ISSN 13596454. doi: 10.1016/j.actamat.2008.03.036. 161

[414] Mazdak Parsi, Kamyar Najmi, Fardis Najafifard, Shokrollah Hassani, Brenton S. McLaury, and Siamack A. Shirazi. A comprehensive review of solid particle erosion modeling for oil and gas wells and pipelines applications. *J. Nat. Gas Sci. Eng.*, 21:850–873, nov 2014. ISSN 18755100. doi: 10.1016/j.jngse.

2014.10.001.   URL `https://www.sciencedirect.com/science/article/pii/S187551001400300X`. 161

[415] Feihu Zhang, Binbin Meng, Yanquan Geng, Yong Zhang, and Zhipeng Li. Friction behavior in nanoscratching of reaction bonded silicon carbide ceramic with Berkovich and sphere indenters. *Tribol. Int.*, 97:21–30, may 2016. ISSN 0301679X.   doi: 10.1016/j.triboint.2016.01.013.   URL `https://www.sciencedirect.com/science/article/pii/S0301679X16000256`. 164, 176

[416] J. D. Kamminga and G. C.A.M. Janssen. Experimental discrimination of plowing friction and shear friction. *Tribol. Lett.*, 25(2):149–152, jan 2007. ISSN 10238883.   doi: 10.1007/s11249-006-9135-3.   URL `http://link.springer.com/10.1007/s11249-006-9135-3`. 164

[417] F. Pöhl, C. Hardes, and W. Theisen. Deformation behavior and dominant abrasion micro mechanisms of tempering steel with varying carbon content under controlled scratch testing. *Wear*, pages 212–222, mar 2019. ISSN 00431648. doi: 10.1016/j.wear.2019.01.073. 164

[418] Bharat Bhushan. *Introduction To Tribology*.   Wiley, 2 edition, 2013.   ISBN 9781119944539. 164

[419] Sina Ebnesajjad and Arthur H. Landrock.   Surface Tension and Its Measurement. In *Adhes. Technol. Handb.*, pages 19–34. Elsevier, jan 2015. doi: 10.1016/b978-0-323-35595-7.00002-4. 164

[420] Hjalti Skulason and C. Daniel Frisbie. Rupture of hydrophobic microcontacts in water: Correlation of pull-off force with AFM tip radius. *Langmuir*, 16(15):6294–6297, 2000. ISSN 07437463. doi: 10.1021/la000208y. 164

[421] Guangtu Gao, Rachel J. Cannara, Robert W. Carpick, and Judith A. Harrison. Atomic-scale friction on diamond: A comparison of different sliding directions on (001) and (111) surfaces using MD and AFM. *Langmuir*, 23(10):5394–5405, 2007. ISSN 07437463. doi: 10.1021/la062254p. 175, 180

[422] Nikhil S. Tambe and Bharat Bhushan. Friction model for the velocity dependence of nanoscale friction. *Nanotechnology*, 16(10):2309–2324, 2005. ISSN 09574484. doi: 10.1088/0957-4484/16/10/054. 164, 175, 227

[423] Samuel J. McMaster, Tomasz W. Liskiewicz, Anne Neville, and Ben D. Beake. Investigating the Interfacial and Ploughing contributions to Friction of DLC coatings using Nano-scratch with varying Probe Radius. . 165

[424] B. D. Beake, B. Shi, and J. L. Sullivan. Nanoscratch and nanowear testing of TiN coatings on M42 steel. *Tribol. - Mater. Surfaces Interfaces*, 5(4):141–147, 2011. ISSN 17515831. doi: 10.1179/1751584X11Y.0000000017. 165, 179

[425] Micro Materials.   — NanoTriboTest — Reciprocating wear tests — Electrical contacts, 2019. URL `https://www.micromaterials.co.uk/techniques/nanotribotest/`. 165, 192, 234, 235

[426] M. Bigerelle, P. E. Mazeran, and M. Rachik. The first indenter-sample contact and the indentation size effect in nano-hardness measurement. *Mater. Sci. Eng. C*, 27 (5-8 SPEC. ISS.):1448–1451, sep 2007. ISSN 09284931. doi: 10.1016/j.msec.2006.09.031. 166

[427] Mirko Weidner, Oscar Borrero-López, Mark Hoffman, Avi Bendavid, and Phil J. Martin. Effect of substrate roughness on the contact damage of thin brittle films on brittle substrates. *Thin Solid Films*, 518(18):5242–5248, jul 2010. ISSN 00406090. doi: 10.1016/j.tsf.2010.04.039. URL `https://www.sciencedirect.com/science/article/pii/S004060901000564X`. 171

[428] T. W. Liskiewicz, B. D. Beake, N. Schwarzer, and M. I. Davies. Short note on improved integration of mechanical testing in predictive wear models. *Surf. Coatings Technol.*, 237:212–218, 2013. ISSN 02578972. doi: 10.1016/j.surfcoat.2013.07.044. URL `http://dx.doi.org/10.1016/j.surfcoat.2013.07.044`. 173, 178, 180, 227, 231, 252, 253, 260

[429] Helena Ronkainen, Anssi Laukkanen, and Kenneth Holmberg. Friction in a coated surface deformed by a sliding sphere. *Wear*, 263(7-12 SPEC. ISS.):1315–1323, sep 2007. ISSN 00431648. doi: 10.1016/j.wear.2007.01.103. URL `https://www.sciencedirect.com/science/article/pii/S004316480700364X`. 175, 179

[430] Feodor M. Borodich, Emmanuel Brousseau, Alastair Clarke, Andrey Pepelyshev, and Juan Carlos Sánchez-López. Roughness of Deposited Carbon-Based Coatings and Its Statistical Characteristics at Nano and Microscales. *Front. Mech. Eng.*, 5 (May):1–13, 2019. ISSN 2297-3079. doi: 10.3389/fmech.2019.00024. 176

[431] Alanazi Ali, Kenji K. Hirakuri, and Gernot Friedbacher. Roughness and deposition mechanism of DLC films prepared by r.f. plasma glow discharge. *Vacuum*, 51(3): 363–368, 1998. ISSN 0042207X. doi: 10.1016/S0042-207X(98)00115-8. 176

[432] André Clausner and Frank Richter. Determination of yield stress from nano-indentation experiments. *Eur. J. Mech. A/Solids*, 51:11–20, 2015. ISSN 09977538. doi: 10.1016/j.euromechsol.2014.11.008. 178

[433] L. Vandeperre and W.J. Clegg. The Correlation between Hardness and Yield Strength of Hard Materials. *Mater. Sci. Forum*, 492-493:555–560, 2005. ISSN 1662-9752. doi: 10.4028/www.scientific.net/msf.492-493.555. 178

[434] Ayesha J. Haq, P. R. Munroe, M. Hoffman, P. J. Martin, and A. Bendavid. Nanoindentation-induced deformation behaviour of diamond-like carbon coatings on silicon substrates. *Thin Solid Films*, 515(3):1000–1004, 2006. ISSN 00406090. doi: 10.1016/j.tsf.2006.07.074. 178

[435] Ayesha J. Haq, P. R. Monroe, M. Hoffman, P. J. Martin, and A. Bendavid. Berkovich indentation of diamondlike carbon coatings on silicon substrates. *J. Mater. Res.*, 23(7):1862–1869, 2008. ISSN 08842914. doi: 10.1557/jmr.2008.0232.

[436] Ayesha J. Haq, P. R. Munroe, M. Hoffman, P. J. Martin, and A. Bendavid. Effect of coating thickness on the deformation behaviour of diamond-like carbon-silicon system. *Thin Solid Films*, 518(8):2021–2028, 2010. ISSN 00406090. doi: 10.1016/j.tsf.2009.08.041. URL `http://dx.doi.org/10.1016/j.tsf.2009.08.041`.

[437] A. J. Haq, P. R. Munroe, M. Hoffman, P. J. Martin, and A. Bendavid. Nanoindentation-induced deformation behaviour of tetrahedral amorphous carbon coating deposited by filtered cathodic vacuum arc. *Diam. Relat. Mater.*, 19(11):

1423–1430, 2010. ISSN 09259635. doi: 10.1016/j.diamond.2010.08.014. URL `http://dx.doi.org/10.1016/j.diamond.2010.08.014`. 178

[438] N. Schwarzer, Q. H. Duong, N. Bierwisch, G. Favaro, M. Fuchs, P. Kempe, B. Widrig, and J. Ramm. Optimization of the Scratch Test for specific coating designs. *Surf. Coatings Technol.*, 206(6):1327–1335, 2011. ISSN 02578972. doi: 10.1016/j.surfcoat.2011.08.051. URL `http://dx.doi.org/10.1016/j.surfcoat.2011.08.051`. 178, 258, 259, 260

[439] B. D. Beake, S. R. Goodes, and B. Shi. Nanomechanical and nanotribological testing of ultra-thin carbon-based and MoST films for increased MEMS durability. *J. Phys. D. Appl. Phys.*, 42(6), 2009. ISSN 00223727. doi: 10.1088/0022-3727/42/6/065301. 179

[440] Baogui Shi, John L. Sullivan, and Ben D. Beake. An investigation into which factors control the nanotribological behaviour of thin sputtered carbon films. *J. Phys. D. Appl. Phys.*, 41(4), 2008. ISSN 00223727. doi: 10.1088/0022-3727/41/4/045303. 179, 254

[441] M. G. Gee and L. Nimishakavi. Model single point abrasion experiments on WC/Co hardmetals. *Int. J. Refract. Met. Hard Mater.*, 29(1):1–9, 2011. ISSN 02634368. doi: 10.1016/j.ijrmhm.2010.04.009. URL `http://dx.doi.org/10.1016/j.ijrmhm.2010.04.009`. 179

[442] Qilong Wei, Jiangang Lü, Qiang Yang, and Xiaoyuan Li. Multi-pass micro-scratching and tribological behaviors of an austenitic steel in media. *Tribol. Int.*, 117(January 2017):112–118, 2018. ISSN 0301679X. doi: 10.1016/j.triboint.2017.08.016. URL `https://doi.org/10.1016/j.triboint.2017.08.016`. 179

[443] K. Meine, T. Schneider, D. Spaltmann, and E. Santner. The influence of roughness on friction Part I: The influence of a single step. *Wear*, 253(7-8):725–732, oct 2002. ISSN 00431648. doi: 10.1016/S0043-1648(02)00159-X. 187, 252

[444] K. Meine, T. Schneider, D. Spaltmann, and E. Santner. The influence of roughness on friction Part II. The influence of multiple steps. *Wear*, 253(7-8):733–738, oct 2002. ISSN 00431648. doi: 10.1016/S0043-1648(02)00160-6. 187, 252

[445] Samuel J. McMaster, Shahriar Kosarieh, Tomasz W. Liskiewicz, Anne Neville, and Ben D. Beake. Multi-scale Fretting Analysis of the Friction of DLC coatings in Dry and Lubricated conditions. . 187

[446] AZoM. AISI 52100 Alloy Steel (UNS G52986), 2012. URL `https://www.azom.com/article.aspx?ArticleID=6704`. 189

[447] A. Fantetti, L.R. Tamatam, M. Volvert, I. Lawal, L. Liu, L. Salles, M.R.W. Brake, C.W. Schwingshackl, and D. Nowell. The impact of fretting wear on structural dynamics: Experiment and Simulation. *Tribol. Int.*, 138:111–124, oct 2019. ISSN 0301679X. doi: 10.1016/j.triboint.2019.05.023. URL `https://www.sciencedirect.com/science/article/pii/S0301679X19302828`. 200

[448] Jouko Hintikka, Antti Mäntylä, Joona Vaara, Tero Frondelius, and Arto Lehtovaara. Stable and unstable friction in fretting contacts. *Tribol. Int.*, 131:73–82, mar 2019. ISSN 0301679X. doi: 10.1016/j.triboint.2018.10.014. URL `https://www.sciencedirect.com/science/article/pii/S0301679X1830495X`. 201

[449] M. Shima, H. Suetake, I. R. McColl, R. B. Waterhouse, and M. Takeuchi. On the behaviour of an oil lubricated fretting contact. *Wear*, 210(1-2):304–310, 1997. ISSN 00431648. doi: 10.1016/S0043-1648(97)00078-1. 205, 226

[450] S. Fouvry, T. Liskiewicz, Ph. Kapsa, S. Hannel, and E. Sauger. An energy description of wear mechanisms and its applications to oscillating sliding contacts. *Wear*, 255(1-6):287–298, aug 2003. ISSN 00431648. doi: 10.1016/S0043-1648(03)00117-0. URL `https://www.sciencedirect.com/science/article/pii/S0043164803001170{#}FIG1`. 224, 225

[451] S. Fouvry, V. Fridrici, C. Langlade, Ph. Kapsa, and L. Vincent. Palliatives in fretting: A dynamical approach. *Tribol. Int.*, 39(10):1005–1015, oct 2006. ISSN 0301679X. doi: 10.1016/j.triboint.2006.02.038. URL `https://www.sciencedirect.com/science/article/pii/S0301679X06000454{#}fig3`. 224, 226

[452] T. Liskiewicz. *Hard coatings durability under fretting wear.* PhD thesis, 2005. URL `http://linkinghub.elsevier.com/retrieve/pii/S0167892205800677`. 224

[453] A. L. Mohd Tobi, P. H. Shipway, and S. B. Leen. Gross slip fretting wear performance of a layered thin W-DLC coating: Damage mechanisms and life modelling. *Wear*, 271(9-10):1572–1584, jul 2011. ISSN 00431648. doi: 10.1016/j.wear.2010.12.073. 225

[454] B. Blanpain, J. P. Celis, J. R. Roos, J. Ebberink, and J. Smeets. A comparative study of the fretting wear of hard carbon coatings. *Thin Solid Films*, 223(1):65–71, jan 1993. ISSN 00406090. doi: 10.1016/0040-6090(93)90728-8. URL `https://www.sciencedirect.com/science/article/pii/0040609093907288`. 225, 227

[455] Antoni Neyman. The influence of oil properties on the fretting wear of mild steel. *Wear*, 152(1):171–181, 1992. ISSN 00431648. doi: 10.1016/0043-1648(92)90212-Q. 226

[456] M. I. De Barros'Bouchet, J. M. Martin, T. Le-Mogne, and B. Vacher. Boundary lubrication mechanisms of carbon coatings by MoDTC and ZDDP additives. In *Tribol. Int.*, volume 38, pages 257–264, mar 2005. doi: 10.1016/j.triboint.2004.08.009. 226

[457] M. De Feo, M. I. De Barros Bouchet, C. Minfray, Th Le Mogne, F. Meunier, L. Yang, B. Thiebaut, and J. M. Martin. MoDTC lubrication of DLC-involving contacts. Impact of MoDTC degradation. *Wear*, 348-349:116–125, feb 2016. ISSN 00431648. doi: 10.1016/j.wear.2015.12.001. 226

[458] Yasir Al-Jeboori, Shahriar Kosarieh, Ardian Morina, and Anne Neville. Investigation of pure sliding and sliding/rolling contacts in a DLC/Cast iron system when lubricated in oils containing MoDTC-Type friction modifier. *Tribol. Int.*, 122:23–37, jun 2018. ISSN 0301679X. doi: 10.1016/j.triboint.2018.02.015. 226

[459] Ardian Morina, Hongyuan Zhao, and J. Fred W. Mosselmans. In-situ reflection-XANES study of ZDDP and MoDTC lubricant films formed on steel and diamond like carbon (DLC) surfaces. *Appl. Surf. Sci.*, 297:167–175, apr 2014.

ISSN 01694332. doi: 10.1016/j.apsusc.2014.01.116. URL `https://www.sciencedirect.com/science/article/pii/S0169433214001688`. 226

[460] G. M. Wilson, J. F. Smith, and J. L. Sullivan. A nanotribological study of thin amorphous C and Cr doped amorphous C coatings. *Wear*, 265(11-12):1633–1641, 2008. ISSN 00431648. doi: 10.1016/j.wear.2008.03.017. 227, 231

[461] Dirk Drees, Jean Pierre Celis, and Satish Achanta. Friction of thin coatings on three length scales under reciprocating sliding. *Surf. Coatings Technol.*, 188-189(1-3 SPEC.ISS.):511–518, 2004. ISSN 02578972. doi: 10.1016/j.surfcoat.2004.07.008. 227, 253

[462] Lúcia V. Santos, Vladimir J. Trava-Airoldi, Evaldo J. Corat, Koshun Iha, Marcos Massi, Rodrigo Prioli, and Richard Landers. Friction coefficient measurements by LFM on DLC films as function of sputtering deposition parameters. *Diam. Relat. Mater.*, 11(3-6):1135–1138, 2002. ISSN 09259635. doi: 10.1016/S0925-9635(01)00600-8. 227

[463] B. Bhushan and S. Sundararajan. Micro/nanoscale friction and wear mechanisms of thin films using atomic force and friction force microscopy. *Acta Mater.*, 46(11): 3793–3804, 1998. ISSN 13596454. doi: 10.1016/S1359-6454(98)00062-7. 227, 253

[464] O. Zwörner, H. Hölscher, U. D. Schwarz, and R. Wiesendanger. The velocity dependence of frictional forces in point-contact friction. *Appl. Phys. A Mater. Sci. Process.*, 66(SUPPL. 1):263–267, 1998. ISSN 09478396. doi: 10.1007/s003390051142. 227

[465] S. Fouvry and K. Kubiak. Introduction of a fretting-fatigue mapping concept: Development of a dual crack nucleation - crack propagation approach to formalize fretting-fatigue damage. *Int. J. Fatigue*, 31(2):250–262, feb 2009. ISSN 01421123. doi: 10.1016/j.ijfatigue.2008.09.002. URL `https://www.sciencedirect.com/science/article/pii/S0142112308002168?via{%}3Dihub{#}fig2`. 227

[466] N. T. Garabedian, H. S. Khare, R. W. Carpick, and D. L. Burris. AFM at the Macroscale: Methods to Fabricate and Calibrate Probes for Millinewton Force Measurements. *Tribol. Lett.*, 67(1):1–10, 2019. ISSN 10238883. doi: 10.1007/s11249-019-1134-2. URL `http://dx.doi.org/10.1007/s11249-019-1134-2`. 227

[467] Ben D. Beake, Adrian J. Harris, Tomasz W. Liskiewicz, Jérémie Wagner, Samuel J. McMaster, S. R. Goodes, Anne Neville, and Lei Zhang. Friction and electrical contact resistance in reciprocating nano-scale wear testing of metallic materials. *Wear*, page 203866, mar 2021. ISSN 00431648. doi: 10.1016/j.wear.2021.203866. URL `https://linkinghub.elsevier.com/retrieve/pii/S0043164821002556`. 231

[468] M. G. Gee and A. D. Gee. A cost effective test system for micro-tribology experiments. *Wear*, 263(7-12 SPEC. ISS.):1484–1491, sep 2007. ISSN 00431648. doi: 10.1016/j.wear.2006.12.042. URL `http://www.sciencedirect.com/science/article/pii/S004316480700395X`. 231

[469] M. G. Gee, J. W. Nunn, A. Muniz-Piniella, and L. P. Orkney. Micro-tribology experiments on engineering coatings. *Wear*, 271(9-10):2673–2680, jul 2011. ISSN 00431648. doi: 10.1016/j.wear.2011.02.031. URL `http://www.sciencedirect.com/science/article/pii/S0043164811003486`. 231, 253, 254

[470] Kirsten I. Schiffmann and Andreas Hieke. Analysis of microwear experiments on thin DLC coatings: Friction, wear and plastic deformation. *Wear*, 254(5-6):565–572, 2003. ISSN 00431648. doi: 10.1016/S0043-1648(03)00188-1. 231, 254

[471] Kirsten Ingolf Schiffmann. Phenomena in microwear experiments on metal-free and metal-containing diamond-like carbon coatings: Friction, wear, fatigue and plastic deformation. *Surf. Coatings Technol.*, 177-178:453–458, 2004. ISSN 02578972. doi: 10.1016/j.surfcoat.2003.08.064. 231, 252, 254

[472] Ben D. Beake, Samuel J. McMaster, Tomasz W. Liskiewicz, and Anne Neville. Influence of Si- and W- doping on micro-scale reciprocating wear and impact performance of DLC coatings on hardened steel. *Tribol. Int.*, page 107063, apr 2021. ISSN 0301679X. doi: 10.1016/j.triboint.2021.107063. URL `https://linkinghub.elsevier.com/retrieve/pii/S0301679X21002115`. 231

[473] Oerlikon Balzers. Coated components: Great Performance and reliability. Technical report, 2010. 232, 253

[474] Ben D. Beake, Sam J. McMaster, Tomasz W. Liskiewicz, and Anne Neville. Influence of Si and W doping on micro-scale reciprocating wear and impact resistance of DLC coatings on hardened steel. 233, 234

[475] D. L. Burris and W. G. Sawyer. Addressing practical challenges of low friction coefficient measurements. *Tribol. Lett.*, 35(1):17–23, 2009. ISSN 10238883. doi: 10.1007/s11249-009-9438-2. 235

[476] Kenneth Holmberg, Anssi Laukkanen, Helena Ronkainen, Richard Waudby, Gwidon Stachowiak, Marcin Wolski, Pawel Podsiadlo, Mark Gee, John Nunn, Carsten Gachot, and Lawrence Li. Topographical orientation effects on friction and wear in sliding DLC and steel contacts, part 1: Experimental. *Wear*, 330-331: 3–22, 2015. ISSN 00431648. doi: 10.1016/j.wear.2015.02.014. 252

[477] T. J. Kamps, J. C. Walker, and A. G. Plint. In situ stylus profilometer for a high frequency reciprocating tribometer. *Surf. Topogr. Metrol. Prop.*, 5(3):1–16, 2017. ISSN 2051672X. doi: 10.1088/2051-672X/aa7da8. 252

[478] Feng Chun Hsia, Fiona M. Elam, Daniel Bonn, Bart Weber, and Steve E. Franklin. Wear particle dynamics drive the difference between repeated and non-repeated reciprocated sliding. *Tribol. Int.*, 142(June 2019):105983, 2020. ISSN 0301679X. doi: 10.1016/j.triboint.2019.105983. URL `https://doi.org/10.1016/j.triboint.2019.105983`. 252

[479] E. Santner, D. Klaffke, K. Meine, Ch Polaczyk, and D. Spaltmann. Demonstration of topography modification by friction processes and vice versa. *Tribol. Int.*, 39(5): 450–455, may 2006. ISSN 0301679X. doi: 10.1016/j.triboint.2005.04.029. 252, 253

[480] Nikhil S. Tambe and Bharat Bhushan. Nanoscale friction-induced phase transformation of diamond-like carbon. *Scr. Mater.*, 52(8):751–755, 2005. ISSN 13596462. doi: 10.1016/j.scriptamat.2004.12.013. 252

[481] Spyridon Korres, Tim Feser, and Martin Dienwiebel. A new approach to link the friction coefficient with topography measurements during plowing. *Wear*, 303 (1-2):202–210, 2013. ISSN 00431648. doi: 10.1016/j.wear.2013.03.010. URL `http://dx.doi.org/10.1016/j.wear.2013.03.010`. 253

[482] J. Koskinen, D. Schneider, H. Ronkainen, T. Muukkonen, S. Varjus, P. Burck, K. Holmberg, and H. J. Scheibe. Microstructural changes in DLC films due to tribological contact. *Surf. Coatings Technol.*, 108-109(1-3):385–390, 1998. ISSN 02578972. doi: 10.1016/S0257-8972(98)00656-2. 254

[483] J. Michler and E. Blank. Analysis of coating fracture and substrate plasticity induced by spherical indentors: Diamond and diamond-like carbon layers on steel substrates. *Thin Solid Films*, 381(1):119–134, jan 2001. ISSN 00406090. doi: 10.1016/S0040-6090(00)01340-7. 254

[484] K. J. Kubiak, T. G. Mathia, and S. Fouvry. Interface roughness effect on friction map under fretting contact conditions. *Tribol. Int.*, 43(8):1500–1507, 2010. ISSN 0301679X. doi: 10.1016/j.triboint.2010.02.010. 259

[485] Ben D. Beake, Andrew Bird, Luis Isern, Jose L. Endrino, and Feng Jiang. Elevated temperature micro-impact testing of TiAlSiN coatings produced by physical vapour deposition. *Thin Solid Films*, jun 2019. ISSN 00406090. doi: 10.1016/j.tsf.2019.06.008. URL `https://www.sciencedirect.com/science/article/pii/S0040609019303773https://linkinghub.elsevier.com/retrieve/pii/S0040609019303773`. 266

[486] Micro Materials. Nanomechanical Testing — High Temperature — 1000 C, 2020. URL `https://www.micromaterials.co.uk/environment/testing1000/`.

[487] Micro Materials. High Temperature Nanomechanical Testing — NanoTest Vantage, 2020. URL `https://www.micromaterials.co.uk/environment/hightemperature/`. 266

[488] J. M. Wheeler and J. Michler. Invited article: Indenter materials for high temperature nanoindentation. *Rev. Sci. Instrum.*, 84(10):1–11, 2013. ISSN 00346748. doi: 10.1063/1.4824710. 266

[489] Micro Materials. Nano Test Vantage Imaging Options, 2020. URL `https://www.micromaterials.co.uk/techniques/imaging-options/`. 266

[490] Bharat Bhushan. Nanotribology, nanomechanics and nanomaterials characterization. *Philos. Trans. R. Soc. London A Math. Phys. Eng. Sci.*, 366(1869): 1351–1381, apr 2008. ISSN 1364-503X, 1471-2962. doi: 10.1098/rsta.2007.2163. URL `http://www.ncbi.nlm.nih.gov/pubmed/18156126http://rsta.royalsocietypublishing.org/content/366/1869/1351{%}5Cnhttp://rsta.royalsocietypublishing.org/content/roypta/366/1869/1351.full.pdf{%}5Cnhttp://www.ncbi.nlm.nih.gov/pubmed/18156126`. 266

[491] T. Haque, A. Morina, and A. Neville. Influence of friction modifier and anti-wear additives on the tribological performance of a non-hydrogenated DLC coating. *Surf. Coatings Technol.*, 204(24):4001–4011, 2010. ISSN 02578972. doi: 10.1016/j.surfcoat.2010.05.017. 266

[492] Monika Madej. The effect of TiN and CrN interlayers on the tribological behavior of DLC coatings. *Wear*, 317(1-2):179–187, sep 2014. ISSN 00431648. doi: 10.1016/j.wear.2014.05.008. URL `http://www.sciencedirect.com/science/article/pii/S004316481400177X`. 267

[493] C. V. Cooper, P. Holiday, and A. Matthews. The effect of TiN interlayers on the indentation behavior of diamond-like carbon films on alloy and compound substrates. *Surf. Coatings Technol.*, 63(3):129–134, mar 1994. ISSN 02578972. doi: 10.1016/0257-8972(94)90089-2. 267

[494] E. Zoestbergen and J. Th. M. De Hosson. Crack resistance of PVD coatings: Influence of surface treatment prior to deposition. *Surf. Eng.*, 18(4):283–288, aug 2002. ISSN 02670844. doi: 10.1179/026708402225006169. URL `http://www.tandfonline.com/doi/full/10.1179/026708402225006169`. 267

[495] Taizo Makino, Takanori Kato, and Kenji Hirakawa. Review of the fatigue damage tolerance of high-speed railway axles in Japan. *Eng. Fract. Mech.*, 78(5):810–825, mar 2011. ISSN 00137944. doi: 10.1016/j.engfracmech.2009.12.013. URL `https://www.sciencedirect.com/science/article/pii/S0013794409003944?via{%}3Dihub`. 268

[496] I. M. Hutchings. Abrasive and erosive wear tests for thin coatings: A unified approach. In *Tribol. Int.*, volume 31, pages 5–15. Elsevier, jan 1998. doi: 10.1016/S0301-679X(98)00004-8. g

[497] H.H. Ku. Notes on the use of propagation of error formulas. *J. Res. Natl. Bur. Stand. Sect. C Eng. Instrum.*, 70C(4):263, 1966. ISSN 0022-4316. doi: 10.6028/jres.070c.025. u

[498] Harvard University. A Summary of Error Propagation - Physical Sciences 2, 2007. u

Appendix A

Conferences And Presentations

A.1   Conferences And Courses Attended

- UK Tribology Launch Event, IOM3, London, 2015

- 24th Mission of Tribology, IMechE, London, 2015

- 50th Anniversary of the Jost Report, IMechE, London, 2016

- TriboUK, University of Leeds, 2016

- 43rd Leeds-Lyon Symposium on Tribology, Leeds, 2016

- Winter Tribology Fair, University of Warwick, 2017

- IET Challenges in Tribology, Birmingham, 2017

- IDC Machining Conference, Advanced Manufacturing Research Centre (AMRC), University of Sheffield, 2017

- Advanced Nano-Mechanical Techniques For Academic and Industrial Research, University of Warwick, 2017

- Nanotribology Summer School, Technical University of Denmark (DTU), 2017

- TriboUK, Imperial College, London, 2018

- European Conference on Nanofilms (ECNF), Cranfield University, 2018

- 45th International Conference on Metallurgical Coatings and Thin Films (ICM-CTF), San Diego, 2018

- Ion and Plasma Surface Interactions Group Conference, University of Huddersfield, 2018

- 45th Leeds-Lyon Symposium on Tribology, Leeds, 2018

- Tribology in Marine Diesel Engines, Harbin, China, 2019

- TriboUK, University of Leeds, 2019

- Advanced nano-mechanical techniques for academic and industrial research, University of Southampton, 2019

A.2   Oral Presentations

- S.J. McMaster *et al.* Nanomechanical Characterisation of DLC Coating Systems, TriboUK, Imperial College, London, 2018

- S.J. McMaster *et al.* Nano-Mechanical Characterisation of DLC Coating Systems, ECNF, Cranfield University, 2018

- S.J. McMaster *et al.* Investigating Erosion Resistance of Advanced DLC Coating Systems with Nano-Impact Method, 45th ICMCTF, San Diego, 2018

- S.J. McMaster *et al.* Predicting the fretting performance of Diamond-Like Carbon coating systems by analysing nanomechanical properties, TriboUK, University of Leeds, 2019 [1]

- S.J. McMaster *et al.* Nanomechanical Characterisation of Diamond-Like Carbon Coatings for Tribological Performance: Nano-Scratch and Multi-Scale Fretting, University of Oxford Materials Group, 2020 [2]

A.3   Poster Presentations

- S.J.McMaster *et al.* Nano-Mechanical characterisation of DLC coatings for tribological performance, Winter Tribology Fair, University of Warwick, 2017

- S.J. McMaster *et al.* Nanomechanical and Impact-Erosion Characterisation of DLC Coating Systems, Ion and Plasma Surface Interactions Group Conference, University of Huddersfield, 2018 [3]

- S.J. McMaster *et al.* Nanomechanical and Impact-Erosion Characterisation of DLC Coating Systems, 45th Leeds-Lyon Symposium on Tribology, Leeds, 2018

- S.J. McMaster *et al.* Multi-Scale Scratch and Fretting Characterisation of Hydrogenated DLC, Advanced nano-mechanical techniques for academic and industrial research, University of Southampton, 2019

---

[1]Won Best Presentation Prize

[2]Invited Speaker

[3]Won Best Poster Prize

Appendix B

Further Erosion Results: Calibration And Mass Change

This appendix will detail the calibration procedures for the SIJ regularly used at the University of Leeds as welll as the bespoke air erosion rig and the sample mass change results gained using both methods. As previously stated in Chapter 6, the mass loss results shown in this appendix were not conclusive necessitating the use of an alternative method (optical image analysis) for evaluating the erosion resistance. All coatings referenced in this appendix are thin and smooth variants, the same designs as tested in Chapter 6.

B.1   Slurry Erosion Rig Description And Calibration

Figure B.1 shows a schematic of the SIJ rig commonly used for slurry erosion testing at the University of Leeds. Various gases are able to be bubbled into the tank to create corrosive environments but for this testing this was not used and it was ran entirely erosive without any corrosive synergistic interactions. The tank has a capacity of 50 l.
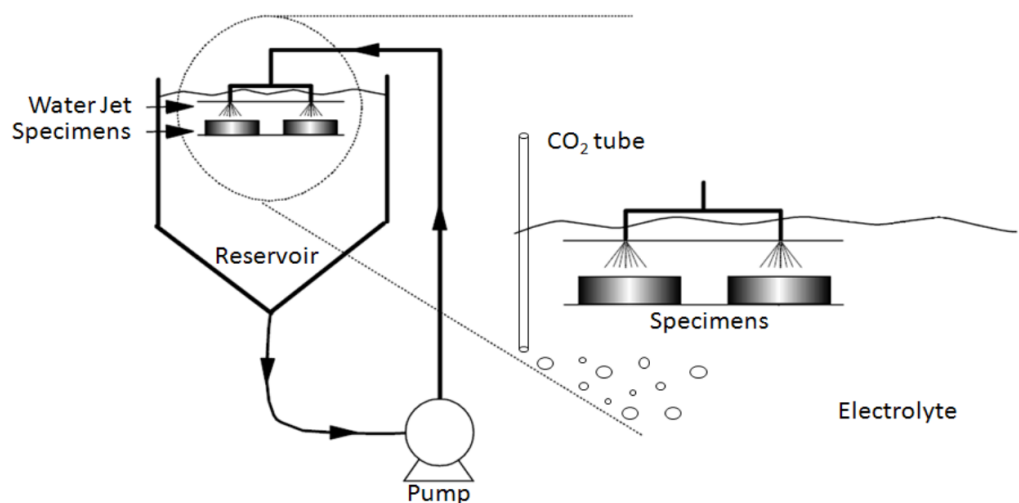
Figure B.1: Schematic of the SIJ used at the University of Leeds. From [394, 395].

A variable frequency pump is used to allow for different flow rates to be attained. The flow rate is calibrated by filling a set volume of water and measuring the time to fill the volume across the frequency range of the pump. 3 repeats were used per pump frequency measured. The flow velocity (in ms^{-1}) is obtained by dividing the average flow rate (in $m^3 s^{-1}$) by the nozzle area (in m^2). A flow velocity of $15\,ms^{-1}$ was used (with a pump frequency of approximately $31\,Hz$) and this was continued with the air erosion rig to maintain the same conditions. Figure B.2 shows the calibration results for the SIJ.

Equation	$y = a + b*x$
Plot	Flow Velocity
Weight	Instrumental
Intercept	-1.1712 ± 0.98709
Slope	0.5001 ± 0.03125
Residual Sum of Squares	4.16778
Pearson's r	0.99038
R-Square (COD)	0.98086
Adj. R-Square	0.97703
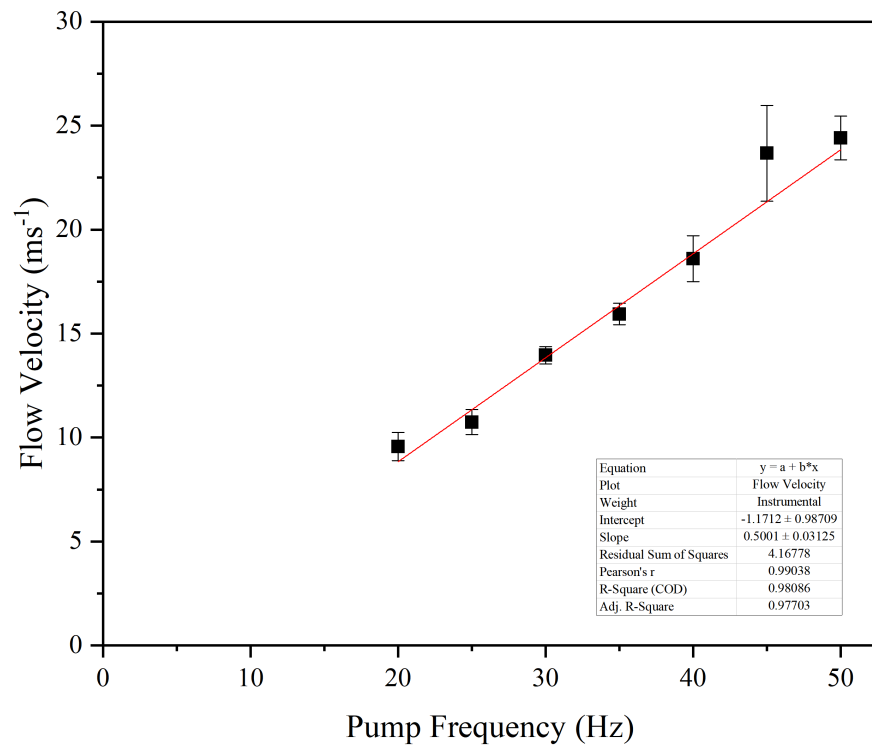
Figure B.2: Calibration of pump frequency to measure flow velocity for the SIJ.

The sand concentration must also be calibrated. The tank is filled to capacity and set volumes of water are removed, this is done prior to adding sand to calculate the ambient levels of sand in the tank. It is extremely difficult to remove all the sand even after cycling fresh water through several times. Incremental masses of sand are added to the tank and samples of the water are taken. The sand is separated from the water using filter paper and left to dry for several days (~ 3) so that the dry mass can be measured. The sand concentration can be found by dividing the dry mass measured against the volume of water removed from the tank for that increment of mass added. Figure B.3 shows calibration graph of the sand concentration in the SIJ. To achieve the sand concentration of $0.524\,kg\,m^{-3}$, $27.68\,g$ was added to the tank.

d

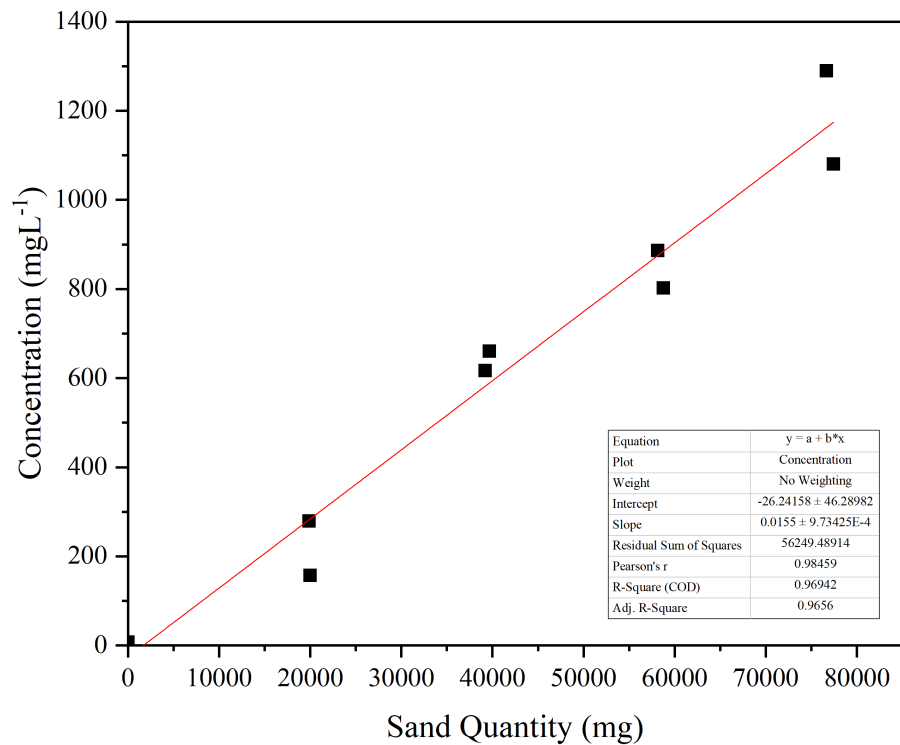| Equation	y = a + b*x
Plot	Concentration
Weight	No Weighting
Intercept	-26.24158 ± 46.28982
Slope	0.0155 ± 9.73425E-4
Residual Sum of Squares	56249.48914
Pearson's r	0.98459
R-Square (COD)	0.96942
Adj. R-Square	0.9656

Figure B.3: Sand quantity added to achieve levels of sand concentration in the SIJ.

The maximum testing time was 8 h (480 min), the mass of the substrates were measured at 30 min, 60 min, 240 min and 480 min (at the conclusion of the test). The substrates were marked to ensure they were returned to the same position under the same nozzle of the erosion rig after each mass measurement.

B.2 Slurry Erosion Results

To measure the mass loss under erosive conditions, the sample is weighed before testing using a micro-gram accurate balance. After removal from the SIJ tank, the sample is dried using compressed air to remove any water or sand adhered to the sample. 5 repeated mass measurements are used to establish the mass loss in each step and the standard deviation due to the small amount lost per erosion step. The mass loss behaviour of uncoated substrates was measured to ensure that when coated substrates were measured their behaviour was different. If similar behaviour is seen with the coated substrates under the same erosive conditions, the environment can therefore be determined to be too extreme or the time-scale too long with the coating delaminating after a short time scale.

B.2.1 Uncoated Substrates Mass Loss

Figures B.4 and B.5 show the mass loss results for the uncoated substrates of SS and HTS respectively. The mass loss of HTS is seen to plateau (Figure B.5) after 60 min, this could be due to hardening of the substrate after repetitive particle impacts.
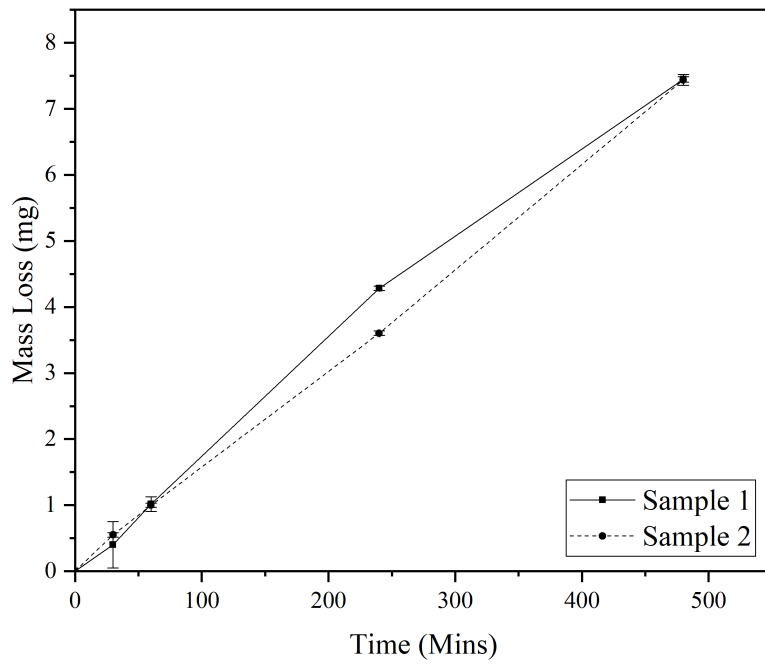
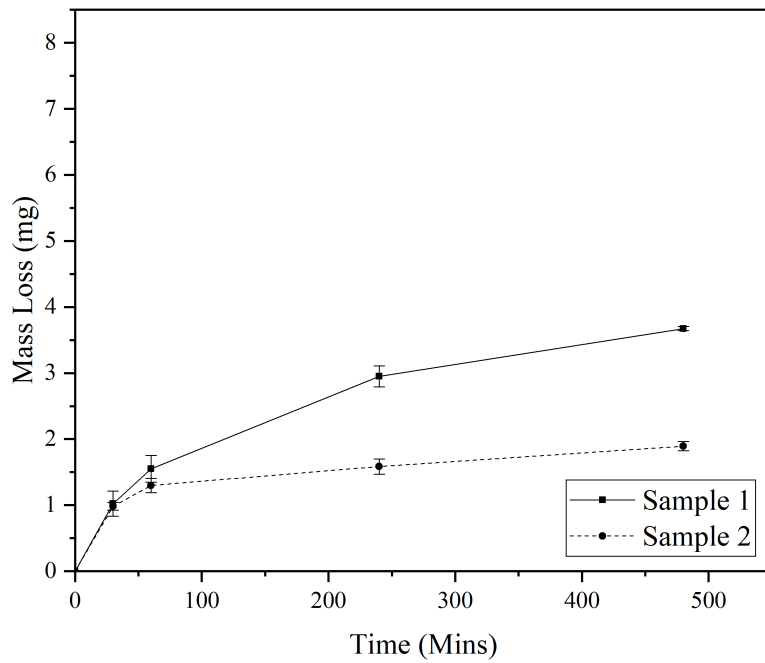Figure B.4: Mass loss results for uncoated SS substrate under slurry erosion conditions.

Figure B.5: Mass loss results for uncoated HTS substrate under slurry erosion conditions.

f

B.2.2   Coating Mass Loss

Figures B.6, B.7 and B.8 show the mass loss results for Coatings A, B and C on SS respectively. For Coatings A (Figure B.6) and B (Figure B.7) the mass loss up to 60 min is seen to be at a higher rate due to protection from the coating, after this time a majority of the coating is removed however the mass loss contains contributions from both coating and substrate [496]. In Figure B.8, Coating C is seen to be removed at a faster rate with behaviour similar to that seen in Figure B.4.
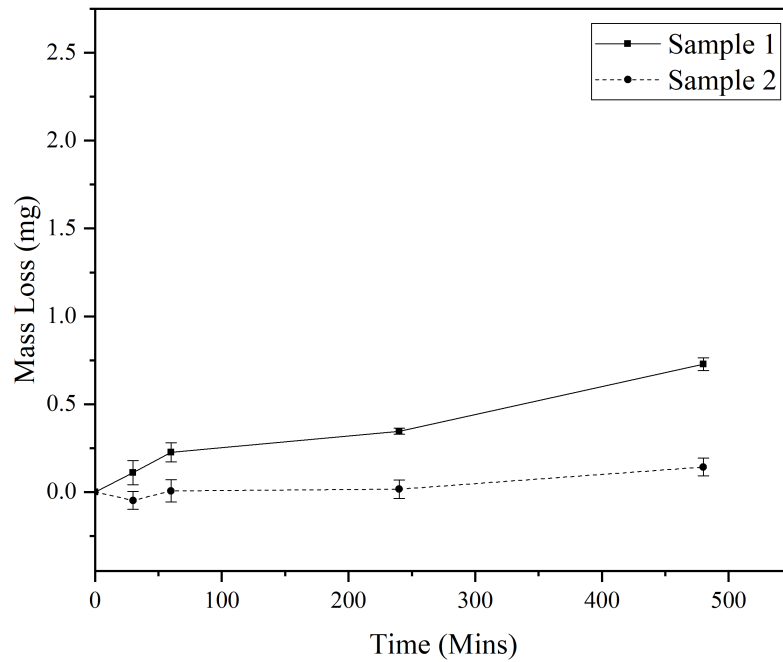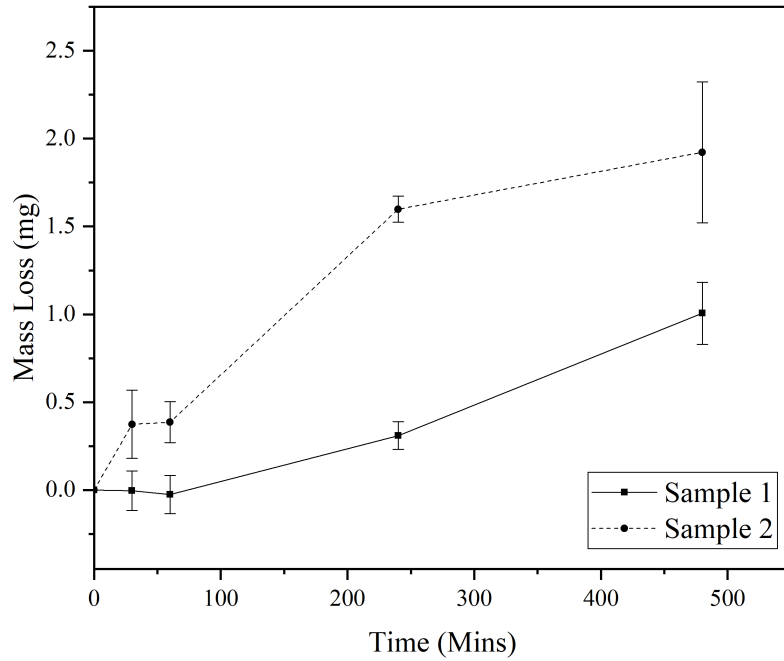

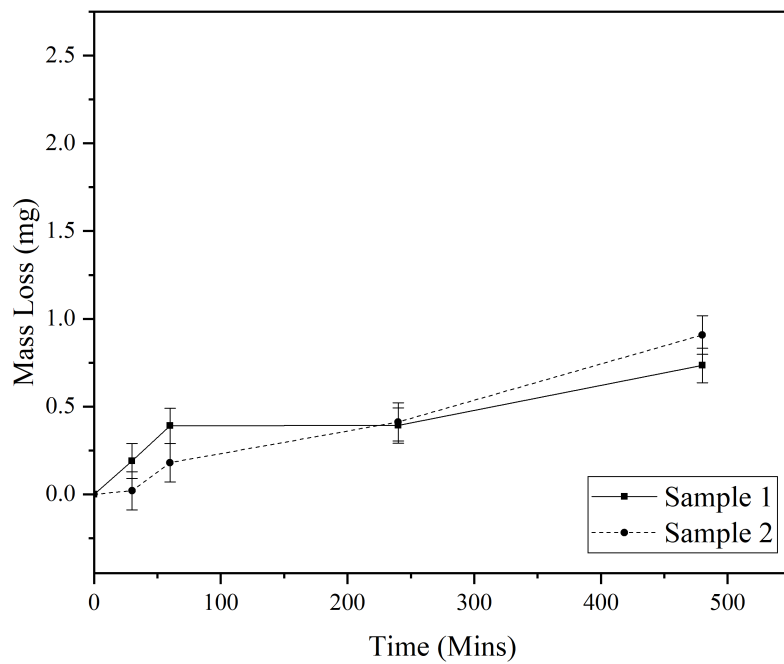Figure B.6: Mass loss results for Coating A on SS under slurry erosion conditions.
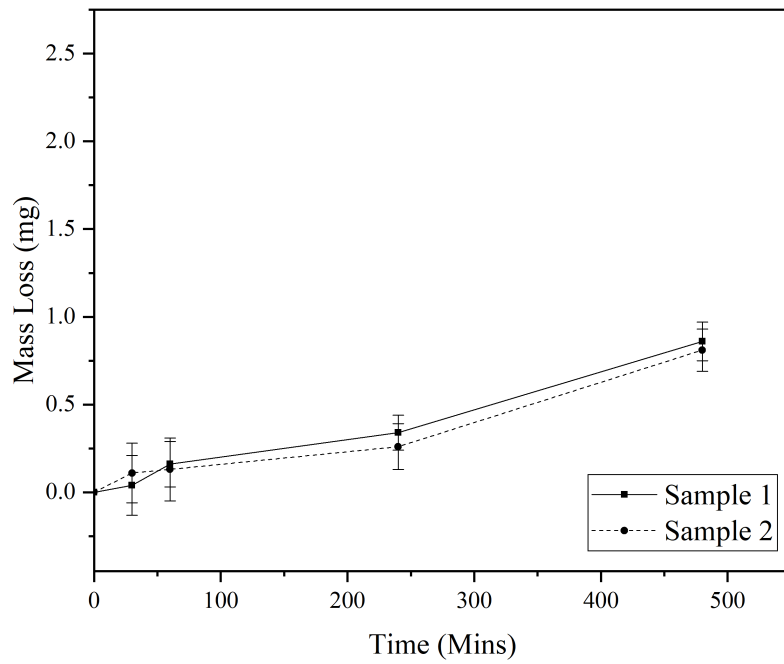
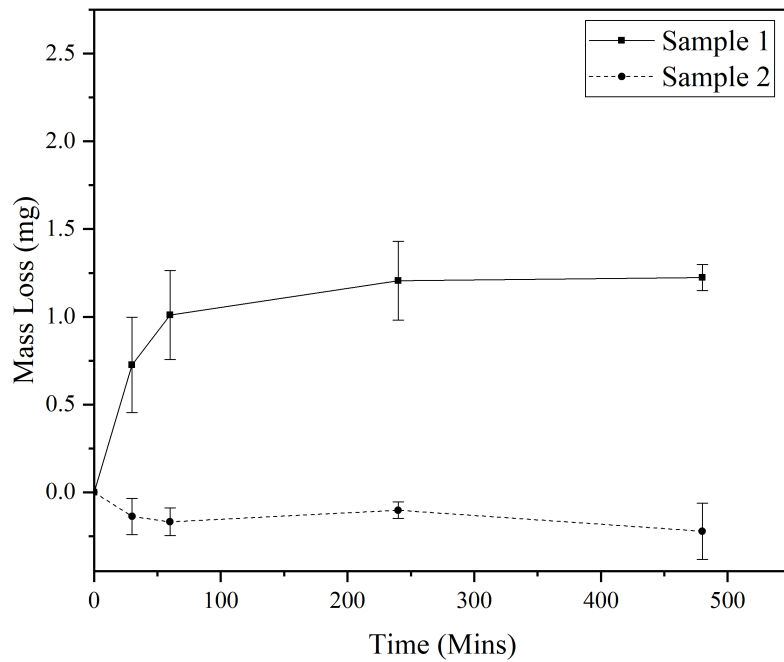Figure B.7: Mass loss results for Coating B on SS under slurry erosion conditions.
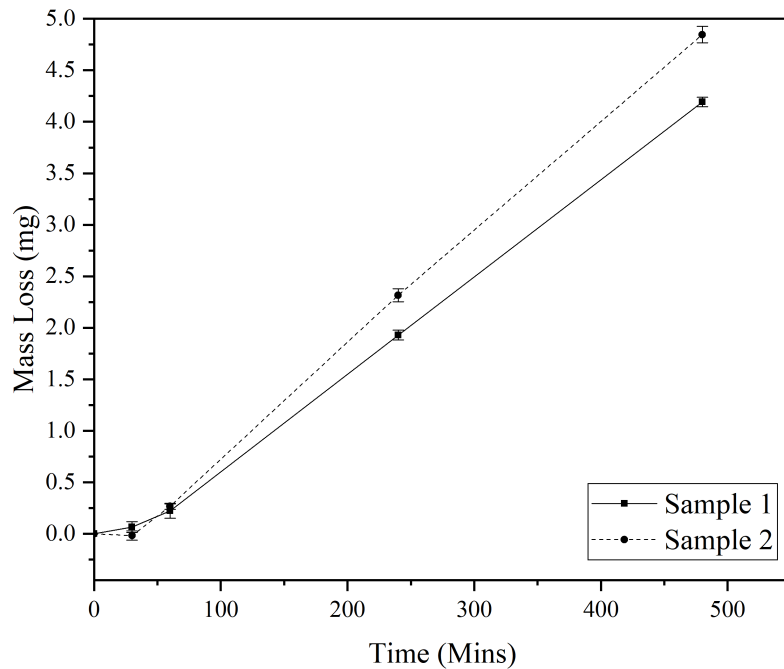
Figure B.8: Mass loss results for Coating C on SS under slurry erosion conditions.

Figures B.9, B.10 and B.11 show the mass loss results for Coating A, B and C on HTS respectively. Similar behaviour is seen compared to the coatings deposited on SS with initially higher mass loss followed by contributions from both coating and substrate. In Fig-

ure B.11 (Coating C), sample 2 is seen to have higher mass gain which can be attributed to greater particle embedding due to the decreased hardness of the coating allowing it to deform without extensive fracture when compared to Coatings A and B.

Figure B.9: Mass loss results for Coating A on HTS under slurry erosion conditions.

Figure B.10: Mass loss results for Coating B on HTS under slurry erosion conditions.

Figure B.11: Mass loss results for Coating C on HTS under slurry erosion conditions.

B.2.3 Topography Change

Figures B.12 and B.13 show the topography of Coatings B and C respectively on SS after 8 h of erosion. These figures are presented as examples to show that at the maximum testing time, the depth reached is enough to be showing substrate behaviour with no protection given by the coatings. Surface profiles were measured using the Talysurf 120L with a scan distance of 15 mm.
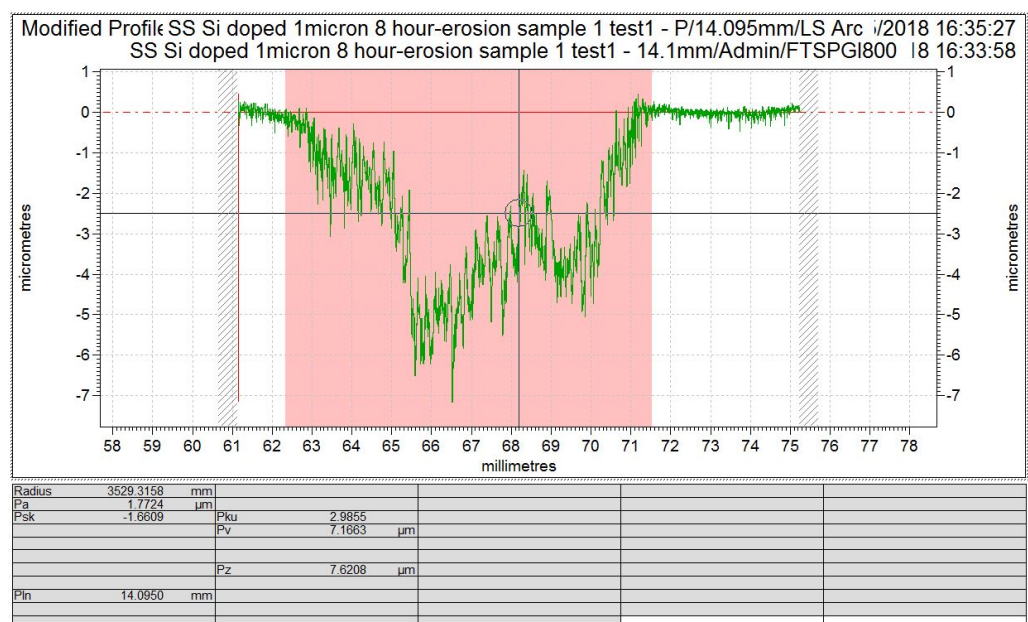

Figure B.12: Topography of Coating B on SS after 8 h of slurry erosion.
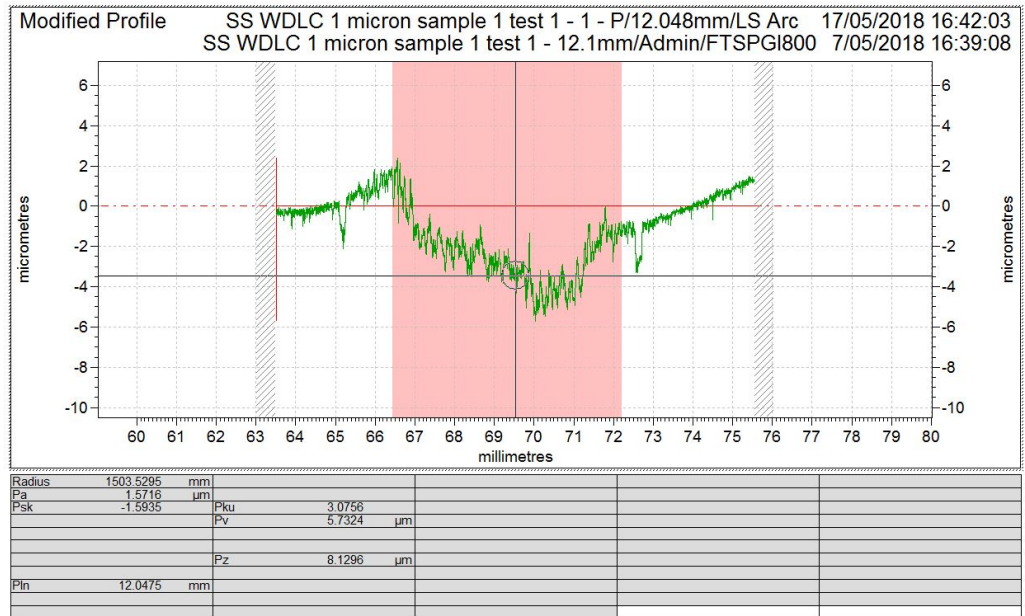
Figure B.13: Topography of Coating C on SS after 8 h of slurry erosion.

B.3 Air Erosion Rig: Further Information

B.3.1 Rig Design Schematics

Figure B.14 shows a cross section of the air erosion nozzle design. The compressed air inlet narrows to exploit the Venturi effect to increase the pressure inside the nozzle. The sand is drawn into the air flow due to the pressure differential between the inlet and interior of the nozzle.
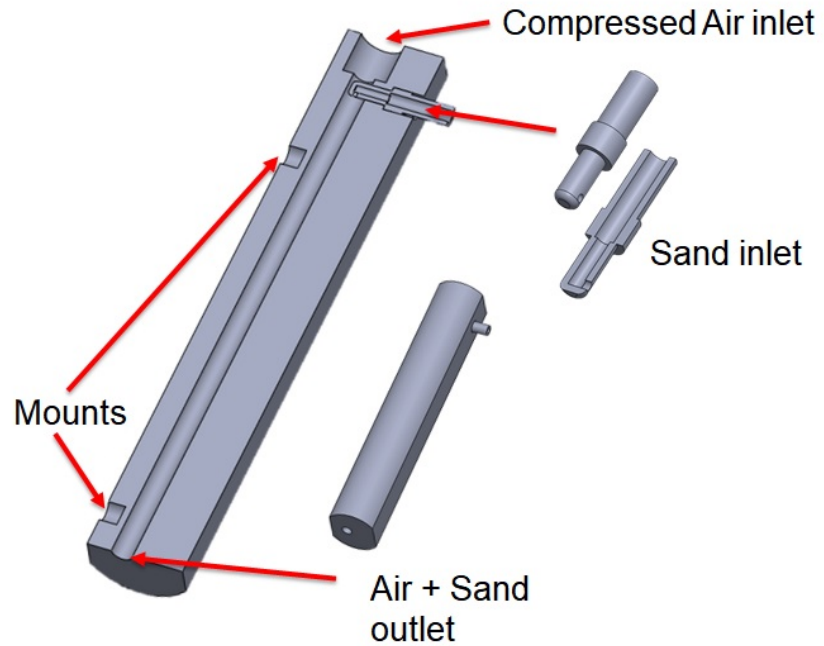
Figure B.14: 3D model of the cross section of the air erosion rig nozzle.

A 3D schematic of the air erosion rig's sample holder is shown in Figure B.15. Samples are hold in place using two fixing bolts, these are used to avoid the sample rotating during particle impingement in test cycles. The samples can also be tilted to allow for a maximum impingement angle of 30°.
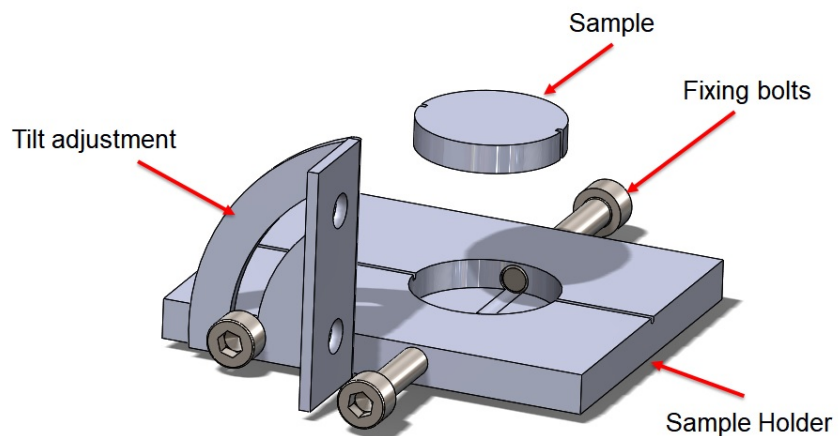

Figure B.15: 3D model of the air erosion rig sample holder.

B.3.2   Air Erosion Mass Change Measurements

Uncoated substrates were tested at 2.03 bar ($15 \, \mathrm{m \, s^{-1}}$) to establish their behaviour to ensure that when the coated substrates were tested, their distinct mass loss patterns could be attributed entirely to the coatings and to rule out any substrate effects. The same procedure is used to determine the mass loss as in the slurry erosion, the sample is weighed before testing and as required for each erosion step. After each erosion step, compressed

air is used to ensure the sample is clean and doesn't have excess sand adhered to any part of the sample surface. Figures B.16 and B.17 show the mass loss results for the uncoated SS and HTS respectively. Note that the scale on each graph is different.
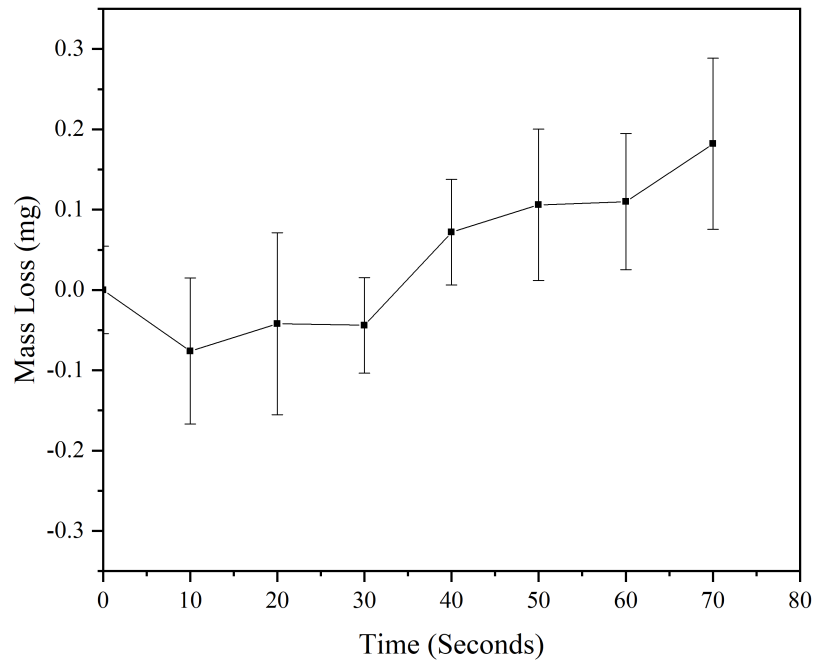

Figure B.16: Mass loss of the uncoated SS substrate at $15\,\mathrm{m\,s^{-1}}$ particle velocity.
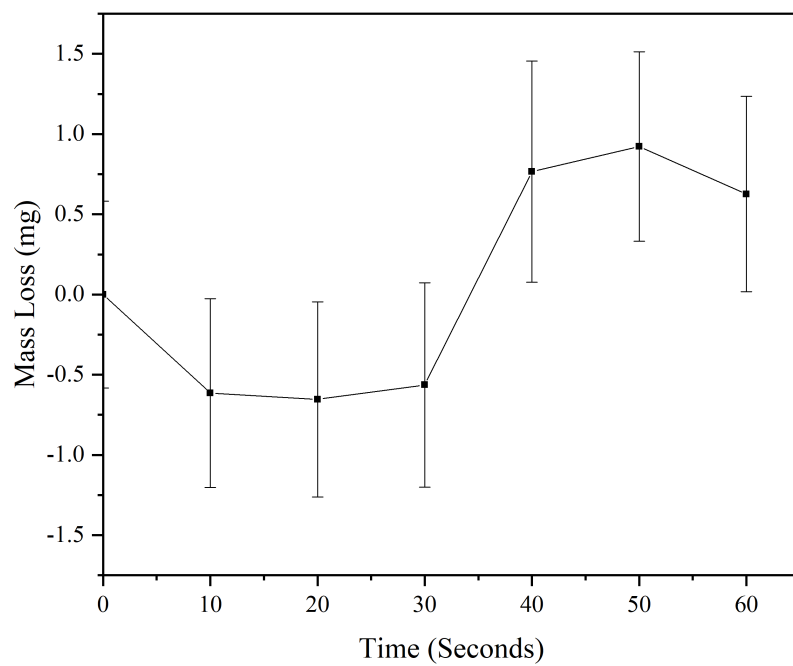

Figure B.17: Mass loss of the uncoated HTS substrate at $15\,\mathrm{m\,s^{-1}}$ particle velocity.

Mass gain is seen in the initial time steps of each graph due to particle embedding [74, 391–393]. The increased mass gain and mass loss seen with HTS can be attributed to its increased hardness giving a more brittle structure that is more likely to crack and fracture [73].

Tests on coated substrates were conducted at both 1 bar (7.39 m s^{-1}) and 2.03 bar (15 m s^{-1}) to assess the affect of particle velocity on mass loss due to the inconclusive results gained particularly on HTS. Mass loss/mass gain did not seem to follow a discernible pattern and the errors associated with each measurement were large enough as to not provide conclusive results. Visual analysis of the erosion scars on SS indicated that the coating was almost entirely eroded within 10 s, this was confirmed with the optical analysis as performed in Chapter 6.

The mass loss results for Coatings A, B and C on HTS at 1 bar (7.39 m s^{-1}) are shown in Figure B.18. Coating A is the only one of the results set to show mass loss however the error bars do not indicate an acceptable confidence level in the results. Coatings B and C show negligible mass loss up to the maximum time under erosive conditions.
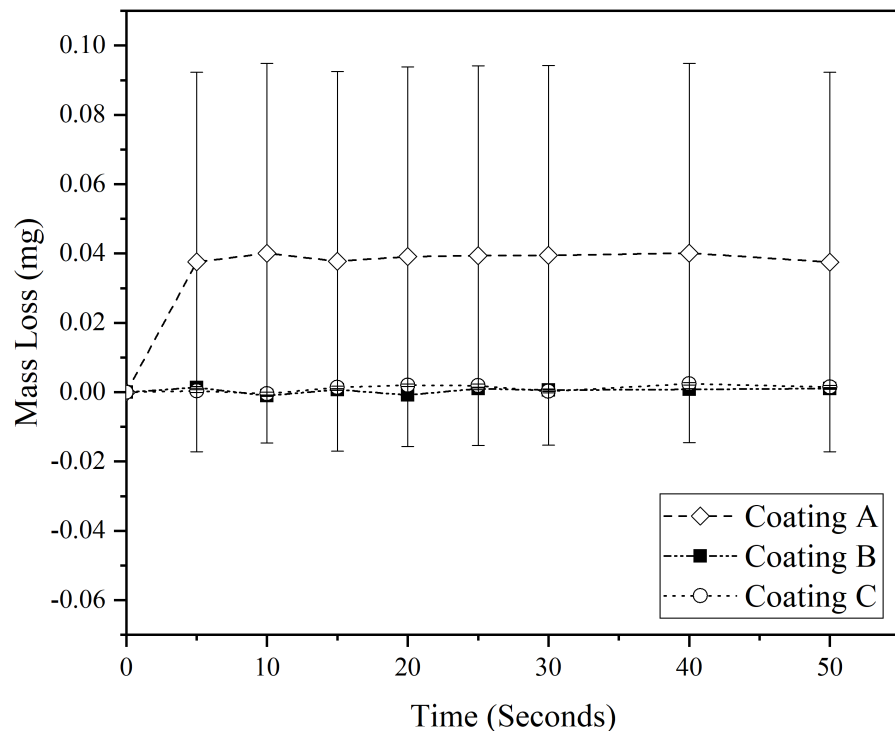

Figure B.18: Mass loss under air based erosion for Coatings A, B and C on HTS at 7.39 m s^{-1} particle velocity.

Figure B.19 shows the mass loss measured for Coatings A, B and C with a particle velocity of 15 m s^{-1}. No clear mass loss trend can be discerned across any of the samples due to the irregular periods of mass loss and mass gain. This was attributed to coating deformation and particle embedding in the coating. Coating C was tested to longer time steps than the other coatings as it was seen to vary in mass to a greater degree therefore an attempt was made to assess whether it would form a stable pattern after further successive periods of erosion.
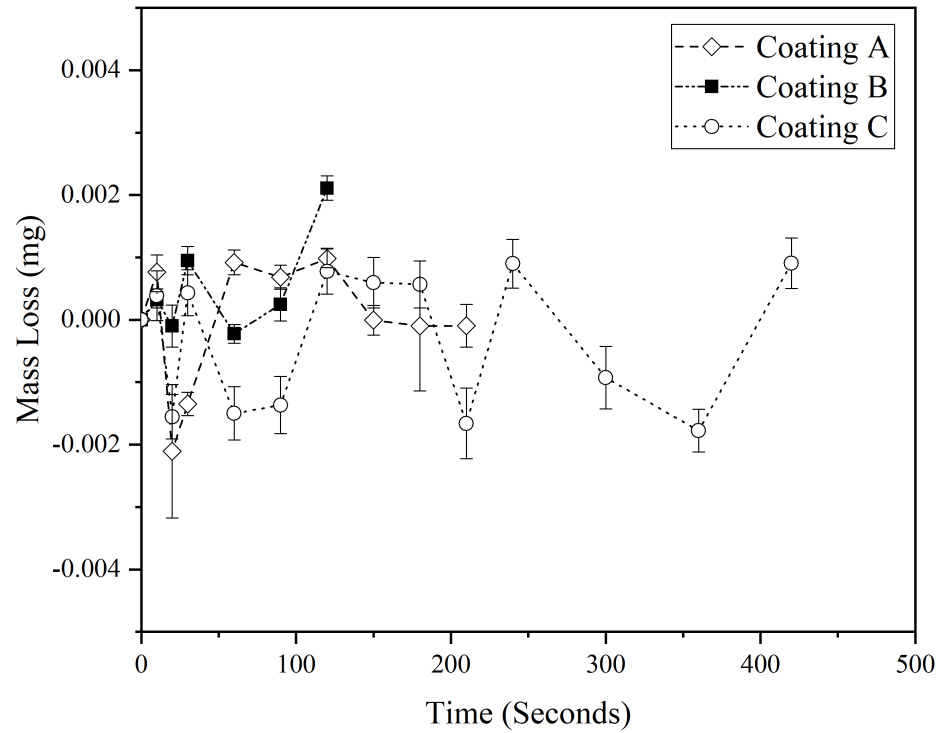
Figure B.19: Mass loss under air based erosion for Coatings A, B and C on HTS at $15\,\mathrm{m\,s^{-1}}$ particle velocity.

B.3.3 Air Erosion Topography Change

Figure B.20 shows the change of surface topography due to the effect of the particle impingement. The surface is worn unevenly due to the presence of the coating. It can be noted that there is some degree of material loss but also distortion of the coating. This could be due to sand particle embedding and cracking of the coating. As this doesn't present a normal erosive volume loss pattern it was decided that this method could not be used to accurately quantify the coating loss. The topography measurement was made with the Talysurf 120L with a scan distance of $10\,\mathrm{mm}$. As it's primary purpose is measuring surface roughness it could be used to assess whether the coatings would present a measurable volume loss.
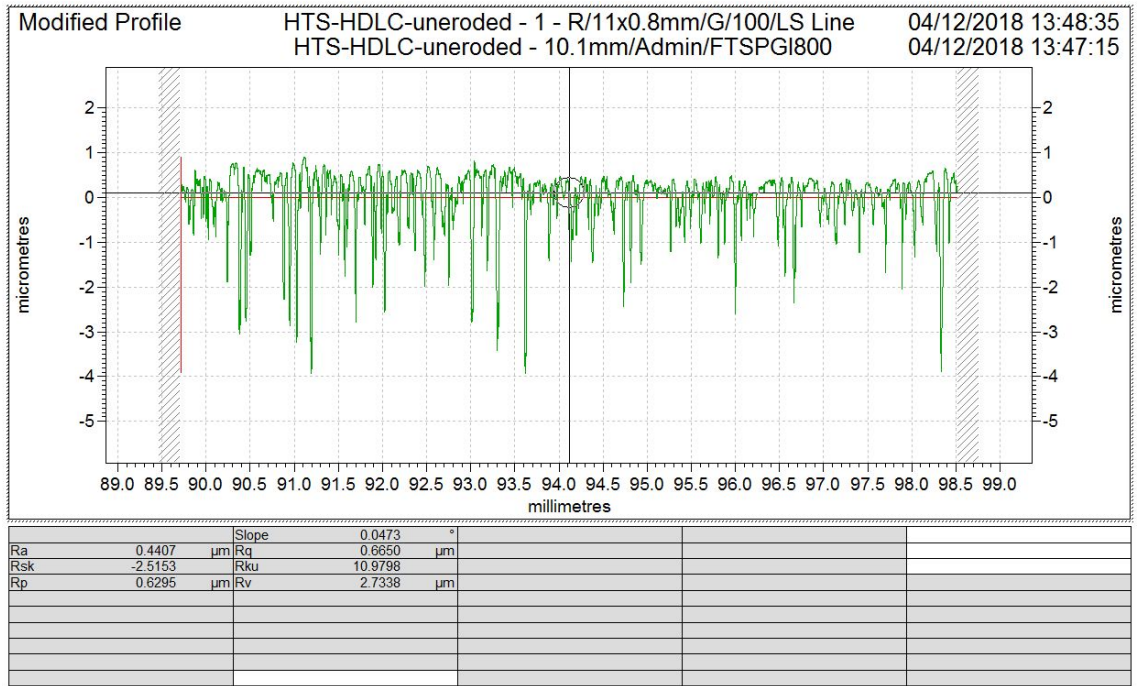
(a) Surface topography before erosion.
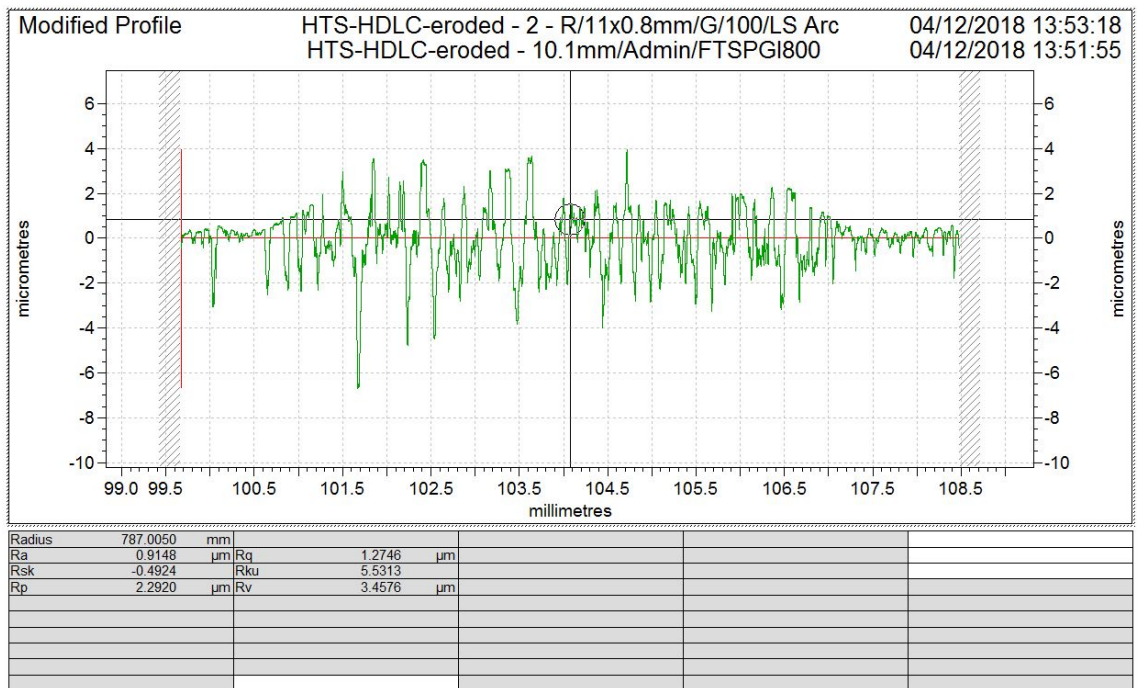
(b) Surface topography after erosion.

Figure B.20: Surface topography measurement of Coating A on HTS prior to and post the erosion cycles as measured by the Talysurf 120L. Note that the scale changes between the two subfigures.

Appendix C

Erosion Particle Quantification

C.1 Slurry Erosion

The radius of the nozzle is equal to 2×10^{-3} m. Therefore we can calculate the area of the nozzle (A_n):

$$A_n = \pi r^2 \tag{C.1}$$
$$= \pi \left(2 \times 10^{-3}\right)^2 \tag{C.2}$$
$$= 1.26 \times 10^{-5}\,\mathrm{m}^2 \tag{C.3}$$

We can now calculate a volumetric flow rate with the calibrated flow velocity ($v = 15\,\mathrm{m\,s^{-1}}$):

$$\dot{V} = v \times A \tag{C.4}$$
$$= 15\,\mathrm{m\,s^{-1}} \times 1.26 \times 10^{-5}\,\mathrm{m}^2 \tag{C.5}$$
$$= 1.88 \times 10^{-4}\,\mathrm{m^3\,s^{-1}} \tag{C.6}$$

Using the sand density (d) in the tank ($0.524\,\mathrm{kg\,m^{-3}}$), a mass rate ($M$) can be calculated:

$$M = \dot{V} \times d \tag{C.7}$$
$$= 1.88 \times 10^{-4} \times 0.524 \tag{C.8}$$
$$= 9.88 \times 10^{-5}\,\mathrm{kg\,s^{-1}} \tag{C.9}$$

The mass of one sand particle can be calculated using the sand density ($\rho_s = 2560\,\mathrm{kg\,m^{-3}}$) and the average diameter of the sand ($d_s = 250\,\mathrm{\mu m}$):

$$m = V_s \times \rho_s \tag{C.10}$$

$$= \frac{4}{3}\pi r_s^3 \times \rho_s \tag{C.11}$$

$$= \frac{4}{3}\pi \left(125 \times 10^{-6}\right)^3 \times 2560 \tag{C.12}$$

$$= 2.09 \times 10^{-8}\,\mathrm{kg} \tag{C.13}$$

The number of particles in this volumetric flow rate (*PPS*) can be calculated by:

$$PPS = \frac{M}{m} \tag{C.14}$$

$$= \frac{9.88 \times 10^{-5}}{2.09 \times 10^{-8}} \tag{C.15}$$

$$= 4716 \tag{C.16}$$

The radius of the impact area ($r_s = 3\,\mathrm{mm}$) allows the impact area (A_s) to be calculated:

$$A_s = \pi r_s^2 \tag{C.17}$$

$$= \pi \times \left(3 \times 10^{-3}\right)^2 \tag{C.18}$$

$$= 2.83 \times 10^{-5}\,\mathrm{m^2} \tag{C.19}$$

Using the ratio of the areas of the nozzle (A_n) and the impact area (A_s), the proportion of particles hitting the surface can be obtained (r_{impact}):

$$r_{impact} = \frac{A_n}{A_s} \tag{C.20}$$

$$= \frac{1.26 \times 10^{-5}}{2.83 \times 10^{-5}} \tag{C.21}$$

$$= 0.44 \tag{C.22}$$

Now the particles impacting the surface per second (I_s) can be calculated:

$$I_s = r_{impact} \times PPS \tag{C.23}$$

$$= 0.44 \times 4716 \tag{C.24}$$

$$= 2096\,\mathrm{s^{-1}} \tag{C.25}$$

r

C.2   Air Based Erosion

The radius of the nozzle is equal to 2.5×10^{-3} m.
Area of the nozzle (A_n):

$$A_n = \pi r^2 \tag{C.26}$$
$$= \pi \left(2.5 \times 10^{-3}\right)^2 \tag{C.27}$$
$$= 1.96 \times 10^{-5} \, \text{m}^2 \tag{C.28}$$

Volumetric flow rate with the calibrated flow velocity ($v = 15 \, \text{m s}^{-1}$):

$$\dot{V} = v \times A \tag{C.29}$$
$$= 15 \, \text{m s}^{-1} \times 1.96 \times 10^{-5} \, \text{m}^2 \tag{C.30}$$
$$= 2.95 \times 10^{-4} \, \text{m}^3 \, \text{s}^{-1} \tag{C.31}$$

Using the sand flow rate ($1.25 \, \text{g s}^{-1}$) and the air flow rate ($10 \, \text{L s}^{-1}$), the sand concentration (c) of $1.25 \times 10^{-4} \, \text{kg L}^{-1}$ can be found and used to calculate the mass rate (M):

$$M = \dot{V} \times c \tag{C.32}$$
$$= 2.95 \times 10^{-4} \times 1.25 \times 10^{-4} \tag{C.33}$$
$$= 3.68 \times 10^{-5} \, \text{kg s}^{-1} \tag{C.34}$$

The mass of the individual sand particle does not change. Number of particles in this volumetric (PPS) flow rate can be calculated by:

$$PPS = \frac{M}{m} \tag{C.35}$$
$$= \frac{3.68 \times 10^{-5}}{2.09 \times 10^{-8}} \tag{C.36}$$
$$= 1757.81 \tag{C.37}$$

The impact area remains the same as in the slurry erosion. Using the ratio of the areas of the nozzle (A_n) and the impact area (A_s), the proportion of particles hitting the surface can be obtained (r_{impact}):

$$r_{impact} = \frac{A_n}{A_s} \tag{C.38}$$

$$= \frac{1.96 \times 10^{-5}}{2.83 \times 10^{-5}} \tag{C.39}$$

$$= 0.69 \tag{C.40}$$

Now the particles impacting the surface per second (I_s) can be calculated:

$$I_s = r_{impact} \times PPS \tag{C.41}$$

$$= 0.69 \times 1757.81 \tag{C.42}$$

$$= 1220.70\,\mathrm{s}^{-1} \tag{C.43}$$

t

Appendix D

Summary Of Gaussian Error Propagation Formulae

This appendix will summarise the Gaussian error propagation formulae used throughout this thesis. This methodology of data processing is used by various physical scientists to ascertain the uncertainties of compound variables so that the reliability of these quantities can be determined [497, 498].

The compound variable to be considered in each case shall be named Q. Each of the sections will describe the general formulae used for that particular operator. As the name implies, each variable is considered to have an uncertainty of a normal Gaussian distribution and the uncertainties of each variable are uncorrelated and random [498]. The full derivation of the formulae will not be given as these are covered by the referenced material and this appendix is simply here to provide a reference for the methods used.

D.1   Addition Or Subtraction

For this section if Q were some combination of sums and differences:

$$Q = a + b - c \tag{D.1}$$

The uncertainty δQ is the sum in quadrature[1] of the constituent variables:

$$\delta Q = \sqrt{(\delta a)^2 + (\delta b)^2 + (\delta c)^2} \tag{D.2}$$

D.2   Multiplication Or Division

If Q were some combination of products or quotients:

$$Q = \frac{ab}{c} \tag{D.3}$$

The uncertainty is:

---

[1]Square root of the sum of the squares.

$$\frac{\delta Q}{Q} = \sqrt{\left(\frac{\delta a}{a}\right)^2 + \left(\frac{\delta b}{b}\right)^2 + \left(\frac{\delta c}{c}\right)^2} \tag{D.4}$$

In effect, this means that for products or quotients, the fractional uncertainties add in quadrature.

D.3   Indices

If Q were the product of some variable raised to exact number index:

$$Q = x^n \tag{D.5}$$

The uncertainty is therefore:

$$\delta Q = |n| x^{x-1} \delta x \tag{D.6}$$

which can otherwise be expressed as:

$$\frac{\delta Q}{Q} = |n| \frac{\delta x}{|x|} \tag{D.7}$$

The form as seen in Equation D.7 is generally the one implemented for calculations. It must be noted that when $n = -1$, the percentage uncertainty is unchanged when the reciprocal is taken. This is also why multiplication and division are treated the same in Section D.2.

D.4   Complex Formulae

For more complex formulae that are combinations of the above methodologies, the best approach is to use the methods in combination or in sequence whichever proves easier.